Regulation of myonuclear domains by microtubules network in skeletal muscle

Alireza Ghasemizadeh

THESE de DOCTORAT DE
L'UNIVERSITE CLAUDE BERNARD LYON 1

Ecole Doctorale N° 340
BIOLOGIE MOLÉCULAIRE INTÉGRATIVE ET CELLULAIRE (BMIC)

Discipline : Biologie

Soutenue publiquement le 14/11/2022, par :
Alireza GHASEMIZADEH

Régulation des domaines nucléaires par le réseau associé aux microtubules dans les muscles striés squelettiques

---

Devant le jury composé de :

KRETZ, Carole	Professeure, Université Lyon 1	Présidente
JANKE, Carsten	Directeur de Recherche, CNRS	Rapporteur
MAIRE, Pascal	Directeur de Recherche, INSERM	Rapporteur
ESTEVES-DE-LIMA, Joana	Chargée de Recherche, INSERM	Examinatrice
LAFANECHERE, Laurence	Directrice de Recherche, CNRS	Examinatrice
GACHE, Vincent	Chargé de Recherche, INSERM	Directeur de thèse

“Rose petals let us scatter and fill the cup with red wine
The sky (limits) let us shatter and come with a new design”

From Divan of Hafez, the 14th century Persian poet, Shiraz, Iran

Preamble

My doctorate thesis was carried out under the supervision of Dr. Vincent GACHE at the laboratory of Physiopathology and Genetics of Neuron and Muscle (PGNM), directed by Dr. Laurent SCHAEFFER, and located at Institut NeuroMyoGene (INMG, Lyon, France). The exceptional support of Dr. GACHE in addition to the rich multidisciplinary environment provided by INMG have allowed me to follow my aims, conduct my thesis project, increase my knowledge, and develop my personal and professional maturity.

In addition to my thesis project, my doctorate gave me the opportunity to engage in complementary teaching activity in the domains of cellular and molecular biology, immunology, and genetics at Claude Bernard Lyon 1 University. A great personal and educational experience which I will always cherish.

I was also honored to be selected as a member of the BMIC doctoral school students representative, a fun collaborative experience, which gave me the chance to help my doctorate fellows, as much as possible, and communicate their needs to members of the doctoral school council. I also learned the difficult responsibility of being a judge during doctoral school entry competitions and to get a sense of the complexity of scientific days organization!

At last, thanks to collaborations and participation in different international conferences during my doctorate, I had the opportunity to contribute to several publications and present my work in front of great scientific communities.

Scientific publications

Simple Methods for Permanent or Transient Denervation in Mouse Sciatic Nerve Injury Models. Bio Protocol. 2022
Osseni A, Thomas JL, **Ghasemizadeh A**, Schaeffer L, Gache V.

MACF1 controls skeletal muscle function through the microtubule-dependent localization of extra-synaptic myonuclei and mitochondria biogenesis.
eLife. 2021.
Ghasemizadeh A, Christin E, Guiraud A, Couturier N, Abitbol M, Risson V, Girard E, Jagla C, Soler C, Laddada L, Sanchez C, Jaque-Fernandez FI, Jacquemond V, Thomas JL, Lanfranchi M, Courchet J, Gondin J, Schaeffer L, Gache V.

Role of SVBP and microtubules detyrosination in skeletal muscle development and homeostasis. (In preparation)
Alireza Ghasemizadeh, Caroline Brun, Emilie Christin, Celine Malleval, Edwige Belotti, Julien Gondin, Marie-Jo Moutin, and Vincent Gache

Cytoplasmic NuMA1 promotes microtubule stabilization and controls myonuclear spreading and dynamics in skeletal muscle. (In preparation)
Nathalie Couturier, **Alireza Ghasemizadeh**, Emilie Christin, Alexandre Janin, Alexis Osseni, Jean-Luc Thomas, Laurent Schaeffer, Stéphane Konig, Jessica Brunetti, Maud Frieden, Yohann Couté, Alexandra Kraut, Julien Courchet and Vincent Gache

SH3KBP1 scaffolds endoplasmic reticulum and controls skeletal myofibers architecture and integrity. (In preparation)
Alexandre Guiraud, Emilie Christin, Nathalie Couturier, Carole Kretz-Remy, Alexandre Janin, **Alireza Ghasemizadeh**, Anne-Cécile Durieux, David Arnould, Norma Beatriz Romero, Mai Thao Bui, Vladimir L. Buchman, Laura Julien, Marc Bitoun and Vincent Gache

Scientific Presentations

❖ **Microtubule network dynamics in myonuclei positioning in muscle fibers**
- **Jun. 2022, Oral communication (Selected for fee waiver grant)**
  EMBO, Microtubules from Atoms to Complex Systems, Heidelberg, Germany
- **May. 2022, Poster presentation**
  Stem Cells, Development & Cancer, Lyon, France
- **Apr. 2022, Poster presentation**
  EMBO, Muscle formation, maintenance, regeneration and pathology, Gouvieux, France
- **Nov.2021, Oral communication**
  Paris Cytoskeleton Talks (Virtual)
- **Nov.2021, Poster presentation (Best poster prize)**
  French Society of Myology, Saint-Etienne, France

❖ **MACF1 maintains myonuclei and mitochondria organization in skeletal muscle**
- **Jun.2021, Oral communication**
  Young Researchers of INMG (Virtual)
- **Nov.2020, Oral communication (Best talk prize)**
  BMIC Doctoral school days (Virtual)
- **Jun.2020, Poster presentation**
  EMBO, Microtubules from Atoms to Complex Systems (virtual)
- **Jun.2020, Oral communication**
  Muscle Science Talks (virtual)
- **Nov.2019, Oral communication (Selected for SFM Prix de voyage)**
  French Society of Myology, Marseille, France
- **Nov.2019, Oral communication**
  BMIC Doctoral School days, Lyon, France
- **Nov.2019, Poster presentation**
  Imaging the cell, Lyon, France
- **July.2019, Poster presentation (Best poster prize)**
  French Microtubule Network, Rennes, France
- **Mar.2019, Oral communication**
  NeuroMuscular Club of Rhone-Alpes Auvergne, Lyon, France
- **Feb.2019, Oral communication**
  Young Researchers of INMG, Lyon, France

❖ **MACF1 governs myonuclear domain organization and controls neuromuscular junction integrity in skeletal muscles**
- **Nov.2018, Poster presentation**
  French Society of Myology, Brest, France
- **Nov.2018, Poster presentation**
  BMIC Doctoral School days, Lyon, France

Acknowledgments

I wish to thank Dr. Vincent Gache, my idol of knowledge in “microtubules and myonuclei worlds”, who believed in me, mentored me every day for the past four years, guided me to develop a better version of myself, and listened to me as a friend whenever I needed one!

I am grateful to Prof. Carole Kretz, Dr. Carsten Janke, Dr. Pascal Maire, Dr. Laurence Lafanechere, and Dr. Joana Esteves-De-Lima who accepted to participate in my thesis defense jury to evaluate and discuss my work.

I would like to thank Drs. Julien Falk, Laurence Lafanechere, and Marie-Jo Moutin who took part in my thesis yearly evaluation committee for their advice and guidance throughout my Ph.D.

I would also like to thank Drs. Sandrine Bretaud, Sophie Richard, Emilie Delaune, and Marie Paschaki, who trusted in me by giving me the opportunity to experience teaching at the university and kindly guiding me along the way.

I would like to thank every member of the Gache Team over the years, especially:

Prof. Carole Kretz, the mother figure of my thesis, for all the technical helps, great advices on teaching, countless support during my professional and personal ups and downs, and her forever optimism and smile!

Emilie Christin, the Wikipedia of Gache Team, for teaching me how to culture muscle cells at the beginning of my thesis, helping me with a lot of experiments all along my thesis, and especially for her great friendship, which I wish to keep forever!

Celine Malleval, who, in addition to her great personality and kindness, saved me hours of “clicking and counting” by generating automated analyzing programs adapted exactly to my experiments.

Drs. Alexandre Janin and Marie Abitbol for their great tips on qRT-PCR!

and Dr. Caroline Brun, the newbie of the Gache Team, for her helps with muscle stem cells handling and her tips on project and time management, and most of all, for her party enthusiasm!

I would like to thank Dr. Evelyne Goillot, for her patience with my million “can I have a question” questions and for countless numbers of great discussions that we had, from science and western blots to politics in the middle east!

And of course, Mis. Andree Defours, who always helped me with all the paper works and administration without any hesitation!
I wish to thank every member of INMG, in particular:

The great minds, Drs. Laurent Schaeffer, Julien Courchet, Benedict Chazaud, Fabien Le Grand, Helene Puccio, Julien Gondin, Remi Mounier, Alexis Osseni, Arnaud Jacquier, Jean-Luc Thomas, Vincent Jacquemond, Christine Berthier, Bruno Allard, Valerie Risson, Edwige Belloti, Michele Weiss-Gayet, Isabella Scionti, Laetitia Mazelin, Maite Carre-Pierrat, and Patric Lemont, in addition to Julien Carras and Sabrina Ben Larbi, from whom I learned a lot, through simple discussions to amazing collaborations.

Fellow juniors of the institute, Laurent C., (Lolo), Elodie F., Nathalie C., Pauline B., Charline R., Romane I., Francisco J., Yoann L., Cloe B., Simon R., Georgiana P., Anita K., Tanushri D., Marine D., Leslie A., Cloe P., Delia C., and Gauthier T., with whom we had countless moments of joy, from picnics to parties!

I would like to thank every member of the BMIC doctoral school representatives, for sharing this fun amazing experience together!

I would also like to thank members of the Ciqle imaging platform, in particular Dr. Christophe Vanbelle, Denis Ressnikoff, Bruno Chapuis, and Elisabeth Errazuriz, in addition to members of PBES, SCAR, and ANIPHY animal facilities, for all their help and flexibility throughout my thesis project.

This thesis gifted me with many dear, forever lasting, friends who I cherish:
Louise G. (Louisou): The coolest ever!
Laura G.: The ultimate optimist!
Thibaut D. (TT): The role model!
Jimmy M.: The kind heart!
Pauline G.: The S.O.S collaborator!
Lea C.: The one you can count on!
Hamy L.: The one who always sees the best in others!
Sozerko Y.: The positive energy!
Martijn K.: The calming one!
and Huong H. (HH) (the special one): Thank you for sharing a countless number of coffees (and even more beers!!), laughter, and nagging with me, and believing in me even when I was doubting myself!

And last but definingly not least, I wish to thank my sweetheart parents, Mahdi and Orinab, who, without their support, I could have never imagined standing where I stand today, my darling sister and brother, Shima and Arsha, for sending me long-distance love, and of course, my amazing beloved Jakub (Kubus) who supported me through the rough days, made me laugh (at least once a day), and never let go of my hand!

Table of contents

Abstract

Skeletal muscle is composed of thousands of giant cells, known as myofibers. To develop myofibers, progenitor mononuclear cells, called myoblasts, fuse together and share their cytoplasm and nucleus with the forming syncytia. Within each myofiber, hundreds of nuclei, also termed myonuclei, are regularly positioned at the periphery, with exception of specialized zones such as neuromuscular junctions (NMJs) where several myonuclei are clustered. This precise myonuclei organization gives rise to myonuclear domains, which are theoretical territories transcriptionally supported by each myonucleus to guarantee a spatial and coordinated transcriptomic activity all along myofibers. Myonuclear domains are challenged in different types of myopathies where mispositioned myonuclei can be observed along and within myofibers. Yet, how myonuclear domains are regulated at the periphery of myofibers and how their disruption may contribute to the development of myopathies remain poorly understood.

Microtubules (MTs) are highly dynamic structures which go through cycles of polymerization and depolymerization under the influence of their microtubules-associated proteins (MAPs) or post-translational modifications (PTMs). During the early steps of myofibers development, MTs actively participate in myonuclear domains formation by serving as railways for motor molecules which disperse myonuclei along the growing myofiber. Later on, it is the assembly of muscular sarcomeres which will push the dispersed myonuclei to the periphery of myofibers. How myonuclei are held at the periphery of myofibers is not clear, however, the presence of dense MTs cage around the peripheral myonuclei suggests that MTs and their associated proteins network may contribute to myonuclei positioning also in mature myofibers.

In this study, we challenged MT dynamics by altering its MAPs network or its PTMs proportion during myogenesis. By using various *in vitro* and *in vivo* knock-down and knock-out models, we show that MT dynamics is reduced during myogenesis toward a more stable network in mature myofibers. We also report that increasing MT dynamics can directly disrupt myonuclear domains at the periphery of myofibers, either by increasing myonuclei dynamics or by increasing myonuclei content per myofiber. In both cases, we propose mechanisms explaining how each form of disrupted myonuclear domains results in reduced muscle functionality.

Institut NeuroMyoGène
Laboratoire Physiopathologie et Génétique du Neurone et du Muscle
CNRS UMR 5261 - INSERM U1315 - Université Claude Bernard Lyon 1
8 Avenue Rockefeller
69008, Lyon, France

Résumé

Le muscle squelettique est composé de milliers de cellules géantes, appelées les myofibres. Pour développer les myofibres, des cellules progénitrices mononucléées, appelées myoblastes, fusionnent et partagent leur cytoplasme et leur noyau avec les syncytiums en formation. Au sein de chaque myofibre, des centaines de noyaux sont régulièrement positionnés à la périphérie, à l'exception de zones spécialisées telles que les jonctions neuromusculaires (NMJs, pour neuromuscular junctions) où plusieurs noyaux sont regroupés. Cette organisation précise des noyaux donne naissance à des domaines nucléaires, qui sont des territoires théoriques supportés transcriptionnellement par chaque noyau pour garantir une activité transcriptomique coordonnée tout au long des myofibres. Les domaines nucléaires sont dérégulés dans différents types de myopathies où on observe des noyaux mal positionnés au long ou à l'intérieur des myofibres. Cependant, comment les domaines nucléaires sont régulés à la périphérie des myofibres et comment leur perturbation peut contribuer au développement de myopathies reste peu compris.

Les microtubules (MT) sont des structures dynamiques qui passent par des cycles de polymérisation et de dépolymérisation sous l'influence de protéines associées (MAPs, pour microtubules associated proteins) ou des modifications post-traductionnelles (PTMs, pour post translational modifications). Au cours des premières étapes du développement des myofibres, les MT participent activement à la formation des domaines nucléaires en servant comme un guide pour les molécules motrices qui dispersent les noyaux le long de la myofibre en croissance. Plus tard, c'est l'assemblage des sarcomères musculaires qui vont pousser les noyaux dispersés à la périphérie des myofibres. Comment les noyaux sont maintenus à la périphérie des myofibres n'est pas clair, cependant, la présence d'une cage dense de MT autour des noyaux périphériques suggère que les MT et leur réseau de protéines associées peuvent contribuer au positionnement des noyaux également dans les myofibres matures.

Dans cette étude, nous avons défié la dynamique des MT en modifiant son réseau des MAPs ou sa proportion des PTMs au cours de la myogenèse. En utilisant divers modèles *in vitro* et *in vivo* de sous expression ou knock-out, nous montrons que la dynamique des MT est réduite au cours de la myogenèse vers un réseau plus stable dans les myofibres matures. Nous rapportons également que l'augmentation de la dynamique des MT peut perturber directement les domaines nucléaires à la périphérie des myofibres, soit en augmentant la dynamique des noyaux soit en augmentant le nombre des noyaux par myofibre. Dans les deux cas, nous proposons des mécanismes expliquant comment chaque forme de perturbation des domaines nucléaires peut entraîner une réduction de la fonctionnalité musculaire.

Institut NeuroMyoGène
Laboratoire Physiopathologie et Génétique du Neurone et du Muscle
CNRS UMR 5261 - INSERM U1315 - Université Claude Bernard Lyon 1
8 Avenue Rockefeller
69008, Lyon, France

Abbreviations

A

ABD: Actin binding domain
ACh: Acetylcholine
AChR: Acetylcholine receptor
ACF7: Actin crosslinking family 7
ADP: Adenosine diphosphate
AKAP450: A-kinase anchoring protein 450
APC: Adenomatous polyposis coli
ATP: Adenosine triphosphate

B

BIN1: bridging integrator-1
BMP: Bone morphogenetic protein
BPAG1: Bullous pemphigoid antigen 1

C

Cas9: CRISPR-associated protein 9
Cdc42: Cell division control protein 42
CDK5RAP2: CDK5 regulatory subunit associated protein 2
CH: Calponin homology
CLASP: CLIP-associating protein
Clip170: Cytoplasmic linker protein 170
CM1: Centrosomin motif 1
CNM: Centronuclear myopathy
CRISPR: Clustered regularly interspaced short palindromic repeats
CSA: cross-sectioned area

D

Dapi: 4′,6-diamidino-2-phenylindole
DMD: Duchenne muscular dystrophy
DMEM: Dulbecco's modified Eagle medium
DNA: Deoxyribonucleic acid
DNM: Dynamin
Dync1i2: Dynein intermediate chain

E

EB: End binding protein
EC: Excitation-contraction
ECC: excitation-contraction-coupling
ECM: Extracellular matrix
EDL: Extensor digitorum longus
EDMD: Emery-dreifuss muscular dystrophy
EdU: 5-ethynyl-2'-deoxyuridine
ELMO: Engulfment and cell motility
ER: Endoplasmic reticulum
ERT2: Estrogen receptor T2

F

FAK-Src: Focal adhesion kinase and steroid receptor coactivator
FBS: Fetal bovine serum
FGF: Fibroblast growth factor

G

G: Gastrocnemius
GAR: Growth arrest specific-2 domain
GCP: γ-tubulin complex protein
GSK3: Glycogen synthase kinase-3
GSR: Glycine-Serine-Arginine repeats domain

H

HBSS: Hanks' balanced salt solution
HDAC6: Histone deacetylase 6
HECTD1: HECT domain E3 ubiquitin protein ligase 1
HES1: Hairy and enhancer of split-1
HSA: Human skeletal actin

I

IMDM: Iscove modified Dulbecco media
INM: Inner nuclear membrane

K

KASH: Klarsicht/Anc-1/Syne homology
KD: Knock-down
KIF: Kinesin superfamily protein
Klar: Klarsicht
KLC: Kinesin light chain
KO: Knock-out

L

LINC: Linker of nucleoskeleton and cytoskeleton
LRP6: Lipoprotein receptor-related protein 6

M

MACF1: Microtubule actin cross-linking factor 1
MAP: Microtubules associated protein
MBD: Microtubules binding domain
MHC: Myosin heavy chain
MRFs: Myogenic regulatory factors
MTs: Microtubules
MTJ: Myotendinous junction
MTM1: Myotubularin 1
MTOC: Microtubules organization center
ncMTOC: Non-centrosomic microtubules organization center
MuSK: Muscle-specific kinase
MYF5: Myogenic factor 5
MyoD: Myoblast determination protein
MyoG: Myogenin
MZT1: MZT1 mitotic spindle organizing protein 1

N

NADPH: Nicotinamide adenine dinucleotide phosphate
NE: Nuclear envelope
NEDD1: Neural precursor cell expressed developmentally down-regulated protein 1
Nesprin: Nuclear envelope spectrin repeat protein
NF-H: Neurofilament heavy chain
NMJ: Neuromuscular junction
NUP153: Nucleoporin 153
N-WASP: Neural Wiskott-Aldrich syndrome protein

O

ONM: Outer nuclear membrane
Op18: Oncoprotein 18

P

P230: Trans Golgi protein 230
Par6β: Partitioning defective 6-β
PAX: Paired box
PBS: Phosphate buffered saline
PCM1: Pericentriolar material 1
PCR: Polymerase chain reaction
qPCR: Quantitative PCR

QRT-PCR: Quantitative reverse transcription PCR
PD: Plakin domain
PGC-1α: Peroxisome proliferator-activated receptor gamma coactivator 1-alpha
PRD: Plakin (or Plectin) repeats domain
PTM: Post-translational modification

R

RNA: Ribonucleic acid
mRNA: Messenger RNA
ROS: Reactive oxygen species
Runx2: Runt-related transcription factor 2

S

SDH: Succinate dehydrogenase
SH3: Src-homology 3
Shot: Shortstop
SIRT2: Sirtuine 2
Six: Sine oculis homeobox
SR: Spectrin repeats
SUN: Sad1/UNC-84 homology
SVBP: Small vasohibin binding protein
Syne: Spectrin repeat containing nuclear envelope protein

T

TA: Tibialis anterior
αTAT1: α-tubulins acetyltransferase
TeDT: Texture detection technique
TGN: Trans Golgi network
TI-VAMP: Tetanus neurotoxin-insensitive vesicle-associated membrane protein
TTL: Tubulin tyrosine ligase
γ-TuRC: γ-tubulin ring complex
γ-TuSC: γ-tubulin small complex

V

VAB-10: Variable abnormal morphology 10
VASH: Vasohibin

W

WT: Wild type
WNT: Wingless and Int-1

Y

YAP: Yes-associated protein

List of Figures

Introduction

Chapter 1: Nuclear movement in cells: from mononucleated to multi-nucleated cells

I) Nucleus

In eukaryotic cells, the nucleus is a double membrane organelle that guards the cell's genetic material and provides a suitable environment for transcription and replication of genome (Alberts, 2019; Pederson, 2011). The bilayer nuclear envelope (NE) is specialized to maintain nuclear shape and is the site of nucleocytoplasmic exchange through nuclear pores. The inner nuclear membrane (INM) participates in the chromatin organization mainly through the interaction of nuclear lamina with the chromatin. The outer nuclear membrane (ONM) faces the cytoplasm and is in continuity with the endoplasmic reticulum (ER) (Figure 1). The INM and ONM are coupled together and to the cytoskeleton through the Linker of Nucleoskeleton and Cytoskeleton (LINC) complex which allows a connection between the interior of the nucleus (through the nucleoskeleton) and the cytoplasmic cytoskeletons (actin, microtubule, and intermediate filaments) and thus contribute to the shape and positioning of the nucleus within cells (Figure 2) (De Magistris and Antonin, 2018; Hetzer, 2010). Indeed, despite the general view on the central positioning of a round-shaped nucleus inside a cell, nucleus subcellular localization and shape are adapted to cell type, cell cycle, and differentiation state and directly affect cell fate (Gundersen and Worman, 2013; Thorpe and Charpentier, 2017).

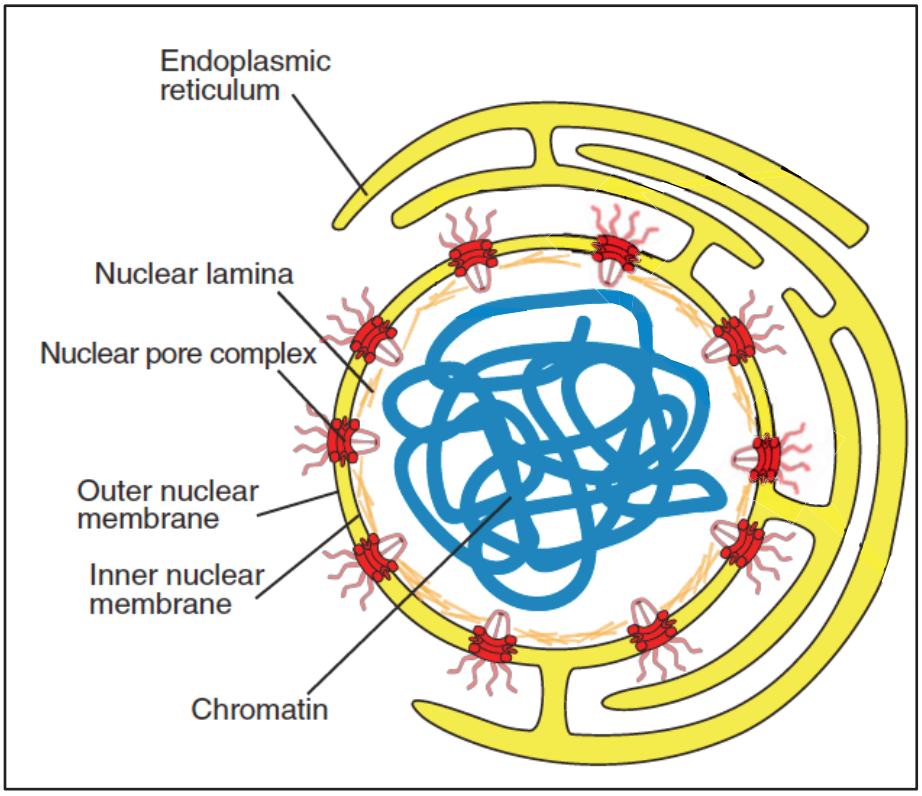

Figure 1: Illustration of the nucleus.
Schema presents INM and its interaction with chromatin through nuclear lamina, in addition to ONM and its prolongation with ER. While NE separates the genetic material from the cytoplasm, the nuclear pores ensure a controlled cargo transport between the nucleus and cytoplasm. Figure adapted from (De Magistris and Antonin, 2018).

II) Managing nucleus in cells

Cells are under constant mechanical stress due to changes in their environment. Any internal or external stress on the cell is translated to the nucleus in order to adapt a proper response. These adaptations are reflected by changes in nuclear positioning and shape. As mentioned previously, the LINC complex is the intermediate player in mechanical message transmission to the nucleus by connecting the nucleoskeleton to the cytoskeleton (Guilluy and Burridge, 2015).

1) The LINC complex

The proteins present in the LINC complex can be divided into two categories, the Sad1/UNC-84 homology (SUN) domain-containing proteins and the Klarsicht/Anc-1/Syne homology (KASH) domain-containing proteins (Janin and Gache, 2018). While SUN domain-containing proteins, such as SUN1 and SUN2 cross the INM and couple to chromatin through nuclear lamins, the KASH domain-containing proteins, such as nuclear envelope spectrin repeats protein (Nesprins), cross the ONM and couple SUN proteins to the cytoskeleton. The interaction between Nesprin proteins and cytoskeleton can be direct through their microtubules binding domain (MBD) and actin-binding domain (ABD) or indirect, through liaison proteins such as plectins, which chain the Nesprins to intermediate filaments (Figure 2) (Janin and Gache, 2018; Marks and Petrie, 2022). The interaction between SUN proteins and Nesprins plays a fundamental role in cytoskeleton force transition to the nucleus (Hao and Starr, 2019).

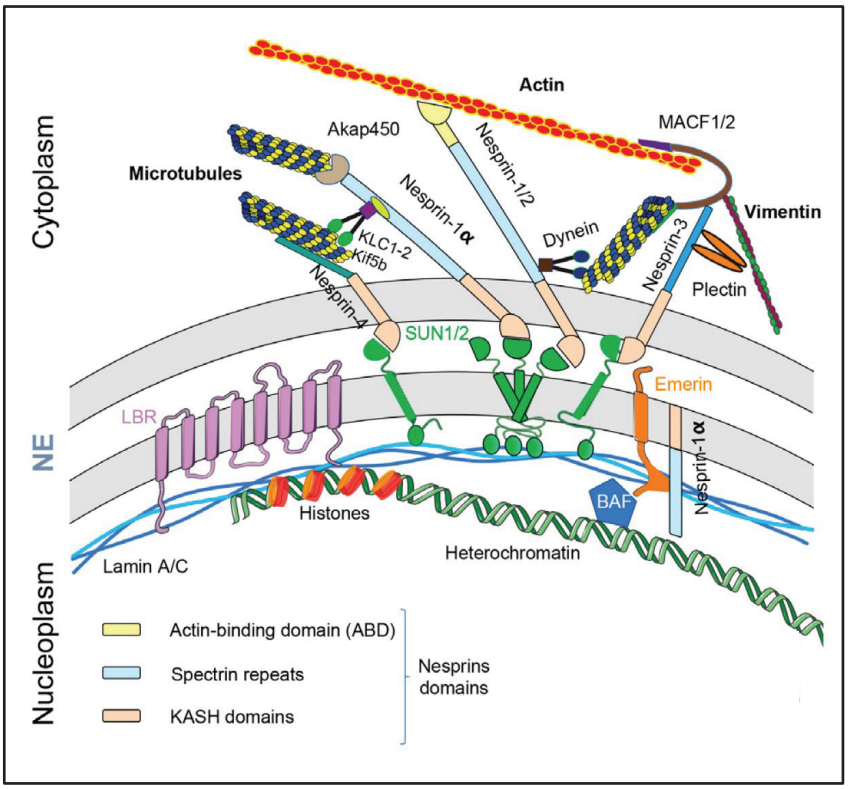

Figure 2: Illustration of NE interaction with the cytoskeleton through LINC complex. From the inside of the nucleus to the outside, nuclear lamins are in direct interaction with SUN proteins, which cross the INM and bind to KASH domain-containing proteins, such as Nesprins. Nesprins present various affinity for different cytoskeleton elements thanks to their specific binding domains, such as ABD, MTB, and plectin-binding domain. Figure adapted from (Janin and Gache, 2018).

2) Mechanotransduction and adaptation of nuclear form

Mechanotransduction groups molecular mechanisms which allow cells to adapt to changes in their environment by transducing mechanical stress into a biochemical signal. These physical changes are applied on the cytoplasmic cytoskeleton and translated to the NE through the LINC complex and can affect the nuclear shape, NE cargo transport, and genes expression (Dahl et al., 2008).

LINC complex protein SUN1 has been shown to colocalize with nuclear pores and interact with the nuclear pore protein, NUP153 (Liu et al., 2007; Talamas and Hetzer, 2011). In human epithelial and mouse fibroblast cell lines, the interaction between SUN1 and NUP153 has been shown to be necessary for NUP153 distribution at NE (Liu et al., 2007). Interestingly, in fibroblast cells, the application of force on the nucleus can result in NE stretching and dilatation of nuclear pores in a more open configuration (Elosegui-Artola et al., 2017; Enyedi and Niethammer, 2017). This can facilitate the cytoplasm/nucleus exchanges and import of regulatory proteins such as transcription factors or coregulators to the nucleus. One example is the nuclear import of the Yes-associated protein (YAP), a transcriptional regulator acting as a coactivator and/or a corepressor. Changes in extracellular matrix rigidity alters the actin-mediated force applied on the NE and results in nucleus flattening and nuclear pore stretching which in turn facilitate the import of YAP inside the nucleus (Elosegui-Artola et al., 2017).

Nuclear lamins are also sensitive to the level of tension present at NE. Following force application on primary mouse mesenchymal cells, nuclear lamins will get phosphorylated and coupled to SUN2 at the periphery of INM and turn the nuclear membrane more rigid (Buxboim et al., 2014; Swift et al., 2013). This change in nuclear stiffness in turn affects the import and export rate at the NE.

In addition, transitory or long-lasting gene expression alterations may occur when chromatin organization is remodeled due to an applied mechanical force. As mentioned before, one of the modulators of chromatin organization is the actin cytoskeleton by interaction with nuclear lamins through the LINC complex. A timescale study has demonstrated that the application of external force on the membrane of the epithelial cells results in increased actin cytoskeleton polymerization close to the NE and as a consequence chromatin reorganization. Interestingly, this study describes a bigger chromatin rearrangement for less condensed euchromatin compared to condensed heterochromatin following mechanical stress, suggesting differential transmission of force between eu- and hetero-chromatin (Iyer et al., 2012). Moreover, studies on adherent mouse and human fibroblasts have demonstrated that accumulation of perinuclear actin at the apical surface of the nucleus redistributes the nuclear lamina and participates in active gene-expression sites organization under NE (Kim and Wirtz, 2015).

Thus, the nucleus is a mechanosensitive organelle within the cell whose activity is directly coupled to the cells' sensing of its microenvironment. Depending on the level of the mechanical stress applied on the cell, nuclear form, permeability, and chromatin organization are modulated and result in short- or long-term gene expression modifications. Indeed, changes in

nucleoskeleton composition and disrupted NE rigidity have been linked to a wide range of diseases such as skin abnormalities, spinocerebral ataxia, and cardiac and skeletal myopathies (Holaska, 2016).

3) Nuclear movement: adaptation to cell state

The nuclear movements are influenced by cells' status and, depending on the origin of the force, can be mono- or bi-directional, continuous or with pause, and can have various velocities (Gundersen and Worman, 2013).

In *S. pombe*, microtubules (MTs) generate pushing forces on NE to keep the nucleus in the center of the cell. This pushing force is due to MTs nucleation and polymerization from the center of the cell, near the nucleus, toward the cell tips. This central positioning of the nucleus is essential for proper cell division (Tran et al., 2001). However, in budding yeast, dynein motor protein generate MT-related pulling forces and moves the nucleus to the bud neck (Figure 3) (Adames and Cooper, 2000).

Following sperm entry into an egg, the emerging centrosomal MTs from male and female pronuclei will direct them to join each other close to the cell center, a process necessary for successful fertilization (Figure 3) (Gundersen and Worman, 2013). Interestingly, the male and female pronuclei move via two different mechanisms. The male pronucleus is positioned at the cell cortex in tight interaction with the centrosome. The growing of MTs from the centrosomes toward the cell cortex pushes the male pronucleus toward the center of the cell (Reinsch and Gonczy, 1998). For the female pronucleus, the neighboring centrosome does not exercise a MTs nucleation activity. Yet the centrosome in the vicinity of the female pronucleus has the capacity to assemble and organize cytoplasmic MTs which results in the movement of the female pronucleus to the center of the cells (Morito et al., 2005).

In zebrafish, it has been shown that nuclear movement toward the apical side of retinal cells is driven by myosin2, an actin-dependent motor protein specific to non-muscular cells (Norden et al., 2009). This type of nuclear movement is suggested to be important for maintaining proper cell polarity and therefore neuroepithelium development (Baye and Link, 2008).

The nuclear movement also has a great impact on neuronal development. In neuronal precursor cells, the apically positioned nucleus is directed by MTs and moves to the basal level of the cell during G1 but goes back to its apical position during G2 to go through mitosis (Figure 3) (Taverna and Huttner, 2010). In migrating neurons, the nucleus moves toward the leading site of the cell in a process dependent on both actin filaments and MTs. Indeed, it has been shown that in these cells, actin-myosin2 force is necessary for pushing the nucleus forward on MT railways that are generated by the centrosome, which is positioned at the leading side of the nucleus (Schaar and McConnell, 2005). Mutations in cytoskeleton components, such as tubulins, can disrupt neuronal migration and are linked to defeats in neuronal development and brain malformations resulting in intellectual retards or mental disorders (Nakazawa and Kengaku, 2020).

In migrating fibroblasts, the nucleus moves toward the forming lamellipodium (Figure 3). Interestingly, LINC complex proteins Nesprin-2 and SUN2 have been shown to use the actin filaments and promote the proper nuclear movement synchronized with the migration of the cell. This movement is essential for fibroblast migration toward wounded sites *in vitro* (Luxton et al., 2010).

Thus, cytoskeleton elements monitor and adapt both nuclear mechanotransduction and nuclear positioning in a cell-dependent manner. As highlighted by different examples, nuclear movement depends greatly on forces generated by MTs. Indeed, MTs are nucleated from the MT organization center which can be the juxtanuclear centrosome in proliferating cells or non-centrosomal sites in differentiated cells, such as the nuclear envelope in muscle cells. In both cases, MT nucleation proposes mechanical support to cargo transport within cells through different mechanisms (Sanchez and Feldman, 2017). For nuclear movement, this can be a direct mechanism, such as pushing forces generated by MT nucleation, or an indirect mechanism through the activity of various MT binding motor proteins (Cadot et al., 2015).

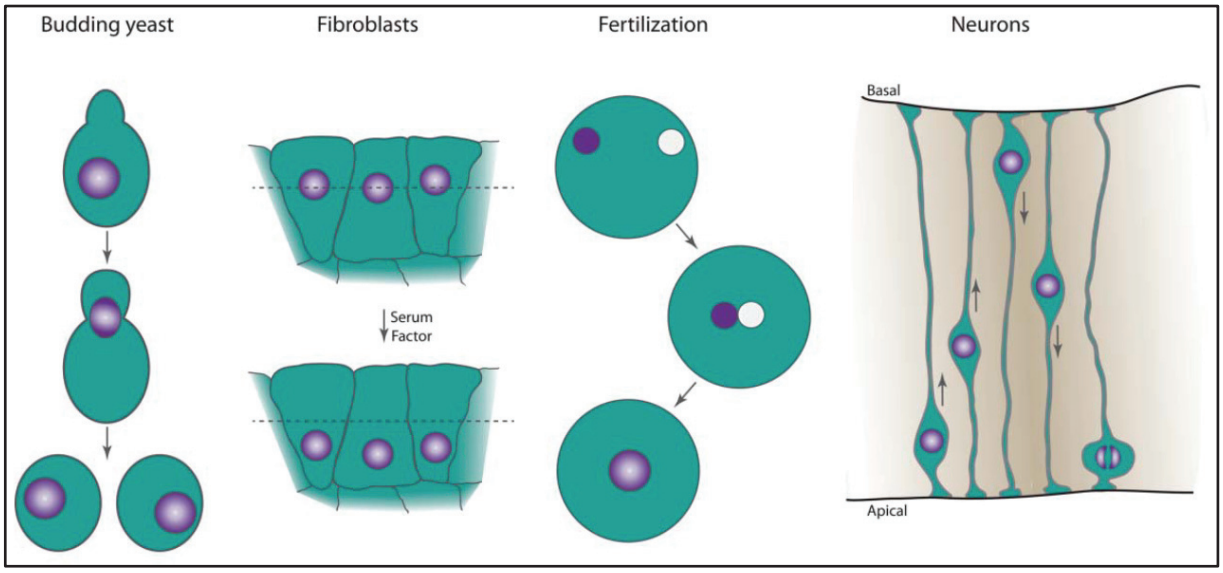

Figure 3: Illustration of nuclear movement in different cell types.
From left to right: In yeast, the nucleus moves toward the bud neck to allow proper cell division, in fibroblasts nucleus moves to the back of the cell prior to cell migration, in fertilizing egg the male and female pronuclei join in the center to mix their DNAs and in developing neurons, nucleus moves between basal and apical levels during the cell cycle. Figure adapted from (Cadot et al., 2015).

III) Myonuclei movement and the particular case of skeletal muscle fibers

The concept of nuclear movement and positioning is more complex in the case of skeletal muscle fibers since each muscle fiber contains hundreds of regularly spaced nuclei located at its periphery. The observation of mispositioned myonuclei in different myopathies has increased the interest in understanding the mechanisms behind myonuclei movement and positioning in the field.

1) Skeletal muscle

Skeletal muscle makes up to 40% of our body mass and allows voluntary contraction and movements due to its connection with our peripheral nervous system. From a physiological point of view, skeletal muscle is necessary for maintaining our posture, breathing, and conducting voluntary movements. From a cellular and tissular point of view, skeletal muscle serves as the reservoir for amino acids and carbohydrates and regulates body temperature by producing heat. The size and volume of each skeletal muscle depend directly on the number and size of its cells, known as myofibers (Frontera and Ochala, 2015). Each myofiber is a syncytium that originates from the fusion of mononuclear muscle cells called myoblasts. In humans, a mature myofiber can be as long as 60 cm and contains hundreds of nuclei, defined as “myonuclei”. During each step of myogenesis, these myonuclei are precisely moved until they are pushed to the periphery of mature myofibers. At the periphery of myofibers, oval-shape myonuclei are regularly spaced, with exception of particular zones such as neuromuscular junctions (NMJs), where several specialized myonuclei, known as post-synaptic myonuclei, can be found clustered (Cadot et al., 2015). While previous studies have been dedicated to mechanisms regulating myonuclei movement during myogenesis, how myonuclei are positioned at the periphery of myofibers and how their spacing is regulated are poorly understood.

A) Myogenesis

In the course of development, embryonic skeletal muscle progenitor cells originate from mesoderm and go through myogenesis following activation of different transcriptional factors, including myogenic regulatory factors (MRFs) (Figure 4) (Buckingham et al., 2003; Hernández-Hernández et al., 2017; Tajbakhsh and Cossu, 1997).

The expression and activity of different members of the sine oculis homeobox (Six) transcription factors family, in particular, Six1 and Six4, is known to initiate myogenic lineage specification in muscle progenitor cells by inducing the expression of transcription factors such as paired box gene 3 (PAX3) (Grifone et al., 2005). Expression of PAX3 will promote the migration of muscle stem cells from mesoderm (Birchmeier and Brohmann, 2000) and is followed by expression and activity of transcription factor paired box gene 7 (PAX7) which will regulate the expression of MFRs, such as myogenic factor 5 (MYF5) (Buckingham and Relaix, 2015; Mayran, 2015). Interestingly, Six1, Six4, and PAX3 have also been shown to activate the expression of MYF5 (Giordani et al., 2007). In addition, Six1 and Six4 together

with MYF5 are necessary for the induction of muscle stem cells commitment to myoblasts by initiating the expression of myoblast determination protein (MyoD) (Relaix et al., 2013). Therefore, Six family members have been suggested to regulate different steps of myogenesis (Maire et al., 2020). Following, MyoD will promote the expression of myogenin (MyoG) which will induce the differentiation of myoblasts to myocytes (Mukund and Subramaniam, 2020; Sabourin and Rudnicki, 2000). At this point, huge membrane and cytoskeleton rearrangement, in parallel with the expression of transmembrane proteins Myomaker and Myomerger (regulated by MyoD and MyoG), will induce myocytes fusion and formation of myotubes, containing myonuclei aligned in their center (Millay, 2022). While fusion continues, myotubes will gain volume and express sarcomeric proteins such as α-actinin and muscle-specific myosin heavy chain (MHC) to form the contractile apparatus and develop into myofibers. This participates in the movement of central myonuclei toward the periphery of myofibers and their dispersion all along the myofiber (Roman et al., 2017). Maturation of myofibers pursues by the expression of different acetylcholine receptors (AChRs) subunits which will cluster together and form post-synaptic NMJs upon the liberation of Agrin from innervating motor neurons (Barbeau et al., 2020; Chal and Pourquié, 2017).

From an extrinsic point of view, different signaling pathways are also known to impact myogenesis. For example, the bone morphogenetic protein (BMP) signaling pathway is known to maintain the proliferation of PAX3 positive cells during early embryogenesis by preventing the expression of differentiation genes, such as MyoD target genes (Amthor et al., 1998; Ono et al., 2011). Later on Wingless and Int-1 (WNT) signaling pathway is important in the regulation of the PAX7+ cells population by inducing the expression of MRFs (Hutcheson et al., 2009; Tajbakhsh et al., 1998). NOTCH is another important signaling pathway that seems to play a crucial role in determining the fate of myogenic progenitor cells. It acts upstream of the hairy and enhancer of split-1 (HES1) transcription regulator which controls the expression of MyoD (Lahmann et al., 2019). Ablation of NOTCH signaling results in premature differentiation of progenitor cells and its activation is enough to prevent progenitor cells differentiation (Esteves de Lima et al., 2016; Vasyutina et al., 2007).

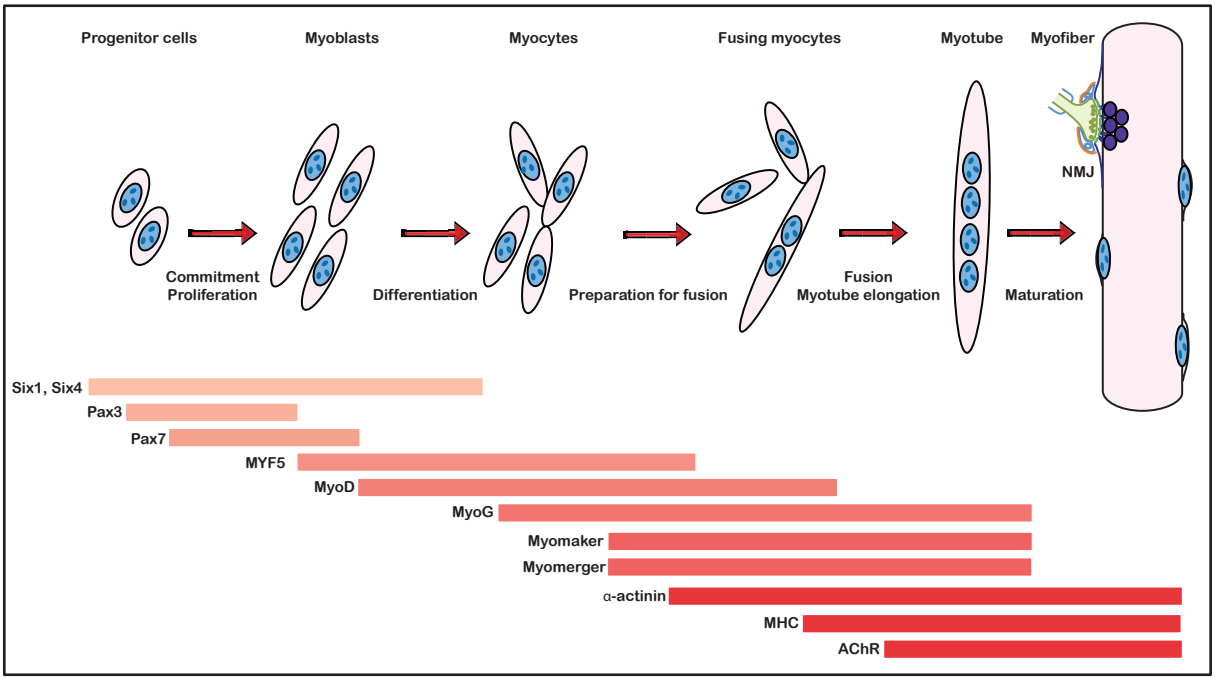

Figure 4: Illustration of sequential steps of myofibers development from progenitor muscle cells.

Each step of myofibers development requires the activity of different transcriptional factors and the expression of specific proteins which will advance myogenesis step by step and enable the structural changes needed to form long contractile multinucleated myofibers from mononuclear myoblasts.

B) Myofibers

As mentioned above, the product of myogenesis is multinucleated contractile myofibers (Frontera and Ochala, 2015). Each myofiber is innervated by one motor neuron, surrounded by blood vessels, and gathered with other myofibers by the connective tissue to form the skeletal muscle. The skeletal muscle is limited between two myotendinous junctions which joint skeletal muscles to bones through tendons (Figure 5) (Frontera and Ochala, 2015). The exterior and interior architecture of each myofiber play critical roles in the functionality of skeletal muscles in our body which are described in the following sections.

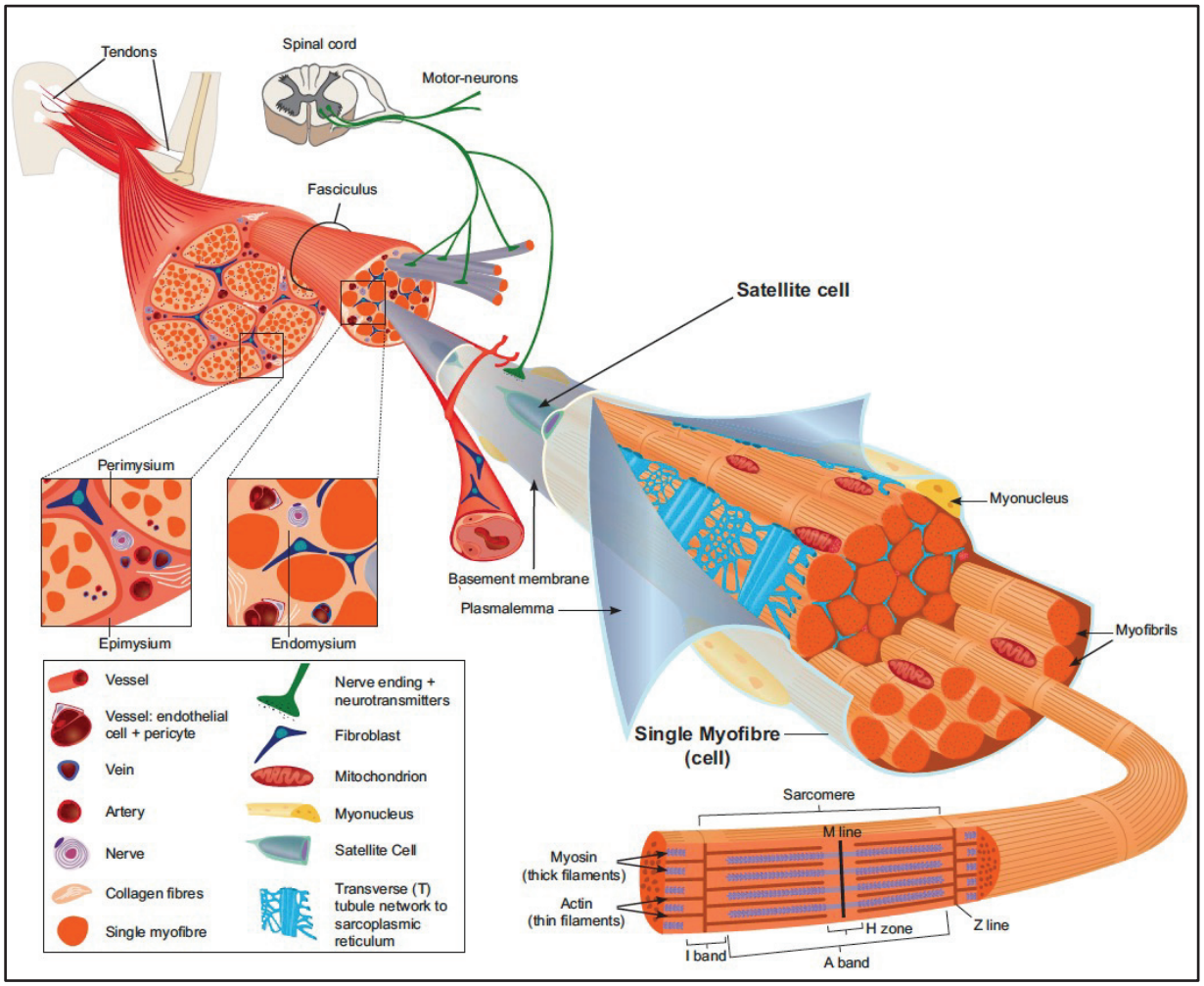

Figure 5: Illustration of skeletal muscle.
Skeletal muscle is connected to tendons by myotendinous junctions and holds onto fasciculi of myofibers. Each myofiber is surrounded by endomysium and covered by a basement membrane. The basement membrane of each myofiber is in direct contact with blood vessels and is innervated by a single motor neuron projection to form an NMJ. Between the basement membrane and plasmalemma, quiescent muscle stem cells can be observed. Passing plasmalemma hundreds of myonuclei can be found regularly positioned at the periphery of the myofiber. Within the myofiber, we can observe the T-Tubule network, sarcomeres, and myofibrils, in addition to residing mitochondria between myofibrils. Figure adapted and modified from (Tajbakhsh, 2009).

B1) Exterior environment of myofibers

Inside the skeletal muscle, fasciculi of myofibers are surrounded by a layer of connective tissue known as epimysium. Inside each fasciculus, myofibers are surrounded by a distinct form of connective tissue, known as endomysium (Figure 5). Both epimysium and endomysium are composed of collagen fibers in a proteoglycan matrix (Purslow, 2020). In epimysium, the collagen matrix is relatively stiff and define the volume and structure of skeletal muscle (Purslow, 1989). In endomysium, the collagen fibers are wavy and run in parallel to muscle fibers (Trotter and Purslow, 1992). Each myofiber is distantly separated from the connective tissue and other myofibers by a cover of the basement membrane made from non-fibrous collagen type IV, laminin, and proteoglycan. However, it is the plasmalemma (also known as sarcolemma) that isolates each myofiber from the extracellular matrix (Figure 5) (Purslow, 2020).

The skeletal muscle is limited between two myotendinous junctions (MTJs), which are the functional units that transduce the muscle contraction to skeletal system movement (Figure 5). During development, myogenic cells and specialized fibroblasts (later called tenocytes) develop their interaction through the extensive long villous processes of their cell membranes. This happens side by side with the enrichment of different extracellular matrix components, such as collagen, elastin, and fibrillin which together ensure the elasticity of MTJs (Charvet et al., 2012).

Another participating element in the extracellular myofibers environment is the blood vessels. In fact, skeletal muscle is a highly vascularized tissue with blood vessels surrounding every myofiber's basement membrane (Figure 5). These vessels are known to provide energy and oxygen to myofibers and are necessary for the proper activity of skeletal muscle (Latroche et al., 2015). Indeed, muscle weakness is one of the main symptoms of juvenile dermatomyositis, an autoimmune disease affecting the vascular system (Aouizerate et al., 2018; Latroche et al., 2015). During embryogenesis, myogenic and endothelial cells drive from the same origin under influence of different transcription factors. Already at the embryonic stage, small blood vessels are formed in parallel with myotubes formation, and the maturation of blood vessels is done along myofibers maturation post birth, to form long meshes of blood vessels around each myofiber (Latroche et al., 2015).

B2) Myofibrils structure and their neighboring mitochondria

Myofibers cytoplasm contains repetitive chains of sarcomeres which are composed of specific structural and motor proteins (Figures 5-6). During development and myogenesis, different components of sarcomeres are sequentially expressed and assembled through a process called myofibrillogenesis, yet the final repetitive sarcomeric striation occurs in mature myofiber (Sanger et al., 2010).

Each sarcomere is defined between two Z-lines (or Z-disks) positioned in the middle of two I-bands from two consecutive sarcomeres. The I-band is mainly composed of thin filaments and gathers different isoforms of actin. When analyzing a single myofiber, this zone appears as a clear transversal line under light microscopy. Passing Z-line and I-band, A-band is positioned in the central zone of each sarcomere where thin and thick filaments can overlap. In the overlapping region, actin and actin-binding proteins such as troponin and tropomyosin, which are essential proteins for the conduction of contraction, are in direct contact with myosin, the main components of thick filaments. Under light microscopy, the dense overlapping region will appear as a dark transversal line. Following, H-zone is the central region of the A-band composed only of thick filaments and is centered itself by the M-line which is the attachment site of thick filaments. After a neuromuscular stimulation, contraction occurs when Ca^{2+} binds to troponin, which results in a conformational change of the troponin-tropomyosin complex. This will give access to myosins to bind to, and slide on, actin filaments. The movement of myosin thick filament on actin thin filaments will result in shortening of sarcomeres length, also known as contraction (Mukund and Subramaniam, 2020). Myosin-related myopathies and myopathies due to mutations in actin or troponin are examples of muscular diseases directly linked to the misassembled sarcomeres and myofibrils (Mukund and Subramaniam, 2020).

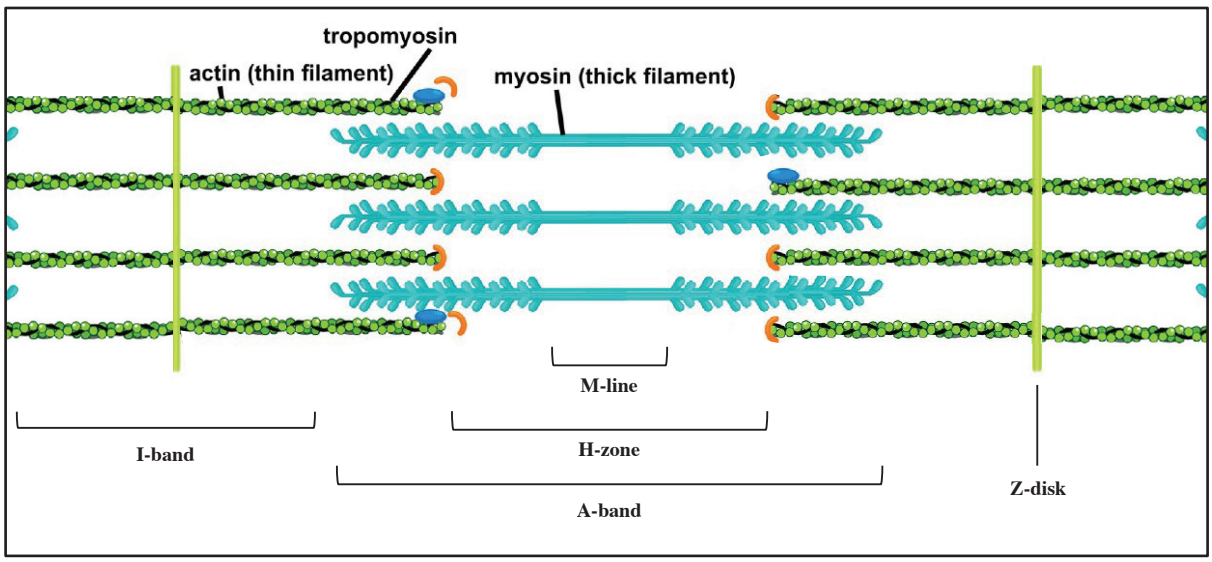

Figure 6: Illustration of skeletal muscle sarcomere organization.
A simplified schema of contractile unit organization in the limit of two Z-disks with the M-line in the center. Schema presents myosin thick filaments in interaction with actin thin filaments and tropomyosin. Figure adapted and modified from (Tolkatchev et al., 2019).

Lateral myofibrils are firmly bound together and to the plasmalemma by desmin intermediate filaments (Mukund and Subramaniam, 2020). Interestingly, desmin filaments also regulate the positioning of mitochondria, which tend to form a tight network that wraps around sarcomeres I bands and chains up longitudinal side by side with myofibrils (Figure 7) (Milner et al., 2000; Willingham et al., 2021).

Mitochondria is one of the most abundant subcellular organelles within myofibers which is responsible for ATP production through oxidative phosphorylation (Mukund and Subramaniam, 2020). It has been shown that PPARG coactivator-1α (PGC-1α), which is a marker of mitochondrial biogenesis, contributes to mitochondrial population growth during myogenesis, probably to address the needs of growing myofiber (Remels et al., 2010). Muscle weakness and exercise intolerance are among the symptoms of a group of myopathies known as mitochondrial myopathies. These myopathies are linked to defective mitochondrial activity, due to mutations in mitochondrial or nuclear genes responsible for the expression of mitochondrial biogenesis markers or mitochondrial respiratory complexes proteins (Ahuja, 2018).

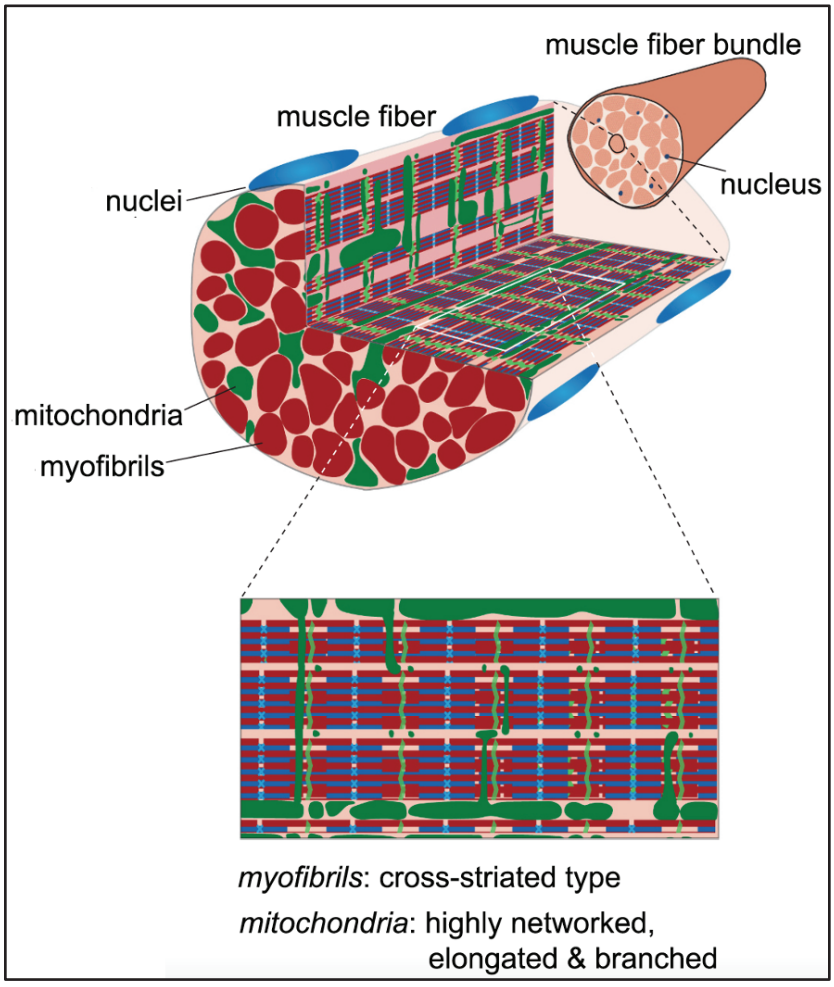

Figure 7: Illustration of the mitochondrial network within myofibers. Myofibers contain bundles of aligned crosslinked myofibrils with mitochondria laying in between. These mitochondria form thin extensions along the sarcomeric I-bands and build a continuous network. Figure adapted from (Luis and Schnorrer, 2021).

In fact, myofibers can be categorized based on their metabolism in addition to the composition of their myofibrils. Slow-twitch myofibers, also known as type I red muscle, rely mostly on mitochondrial respiration, while fast-twitch myofibers, also known as type II white muscle, get most of their energy from glycolytic metabolism. Type I myofibers are known to mainly express the muscle-specific myosin heavy chain (MHC) isotype I. However, type II myofibers can be further subcategorized to IIa, IIb, and IIx based on their expression level of different isotypes of MHC, which are MHC IIa, IIb, and IIx respectively (Figure 8). The metabolism mechanism and MHC isotype expression have a direct impact on myofibers' resistance to fatigue and force production. Type I myofibers are more resistant to fatigue, their contraction speed is slow and produce low amount of force. However, type II myofibers, from IIa to IIx, are less resistant to fatigue, and their faster and stronger contraction results in higher force production. (Schiaffino and Reggiani, 2011).

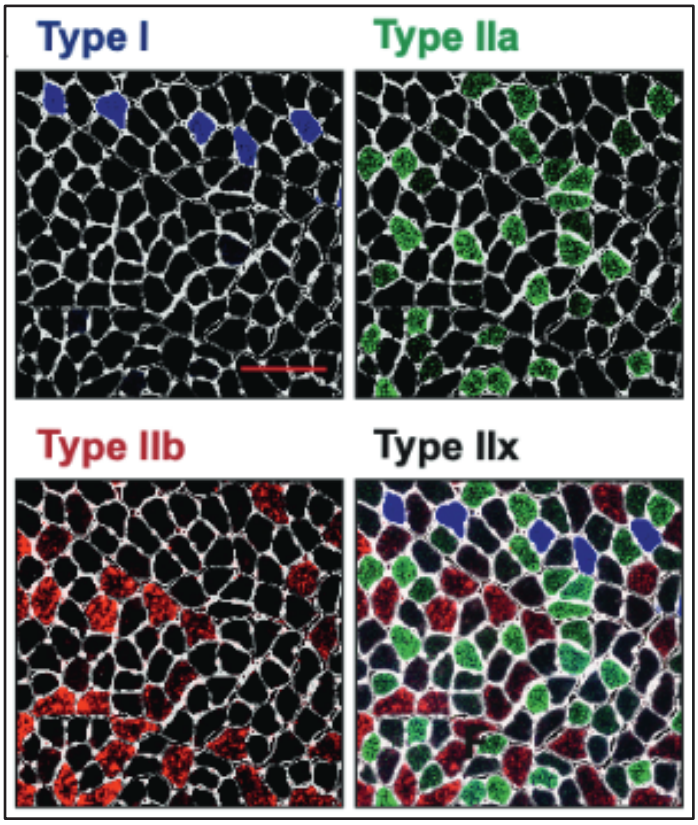

Figure 8: Representative photos of different myofibers type proportions in mouse quadriceps.
To visualize different myofibers subtypes, a mouse quadricep cross-section was subjected to immunofluorescence staining to detect the presence of specific MHC isotypes. Type I myofibers (presented in blue) show the lowest proportion compared to type II myofibers (presented in green for IIa, red for IIb, and black (remaining nonstained myofibers) for IIx). Figured adapted from (Kastenschmidt et al., 2019).

B3) Neuromuscular junctions and message transmission

Motor neurons innervation of the basement membrane is another event that accompanies the development of myofibers (Figure 5). With the formation of myotubes, transmembrane AChR subunits expression will result in their clustering within the developing myofibers through a process called prepatterning (Witzemann, 2006). The clusters are formed from two α-, one β-, and one δ-subunits in addition to one γ-subunit at the embryonic stage which will be replaced by one ε-subunit once the synapse is formed (Figure 9) (Cetin et al., 2020). During embryogenesis, the clustering is initiated by the post-synaptic protein MuSK and is continued by the activity of proteins such as rapsyn, which will act as stabilizers. While the clustering itself happens independent of neuronal signal, the liberation of acetylcholine (ACh) from the axonal projections of developing motor neurons (which originate from the peripheral nervous system) will relocate AChRs clusters within the myofiber to prepare for innervation and synapse formation. The liberation of neuronal Agrin will serve as a secondary stabilizer for forming NMJs by linking to post-synaptic endplates and preventing their dispersion. In mice, several innervation sites can be observed during embryonic stages, while during post-natal maturation, most of the surplus innervation sites are eliminated and only one single motor neuron-myofiber synapse will remain (Li et al., 2018; Witzemann, 2006). This happens side by side with the shift from γ-subunit to ε-subunit and results in the final pretzel-like pattern of AChRs clusters (Cetin et al., 2020; Witzemann, 2006). The construction of NMJs is completed by their coverage with terminal Schwann cells which are essential for the maintenance of NMJs (Barik et al., 2016).

To conduct muscular stimulation, synaptic vesicles produced by the innervating motor neuron will fuse with the presynaptic membrane of the motor neuron and liberate ACh in the synapse which will bind to AChR (Figure 10). This will result in the opening of ion channels all along the myofibers plasmalemma and the creation of an influx of Na^+ and efflux of K^+. This action potential will in turn result in the liberation of Ca^{2+} inside the myofiber and the generation of contraction which is discussed in the next section (Zou and Pan, 2022).

NMJs are essential for skeletal muscle activity and voluntary movements. Neuromuscular diseases can occur due to injury or dysfunction of any of the participating cells, myofibers, motor neurons, or Schwann cells, and can cause life-altering complications such as muscular atrophy or problems in movement and balance maintenance (Li et al., 2018; Morrison, 2016).

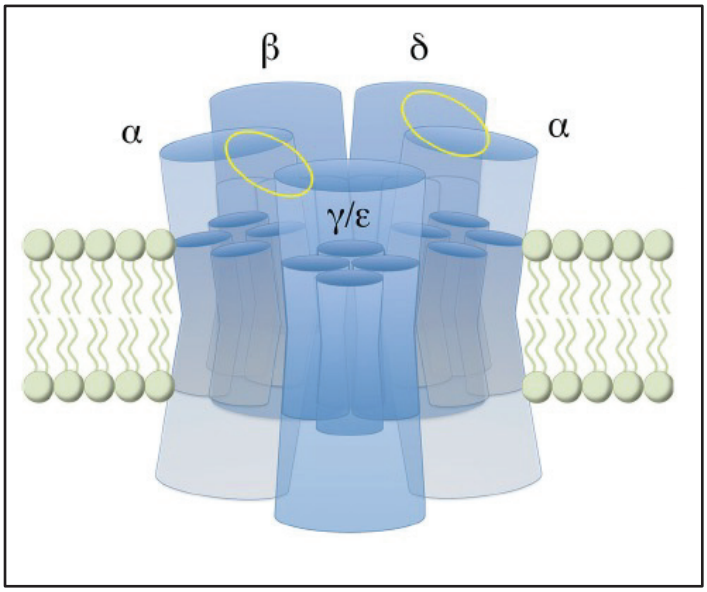

Figure 9: Illustration of AChR subunits at NMJs.
All AChR subunits are transmembrane proteins and pass the bilayer cell membrane facing the synapse. Yellow ellipses specify the binding sites of ACh on the cluster. Figure adapted from (Cetin et al., 2020).

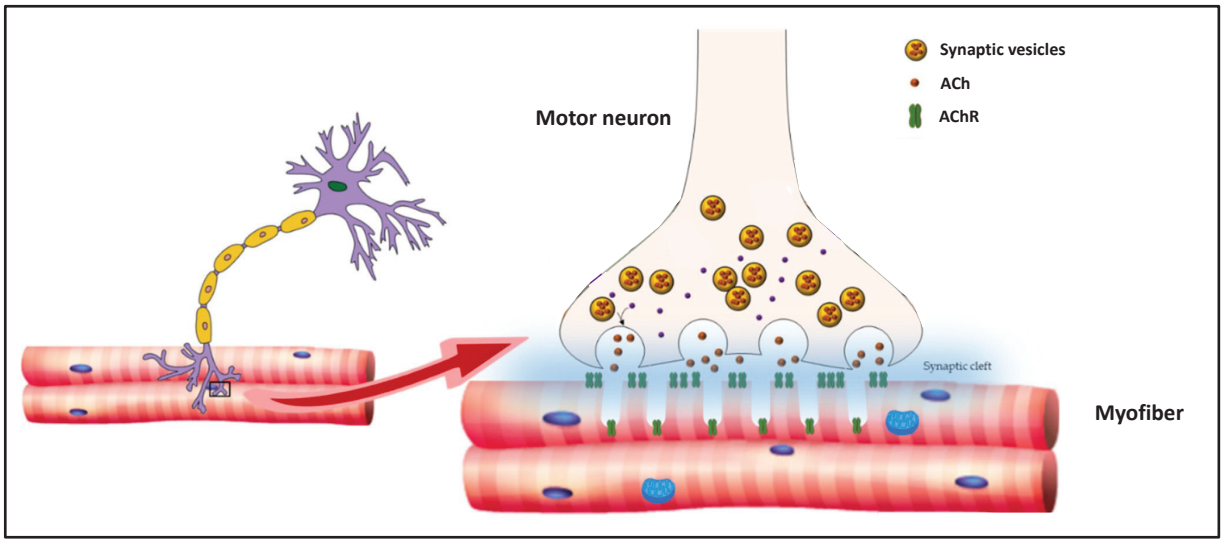

Figure 10: Illustration of NMJ and neuromuscular message transmission.
Following the fusion of presynaptic vesicles with motor neuron membrane, ACh is liberated in the synapse and will bind to AChR clusters present on the post-synaptic myofiber to enchain the action potential propagation. Figure adapted and modified from (Dobrowolny et al., 2021).

B4) Transverse tubules, sarcoplasmic reticulum, and excitation-contraction coupling

Following neuronal stimulation and action potential generation, the excitation-contraction (EC) signal has to pass through the basement membrane and plasmalemma and arrive at sarcomeric contractile units to conduct myofibers contraction, a complex process known as excitation-contraction-coupling (ECC). This happens through the invaginations of plasmalemma between myofibrils which are known as transverse tubules (T-Tubules) and are in tight contact with the sarcoplasmic reticulum (SR, the specialized endoplasmic reticulum of myofibers and main muscle reservoir for calcium within myofibers) in specific regions called cisternae (Figure 11). The transmitted nerve action potential depolarizes T-Tubules and results instantly in Ca^{2+} release from the cisternae of SR along the whole myofiber (Al-Qusairi and Laporte, 2011). Ca^{2+} will further result in sarcomeric proteins conformational change and myosin thick filaments sliding.

During myofibers development, SR proteins expression is detected in early myotubes and their assembly occurs almost at the same time as sarcomeric proteins. However, expression of T-Tubule-associated proteins begins slightly later with myotubes development and keeps increasing with myofibers maturation (Al-Qusairi and Laporte, 2011). Mutations in Ca^{2+} channels and ECC proteins can be linked to myopathies such as central core myopathy which present reduced muscle tone and muscle weakness (Mukund and Subramaniam, 2020).

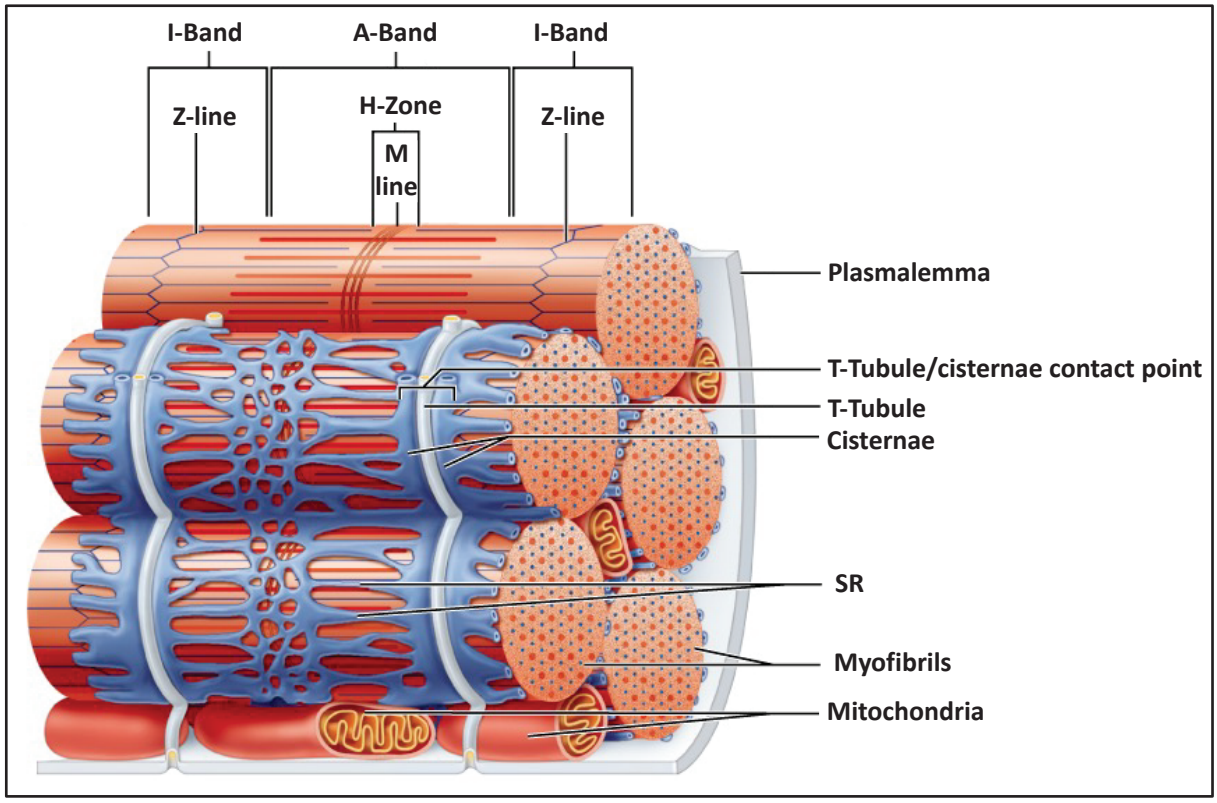

Figure 11: Illustration of sarcomeres and EC complexes.
Scheme illustrating sarcomeres organization in addition to the tight relation between SR with sarcomeres on one side and SR with T-tubules on the other side. Figure adapted and modified from (Marieb, 2001).

B5) Adjacent muscle stem cells and muscle regeneration

Skeletal muscle is one of the most regenerative tissues thanks to the presence of its quiescent muscle stem cells (MuSCs, also known as satellite cells) which reside between the basement membrane and plasmalemma (Figure 5). It is known that following myogenesis at the embryonic stage, a subset of cells positive for PAX3 and PAX7 will begin to take position under the forming basement membrane and eventually give rise to the adult MuSCs. The majority of these cells will drastically lose their positivity for PAX3 and therefore PAX7 will be the main marker of postnatal MuSCs. These cells can participate in myofibers' growth during postnatal development or myofibers regeneration following injury (Aziz et al., 2012; Tajbakhsh, 2009; Zhu et al., 2021).

The maintenance of MuSCs quiescence depends enormously on the composition of their niche and their interaction with myofiber which inform MuSCs on myofibers status. In particular, the stiffness of ECM, which depends on its components such as Collagens, Fibrillins, or Elastins, in addition to the active or inactive state of different signaling pathways, such as NOTCH and WNT, have been described to have a direct regulatory impact on MuSCs status (Loreti and Sacco, 2022; Relaix et al., 2021).

Following muscular damage, alerted activated MuSCs will gradually lose their PAX7 and will express myogenic factors such as MyoD and further MyoG to differentiate and fuse with damaged myofibers, resulting in the presence of central myonuclei within regenerating myofibers (Figure 12) (Almada and Wagers, 2016; Fukada et al., 2022). Depending on the level of damage, the vascular system may also need to be repaired, new NMJs may need to form and the extracellular matrix (ECM) may need to be rebuilt (Figure 13) (Loreti and Sacco, 2022). Yet, no matter the depth of tissue damage and repair, central myonuclei resulting from fusing MuSCs will have to move to the myofiber periphery, a process which can take up to several months (Forcina et al., 2020; Fukada et al., 2022). . When regeneration is completed, a subset of proliferated MuSCs negative for MyoD will go back to quiescence to maintain MuSCs pool (Almada and Wagers, 2016).

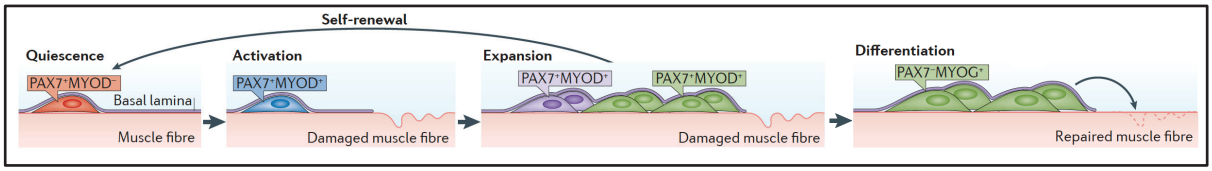

Figure 12: Illustration of MuSCs at the periphery of healthy and regenerating myofibers. Following injury or change in ECM, quiescent PAX7+ MuSCs will get activated and start expressing MyoD. The PAX7+ MyoD+ myoblasts have a high proliferative capacity which results in the expansion of their population. While some of the new myoblasts will regain their stemness by losing MyoD and go back to quiescent, the majority of them will start expressing MyoG which will induce their differentiation and their fusion with damaged myofiber. Figure adapted from (Almada and Wagers, 2016).

Pathological changes in the MuSCs niche and ECM can be observed in different muscular diseases such as muscular dystrophies or neuromuscular diseases. For example, in muscular dystrophies, the presence of pathological myofibers fragility and damage is accompanied by persistent local inflammation and altered composition of MuSCs nice. This results in excessive MuSCs alert and long-term loss of self-renewal and regenerative capacity of MuSCs, which contributes to the progression of the disease (Mashinchian et al., 2018).

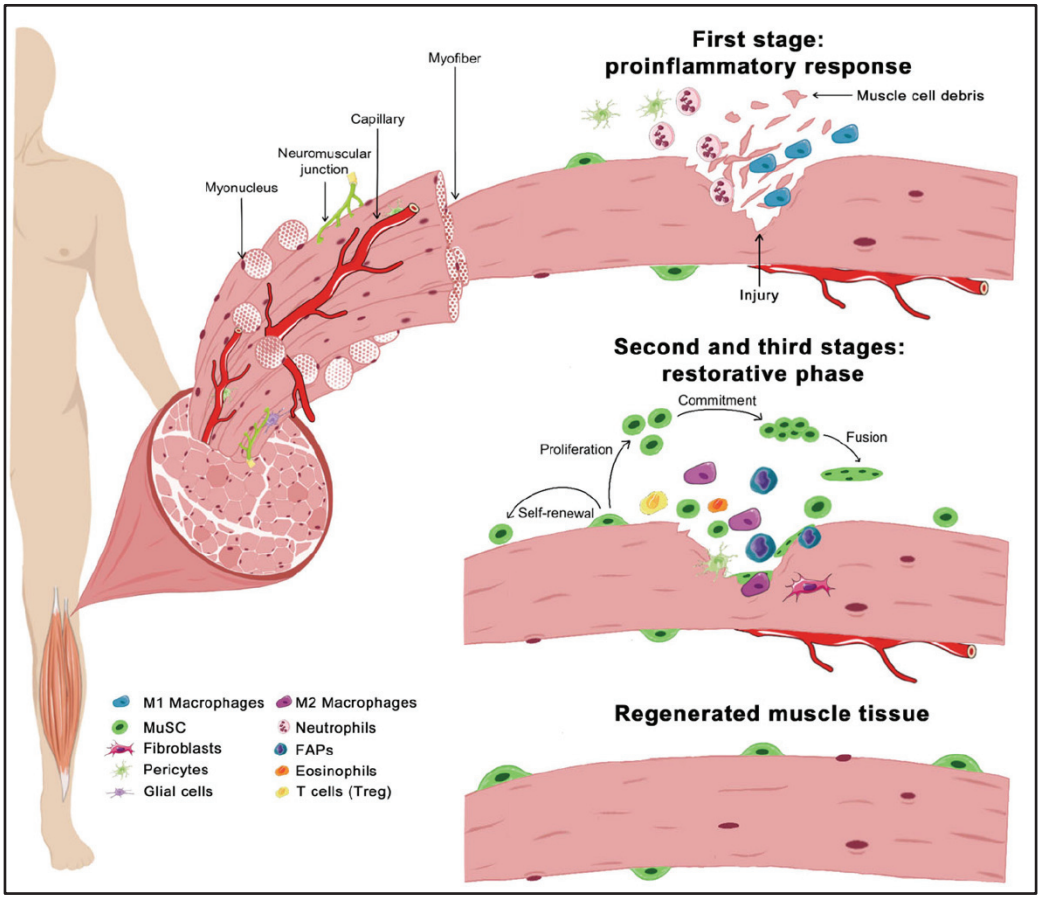

Figure 13: Illustration of muscle regeneration at a glance.
Following injury, several cell types, including MuSCs, participate to repair the myofibers. During the proinflammatory step, immune cells such as neutrophils and proinflammatory macrophages (M1) will clear the site of injury from damaged myofibers. During the second stage, alerted MuSC begin to proliferate and expand. In parallel, other immune cells such as T cells and eosinophils enter the injury site. In particular, eosinophils will stimulate the proliferation of fibro-adipogenic progenitor cells which will later help remodel the ECM. Through the third step, M1 macrophages are replaced by M2 or anti-inflammatory macrophages. M2 macrophages will express anti-inflammatory markers as a signal for other immune cells and will express ECM-related genes to participate in ECM remodeling and promote MuSCs differentiation. Following MuSCs differentiation, they will fuse together or with damaged myofiber and participate in tissue regeneration. Figure adapted from (Loreti and Sacco, 2022).

B6) Peripheral myonuclei

As mentioned before, hundreds of myonuclei can be found, under the plasmalemma, regularly positioned at the periphery of the myofiber or clustered under NMJs or in the vicinity of MTJs (Figure 5). Based on the dispersed positioning of myonuclei, it has been suggested that each myonucleus transcriptionally serves a specific region of myofiber around it, known as the myonuclear domain. Indeed, disruption of myonuclei spreading results in defects in myogenesis, and mispositioned myonuclei can be observed in different types of myopathies (Cadot et al., 2015; Folker and Baylies, 2013). The detailed myonuclei movement and positioning during myogenesis as well as the links between myonuclei mispositioning or malformation with myopathies are described in the following sections.

2) Step by step with myonuclei movement during myogenesis

Depending on the myogenesis step, myonuclear movement is regulated by different members of the cytoskeleton, MTs, actin, or intermediate filaments in addition to their binding proteins, such as microtubules associated proteins (MAPs).

This section is focused on the regulation of myonuclei dynamics during mammalian myogenesis (which is resumed in Figure 14). MTs and MT organization in skeletal muscle will be exclusively introduced and detailed in chapter two.

A) Myonuclei centration in myotubes

As previously described, fusion occurs in differentiated myocytes and results in myotubes formation.

The fusion of myocytes is synchronized with changes in the cytoskeleton, notably the MT network and their organization. In mononuclear myoblasts and early differentiated myocytes, MTs are nucleated from the centrosomic microtubules organization center (MTOC) in the vicinity of the nucleus. However, MT nucleation center begins to change as myocytes prepare themselves for fusion, from MTOC to the non-centrosomic microtubules organization center (ncMTOC), located mainly at the myonuclear envelope (Bugnard et al., 2005; Tassin et al., 1985). Therefore, throughout myogenesis and further in myofibers, each myonucleus will serve as an individual ncMTOC which is essential in the production of pulling and pushing forces and driving myonuclei positioning.

As MT organization center changes and myocytes begin to fuse, arriving myonuclei move to the center of the forming myotube, an event that is known as myonuclei centration. Interestingly, studies have shown that myonuclei are prepared for their movement even before fusion occurs. To initiate, Partitioning defective 6-β (Par6β) and the GTPase Cdc42 are relocated to the NE, where together with the dynein, they form a complex which is necessary for the recruitment of the dynactin, a microtubule-binding protein, to the NE of differentiated myocytes. This dynactin recruitment is necessary for the dynein/dynactin/MTs complex formation. As myocytes fuse, the dynein/dynactin present at each NE will begin to pull the arriving myonucleus using MTs which brings all the myonuclei to the center of myotubes. Manipulation of MT network by stabilizing drugs such as Taxol disrupts myonuclei centration in forming myotubes which suggests that myonuclei centration in early myotubes is mainly dependent on MT network rather than other cytoskeleton elements (Cadot et al., 2012).

B) Myonuclei alignment along myotubes

Shortly after centration, myonuclei will begin to align in the center of myotubes, an event that requires not only the sliding of myonuclei but also a 3D rotatory movement.

Post fusion, the nuclear envelope spectrin repeats protein 1 (Nesprin-1), one of the main members of the LINC complex, will recruit pericentriolar proteins such as pericentrin, pericentriolar material 1(PCM1), and A-kinase Anchoring Protein 450 (AKAP450) to ncMTOC at the NE of centered myonuclei inside myotubes. Knock-down (KD) of either of these proteins perturbs myonuclei alignment *in vitro* (Espigat-Georger et al., 2016; Gimpel et al., 2017). This means that the LINC complex indirectly participates in MT organization and nucleation from NE.

While Nesprin-1 and LINC complex participates in ncMTOC formation and MTs continue to nucleate from NE, Nesprin-1 recruits other MT-associated motor proteins, such as Kinesin Family Member 5B (KIF5B) and dynein to the NE (Espigat-Georger et al., 2016; Gimpel et al., 2017; Wilson and Holzbaur, 2015). The arrival of motor proteins to the NE is in particular essential for proper myonuclei 3D rotation. These proteins will walk on MTs in antiparallel directions (KIF5B toward the growing end and dynein toward the nucleation center) which will generate a rotatory movement for the myonucleus (Wilson and Holzbaur, 2012). KIF5B muscle-specific KO mice present aggregates of myonuclei within myofibers and die shortly after death due to insufficient diaphragm capacity (Wang et al., 2013).

Therefore, maturation of ncMTOC and MT nucleation will generate a pushing force on myonuclei while the presence of motor proteins at the NE will generate myonuclei rotation. Altogether, this will result in separation and alignment of myonuclei in the middle of myotubes.

Following myonuclei alignment, nucleating MTs from the NE of adjacent myonuclei begin to grow in an antiparallel sense which will play a crucial role in myonuclei spreading.

C) Myonuclei spreading in maturing myotubes

As myotubes grow to form myofibers, aligned myonuclei will begin to spread at a mean speed of around 0.27µm/min within the long myotubes (Gache et al., 2017). For this movement, both MTs and LINC complex have been shown to participate through interconnected mechanisms.

For MTs, it has been shown that microtubule-associated protein 7 (MAP7) will bind to, and install, the motor protein KIF5B on MTs. In this complex, both MAP7 and KIF5B attach to MTs, but on two antiparallel chains. MAP7 will stably attach to one MT while KIF5B will slide toward the growing end of the anti-parallel MT. As MTs continue to nucleate from the NE, the movement generated by this sliding on the anti-parallel MT simultaneously results in MT-dependent myonuclei spreading in elongated myotubes (Gimpel et al., 2017; Metzger et al., 2012).

During myonuclei alignment, both Nesprin-1 and Nesprin-2 participate in the recruitment of KIF5B to the NE and LINC complex by binding to the kinesin light chain (KLC), another regulatory mechanism necessary for KIF5B-dependent myonuclei spreading on anti-parallel MTs (Wilson and Holzbaur, 2015). KO of either Nesprin-1 or Nesprin-2 disrupts KIF5B recruitment to the NE and results in aggregated myonuclei within myotubes (Stroud et al., 2017).

Several other MT-associated proteins have been described to affect myonuclei spreading within myotubes. Downregulation of different members of the kinesin and dynein family of proteins affects myonuclei movement at different levels during myonuclei alignment. While some such as KIF12A, KIF27, dynamin-2 (DNM2), or dynein intermediate chain (Dync1i2) (in addition to several other members of each family) have been shown to affect myonuclei speed or their time in motion during their alignment in myotubes, others, such as KIF1C, KIF9 and KIF2B have been shown to regulate myonuclei spreading and alignment without causing any changes in myonuclei speed parameters (Gache et al., 2017). These results indicate a vaster and more complex role of MTs and their associated proteins network in proper myonuclei movement during myotubes maturation. However, the underlying mechanism behind each of these regulators is yet to be defined.

D) Myonuclei peripherization in developing myofibers

While myonuclei movement within myotubes is a direct MT-dependent process, their movement to the periphery of myofibers is known to be a secondary result of myofibrils formation and occurs at different steps.

Indeed, with myofibers development, the cytoplasm will begin to be filled with sarcomeric proteins. As chains of sarcomeres tightly joint together and form myofibrils within myofibers, the tightening of free space between myofibrils, in addition to their contraction, will squeeze myonuclei between myofibrils toward the periphery of myofibers. During this step, Nesprins have been shown to recruit actin and N-WASP (the actin polymerization factor) to the vicinity of the NE, a process that results in actin nucleation and organization (Falcone et al., 2014). Actin nucleation will further impact desmin organization. As a consequence, desmin intermediate filaments will begin to crosstalk myofibrils which will zip up the sarcomeres and result in myofibrils formation (Roman et al., 2017).

During myofibrillogenesis, nuclear lamina plays an essential role in the maintenance of myonuclei rigidity and structure as myonuclei are squeezed to the periphery of myofibers. Once at the periphery, the tightness of space available between myonuclei and myofibers plasma membrane will result in the reduction of myonuclei sphericity and their flattening at the periphery of myofibers (Roman et al., 2017).
Exceptionally, a recent study shows that secreted fibronectin from neighboring fibroblasts activates the α5-Integrin receptor in forming myofibers. This results in a cascade activation of the FAK-Src signaling pathway and downstream actin nucleation, which as explained before, participates in desmin organization and myofibrils crosslink (Roman et al., 2018). This study has opened a new window on regulatory mechanisms of myonuclei movement and positioning

during myofibers formation, pointing to the importance of extracellular environment, stiffness, and signaling, hand to hand with intracellular molecular changes.

E) Myonuclei anchoring at the periphery of myofibers

As mentioned before, myonuclei are found evenly spaced at the periphery of myofibers, with exception of a few myonuclei that form clusters under NMJs or in the vicinity of MTJs (Perillo and Folker, 2018).

Different proteins have been cited to be important in the maintenance of myonuclei peripheral positioning, however, for most of them, the exact mechanism behind their regulatory role remains unidentified.

Mutation in spectrin repeat containing nuclear envelope protein 1 (Syne-1) results in disrupted peripheral myonuclei organization. It has been shown that Syne-1 uses its KASH domain to couple to myonuclei (Zhang et al., 2007). The fact that Syne-1 bears an actin-binding domain could suggest that Syne-1 regulatory role on myonuclei positioning is dependent on the actin cytoskeleton. In addition, it has also been shown that SUN domain-bearing proteins, Sun1 and Sun2, mutually participate in myonuclei peripheral distribution. Their double knock-out (KO) results in disorganized myonuclei at the periphery of myofibers (Lei et al., 2009). Interestingly, Sun-bearing proteins have been shown to bind to KASH-bearing proteins at the NE (Starr and Fischer, 2005). This could suggest a more complex role for Syne-1 and Nesprins (as KASH domain baring proteins) in addition to Sun1, and Sun2 (as SUN domain baring proteins) in peripheral myonuclei positioning.

It is important to know that in mammalian myofibers, MTs form a dense astral cage around the peripheral myonuclei and are exceptionally dense at the junctional zones, which implies their potential regulatory role in myonuclei positioning at the periphery of myofibers (Jasmin et al., 1990; Ralston et al., 1999). However, little is known about MT network participation in final myonuclei positioning in mammalian myofibers. What is known, from *Drosophila* myofibers, is that Nesprin-1 is important for proper MT cage formation around myonuclei and therefore myonuclei positioning. At the same time, Nesprin-1 is known to co-operate with spectraplakin and microtubules end binding protein 1 (EB1) to provide elasticity to the peripheral myonuclei, a notion important for the maintenance of myonuclei shape, and therefore, chromatin organization (Wang et al., 2015).

Intermediate filament desmin is another protein that has been shown to interact with plectin-1 and participate in myonuclei maintenance at the periphery of myofibers. Loss of myonuclei anchoring at the periphery of myofibers can be observed in models with disrupted desmin organization (Chapman et al., 2014; Konieczny et al., 2008). It is interesting to know that myonuclei have been shown to preferentially locate near blood vessels at the periphery of myofibers. However, while disruption of the desmin intermediate filaments network results in disorganized myonuclei, it does not affect the close positioning of myonuclei to blood vessels,

which leaves the mysterious mechanism and reason behind myonuclei affection for blood vessels unsolved (Ralston et al., 2006).

F) Myonuclei aggregation

Clustered myonuclei under NMJ or close to MTJ are particularly important since they address local transcriptional needs of the myofiber and monitor muscle excitation and contraction (Roman and Gomes, 2018).

As previously described, both NMJ and MTJ begin to form and structure during embryonic stages, which makes it difficult to understand the exact mechanism responsible for myonuclei aggregation in the vicinity of these cell-cell junctions.

While almost no data is available on myonuclei organization at MTJ in mammalian cells, our current knowledge of post-synaptic myonuclei organization at NMJs is based on clinical observations from patients or based on murine KO models. Indeed, patients with mutations in Nesprin-1 or SUN proteins present defeats in myonuclei aggregation under NMJs. The same phenotype has been observed for mouse mutant models confirming the importance of these proteins in post-synaptic myonuclei organization. This can suggest the implication of the LINC complex in post-synaptic myonuclei organization (Chapman et al., 2014; Lei et al., 2009). In addition, while only Syne-1 was shown to participate in non-synaptic myonuclei organization through its KASH domain, both Syne-1 and Syne-2 KO models present a lost post-synaptic myonuclei clustering (Zhang et al., 2007).

In *Drosophila* myofibers, dynein and kinesin have been shown to manage the distance between myonuclei specifically close to NMJs, while the KASH-domain protein of *Drosophila,* Klar, has been shown to organize the distance between myonuclei at both NMJs and MTJs (Perillo and Folker, 2018). Whether these mechanisms are conserved in mammalian myofibers has to yet be defined.

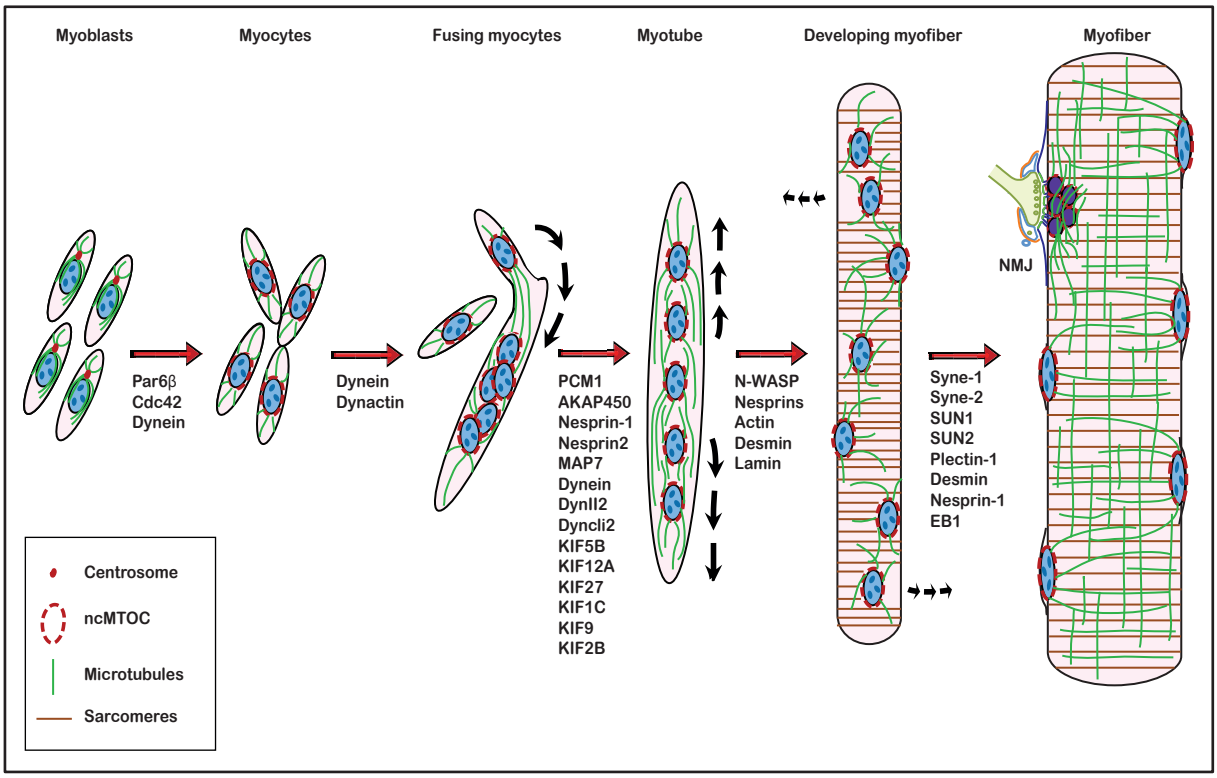

Figure 14: Illustration of stepwise myonuclear movement during myogenesis.
Global overview of myonuclei positioning synchronized with major changes in cytoskeleton during myogenesis from mononuclear myoblasts to mature myofibers (black arrows show the direction of myonuclei movement). In myoblasts, MTs are nucleated from the centrosome. As differentiation starts, myocytes prepare themselves for fusion. During this step, non-centrosomic MTOCs begin to form at the NE. In fusing myocytes, MT and dynein-dependent myonuclei centration gather all the myonuclei in the center of the forming myotube. Next, different members of Dyneins and Kinesins family, in addition to LINC complex proteins such as Nesprins, participate in myonuclei alignment in the middle of the myotubes and in their spreading as myotubes grow. In developing myofibers, sarcomeres crosslink mediated by proteins such as desmin results in the formation of myofibrils within myofibers. The tightness of space between forming sarcomeres in addition to myofibrils contraction once the sarcomeres are formed squeeze myonuclei to the periphery of myofibers. In mature myofiber, myonuclei can be found regularly spaced at the periphery or clustered under NMJ, in direct contact with cytoskeleton components such as MTs and sarcomeric desmin.

3) Myonuclei movement in myofibers during stability, muscle tear, or muscle regeneration

What happens when mature myofibers are formed? Are myonuclei stable at the periphery? Or do they move, either spontaneously and regularly or under special circumstances? The answer to these questions depends greatly on myofibers' status.

Live imaging of myonuclei *in vivo* in intact healthy skeletal myofibers has shown that myonuclei are stable and do not move even when filmed for several days (Bruusgaard et al., 2003). The same study, which follows myonuclei positioning by intramuscular injection of labeled DNA, describes a regularly-spaced stationary positioning for myonuclei at the periphery of myofibers and reports a stable ratio between myonuclei density to myofiber cytoplasm (referring to the myonuclear domain which is exclusively discussed in the following section). However, a more recent study shows that on *ex vivo* isolated live myofibers issued from WT mice, myonuclei move slightly at the periphery of myofibers with a speed around 0.027µm/min (almost ten times slower than myonuclei speed during myonuclei alignment in myotubes *in vitro*) (Iyer et al., 2017). Together, these studies suggest a rather stable positioning with low movements for myonuclei at the periphery of healthy myofibers.

Interestingly, the later study has also described an increase in myonuclei velocity in myofibers of myopathic mice (Iyer et al., 2017). Duchenne muscular dystrophy (DMD) is a progressive myopathy which results in severe muscle wasting and premature death. DMD occurs due to mutations in the gene coding for dystrophin, a transmembrane protein that couples the cytoskeleton to the extracellular matrix through myofibers plasmalemma (Duan et al., 2021). In this study, myonuclei at the periphery of isolated myofibers from DMD mice (known as MDX) are shown to move more frequently and at a greater speed compared to WT myonuclei (Iyer et al., 2017). It is interesting to know that MDX mice exhibit disorganized MTs and reduced Nesprin-1 expression (Belanto et al., 2014; Iyer et al., 2017). This could suggest that the LINC complex (through Nesprin-1) and MTs participate in myonuclei maintenance at the periphery of mature healthy myofibers.

Another example of a situation leading to myonuclei movement post myofibers formation could be muscle regeneration. As described before, muscle regeneration is accompanied by proliferation and fusion of MuSCs which results in the presence of central myonuclei within regenerating myofibers. It is known that following final tissue repair, the number of central myonuclei will gradually reduce, suggesting the movement of the newly accreted myonuclei to the periphery of myofibers (Forcina et al., 2020; Fukada et al., 2022). However, the mechanisms behind this particular myonuclei movement remain completely unknown. Is this an inactive process, due to the realignment of sarcomeres and new myofibrils formation which would squeeze the myonuclei to the periphery of myofibers just like during myogenesis, or is there active molecular machinery regulated by cytoskeleton elements that set the myonuclei positioning post-regeneration have to be yet determined.

But what happens if small muscle tears occur? Do myofibers go through the trouble of regeneration only to repair a small fissure? Several studies have shown that myonuclei number

will increase as hypertrophy happens following continuous exercise (Dungan et al., 2019; Goh et al., 2019; Masschelein et al., 2020). This is generally linked to muscle tearing due to strong physical activity and myofibers rebuilding by MuSCs. However, a very recent study has challenged this question by inducing micro-damage on *ex vivo* isolated myofibers and *in vitro* developed myofibers. In this study, they show that myofibers can repair small muscle tears in a mechanism independent of MuSCs activation and surprisingly dependent on myonuclei movement (Roman et al., 2021). They indicate that following a small local injury, the closest peripheral myonuclei will move to the injury site and participate in myofiber repair. This study describes myonuclei movement to the injury site *in vivo* following eccentric exercise in addition to movement to the injury site *ex vivo* and *in vitro* following myofibers punctual laser damage. Interestingly, the mechanism behind this myonuclei movement is shown to be regulated by dynein through the MT network, indicating the existence of a MT-dependent myonuclear movement post myonuclei anchoring at the periphery of myofibers. Whether other motor proteins participate in this type of myonuclei dynamic remains unknown for the moment.

Thus, while myonuclei were thought to be fixed at the periphery of myofibers, recent studies claim that myonuclei stationary depends on myofibers' status. Yet the exact molecular machinery monitoring myonuclei movement in mature myofibers has to be discovered.

4) Myonuclear domains: nuclear accretion, muscular hypertrophy, and muscular atrophy

The myonuclear domain refers to a theoretical amount of cytoplasm that can be supported by myonucleus (Hall and Ralston, 1989). This theory tries to answer different questions regarding myonuclei within myofibers, such as why are they this numerous and regularly arranged.

During the past decades, many studies have been dedicated to exploring the correlation between muscle fiber size and myonuclei number. It has been long established that during post-natal development, muscle size grows in parallel with new myonuclei accretion due to MuSCs proliferation and their fusion with growing myofibers (Burleigh, 1977; Cardasis and Cooper, 1975; Moss, 1968). In addition, physical activity can induce local muscle damage or “muscular tears”, which will result in muscle hypertrophy, accompanied by increased myonuclei number due to MuSCs activation independent of muscle regeneration (Rosenblatt et al., 1994; Roy et al., 1991; Timson, 1990). Interestingly, it has been shown that myonuclei accretion precedes myofibers hypertrophy in training muscles (Kadi et al., 1999). Suggesting that arriving myonuclei participate in increasing the volume of the myofiber. These pioneer studies are followed by more recent studies which confirm the myonuclei accretion before muscle hypertrophy and suggest a restricted diffusion limit for myonuclei products (RNAs and proteins) within the myofibers cytoplasm (Abou Sawan et al., 2021; Crameri et al., 2007; Denes et al., 2021; Goh et al., 2019; Hyldahl et al., 2014; Pavlath et al., 1989; Ralston and Hall, 1992). Together, these studies are concordant with the myonuclear domain theory and suggest that hundreds of myonuclei are dispensed precisely and regularly within the myofiber to simultaneously support limited zones of cytoplasm and ensure correct myofibers functionality.

However, the myonuclear domain theory gets a bit challenged when we look at muscular atrophy. Hypothetically, one could expect a loss of myonuclei following muscular atrophy to maintain the proposed myonuclei vs cytoplasm ratio. This idea was supported during the previous decades since the loss of myonuclei was described following muscular atrophy and this myonuclei loss was suggested to be a result of individual myonuclei apoptosis (Adhihetty et al., 2007; Allen et al., 1997, 1996; Alway et al., 2003; de Castro Rodrigues and Schmalbruch, 1995; Viguie et al., 1997). However, more recent studies have suggested that the previously detected nuclear apoptosis was due to the presence of apoptotic cells in the muscle microenvironment and that myonuclei number remains untouched following muscular atrophy (Bruusgaard and Gundersen, 2008; Hansson et al., 2020). Another contradictory phenomenon against the myonuclei apoptosis hypothesis is the stability of myonuclei number following age-related atrophy known as sarcopenia (Manta et al., 1987). In contrast, the absence of myonuclei accretion, due to the prevention of MuSCs fusion with myofibers, is linked to inhibition of myofibers growth and is shown to follow a sublinear rule (Cramer et al., 2020; Darr and Schultz, 1989; Hansson et al., 2020; Murach et al., 2017). So reduced accretion results in smaller fiber size, but muscular atrophy does not reduce myonuclei number.

Therefore, while the positive correlation between myonuclei accretion and fiber hypertrophy agrees with myonuclear theory, the stability of myonuclei number per myofiber following muscular atrophy remains an unsolved puzzle.

5) Myonuclei and myopathies

Peripheral myonuclei positioning has physiological importance in myofibers. This is highlighted by the presence of mispositioned or central myonuclei in different myopathies and by studies on myofibers from the *Drosophila* model which directly correlate the mispositioning of myonuclei to myofibers dysfunction (Auld and Folker, 2016; Folker and Baylies, 2013; Metzger et al., 2012).

In that regard, one example would be centronuclear myopathies (CNMs), a group of inherited genetic disorders distinguished by the presence of central myonuclei within myofibers (Jungbluth et al., 2008). Patients with CNM present heterogeneous phenotypes, which can be muscular atrophy and weakness with age or early respiratory failure post birth. The main genes affected in CNMs are *BIN1*, coding for bridging integrator-1 (BIN1) protein, *DNM2* coding for dynamin-2 (DNM2) protein, and *MTM1*, which codes for Myotubularin 1 (MTM1) protein. All three proteins can be detected at the junction between myofibers T-Tubules and SR and are involved in membrane remodeling (Jungbluth et al., 2008; Romero and Bitoun, 2011). In addition, MTM1 has been shown to bind to desmin and participate in its organization, while BIN1 has been shown to participate in N-WASP activity, actin nucleation, and sarcomeres organization (Falcone et al., 2014; Hnia et al., 2011). Indeed, patients bearing mutations in any of these genes present defects in both the desmin network and T-Tubules organization (Cowling et al., 2011; Dowling et al., 2009; Hnia et al., 2011; Romero and Bitoun, 2011; Toussaint et al., 2011). In correlation, studies on mouse and zebrafish models have linked the T-Tubules disorganization to dysfunctions in myofibers contractility and ECC (Al-Qusairi et al., 2009;

Cowling et al., 2011; Dowling et al., 2009; Falcone et al., 2014; Lee et al., 2002; Prokic et al., 2020; Razzaq et al., 2001; Toussaint et al., 2011). As previously mentioned, sarcomeres formation and myofibers contraction during myogenesis are necessary for peripheral myonuclei positioning (Falcone et al., 2014; Roman et al., 2017). Thus, the central myonuclei positioning in these CNMs could be due to defective contraction and reduced peripherization of myonuclei, in addition to reduced force to keep the myonuclei at the periphery of myofibers due to disorganized sarcomeres. Mispositioned myonuclei can be observed in various other myopathies. Desminopathy refers to a group of genetic diseases caused by mutations in the desmin gene, which results in the formation of desmin aggregates within the cell. In skeletal muscle, this results in myofibrils disorganization which is accompanied by mispositioned myonuclei (Clemen et al., 2013). Emery-dreifuss muscular dystrophy (EDMD) is another group of myopathies in which mispositioned myonuclei can be found following mutations in genes coding for NE proteins such as Nesprin-1 and Nesprin-2, SUN1, and SUN2 or nuclear lamins (Heller et al., 2020). What these myopathies have in common, in addition to mispositioned myonuclei, is muscular atrophy and weakness. The mispositioning of myonuclei observed in any of the mentioned myopathies can result in disequilibrated myonuclear domain along myofiber and in turn improper protein production. In addition, the difference in pressure at the NE between peripheral and central myonuclei can affect nuclear mechanotransduction and chromatin organization. For example, mutations in lamin have been linked to nuclear deformation and genes expression alteration (Davidson and Cadot, 2021). Therefore, the contribution of the altered myonuclear domain and nuclear mechanotransduction in the development of each of these myopathies remains an open case.

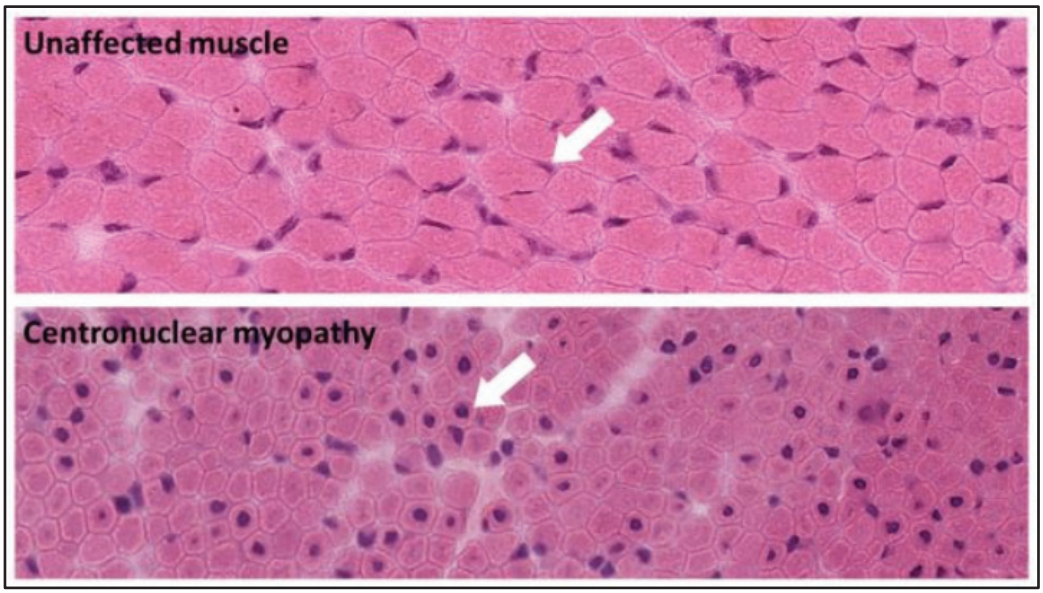

Figure 15: Representative photos of peripheral and central myonuclei positioning.
Example photos from cross-sectioned skeletal muscle biopsies from healthy and CNM diagnosed individuals, reflecting the proper myonuclei positioning at the periphery of healthy myofibers (upper panel) compared to central myonuclei positioning in myofibers from a CNM patient (lower panel). Muscular atrophy can also be noticed in CNM patients myofibers. Figure adapted from (https://www.musculardystrophyuk.org/book/export/html/6807).

6) Identification of new regulators of myonuclei positioning in myofibers

As previously mentioned, in order to gain their peripheral positioning, myonuclei are constantly moved during myofibers formation. We know that during early steps, these myonuclei movements are dependent on MTs and different MAPs such as MAP7 and KIF5B (Cadot et al., 2012; Gache et al., 2017; Gimpel et al., 2017; Metzger et al., 2012). Interestingly, MTs form a dense cage around the peripheral myonuclei in mature myofibers, suggesting a potential role for MTs network in the maintenance of myonuclei positioning (Ralston et al., 1999). Identification of the actors participating in peripheral myonuclei positioning can help in understanding the irregulated mechanisms which lead to myonuclei mispositioning in different myopathies.

To address this hypothesis, a large screen has been done in the team of Dr. Gache, looking for new MT binding proteins with a potential role in myonuclei positioning during myofibers development or at the periphery of myofibers (Figure 16) (Couturier and Gache, 2017). To do so, primary myoblasts were isolated from WT mice pups and were maintained in culture until the development of immature myotubes *in vitro*. Sequential steps of this culture method consist of the application of a thick Matrigel layer onto myotubes in addition to supplementing neuronal Agrin to the culture medium. By maintaining myotubes for up to ten days on culture, this technique permits the development of mature contractile myofibers with peripherized myonuclei *in vitro* (Falcone et al., 2014). To purify MT-related proteome from immature myotubes and mature myofibers, the MT network was stabilized by Taxol and total protein extracts from myotubes or myofibers were centrifuged through a glycerol cushion as described before (Gache et al., 2007). By performing mass spectrometry, 2247 total proteins were detected which were narrowed down to 240 candidates based on their representation in the extract and their known molecular function. These 240 candidates were divided into the three following categories: proteins detected specifically in myotubes, proteins detected specifically in myofibers, and proteins shared between myotubes and myofibers (Couturier and Gache, 2017).

Among the shared proteins, the huge spectraplakin microtubule actin cross-linking factor 1 (MACF1) was highly present in both myotubes and myofibers. MACF1 was selected as a potential candidate with a role in peripheral myonuclei positioning in mature myofibers based on the data available in the literature which are introduced in the following section.

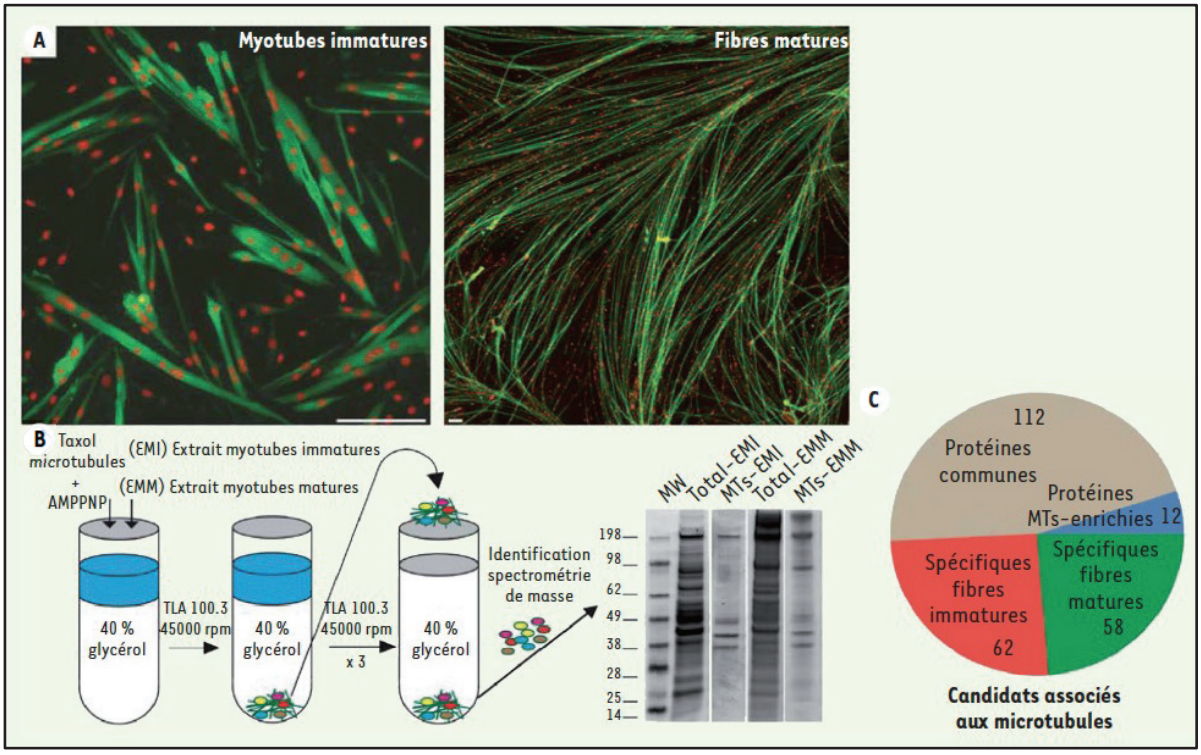

Figure 16: Isolation of MT-related proteome of myotubes and myofibers.
(A) representative photos from *in vitro* immature myotubes and mature myofibers stained for nuclei (red) and Myosin Heavy Chain (MHC, green). Scale bars = 150µm. (B) sequential steps of the biochemical approach used to purify the MT-related proteome from myotubes and myofibers. (C) proportional representation of the selected 240 MT-related proteins. Figure adapted from (Couturier and Gache, 2017).

A) Microtubule Actin Cross-linking Factor 1

MACF1 was first described as ACF7 for Actin Crosslinking Family 7 due to the homology of its actin-binding domain (ABD) with Spectrins. The gene coding for MACF1 was located on chromosome 1 and was hypothesized to give rise to huge proteins (Byers et al., 1995). A year later, the mouse homolog was described to be present on chromosome 4. Its mRNA was highly expressed in lungs, nervous system, and skeletal or cardiac muscles, with probabilities of tissue-specific isoforms due to the presence of several promoters (Bernier et al., 1996). It was only in 1999 that a change of name from ACF7 to MACF1 was suggested, as mouse MACF1 was revealed to bind to, and stabilize, microtubules through a domain present at its C-terminal, in addition to binding to actins through its ABD present at its N-terminal (C. L. Leung et al., 1999; Sun et al., 1999). In the past two decades, MACF1 has been studied in a variety of tissues and in the context of different cellular events, using *in vitro* or tissue-specific *in vivo* models, as the total MACF1 KO mice are embryonically lethal (Chen et al., 2006).

A1) MACF1 family

MACF1 is a member of the Spectraplakins cytoskeleton-linkers family. Spectraplakins are a small group of two huge proteins with high structural homology, known as MACF1 and Bullous pemphigoid antigen 1 (BPAG1 – also known as MACF2 and Dystonin) in mammalian cells, Magellan (also known as macf1) in Zebrafish, Shortstop (Shot – orthologue to MACF1) in *Drosophila* and Variable Abnormal morphology 10 (VAB-10 – orthologue to MACF1) in *C. elegans*. Structurally, these proteins share domains with both Spectrins and Plakins family members, giving them the possibility to bind actin and intermediate filaments. In addition, these huge proteins bear a special domain which allows them to bind to MTs, and therefore, they are able to interconnect all members of the cytoskeleton (Zhang et al., 2017).

Spectrins gather some of the most well-studied cytoskeleton-associated proteins named Dystrophin, Utrophin, α-actinin, Nesprins, and α-/β-spectrin. Members of this family are characterized by a central spectrin repeat domain (SRs) which gives them the possibility to dimerize in parallel or anti-parallel manners. SRs are also known to provide flexibility to the proteins and to separate the N-terminus and C-terminus of the protein which bind to different partners (Liem, 2016).

Plakins family includes Plectin, Desmoplakin, Envoplakin, Periplakin, and Epiplakin. Compared to Spectrins, these proteins are bigger, vertebrate-specific, and have two signature domains: Plakin domain (PD) and Plakin (or Plectin) Repeats Domain (PRD).The PD is a series of spectrin repeats with a Src-homology 3 (SH3) domain in the middle. PD is important for the interaction of all the members, except Epiplakin which lacks PD, with desmosomes and hemidesmosomes. Each PRD is a chain of 38 amino acids that have been repeated around 4.5 times. Based on the sequence, this domain itself can be further subcategorized into A-, B-, and C-PRD classes. These PRDs permit the Plakins, except for Periplakin which lacks the PRD, to interact with intermediate filaments. The strength of this interaction is coherent with the number of PRD (Hu et al., 2018).

A2) MACF1 structure

MACF1 is a huge protein with two main isoforms of 680 and 800kD (Figure 17) (Gong et al., 2001; Lin et al., 2005). Starting from N-terminal, the largest MACF1 isoforms contain two calponin homology (CH) domains, known as CH1 and CH2, which form the ABD of the protein (Bernier et al., 1996; C. L. Leung et al., 1999). The activity of this domain is regulated by the phosphorylation of a tyrosine residue within the CH2 domain which results in conformational changes and allows MACF1 to interact with actin (Bernier et al., 1996). However, due to alternative splicing or the presence of several transcription initiation sites within the *MACF1* gene, the smaller MACF1 isoforms do not contain the CH domains and are not able to bind to actin cytoskeleton (Gong et al., 2001; Goryunov et al., 2010). As previously mentioned, Spectraplakins inherit their name by bearing domains originally designated to Spectrins or Plakins. Following the ABD, MACF1 contains a PD, which is known to allow protein-protein interactions at cellular junctions (Bernier et al., 1996; C. L. Leung et al., 1999). Interestingly, MACF1 has been reported to be present at the junctions of the intestinal epithelium, however, whether this is dependent on its PD remains to be investigated (Ma et al., 2017, p. 7). The largest MACF1 isoform contains PRDs following its PD (Lin et al., 2005). While in members of the Plakins family, this domain is known to facilitate the interaction of proteins with intermediate filaments, in MACF1, the PRDs have been shown to enable MACF1 association with Golgi complex (Lin et al., 2005). The central region of MACF1 is composed of several long SRs, each containing around 110 to 120 residues (C. L. Leung et al., 1999). These repeats are known to bring flexibility to the structure of MACF1 and give broad responsibility to the protein by allowing its partnership with different proteins involved in cell signaling or cargo trafficking such as Axin from Wnt signaling and P230 from Golgi complex (Chen et al., 2006; Kakinuma et al., 2004). At their C-terminal, all MACF1 isoforms contain two EF-hand domains (EF1 and EF2) followed by a growth arrest specific-2 domain (GAR) and a Glycine-Serine-Arginine repeats domain (GSR) (C. L. Leung et al., 1999; Sun et al., 1999). These domains are essential for MACF1 ability to bind to MTs or interact with MAPs. In fact, structural and functional analyses have revealed that the GAR domain alone is sufficient for MACF1 binding to MTs, while EF domains interaction with MTs requires the presence of adjacent GAR domain (Lane et al., 2017). Complementarily, the GSR domain is able to bind to proteins such as EB1, present at MT growing-ends (Slep et al., 2005). Since the MT binding domain is shared at the C-terminus by all MACF1 isoforms, the capacity of this giant protein to cross-link MTs to actins depends on the presence of CH domains at the N-terminal of the isoform.

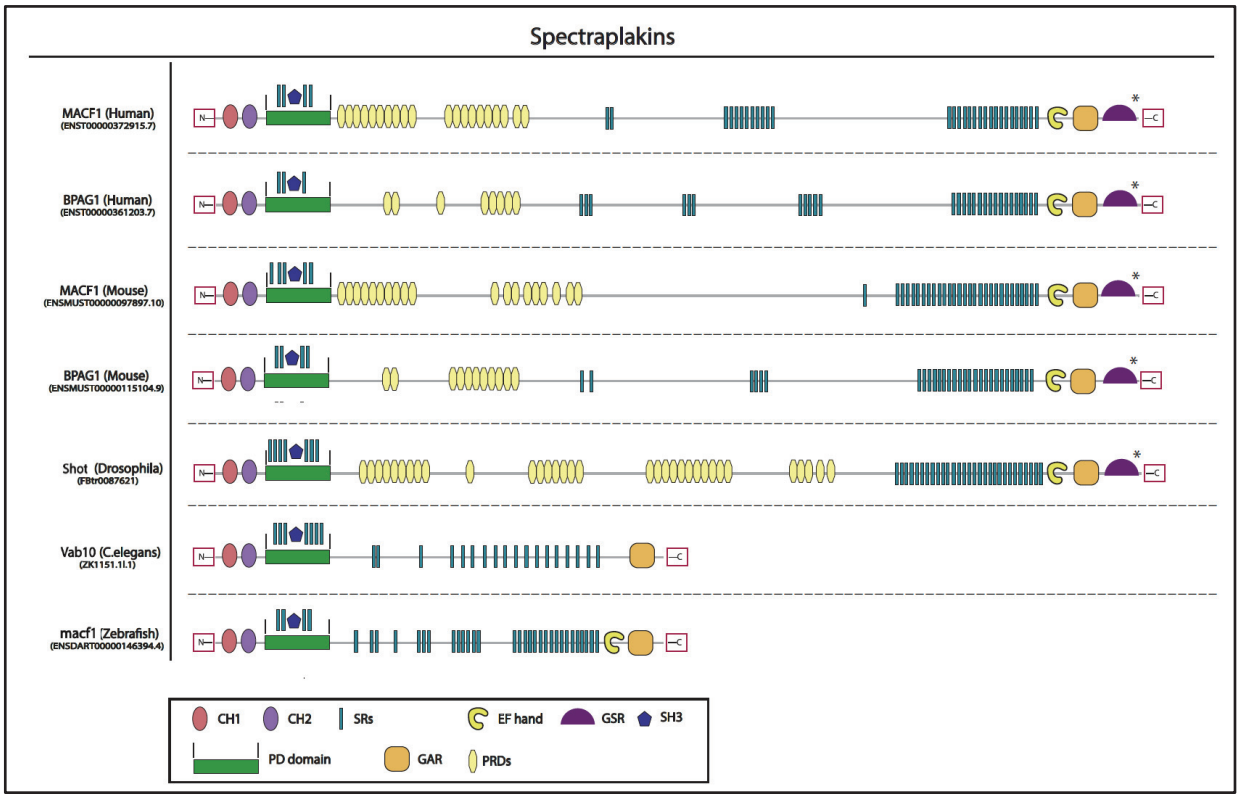

Figure 17: Illustration of Spectraplakins domains.
Representative structure of Spectraplakins designed according to information provided by Ensembl, UniProt, and SMART databases. The corresponding Ensembl reference ID is indicated below each protein (only the largest isoform of each protein is presented). The "*" above the GSR domain signifies its prediction based on literature and not the mentioned databases. Please note that while the length of proteins can be compared to one another or to proteins presented in figure 26, the predicted structures are not set to scale.

A3) MACF1 in skeletal and cardiac muscles

While MACF1 was described highly expressed in skeletal muscle, its role in the tissue was not explored for more than ten years following its discovery. In 2008, in a study focused on the identification of genes differentially expressed between quiescent myoblasts and activated states, the expression of mouse MACF1 was described to increase with skeletal muscle differentiation in the C2C12 skeletal muscle cell line (Sambasivan et al., 2008). A few years later, a case study described a family in Denmark with individuals presenting signs of neuromuscular disorder, including problems in motility, lax muscle, and diminished motor skills associated with a heterozygote duplication in the *MACF1* gene that resulted in reduced protein expression (Jørgensen et al., 2015). Additionally, another case report has described two affected brothers harboring a de-novo missense mutation in the *MACF1* gene with progressive spastic tetraplegia, dystonia, joint contracture, feeding difficulty, and developmental delay (Kang et al., 2020).

In *Drosophila* larva myofibers, Shot has been shown to protect myonuclei structure from the stress applied by stretching/contraction. In these myofibers, Shot actively participates in myonuclei elasticity, by regulating the distribution of *Drosophila* Nesprin. At the same time, Shot participates in myonuclei rigidity by collaborating with EB1 to organize a dense perinuclear MT network. Thereby, ablation of Shot from myofibers results in changes in myonuclei morphology in *Drosophila* (Wang et al., 2015). This suggests that Shot/MACF1 could play an essential role in the control of mechanical stress transmission to myonuclei.

In addition, mouse MACF1 homolog BPAG1 is present at Z-bands of skeletal myofibers and interacts with essential structural proteins, actin, α-actinin, and desmin. In mice cardiac muscle, BPAG1 is not only present at Z- and H-bands, partnering with the same proteins as in skeletal muscles, but also at intercalated discs where it has been shown to connect with Desmoplakin (Steiner-Champliaud et al., 2010). Interestingly, *in vivo* and *in vitro* studies on skeletal muscles from BPAG1 null mice report disrupted myofibril organization, accumulated mitochondria, and muscular weakness compared to control mice (Dalpé et al., 1999). However, cardiac muscle from BPAG1 null mice presents normal actin and desmin organization, suggesting a differential role for the protein between skeletal and cardiac muscles (Boyer et al., 2010).

In 2019, only a few months after the beginning of my thesis project, mouse MACF1 was described to participate in NMJs stability by linking AChRs through the post-synaptic protein Rapsyn and by docking MTs through interaction with EB1 and MAP1b to NMJs (Figure 18). In this study, MACF1 KO mice present fragmented NMJs and muscular atrophy in addition to signs of centralized myonuclei and disorganized mitochondria compared to control mice (Oury et al., 2019). However, it was not clarified how the absence of MACF1 disturbs non-synaptic myonuclei and mitochondria organization and whether these phenotypes depend on disrupted MACF1 interaction with actin, MTs, or both cytoskeleton networks.

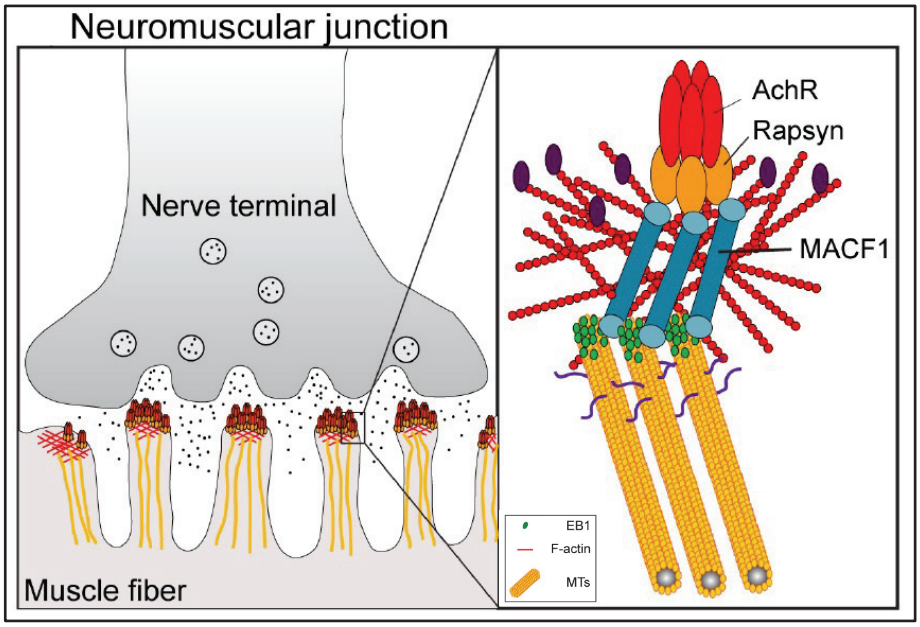

Figure 18: Illustration of MACF1 role at NMJs.
At post-synaptic NMJs, MACF1 links AChRs to MTs through Rapsyn and EB1 proteins and participates in NMJs stability. Figure adapted from (Cusseddu et al., 2021).

Chapter 2: Microtubules from molecules to network in skeletal muscle

I) Cytoskeleton

The cytoplasmic cytoskeleton is mainly composed of (1) actin filaments and actin-associated proteins, (2) intermediate filaments, and (3) microtubules and their microtubules-associated proteins (MAPs). These cytoskeleton elements can be interconnected by specialized proteins, and together, they master a large set of cellular events, from cell division to cellular shape, movement, and fusion, and takes part in subcellular organelles organization, cell signaling, and gene expression (Pollard and Goldman, 2018).

In eucaryotes, the *Actin* genes, codes for one of the most conserved proteins among different species. ATP-binding actin monomers can polymerize to form long two-strand filaments also known as stress filaments (Figure 19). These actin filaments can undergo depolymerization phases and thus are dynamic structures (Pegoraro et al., 2017). Actin filaments are essential for cell shape and structure and create short paths for the movement of motor proteins such as myosin (Pollard, 2016). In skeletal muscle, actin-mediated membrane remodeling is essential for differentiated myocytes fusion (Nowak et al., 2009). In addition, as described previously, actin is one of the main components of sarcomeres in skeletal muscle that promotes myofibers contraction by being a railway for myosin motor proteins (Figure 6). Six different actin isoforms exist, among which the skeletal muscle actin is specifically expressed in skeletal muscle and is the dominant isoform participating in sarcomeres formation (Gunning et al., 2015). The skeletal muscles of skeletal-muscle-actin KO mice are similar to control mice at birth, yet do not grow as control mice, present low muscle strength, and die shortly after birth (Crawford et al., 2002).

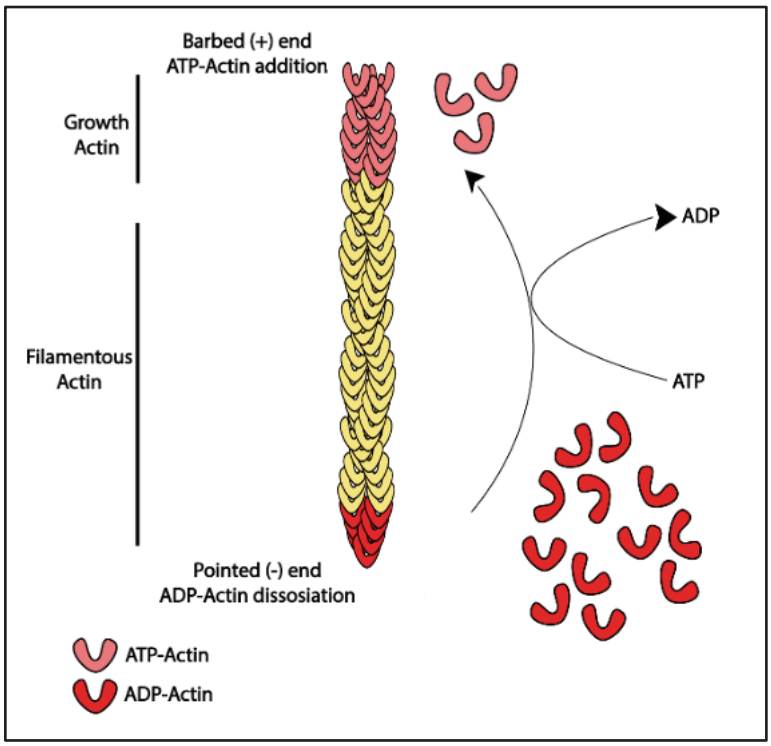

Figure 19: Illustration of actin filaments polymerization and depolymerization. Following expression, actin monomers will bind to, and carry, an ATP molecule that will be used as an energy source during polymerization. Thus, the actin filament is a chain of ADP-actins. These ADP-actins can further be stabilized or dissociate from the filament, events that require specific actin-associated proteins. When separated from the filament, free ADP-actin can re-enter the cycle by exchanging its ADP with ATP.

Intermediate filaments group a variety of proteins including nuclear lamins and cytoplasmic desmin. Compared to MTs and actins, the monomers forming intermediate filaments do not bind nucleotides and are self-assembled in tetrameric subunits to form intermediate filaments which are thicker than actin filaments (Figure 20). They are known to play a critical role in anchoring cytoskeleton members to intercellular junctions (desmosomes) or cell-extracellular matrix junctions (hemidesmosomes) where they play structural roles and participate in signal transduction (Goldmann, 2018). Intermediate filaments are important for many other subcellular organizations, notably rigidity of myonuclei form, myonuclei peripherization, and sarcomeres stability, as described in the first chapter.

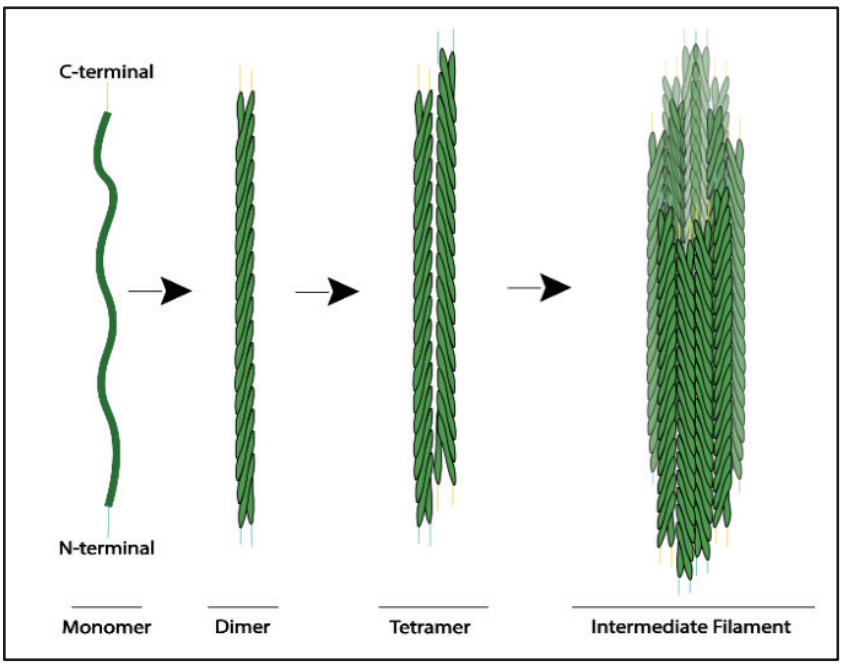

Figure 20: Illustration of intermediate filaments organization. The polymerization of intermediate filaments is a spontaneous process that does not require any type of energy. The monomers will twist together to form the dimers which will bound in an anti-paralleled manner to another dimer and form the tetramers as the basic unit of intermediate filaments. On average, around eight tetramers will round up to form the intermediate filament.

II) From tubulin monomers to MTs

Microtubules are highly dynamic structures that go through constant polymerization and depolymerization, respectively called MT rescue and catastrophe (Figure 21). MTs are made of α- and β-tubulin monomers and are nucleated from microtubule nucleation centers, which can be centrosomic in proliferating cells or non-centrosomic in differentiated cells, for example, myofibers. No matter the nucleation site, MT chains form a fascinating network and serve as a backbone for many cellular structures, and are essential for many cellular events, from the formation of mitotic spindles and chromosome separation during cell division to the organization and movement of subcellular organelles and molecules such as myonuclei during myogenesis, mitochondria, and even RNA. The stability and dynamics of this network depend on a variety of MAPs or post-translational modifications (PTMs) (Figure 27) (Goodson and Jonasson, 2018).

1) Tubulin isoforms and isotypes

In addition to α- and β-tubulin, there exist several other tubulin isoforms, such as γ-tubulin, which is essential for MT nucleation from MT organization centers. While these three isoforms are highly conserved, the δ-,ε-, and ζ-tubulin are specific to species and cells with either cilia or flagella (Findeisen et al., 2014).

In mammalian cells, nine different isotypes can be found for each of the α- and β-tubulin with slight differences in their C-terminal (Sullivan, 1988). In multi-cellular organisms, most cells express multiple tubulins, yet, the proportion of expressing isotypes can vary from one cell to another. For example, the β2-tubulin isotype is highly expressed during spermatogenesis, and platelet cells specifically express β1-tubulin, while skeletal muscle has higher expression of α8-, β5-, and β6-tubulin isotypes (Ludueña and Banerjee, 2008; Michiels et al., 1989; Randazzo et al., 2019). Interestingly, exceeded β6-tubulin expression has been linked to MTs disorganization in DMD myofibers (Randazzo et al., 2019). This could suggest that in addition to tissue-specific expression, the balance of expression of different tubulin isotypes can also have physiological importance. However, little is known about the cell-specific tubulin-isotype-specific gene expression regulation or the particular role/importance of each isotype in different cells' fate. The structural similarities of tubulin isotypes and their capacity to freely dimerize together make it even harder to study the importance of each isotype for each cellular event (Gasic, 2022).

2) MT assembly and structure

To assemble MTs, α- and β-tubulin dimerize and form a linear tubulin protofilaments (McIntosh et al., 2009). Outside a living cell, this dimerization can occur spontaneously in high tubulin concentration (Margolis and Wilson, 1978). However, MT nucleation is a complex process which requires not only the assembly and direction of the nucleation center but also a high amount of energy in the form of GTP (Caudron et al., 2002). This means that within a living cell, MT assembly is strictly monitored and is in direct correlation with the cell's needs, such as during the mitotic process.

Both α- and β-tubulin monomers are bound to a GTP molecule, which they will hold onto even when they dimerize. As the MT nucleation starts, α-tubulin will bind to the nucleation center therefore the β-tubulin will be located at the growing end of the protofilament. In this process, while the GTP bound to α-tubulin remains untouched, the GTP bound to β-tubulin is hydrolyzed to GDP as the dimers repetitively bind together in a head-to-tail fashion and build the protofilaments. In fact, when a new dimer is added to the growing lattice, β-tubulins GTP hydrolysis is activated by the interaction of the catalytic domain of incoming α-tubulin with previous β-tubulin (Caplow, 1992; Caplow and Shanks, 1990; Erickson and O'Brien, 1992). A MT is generally formed of thirteen protofilaments, laterally rounded up in a helical structure where similar subunits of tubulin from neighboring protofilaments interact with one another and form α-α or β-β bounds. This result in the formation of the final MT as a hollow tube with a minus-end located at the nucleation center, a lattice composed of GTP-α-tubulins bound to

GDP-β-tubulins, and a free-growing plus-end (or plus-tip) made of GTP-β-tubulins, known as GTP cap (Goodson and Jonasson, 2018; McIntosh et al., 2009; Metoz et al., 1997).

As previously mentioned, MTs can go through sudden depolymerization, known as catastrophe, followed by a new phase of polymerization, known as rescue (Mitchison and Kirschner, 1984; Walker et al., 1988). MTs continue to polymerize with a slight curve as long as new GTP-bound dimers are available and sit on the GTP cap (Caplow and Shanks, 1996; Chrétien et al., 1995; Drechsel and Kirschner, 1994). However, if the GTP cap is lost, due to hydrolysis or dissociation, MT catastrophe occurs. In the absence of a GTP cap, GDP-β-tubulins, which are more prone to curve and whose interaction with α-tubulin is less stable, begin to peel off from MT lattice and result in the shrinking of MTs (Coombes et al., 2013; Odde et al., 1995). In addition, more recent studies have shown that motor proteins can damage MTs as they move along the MT lattice and can induce MT breakage (Triclin et al., 2021). MT rescue has been described to depend on GTP-islands on MT lattice, which refers to zones on the MT lattice composed of GTP-β-tubulins that have escaped GTP hydrolysis during polymerization (Dimitrov et al., 2008). Thanks to these GTP islands, the reappearance of GTP-β-tubulins at the plus-tip of shrinking MT lattice can stop the catastrophe and restart the polymerization process.

The constant cycles of MT cytoskeleton catastrophe and rescue, allow the cells to adapt their shape in response to environmental changes and to manage their subcellular organelles organization, and thereby activity, in response to internal and external signals. The turnover of these events is under the influence of MAPs, motor molecules, or plus-tip proteins, in addition to tubulins PTMs, which are further discussed in the following sections.

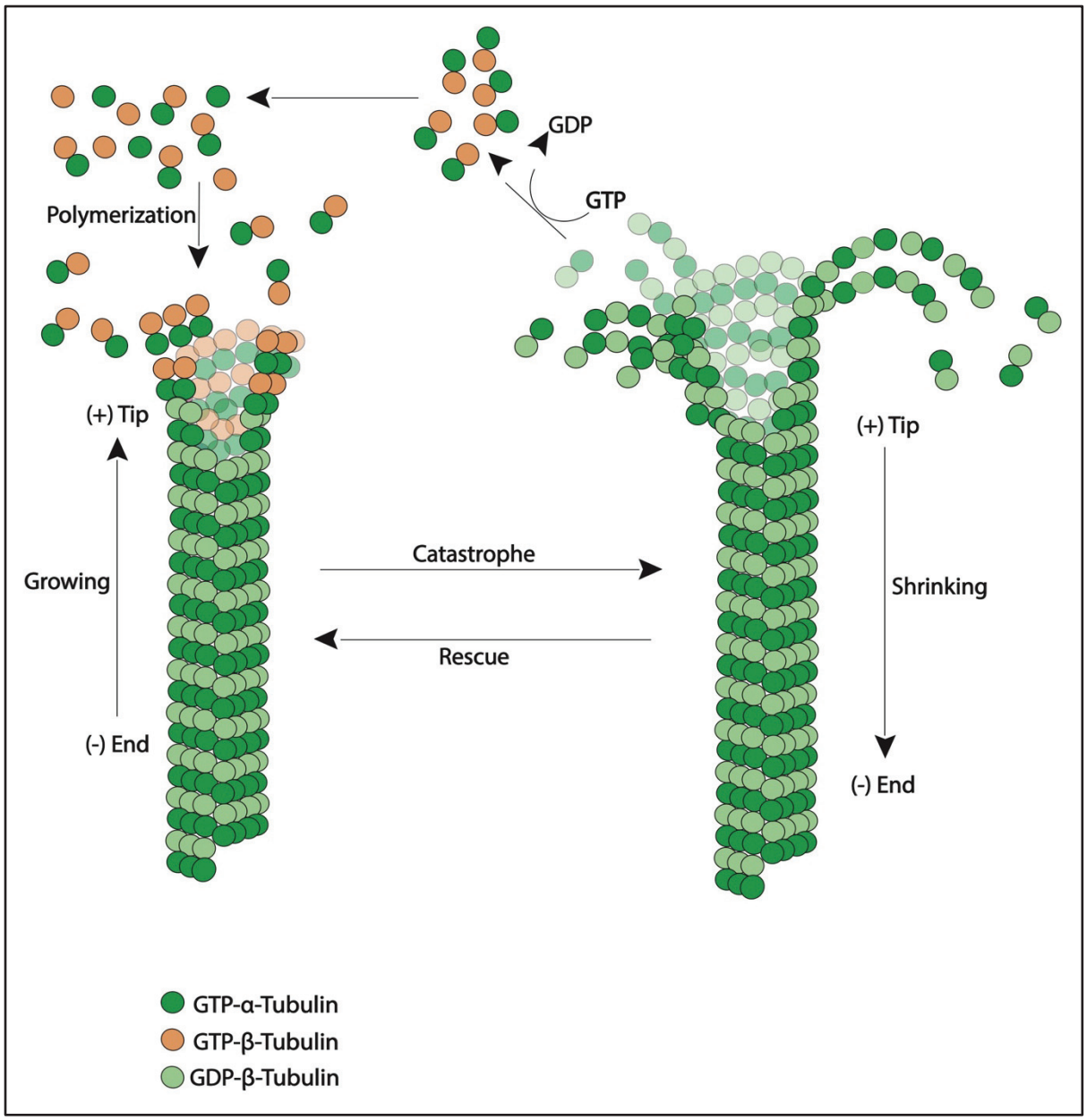

Figure 21: Illustration of MT dynamics.
MT polymerization initiates by dimerization of GTP-α-tubulin and GTP-β-tubulin. GTP-α-tubulin will sit at the nucleation site and therefore GTP-β-tubulin will be at the growing tip. As polymerization continues, new dimers will bind to the lattice in a head-to-tail fashion. In this process, new α-tubulin will catalyze the hydrolysis of the plus-tip GTP to GDP. Therefore, the lattice is made from GTP-α-tubulins bound to GDP-β-tubulins with a growing tip composed of GTP-β-tubulin, termed the GTP cap. If the cap is lost, dimers of GTP-α-tubulin/GDP-β-tubulin will detach from the lattice and result in MT lattice shrinking. These dimers can join back the polymerization cycle once the GDP-β-tubulin exchanges its GDP for GTP. Sudden alterations between MT growing and shrinking are known as MT rescue and catastrophe respectively.

3) MT nucleation

Within a eukaryotic cell, MTs long chains polymerization requires the recruitment of γ-tubulin and its associated proteins, known as γ-tubulin ring complex (γ-TuRC), to the microtubules organization centers (MTOCs) (Farache et al., 2018). Each γ-TuRC is made from seven γ-tubulin small complex (γ-TuSC) which bind and spin in a single-turn helix template (Kollman et al., 2010). Each γ-TuSC itself is made from two γ-tubulin which are individually bound to two different γ-tubulin complex proteins (GCPs). While in simpler organisms such as yeast, GCP2, and GCP3 are the main members of the complex, in higher organisms such as humans, other GCPs (GCP4, GCP5, and GCP6) have been described to be capable of replacing either GCP2 and GCP3 within the γ-TuSC structure (Guillet et al., 2011; Teixidó-Travesa et al., 2012).

However, γ-TuRCs need to be recruited to MTOCs in order to be activated and initiate the nucleation of MTs.

While γ-tubulin and GCPs form the core of γ-TuRC, the γ-TuRC installation process at MTOCs is mediated by other proteins that couple to the γ-TuRCs ring and promote the assembly of γ-TuRC at the MTOC. For example, MOZART1 (MZT1) binds to the GCPs in the base of γ-TuRCs and plays an intermediary role between γ-TuRC and γ-TuRC-tethering proteins (Cota et al., 2016; Lin et al., 2016). In mammalian cells, pericentrin, CDK5 regulatory subunit associated protein 2 (CDK5RAP2), and neural precursor cell expressed developmentally down-regulated protein 1 (NEDD1) are also among the regulators of γ-TuRCs installation at microtubules organization centers (Choi et al., 2010; Haren et al., 2006; Manning et al., 2010). Most of these proteins contain a centrosomin motif 1 (CM1) domain which is suggested to bind to GCP proteins and therefore dock γ-TuRCs to MTOC (Choi et al., 2010; Haren et al., 2006).

Once γ-TuRC is properly formed and installed at MTOCs, α- and β-tubulin will begin to form the tubulin polymers, the MTs.

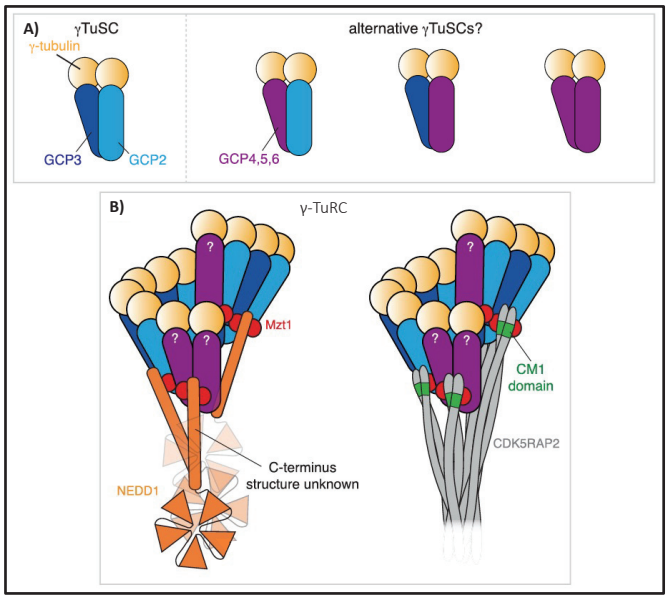

Figure 22: Illustration of γ-TuSC and γ-TuRC.
(A) The conserved organization for γ-TuSC is composed of two γ-tubulins that are bound to GCP2 and GCP3 while alternative γ-TuSC organizations may exist in higher organisms in which one or both GCP2 and GCP3 can be replaced by GCP4, 5 or 6. (B) MZT1 binds to the N-terminal of GCP proteins and joins them to proteins such as NEDD1 or CDK5RAP2 and together they will dock γ-TuRCs to MTOCs. Figure adapted from (Tovey and Conduit, 2018).

4) MT organization centers

As previously mentioned, while centrosomes are the most common and best characterized MTOCs, other cellular organelles such as the Golgi apparatus and the nucleus can also participate in MT nucleation and organization. The switch between centrosomic to non-centrosomic MTOCs depends on cell state and cell type.

A) Centrosomic MTOC

The centrosome is made from two individual centrioles that are perpendicularly positioned to each other. Each centriole itself is formed of nine microtubule triplets which together form a cylindric structure (Figure 23) (Doxsey, 2001). Centrioles are themselves surrounded by pericentriolar material (PCM). The PCM gathers molecules that are necessary for centrosome formation and stability but also γ-TuRC installation at the centrosome. For example, pericentrin and AKAP450 are both known to interact with GCP2 and GCP3, while pericentrin can also interact with NEDD1 from γ-TuRC (Lawo et al., 2012; Takahashi et al., 2002; Zimmerman et al., 2004).

During mitosis, centrosomes are essential for the formation of mitotic spindles, MT astral projections, and thereby proper chromosome separation (Wu et al., 2017). However, during interphase, the centrosome gains a juxtanuclear position within the cell and regulates subcellular organelles positioning and dynamics by supporting MT nucleation and railway formation (Bornens, 2012).

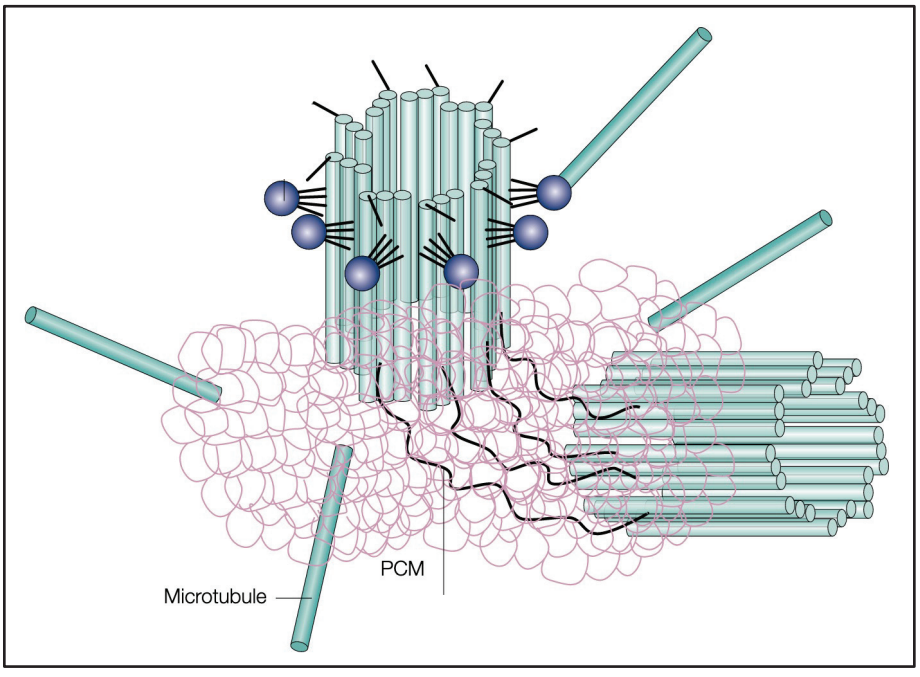

Figure 23: Illustration of centrosome and centrioles.
Schema presenting the perpendicular positioning of two centrioles within the centrosome and the PCM which participate in MT nucleation. Figure adapted from (Doxsey, 2001).

B) Non-centrosomic MTOC

Although centrosome is the most studied MT nucleation center, most differentiated cells in multicellular organisms set up non-centrosomic MT organization center (ncMTOC), the location of which varies depending on cell type (Figure 24).

Studies from *Drosophila* and *C. elegans* epithelial cells have shown that prior to ncMTOC formation, γ-TuRC is released from centrosomic MTOC, and PCMs lose their association with the centrosome (Brodu et al., 2010; Lu and Roy, 2014; Sanchez and Feldman, 2017). In mice keratinocytes, attenuation of MT nucleating activity of centrosome occurs following NEDD1 dissociation from the centrosome during differentiation (Muroyama et al., 2016).

Following dissociation, centrosomal proteins are relocalized to designated ncMTOC sites within the cells.

For example, in human pigmental epithelial cells, installation of γ-tubulin at the Golgi complex is needed for Golgi-centered MT nucleation. When moving, Golgi-nucleated MTs are projected toward the leading edge of these cells and has been suggested to participate in the transport of Golgi complex products within the cell (Efimov et al., 2007).

In mammalian cochlea cells and epithelial cells of colon origin, ncMTOCs are positioned apically under the cell membrane where γ-tubulin can be localized (Meads and Schroer, 1995; Mogensen et al., 2000; Toya et al., 2016; Tucker et al., 1992). In Caco-2 human epithelial cells, these MT apical to basial polarity are important for cells structural stability and subcellular organelles (such as Golgi complex) organization (Toya et al., 2016).

Another example of MT nucleation and organization from ncMTOCs can be differentiated neurons. In these cells, γ-tubulin and γ-TuRC have been shown to nucleate MTs at different centers within the cytoplasm (Sanchez and Feldman, 2017). Interestingly, MTs are homogenously oriented in axons with their plus ends facing the tips, while in dendrites, minus-ends and plus-tips of different MTs can be found randomly oriented (Baas et al., 1988; Berbari et al., 2007; Stepanova et al., 2003). This particular MT organization has been suggested to contribute to polarized trafficking of molecular motors, such as dynein, from axon to dendrites (Kapitein and Hoogenraad, 2015).

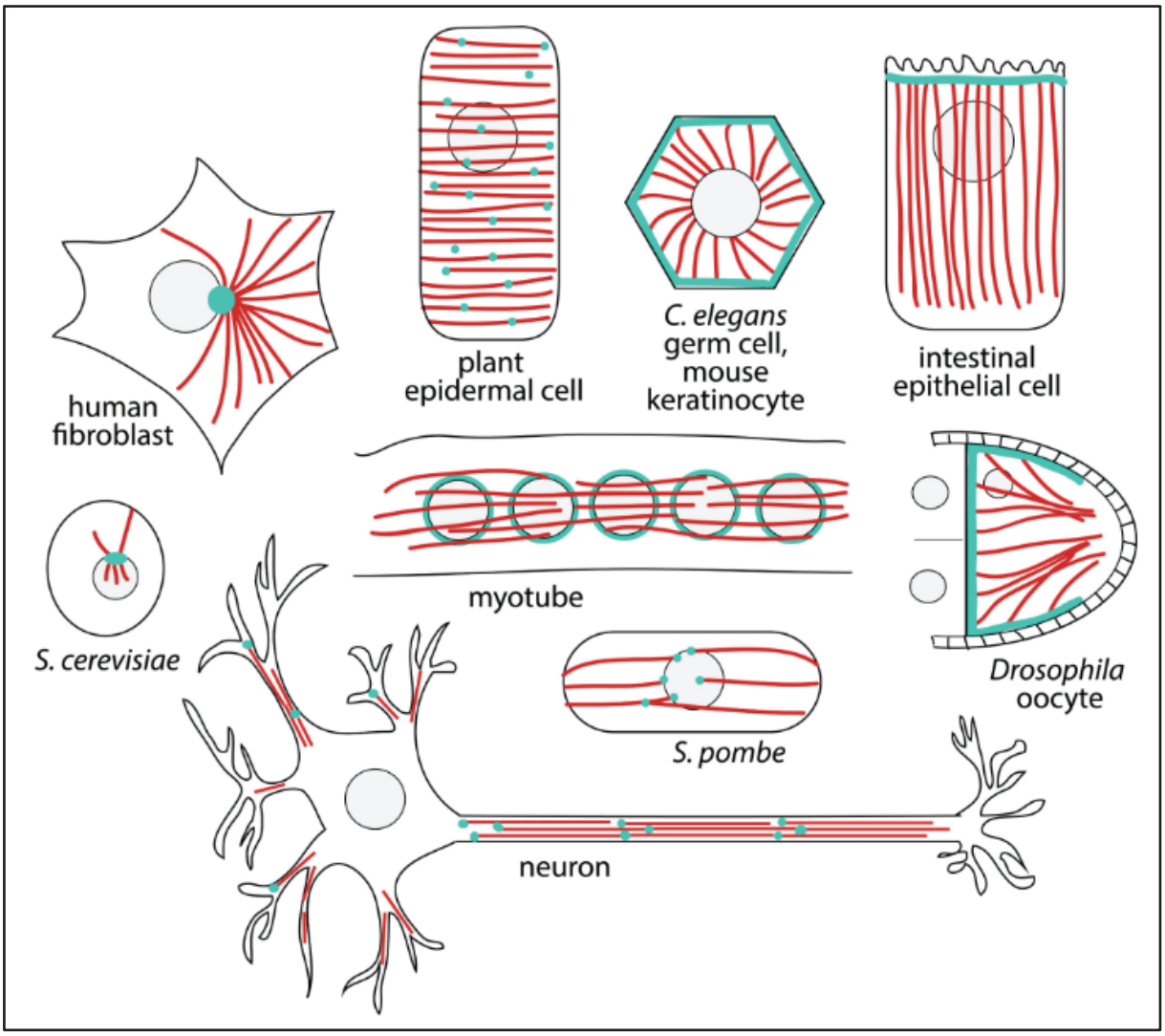

Figure 24: Illustration of MTOCs.
Schema presenting the heterogeneity of MTOCs (presented in blue) between different organisms and even different cell types within the same organism. MTs (presented in red) organization is fundamentally directed by MTOC and differs between MT nucleating from centrosomic MTOCs or ncMTOCs. Figure adapted from (Sanchez and Feldman, 2017).

C) MT organization in skeletal muscle

In proliferating myoblasts, MTs nucleate in a sun-like pattern from the centrosome which is in close contact with the nucleus (Figure 26) (Tassin et al., 1985; Warren, 1974). In these mononuclear cells, the Golgi apparatus is in the vicinity of the nucleus with a polar orientation while the endoplasmic reticulum (ER) is dispersed all around in the cytoplasm in a reticular pattern (Ralston, 1993). It has been shown that in myoblasts MTs are essential for the stability of Golgi apparatus organization (Tassin et al., 1985).

Myoblasts differentiation to myocytes and further myocytes fusion to myofibers is accompanied by relocalization of γ-tubulin, CDK5RAP2, pericentrin, and AKAP450 from centrosomes to NE (Bugnard et al., 2005; Fant et al., 2009; Oddoux et al., 2013; Srsen et al., 2009). In these myotubes, MTs are nucleated and elongated in parallel to one another from NE (Figure 25) (Tassin et al., 1985). In addition, the Golgi apparatus takes a perinuclear positioning and ER forms a thinner longitudinal-like organization all along the myotube (Lu et al., 2001; Ralston, 1993).

As development continues, centrioles gradually disappear and centrosomes get almost undetectable (Connolly et al., 1986; Przybylski, 1971; Ralston, 1993; Tassin et al., 1985). In myofibers, MTs continue to majorly nucleate from NE and form a grid-like transversally and longitudinally crossed network all along myofiber (Figure 25-26) (Ralston et al., 1999). In this grid-like network, longitudinal MTs align with myofibrils along myofiber, while transversal MTs align with sarcomeres Z-disks. Interestingly, dystrophin, which is mainly known for connecting sarcomeres to myofibers membrane, has been shown to bind MTs and guide MT organization in myofibers (Prins et al., 2009).

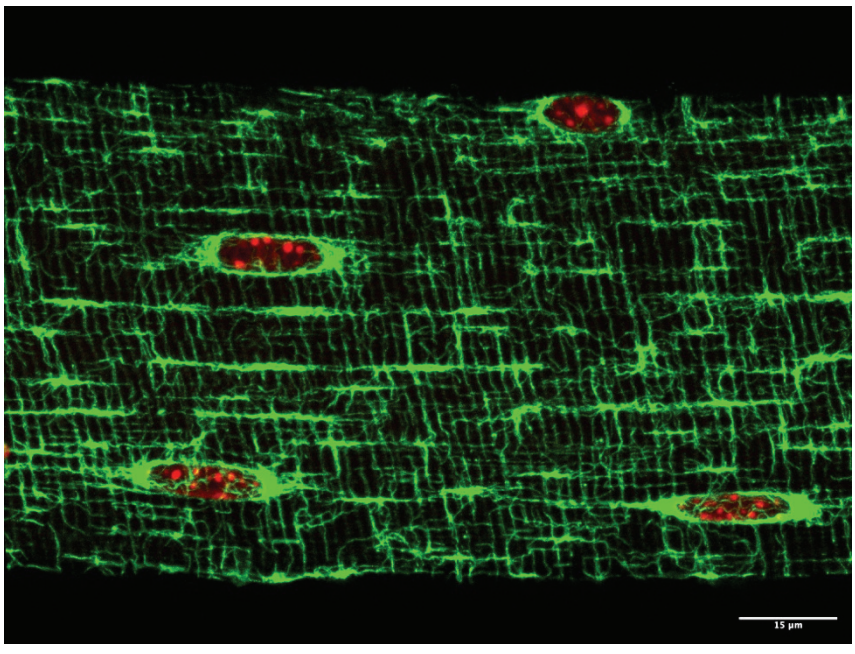

Figure 25: MT network in myofibers. Representative photo (63X) presenting MT network (green) gride-like organization within a healthy mature myofiber isolated from mouse *tibialis anterior* muscle. Myonuclei (red) can be observed regularly spaced at the myofiber's periphery with a dense MT cage around them.

Golgi complex has been previously described to participate in MT nucleation in differentiated cells (Efimov et al., 2007). Regarding myofibers, the Golgi complex can be found both in the vicinity of the NE at the periphery of myofibers and at the crossing points of MT grids (Figure 26). At both sites, the Golgi complex is detected hand to hand with γ-tubulin and pericentrin and is known to participate in local MT nucleation (Oddoux et al., 2013). In addition, the Golgi complex is also present around post-synaptic myonuclei clustered under NMJs where MT networks present great density (Ralston et al., 1999). In mature myofibers, the highly specialized SR can be found aligned with MTs. A close relationship between the Golgi complex and SR exit points can be observed all along the myofibers (Lu et al., 2001).

Growing evidence shows that changes in MTOC are necessary for proper myofibers development. In early myogenesis, MTs have been suggested to participate in myocytes fusion and further in myotubes elongation (Saitoh et al., 1988; Straube and Merdes, 2007). During myogenesis, MT rearrangement is synchronized with the great myonuclei dynamics and both mechanisms seem to be dependent on one another. NE serves as the MT nucleation center while MTs provide the roads and motor molecules to ensure proper myonuclei distribution during myofibers development (Gache et al., 2017; Metzger et al., 2012; Ralston et al., 1999; Wilson and Holzbaur, 2012). In parallel to NE, Golgi elements begin to nucleate MTs as myofibers develop (Oddoux et al., 2013). Indeed, Nesprin-1 has been shown to recruit AKAP450 to the NE and promotes MT nucleation from the NE ncMTOC in developing myotubes (Gimpel et al., 2017). What other proteins participate in MT nucleation at the NE or Golgi elements within myofibers and how are they recruited/arranged at these sites remain unknown for the moment. However, as MTs continue to nucleate from NE and Golgi elements, proteins such as dystrophin and MAP4 guide and orient MTs to form the gride-like MT network in myofibers (Mogessie et al., 2015; Prins et al., 2009). In return, MT network has been suggested to direct and orient myosin organization during sarcomeres formation (Antin et al., 1981; Pizon et al., 2005). Additionally, the final gride-like organization of MTs in mature myofibers serves as a mechanical support for sarcomeres during contraction and provides an interconnected railway for the shipment of cargos such as RNA along the myofibers (Denes et al., 2021; Kerr et al., 2015). Thus, MT organization seems to be essential for proper myofibers formation and activity through different mechanisms. This suggests that any disruption in MT nucleation or MT dynamics can affect myofibers functionality.

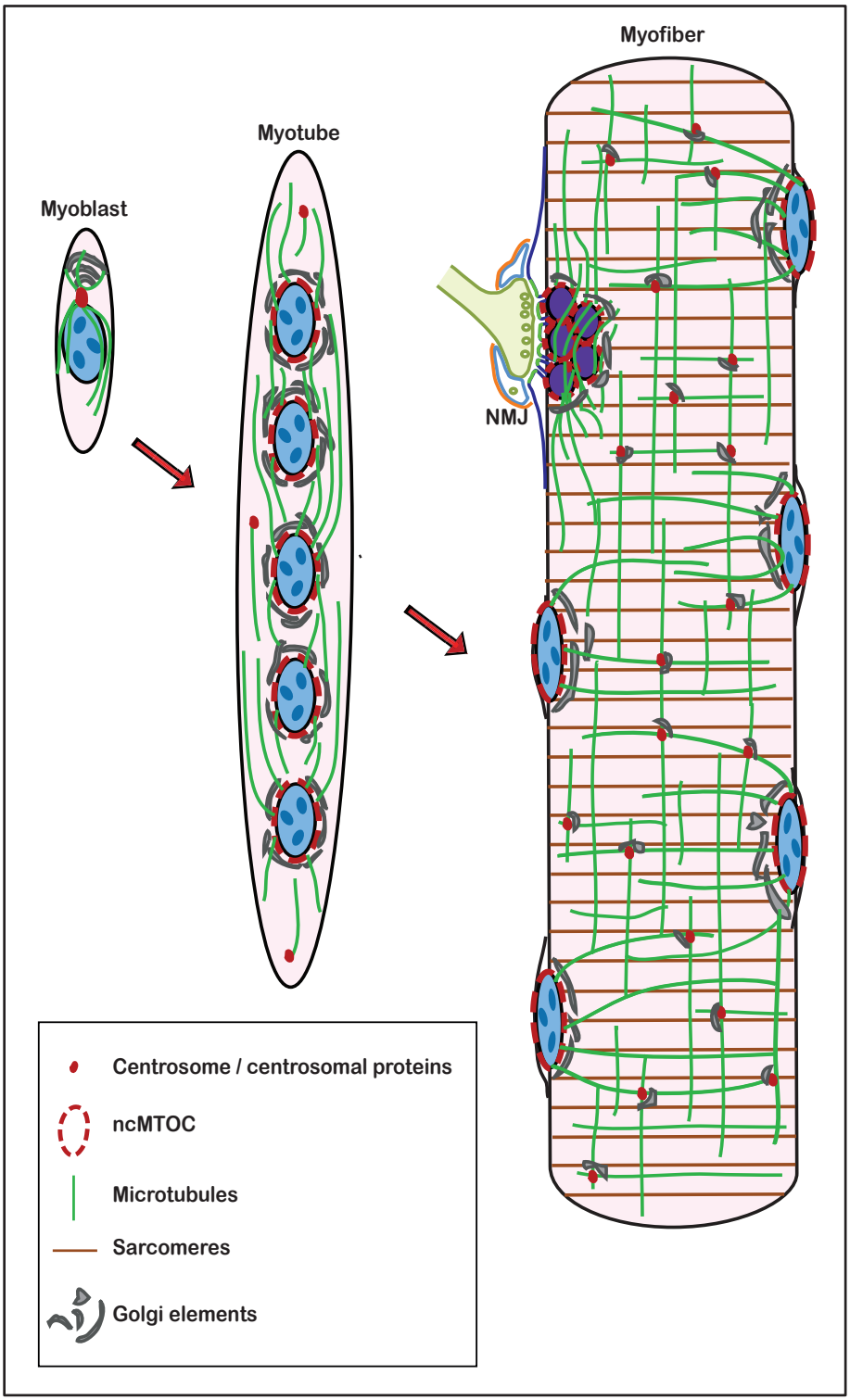

Figure 26: Illustration of MTOC rearrangement through myogenesis.
Before differentiation, MTs are radially nucleated from the juxtanuclear centrosome of myoblasts. As differentiation begins, centrosomal proteins, in addition to the Golgi complex, are moved to the NE. Therefore, in myotubes, NE is in charge of MTs longitudinal nucleation as a ncMTOC. In a mature myofiber, centrosomal proteins surround the NE of peripheral or post-synaptic myonuclei and sit next to Golgi elements all along the myofiber. In these fibers, both peripheral myonuclei NE and dispersed Golgi elements along myofiber participate in MT grid-like organization. The illustration is not drawn to scale.

III) Dynamics of MTs

As previously mentioned, MT dynamics is spatiotemporally under the influence of MAPs associated with MT lattice or of PTMs, which, depending on their nature, could promote or prevent MT assembly or disassembly. While compared to MAPs, much less is known about the importance PTMs in MT dynamics, a review of the current data available on MT PTMs in skeletal muscles can be found in the following sections.

1) Impact of post-translational modifications on MT dynamics

As different isotypes of α- and β-tubulins chain up, they can be subjected to various PTMs and generate specific MT patterns known as the tubulin code (Figure 27). Most of these tubulin PTMs are reversible and the dominance of different PTMs can vary depending on the cell type or cell state. Some PTMs have been shown to support MTs structurally and maintain MTs stability. In addition, different tubulin code patterns created by PTMs can guide and attract specific MAPs, plus-tip, or motor proteins and thus can influence not only the dynamics of MTs but also the dynamics of subcellular cargos (Gadadhar et al., 2017).

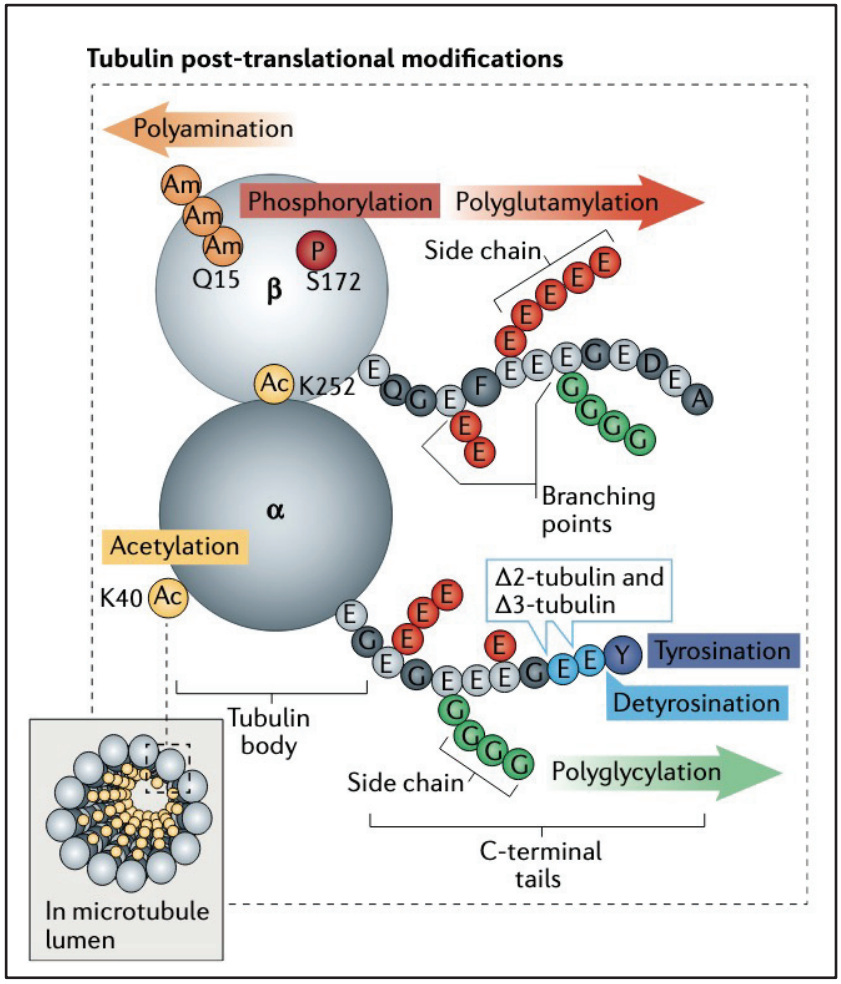

Figure 27: Illustration of different PTMs on tubulins.
Schema presenting the variety of PTMs that could occur to α- and β-tubulins. Except for α-tubulins acetylation which occurs inside the MT lumen, the rest of the PTMs are known to be present on the exterior lattice of MTs. Figure adapted from (Janke and Magiera, 2020).

A) Acetylation

α-tubulin acetylation occurs on lysine residues of α-tubulins, located inside the MT lumen, which is unique to this PTM (Howes et al., 2014; L'Hernault and Rosenbaum, 1985). The acetylation is regulated by α-tubulins acetyltransferase (αTAT1) which specifically acetylates the lysin40 of α-tubulin and is reversible by the Histone deacetylase 6 (HDAC6) and sirtuine2 (SIRT2) (Akella et al., 2010; Hubbert et al., 2002; North et al., 2003).

It has been suggested that α-tubulin acetylation supports MT flexibility and prevents their breakage (Portran et al., 2017; Xu et al., 2017). Actually, this PTM has been long associated with stable long-lived MTs. There is no data available on whether α-tubulins acetylation affects the binding affinity of MAPs related to the fact that acetylation does not occur on the MT lattice where MAPs bind.

In skeletal muscle, acetylation is highly present at the post-synaptic NMJs site (Jasmin et al., 1990). In that regard, two independent studies have investigated the importance of the α-tubulins acetylation PTM in skeletal myofibers. The first one describes that inhibition of HDAC6 results in smaller AChR clusters both *in vitro* and *in vivo*. They show that α-tubulins acetylation modulates the entry and exit rate of AChRs into clusters and propose α-tubulins acetylation to be necessary for post-synaptic NMJs stability (Osseni et al., 2020). The second study highlights the importance of the balance between the presence and absence of α-tubulins acetylation in myofibers activity. They show that increased α-tubulin acetylation results in a stiffer MT network and affects the mechanotransduction rate of skeletal muscle. Interestingly, the same study describes a similar acetylation-dependent effect upon the increase of α-tubulins acetylation in cardiac muscle as well (Coleman et al., 2021).

B) Tyrosination/detyrosination and SVBP

Except for a few isotypes, most α-tubulins are expressed with a tyrosine in their C-terminal. As a PTM, the C-terminal tyrosine can be enzymatically removed and generate detyrosinated α-tubulins. This PTM has been described reversible through the re-addition of a new tyrosine to the C-terminal of α-tubulins (Arce et al., 1975; Hallak et al., 1977; Valenzuela et al., 1981). The α-tubulins detyrosinating enzyme was discovered only last decade. It is a complex formed from a small vasohibin binding protein (SVBP) and either of its partners, vasohibin 1 or 2 (VASH1/2) (Aillaud et al., 2017; Nieuwenhuis et al., 2017). However, the tubulin tyrosine ligase (TTL), which is the enzyme responsible for the re-addition of tyrosine to α-tubulins, has been known since three decades (Ersfeld et al., 1993).

SVBP (also known as CCDC23) is a small protein of about 7kD whose gene is located on chromosome 1 in humans and chromosome 4 in mice. Before being described as the coenzyme for α-tubulin detyrosination, it was for its role as a secretory chaperon for VASH1 and VASH2 in endothelial cells to promote their anti-angiogenic and pro-angiogenic activity, respectively (Kimura et al., 2009; Suzuki et al., 2010; Xue et al., 2013). Following their identification as α-tubulins detyrosinating complex, crystallography analysis and functional assays have revealed

that VASH1 can recognize and bind to α-tubulins on MT lattice but it is SVBP which will stabilize the complex on MTs and promote the activity of VASH1 catalytic site. However, compared to VASH1, VASH2 can commit to low levels of MT detyrosination independent of SVBP, but its detyrosinating activity is strongly boosted in the presence of SVBP (Li et al., 2019; van der Laan et al., 2019). These results indicate that both VASH1 and VASH2 α-tubulins detyrosinating activity is predominantly dependent on their coactivator, SVBP. Indeed, Down-regulation of SVBP, VASH1, or VASH2 in cultured neurons resulted in a strong decrease in MT detyrosination, increased neurons branches, and decreased neurons axonal length (Aillaud et al., 2017).

While tyrosinated α-tubulins can be found both free in the cytoplasm and on MTs, detyrosinated can only be observed on MT lattice. This is due to the preference of the SVBP/VASH complexes for MTs and the inability of TTL to add a new tyrosine to α-tubulins on MT lattice. This is due to the difference in tubulin dimers structure in MTs (straight) compared to detached dimers (curved) and accessibility of TTL to α-tubulins (Prota et al., 2013). Therefore, TTL has a great affinity for detyrosinated α-tubulins once they are detached from MT lattice during catastrophe (Aillaud et al., 2017; Arce et al., 1978; Gundersen et al., 1987; G. G. Gundersen and Bulinski, 1986; Kumar and Flavin, 1981; Raybin and Flavin, 1977; Thompson et al., 1979).

Growing evidence shows the preference of different MT binding proteins for either tyrosinated or detyrosinated MTs. As a result, tyrosinated MTs are associated with dynamic MTs while detyrosinated MTs are associated with stable MTs. By studying neuronal or epithelial cells, it has been shown that different motor proteins such as KIF2A and KIF3C preferentially bind to tyrosinated MTs and promote MT depolymerizing activity (Ferreira et al., 2020; Gumy et al., 2013; Peris et al., 2009). Thus, MT detyrosination indirectly increases the stability of MTs by preventing the activity of these motor molecules. In addition, MT end-binding proteins such as EB1 have been shown facilitate the installation of MT plus tips proteins, such as CLIP-170, on the growing ends of tyrosinated MTs and increase MT dynamics (Chen et al., 2021; Honnappa et al., 2009). Interestingly, another kinesin known as KIF17 preferentially promotes the installation of adenomatous polyposis coli (APC) on detyrosinated MTs which participates in MT stabilization (Jaulin and Kreitzer, 2010). Whether these PTMs have the same or similar molecular impacts on MTs in skeletal muscle has to be determined.

In skeletal muscle, the tyrosination/detyrosination cycle seems to be important for both development and function of myofibers. In chicken embryos, TTL has been shown to be highly active during skeletal muscle embryonic development and decrease as myofibers grow (Deanin et al., 1977). In addition, post-natal studies on different tissues from rats have demonstrated that TTL activity in skeletal muscle is much stronger than in other tissues, except for the brain (Deanin and Gordon, 1976). In myofibers, MTs participate in the transduction of mechanical stress by regulating the NADPH-dependent oxidation of reactive oxygen species (ROS) upon mechanical stress which in turn can modulate the activation of Ca^{2+} channels and thereby contraction. It is interesting to know that in the skeletal muscles of the DMD mouse model, MTs are highly dense, stiff, and disorganized. This alteration of MT rigidity results in increased ROS oxidation and increased Ca^{2+} channels activation (Khairallah et al., 2012; Prins et al.,

2009). In turn, this increased Ca^{2+} channels activation has been suggested to induce myofibers damage due to excessive contraction (Ward et al., 2014). Remarkably, MT stiffness in DMD myofibers has been linked to increased MT detyrosination. Accordingly, the reduction of MT detyrosination has been shown to reduce ROS oxidation and Ca^{2+} channels activation and ameliorate the speed of skeletal muscle contraction and relaxation (Kerr et al., 2015). These data suggest that the control of the balance between tyrosinated and detyrosinated α-tubulins can have a great developmental and physiological impact on skeletal muscles. Especially when combined with observation of muscular hypotonia in patients bearing mutations in SVBP (Iqbal et al., 2019).

Furthermore, the same studies on DMD mice present identical mechanical disruption of cardiac muscle contraction due to increased MT detyrosination and stiffness (Kerr et al., 2015; Khairallah et al., 2012; Prins et al., 2009). A complementary study on cardiac muscle has addressed the question of the mechanical importance of MT detyrosination during muscle contraction. In this study, they have shown that MT detyrosination is necessary to establish a strong joint between MT network and desmin and thereby between MT network and sarcomeres. Under these circumstances, MTs buckle up with each sarcomere shortening and manage the mechanical stress transduction. However, in the absence of MT detyrosination, MT interaction with sarcomeres is disrupted. This results in MTs sliding in parallel to each other following a contraction instead of buckling up and is correlated to faster sarcomeres shortening (Robison et al., 2016). In fact, the same study and others have described increased MT detyrosination in different cardiomyopathies with phenotypes such as cardiac arrhythmia. In these cells, reduction of MT detyrosination by drugs which prevent MT grow, by increasing TTL activity/expression, or directly by targeting the MT detyrosinating complex through down-regulation of VASH1, all results in reduced cardiac muscle stiffness and improved contraction (Caporizzo et al., 2018; Chen et al., 2020, 2018; Hotta et al., 2021; Robison et al., 2016). These data suggest a direct regulatory role for MT detyrosination in mechanotransduction of stress during muscle contraction.

Interestingly, patients with a stop-gain mutation in SVBP also present signs of muscular hypotonia (Iqbal et al., 2019). However, whether the same SVBP/VASH1 and/or SVBP/VASH2 complexes are responsible for MTs detyrosination in skeletal and how mutation in SVBP can lead to skeletal muscle weakness have never been addressed. In addition, while these studies indicate the importance of a balance between tyrosinated/detyrosinated MTs in skeletal muscle, they are based on irregular MT tyrosination/detyrosination balance in diseased models or challenging the balance via different drugs. A direct study on the evolution of MT tyrosination/detyrosination balance during myogenesis and in myofibers can increase our knowledge on the potential importance of controlled MT dynamics for skeletal muscle homeostasis.

C) Other tubulin PTMs

As cited in figure 27, there exist other tubulin PTMs - for α-tubulins: methylation, phosphorylation, ubiquitinylation, sumoylation, palmitoylation, and Δ2-/Δ3-α-tubulins (lacking 2 or 3 glutamines at their C-terminal), for β-tubulins: acetylation or phosphorylation, and finally for both α- and β-tubulins: (poly) glutamylation, (poly) glycation or polyamination (Janke and Magiera, 2020). For each of these PTMs, their presence in skeletal muscle in addition to their physiological importance in this tissue have yet to be studied.

2) Role of MAPs in MT dynamics

As previously mentioned, different MAPs, including motor proteins, plus-tip proteins, and cytoskeleton cross-linkers can also participate/regulate MT dynamic, either by favoring MT catastrophe or helping MT stabilization. Here, a few examples are given to highlight different mechanisms through which MAPs can modulate MT dynamics, with an emphasize on skeletal muscle, when data were available.

One example of MAPs promoting MT stability can be MAP4. During myogenesis, oMAP4 (a smaller isoform of muscle specific MAP4 protein) is specifically expressed with differentiation and regulates myocytes elongation for fusion. Further in developing myotubes, it participates in MT paraxial organization by zipping and stabilizing antiparallel MTs (Mogessie et al., 2015). In myofibers, MAP6 has been shown to be important for the proper gride-like organization of MTs. MAP6 KO mice present disorganized MTs as reflected by increased transversal MTs in skeletal muscle myofibers. They also present disorganized SR and reduced calcium release from the SR which in turn results in increased muscle weakness (Sébastien et al., 2018). It is interesting to know that some MAPs can bear a phosphorylation site in their C-terminal. In neurons, the phosphorylation state of these MAPs can directly affect their activity on MTs (Ozer and Halpain, 2000; Szebenyi et al., 2005). Since this could be a mechanism through which cell monitors MT stability, the study of the phosphorylated/dephosphorylated state of different MAPs in skeletal muscle during myogenesis can bring valuable information to understanding skeletal muscle-specific MTs regulating mechanisms.
Another group of proteins that can act on MT stability are cytoskeleton crosslinkers. These proteins are able to couple MTs, actins, and intermediate filaments together to ensure cytoskeleton stability and synchronized activity. One example of these proteins can be dystrophin. In skeletal muscle, dystrophin can bind actin to the plasma membrane through its actin-binding domain. Together with its partners, they form the dystrophin complex which creates a network connecting myofibers ECM to intracellular sarcomeres through plasma membrane (Allen et al., 1996). In mature myofibers, this protein has been shown to be essential for proper localization of Golgi apparatus and MT nucleation, in addition to guiding MT gride-like organization and stabilization (Oddoux et al., 2019; Prins et al., 2009).

Plus-tip proteins, such as MT end binding EB1 and EB3 can also modulate MT dynamics. As indicated by their name, these proteins bind, and form complexes, specifically at the growing tips of MTs (Akhmanova and Steinmetz, 2010). Their constant binding to MT plus-tips is

known to prevent the binding of MT depolymerizes (Komarova et al., 2009; Tirnauer et al., 2002). In skeletal muscle, EB3 has been shown to increase during myogenesis and to regulate MT organization specifically under the cell cortex, a phenomenon necessary for myocytes elongation and fusion (Straube and Merdes, 2007).

Other microtubule-binding proteins, such as kinesin-8 can have MT destabilizing activity. *In vitro* studies have shown that this protein binds strongly to MTs and moves on MT lattice toward growing plus-tips. When dissociating, it removes one or two MT dimers and causes MT catastrophe (Varga et al., 2009). Another example of catastrophe-promoting protein could be Oncoprotein 18/stathmin (Op18), a member of the kinesin-13 family. In the hamster ovarian epithelial cell line, this protein binds to tubulin heterodimers and provokes a conformational change which facilitates MT catastrophe (Komarova et al., 2009).

Aim of the project

The homogenous myonuclei positioning along myofiber guarantees a spatial and coordinated transcription activity within a territory around each myonucleus, the myonuclear domain, and contributes to myofiber functional integrity (Denes et al., 2021; Hall and Ralston, 1989; Pavlath et al., 1989; Ralston and Hall, 1992). The loss of peripheral myonuclei in skeletal muscles is the hallmark of different myopathies, such as centronuclear myopathies (Collins et al., 2017; Falcone et al., 2014; Perillo and Folker, 2018). In addition, changes in myonuclei shape have been suggested to participate in the development of different muscular diseases (Janin and Gache, 2018; Puckelwartz et al., 2009). Yet it still is unclear why the peripheral myonuclei positioning is lost and how changes in myonuclei shape and their mispositioning contribute to the development of different myopathies. Moreover, the exact mechanisms regulating myonuclei spacing and anchoring at the periphery of myofibers remain unknown.

As MTs are the main railway for myonuclei guidance and movement during myogenesis and form a dense network around the peripheral myonuclei dispersed along mature myofibers or under NMJs (Gache et al., 2017; Ralston et al., 1999), I aimed to decipher the contribution of MT network in peripheral myonuclei positioning, and thus myonuclear domains organization/maintenance, in mature myofibers.

To address this question, I took advantage of the library of the MT related proteomic in myotubes and myofibers that was previously generated in the team of Dr. Gache (Couturier and Gache, 2017). Among the candidates, I aimed to decipher the role of MACF1 in skeletal muscle, during development and more specifically in mature myofibers because:

- in enriched MTs samples, MACF1 was detected almost as high as KIF5B, a major regulator of myonuclei dynamics during myofibers development,

- MACF1 orthologue in *Drosophila*, Shot, has been shown to be present around myonuclei to maintain perinuclear MTs in myofibers of *Drosophila* larva and thereby regulate myonuclei shape and positioning (S. Wang et al., 2015),

- a mutation in the *MACF1* gene has been linked to a neuromuscular disease with muscular hypotonia (Jørgensen et al., 2015).

This first study allowed me to dissect and identify the importance of MACF1 in skeletal muscle health and homeostasis, not only by participating in myonuclei positioning but also through its regulatory roles on MT network dynamics. Interestingly, my studies on different MT PTMs in MACF1 depleted myofibers suggested potential importance for the balance between tyrosinated and detyrosinated α-tubulins in myonuclei stability within myofibers. Therefore, the second study of my thesis is dedicated to studying the regulation and importance of the balance between tyrosinated and detyrosinated α-tubulins during skeletal muscle development by manipulating the α-tubulins detyrosinating coenzyme, SVBP.

The ensemble of results from these two projects provide new information on importance of regulated MT dynamics for skeletal muscle homeostasis.

During my thesis, I also development a new culture method in order to increase MT network maturity *in vitro* and closer to their gride-like organization *in vivo.* The data obtained related to the model development are introduced in the third study. In future, this method can be used to identify mechanisms regulating MT gride-like organization in addition to myonuclear domains maintenance *in vitro.*

Results

Study 1

To study the role of MACF1 in myonuclei positioning during myogenesis and in mature myofibers, first I checked whether absence of MACF1 affects myonuclei positioning *in vitro*. Then I searched for the mechanism through which MACF1 regulates myonuclei positioning during myofibers development. These experiments allowed me to show that MACF1 controls myonuclei dynamics though MTs. To have deeper insights on the role of MACF1 in skeletal muscle, I used a skeletal muscle specific MACF1 KO mouse model which was developed in the team of Dr. Gache by Dr. Alexandre Guiraud. My microscopy images of isolated myofibers from adult 12-month-old MACF1 KO mice directly revealed disorganized myonuclei and MTs organization compared to WT mice, recapitulating my observations *in vitro*. In parallel, I observed that NMJs of 12-month-old MACF1 KO and WT mice are fragmented and have a smaller number of post-synaptic myonuclei compared for MACF1 KO myofibers to WT. These observations led me to questions whether these phenotypes occur simultaneously or as chains of events. Thus, I studied myofibers of skeletal muscle specific inducible MACF1 KO mouse model. However, except for NMJs fragmentation, I did not observe the phenotypes related to MTs or myonuclei disorganization in this model even four month post induction of MACF1 down regulation *in vivo* (data obtained from skeletal muscle specific inducible MACF1 KO model are presented in the "complementary data 1" following the published article). Thus, to study the evolution of myonuclei, MTs and NMJs disorganizations in MACF1 KO myofibers, I compared myofibers of WT and MACF1 KO mice, at different ages, from 2-month-old to 12-month-old. This time-course analysis allowed me to show a progressive MTs and myonuclei disorganization in MACF1 KO myofibers and some myonuclei internalization inside myofibers which occurs only in 12-month-old. In parallel, my collaboration with Dr. Julien Gondin from our institute allowed us to show that MACF1 KO mice skeletal muscle present a resistance to fatigure in response to stimulation compared to WT mice, suggesting a potential alteration in skeletal myofibers metabolism in the absence of MACF1. As skeletal myofibers are rich on mitochondria, and mitochondria use MTs cytoskeleton as a support for their organization, I compared the mitochondrial population of WT and skeletal muscle specific MACF1 KO mice from different points of view. I observed that in the absence of MACF1, mitochondrial biogenesis is progressively increased, resulting in the accumulation of round mitochondria within myofibrils of skeletal myofibers, thus I hypothesized that this progressive myofibril disorganization is potentially contributing to myonuclei internalization in MACF1 KO myofibers with age.

This study allowed me to demonstrate the role of microtubule associated protein MACF1, and thus MT network, in myonuclear domains organization, not only during myogenesis, but specially in mature myofibers *in vitro* and *in vivo*. The ensemble of data obtained along this project are presented in the following article.

Publication 1:

MACF1 controls skeletal muscle function through the microtubule-dependent localization of extra-synaptic myonuclei and mitochondria biogenesis.

eLife, 2021

Alireza Ghasemizadeh*, *Emilie Christin*, *Alexandre Guiraud*, *Nathalie Couturier*, *Marie Abitbol*, *Valerie Risson*, *Emmanuelle Girard*, *Christophe Jagla*, *Cedric Soler*, *Lilia Laddada*, *Colline Sanchez*, *Francisco-Ignacio Jaque-Fernandez*, *Vincent Jacquemond*, *Jean-Luc Thomas*, *Marine Lanfranchi*, *Julien Courchet*, *Julien Gondin*, *Laurent Schaeffer*, *Vincent Gache

RESEARCH ARTICLE

MACF1 controls skeletal muscle function through the microtubule-dependent localization of extra-synaptic myonuclei and mitochondria biogenesis

Alireza Ghasemizadeh[1], Emilie Christin[1], Alexandre Guiraud[1], Nathalie Couturier[1], Marie Abitbol[1,2], Valerie Risson[1], Emmanuelle Girard[1], Christophe Jagla[3], Cedric Soler[3], Lilia Laddada[3], Colline Sanchez[1], Francisco-Ignacio Jaque-Fernandez[1], Vincent Jacquemond[1], Jean-Luc Thomas[1], Marine Lanfranchi[1], Julien Courchet[1], Julien Gondin[1], Laurent Schaeffer[1], Vincent Gache[1]*

[1]Institut NeuroMyoGène, CNRS UMR5310, INSERM U1217, Faculté de Médecine Rockefeller, Université Claude Bernard Lyon I, Lyon Cedex, France; [2]Université Marcy l'Etoile, VetAgro Sup, Lyon, France; [3]GReD Laboratory, Clermont-Auvergne University, INSERM U1103, CNRS, Clermont-Ferrand, France

Abstract Skeletal muscles are composed of hundreds of multinucleated muscle fibers (myofibers) whose myonuclei are regularly positioned all along the myofiber's periphery except the few ones clustered underneath the neuromuscular junction (NMJ) at the synaptic zone. This precise myonuclei organization is altered in different types of muscle disease, including centronuclear myopathies (CNMs). However, the molecular machinery regulating myonuclei position and organization in mature myofibers remains largely unknown. Conversely, it is also unclear how peripheral myonuclei positioning is lost in the related muscle diseases. Here, we describe the microtubule-associated protein, MACF1, as an essential and evolutionary conserved regulator of myonuclei positioning and maintenance, in cultured mammalian myotubes, in *Drosophila* muscle, and in adult mammalian muscle using a conditional muscle-specific knockout mouse model. In vitro, we show that MACF1 controls microtubules dynamics and contributes to microtubule stabilization during myofiber's maturation. In addition, we demonstrate that MACF1 regulates the microtubules density specifically around myonuclei, and, as a consequence, governs myonuclei motion. Our in vivo studies show that MACF1 deficiency is associated with alteration of extra-synaptic myonuclei positioning and microtubules network organization, both preceding NMJ fragmentation. Accordingly, MACF1 deficiency results in reduced muscle excitability and disorganized triads, leaving voltage-activated sarcoplasmic reticulum Ca^{2+} release and maximal muscle force unchanged. Finally, adult MACF1-KO mice present an improved resistance to fatigue correlated with a strong increase in mitochondria biogenesis.

***For correspondence:** vincent.gache@inserm.fr

Competing interests: The authors declare that no competing interests exist.

Funding: See page 27

Preprinted: 15 May 2019
Received: 18 May 2021
Accepted: 10 August 2021
Published: 27 August 2021

Reviewing editor: Mohammed Akaaboune, University of Michigan, United States

Introduction

Throughout skeletal muscle development, myonuclei actively move to settle at specific locations in the fully differentiated muscle fibers (myofibers) where they are regularly spaced along the longitudinal fiber axis, sitting at the periphery underneath the surface membrane (***Roman and Gomes, 2018***). The density of myonuclei along myofibers' length remains relatively constant with the exception of the neuromuscular junction (NMJ), where ~5–6 myonuclei (synaptic myonuclei) are clustered immediately below the NMJ (***Bruusgaard et al., 2006***; ***Manhart et al., 2018***; ***Ravel-Chapuis et al., 2007***).

Failure in proper extra-synaptic myonuclei patterning has been linked to different myopathies and muscle weakness (**Collins et al., 2017**; **Falcone et al., 2014**; **Metzger et al., 2012**; **Perillo and Folker, 2018**; **Roman et al., 2017**). This precise organization is correlated with a particular 'flatten' shape of the myonuclei, whose alteration has recently emerged as a potential contributor to several muscular diseases (**Cho et al., 2017**; **Janin and Gache, 2018**; **Norton and Phillips-Cremins, 2017**; **Puckelwartz et al., 2009**).

Proteins localized inside myonuclei such as Lamin A/C, Emerin, or Nuclear Envelope Proteins (NEPs), connect the nuclear lamina to the cytoskeleton through the 'LInker of Nucleoskeleton and Cytoskeleton' (LINC) complex, which plays a critical role in the maintenance of myonuclei shape and localization (**Chang et al., 2015**; **Lee and Burke, 2018**; **Levy et al., 2018**; **Mattioli et al., 2011**). Additionally, molecular motors and Microtubule-Associated Proteins (MAPs), in interaction with actin/microtubule networks, are also involved in myonuclei localization during muscle formation (**Casey et al., 2003**; **Gache et al., 2017**; **Metzger et al., 2012**; **Rivero et al., 2009**). Importantly, the specific localization and shape of myonuclei, determined by mechanical forces emanating from different cytoskeleton networks, act directly on chromatin organization and gene expression (**Chojnowski et al., 2015**; **Kirby and Lammerding, 2018**; **Ramdas and Shivashankar, 2015**; **Robson et al., 2016**). Yet, how myonuclei positioning in mature myofibers is set and how it regulates the signaling pathways maintaining myofiber integrity is still poorly understood.

To identify proteins involved in the maintenance of myonuclei positioning, we used an in vitro primary myotubes/myofibers culture system and identified MACF1 (Microtubule Actin Crosslinking Factor 1) as a regulator of myonuclei positioning during the late phases of myofiber maturation. MACF1 is a member of the spectraplakin family of proteins. It is a huge protein composed of multiple domains that allow its interaction with actin filaments and microtubules to stabilize them as adhesion structures in a variety of tissues (**Kodama et al., 2003**; **Sanchez-Soriano et al., 2009**). *MACF1* gene duplication (resulting in a decrease of MACF1 protein) is linked with a neuromuscular disease condition (**Jørgensen et al., 2014**) and *MACF1* variants are associated with congenital myasthenia (**Oury et al., 2019**). The *C. elegans* orthologous, VAB-10 and the *Drosophila* orthologous, Shot, are essential for nuclei migration in distal tip cells of the somatic gonad and myotendinous junction formation, respectively (**Bottenberg et al., 2009**; **Kim et al., 2011**; **Lee and Kolodziej, 2002**). Interestingly, Shot was proposed to contribute to the formation and maintenance of a perinuclear shield in muscle from drosophila larvae, contributing to myonuclei localization (**Wang and Volk, 2015**). However, the analysis of MACF1 functions in the control of extra-synaptic myonuclei position and muscle homeostasis is still pending.

Here, using in vitro and in vivo models, we report that MACF1 is important for the maintenance of myonuclei patterning in mammalian myofibers. MACF1 contributes to extra-synaptic myonuclei motion and positioning through the regulation of microtubules dynamics. We also reveal that MACF1 is essential for proper NMJ formation and mitochondria homeostasis.

Results

MACF1 uses microtubules to set myonuclei spreading during myofibers maturation

To identify new factors that contribute to myonuclei spreading in myofibers, we purified proteins able to bind to Taxol-stabilized microtubules from 3 days primary mouse myotubes and 13 days differentiated myofibers (**Figure 1A**). The major Microtubule-Associated-Proteins (MAPs) identified by mass-spectrometry using this protocol revealed the significant presence of MACF1 protein (**Figure 1—figure supplement 1A–B**). MACF1 is a member of the spectraplakin family known to play an architectural role through regulation of the spatial arrangement and function of specific organelles such as the nucleus, the mitochondria, the Golgi apparatus, and the sarcoplasmic reticulum (**Boyer et al., 2010**). MACF1 is a large protein mainly described as a cytoskeleton linker that binds and aligns microtubules and actin networks (**Preciado López et al., 2014**). In developing myofibers, actin is actively involved in myoblasts fusion and contributes to sarcomere formation (**Kim et al., 2015**; **Sanger et al., 2010**) while microtubules actively participate in myofiber elongation and myonuclei spreading (**Metzger et al., 2012**). Although MACF1 was initially described to be predominantly expressed in neurons and muscle (**Bernier et al., 2000**), its role in muscle fibers remains

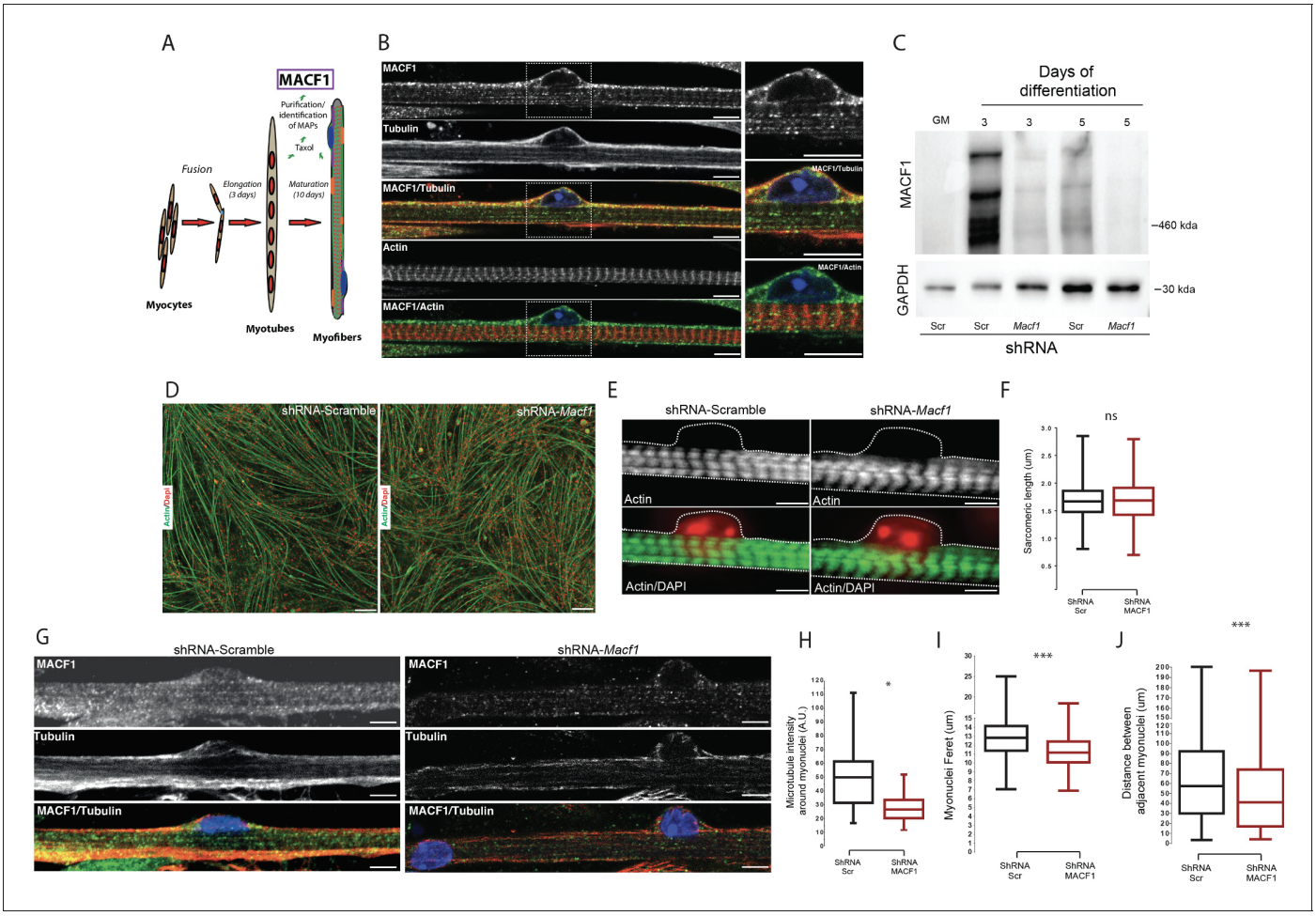

Figure 1. MACF1 is an essential regulator of myonuclei positioning in mature myofibers. (**A**) Scheme presentation of the sequential steps to obtain immature myotubes and mature myofibers from primary mouse myoblasts. Taxol stabilized microtubules proteome was collected either from WT elongated myotubes or from mature contractile myofibers. For downregulating experiments, siRNA/shRNA were transfected in early steps of differentiation just before myotubes formation. (**B**) Confocal immunofluorescence images (63×) presenting the organization of MACF1 (green) and total alpha tubulin or F-actin (red) in WT mature mouse primary myofibers. Scale bar = 10 µm. (**C**) Western blot analysis of MACF1 protein expression (main two isoforms at 830 and 630 kD) in total protein extracts of primary cells at proliferation cycle (GM for growth media) and in 3- or 5 days post-differentiation myotubes or myofibers. Cells were treated either with a scramble shRNA or a pool of four shRNAs targeting *Macf1*. GAPDH was used as loading control. (**D**) Immunofluorescence staining (10×) of F-actin (green) and myonuclei (red) in primary myofibers treated either with scramble shRNA (left panel) or with a pool of four distinct shRNAs targeting *Macf1* (right panel) after 13 days of differentiation. Scale Bar = 50 µm. (**E**) Representative immunofluorescence microscopy images (63×) of F-actin (green) and myonuclei (red) in primary myofibers treated with scramble shRNA (left panel) or with a pool of four distinct shRNAs targeting *Macf1* (right panel) after 13 days of differentiation. Scale Bar = 10 µm. (**F**) Sarcomere length measured on the immunofluorescence images of F-actin from 13 days mature primary myofibers treated with either scramble shRNA or a pool of four distinct shRNAs targeting *Macf1*. Data were obtained from three individual experiments. Line is set at median. Ns stands for not significant (Student's t test). (**G**) Confocal immunofluorescence images (63×) presenting the organization of total alpha tubulin (red) or MACF1 (green) in mature primary myofibers following treatment with either scramble shRNA (left panel) or a pool of four distinct shRNAs (right panel) targeting *Macf1*. Scale bar = 10 µm. (**H–J**) Mean values for fluorescent intensity of total alpha tubulin (**H**), myonuclei ferret (**I**) and distance between adjacent myonuclei (**J**) measured on mature primary myofibers following treatment with either scramble shRNA or a pool of four distinct shRNAs targeting *Macf1*. All panels were generated from data obtained from three individual experiments. Line is set at median. *p<0.05 and ***p<0.001 (Student's t test).
The online version of this article includes the following source data and figure supplement(s) for figure 1:

Source data 1. Table showing data from experiments plotted in ***Figure 1F,H,I and J***.
Source data 2. Whole immunoblotting membrane for MACF1 and GAPDH plotted in ***Figure 1C***.
Figure supplement 1. Reduction of MACF1 does not affects myotubes formation or myonuclei spreading within myotubes.
Figure supplement 1—source data 1. Table showing data from experiments plotted in ***Figure 1—figure supplement 1D,F and G***.
Figure supplement 1—source data 2. Whole immunoblotting membrane for MACF1 and GAPDH plotted in ***Figure 1—figure supplement 1C***.
Figure supplement 2. MACF1 is essential for myonuclei positioning and shape in mature myofibers.
Figure 1 continued on next page

Figure 1 continued

Figure supplement 2—source data 1. Table showing data from experiments plotted in ***Figure 1—figure supplement 2A–C***.

elusive. We first addressed the localization of MACF1 in mature myofibers formed in vitro. Our immunofluorescence approach revealed a dotted pattern all along the myofibers that mainly colocalized with its cortical microtubule network, in agreement with our mass-spectrometry results (***Figure 1B***). Of importance, MACF1 accumulates preferentially around the peripheral myonuclei in mature myofibers (***Figure 1B***, zoom panels). Conversely, MACF1 is clearly excluded from actin network structures (***Figure 1B***).

To determine whether MACF1 is important for skeletal muscle development, we addressed its role during myotubes formation and in mature myofibers. Mouse *Macf1* mRNA was previously shown to increase steadily during myogenesis (***Leung et al., 1999***). We first observed an absence of MACF1 in proliferating myoblasts and confirmed a burst of MACF1 protein expression during the early steps of myotubes formation using primary mouse myoblasts cells and the C2C12 myogenic cell line (***Figure 1C***, ***Figure 1—figure supplement 1C–D***). MACF1 expression was dramatically reduced upon transfection of siRNA or small hairpin RNA (shRNA) targeting the MACF1 mRNA compared to their respective scrambled (Scr) controls (***Figure 1C***, ***Figure 1—figure supplement 1C***). MACF1 down-regulation had no impact on myotubes formation and architecture, as reflected by the unaffected ratio of myotube length to myonuclei content (***Figure 1—figure supplement 1E–F***). In accordance, neither myonuclei distribution as assessed by the mean distance between myonuclei and myotube's centroid nor the statistical distribution of myonuclei along myotubes length were affected following MACF1 down-regulation (***Figure 1—figure supplement 1G–I***). These results were confirmed in C2C12 myotubes cells where no alteration in myonuclei spreading was observed following MACF1 downregulation (***Figure 1—figure supplement 1J***).

To further investigate the implication of MACF1 in mature myofibers, primary mouse myotubes were maintained in differentiation media for 10 additional days using a protocol that allows myofibrillogenesis, sarcomeric structures formation and peripheral myonuclei adopting a flatten architecture and regular spreading along myofibers (***Falcone et al., 2014***). This long-term differentiation approach showed that MACF1 depletion did not impact the global maturation of myofibers, as reflected by homogeneous myofibers width and unaffected actin network striation (***Figure 1D–F***; ***Figure 1—figure supplement 2A***). Yet, when addressing the global integrity of the microtubule network in these mature myofibers by immunofluorescence, we found a 50% decrease of the microtubule staining intensity in the vicinity of the myonuclei perimeter and an apparently less dense cortical network (***Figure 1G–H***). Accordingly, myonuclei shape was much rounder in MACF1-depleted condition, as appreciated by a significant reduction of the myonuclei feret diameter (***Figure 1I***, ***Figure 1—figure supplement 2B***). As microtubules are used in developing myofibers by multiple molecular motors to determine myonuclei spreading (***Gache et al., 2017***), we investigated the impact of MACF1 depletion on this process and observed a significant reduction in the mean distance between adjacent myonuclei (***Figure 1J***, ***Figure 1—figure supplement 2C***) in MACF1-depleted myotubes.

MACF1 controls microtubules dynamics and myonuclei motion in developing muscle fibers

To better understand the localization of MACF1, as driven by its Microtubule Binding Domain (MTBD), we expressed only the MTBD of MACF1 in immature primary myotubes and in mature primary myofibers (***Figure 2A–B***). Interestingly, in primary myotubes, MACF1-MTBD appeared as small comets that merged with the microtubule network all along myotubes length (***Figure 2A***). In contrast, in mature myofibers, we observed a strong accumulation of stable MACF1-MTBD longitudinal bundles close to myonuclei, in addition to small comets dispersed along the myofibers (***Figure 2B***).

MACF1 was previously shown to regulate microtubules polymerization (***Alves-Silva et al., 2012***; ***Ka et al., 2016***; ***Wang et al., 2015***). We thus questioned, in our system, how microtubule dynamics evolve during the myofibers maturation steps and whether MACF1 depletion impacts this process. To study the microtubule network dynamics in developing myofibers, we used the tracking of a fluorescently-tagged End Binding protein member (EB3) at different time points during maturation of in

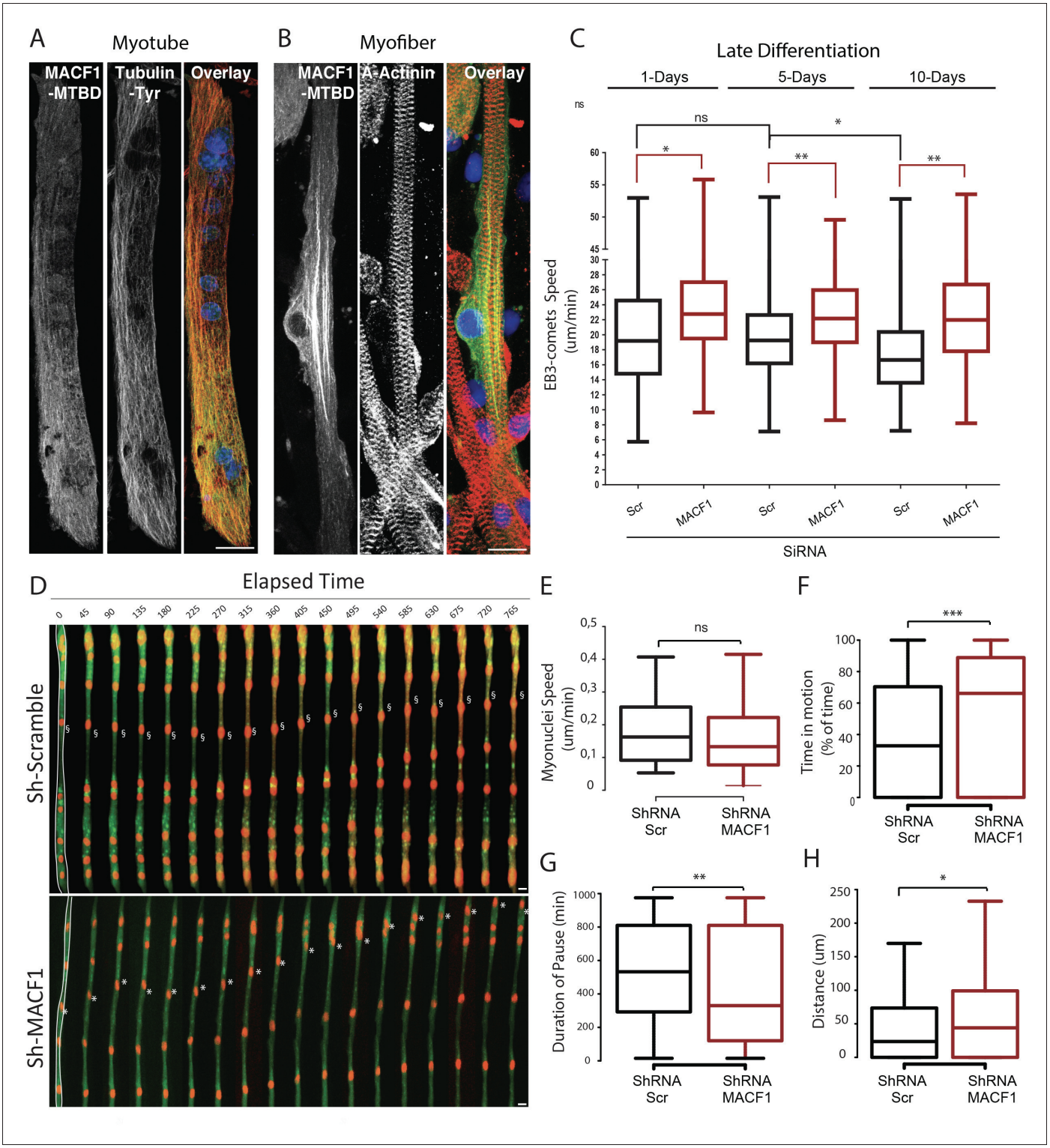

Figure 2. MACF1 regulates myonuclei dynamics through the control of microtubules. (**A–B**) representative confocal immunofluorescence images (63×) presenting MACF1-MTBD (green) and tyrosinated alpha tubulin (red) in primary myotubes (**A**) or alpha actinin (red) in primary myofibers (**B**). Scale bar = 10 µm. (**C**) Quantification of EB3 comets speed in primary cells treated with either scramble siRNA or a pool of 3 individual siRNAs targeting *Macf1* in primary myotubes at three different time points during maturation. At least 200 comets from three individual experiments were mapped per condition. Line is set at median. Ns stands for not significant, *p<0.05 and **p<0.01 (Student's t test). (**D**) Frames from a 14 hr time-lapse movie of two channels

Figure 2 continued on next page

Figure 2 continued

(shRNA in green and lamin-chromobody in red) taken 5 days post differentiation from primary myotubes treated with either a scramble shRNA (upper panel) or a mix of shRNAs targeting *Macf1* (lower level). In the first frame (on the left), myofibers are selected in white, which corresponds to the region used to create the adjacent kymograph. Scale bar = 10 µm. (**E–H**) Speed (**E**), Time in motion (**F**), Duration of pauses (**G**), and Distance travelled by myonuclei (**H**) were quantified using SkyPad analysis (***Cadot et al., 2014***). Quantifications were done on myonuclei within different myofibers from three individual experiments. Line is set at median. Ns stands for not significant, *p<0.05, **p<0.01, and ***p<0.001 (Student's t test).
The online version of this article includes the following source data for figure 2:

Source data 1. Table showing data from experiments plotted in ***Figure 2C and E–H***.

vitro primary myofibers (***Figure 2C***, ***Video 1***). During myofibers maturation process, EB3-comets speed was relatively constant (≈ 19 µm/min) until 5 days of maturation. After this time point, EB3-comets speed decreased significantly, reflecting a progressive downturn in microtubule dynamics (***Oddoux et al., 2013***; ***Figure 2C***). However, the velocity of EB3 comets was increased by 15% upon MACF1 downregulation and remained high (≈ 23 µm/min) all along the process of myofibers maturation (***Figure 2C***). This is consistent with a role for MACF1 in the regulation of microtubule polymerization, mainly as a stabilization factor. As myonuclei preferentially use the microtubule network to move longitudinally along myotubes (***Gache et al., 2017***; ***Metzger et al., 2012***), we next investigated the impact of the increase in microtubule dynamics on myonuclei movements during myofibers maturation. Just before fusion, myoblasts were co-transfected with the lamin-chromobody to visualize myonuclei concomitantly with a shRNA targeting either a scramble sequence or *Macf1*, and a GFP reporter (***Figure 2D***, ***Video 2***). We tracked myonuclei in 5-day-differentiated myofibers every 15 min for 14 hr and analyzed their displacement parameters by the SkyPad method (***Cadot et al., 2014***). In control conditions, myonuclei spent 32% of the time in motion at a median speed of 0.16 µm/min, resulting in a displacement of 24 µm after 14 hr (more than twice bigger than the mean myonuclei feret). Interestingly, in the absence of MACF1, the median velocity of myonuclei was not significantly changed (***Figure 2E***) but the percentage of time that myonuclei spent in motion was doubled, reaching 66% of the time (***Figure 2F***). Accordingly, the median motion pause was 530 min in the control conditions while it fell down to 330 min in the absence of MACF1 (***Figure 2G***). Overall, in the absence of MACF1, myonuclei traveled twice more distance than in control conditions with a mean distance of 44 µm in 14 hr (***Figure 2H***).

Thus, depletion of MACF1 generates increased microtubule dynamics, which in turn elevate myonuclei motion during myofibers maturation, inducing failure in myonuclei spreading in mature myofibers.

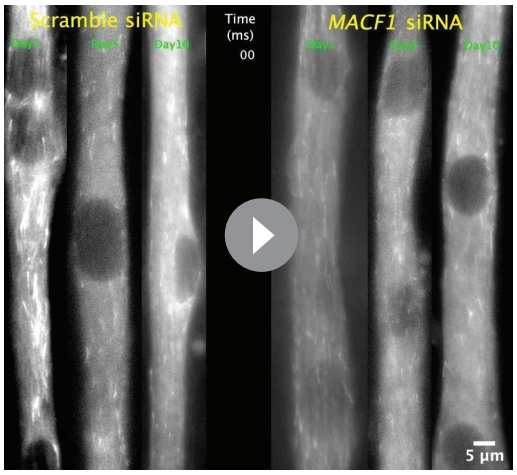

Video 1. Time-lapse experiments of primary myoblasts co-transfected with EB3-GFP plasmid and Scramble-siRNA at 1 day, 5 days, and 10 days post 'late differentiation' initiation (left panels) or primary myoblasts co-transfected with EB3-GFP plasmid and *Macf1*- siRNA at 1 day, 5 days, and 10 days post 'late differentiation' initiation (right panels). Each frames represent 500 milliseconds and was recorded for a period of time of 7 s.
https://elifesciences.org/articles/70490#video1

Conditional MACF1-KO adult mice show microtubule network disorganization in their skeletal muscle fibers

To further investigate the role of MACF1 in skeletal muscle development, we used a conditional *Macf1* knockout mouse line in which exons 6 and 7 of the *Macf1* gene are floxed (***Goryunov et al., 2010***). Homozygous mice were crossed with mice carrying the Cre-recombinase expression under the control of the Human Skeletal muscle Actin (HSA) promoter (***Miniou, 1999***). Briefly, mice carrying two floxed alleles of *Macf1* (*Macf1*$^{f/f}$) were crossed with heterozygous mice for *Macf1* (*Macf1*$^{f/-}$) that carried the HSA::Cre transgene (HSA::Cre; *Macf1*$^{f/-}$), generating the conditional

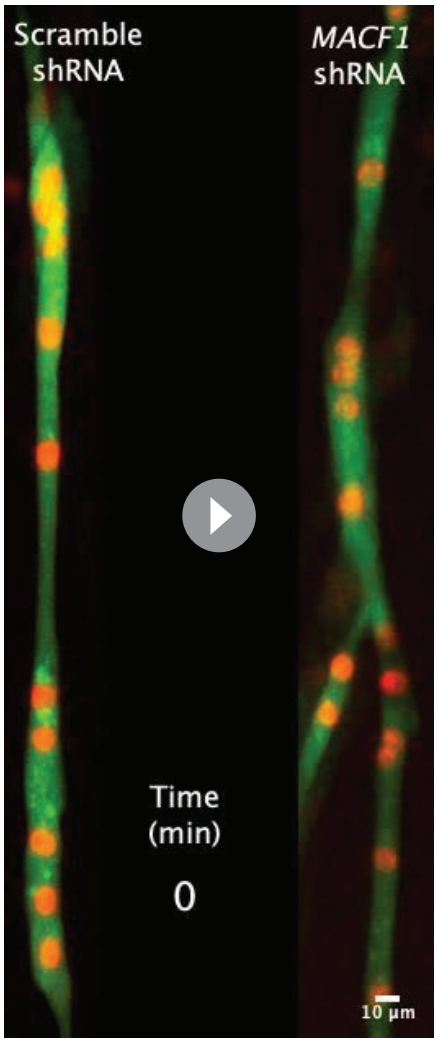

Video 2. Time-lapse experiments of primary myoblasts co-transfected with Lamin-Chromobody-RFP plasmids and either Scramble shRNA (left panel) or a pool of four individual *Macf1* shRNA (rigth panel). Time laps images were captured form myotubes 5 days after starting differentiation process. Primary myotubes were recorded every 15 min for a period of time of 14 hr.
https://elifesciences.org/articles/70490#video2

mutant (HSA::Cre; *Macf1*$^{f/f}$; hereafter referred to as *Macf1* Cre+) and control mice (WT; *Macf1*$^{f/f}$ referred as *Macf1* Cre-) (***Figure 3A–B***). We quantified the efficiency of this approach by measuring the loss of MACF1 mRNA in muscle lysates and observed that its levels were reduced by 70% (***Figure 3C***, ***Figure 3—figure supplement 1A***). Besides, MACF1 downregulation was confirmed by western blotting (***Figure 3—figure supplement 1B***). *Macf1* conditional-KO mice were born at Mendelian frequency and appeared indistinguishable from WT littermates (data not shown). Comparing the body weight evolution between conditional-KO (*Macf1* Cre+) and control mice (*Macf1* Cre-) throughout growing and maturation did not reveal any difference between the two groups (***Figure 3—figure supplement 1C–E***).

We first addressed the impact of MACF1 depletion on the cytoskeleton network using mature myofibers extracted from the *Tibialis Anterior* muscles of WT and conditional MACF1-KO mice. As expected from our in vitro experiments, immunofluorescence approach confirmed the preferred co-localization of MACF1 with the microtubule network rather than with the actin network (***Figure 3D***). We also observed a clear accumulation of MACF1 in the vicinity of myonuclei (***Figure 3D***, arrows) as previously reported in *Drosophila* myofibers but not in murine myofibers (***Oury et al., 2019***; ***Wang et al., 2015***). In *Macf1* Cre+ muscle myofibers, MACF1 staining was clearly less intense all along the myofibers and particularly within the myonuclei vicinity. Also, the microtubule network organization was clearly altered in *Macf1* Cre+ myofibers while there was no concurrent sign of actin network defect (***Figure 3D***). The preserved integrity of the actin network was confirmed by the absence of change in sarcomere length at different ages (***Figure 3E***, ***Figure 3—figure supplement 1F***). To quantify the spatial disorganization of the microtubule network, we used a texture detection tool (TeDT) (***Liu and Ralston, 2014***). Our data show that the longitudinal microtubule network is the most affected regardless of the age of the animals (2-, 6-, or 12-month-old mice (***Figure 3F***, ***Figure 3—figure supplement 1G–H***)), in agreement with the loss of MACF1 staining in the *Macf1* Cre+ muscle myofibers (***Figure 3D***). Altogether, these evidences demonstrate that MACF1 stabilizes the microtubule network during myofibers maturation.

MACF1 can modulate microtubule dynamics through the interaction with different partners such as CLAPS2, EB1, CAMSAP3, Nesprin, Map1B, ErbB2 (***Ka et al., 2014***; ***Noordstra et al., 2016***; ***Pereira et al., 2006***; ***Ryan et al., 2012***; ***Zaoui et al., 2010***). In addition, microtubules are subject to a variety of post-translational modifications (PTMs) that are associated with changes in microtubules dynamics (***Nieuwenhuis and Brummelkamp, 2019***). Among these, tubulin de-tyrosination is associated with longer-living microtubules, whereas dynamic microtubules are mainly tyrosinated (***Bulinski and Gundersen, 1991***). To further investigate the role of MACF1 in the long-term balance of microtubule dynamic in myofibers, we addressed the microtubule tyrosination/de-tyrosination

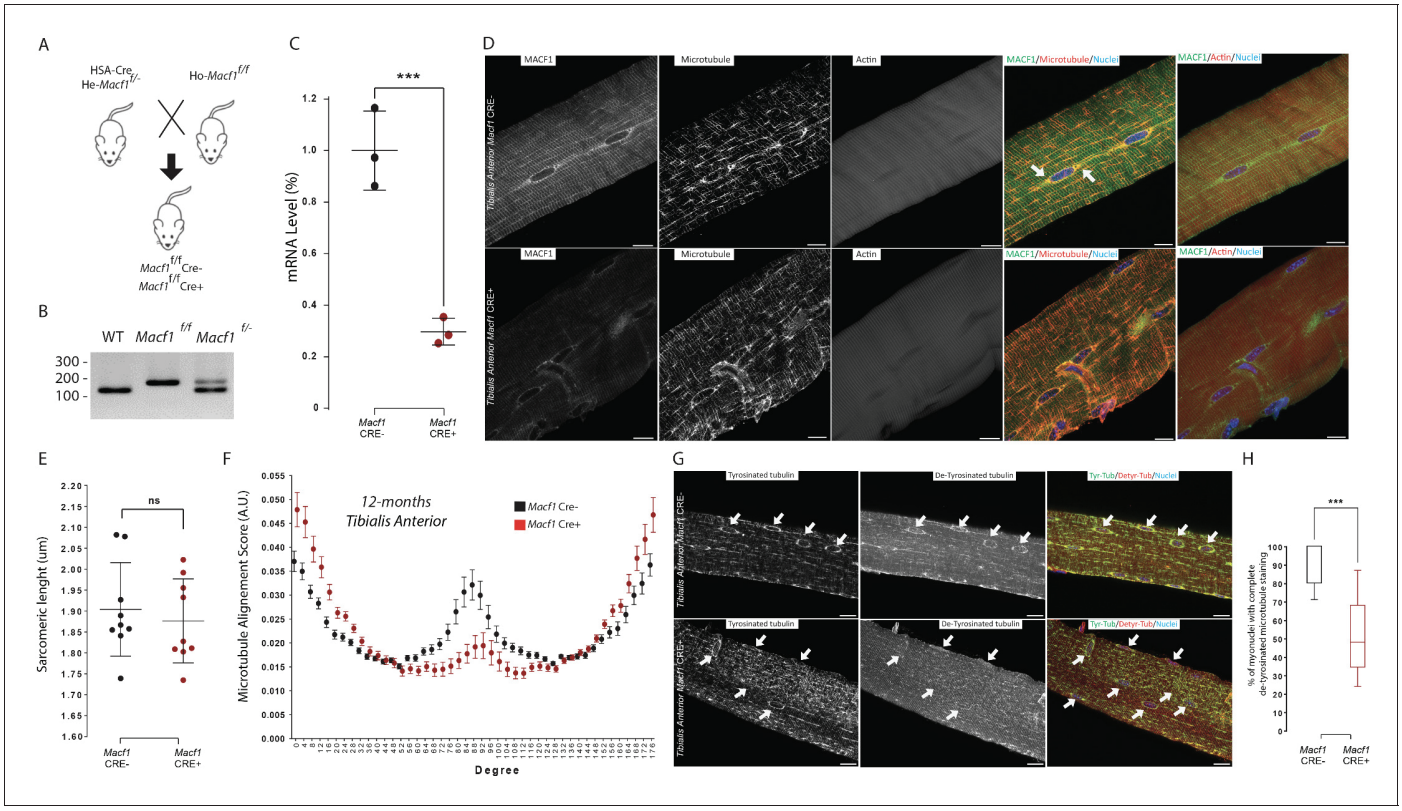

Figure 3. MACF1 is necessary for global and perinuclear microtubules organization within skeletal muscles in vivo. (**A**) Scheme of the strategy used to generate muscle specific *Macf1* knockout mouse model. (**B**) Representative PCR gel confirming the floxed *Macf1* gene in mutant mice carrying Cre transgene. (**C**) Quantification of efficacy of the Cre-lox system in our muscle specific mouse model by analyzing the *Macf1* gene expression level. qRT-PCR was carried out on total mRNA extracted from *Gastrocnemius* of 3 WT and 3 *Macf1* KO mice of 12-month-old. Following the calculation of relative gene expression level on housekeeping genes for each mouse, the mean expression level of *Macf1* was calculated for the WT mice. To generate the graph, the *Macf1* expression level of each WT and KO mouse was then normalized on the previously calculated mean value. Line is set at mean (with SEM). ***p<0.001 (Student's t test). (**D**) Representative confocal images (63×) of isolated myofibers from *Tibialis Anterior* of *Macf1* Cre- (upper panel) and Cre+ (lower panel) mice, showing MACF1 (green), myonuclei (blue) and microtubules or F-actin (red). Scale Bar = 15 µm. (**E**) Sarcomere length quantified from the alpha actinin staining from 3 *Macf1* Cre- and 3 *Macf1* Cre+ 12-month-old mice. Following myofibers isolation from *Tibialis Anterior*, the distance between alpha actinin transverse bands of 3 myofibers per mouse was measured. Line is set at mean (with SD). Ns stands for not significant (Mann-Whitney test). (**F**) Microtubules network organization analysis of at least three myofibers from each of the three WT and three conditional *Macf1*-KO mice using TeDT software. The final generated graph presents a global score for each given degree of microtubules orientation, with 0 and 180 degrees corresponding to the longitudinal microtubules and 90 degrees corresponding to the transverse microtubules. Mean values (with SEM) is presented. (**G**) Representative confocal images (63×) from myofibers isolated from *Tibialis Anterior* issued from 12-month-old *Macf* Cre- (upper panel) or Cre+ (lower panel) mice, presenting tyrosinated tubulin (green), de-tyrosinated tubulin (red) and myonuclei (blue). White arrows point to myonuclei. Scale Bar = 15 µm. (**H**) Quantification of the percentage of myonuclei presenting the total de-tyrosinated tubulin ring. Quantifications were done on confocal images obtained from several isolated myofibers from *Tibialis Anterior* of three WT and three conditional *Macf1*-KO mice at the age of 12 months. Line is set at median. ***p<0.001 (Student's t test).

The online version of this article includes the following source data and figure supplement(s) for figure 3:

Source data 1. Table showing data from experiments plotted in ***Figure 3C,E,F and H***.

Figure supplement 1. MACF1 conditional KO mice present progressive microtubules disorganization.

Figure supplement 1—source data 1. Table showing data from experiments plotted in ***Figure 3—figure supplement 1A and C–I***.

status in muscles from our conditional-KO and control mice (***Figure 3G–H***). In *Macf1* Cre- muscle fibers, tyrosinated tubulin is found all along microtubules and in the vicinity of myonuclei along myofibers. Conversely, de-tyrosinated tubulin was found preferentially in the vicinity of myonuclei. While in *Macf1* Cre+ muscles, there was no change in the tyrosinated tubulin pattern, de-tyrosinated tubulin staining at myonuclei periphery was either severely reduced or absent (***Figure 3G***, arrows). Interestingly, this modification was relevant only in muscles from 12-month-old *Macf1* Cre+ mice

(***Figure 3H***, ***Figure 3—figure supplement 1I***), suggesting a progressive impact of MACF1 loss on the microtubules pattern. Therefore, MACF1 plays a critical role in the long-term maintenance of stability of the peri-nuclear and longitudinal microtubule network of myofibers.

Muscle-specific conditional MACF1-KO mice exhibit progressive myonuclei mislocalization

We next assessed myonuclei localization along muscle fibers of *Macf1* Cre+ mice. *Tibialis Anterior* myofibers were extracted from 2-, 6-, and 12 months old *Macf1* Cre- and *Macf1* Cre+ mice and immunofluorescence staining was used to analyze myonuclei distribution (***Figure 4A***). We found that the shortest distance between neighboring myonuclei was increasing throughout development in wild-type muscles, reaching a plateau at 6 months of age (***Figure 4B***). In MACF1 depleted myofibers, not only this increase was not observed during development but there was also a significant drop in the value for the distance between myonuclei in myofibers from 12-month-old mice (***Figure 4B***). In addition, the increase in the myonuclei feret value observed in control myofibers, was abolished in *Macf1* Cre+ myofibers (***Figure 4C***), leading to an increase in myonuclei roundness (***Figure 4D***), consistent with the slackening of the cytoskeleton pressure on the myonuclei membrane (***Wang et al., 2015***).

In normal conditions, myonuclei are regularly spaced at the periphery along muscle fibers (***Bruusgaard et al., 2006***). We compared myonuclei localization in different types of muscles from *Macf1* Cre- and *Macf1* Cre+ mice by analyzing muscle cross-sections stained with DAPI and laminin (to determine the limit of each myofiber) (***Figure 4E***, ***Figure 4—figure supplement 1A***). We observed a significant increase in the number of delocalized myonuclei in the *Macf1* Cre+ muscles, either at the center or elsewhere dispatched within the myofibers of several skeletal muscles (*Tibialis Anterior, Soleus* and *Gastrocnemius*) in 12-month-old mice (***Figure 4E–F***, ***Figure 4—figure supplement 1A–B***). Interestingly, no significant delocalization of myonuclei was observed in 3- and 8-month-old mice (***Figure 4—figure supplement 1A–B***), suggesting that peripheral myonuclei alteration precede myonuclei internalization. Remarkably, peripheral myonuclei spreading is altered concomitantly with microtubules disorganization, while myonuclei internalization correlates with the disappearance of stable microtubules around myonuclei. With respect to myofiber size, no significant alteration was detected in the cross-sectional area (CSA) in *Tibialis Anterior* muscles from 3-month-old mice (***Figure 4G***). Nonetheless, we observed a shift of the distribution towards a smaller CSA in muscles from 8-month-old *Macf1* Cre+ mice, which was maintained at 12 months of age (***Figure 4G***). Of note, changes in myonuclei positioning were not associated with an alteration in the total number of myofibers per muscle (***Figure 4—figure supplement 1C***), nor with a massive regeneration process, as evidenced by the absence of *Myogenin* or *MyoD* mRNA upregulation (***Figure 4—figure supplement 1D–E***). Thus, MACF1 is implicated in the maintenance of peripheral myonuclei spreading in adult myofibers as well as in the prevention of myonuclei internalization.

MACF1-deficient muscles exhibit progressive neuromuscular junction alteration

MACF1 contributes to the maintenance of the neuromuscular junction (NMJ) by recruiting microtubules at that location (***Oury et al., 2019***) where synaptic myonuclei are clustered underneath the junction (***Bruusgaard et al., 2006***). We thus investigated the potential implication of MACF1 in myonuclei clustering at the NMJ. Immunofluorescence staining revealed no clear accumulation or specific localization of MACF1 at the NMJ, in contrast with a previous report on mouse muscle (***Oury et al., 2019***). However, consistent with observations from this group, there was a clear progressive alteration of acetylcholine receptors (AChRs) patterning in myofibers from *Macf1* Cre+ mice, characterized by a decrease of AChRs clusters size and an increase of NMJ fragmentation (***Figure 5A–C***). This AChRs clustering impairment was confirmed in different muscles (*Tibialis Anterior*, *Extensor Digitorum Longus, and Rectus Lateralis*) (***Figure 5—figure supplement 1A–B***). We also confirmed these results on the neuromuscular junction of *Drosophila* model, using the muscle-specific driver *(Mef2-GAL4)* to express RNAi against *Drosophila Shot* (*Macf1* orthologous) (***Wang et al., 2015***). Immunostaining against Shot confirmed a preferential localization of the protein around myonuclei but not at the NMJ and showed a significant reduction of protein level around myonuclei in Shot-KD larval muscles (***Figure 5—figure supplement 1C–D***). In accordance with the conditional-KO mouse model,

we found that the size of active zones of synaptic buttons and post-synaptic terminals were decreased in Shot-KD larval muscles (***Figure 5—figure supplement 1E–F***).

We next studied the association of synaptic myonuclei with the NMJ. We observed a progressive recruitment of myonuclei underneath the NMJ in *Tibialis Anterior* myofibers of control mice with age, concomitant with an enlargement of the area occupied by AChRs. In control mice, the number of synaptic myonuclei increased from approximately 7 at 2 months of age to 11 at 12 months of age (***Figure 5D***). In MACF1-depleted myofibers (*Macf1* Cre+), there was no new recruitment of synaptic myonuclei over the same period and the number of synaptic myonuclei remains close to 7 from 2- to 12 months of age (***Figure 5D***). As we identified that microtubule network is altered along muscle fibers in MACF1-depleted condition, we analyzed the potential changes in tyrosinated/de-

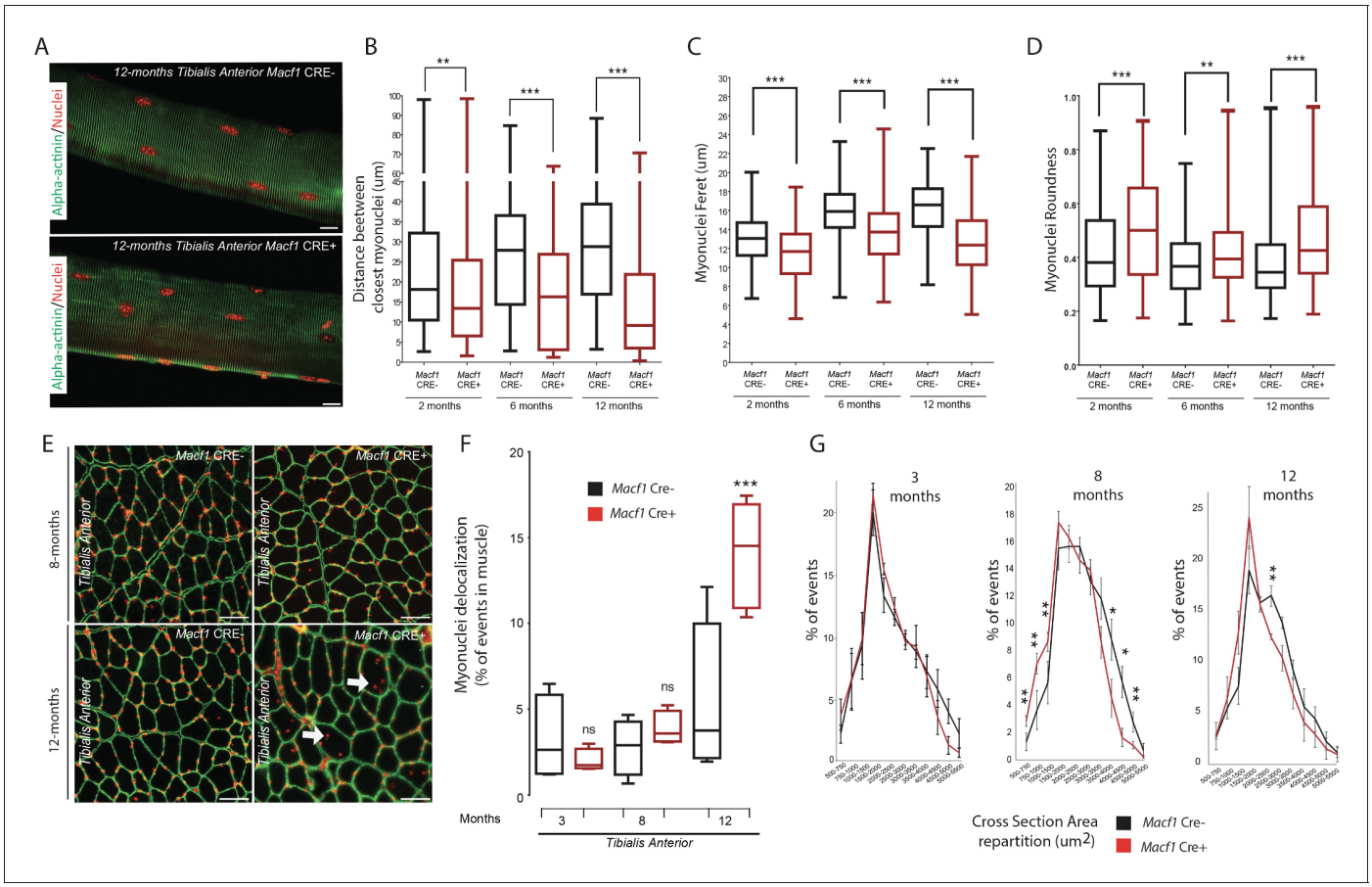

Figure 4. Loss of MACF1 alters myonuclei shape and positioning progressively with age. (**A**) Representative confocal images (63×) of myofibers isolated from *Tibialis Anterior* of *Macf1* Cre- (upper panel) and Cre+ (lower panel) mice at the age of 12 months presenting alpha-actinin (green) and myonuclei (red). Scale Bar = 15 µm. (**B–D**) Quantification of distance between the nearest myonuclei (**B**), myonuclei feret (**C**) and myonuclei roundness (**D**) measured on isolated myofibers from *Tibialis Anterior* of *Macf1* Cre- and Cre+ mice (as presented in panel A) at 2-, 6-, and 12 months of age. Several myofibers were subjected to analysis per mouse. Each group gathers data obtained from myofibers of 3 or more mice. Line is set at median. **p<0.01 and ***p<0.001 (Student's t test). (**E**) Representative images of *Tibialis Anterior* muscle cross-section from *Macf1* Cre- (left panels) and *Macf1* Cre+ (right panels) mice at the age of 8 and 12 months, stained for myonuclei (red) and Laminin (green). Examples of myofibers with mis-localized myonuclei are indicated by white arrows. Scale Bar = 150 µm. (**F**) Quantification of the percentage of myofibers with mis-localized myonuclei in *Tibialis Anterior* of 3, 8, and 12 months-old *Macf1* Cre- and *Macf1* Cre+ mice. Line is set at median. Ns stands for not significant and ***p<0.001 (Student's t test). (**G**) Distribution of myofibers cross-section area in the *Tibialis Anterior* from 3-, 8-, and 12-months-old *Macf1* Cre- and *Macf1* Cre+ mice. Line is set at mean (with SEM). Ns stands for not significant, *p<0.05 and **p<0.01 (Student's t test).

The online version of this article includes the following source data and figure supplement(s) for figure 4:

Source data 1. Table showing data from experiments plotted in ***Figure 4B–D and F–G***.

Figure supplement 1. Mis-localization of myonuclei in MACF1 conditional KO mice is independent from muscular regeneration.

Figure supplement 1—source data 1. Table showing data from experiments plotted in ***Figure 4—figure supplement 1B–E***.

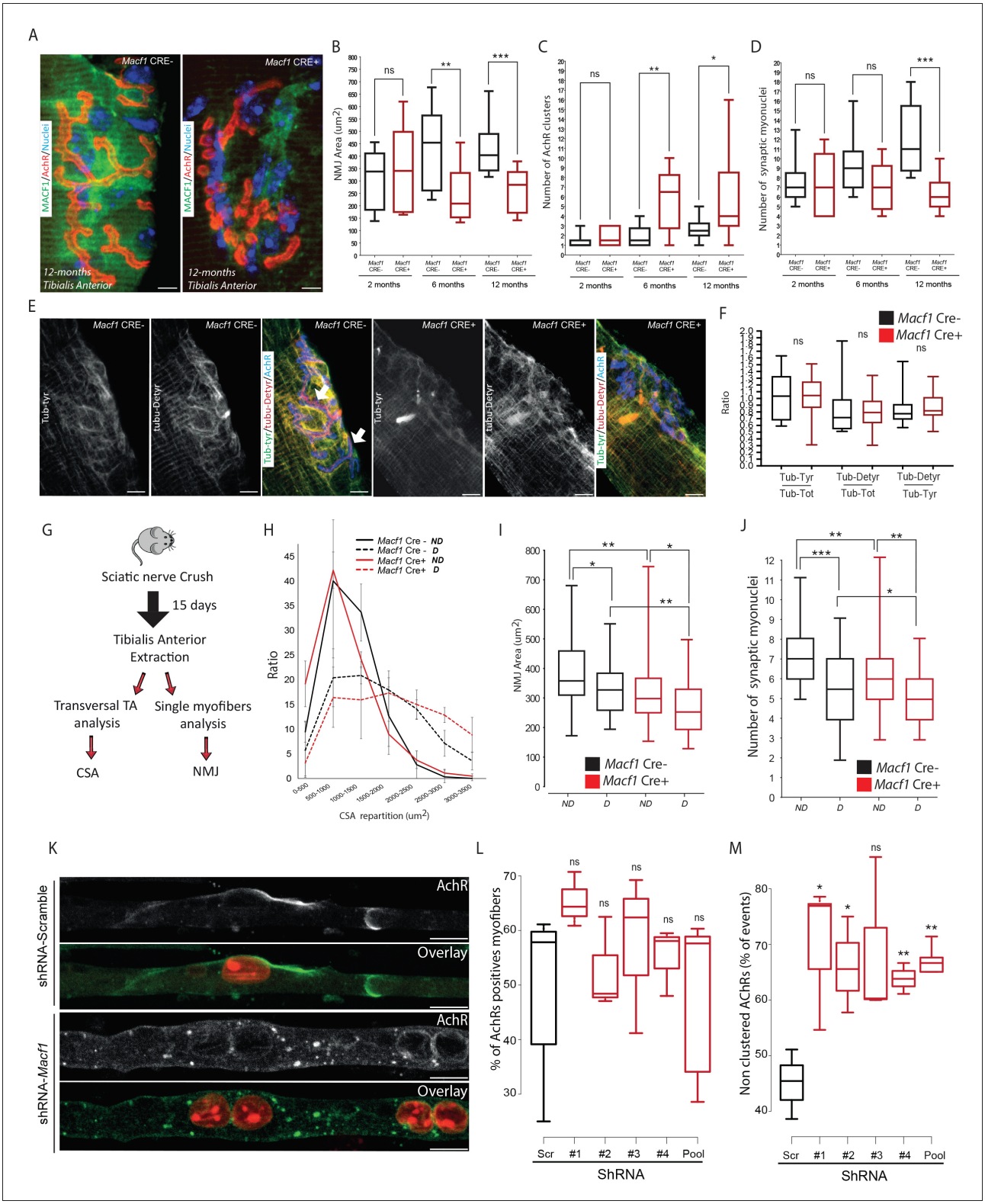

Figure 5. MACF1 controls AChRs clustering but has no impact on synaptic myonuclei at the NMJ. (**A**) Representative confocal images (63×) of post-synaptic NMJs within isolated myofibers from *Tibialis Anterior* of *Macf1* Cre- (left panel) and Cre+ (right panel) mice at the age of 12 months presenting MACF1 (green), AChRs clusters (red) and myonuclei (blue). Scale Bar = 10 µm. (**B–D**) Quantification of post-synaptic NMJs area (**B**), number of AChRs clusters (**C**) and number of synaptic myonuclei (**D**) measured on myofibers isolated from *Tibialis Anterior* of *Macf1* Cre- and Cre+ mice (as presented in

Figure 5 continued on next page

Figure 5 continued

panel A) at 2-, 6-, and 12 months of age. Several myofibers were subjected to analysis per mouse and each group is formed from at least three mice. Line is set at median. Ns stands for not significant, *p<0.05, **p<0.01 and ***p<0.001 (Student's t test). (**E**) Representative confocal images (63×) presenting tyrosinated tubulin (green), de-tyrosinated tubulin (red), and AChRs clusters (blue) in myofibers isolated from *Tibialis Anterior* of *Macf1* Cre- (three left panels) and Cre+ (three right panels) mice at the age of 12 months. Scale Bar = 10 µm. (**F**) Quantification of the ratios of fluorescence intensity from tyrosinated tubulin to total tubulin, de-tyrosinated tubulin to total tubulin and de-tyrosinated tubulin to tyrosinated tubulin. The mean fluorescence intensity of each given staining was measured specifically for the post-synaptic NMJs area (as presented in panel E) on NMJs of myofibers isolated from *Tibialis Anterior* of *Macf1* Cre- and Cre+ mice at the age of 12 months. Line is set at median. Ns stands for not significant (Student's t test). (**G**) Scheme of the strategy used to induce sciatic nerve crush and subsequent analysis of muscle fibers from *Macf1* Cre- and Cre+ mice. (**H**) Distribution of myofibers cross-section areas from non-denervated (referred as ND) and denervated (referred as D) *Tibialis Anterior* muscles of *Macf1* Cre- and Cre+ mice at the age of 8 months. Line is set at mean (with SEM). (**I–J**) Quantification of post-synaptic NMJs area (**I**) and number of synaptic myonuclei (**J**) measured on isolated myofibers from non-denervated (referred as ND) and denervated (referred as D) *Tibialis Anterior* muscles of *Macf1* Cre- and Cre+ mice at the age of 8 months. Line is set at median. *p<0.05, **p<0.01, and ***p<0.001 (Student's t test). (**K**) Representative fluorescence images (63×) of AChRs clusters (green) and myonuclei (red) in myofibers treated with scramble shRNA (two upper panels) or with a pool of the four distinct shRNAs targeting *Macf1* (two lower panels) after 10 days of differentiation in presence of Agrin in culture medium. Scale Bar = 10 µm. (**L**) Percentage of myofibers expressing immunofluorescence staining for AChRs in primary myofibers treated with scramble shRNA, with each of the four distinct shRNAs or with a pool of these four distinct shRNAs targeting *Macf1* after 10 days of differentiation in the presence of Agrin. Data are from three individual experiments. Line is set at median. Ns stands for not significant (Student's t test). (**M**) AChRs clustering distribution in cells treated with scramble shRNA, with each of the four individual shRNAs or with a pool of the four individual shRNAs targeting *Macf1* after 10 days of differentiation in the presence of Agrin. Data was collected from three individual experiments for each condition. Line is set at median. Ns stands for not significant, *p<0.05 and **p<0.01 (Student's t test).

The online version of this article includes the following source data and figure supplement(s) for figure 5:

Source data 1. Table showing data from experiments plotted in ***Figures 5B–D,F,H–J and L–M***.
Figure supplement 1. MACF1 orthologue, Shot, is essential for NMJs organization in *Drosophila*.

tyrosinated tubulin distribution at the NMJ. Surprisingly, tubulin accumulation was not observed around the synaptic myonuclei of control myofibers, in contrast with the pattern observed at extra-synaptic nuclei (***Figure 5E***, ***Figure 3G***). Instead, we detected tubulin accumulation close to the NMJ site of MACF1 mutant mice with a blurry patterning. Nonetheless, de-tyrosinated tubulin accumulation appeared highly correlated with AChRs staining even when AChR clusters were fragmented in the conditional-KO mice (***Figure 5E***, arrows). Finally, the ratio of both tyrosinated and de-tyrosinated tubulin vs total tubulin at NMJs were not different between *Macf1* Cre- and *Macf1* Cre+ mice (***Figure 5F***). This suggests that the role of MACF1 at the NMJ is not related to myonuclei clustering nor to the control of microtubule dynamics but is instead associated with AChRs clustering.

To further check that synaptic myonuclei location does not depend on MACF1, we used a sciatic nerve crush protocol to induce denervation (***Figure 5G***; ***Milanic et al., 1999***). Using this technique, we clearly observed atrophy of the muscle fibers together with a reduction in the AChRs area in both *Macf1* Cre- and *Macf1* Cre+ conditions (***Figure 5H–I***). Interestingly, 15 days following denervation, the similar number of synaptic myonuclei per NMJ was lost in both *Macf1* Cre- and *Macf1* Cre+ conditions (***Figure 5J***), confirming that MACF1 is not directly implicated in the maintenance of synaptic myonuclei.

As the role of MACF1 at the NMJ seemed specifically related to AChR clustering, we tested whether MACF1 depletion in myofibers in vitro would fail to precociously cluster AChRs. For this, agrin-supplemented culture medium was used during in vitro differentiation of myofibers as this is known to induce clustering of AChRs (***Lin et al., 2005***; ***Schmidt et al., 2012***; ***Vilmont et al., 2016***; ***Figure 5K***). Using immunofluorescence staining, we found that, even though the proportion of shRNA-MACF1-transfected myofibers expressing AChRs was not changed (***Figure 5L***), they displayed a 20% drop in the number of those presenting AChR clusters with a diameter larger than 8 µm (***Figure 5M***). This demonstrates that MACF1 is required for efficient AchR clustering in the myofiber.

Altogether, MACF1 is required to maintain the neuromuscular synapse integrity through AChRs clustering in developing and differentiated myofibers, which in turn controls synaptic myonuclei recruitment at the NMJ.

Muscle fibers from MACF1-KO mice show muscle excitability defects and T-tubules alteration with preserved excitation-contraction coupling

To determine whether the above-described alterations impact muscle function, we tested muscular performance in young (4-month-old) and in adult (12-month-old) *Macf1* conditional-KO mice compared to age-matched control animals. The formers are mainly characterized by peripheral extra-synaptic myonuclei disorganization, while the latters also exhibit large internalization of extra-synaptic myonuclei mice. We used a strictly non-invasive experimental setup offering the possibility to stimulate the hindlimb muscles in vivo to record force production. Force was measured in response to incremental stimulation frequencies (from 1 to 100 Hz) to obtain the force-frequency relationship. There was no significant difference in the values for maximum force produced between the two groups, irrespective of the mouse age. However, in young mice, there was a large rightward shift of the force production capacity in conditional *Macf1* KO mice (***Figure 6A***), suggesting alteration of either the neuromuscular transmission or of the excitation-contraction coupling process. Of note, this shift was also maintained in adult mice, although in a less pronouced manner (***Figure 6A***).

In skeletal muscle, triads consist of one transverse tubule (T-tubule) with two appended terminal cisternae of sarcoplasmic reticulum (SR). The triad is the structure where excitation-contraction coupling (ECC) takes place. Efficient triad formation has been linked to microtubule organization in muscle cells (***Osseni et al., 2016***). Since *Macf1* conditional-KO myofibers exhibit microtubule disorganization, we used electron microscopy to study the ultrastructure of muscle in *Macf1* Cre+ mice and analyzed T-tubules and SR organization (***Figure 6B***). We found signs of alteration of the T-tubules in some *Macf1* Cre+ myofibers (***Figure 6B***, white arrows) consistent with a possible alteration of ECC. To test this possibility, we compared voltage-activated SR Ca^{2+} release in *Flexor Digitalis Brevis* (FDB) muscle fibers isolated from conditional *Macf1* Cre+ mice and control mice. Confocal staining using di-8-anepps showed an overall comparable structure of T-tubule network in *Macf1* Cre- and in *Macf1* Cre+ FDB muscle fibers (***Figure 6C*** -top and -middle panels). However, some isolated muscle fibers from the conditional mutant mice exhibited strong alteration of T-tubule orientation without perturbation in T-tubules density or sarcomere length (***Figure 6C*** -Bottom panel, D-F). We next tested if SR Ca^{2+} release amplitude and kinetics are affected in *Macf1* Cre+ muscle fibers. ***Figure 6G*** shows rhod-2 Ca^{2+} transients elicited by membrane depolarizing steps of increasing amplitude in a *Macf1* Cre- and in a *Macf1* Cre+ fibers. As routinely observed under these conditions (***Kutchukian et al., 2017***), transients in control fibers exhibit a fast early rising phase upon depolarization followed by a slower phase at low and intermediate voltages and by a slowly decaying phase for the largest depolarizing steps. As shown in ***Figure 6H***, rhod-2 transients from *Macf1* Cre+ fibers exhibited an overall similar time-course, not distinguishable from control muscle fibers. In each tested fiber, the rate of SR Ca^{2+} release was calculated from the rhod-2 Ca^{2+} transients. Traces for the calculated rate of SR Ca^{2+} release corresponding to the transients shown in ***Figure 6H*** are shown in ***Figure 6I***. In both fibers, the rate exhibits a similar early peak, whose amplitude increases with that of the pulse, followed by a spontaneous decay down to a low level. The SR Ca^{2+} released peak amplitude was similar in *Macf1* Cre- and in *Macf1* Cre+ muscle fibers for all voltages (***Figure 6I***) and the time to reach the peak was also not affected in the *Macf1* Cre+ muscle fibers (***Figure 6I***, values not shown). Mean values for maximal rate of SR Ca^{2+} release (Max $d[Ca_{tot}]/dt$), mid-activation voltage ($V_{0.5}$) and slope factor (k) of the voltage-dependence were statistically unchanged in *Macf1* Cre+ muscle fibers compared to control fibers (***Figure 6J***). Accordingly, there was also no change in the voltage-dependent Ca^{2+} channel activity of the dihydropyridine receptor (also referred to as $Ca_V1.1$, the voltage-sensor of excitation-contraction coupling) in fibers from *Macf1* Cre+ mice (not shown).

Overall, despite some structure alterations, myofibers isolated from *Macf1* conditional-KO mice exhibit efficient voltage-activated SR-Ca^{2+} release, strongly suggesting that altered force-frequency relationship is related to neuromuscular transmission deficiency.

MACF1 controls mitochondria biogenesis in skeletal muscle

During our studies on muscle excitability, measurement of the absolute maximal force developed by *Macf1* conditional KO mice was not changed compared to control mice (data not shown) but when we questioned the fatigability of those muscles, we found that in both young and old mice, *Macf1* Cre+ are more resistant to fatigue compared to control mice (***Figure 7A***). Since skeletal muscles are

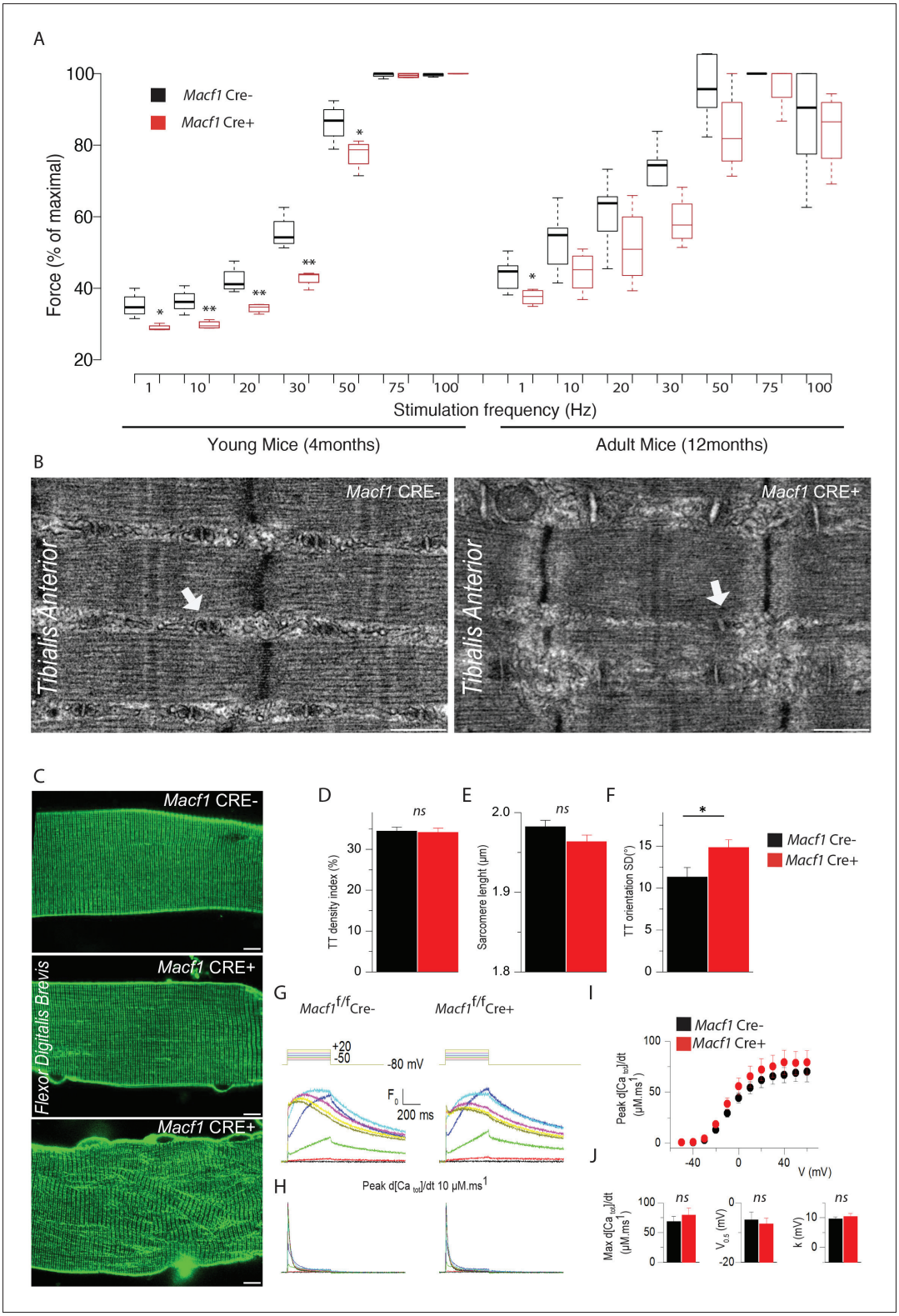

Figure 6. Muscle-specific *Macf1* knockout affects muscle force production and T-tubule organization but leaves SR Ca^{2+} release unchanged. (**A**) Force production from the *Hindlimb* muscles in young (4 months) and adult (12 months) *Macf1* Cre- and *Macf1* Cre+ mice in response to various incremental stimulation frequencies (from 1 to 100 Hz). Line is set at median. *p<0.05 and **p<0.01 (Student's t test). (**B**) Representative electron microscopy images of myofibrils and T-tubule organization within *Tibialis Anterior* muscles from 12-month-old *Macf1* Cre- and *Macf1* Cre+ mice. Scale Bar = 0.5 µm. (**C**)

Figure 6 continued on next page

Figure 6 continued

Representative fluorescence microscopy images of di-8-anepps staining of the T-tubule network in *Flexor Digitalis Brevis* muscle fibers of 12-month-old *Macf1* Cre- and *Macf1* Cre+ mice. Scale Bar = 15 µm. (**D–F**) Quantification of T-tubules density index (**D**), Sarcomere length (**E**) and T-tubules orientation (**F**) in *Flexor Digitalis Brevis* muscle fibers from 12-month-old *Macf1* Cre- and *Macf1* Cre+ mice. Mean with SD is showing. Ns stands for not significant and *p<0.05 (Student's t test). (**G**) Representative rhod-2 Ca^{2+} transients in a *Macf1* Cre- and in a *Macf1* Cre+ fiber in response to 0.5 s-long depolarizing pulses from −80 mV to the range of indicated values, with intervals of 10 mV. (**H**) Corresponding Ca^{2+} release flux ($d[Ca_{Tot}]/dt$) traces calculated as described in the Materials and methods. (**I**) Mean voltage-dependence of the peak rate of SR Ca^{2+} release in *Macf1* Cre- and in a *Macf1* Cre+ fibers. (**J**) Inset shows the mean values for maximal rate, half-activation voltage and steepness factor (**k**) for SR Ca^{2+} release in the two groups of fibers, as assessed from Boltzmann fits to data from each fiber.

The online version of this article includes the following source data for figure 6:

Source data 1. Table showing data from experiments plotted in ***Figure 6A,D–F and I***.

composed of a functional and metabolic continuum of slow (type I) and fast fibers (types IIa and IIx) known to distinctively rely on metabolic pathways and mitochondrial activity, we first questioned whether there were changes in the mitochondrial pool of adult conditional-KO mice. We measured the intensity of succinate dehydrogenase (SDH) staining, indicative of mitochondrial activity, and found a significant increase in the number of fibers with strong positive succinate dehydrogenase staining in *Tibialis Anterior* muscle from 12-month-old *Macf1* Cre+ compared to control mice (***Figure 7B–C***). As the intensity of SDH staining is commonly used to discriminate slow and fast fibers, we investigated if the proportion of slow fibers was changed in *Macf1* Cre+ mice. Cross-sections of 12-month-adult muscles from the *Tibialis Anterior, Soleus* and *Gastrocnemius* were analyzed for slow myosin content and no alteration was observed (***Figure 7—figure supplement 1A–B***).

We next quantified the content of mitochondria and of proteins of the electron transport chain. There was an increase in the total amount of mitochondria (Tom20 relative to actin) in total protein extracts from *Gastrocnemius* of 12-month-old *Macf1* Cre+ mice, as compared to control mice. However, there were no changes in the levels of mitochondrial electron transport chain proteins (CI, II, III, IV, and V, relative to Tom20) (***Figure 7D***). To confirm the increase of mitochondria pool, we measured the ratio of Mitochondrial-DNA to Genomic-DNA. This ratio did not differ between young (3-month-old) and adult (12-month-old) control mice, nor did it between young *Macf1* Cre+ and control mice (***Figure 7E***). Interestingly, adult *Macf1* Cre+ mice showed an increased amount of mitochondrial DNA compared to the other groups (***Figure 7E***). To understand this phenomenon, we followed the expression level of different genes known to contribute to mitochondria fusion/fission/biogenesis such as *DNM1, DNM2, PPARGC1A* and *SLN*. Remarkably, we found that only the expression of Sarcolipin, known to promote mitochondria biogenesis in skeletal muscle (***Maurya et al., 2018***; ***Maurya et al., 2015***) was increased in *Macf1* Cre+ mice compared to control mice (***Figure 7F***, ***Figure 7—figure supplement 1C***). We next checked the staining of Cytochrome C, indicative of mitochondria content and spatial organization, in myofibers isolated from *Tibialis Anterior* muscles from 12-month-old mice. Our immunofluorescence approach showed a strong accumulation of mitochondria in different areas at the periphery of myofibers from the conditional-KO mice compared to control mice (***Figure 7G***, arrow). Additionally, there was an accumulation of mis-oriented longitudinal staining (***Figure 7H***), reminiscent of what was observed with the T-tubules staining in certain *Macf1* Cre+ myofibers (***Figure 6C***). This suggests an alteration of myofibrils cohesion at the periphery of the myofibers. In this view, since mitochondria are linked to both the microtubule network and to Desmin intermediate filaments (***Reipert et al., 1999***), we questioned the integrity of the Desmin network and found a similar disruption as observed for mitochondria staining (***Figure 7—figure supplement 1D-E***). Electron microscopy was next used to visualize the ultrastructure of mitochondria in *Tibialis Anterior* muscle of *Macf1* Cre+ mice. This approach confirmed the increase in mitochondria content in *Macf1* Cre+ myofibers, associated with the presence of spherical mitochondria in-between myofibrils (***Figure 7I***). We next questioned if the mitochondrial network distribution was altered in vitro, in primary myofibers (***Figure 7J***). In myofibers treated with scrambled siRNA/shRNA, mitochondria lined up in the bulk of myofibers, in-between myofibrils, where they followed the longitudinal axis, just like the microtubule network. However, in *Macf1* siRNA/shRNA-treated myofibers, we observed a 30% increase of mitochondria content (***Figure 7K***). These results confirmed a role of MACF1 in muscles specifically related to mitochondria biogenesis. Consequently, MACF1 is involved

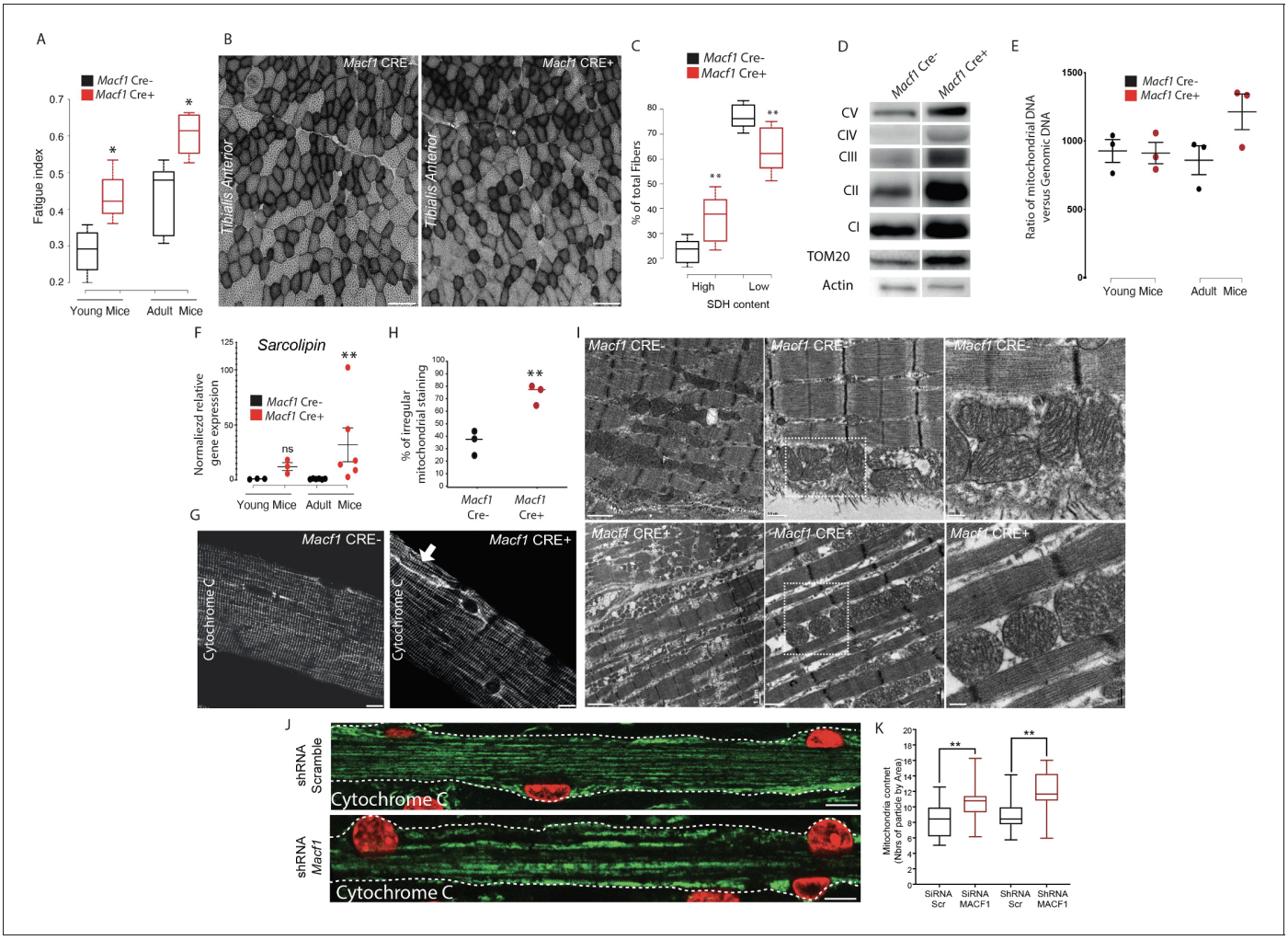

Figure 7. Muscle specific MACF1 knockout affects mitochondrial content and organization. (**A**) Quantification of the fatigue index from the *Hindlimb* muscles in young (4 months) and adult (12 months) *Macf1* Cre- and *Macf1* Cre+. Line is set at median. *p<0.05 (Student's t test). (**B**) Representative images of transversal cross-section of *Tibialis Anterior* muscle from 12-month-old *Macf1* Cre- (left panel) and *Macf1* Cre+ (right panel) mice stained for Succinate DeHydrogenase activity. Scale Bar = 150 µm. (**C**) Quantification of the Succinate DeHydrogenase activity relative to myofibers distribution in conditional *Macf1*-KO mice compared to control mice. Line is set at median. Ns stands for not significant, **p<0.01 (Student's t test). (**D**) Western blot analysis of OXPHOS mitochondrial electron transport chain, TOM20 and actin proteins expression in total extracts from *Gastrocnemius* muscles of 12-month-old *Macf1* Cre- and *Macf1* Cre+ mice. (**E**) QPCR quantification of the ratio between mitochondrial and genomic DNA in total DNA extracts obtained from *Gastrocnemius* muscles of three individual *Macf1* Cre- and *Macf1* Cre+ mice at each given age. Line is set at mean (with SEM). (**F**) QRT-PCR results presenting relative gene expression level for SLN in *Macf1* Cre- and Cre+ at each given age. Following the calculation of relative gene expression level with reference to housekeeping genes for each mouse, the mean expression level of SLN was calculated for the WT mice. Next, the expression level of each WT and KO mouse was normalized to the previously calculated mean value. Line is set at mean (with SEM). Ns stands for not significant and **p<0.01 (Mann-Whitney test). (**G**) Representative confocal images (63×) from isolated myofibers of *Tibialis Anterior* stained for Cytochrome C in *Macf1* Cre- (left panel) and Cre+ (right panel) mice of 12-month-old mice. Scale Bar = 15 µm. (**H**) Quantification of the percentage of myofibers with irregular (broken/oriented/accumulated) mitochondrial staining in isolated myofibers of *Tibialis Anterior* muscles from three individual *Macf1* Cre- and Cre+ mice at the age of 12 months. Line is set at median. **p<0.01 (Student's t test). (**I**) Representative electron microscopy images of myofibrils and mitochondria organization within *Tibialis Anterior* muscles from 12-month-old *Macf1* Cre- (upper panels) and *Macf1* Cre+ (lower panels) mice. Scale Bar = 1, 0.5, 0.2 µm. (**J**) Confocal immunofluorescence images (63×) presenting the organization of Cytochrome C (green) in primary myofibers treated either with scramble shRNA (upper panel) or with a pool of four distinct shRNAs targeting *Macf1* (lower panel) after 13 days of differentiation. Myonuclei are presented in red. Scale Bar = 10 µm. (**K**) Quantification of mitochondrial content per area in primary myofibers treated either with scramble shRNA or with a pool of four distinct shRNAs targeting *Macf1* after 13 days of differentiation. Line is set at median. **p<0.01 (Student's t test).

The online version of this article includes the following source data and figure supplement(s) for figure 7:

Source data 1. Table showing data from experiments plotted in ***Figure 7A,C,E–F,H and K***.

Figure 7 continued on next page

Figure 7 continued

Source data 2. Whole immunoblotting membrane for OXPHOS, TOM20, and actin plotted in ***Figure 7D***.
Figure supplement 1. MACF1 conditional KO mice present normal distribution of different skeletal muscles types but disorganized Desmin network.
Figure supplement 1—source data 1. Table showing data from experiments plotted in ***Figure 7—figure supplement 1B–C and E***.

in the regulation of mitochondria biogenesis as loss of MACF1 is associated with an increase in Sarcolipin level and redistribution of mitochondrial content.

Discussion

Different mechanisms involving actin and microtubule network control myonuclei positioning during muscle fiber development and differentiation (***Azevedo and Baylies, 2020***). However, the long-term mechanisms allowing myonuclei patterning maintenance in mature muscle fibers are still pending. The present study describes a MACF1-dependent pathway that is critical for proper myonuclei distribution at the periphery of the myofibers, through the ability of MACF1 to control microtubule network dynamics. MACF1 is a giant member of the spectraplakin family, able to simultaneously bind to different cytoskeleton members. Spectraplakins are involved in intracellular trafficking, cellular polarization migration and shaping, cell-cell adhesion and mechanical strength (***Suozzi et al., 2012***). In mononuclear cells, MACF1 acts as a hub between the actin and microtubule networks to promote their alignment, allowing cells structure maintenance (***Preciado López et al., 2014***). In skeletal muscle, MACF1 has been implicated in the integrity of the NMJ through its association with rapsyn and actin (***Antolik et al., 2007***; ***Oury et al., 2019***). Shot, the *Drosophila* orthologue participates in the formation and maintenance of a perinuclear shield in muscle (***Wang et al., 2015***). Still, MACF1 function in muscle remained puzzling as *drosophila* Shot exhibits a myonuclei-related localization while previous studies in murine models identified MACF1 specifically accumulated at the NMJ.

Our in vitro results show that MACF1 is progressively expressed during muscle fiber maturation and differentiation and accumulates at the periphery of the myofibers where it colocalizes with cortical microtubules (***Figure 1***, ***Figure 1—figure supplement 1***). In vivo, muscle MACF1 also accumulates strongly in the vicinity of extra-synaptic myonuclei and colocalizes mainly with the longitudinal microtubule network (***Figure 3***), in accordance with observations from *Drosophila* myofibers (***Figure 5—figure supplement 1***; ***Wang et al., 2015***). Interestingly, the MACF1 accumulation pattern along the extrasynaptic myofibers differs from that at the NMJ where there isn't a particular MACF1 meshwork around synaptic myonuclei, nor a colocalization of MACF1 with AChRs (***Figure 5***, ***Figure 5—figure supplement 1***). Accordingly, extra-synaptic myonuclei positioning is altered in developing myofibers of MACF1-depleted muscles (***Figures 1*** and ***4***), whereas synaptic myonuclei positioning is not affected (***Figure 5***). Our in vitro results suggest that the progressive alteration of myonuclei positioning is mainly due to the capacity of MACF1 to freeze myonuclei displacement events (***Figure 2***). Thus, in the MACF1-depleted condition, myonuclei motion is increased and contributes to the alteration of myonuclei distribution along myofibers that translates into a reduction in the distance between adjacent myonuclei (***Figures 1*** and ***4***). Interestingly, the in vivo long-term depletion of muscle MACF1 leads to a dramatic change in the location of myonuclei in 12 month-old mice. In these mice, myonuclei are internalized, with no associated signs of regeneration (***Figure 4***, ***Figure 4—figure supplement 1***). Myonuclei internalizations is concomitant with the appearance of T-tubules enlargement and with continuity breaks of membranes and Desmin structures in the myofibers (***Figures 6*** and ***7***). In mature myofibers, myonuclei have been found to reach the periphery of myofibers by a process dependent on an interplay between myonuclei rigidity, actin and Desmin network (***Roman et al., 2017***). Depletion of MACF1 in vitro or in vivo does not impact the actin network integrity, as reflected by unmodified sarcomere's structure (***Figures 1*** and ***3***, ***Figure 3—figure supplement 1***). In contrast, the myonuclei morphology is modified (***Figures 1*** and ***4***). We believe that in MACF1 depleted myofibers, the loosened anchorage of peripheral myonuclei is the initial cause of changes in their morphology. Over time, MACF1 depletion affects the Desmin network, which is a myofibril linker known to play a hub role between the sarcolemmal cytoskeleton and nuclei (***Hnia et al., 2015***). In this perspective, myonuclei internalization in MACF1-depleted myofibers from old mice is likely the consequence of loosening of the MACF1-dependent meshwork in the vicinity

of the myonuclei. This contributes to the long-term enhancement of myonuclei motion, associated with myonuclei shape alteration. Altogether, this internalization requires loss of cohesion within myofibrils, achieved through reorganization of the Desmin network.

Our study shows that MACF1 controls myonuclei displacement through the regulation of microtubules dynamics during myofibers maturation (***Figures 2*** and ***3***). Early steps of myonuclei positioning in immature myofibers (myotubes) depend on an interplay between microtubules, microtubule-associated-proteins and motors proteins such as MAP4, MAP7, Dynein, and Kif5b (***Cadot et al., 2012***; ***Gache et al., 2017***; ***Metzger et al., 2012***; ***Mogessie et al., 2015***). Interestingly, we found that MACF1 is not involved in the early steps of myonuclei spreading in myotubes (***Figure 1—figure supplement 1***). Using EB3 comets tracking, we show that microtubule dynamic progressively decreases within myofibers during maturation, leading to more stabilized microtubules structures (***Figure 2***). Interestingly, the absence of MACF1 impairs this stabilization and leads to microtubule with a higher polymerization rate (***Figure 2***). We propose that this enhanced dynamic is correlated with the increased myonuclei movement along myofibers, especially because endogenous MACF1 is in vitro and in vivo clearly located around myonuclei and is co-localized with the longitudinal microtubule network (***Figures 1*** and ***3***). Progressive microtubule network stabilization during myofibers maturation is associated with de-tyrosinated tubulin accumulation. Interestingly, our microscopy images show that a de-tyrosinated pool of microtubules is present in the vicinity of myonuclei in control mice (***Figure 3***; ***Gadadhar et al., 2017***). In accordance with the elevated microtubule dynamics, de-tyrosinated tubulin staining around myonuclei is lost in *Macf1* KO muscles (***Figure 3***), supporting a link between microtubule dynamics and myonuclei motion. No direct interplay between MACF1 and tubulin post translational modification (PTMs) has been so far documented, but one can hypothesize that regarding already described MACF1 localization, at the Minus-End of microtubules throught CAMSAP/patronin or at the Plus-End of microtubules throught EB1, MACF1 can influence localization of enzymes controlling tubulin PTMs such as TTL or SVBP (***Aillaud et al., 2017***; ***Noordstra et al., 2016***; ***Peris et al., 2006***; ***Su et al., 2020***). Thus, it is tempting to postulate that in MACF1-depleted myofibers from old mice, this elevated microtubule dynamic is constantly challenging the cohesion between myofibrils through Desmin reorganization, hence contributing to the myonuclei internalization process (***Heffler et al., 2020***). Interestingly, in the MACF1-depleted myofibers, the tyrosinated/de-tyrosinated ratio of microtubules is not changed at the NMJ supporting alternative tubulin PTMs in the maintenance of the microtubule network cohesion at that location (***Osseni et al., 2020***). Nonetheless, we show that MACF1 is important for the control of AChR clustering in mature myofibers (***Figure 5***). Failure of this mechanism in the MACF1-depleted myofibers is the most likely reason for the observed decrease in muscle excitability since it will affect neuromuscular transmission (***Figure 6***). This interpretation is strengthened by the fact that myofibril genesis is not impacted neither in vitro nor in vivo upon MACF1-depletion and by the fact that there is also no alteration in SR-Ca^{2+} release even though the overall structure of T-tubule network was found affected in some of the myofibers (***Figure 6***).

Our study has also revealed an unexpected role for muscle MACF1 related to mitochondria biogenesis. We observed an increase in the number of oxidative fibers in MACF1-depleted muscles from old mice, with no associated change in the myosins expression levels (***Figure 7***, ***Figure 7—figure supplement 1***). This alteration is correlated with an increase of mitochondrial DNA and with the increased fatigue resistance of the MACF1 KO mice (***Figure 7***). In addition, our electron and fluorescence microscopy images revealed an alteration of mitochondria shape and patterning as they appear rounder and accumulated in-between myofibrils (***Figure 7***). Molecular motors such as Kif5b and Dynein control mitochondrial motion in myoblasts (iqbal and ***Iqbal and Hood, 2014***). Microtubule network disorganization and loss of myofibrils cohesion may explain mitochondria mislocalization along myofibers. Accordingly, MACF1 has been previously implicated in mitochondria localization and nuclear positioning in oocytes (***Escobar-Aguirre et al., 2017***). In addition, an increase in microtubules instability directly impacts the local concentration of free tubulin (***Gache et al., 2005***) and free tubulin-βII level can affect mitochondrial metabolism and organization (***Guerrero et al., 2010***; ***Guzun et al., 2011***; ***Kumazawa et al., 2014***). Finally, our investigations revealed that the mRNA levels of proteins related to mitochondrial fusion/fission such as DNM1 and DNM2 were unchanged in MACF1 depleted myofibers but the transcripts of Sarcolipin, a protein related to mitochondrial biogenesis, were dramatically increased in conditional old mutant mice compared to controls. One possibility is that this alteration is due to the aberrant myonuclei size/

shape of MACF1 KO myofibers since it has been reported that nuclear alterations can impact gene expression through changes in mechanotransduction processes (***Robson et al., 2016***; ***Wang et al., 2018***). In any case, our results indicate that the increase in mitochondria number is already present in young mice (***Figure 7***) and is the most likely explanation for the resistance of both young and old KO mice to fatigue. We thus provide evidence that microtubule organization and dynamics in muscle cells are imporant not only for mitochondria motion and positioning, but also to maintain mitochondria biogenesis (***Mado et al., 2019***).

The present results have physiopathological relevance as there are several disease conditions associated with peripheral myonuclei mis-localization in muscle fibers. This is the case for a heterogeneous group of inherited muscle diseases, called CentroNuclear Myopathies (CNMs), which are defined pathologically by an abnormal localization of myonuclei in the center of the myofibers (***Jungbluth and Gautel, 2014***). Genes implicated in the various forms of CNMs encode proteins that participate in different aspects of membrane remodeling and trafficking such as MTM1, Amphyphisin-2/BIN1, DNM2, and HACD1 (***Bitoun et al., 2005***; ***Laporte et al., 1996***; ***Muhammad et al., 2013***; ***Muller et al., 2003***). Another example is skeletal muscle biopsies from patients with desminopathies which also present internalized myonuclei (***Clemen et al., 2013***). Here, we have identified MACF1, as a critical contributor in the maintenance of extra-synaptic myonuclei positioning, in the maintenance of the NMJ integrity and in mitochondria location and biogenesis. This is of strong relevance to our understanding of muscle diseases associated with centralization of myonuclei and potentially to other pathological muscle defects.

Materials and methods

Cell culture

Primary myoblasts were collected from wild type C57BL6 mice as described before (***Falcone et al., 2014***; ***Pimentel et al., 2017***). Briefly, Hindlimb muscles from 6 days pups were extracted and digested with collagenase (Sigma, C9263-1G) and dispase (Roche, 04942078001). After a pre-plating step to discard contaminant cells such as fibroblasts, myoblasts were cultured on 1% matrigel coated-dish (Corning, 356231) in growth media (GM: IMDM (Gibco, 21980–032), 20% fetal bovine serum (Gibco, 10270–106), 1% chicken embryo extract (USBiological, C3999), and 1% penicillin-streptomycin (Gibco, 15140–122)). When reached to 90% of confluence, myocytes were induced to differentiate in myotubes for 2–3 days in differentiation media (DM: IMDM (Gibco, 21980–032), 2% of horse serum (Gibco, 16050–122) and 1% penicillin-streptomycin (Gibco, 15140–122)). Myotubes were then covered by a concentrated layer of matrigel and maintained for up to 10 days in long differentiation culture medium (LDM: IMDM (Gibco, 21980–032), 2% of horse serum (Gibco, 16050–122), 0.1% Agrin + 1% penicillin-streptomycin (Gibco, 15140–122)) until the formation of mature and contracting myofibers. LDM was changed every two days.

Mouse myoblast C2C12 cells (ATCC, CRL-1772, RRID:CVCL_0188), tested negative form mycoplasma, were cultured in growth media (DMEM (Gibco, 41966029), 15% fetal bovine serum (Gibco, 10270–106) and 1% penicillin-streptomycin (Gibco, 15140–122)) and were plated on 1% Matrigel-coated dishes for 1–2 days before differentiation. Differentiation was induced by switching to differentiation media (DMEM (Gibco, 41966029)) with 1% horse serum (Gibco, 16050–122).

Production of wild-type Agrin recombinant proteins

For the production of recombinant proteins, the stably transfected HEK293-EBNA cells were grown to about 80% confluence and were transferred to expression medium without FBS. Conditioned medium containing secreted proteins was collected every 3 days and replaced with fresh expression media for 12 days. Conditioned medium was centrifuged at 2000xg for 10 min to pellet the cells before storing at −20˚C. After thawing, recombinant proteins were purified from conditioned media by HPLC, on a HiTRAP Imac HP column (GE Healthcare, 17-0920-03), eluted with imidazol and desalted on silica column with PBS (GE Healthcare, HiPrep 26 /10Desalting) or on a Vivaspin column (Vivaspin Sartorius). The absolute concentration of soluble Agrins was estimated on a coomassie blue stained gel by comparison with a known amount of a commercial purified Agrin.

Cell transfection

For C2C12 cells, scramble or *Macf1* targeting siRNAs were transfected in cells using Lipofectamine 2000 (ThermoFisher Scientifics, 11668–019) at the final concentration of 10 nM, following manufacturer instructions, just before differentiation. Same transfection methode was used according to the instructions to deliver scramble or *Macf1* targeting shRNAs to cells.

For primaries cells, siRNAs were transfected using Lipofectamine 2000 (ThermoFisher Scientifics, 11668–019) at the final concentration of 2 nM. shRNAs (Geneocopia), MACF1-MTBD-GFP (gift from Carsten Janke team, Institut Curie, Paris, France), EB3-GFP (gift from Annie Andrieux team, Grenoble Institute Neurosciences, Grenoble, France) or RFP-Lamin-chromobody (Chromotek) cDNA were transfected to cells using Lipofectamine 3000 (ThermoFisher Scientifics, L3000-008) following manufacturer instructions, just before differentiation.

siRNA	Sense oligonucleotide sequence	Anti-Sense oligonucleotide sequence
MACF1 #952	GAGUUUCAAAAGAACCUUAtt	UAAGGUUCUUUUGAAACUCtt
MACF1 #954	CAAUACAGCUGAAAAAGUUtt	AACUUUUUCAGCUGUAUUGgg
MACF1 #958	GGAUGAAAUUAAUACUCGAtt	UCGAGUAUUAAUUUCAUCCat
shRNA	Clone Name	Target Sequence
MACF1 #1	MSH071923-1-CU6 (OS398499)	GCACATCAATGATCTCTATGA
MACF1 #2	MSH071923-2-CU6 (OS398500)	GCAGGTGAAGCTAGTGAATAT
MACF1 #3	MSH071923-3-CU6 (OS398501)	GCAGATTGCAAACAAGATACA
MACF1 #4	MSH071923-4-CU6 (OS398502)	GCTAAAGAATATCCGACTACT

Mouse model

Mice that carry a loxP-flanked allele of *Macf1* (***Goryunov et al., 2010***) and Hsa-Cre transgenic mice (***Miniou, 1999***) have been described previously. All of the experiments and procedures were conducted in accordance with the guidelines of the local animal ethics committee of the University Claude Bernard – Lyon one and in accordance with French and European legislation on animal experimentation and approved by the ethics committee CECCAPP and the French ministry of research (CECCAPP_ENS_2018_022).

In vivo force measurements

Mice were initially anesthetized in an induction chamber using 4% isoflurane. The right *Hindlimb* was shaved before an electrode cream was applied at the knee and heel regions to optimize electrical stimulation. Each anesthetized mouse was placed supine in a cradle allowing for a strict standardization of the animal positioning. Throughout a typical experiment, anesthesia was maintained by air inhalation through a facemask continuously supplied with 1.5% isoflurane. The cradle also includes an electrical heating blanket in order to maintain the animal at a physiological temperature during anesthesia. Electrical stimuli were delivered through two electrodes located below the knee and the Achille's tendon. The right foot was positioned and firmly immobilized through a rigid slipper on a pedal of an ergometer (NIMPHEA_Research, AII Biomedical SAS) allowing for the measurement of the force produced by the Hindlimb muscles (i.e. mainly the *Gastrocnemius* muscle). The right knee was also firmly maintained using a rigid fixation in order to optimize isometric force recordings. Monophasic rectangular pulses of 0.2 ms were delivered using a constant-current stimulator (Digitimer DS7AH, maximal voltage: 400V). The force-frequency curves were determined by stepwise increasing stimulation frequency, with resting periods > 30 s between stimuli in order to avoid effects due to fatigue. For each stimulation train, isometric peak force was calculated. After a 3 min recovery period, force was assessed during a fatigue protocol consisting of 30 Hz stimulation trains of 0.3 s delivered once every second for 180 s. The peak force of each contraction was measured and averaged every five contractions. A fatigue index corresponding to the ratio between the last five and the first five contractions was determined. Force signal was sampled at 1000 Hz using a Powerlab system and Labchart software (ADinstruments).

Sciatic nerve crush

The mice were made unconscious by isoflurane anesthesia prior to the intraperitoneal injection of ketamine (100 mg/kg) and xylazine (10 mg/kg) in order to obtain a deep state of general anesthesia. To limit the pain on awakening, mice received a subcutaneous injection of buprenorphine at 30 µg/ml (0.1 µg/g of bodyweight). Once deeply anesthetized mice were shaved at the level of the left hip and the skin incised over 3 mm, then the connective tissue (muscle fascia) was incised. In order to reach the sciatic nerve the muscle mass was pushed back with the delicate help of fine forceps. The exposed sciatic nerve was subjected for two minutes to a drop of lurocaïne in order to inhibit any nociceptive impulse. Then the nerve was seized using fine forceps and sectioned by ablation of 2–3 mm to avoid any reconnection by scarring. The wound was then stitched up using suture. 15 days later, after killing the mice according to the ethical rules of the establishment, *Tibialis anterior* muscles were collected for examination.

Mouse genotyping

In order to extract the DNA, samples (mice tales) were incubated in extraction solution (25 mM NAOH, 0.2 mM EDTA) for 30 min at 95˚C. Following the addition of neutralization solution (40 mM Tris-HCL), samples were centrifuged at 13000 RPM for 2 min at RT and the DNA were collected. DNA concentration was evaluated using Nanodrop (ThermoFisher Scientifics). PCR were carried (Hot Start Taq polymerase (QIAGEN, 1007837), PCR buffer mix (QIAGEN, 1005479) DNTP mix (Biolabs, 447)) using the following primers. The same amount of PCR products was loaded in 2X Agarose-1X TAE gels and were migrated for 2H at 130V. Results were obtained using GelDoc (BioRad).

List of the primers used for PCR:

Primer	Sequence
MACF1 F	CATCAGAAGAGATCAACCAACC
MACF1 R	AAAGGAAGAGAGGTCCAAGGT
Cre F	GAGTTGATAGCTGGCTGGTGGCAGATG
Cre R	CCTGGAAAATGCTTCTGTCCGTTTGCC
CD8 F	GGTGCATTCTCACTCTGAGTTCC
CD8 R	GCAGACAGAGCTGATTTCCTATGTG

Protein extraction, western blot, and dot blot analysis

For primary cultured cells or C2C12 cell lines, cells were harvested, using 1X Trypsin for 5 min at 37˚C and centrifuged at 1500 RPM for 5 min at 4˚C. Cell pellets were diluted and incubated in the optimal volume of RIPA lysis buffer containing phosphatases inhibitors (Sigma, P5726-5mL) and proteases inhibitors (Sigma, P8340) for 30 min at 4˚C. Following a sonication and a centrifugation at 12,000 RPM for 10 min at 4˚C, protein samples were collected for further uses. The concentration of proteins was determined using BCA protein assay kit (Thermo Fisher Scientifics, 23225) as described by the manufacturer.

To obtain protein extracts from dissected muscles or other organs, the samples were finely cut onto tubes containing ceramic beads (MP Biomedicals Lysing Matrix D, 6913100) with the optimal volume of RIPA lysis buffer completed with phosphatases inhibitors (Sigma, P5726-5mL) and proteases inhibitors (Sigma, P8340). Tubes were subjected to harsh shaking (6500 rpm, 3 cycles of 15 s with 30 s pause intervals at 4˚C) and rested at 4˚C for 1H. Following a sonication and a centrifugation at 12000 RPM for 10 min at 4˚C, protein samples were collected for further uses. The concentration of proteins was determined using BCA protein assay kit (Thermo Fisher Scientifics, 23225) as described by the manufacturer.

To carry out dot blots, Bio-Dot SF Microfiltration Apparatus plates (BioRad) were used to transfer the protein samples onto the nitrocellulose membranes following protein extraction and dosage.

Western blot or dot blot Membranes were then saturated in 5% milk in TBS for 1H at RT and were incubated in primary antibodies over night at 4˚C. Following washes by 0.1% Tween-20-1X TBS, the membranes were incubated in HRP conjugated secondary antibodies in 5% milk in TBST for

1H at RT. Following washes by 0.1% Tween-20 in TBS the detection of the target proteins was carried out using Super Signal West Femto (Thermo Fisher Scientifics, 34095) and ChemiDoc imaging system (BioRad).

List of antibodies used for western blot:

Antibody	Species and utility	Dilution factor	Manufacturer and reference
Anti-MACF1	Rabbit - primary	1:1000	Novus Biologicals NBP2-36528 (RRID:AB_2893083)
Anti-GAPDH	Mouse - primary	1/1000	Sigma-Aldrich MAB374 (RRID:AB_2107445)
Anti-TOM20	Rabbit - primary	1:1000	Cell Signaling Technologies D8T4N (RRID:AB_2687663)
Anti-OXPHOS	Mouse - primary	1:1000	Abcam Ab110413 (RRID:AB_2629281)
Anti-mouse-HRP	Goat - secondary	1:5000	Invitrogen 62–6520 (RRID:AB_2533947)
Anti-rabbit-HRP	Goat - secondary	1:5000	Invitrogen 65–6120 (RRID:AB_2533967)

Primary cells immunofluorescence staining

Cells were fixed in 4% PFA in PBS for 20 min at 37˚C followed by washes with PBS and permeabilization with 0.5% Triton-X100 in PBS for 5 min at RT. Following washes with PBS, cells were saturated with 1% BSA in PBS for 30 min at RT and incubated in primary antibodies over night at 4˚C. After several washes with 0.05% Triton-X100-1X PBS, cells were incubated in secondary antibodies or dyes for 2H at RT and washed with 0.05% Triton-X100 in PBS before image acquisition. The list of the antibodies used for each staining can be found in the following section.

Isolation of mono-myofibers and immunofluorescence staining

Following the dissection of the whole muscle from the mice, muscle blocks were fixed in 4% PFA in PBS for 2H at RT. After several washes, 30– 50 mono-myofibers were isolated per staining from each muscle. Myofibers were then permeabilized using 1% Triton-X100 in PBS for 15 min at 37˚C and saturated in 1% BSA in PBS for 30 min at RT. Based on the experiments, myofibers were incubated in desired primary antibodies at 4˚C for two nights. Following washes with 0.05% Triton-X100 in PBS, myofibers were incubated in secondary antibodies or dyes for 2H at RT and washed several times with 0.05% Triton-X100 in PBS before mounting on slides. Myofibers were mounted on slides using fluromount Aqueous mounting (Sigma, F4680-25mL) and kept at 4˚C utile image acquisition.

List of the antibodies used for immunofluorescent staining:

Antibody or dye	Species and utility	Dilution factor	Manufacturer and reference
Anti-Cytochrome C	Mouse - primary	1:300	Cell Signaling Technologies 12963S (RRID:AB_2637072)
Anti-MACF1	Rabbit - primary	1:200	Novus Biologicals NBP2-36528 (RRID:AB_2893083)
Anti-alpha tubulin	Mouse - primary	1:1000	Sigma T6074 (RRID:AB_477582)
Anti-Tyrosinated tubulin	Rat - primary	1:100	Andrieux's Lab gift
Anti-De-tyrosinated tubulin	Rabbit - primary	1:100	Andrieux's Lab gift
MF20	Mouse-primary	1:10	DSHB MF20 (RRID:AB_2147781)
Anti-alpha actinin	Mouse – primary	1:350	Sigma A7811 (RRID:AB_476766)

Continued on next page

Continued

Antibody or dye	Species and utility	Dilution factor	Manufacturer and reference
Anti-Desmin	Rabbit - primary	1:500	Cell Signaling Technologies D93F5 (RRID:AB_1903947)
Dapi-brilliant blue	Dye	1:50000	Thermo Fisher Scientifics D1306 (RRID:AB_2629482)
α-Bungarotoxin-Alexa Flour 488	Dye	1:1000	Thermo Fisher Scientifics B13422
α-Bungarotoxin-Alexa Flour 555	Dye	1:200	Thermo Fisher Scientifics B35451
Phalloidin-Alexa Flour 647	Dye	1:100	Thermo Fisher Scientifics A22287
Anti-rat-Alexa Flour 488	Donkey - secondary	1:500	Thermo Fisher Scientifics A-21208 (RRID:AB_2535794)
Anti-rabbit-Alexa Flour 647	Goat - secondary	1:500	Thermo Fisher Scientifics A-21245 (RRID:AB_2535813)
Anti-mouse-Alexa Flour 647	Goat - secondary	1:500	Thermo Fisher Scientifics A-21240 (RRID:AB_2535809)

Histological staining and analysis

Tibialis anterior, *Soleus* and *Gastrocnimius* muscles were collected, embedded in tragacanth gum, and quickly frozen in isopentane cooled in liquid nitrogen. Cross-sections were obtained from the middle portion of frozen muscles and processed for histological, immunohistochemical or enzymo-histological analysis according to standard protocols.

The fiber cross-sectional area and the number of centrally nucleated fibers were determined using Laminin (Sigma L9393) and Dapi-stained sections. Slow myosin antibody (MyHC-I BA-D5) was used to classify muscle fibers types.

SDH staining was performed as previously described (***Nachlas et al., 1957***). Briefly, transverse sections (8 µm) were cut from the mid-belly of the TA muscles on a cryostat at −20˚C and stored at −80˚C until SDH staining was performed. The sections were dried at room temperature for 30 min before incubation in a solution made up of 0.2M phosphate buffer (pH 7.4), 0.1M MgCl2, 0.2M Succinic Acid (Sigma), and 2.4 mM NitroBlue Tetrazolium (NBT, Sigma) at 37˚C in a humidity chamber for 45 min. The sections were then washed in deionized water for 3 min, dehydrated in 50% ethanol for 2 min, and mounted for viewing with DPX mount medium (Electron Microscopy Sciences). Images were acquired as described above.

Fluorescence microscopy and transmission microscopy were performed using Axioimager Z1 microscope with CP Achromat 5x/0.12, 10x/0.3 Ph1, or 20x/0.5 Plan NeoFluar objectives (Zeiss). Images were captured using a charge- coupled device monochrome camera (Coolsnap HQ, Photometrics) or color camera (Coolsnap colour) and MetaMorph software. For all imaging, exposure settings were identical between compared samples. Fiber number and size, central nuclei and peripheral myonuclei were calculated using ImageJ software.

Analysis of T-tubule network and intracellular Ca^{2+} in voltage-clamped fibers

FDB muscle fibers were incubated for 30 min in the presence of 10 µm di-8-anepps in Tyrode solution. Estimation of the T-tubule density from the di-8-anepps fluorescence was carried out from a largest possible region of interest excluding the plasma membrane, within each fiber. For each fiber, two images taken at distinct locations were used. Analysis was carried out with the ImageJ software (National Institute of Health). Automatic threshold with the Otsu method was used to create a binary image of the surface area occupied by T-tubules. The 'skeletonize' function was then used to delineate the T-tubule network. T-tubule density was expressed as the percent of positive pixels within the region. Sarcomere length was estimated from half the number of fluorescence peaks (T-tubules) along the length of the main axis of a given fiber. To assess variability in T-tubule orientation, objects within two T-tubule binary images of each fiber were outlined and particle analysis was performed to

determine the angle of all objects yielding a perimeter larger than an arbitrary value of 10 µm. For each fiber, the standard deviation of angle values was then calculated. This analysis was performed on 10 muscle fibers from 3 Macf1f/f Cre- and from 3 Macf1f/f Cre+ mice, respectively.

Single fibers were isolated from *FDB* muscles as described previously (Jacquemond, 1997). In brief, muscles were incubated for 60 min at 37˚C in the presence of external Tyrode containing 2 mg.mL collagenase (Sigma, type 1). Single fibers were obtained by triturating the collagenase-treated muscles within the experimental chamber.

Isolated muscle fibers were handled with the silicone voltage-clamp technique (***Lefebvre et al., 2014***). Briefly, fibers were partly insulated with silicone grease so that only a short portion (50–100 µm long) of the fiber extremity remained out of the silicone. Fibers were bathed in a standard voltage-clamp extracellular solution containing (in mM) 140 TEA-methanesulfonate, 2.5 CaCl2, 2 MgCl2, 1 4-aminopyridine, 10 HEPES and 0.002 tetrodotoxin. An RK-400 patch-clamp amplifier (Bio-Logic, Claix) was used in whole-cell conFigureuration in combination with an analog-digital converter (Axon Instruments, Digidata 1440A) controlled by pClamp nine software (Axon Instruments). Voltage-clamp was performed with a micropipette filled with a solution containing (in mM) 120 K-glutamate, 5 Na2-ATP, 5 Na2-phosphocreatine, 5.5 MgCl2, 15 EGTA, 6 CaCl2, 0.1 rhod-2, five glucose, 5 HEPES. The tip of the micropipette was inserted through the silicone within the insulated part of the fiber and was gently crushed against the bottom of the chamber to ease intracellular equilibration and decrease the series resistance. Intracellular equilibration of the solution was allowed for 30 min before initiating measurements. Membrane depolarizing steps of 0.5 s duration were applied from −80 mV. Confocal imaging was conducted with a Zeiss LSM 5 Exciter microscope equipped with a 63x oil immersion objective (numerical aperture 1.4). Rhod-2 fluorescence was detected in line-scan mode (x,t, 1.15 ms per line) above 560 nm, upon excitation from the 543 nm line of a HeNe laser. Rhod-2 fluorescence transients were expressed as F/F0 where F0 is the baseline fluorescence. The Ca2+ release flux (rate of SR Ca2+ release) was estimated from the time derivative of the total myoplasmic Ca2+ ([Catot]) calculated from the occupancy of intracellular calcium binding sites following a previously described procedure (***Kutchukian et al., 2017***).

q-PCR

RNA extraction and RT-PCR

After the addition of Trizol (Sigma, T9424-200mL) on each sample, lysing matrix D and fast prep system (MPbio, 6913–100) were used for sample digestion and pre-RNA extraction. In order to extract RNA, samples were incubated in chloroform for 5 min at RT, centrifuged for 15 min at 12,000 rcf at 4˚C and incubated in the tubes containing isopropanol (precipitatation of RNA) for 10 min at RT. following a centrifuge of samples for 15 min at 12,000 rcf at 4˚C, samples were washed 2 times with 70% ethanol and the final RNA pellets were diluted in ultra-pure RNase free water (Invitrogen, 10977–035). RNA concentration was calculated using Nanodrop (ThermoFisher Scientifics). Goscript Reverse Transcriptase System (Promega, A5001) was used as described by the manufacturer to produce the cDNA.

DNA extraction

DNA was extracted from frozen whole *Gastrocnimius* according to the manufacturers' protocol, using a Maxwell 16 Instrument (Promega Corporation, Madison, USA) and a Maxwell 16 Tissue DNA Purification Kit ((Promega Corporation, Madison, USA)). DNA concentration was calculated using Nanodrop (ThermoFisher Scientifics).

q-PCR

Fast Start Universal SYBR Green Master (Rox)(Roche, 04913914001) and CFX Connect Real-Time PCR Detection System (BioRad) were used to carry out the quantitative PCR using the following primer sets. For analysis of genes expression level, The CT of target genes was normalized on four control genes. To compare the level of mitochondrial DNA, CT of mitochondrial DNA was normalized on genomic DNA.

List of the primares used for q-PCR:

Primers	Sequence
MACF1 F	ATTGATTCACCGATACAGGCCC
MACF1 R	ATCTTCTGCATCTAGCAGTCGG
MyoD F	AGCACTACAGTGGCGACTCA
MyoD R	GCTCCACTATGCTGGACAGG
Myogenin F	CAATGCACTGGAGTTCGGTC
Myogenin R	ACAATCTCAGTTGGGCATGG
Sarcolipin F	GGTCCTTGGTAGCCTGAGTG
Sarcolipin R	CGGTGATGAGGACAACTGTG
DNM1 F	ATTTCGTGGGCAGGGACTTTC
DNM1 R	CAGTGCAGGAACTCGGCATA
DNM2 F	GGACCAGGCAGAGAATGAGG
DNM2 R	ACGTAGGAGTCCACCAGGTT
PPARGC1A F	GCAGGTCGAACGAAACTGAC
PPARGC1A R	CTTGCTCTTGGTGGAAGCAG
Gusb F	GAGGATTGCCAACGAAACCG
Gusb R	GTGTCTGGGGACCACCTTTGA
RpL4 F	GCCATGAGAGCGAAGTGG
RpL4 R	CTCCTGCAGGCGTCGTAG
Myoglobin F	CCTGGGTACTATCCTGAAGA
Myoglobin R	GAGCATCTGCTCCAAAGTCC
Betatub F (gDNA)	GCCAGAGTGGTGCAGGAAA
Betatub R (gDNA)	TCACCACGTCCAGGACAG
ND1 F (mDNA)	CCCAGCTACTACCATCATTCAAGT
ND1 R (mDNA)	GATGGTTTGGGAGATTGGTTGATGT

Drosophila model and sample preparation

Shot GD9507 UAS-RNAi line from VDRC collection crossed to Mef2-GAL4 driver has been used to attenuate shot gene expression specifically in muscles. Third instar larvae were dissected in physiological salt with 25 mM EDTA. Body wall muscles were fixed with 4% formaldehyde in PBS for 15 min and then rinsed three times for 5 min each in PBS with 0.5% Tween 20 (PBT). Muscles were blocked for 30 min with 20% horse serum in PBT at RT. Staining was performed by using primary antibodies applied overnight at 4˚C and after washing three times in PBT secondary antibodies were applied at RT for 1 hr. The following primary antibodies were used: anti-Brp1 (1:100; DSHB, Nc82-s), anti-Shot (1:100; DSHB, mAbRod1).

Electronic-microscopy

Tissues were cut into small pieces and fixed in 2% glutaraldehyde for 2 hr at 4˚C. Samples were washed three times for 1H at 4˚C and post-fixed with 2% $OsO_4$1 hr at 4˚C. Then tissues were dehydrated with an increasing ethanol gradient (5 min in 30%, 50%, 70%, 95%) and tree times for 10 min in absolute ethanol. Impregnation was performed with Epon A (75%) plus Epon B (25%) plus DMP30 (1.7%). Inclusion was obtained by polymerization at 60˚C for 72 hr. Ultrathin sections (approximately 70 nm thick) were cut on a UC7 (Leica) ultra-microtome, mounted on 200 mesh copper grids coated with 1:1000 polylysine, and stabilized for 1 day at room temperature and contrasted with uranyl acetate and lead citrate. Sections were acquired with a Jeol 1400JEM (Tokyo, Japan) transmission electron microscope, 80Kv, equipped with a Orius 600 camera and Digital Micrograph.

Video-microscopy

To analyze the movement of myonuclei, time-lapse 10X images were acquired using Z1-AxioObserver (Zeiss) with intervals of 15 min. Final videos were analyzed using Metamorph (Zeiss) and SkyPad plugin as described before (***Cadot et al., 2014***).

To analyze the dynamic of EB3, 50 stream acquisitions were obtained at 63X with 500 ms of intervals using Z1-AxioObserver (Zeiss). The movement and speed of each comet was further analyzed as described before (***Sbalzarini and Koumoutsakos, 2005***).

Quantification methods for myonuclei spreading in myotubes in vitro

Quantifications in immature myotubes were assessed using an analysis tool developed in our team. An image analysis performed in ImageJ software is combined with a statistical analysis in RStudio software. This provides quantifications of parameters, ranked by myonuclei content per myotubes, regarding phenotype of myotubes (area, length) and their respective myonuclei positioning compare to centroid of myotubes (DMcM).

MSG diagrams were obtained through the normalization of lengths of all analyzed myotubes (independently to their myonuclei content) to 100%. White lines represent myonuclei density curves assessing the statistical frequency for myonuclei positioning along myotubes. Each color group reflects statistical estimation of myonuclei clustering along myotubes.

Quantification methods for fixed myofibers in vitro

Following fixation and immunofluorescent staining, the following steps were taken to generate data.

The measurement of distance between adjacent myonuclei, myonuclei feret and roundness were done on fibers stained for myonuclei and F-actin.

Microtubules intensity around the myonuclei was assessed on confocal images from total alpha tubulin. An ROI around each myonuclei was selected to measure the mean fluorescent intensity.

The width of each myofiber was measured on F-actin staining in myofibers presenting formed sarcomeres and the sarcomeric length was measured on alpha actinin staining.

Bungarotoxin staining was used to analyze formation of acetylcholine receptors clusters in mature myofibers. Representative images were taken from myofibers of each condition as described. Briefly, a threshold of 8 µm was set as the minimal size for AChRs clusters. Myofibers with at least one cluster of 8 µm or bigger were considered as positive.

Cytochrome C was used to study the mitochondrial content of each myofiber in vitro. On each myofiber, several Regions Of Interest (ROI) were selected randomly. Next, the total number of particles stained for Cytochrome C were quantified per ROI. The particles with circularity equivalent to one were eliminated in order to purify our results from any unwanted background errors. Particles with feret less than 0.75 µm (mean size of mitochondria) were eliminated to purify our results. Finally, the ratio of number of particles per area of ROI was calculated.

All the quantifications/measurements were done using ImageJ software (RRID:SCR_003070).

Quantification methods for fixed myofibers isolated from control or conditional KO mice

After immunofluorescence staining, the distance between each myonuclei and its closest neighbor, myonuclei feret and myonuclei roundness were quantified on 3 µM peripheral Z stacks of each myofiber.

The microtubules orientation was assessed on mono Z images of tubulin staining using TeTD directionality tool as described before (***Liu and Ralston, 2014***).

To study the microtubules pool around myonuclei, 3 µM peripheral Z stacks of each myofiber were analyzed for tyrosinated or de-tyrosinated tubulin staining. Myonuclei presenting a complete de-tyrosinated tubulin ring around them were considered as positive for stable microtubule.

Each NMJs was studied on Z stack images of bungarotoxin staining as described previously (***Jones et al., 2016***). To study different pools of microtubules at the NMJs, Z series images were quantified for total, tyrosinated or de-tyrosinated alpha tubulin specifically at post-synaptic muscular region based on the bungarotoxin staining to select the NMJs ROI.

To analyze the organization of mitochondria and Desmin, 3 µM peripheral Z stacks of each myofiber were studied. Any fiber presenting broken or oriented organization instead of clear transversal/

longitudinal organization (that was observed in control myofibers) was considered as a myofiber with irregular staining.

All the quantifications/measurements were done using ImageJ software (RRID:SCR_003070).

Statistical analysis

GraphPad Prism (RRID:SCR_002798) was used to perform statistical analysis (Student's t test or the Mann-Whitney test) according to samples amount and distribution.

Acknowledgements

This work was supported by an ATIP-Avenir and MyoNeurAlp Alliance grants. We thank Pr. Ronald Liem and Dr. Alper (Columbia University of New York) for providing cKO *Macf1* embryos. We would like to thank Jijumon AS from the team of Dr. Carsten Janke (Institut Curie de Paris) for providing the MACF1-MTBD plasmid. We acknowledge the contributions of the CELPHEDIA Infrastructure (http://www.celphedia.eu/), especially the center AniRA of Lyon in addition to members of CIQLE imaging center (Faculté de Médecine Rockefeller, Lyon-Est). We thank Dr. Yoan Couté for the mass spectrometry analysis performed at EDyP Lab. We are grateful to Caroline Brun, Leonardo Beccari, Hélène Puccio and Bénédicte Chazaud for helping us with proofreading.

Additional information

Funding

Funder	Grant reference number	Author
Programme AVENIR 2014 (ATIP-Avenir)	R14074CS	Vincent Gache
AFM-Téléthon	Alliance MyoNeurAlp	Vincent Gache

The funders had no role in study design, data collection and interpretation, or the decision to submit the work for publication.

Author contributions

Alireza Ghasemizadeh, Conceptualization, Formal analysis, Investigation, Visualization, Methodology, Writing - original draft, Writing - review and editing; Emilie Christin, Formal analysis, Visualization, Methodology; Alexandre Guiraud, Colline Sanchez, Vincent Jacquemond, Formal analysis, Investigation, Methodology; Nathalie Couturier, Francisco-Ignacio Jaque-Fernandez, Formal analysis, Methodology; Marie Abitbol, Formal analysis, Methodology, Writing - original draft; Valerie Risson, Laurent Schaeffer, Resources; Emmanuelle Girard, Resources, Methodology; Christophe Jagla, Cedric Soler, Lilia Laddada, Investigation; Jean-Luc Thomas, Marine Lanfranchi, Methodology; Julien Courchet, Resources, Methodology, Writing - original draft; Julien Gondin, Resources, Formal analysis, Investigation, Methodology; Vincent Gache, Conceptualization, Resources, Formal analysis, Supervision, Funding acquisition, Validation, Investigation, Visualization, Methodology, Writing - original draft, Project administration, Writing - review and editing

Author ORCIDs

Alireza Ghasemizadeh https://orcid.org/0000-0002-8202-8546
Valerie Risson http://orcid.org/0000-0002-6812-6297
Emmanuelle Girard http://orcid.org/0000-0001-6730-9596
Cedric Soler http://orcid.org/0000-0002-2312-5370
Julien Courchet http://orcid.org/0000-0002-1199-9329
Vincent Gache https://orcid.org/0000-0002-2928-791X

Ethics

Animal experimentation: All of the experiments and procedures were conducted in accordance with the guidelines of the local animal ethics committee of the University Claude Bernard - Lyon 1 and in

accordance with French and European legislation on animal experimentation and approved by the ethics committee CECCAPP (ref APAFIS#17455-2018091216033835v5) and the French Ministry of Research.

Decision letter and Author response

Decision letter https://doi.org/10.7554/eLife.70490.sa1
Author response https://doi.org/10.7554/eLife.70490.sa2

Additional files

Supplementary files

- Transparent reporting form

Data availability

All data generated or analysed during this study are included in the manuscript and supporting files. Source data files have been provided for all figures.

References

Aillaud C, Bosc C, Peris L, Bosson A, Heemeryck P, Van Dijk J, Le Friec J, Boulan B, Vossier F, Sanman LE, Syed S, Amara N, Couté Y, Lafanechère L, Denarier E, Delphin C, Pelletier L, Humbert S, Bogyo M, Andrieux A, et al. 2017. Vasohibins/SVBP are tubulin carboxypeptidases (TCPs) that regulate neuron differentiation. *Science* **358**: 1448–1453. DOI: https://doi.org/10.1126/science.aao4165, PMID: 29146868

Alves-Silva J, Sánchez-Soriano N, Beaven R, Klein M, Parkin J, Millard TH, Bellen HJ, Venken KJ, Ballestrem C, Kammerer RA, Prokop A. 2012. Spectraplakins promote microtubule-mediated axonal growth by functioning as structural microtubule-associated proteins and EB1-dependent +TIPs (tip interacting proteins). *Journal of Neuroscience* **32**:9143–9158. DOI: https://doi.org/10.1523/JNEUROSCI.0416-12.2012, PMID: 22764224

Antolik C, Catino DH, O'Neill AM, Resneck WG, Ursitti JA, Bloch RJ. 2007. The actin binding domain of ACF7 binds directly to the tetratricopeptide repeat domains of rapsyn. *Neuroscience* **145**:56–65. DOI: https://doi.org/10.1016/j.neuroscience.2006.11.047, PMID: 17222516

Azevedo M, Baylies MK. 2020. Getting into position: nuclear movement in muscle cells. *Trends in Cell Biology* **30**:303–316. DOI: https://doi.org/10.1016/j.tcb.2020.01.002, PMID: 32008895

Bernier G, Pool M, Kilcup M, Alfoldi J, De Repentigny Y, Kothary R. 2000. Acf7 (MACF) is an actin and microtubule linker protein whose expression predominates in neural, muscle, and lung development. *Developmental Dynamics* **219**:216–225. DOI: https://doi.org/10.1002/1097-0177(2000)9999:9999<::AID-DVDY1041>3.0.CO;2-O, PMID: 11002341

Bitoun M, Maugenre S, Jeannet PY, Lacène E, Ferrer X, Laforêt P, Martin JJ, Laporte J, Lochmüller H, Beggs AH, Fardeau M, Eymard B, Romero NB, Guicheney P. 2005. Mutations in dynamin 2 cause dominant centronuclear myopathy. *Nature Genetics* **37**:1207–1209. DOI: https://doi.org/10.1038/ng1657, PMID: 16227997

Bottenberg W, Sanchez-Soriano N, Alves-Silva J, Hahn I, Mende M, Prokop A. 2009. Context-specific requirements of functional domains of the spectraplakin short stop in vivo. *Mechanisms of Development* **126**: 489–502. DOI: https://doi.org/10.1016/j.mod.2009.04.004, PMID: 19409984

Boyer JG, Bernstein MA, Boudreau-Larivière C. 2010. Plakins in striated muscle. *Muscle & Nerve* **41**:299–308. DOI: https://doi.org/10.1002/mus.21472, PMID: 19768769

Bruusgaard JC, Liestøl K, Gundersen K. 2006. Distribution of myonuclei and microtubules in live muscle fibers of young, middle-aged, and old mice. *Journal of Applied Physiology* **100**:2024–2030. DOI: https://doi.org/10.1152/japplphysiol.00913.2005, PMID: 16497845

Bulinski JC, Gundersen GG. 1991. Stabilization of post-translational modification of microtubules during cellular morphogenesis. *BioEssays* **13**:285–293. DOI: https://doi.org/10.1002/bies.950130605, PMID: 1892478

Cadot B, Gache V, Vasyutina E, Falcone S, Birchmeier C, Gomes ER. 2012. Nuclear movement during myotube formation is microtubule and dynein dependent and is regulated by Cdc42, Par6 and Par3. *EMBO Reports* **13**: 741–749. DOI: https://doi.org/10.1038/embor.2012.89, PMID: 22732842

Cadot B, Gache V, Gomes ER. 2014. Fast, multi-dimensional and simultaneous kymograph-like particle dynamics (SkyPad) analysis. *PLOS ONE* **9**:e89073. DOI: https://doi.org/10.1371/journal.pone.0089073, PMID: 24586511

Casey LM, Lyon HD, Olmsted JB. 2003. Muscle-specific microtubule-associated protein 4 is expressed early in Myogenesis and is not sufficient to induce microtubule reorganization. *Cell Motility and the Cytoskeleton* **54**: 317–336. DOI: https://doi.org/10.1002/cm.10105

Chang W, Antoku S, Östlund C, Worman HJ, Gundersen GG. 2015. Linker of nucleoskeleton and cytoskeleton (LINC) complex-mediated actin-dependent nuclear positioning orients centrosomes in migrating myoblasts. *Nucleus* **6**:77–88. DOI: https://doi.org/10.1080/19491034.2015.1004947, PMID: 25587885

Cho S, Irianto J, Discher DE. 2017. Mechanosensing by the nucleus: from pathways to scaling relationships. *Journal of Cell Biology* **216**:305–315. DOI: https://doi.org/10.1083/jcb.201610042, PMID: 28043971

Chojnowski A, Ong PF, Dreesen O. 2015. Nuclear Lamina remodelling and its implications for human disease. *Cell and Tissue Research* **360**:621–631. DOI: https://doi.org/10.1007/s00441-014-2069-4

Clemen CS, Herrmann H, Strelkov SV, Schröder R. 2013. Desminopathies: pathology and mechanisms. *Acta Neuropathologica* **125**:47–75. DOI: https://doi.org/10.1007/s00401-012-1057-6, PMID: 23143191

Collins MA, Mandigo TR, Camuglia JM, Vazquez GA, Anderson AJ, Hudson CH, Hanron JL, Folker ES. 2017. Emery-Dreifuss muscular dystrophy-linked genes and centronuclear myopathy-linked genes regulate myonuclear movement by distinct mechanisms. *Molecular Biology of the Cell* **28**:2303–2317. DOI: https://doi.org/10.1091/mbc.e16-10-0721, PMID: 28637766

Escobar-Aguirre M, Zhang H, Jamieson-Lucy A, Mullins MC. 2017. Microtubule-actin crosslinking factor 1 (Macf1) domain function in balbiani body dissociation and nuclear positioning. *PLOS Genetics* **13**:e1006983. DOI: https://doi.org/10.1371/journal.pgen.1006983, PMID: 28880872

Falcone S, Roman W, Hnia K, Gache V, Didier N, Lainé J, Auradé F, Marty I, Nishino I, Charlet-Berguerand N, Romero NB, Marazzi G, Sassoon D, Laporte J, Gomes ER. 2014. N-WASP is required for Amphiphysin-2/BIN1-dependent nuclear positioning and triad organization in skeletal muscle and is involved in the pathophysiology of centronuclear myopathy. *EMBO Molecular Medicine* **6**:1455–1475. DOI: https://doi.org/10.15252/emmm.201404436, PMID: 25262827

Gache V, Louwagie M, Garin J, Caudron N, Lafanechere L, Valiron O. 2005. Identification of proteins binding the native tubulin dimer. *Biochemical and Biophysical Research Communications* **327**:35–42. DOI: https://doi.org/10.1016/j.bbrc.2004.11.138, PMID: 15629426

Gache V, Gomes ER, Cadot B. 2017. Microtubule motors involved in nuclear movement during skeletal muscle differentiation. *Molecular Biology of the Cell* **28**:865–874. DOI: https://doi.org/10.1091/mbc.e16-06-0405

Gadadhar S, Bodakuntla S, Natarajan K, Janke C. 2017. The tubulin code at a glance. *Journal of Cell Science* **130**:1347–1353. DOI: https://doi.org/10.1242/jcs.199471, PMID: 28325758

Goryunov D, He CZ, Lin CS, Leung CL, Liem RK. 2010. Nervous-tissue-specific elimination of microtubule-actin crosslinking factor 1a results in multiple developmental defects in the mouse brain. *Molecular and Cellular Neuroscience* **44**:1–14. DOI: https://doi.org/10.1016/j.mcn.2010.01.010, PMID: 20170731

Guerrero K, Monge C, Brückner A, Puurand U, Kadaja L, Käämbre T, Seppet E, Saks V. 2010. Study of possible interactions of tubulin, microtubular network, and STOP protein with mitochondria in muscle cells. *Molecular and Cellular Biochemistry* **337**:239–249. DOI: https://doi.org/10.1007/s11010-009-0304-1, PMID: 19888554

Guzun R, Karu-Varikmaa M, Gonzalez-Granillo M, Kuznetsov AV, Michel L, Cottet-Rousselle C, Saaremäe M, Kaambre T, Metsis M, Grimm M, Auffray C, Saks V. 2011. Mitochondria-cytoskeleton interaction: distribution of β-tubulins in cardiomyocytes and HL-1 cells. *Biochimica Et Biophysica Acta (BBA) - Bioenergetics* **1807**:458–469. DOI: https://doi.org/10.1016/j.bbabio.2011.01.010, PMID: 21296049

Heffler J, Shah PP, Robison P, Phyo S, Veliz K, Uchida K, Bogush A, Rhoades J, Jain R, Prosser BL. 2020. A balance between intermediate filaments and microtubules maintains nuclear architecture in the cardiomyocyte. *Circulation Research* **126**:e10–e26. DOI: https://doi.org/10.1161/CIRCRESAHA.119.315582, PMID: 31822208

Hnia K, Ramspacher C, Vermot J, Laporte J. 2015. Desmin in muscle and associated diseases: beyond the structural function. *Cell and Tissue Research* **360**:591–608. DOI: https://doi.org/10.1007/s00441-014-2016-4, PMID: 25358400

Iqbal S, Hood DA. 2014. Cytoskeletal regulation of mitochondrial movements in myoblasts. *Cytoskeleton* **71**:564–572. DOI: https://doi.org/10.1002/cm.21188, PMID: 25147078

Janin A, Gache V. 2018. Nesprins and lamins in health and diseases of cardiac and skeletal muscles. *Frontiers in Physiology* **9**:97. DOI: https://doi.org/10.3389/fphys.2018.01277, PMID: 30245638

Jones RA, Reich CD, Dissanayake KN, Kristmundsdottir F, Findlater GS, Ribchester RR, Simmen MW, Gillingwater TH. 2016. NMJ-morph reveals principal components of synaptic morphology influencing structure-function relationships at the neuromuscular junction. *Open Biology* **6**:160240. DOI: https://doi.org/10.1098/rsob.160240, PMID: 27927794

Jørgensen LH, Mosbech MB, Færgeman NJ, Graakjaer J, Jacobsen SV, Schrøder HD. 2014. Duplication in the microtubule-actin cross-linking factor 1 gene causes a novel neuromuscular condition. *Scientific Reports* **4**:5180. DOI: https://doi.org/10.1038/srep05180, PMID: 24899269

Jungbluth H, Gautel M. 2014. Pathogenic mechanisms in centronuclear myopathies. *Frontiers in Aging Neuroscience* **6**:339. DOI: https://doi.org/10.3389/fnagi.2014.00339, PMID: 25566070

Ka M, Jung EM, Mueller U, Kim WY. 2014. MACF1 regulates the migration of pyramidal neurons via microtubule dynamics and GSK-3 signaling. *Developmental Biology* **395**:4–18. DOI: https://doi.org/10.1016/j.ydbio.2014.09.009, PMID: 25224226

Ka M, Moffat JJ, Kim W-Y. 2016. MACF1 controls migration and positioning of cortical GABAergic interneurons in mice. *Cerebral Cortex* **77**:5525–5538. DOI: https://doi.org/10.1093/cercor/bhw319

Kim HS, Murakami R, Quintin S, Mori M, Ohkura K, Tamai KK, Labouesse M, Sakamoto H, Nishiwaki K. 2011. VAB-10 spectraplakin acts in cell and nuclear migration in *Caenorhabditis elegans*. *Development* **138**:4013–4023. DOI: https://doi.org/10.1242/dev.059568, PMID: 21831923

Kim JH, Jin P, Duan R, Chen EH. 2015. Mechanisms of myoblast fusion during muscle development. *Current Opinion in Genetics & Development* **32**:162–170. DOI: https://doi.org/10.1016/j.gde.2015.03.006, PMID: 25989064

Kirby TJ, Lammerding J. 2018. Emerging views of the nucleus as a cellular mechanosensor. *Nature Cell Biology* **20**:373–381. DOI: https://doi.org/10.1038/s41556-018-0038-y

Kodama A, Karakesisoglou I, Wong E, Vaezi A, Fuchs E. 2003. ACF7: an essential integrator of microtubule dynamics. *Cell* **115**:343–354. DOI: https://doi.org/10.1016/s0092-8674(03)00813-4, PMID: 14636561

Kumazawa A, Katoh H, Nonaka D, Watanabe T, Saotome M, Urushida T, Satoh H, Hayashi H. 2014. Microtubule disorganization affects the mitochondrial permeability transition pore in cardiac myocytes. *Circulation Journal* **78**:1206–1215. DOI: https://doi.org/10.1253/circj.CJ-13-1298, PMID: 24614510

Kutchukian C, Szentesi P, Allard B, Trochet D, Beuvin M, Berthier C, Tourneur Y, Guicheney P, Csernoch L, Bitoun M, Jacquemond V. 2017. Impaired excitation-contraction coupling in muscle fibres from the dynamin2 R465W mouse model of centronuclear myopathy. *The Journal of Physiology* **595**:7369–7382. DOI: https://doi.org/10.1113/JP274990, PMID: 29071728

Laporte J, Hu LJ, Kretz C, Mandel JL, Kioschis P, Coy JF, Klauck SM, Poustka A, Dahl N. 1996. A gene mutated in X-linked myotubular myopathy defines a new putative tyrosine phosphatase family conserved in yeast. *Nature Genetics* **13**:175–182. DOI: https://doi.org/10.1038/ng0696-175, PMID: 8640223

Lee YL, Burke B. 2018. LINC complexes and nuclear positioning. *Seminars in Cell & Developmental Biology* **82**: 67–76. DOI: https://doi.org/10.1016/j.semcdb.2017.11.008, PMID: 29191370

Lee S, Kolodziej PA. 2002. Short stop provides an essential link between F-actin and microtubules during axon extension. *Development* **129**:1195–1204. DOI: https://doi.org/10.1242/dev.129.5.1195, PMID: 11874915

Lefebvre R, Pouvreau S, Collet C, Allard B, Jacquemond V. 2014. Whole-Cell voltage clamp on skeletal muscle fibers with the Silicone-Clamp technique. *Methods Mol Biol.* **1183**:159–170. DOI: https://doi.org/10.1007/978-1-4939-1096-0_9

Leung CL, Sun D, Zheng M, Knowles DR, Liem RK. 1999. Microtubule actin cross-linking factor (MACF): a hybrid of dystonin and dystrophin that can interact with the actin and microtubule cytoskeletons. *The Journal of Cell Biology* **147**:1275–1286. DOI: https://doi.org/10.1083/jcb.147.6.1275, PMID: 10601340

Levy Y, Ross JA, Niglas M, Snetkov VA, Lynham S, Liao C-Y, Puckelwartz MJ, Hsu Y-M, McNally EM, Alsheimer M, Harridge SDR, Young SG, Fong LG, Español Y, Lopez-Otin C, Kennedy BK, Lowe DA, Ochala J. 2018. Prelamin A causes aberrant myonuclear arrangement and results in muscle fiber weakness. *JCI Insight* **3**: e120920. DOI: https://doi.org/10.1172/jci.insight.120920

Lin CM, Chen HJ, Leung CL, Parry DA, Liem RK. 2005. Microtubule actin crosslinking factor 1b: a novel plakin that localizes to the golgi complex. *Journal of Cell Science* **118**:3727–3738. DOI: https://doi.org/10.1242/jcs.02510, PMID: 16076900

Liu W, Ralston E. 2014. A new directionality tool for assessing microtubule pattern alterations. *Cytoskeleton* **71**: 230–240. DOI: https://doi.org/10.1002/cm.21166, PMID: 24497496

Mado K, Chekulayev V, Shevchuk I, Puurand M, Tepp K, Kaambre T. 2019. On the role of tubulin, plectin, Desmin, and vimentin in the regulation of mitochondrial energy fluxes in muscle cells. *American Journal of Physiology-Cell Physiology* **316**:C657–C667. DOI: https://doi.org/10.1152/ajpcell.00303.2018, PMID: 30811221

Manhart A, Windner S, Baylies M, Mogilner A. 2018. Mechanical positioning of multiple nuclei in muscle cells. *PLOS Computational Biology* **14**:e1006208. DOI: https://doi.org/10.1371/journal.pcbi.1006208, PMID: 29889846

Mattioli E, Columbaro M, Capanni C, Maraldi NM, Cenni V, Scotlandi K, Marino MT, Merlini L, Squarzoni S, Lattanzi G. 2011. Prelamin A-mediated recruitment of SUN1 to the nuclear envelope directs nuclear positioning in human muscle. *Cell Death & Differentiation* **18**:1305–1315. DOI: https://doi.org/10.1038/cdd.2010.183, PMID: 21311568

Maurya SK, Bal NC, Sopariwala DH, Pant M, Rowland LA, Shaikh SA, Periasamy M. 2015. Sarcolipin is a key determinant of the basal metabolic rate, and its overexpression enhances energy expenditure and resistance against Diet-induced obesity. *Journal of Biological Chemistry* **290**:10840–10849. DOI: https://doi.org/10.1074/jbc.M115.636878, PMID: 25713078

Maurya SK, Herrera JL, Sahoo SK, Reis FCG, Vega RB, Kelly DP, Periasamy M. 2018. Sarcolipin signaling promotes mitochondrial biogenesis and oxidative metabolism in skeletal muscle. *Cell Reports* **24**:2919–2931. DOI: https://doi.org/10.1016/j.celrep.2018.08.036, PMID: 30208317

Metzger T, Gache V, Xu M, Cadot B, Folker ES, Richardson BE, Gomes ER, Baylies MK. 2012. MAP and kinesin-dependent nuclear positioning is required for skeletal muscle function. *Nature* **484**:120–124. DOI: https://doi.org/10.1038/nature10914, PMID: 22425998

Milanic T, Kunstelj A, Mars T, Grubic Z. 1999. Morphometric characteristics of myonuclear distribution in the normal and denervated fast rat muscle fiber. *Chemico-Biological Interactions* **119-120**:321–326. DOI: https://doi.org/10.1016/S0009-2797(99)00042-3, PMID: 10421467

Miniou P. 1999. Gene targeting restricted to mouse striated muscle lineage. *Nucleic Acids Research* **27**:27e. DOI: https://doi.org/10.1093/nar/27.19.e27

Mogessie B, Roth D, Rahil Z, Straube A. 2015. A novel isoform of MAP4 organises the paraxial microtubule array required for muscle cell differentiation. *eLife* **4**:e05697. DOI: https://doi.org/10.7554/eLife.05697, PMID: 25898002

Muhammad E, Reish O, Ohno Y, Scheetz T, Deluca A, Searby C, Regev M, Benyamini L, Fellig Y, Kihara A, Sheffield VC, Parvari R. 2013. Congenital myopathy is caused by mutation of HACD1. *Human Molecular Genetics* **22**:5229–5236. DOI: https://doi.org/10.1093/hmg/ddt380, PMID: 23933735

Muller AJ, Baker JF, DuHadaway JB, Ge K, Farmer G, Donover PS, Meade R, Reid C, Grzanna R, Roach AH, Shah N, Soler AP, Prendergast GC. 2003. Targeted disruption of the murine Bin1/Amphiphysin II gene does not disable endocytosis but results in embryonic cardiomyopathy with aberrant myofibril formation. *Molecular and Cellular Biology* **23**:4295–4306. DOI: https://doi.org/10.1128/MCB.23.12.4295-4306.2003, PMID: 12773571

Nachlas MM, Tsou KC, De Souza E, Cheng CS, Seligman AM. 1957. Cytochemical demonstration of succinic dehydrogenase by the use of a new p-nitrophenyl substituted ditetrazole. *The Journal of Histochemistry and Cytochemistry* **5**:420–436. DOI: https://doi.org/10.1177/5.4.420, PMID: 13463314

Nieuwenhuis J, Brummelkamp TR. 2019. The tubulin detyrosination cycle: function and enzymes. *Trends in Cell Biology* **29**:80–92. DOI: https://doi.org/10.1016/j.tcb.2018.08.003, PMID: 30213517

Noordstra I, Liu Q, Nijenhuis W, Hua S, Jiang K, Baars M, Remmelzwaal S, Martin M, Kapitein LC, Akhmanova A. 2016. Control of apico-basal epithelial polarity by the microtubule minus-end-binding protein CAMSAP3 and spectraplakin ACF7. *Journal of Cell Science* **129**:4278–4288. DOI: https://doi.org/10.1242/jcs.194878, PMID: 27802168

Norton HK, Phillips-Cremins JE. 2017. Crossed wires: 3d genome misfolding in human disease. *Journal of Cell Biology* **216**:3441–3452. DOI: https://doi.org/10.1083/jcb.201611001, PMID: 28855250

Oddoux S, Zaal KJ, Tate V, Kenea A, Nandkeolyar SA, Reid E, Liu W, Ralston E. 2013. Microtubules that form the stationary lattice of muscle fibers are dynamic and nucleated at Golgi elements. *Journal of Cell Biology* **203**:205–213. DOI: https://doi.org/10.1083/jcb.201304063, PMID: 24145165

Osseni A, Sébastien M, Sarrault O, Baudet M, Couté Y, Fauré J, Fourest-Lieuvin A, Marty I. 2016. Triadin and CLIMP-63 form a link between triads and microtubules in muscle cells. *Journal of Cell Science* **129**:3744–3755. DOI: https://doi.org/10.1242/jcs.188862, PMID: 27562070

Osseni A, Ravel-Chapuis A, Thomas JL, Gache V, Schaeffer L, Jasmin BJ. 2020. HDAC6 regulates microtubule stability and clustering of AChRs at neuromuscular junctions. *Journal of Cell Biology* **219**:e201901099. DOI: https://doi.org/10.1083/jcb.201901099, PMID: 32697819

Oury J, Liu Y, Töpf A, Todorovic S, Hoedt E, Preethish-Kumar V, Neubert TA, Lin W, Lochmüller H, Burden SJ. 2019. MACF1 links rapsyn to microtubule- and actin-binding proteins to maintain neuromuscular synapses. *Journal of Cell Biology* **218**:1686–1705. DOI: https://doi.org/10.1083/jcb.201810023

Pereira AL, Pereira AJ, Maia AR, Drabek K, Sayas CL, Hergert PJ, Lince-Faria M, Matos I, Duque C, Stepanova T, Rieder CL, Earnshaw WC, Galjart N, Maiato H. 2006. Mammalian CLASP1 and CLASP2 cooperate to ensure mitotic fidelity by regulating spindle and kinetochore function. *Molecular Biology of the Cell* **17**:4526–4542. DOI: https://doi.org/10.1091/mbc.e06-07-0579, PMID: 16914514

Perillo M, Folker ES. 2018. Specialized positioning of myonuclei near Cell-Cell junctions. *Frontiers in Physiology* **9**:1531. DOI: https://doi.org/10.3389/fphys.2018.01531, PMID: 30443220

Peris L, Thery M, Fauré J, Saoudi Y, Lafanechère L, Chilton JK, Gordon-Weeks P, Galjart N, Bornens M, Wordeman L, Wehland J, Andrieux A, Job D. 2006. Tubulin tyrosination is a major factor affecting the recruitment of CAP-Gly proteins at Microtubule plus ends. *Journal of Cell Biology* **174**:839–849. DOI: https://doi.org/10.1083/jcb.200512058, PMID: 16954346

Pimentel MR, Falcone S, Cadot B, Gomes ER. 2017. In VitroDifferentiation of mature myofibers for live imaging. *Journal of Visualized Experiments : JoVE* **7**:55141. DOI: https://doi.org/10.3791/55141

Preciado López M, Huber F, Grigoriev I, Steinmetz MO, Akhmanova A, Koenderink GH, Dogterom M. 2014. Actin-microtubule coordination at growing microtubule ends. *Nature Communications* **5**:4778. DOI: https://doi.org/10.1038/ncomms5778, PMID: 25159196

Puckelwartz MJ, Kessler E, Zhang Y, Hodzic D, Randles KN, Morris G, Earley JU, Hadhazy M, Holaska JM, Mewborn SK, Pytel P, McNally EM. 2009. Disruption of nesprin-1 produces an emery Dreifuss muscular dystrophy-like phenotype in mice. *Human Molecular Genetics* **18**:607–620. DOI: https://doi.org/10.1093/hmg/ddn386, PMID: 19008300

Ramdas NM, Shivashankar GV. 2015. Cytoskeletal control of nuclear morphology and chromatin organization. *Journal of Molecular Biology* **427**:695–706. DOI: https://doi.org/10.1016/j.jmb.2014.09.008, PMID: 25281900

Ravel-Chapuis A, Vandromme M, Thomas JL, Schaeffer L. 2007. Postsynaptic chromatin is under neural control at the neuromuscular junction. *The EMBO Journal* **26**:1117–1128. DOI: https://doi.org/10.1038/sj.emboj.7601572, PMID: 17304221

Reipert S, Steinböck F, Fischer I, Bittner RE, Zeöld A, Wiche G. 1999. Association of mitochondria with plectin and desmin intermediate filaments in striated muscle. *Experimental Cell Research* **252**:479–491. DOI: https://doi.org/10.1006/excr.1999.4626, PMID: 10527638

Rivero S, Cardenas J, Bornens M, Rios RM. 2009. Microtubule nucleation at the cis-side of the golgi apparatus requires AKAP450 and GM130. *Emboj* **1**:13. DOI: https://doi.org/10.1038/emboj.2009.47

Robson MI, de Las Heras JI, Czapiewski R, Lê Thành P, Booth DG, Kelly DA, Webb S, Kerr ARW, Schirmer EC. 2016. Tissue-Specific gene repositioning by muscle nuclear membrane proteins enhances repression of critical developmental genes during myogenesis. *Molecular Cell* **62**:834–847. DOI: https://doi.org/10.1016/j.molcel.2016.04.035, PMID: 27264872

Roman W, Martins JP, Carvalho FA, Voituriez R, Abella JVG, Santos NC, Cadot B, Way M, Gomes ER. 2017. Myofibril contraction and crosslinking drive nuclear movement to the periphery of skeletal muscle. *Nature Cell Biology* **19**:1189–1201. DOI: https://doi.org/10.1038/ncb3605

Roman W, Gomes ER. 2018. Nuclear positioning in skeletal muscle. *Seminars in Cell & Developmental Biology* **82**:51–56. DOI: https://doi.org/10.1016/j.semcdb.2017.11.005, PMID: 29241690

Ryan SD, Bhanot K, Ferrier A, De Repentigny Y, Chu A, Blais A, Kothary R. 2012. Microtubule stability, golgi organization, and transport flux require dystonin-a2-MAP1B interaction. *Journal of Cell Biology* **196**:727–742. DOI: https://doi.org/10.1083/jcb.201107096, PMID: 22412020

Sanchez-Soriano N, Travis M, Dajas-Bailador F, Gonçalves-Pimentel C, Whitmarsh AJ, Prokop A. 2009. Mouse ACF7 and *Drosophila* short stop modulate filopodia formation and microtubule organisation during neuronal growth. *Journal of Cell Science* **122**:2534–2542. DOI: https://doi.org/10.1242/jcs.046268, PMID: 19571116

Sanger JW, Wang J, Fan Y, White J, Sanger JM. 2010. Assembly and dynamics of myofibrils. *Journal of Biomedicine and Biotechnology* **2010**:1–8. DOI: https://doi.org/10.1155/2010/858606, PMID: 20625425

Sbalzarini IF, Koumoutsakos P. 2005. Feature point tracking and trajectory analysis for video imaging in cell biology. *Journal of Structural Biology* **151**:182–195. DOI: https://doi.org/10.1016/j.jsb.2005.06.002, PMID: 16043363

Schmidt N, Basu S, Sladecek S, Gatti S, van Haren J, Treves S, Pielage J, Galjart N, Brenner HR. 2012. Agrin regulates CLASP2-mediated capture of microtubules at the neuromuscular junction synaptic membrane. *Journal of Cell Biology* **198**:421–437. DOI: https://doi.org/10.1083/jcb.201111130, PMID: 22851317

Su P, Yin C, Li D, Yang C, Wang X, Pei J, Tian Y, Qian A. 2020. MACF1 promotes preosteoblast migration by mediating focal adhesion turnover through EB1. *Biology Open* **9**:bio048173. DOI: https://doi.org/10.1242/bio.048173, PMID: 32139394

Suozzi KC, Wu X, Fuchs E. 2012. Spectraplakins: master orchestrators of cytoskeletal dynamics. *Journal of Cell Biology* **197**:465–475. DOI: https://doi.org/10.1083/jcb.201112034

Vilmont V, Cadot B, Vezin E, Le Grand F, Gomes ER. 2016. Dynein disruption perturbs post-synaptic components and contributes to impaired MuSK clustering at the NMJ: implication in ALS. *Scientific Reports* **6**:27804. DOI: https://doi.org/10.1038/srep27804, PMID: 27283349

Wang S, Reuveny A, Volk T. 2015. Nesprin provides elastic properties to muscle nuclei by cooperating with spectraplakin and EB1. *Journal of Cell Biology* **209**:529–538. DOI: https://doi.org/10.1083/jcb.201408098, PMID: 26008743

Wang S, Stoops E, Cp U, Markus B, Reuveny A, Ordan E, Volk T. 2018. Mechanotransduction via the LINC complex regulates DNA replication in myonuclei. *Journal of Cell Biology* **217**:2005–2018. DOI: https://doi.org/10.1083/jcb.201708137, PMID: 29650775

Wang S, Volk T. 2015. Composite biopolymer scaffolds shape muscle nucleus: insights and perspectives from *Drosophila*. *BioArchitecture* **5**:35–43. DOI: https://doi.org/10.1080/19490992.2015.1106061, PMID: 26605802

Zaoui K, Benseddik K, Daou P, Salaün D, Badache A. 2010. ErbB2 receptor controls microtubule capture by recruiting ACF7 to the plasma membrane of migrating cells. *PNAS* **107**:18517–18522. DOI: https://doi.org/10.1073/pnas.1000975107, PMID: 20937854

RESEARCH ARTICLE

Figures and figure supplements

MACF1 controls skeletal muscle function through the microtubule-dependent localization of extra-synaptic myonuclei and mitochondria biogenesis

Alireza Ghasemizadeh *et al*

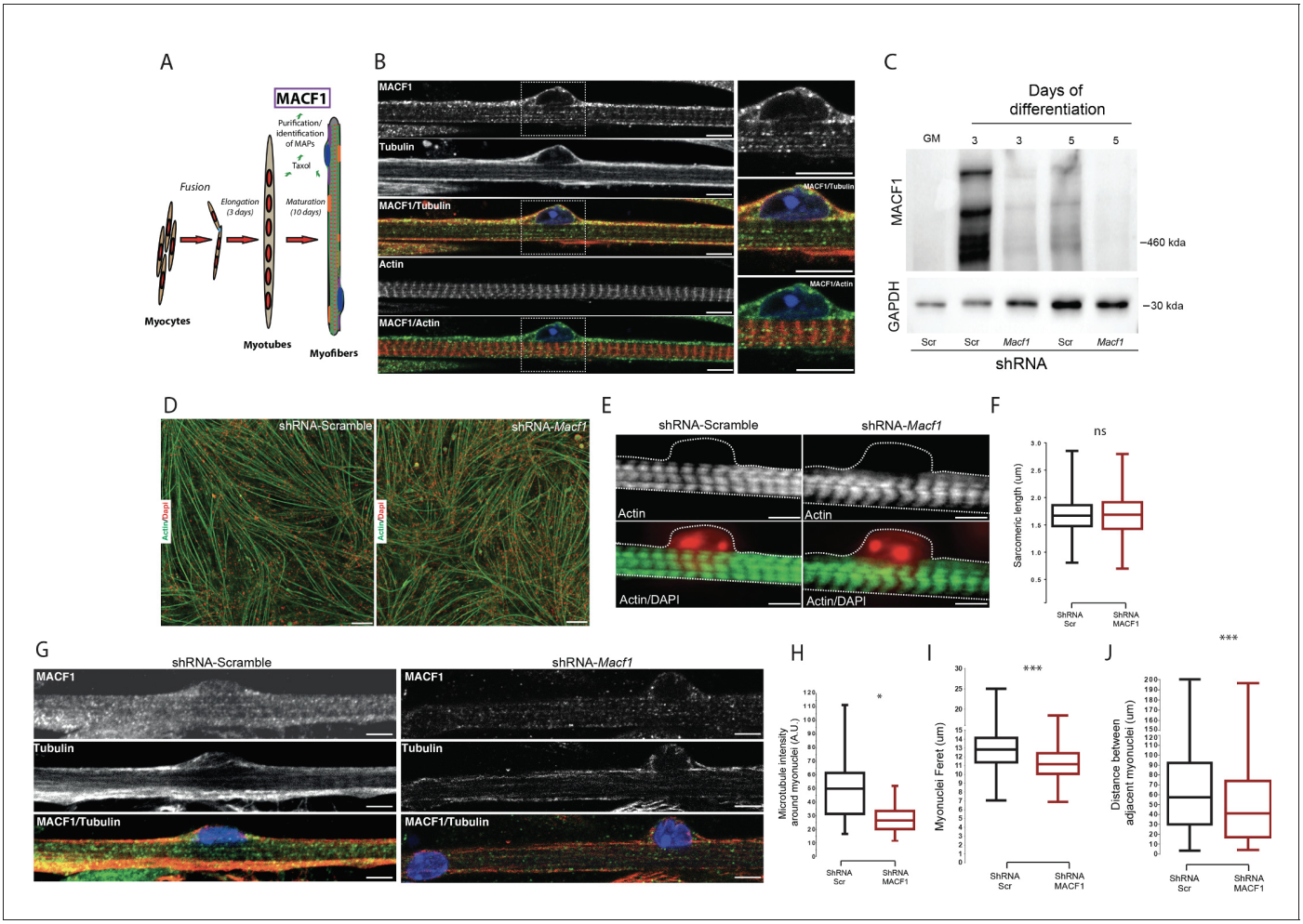

Figure 1. MACF1 is an essential regulator of myonuclei positioning in mature myofibers. (**A**) Scheme presentation of the sequential steps to obtain immature myotubes and mature myofibers from primary mouse myoblasts. Taxol stabilized microtubules proteome was collected either from WT elongated myotubes or from mature contractile myofibers. For downregulating experiments, siRNA/shRNA were transfected in early steps of differentiation just before myotubes formation. (**B**) Confocal immunofluorescence images (63×) presenting the organization of MACF1 (green) and total alpha tubulin or F-actin (red) in WT mature mouse primary myofibers. Scale bar = 10 µm. (**C**) Western blot analysis of MACF1 protein expression (main two isoforms at 830 and 630 kD) in total protein extracts of primary cells at proliferation cycle (GM for growth media) and in 3- or 5 days post-differentiation myotubes or myofibers. Cells were treated either with a scramble shRNA or a pool of four shRNAs targeting *Macf1*. GAPDH was used as loading control. (**D**) Immunofluorescence staining (10×) of F-actin (green) and myonuclei (red) in primary myofibers treated either with scramble shRNA (left panel) or with a pool of four distinct shRNAs targeting *Macf1* (right panel) after 13 days of differentiation. Scale Bar = 50 µm. (**E**) Representative immunofluorescence microscopy images (63×) of F-actin (green) and myonuclei (red) in primary myofibers treated with scramble shRNA (left panel) or with a pool of four distinct shRNAs targeting *Macf1* (right panel) after 13 days of differentiation. Scale Bar = 10 µm. (**F**) Sarcomere length measured on the immunofluorescence images of F-actin from 13 days mature primary myofibers treated with either scramble shRNA or a pool of four distinct shRNAs targeting *Macf1*. Data were obtained from three individual experiments. Line is set at median. Ns stands for not significant (Student's t test). (**G**) Confocal immunofluorescence images (63×) presenting the organization of total alpha tubulin (red) or MACF1 (green) in mature primary myofibers following treatment with either scramble shRNA (left panel) or a pool of four distinct shRNAs (right panel) targeting *Macf1*. Scale bar = 10 µm. (**H–J**) Mean values for fluorescent intensity of total alpha tubulin (**H**), myonuclei ferret (**I**) and distance between adjacent myonuclei (**J**) measured on mature primary myofibers following treatment with either scramble shRNA or a pool of four distinct shRNAs targeting *Macf1*. All panels were generated from data obtained from three individual experiments. Line is set at median. *p<0.05 and ***p<0.001 (Student's t test).

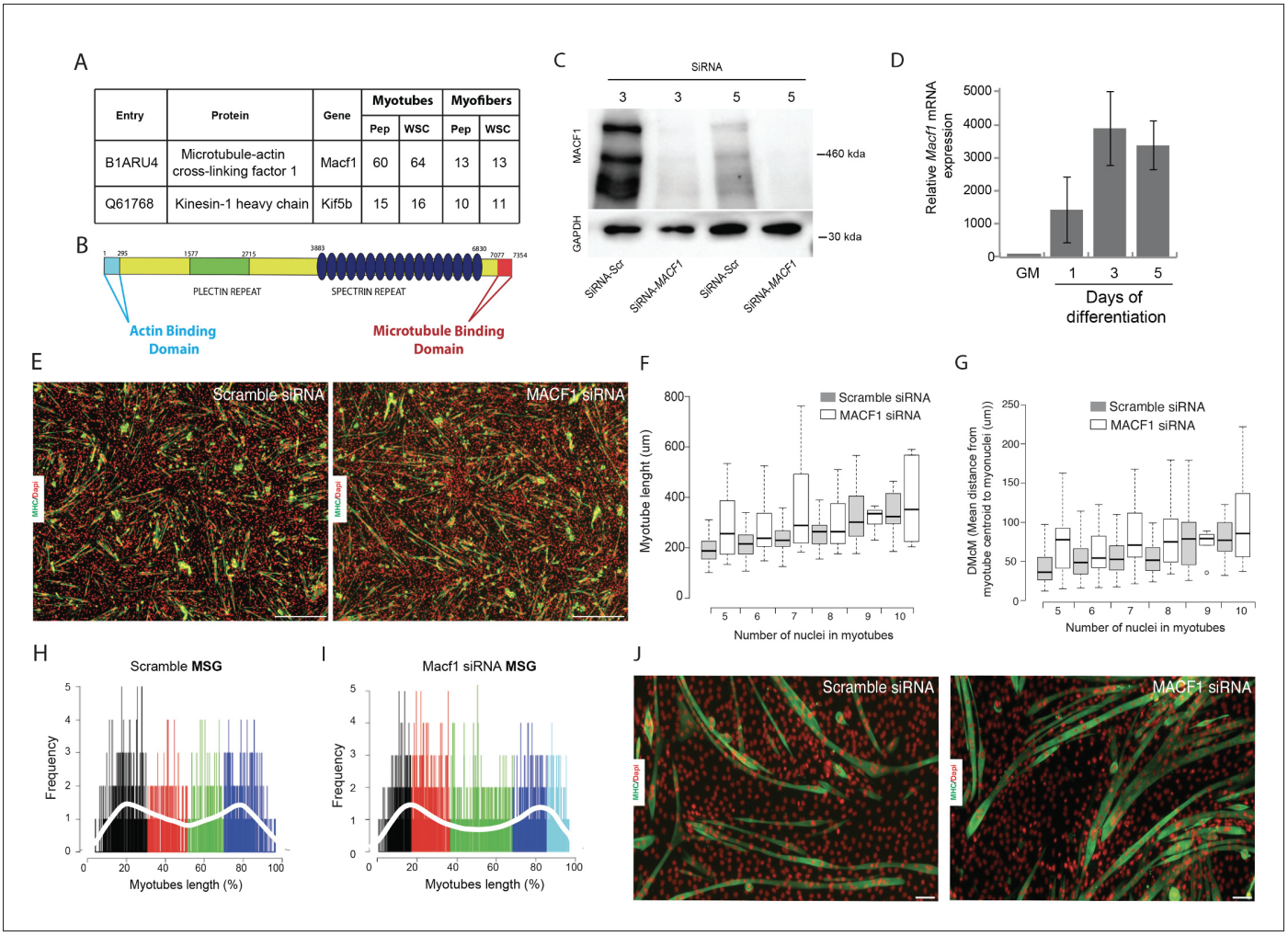

Figure 1—figure supplement 1. Reduction of MACF1 does not affects myotubes formation or myonuclei spreading within myotubes. (**A**) Table showing mass spectrometry identification of MACF1 and Kif4b in 3- and 13-day-old primary myotubes and myofibers, respectively. (**B**) Schematic representation of MACF1 identified domains. ABD is the 'Actin Binding Domain' and MTBD is the 'Microtubule Binding Domain'. (**C**) Western blot analysis of MACF1 protein expression (main two isoforms at 830 and 630 kD) in total protein extracts of primary cells in myotubes and myofibers at 3- and 5 days post-differentiation, respectively. Cells were treated with a scramble siRNA or a pool of three individual siRNAs targeting *Macf1*. GAPDH was used as loading control. (**D**) QRT-PCR analysis of *Macf1* gene expression level relative to housekeeping genes in proliferating C2C12 cells (GM) and after 1, 3, or 5 days of differentiation. Data are from three individual experiments. Mean (with SEM) values are presented. (**E**) Immunofluorescence staining of Myosin Heavy Chain (green) and myonuclei (red) in primary myotubes treated with scramble siRNA (left panel) or a pool of three distinct siRNAs targeting *Macf1* (right panel) after 3 days of differentiation. Scale Bar = 150 µm. (**F–G**) Values for myotube's length (**F**) and mean distance between myonuclei and myotube's centroid (**G**) ranked by myonuclei content per myotubes were quantified after 3 days of differentiation on cells treated with a scramble siRNA or a pool of three individual *Macf1* siRNAs. At least three individual experiments per condition were quantified. Line is set at median. (**H–I**) Myonuclei Spreading Graph (MSG) representing the statistical spatial distribution of myonuclei along myotubes in cells treated with scramble siRNA (**H**) or with a pool of three individual siRNAs (**I**) after 3 days of differentiation. (**J**) Immunofluorescence staining of Myosin Heavy Chain (green) and myonuclei (red) in 5-day-differentiated C2C12 myotubes treated with scramble siRNA (left panel) or a pool of three individual siRNAs targeting *Macf1* (right panel). Scale Bar = 50 µm.

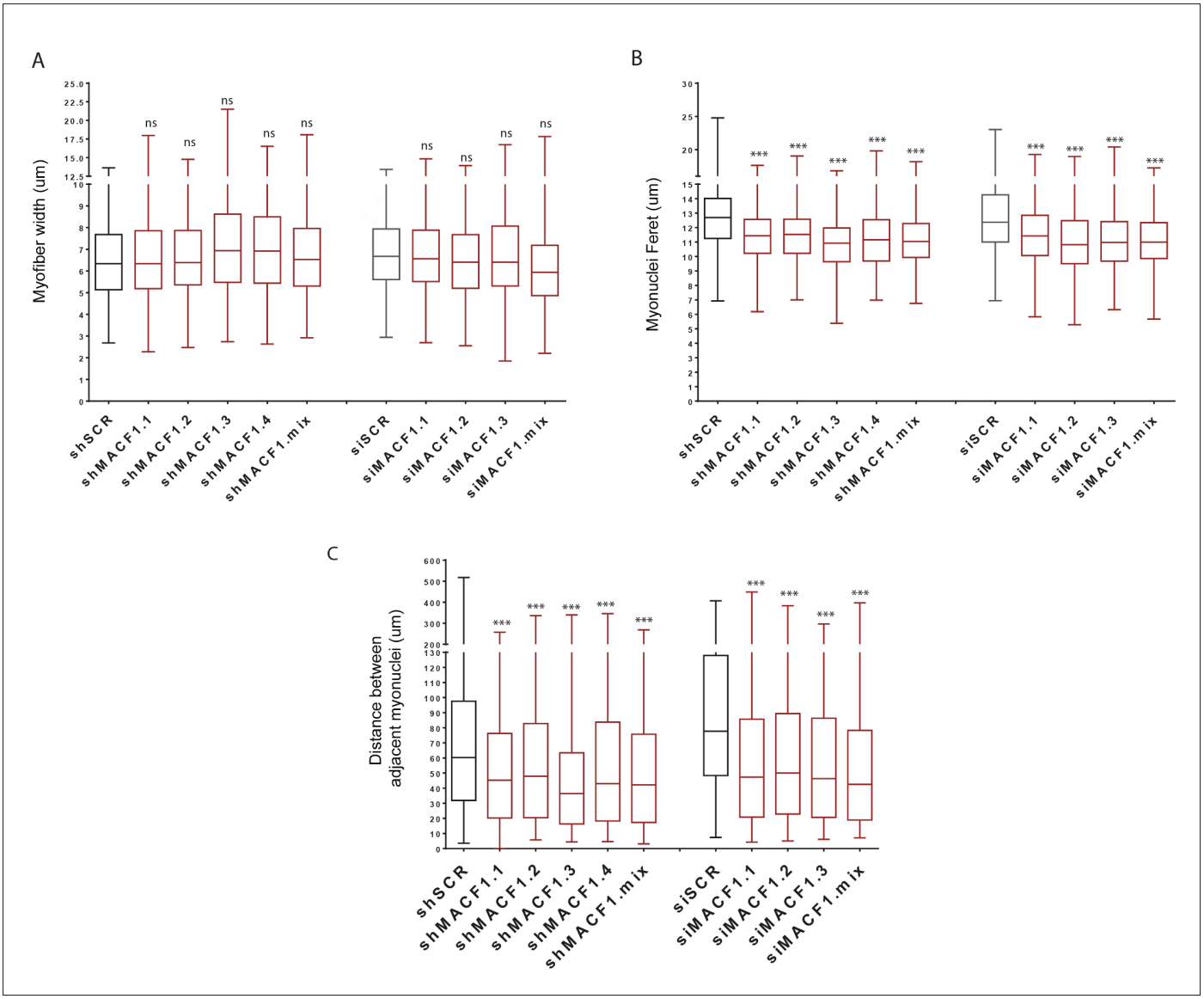

Figure 1—figure supplement 2. MACF1 is essential for myonuclei positioning and shape in mature myofibers. (**A–C**) Myofibers width (**A**), myonuclei ferret (**B**) and distance between adjacent myonuclei (**C**) measured on mature primary myofibers treated with either scramble siRNA, three individual siRNAs targeting *Macf1* or a pool of the three siRNAs targeting *Macf1* in addition to cells treated with scramble shRNA, four individual shRNAs targeting *Macf1* or a pool of the four shRNAs targeting *Macf1*. All panels were generated from data obtained from three individual experiments. Line is at median. Ns stands for not significant and ***p<0.001 (Student's t test).

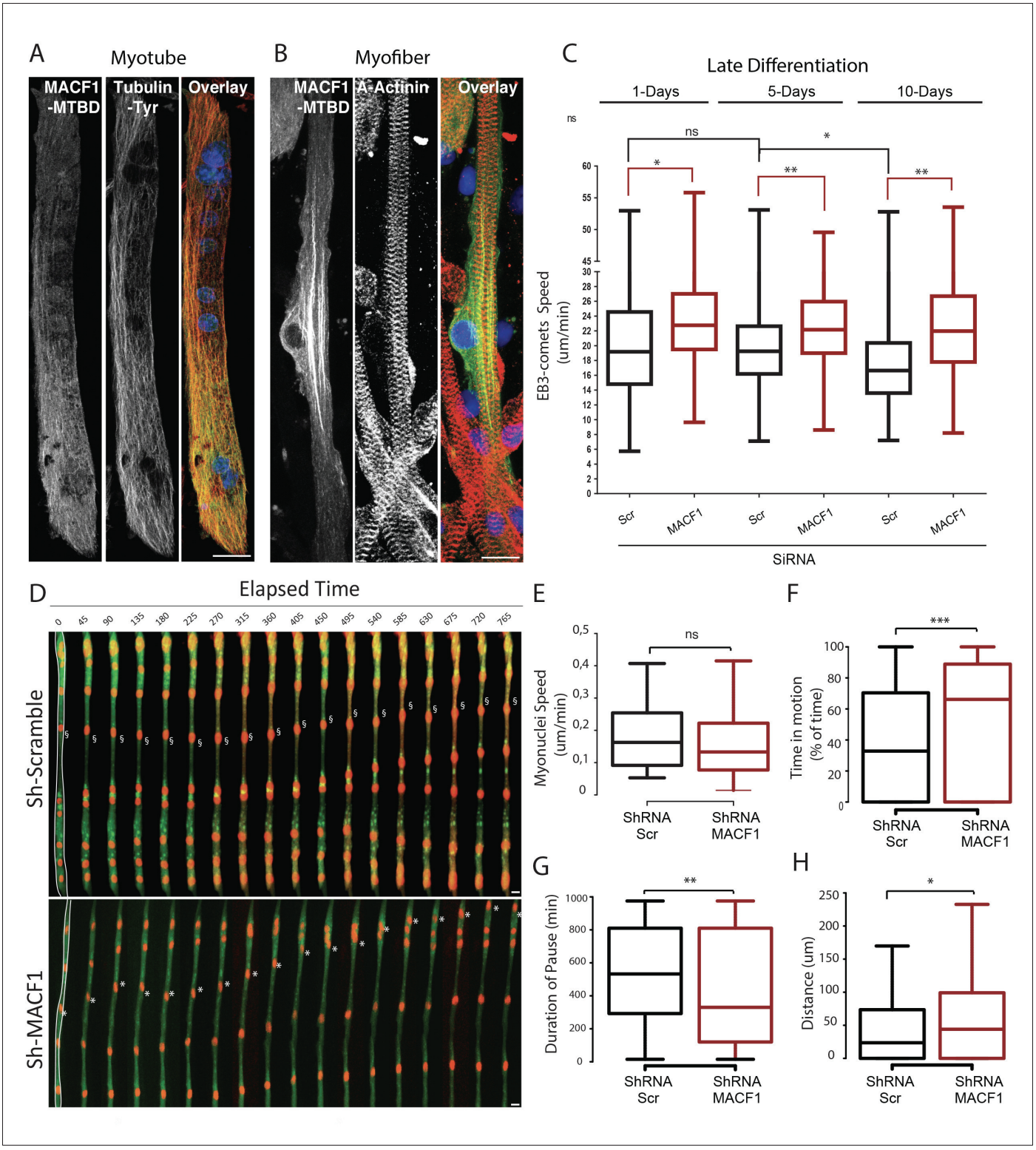

Figure 2. MACF1 regulates myonuclei dynamics through the control of microtubules. (**A–B**) representative confocal immunofluorescence images (63×) presenting MACF1-MTBD (green) and tyrosinated alpha tubulin (red) in primary myotubes (**A**) or alpha actinin (red) in primary myofibers (**B**). Scale bar = 10 µm. (**C**) Quantification of EB3 comets speed in primary cells treated with either scramble siRNA or a pool of 3 individual siRNAs targeting *Macf1* in primary myotubes at three different time points during maturation. At least 200 comets from three individual experiments were mapped per condition.

Figure 2 continued on next page

Figure 2 continued

Line is set at median. Ns stands for not significant, *p<0.05 and **p<0.01 (Student's t test). (**D**) Frames from a 14 hr time-lapse movie of two channels (shRNA in green and lamin-chromobody in red) taken 5 days post differentiation from primary myotubes treated with either a scramble shRNA (upper panel) or a mix of shRNAs targeting *Macf1* (lower level). In the first frame (on the left), myofibers are selected in white, which corresponds to the region used to create the adjacent kymograph. Scale bar = 10 µm. (**E–H**) Speed (**E**), Time in motion (**F**), Duration of pauses (**G**), and Distance travelled by myonuclei (**H**) were quantified using SkyPad analysis (***Cadot et al., 2014***). Quantifications were done on myonuclei within different myofibers from three individual experiments. Line is set at median. Ns stands for not significant, *p<0.05, **p<0.01, and ***p<0.001 (Student's t test).

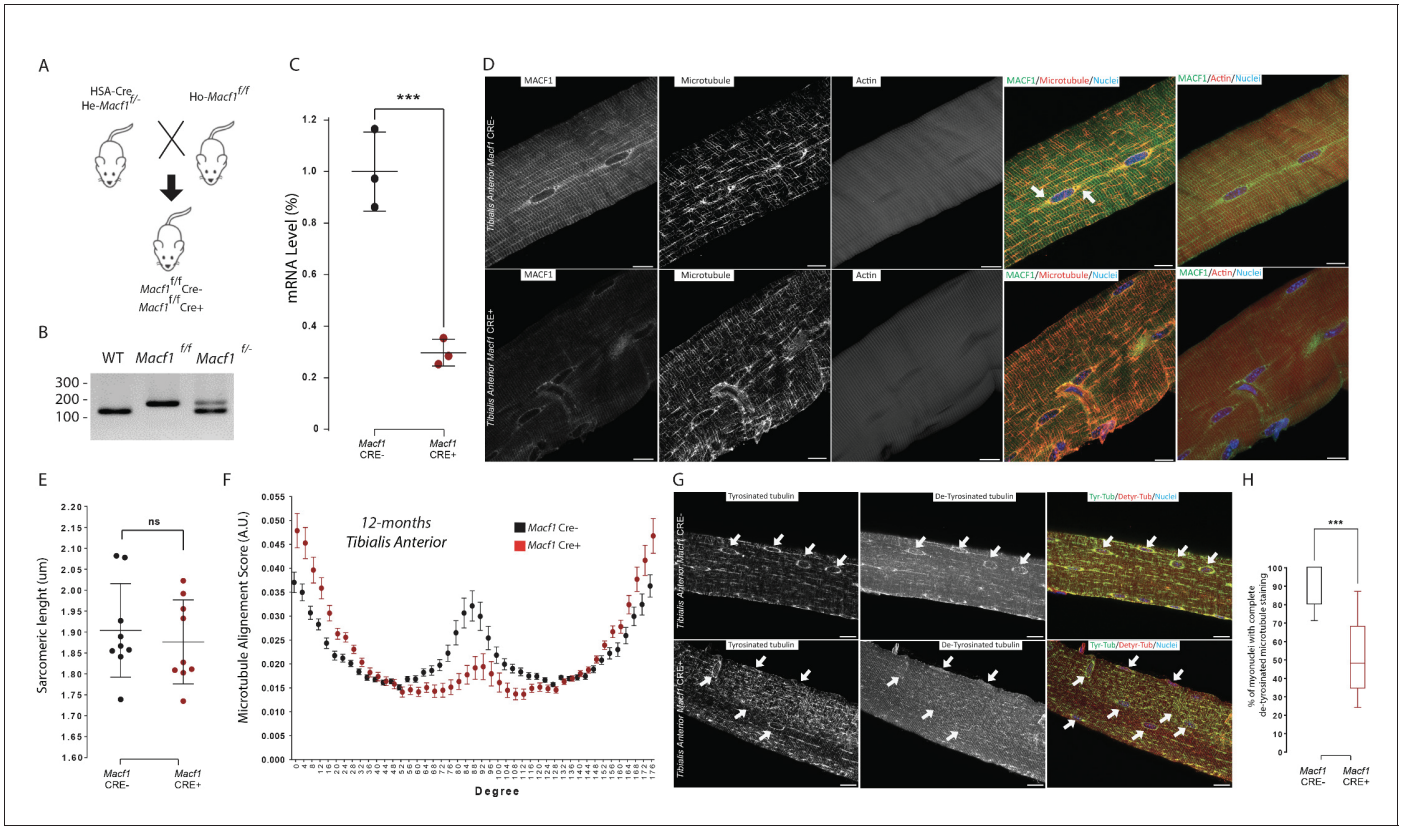

Figure 3. MACF1 is necessary for global and perinuclear microtubules organization within skeletal muscles in vivo. (**A**) Scheme of the strategy used to generate muscle specific *Macf1* knockout mouse model. (**B**) Representative PCR gel confirming the floxed *Macf1* gene in mutant mice carrying Cre transgene. (**C**) Quantification of efficacy of the Cre-lox system in our muscle specific mouse model by analyzing the *Macf1* gene expression level. qRT-PCR was carried out on total mRNA extracted from *Gastrocnemius* of 3 WT and 3 *Macf1* KO mice of 12-month-old. Following the calculation of relative gene expression level on housekeeping genes for each mouse, the mean expression level of *Macf1* was calculated for the WT mice. To generate the graph, the *Macf1* expression level of each WT and KO mouse was then normalized on the previously calculated mean value. Line is set at mean (with SEM). ***p<0.001 (Student's t test). (**D**) Representative confocal images (63×) of isolated myofibers from *Tibialis Anterior* of *Macf1* Cre- (upper panel) and Cre+ (lower panel) mice, showing MACF1 (green), myonuclei (blue) and microtubules or F-actin (red). Scale Bar = 15 µm. (**E**) Sarcomere length quantified from the alpha actinin staining from 3 *Macf1* Cre- and 3 *Macf1* Cre+ 12-month-old mice. Following myofibers isolation from *Tibialis Anterior*, the distance between alpha actinin transverse bands of 3 myofibers per mouse was measured. Line is set at mean (with SD). Ns stands for not significant (Mann-Whitney test). (**F**) Microtubules network organization analysis of at least three myofibers from each of the three WT and three conditional *Macf1*-KO mice using TeDT software. The final generated graph presents a global score for each given degree of microtubules orientation, with 0 and 180 degrees corresponding to the longitudinal microtubules and 90 degrees corresponding to the transverse microtubules. Mean values (with SEM) is presented. (**G**) Representative confocal images (63×) from myofibers isolated from *Tibialis Anterior* issued from 12-month-old *Macf* Cre- (upper panel) or Cre+ (lower panel) mice, presenting tyrosinated tubulin (green), de-tyrosinated tubulin (red) and myonuclei (blue). White arrows point to myonuclei. Scale Bar = 15 µm. (**H**) Quantification of the percentage of myonuclei presenting the total de-tyrosinated tubulin ring. Quantifications were done on confocal images obtained from several isolated myofibers from *Tibialis Anterior* of three WT and three conditional *Macf1*-KO mice at the age of 12 months. Line is set at median. ***p<0.001 (Student's t test).

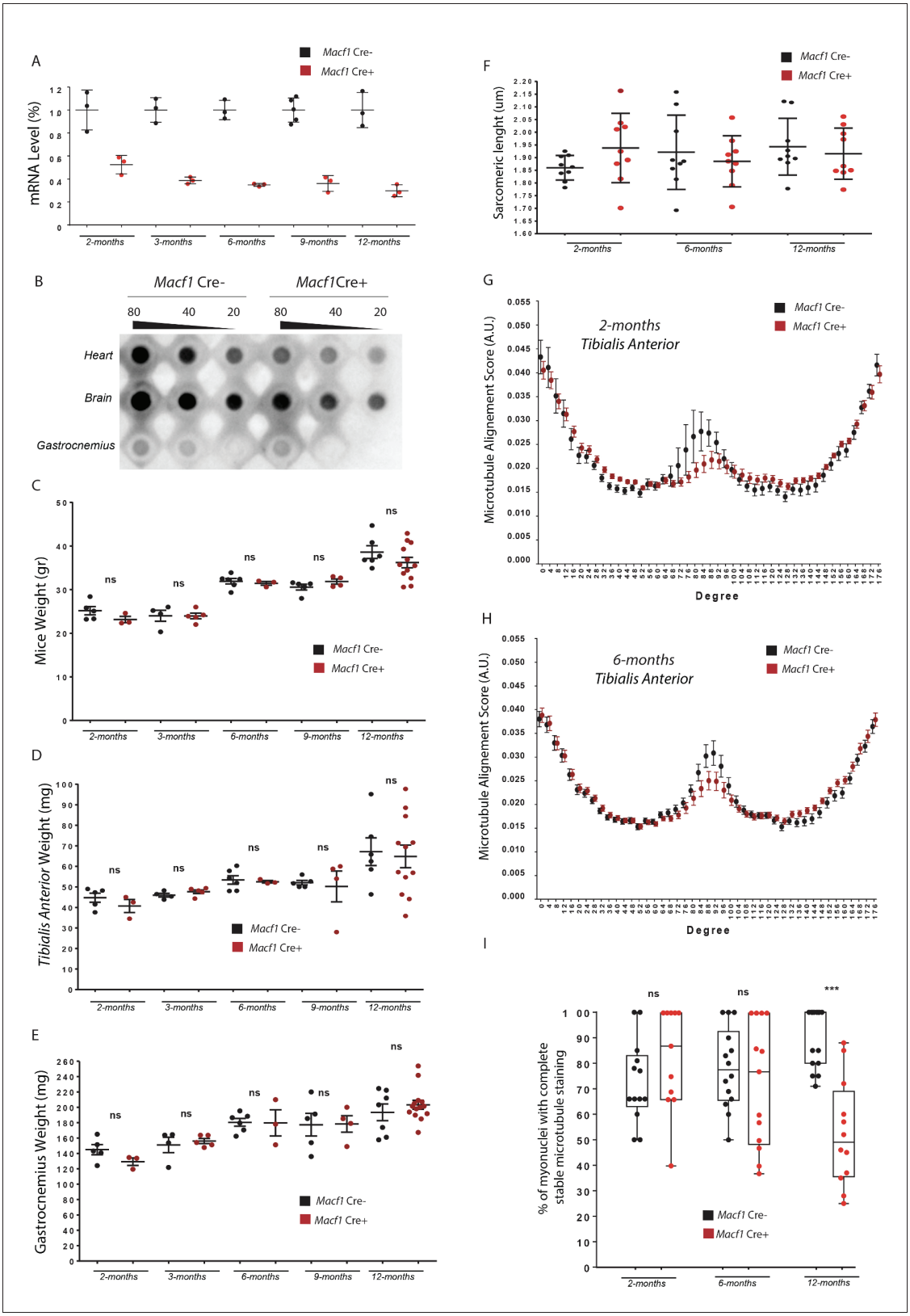

Figure 3—figure supplement 1. MACF1 conditional KO mice present progressive microtubules disorganization. (**A**) Quantification of efficacy of Cre-lox system in our muscle specific mouse model by analyzing the *Macf1* gene expression level. QRT-PCR was carried out on total mRNA extracted from

Figure 3—figure supplement 1 continued on next page

Figure 3—figure supplement 1 continued

Gastrocnemius of three individual *Macf1* Cre- and *Macf1* Cre+ mice at different ages. Following the calculation of relative gene expression level to housekeeping genes for each mouse, the mean expression level of *Macf1* was calculated for the WT mice. To generate the graph, the *Macf1* expression level of each WT and KO mouse was then normalized on the previously calculated mean value. Line is set at mean (with SEM). (**B**) Dot blot assay for MACF1 expression in Heart, Brain and *Gastrocnemius* lysates from 12-month-old *Macf1* Cre- and *Macf1* Cre+ mice. (**C–E**) Evaluation of total body weight (**C**), weight of *Tibialis Anterior* (**D**) and weigh of *Gastrocnemius* (**E**) of *Macf1* Cre- and *Macf1* Cre+ mice at different ages. Line is set at mean (with SEM). Ns stands for not significant (Student's t test). (**F**) Measurements of sarcomere length quantified on alpha actinin staining in three individual *Macf1* Cre- and *Macf1* Cre+ mice at each given age. Following myofibers isolation from *Tibialis Anterior*, the distance between alpha actinin transverse bands of 3 myofibers per mouse was measured. Line is set at mean (with SD). (**G–H**) Microtubule network organization analysis from at least three myofibers from three individual *Macf1* Cre- or conditional KO *Macf1* Cre+ mice at 2 months (**G**) or 6 months (**H**) of age, using TeDT software. The final graph presents a global score for each given degree of microtubules orientation, with 0 and 180 degrees corresponding to the longitudinal microtubules and 90 degrees to the transverse microtubules. Mean values (with SEM) is presented. (**I**) Quantification of the percentage of myonuclei presenting the total de-tyrosinated tubulin ring. Quantifications were done on confocal images obtained from several myofibers isolated from *Tibialis Anterior* muscles of three *Macf1* Cre- and three conditional KO *Macf1* Cre+ mice at different ages. Line is set at median. Ns stands for not significant and ***p<0.001 (Student's t test).

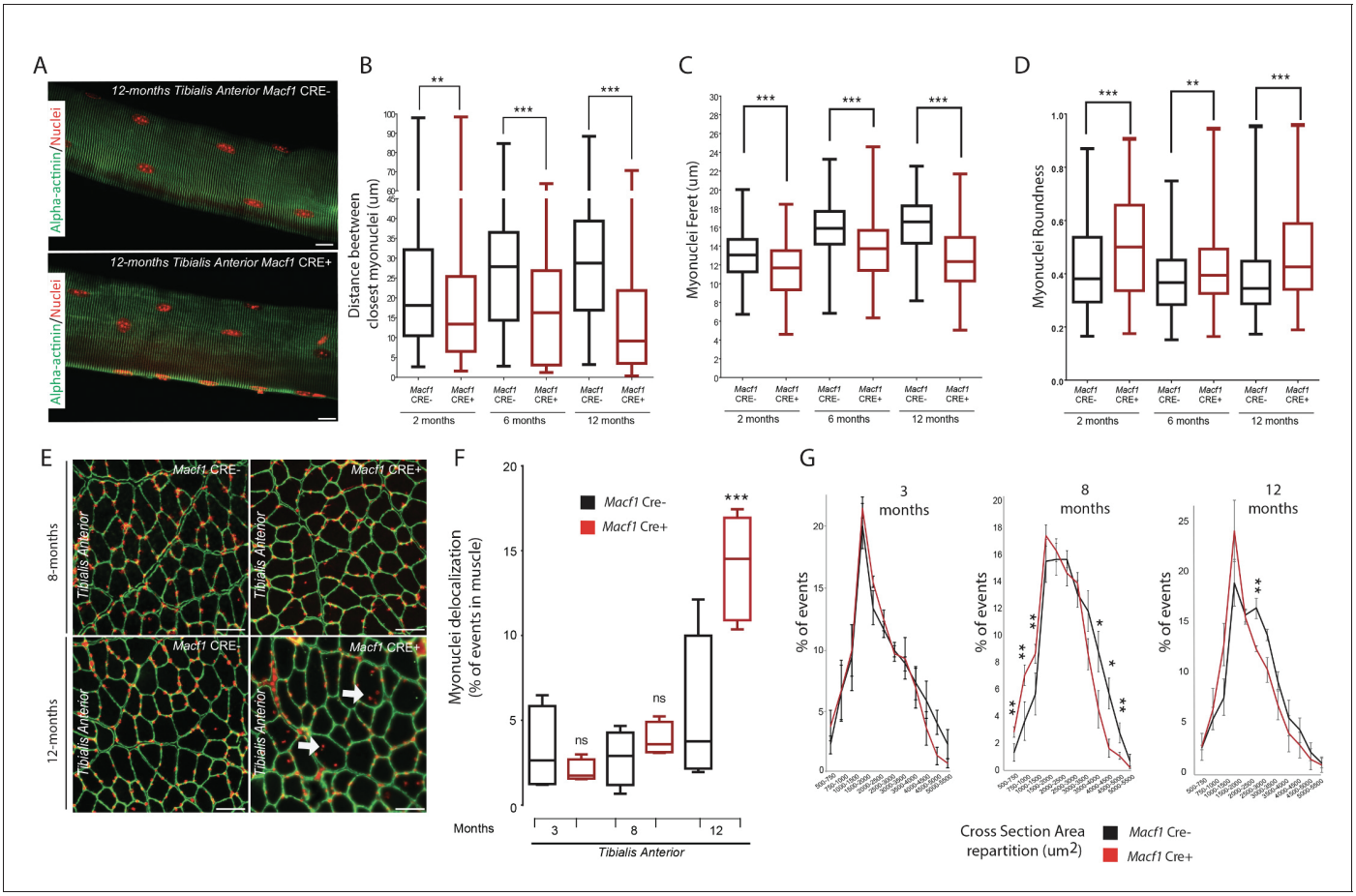

Figure 4. Loss of MACF1 alters myonuclei shape and positioning progressively with age. (**A**) Representative confocal images (63×) of myofibers isolated from *Tibialis Anterior* of *Macf1* Cre- (upper panel) and Cre+ (lower panel) mice at the age of 12 months presenting alpha-actinin (green) and myonuclei (red). Scale Bar = 15 µm. (**B–D**) Quantification of distance between the nearest myonuclei (**B**), myonuclei feret (**C**) and myonuclei roundness (**D**) measured on isolated myofibers from *Tibialis Anterior* of *Macf1* Cre- and Cre+ mice (as presented in panel A) at 2-, 6-, and 12 months of age. Several myofibers were subjected to analysis per mouse. Each group gathers data obtained from myofibers of 3 or more mice. Line is set at median. **p<0.01 and ***p<0.001 (Student's t test). (**E**) Representative images of *Tibialis Anterior* muscle cross-section from *Macf1* Cre- (left panels) and *Macf1* Cre+ (right panels) mice at the age of 8 and 12 months, stained for myonuclei (red) and Laminin (green). Examples of myofibers with mis-localized myonuclei are indicated by white arrows. Scale Bar = 150 µm. (**F**) Quantification of the percentage of myofibers with mis-localized myonuclei in *Tibialis Anterior* of 3, 8, and 12 months-old *Macf1* Cre- and *Macf1* Cre+ mice. Line is set at median. Ns stands for not significant and ***p<0.001 (Student's t test). (**G**) Distribution of myofibers cross-section area in the *Tibialis Anterior* from 3-, 8-, and 12-months-old *Macf1* Cre- and *Macf1* Cre+ mice. Line is set at mean (with SEM). Ns stands for not significant, *p<0.05 and **p<0.01 (Student's t test).

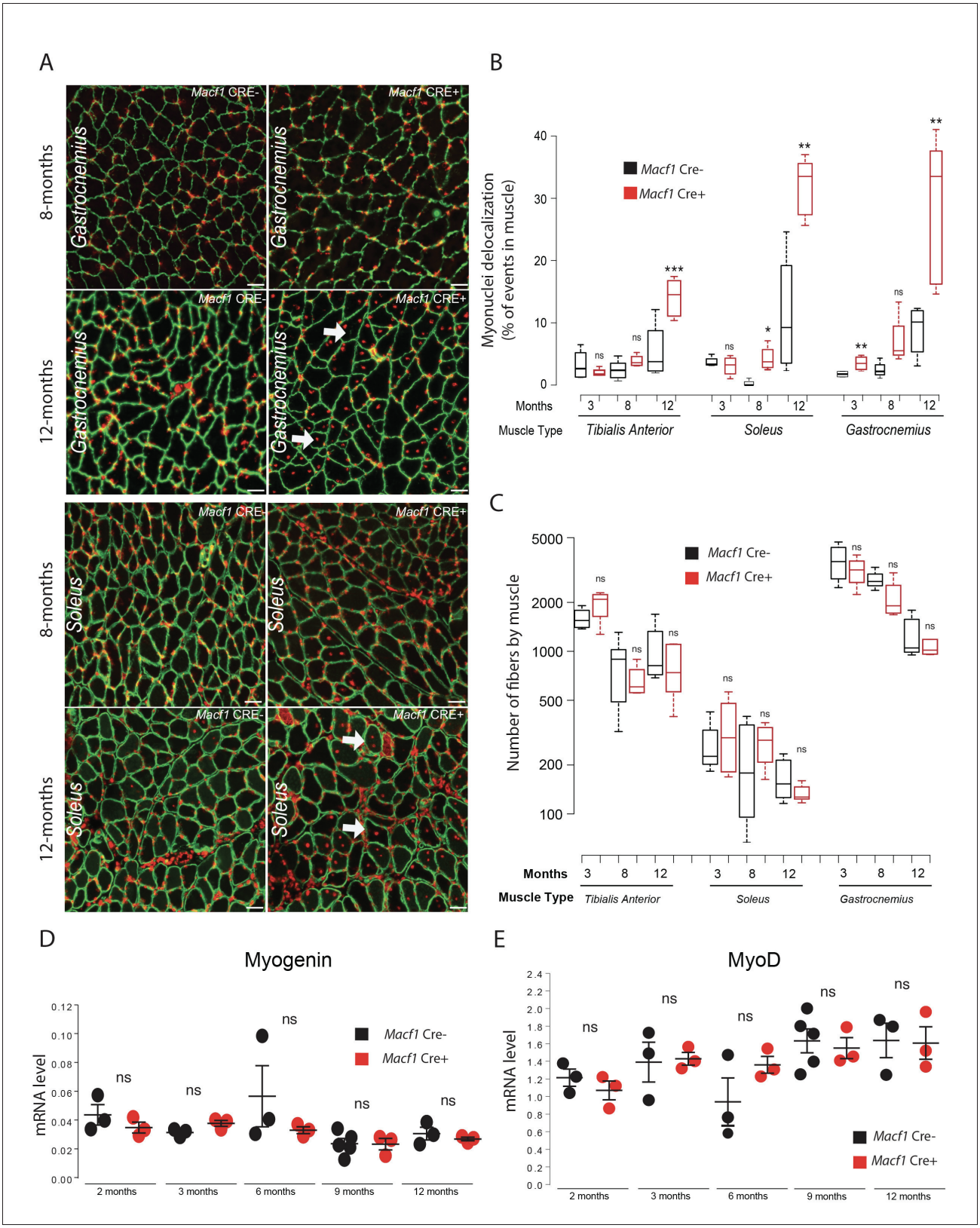

Figure 4—figure supplement 1. Mis-localization of myonuclei in MACF1 conditional KO mice is independent from muscular regeneration. (**A**) Representative images of *Gastrocnemius* and *Soleus* muscles cross-sections from *Macf1* Cre- (left panels) and *Macf1* Cre+ (right panels) mice at the age

Figure 4—figure supplement 1 continued on next page

Figure 4—figure supplement 1 continued

of 8 and 12 months, stained for myonuclei (red) and Laminin (green). Example of myofibers with mis-localized myonuclei are indicated by white arrows. Scale Bar = 100 μm. (**B**) Quantification of the percentage of myofibers with mis-localized myonuclei in *Tibialis Anterior, Soleus* and *Gastrocnemius* of 3-, 8-, and 12-month-old *Macf1* Cre- and *Macf1* Cre+ mice. Line is set at median. Ns stands for not significant, *p<0.05, **p<0.01, and ***p<0.001 (Student's t test). (**C**) Quantification of the number of muscle fibers per cross-sections of *Tibialis Anterior, Soleus* and *Gastrocnemius* of 3-, 8-, and 12-month-old *Macf1* Cre- and *Macf1* Cre+ mice. Line is set at median. Ns stands for not significant (Student's t test). (**D–E**) QRT-PCR results presenting relative gene expression levels for Myogenin (**D**) and MyoD (**E**) in total mRNA extracts from *Gastrocnemius* of *Macf1* Cre- and Cre+ at each given age. Target genes relative expression level to housekeeping genes is presented on each panel. Line is set at mean (with SEM). Ns stands for not significant (Student's t test).

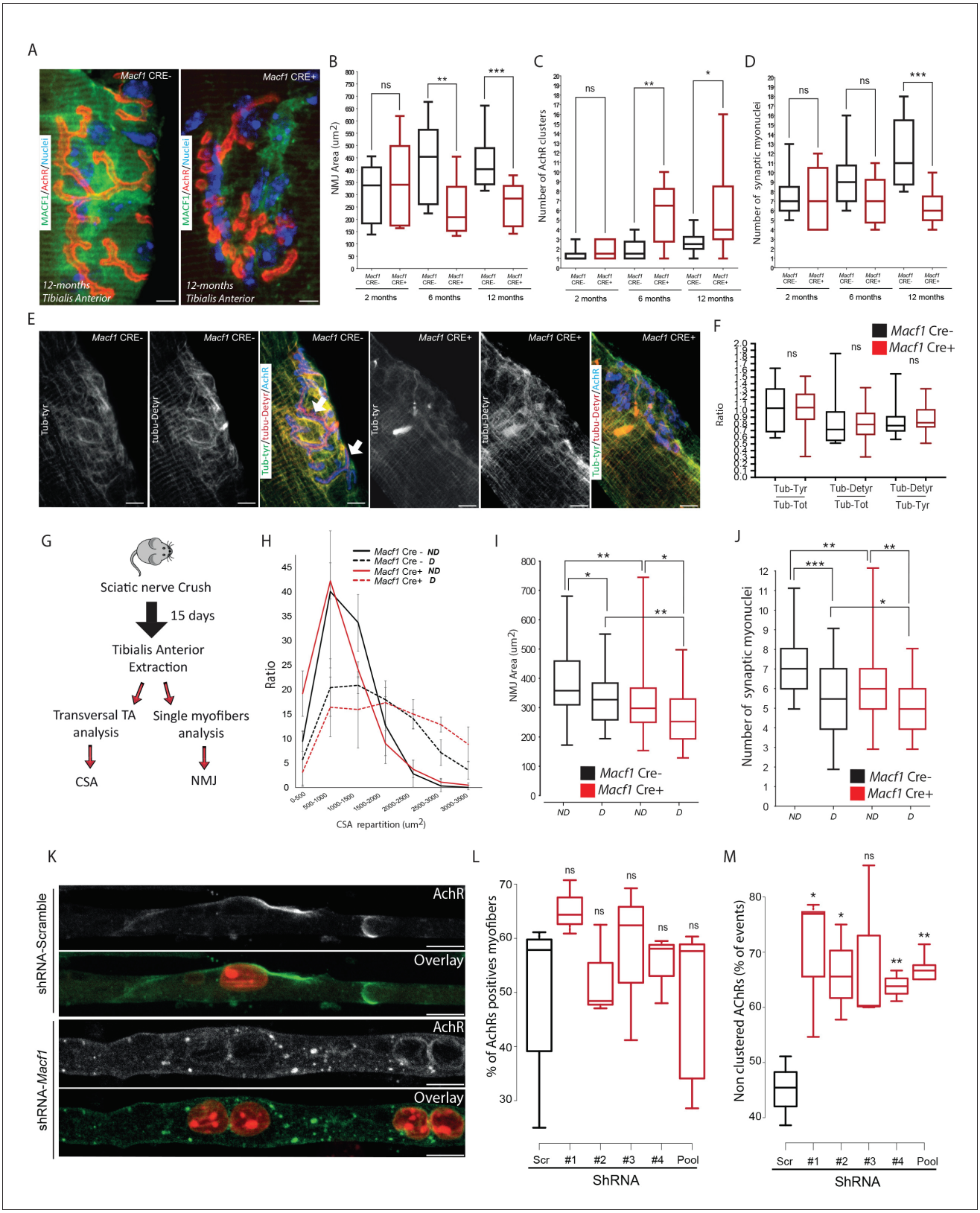

Figure 5. MACF1 controls AChRs clustering but has no impact on synaptic myonuclei at the NMJ. (**A**) Representative confocal images (63×) of post-synaptic NMJs within isolated myofibers from *Tibialis Anterior* of *Macf1* Cre- (left panel) and Cre+ (right panel) mice at the age of 12 months presenting

Figure 5 continued on next page

Figure 5 continued

MACF1 (green), AChRs clusters (red) and myonuclei (blue). Scale Bar = 10 μm. (**B–D**) Quantification of post-synaptic NMJs area (**B**), number of AChRs clusters (**C**) and number of synaptic myonuclei (**D**) measured on myofibers isolated from *Tibialis Anterior* of *Macf1* Cre- and Cre+ mice (as presented in panel A) at 2-, 6-, and 12 months of age. Several myofibers were subjected to analysis per mouse and each group is formed from at least three mice. Line is set at median. Ns stands for not significant, *p<0.05, **p<0.01 and ***p<0.001 (Student's t test). (**E**) Representative confocal images (63×) presenting tyrosinated tubulin (green), de-tyrosinated tubulin (red), and AChRs clusters (blue) in myofibers isolated from *Tibialis Anterior* of *Macf1* Cre- (three left panels) and Cre+ (three right panels) mice at the age of 12 months. Scale Bar = 10 μm. (**F**) Quantification of the ratios of fluorescence intensity from tyrosinated tubulin to total tubulin, de-tyrosinated tubulin to total tubulin and de-tyrosinated tubulin to tyrosinated tubulin. The mean fluorescence intensity of each given staining was measured specifically for the post-synaptic NMJs area (as presented in panel E) on NMJs of myofibers isolated from *Tibialis Anterior* of *Macf1* Cre- and Cre+ mice at the age of 12 months. Line is set at median. Ns stands for not significant (Student's t test). (**G**) Scheme of the strategy used to induce sciatic nerve crush and subsequent analysis of muscle fibers from *Macf1* Cre- and Cre+ mice. (**H**) Distribution of myofibers cross-section areas from non-denervated (referred as ND) and denervated (referred as D) *Tibialis Anterior* muscles of *Macf1* Cre- and Cre+ mice at the age of 8 months. Line is set at mean (with SEM). (**I–J**) Quantification of post-synaptic NMJs area (**I**) and number of synaptic myonuclei (**J**) measured on isolated myofibers from non-denervated (referred as ND) and denervated (referred as D) *Tibialis Anterior* muscles of *Macf1* Cre- and Cre+ mice at the age of 8 months. Line is set at median. *p<0.05, **p<0.01, and ***p<0.001 (Student's t test). (**K**) Representative fluorescence images (63×) of AChRs clusters (green) and myonuclei (red) in myofibers treated with scramble shRNA (two upper panels) or with a pool of the four distinct shRNAs targeting *Macf1* (two lower panels) after 10 days of differentiation in presence of Agrin in culture medium. Scale Bar = 10 μm. (**L**) Percentage of myofibers expressing immunofluorescence staining for AChRs in primary myofibers treated with scramble shRNA, with each of the four distinct shRNAs or with a pool of these four distinct shRNAs targeting *Macf1* after 10 days of differentiation in the presence of Agrin. Data are from three individual experiments. Line is set at median. Ns stands for not significant (Student's t test). (**M**) AChRs clustering distribution in cells treated with scramble shRNA, with each of the four individual shRNAs or with a pool of the four individual shRNAs targeting *Macf1* after 10 days of differentiation in the presence of Agrin. Data was collected from three individual experiments for each condition. Line is set at median. Ns stands for not significant, *p<0.05 and **p<0.01 (Student's t test).

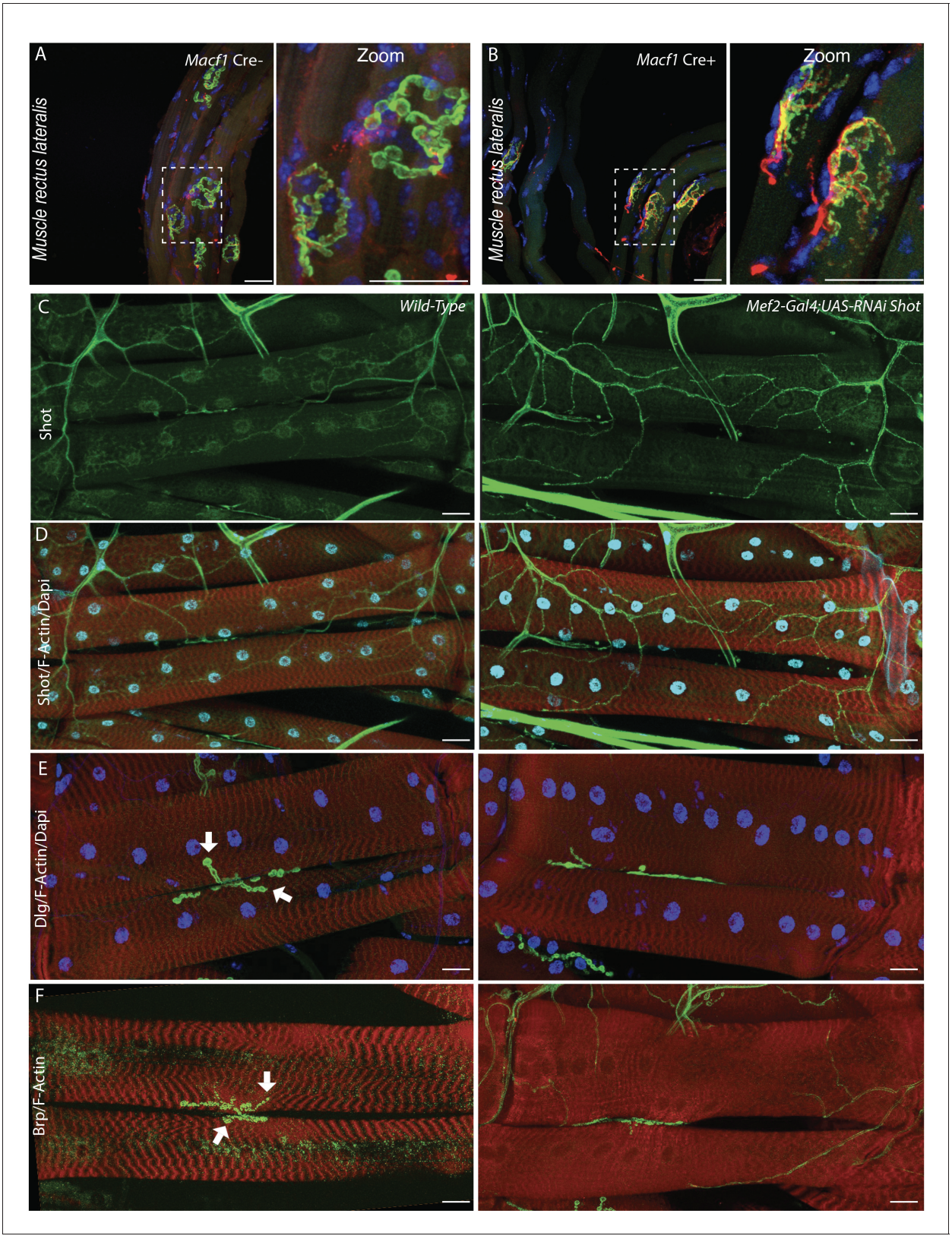

Figure 5—figure supplement 1. MACF1 orthologue, Shot, is essential for NMJs organization in *Drosophila*. (**A–B**) Representative images of myofibers extracted from *Rectus Lateralis* muscle stained for myonuclei (blue), presynaptic markers (Neurofilament and Synaptic vesicles 2) (red) and AChRs

Figure 5—figure supplement 1 continued on next page

Figure 5—figure supplement 1 continued

(green) from 4-month-old *Macf1* Cre- (**A**) and *Macf1* Cre+ (**B**) mice. Scale Bar = 150 μm. (**C–D**) Larval muscles labeled for Shot (Green), myonuclei (blue) and F-actin (red) in WT (left panels) or RNAi treated muscle-targeting *Shot* (right panels). (**E**) Larval muscles labeled for Discs-Large, Dlg (Green), myonuclei (blue) and F-actin (red) in WT (left panel) or RNAi treated muscle targeting *Shot* (right panel). (**F**) Larval muscles labeled for Bruchpilot, BRP (Green), myonuclei (blue) and F-actin (red) in WT (left panel) or RNAi-treated muscle targeting *Shot* (right panel). Scale Bar = 50 μm.

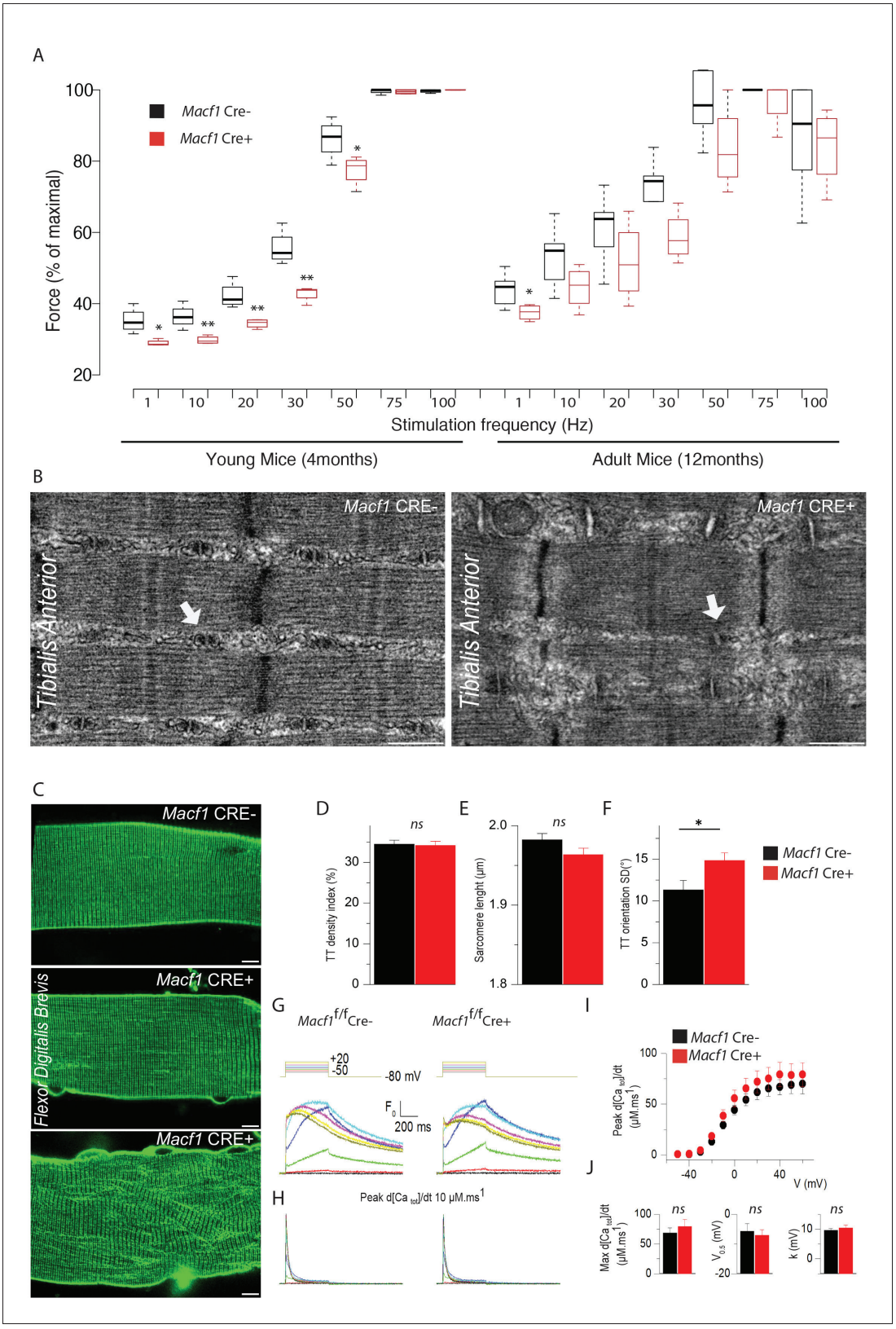

Figure 6. Muscle-specific *Macf1* knockout affects muscle force production and T-tubule organization but leaves SR Ca^{2+} release unchanged. (**A**) Force production from the *Hindlimb* muscles in young (4 months) and adult (12 months) *Macf1* Cre- and *Macf1* Cre+ mice in response to various incremental

Figure 6 continued on next page

Figure 6 continued

stimulation frequencies (from 1 to 100 Hz). Line is set at median. *p<0.05 and **p<0.01 (Student's t test). (**B**) Representative electron microscopy images of myofibrils and T-tubule organization within *Tibialis Anterior* muscles from 12-month-old *Macf1* Cre- and *Macf1* Cre+ mice. Scale Bar = 0.5 µm. (**C**) Representative fluorescence microscopy images of di-8-anepps staining of the T-tubule network in *Flexor Digitalis Brevis* muscle fibers of 12-month-old *Macf1* Cre- and *Macf1* Cre+ mice. Scale Bar = 15 µm. (**D–F**) Quantification of T-tubules density index (**D**), Sarcomere length (**E**) and T-tubules orientation (**F**) in *Flexor Digitalis Brevis* muscle fibers from 12-month-old *Macf1* Cre- and *Macf1* Cre+ mice. Mean with SD is showing. Ns stands for not significant and *p<0.05 (Student's t test). (**G**) Representative rhod-2 Ca^{2+} transients in a *Macf1* Cre- and in a *Macf1* Cre+ fiber in response to 0.5 s-long depolarizing pulses from −80 mV to the range of indicated values, with intervals of 10 mV. (**H**) Corresponding Ca^{2+} release flux ($d[Ca_{Tot}]/dt$) traces calculated as described in the Materials and methods. (**I**) Mean voltage-dependence of the peak rate of SR Ca^{2+} release in *Macf1* Cre- and in a *Macf1* Cre+ fibers. (**J**) Inset shows the mean values for maximal rate, half-activation voltage and steepness factor (**k**) for SR Ca^{2+} release in the two groups of fibers, as assessed from Boltzmann fits to data from each fiber.

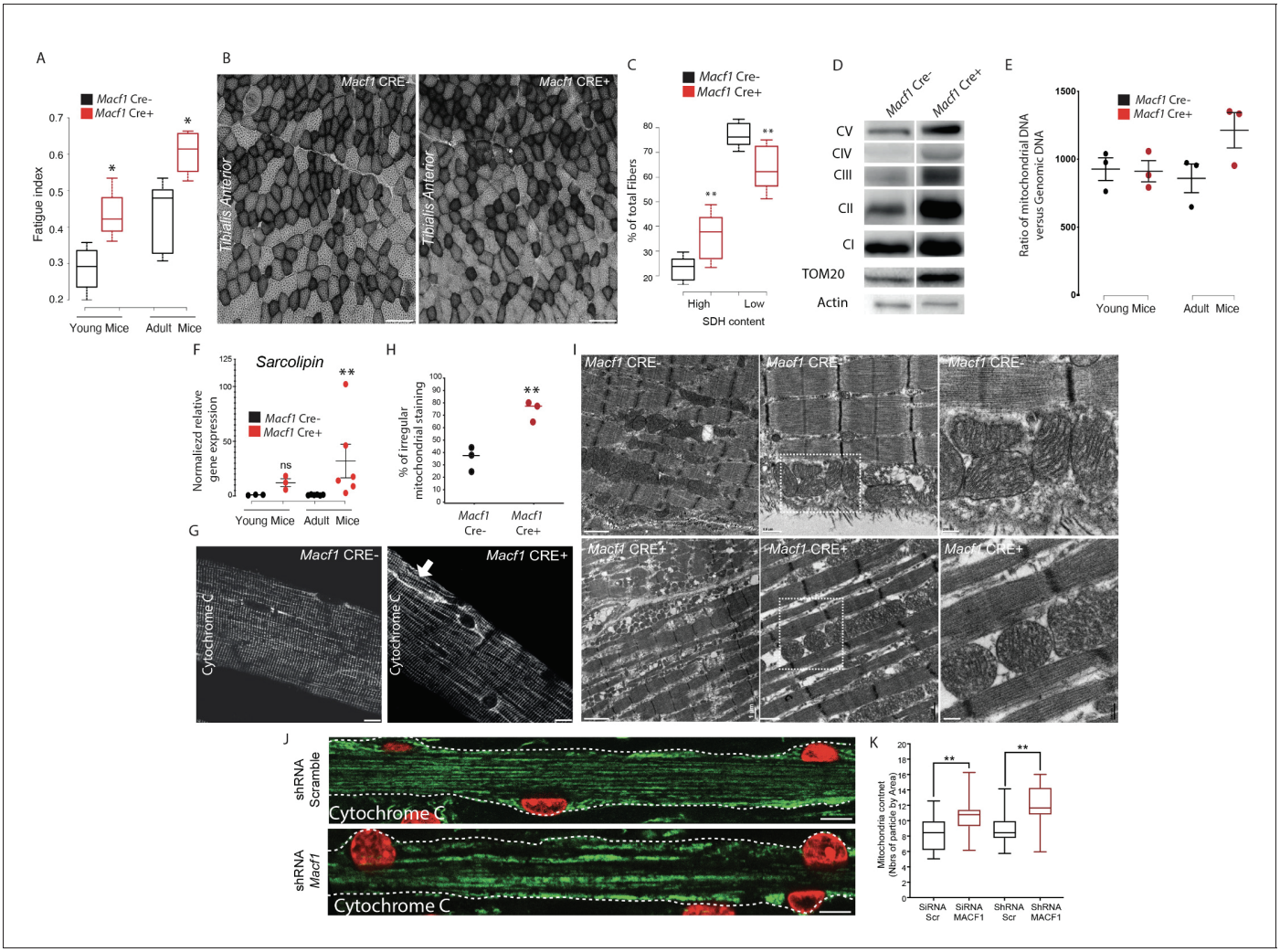

Figure 7. Muscle specific MACF1 knockout affects mitochondrial content and organization. (**A**) Quantification of the fatigue index from the *Hindlimb* muscles in young (4 months) and adult (12 months) *Macf1* Cre- and *Macf1* Cre+. Line is set at median. *p<0.05 (Student's t test). (**B**) Representative images of transversal cross-section of *Tibialis Anterior* muscle from 12-month-old *Macf1* Cre- (left panel) and *Macf1* Cre+ (right panel) mice stained for Succinate DeHydrogenase activity. Scale Bar = 150 µm. (**C**) Quantification of the Succinate DeHydrogenase activity relative to myofibers distribution in conditional *Macf1*-KO mice compared to control mice. Line is set at median. Ns stands for not significant, **p<0.01 (Student's t test). (**D**) Western blot analysis of OXPHOS mitochondrial electron transport chain, TOM20 and actin proteins expression in total extracts from *Gastrocnemius* muscles of 12-month-old *Macf1* Cre- and *Macf1* Cre+ mice. (**E**) QPCR quantification of the ratio between mitochondrial and genomic DNA in total DNA extracts obtained from *Gastrocnemius* muscles of three individual *Macf1* Cre- and *Macf1* Cre+ mice at each given age. Line is set at mean (with SEM). (**F**) QRT-PCR results presenting relative gene expression level for SLN in *Macf1* Cre- and Cre+ at each given age. Following the calculation of relative gene expression level with reference to housekeeping genes for each mouse, the mean expression level of SLN was calculated for the WT mice. Next, the expression level of each WT and KO mouse was normalized to the previously calculated mean value. Line is set at mean (with SEM). Ns stands for not significant and **p<0.01 (Mann-Whitney test). (**G**) Representative confocal images (63×) from isolated myofibers of *Tibialis Anterior* stained for Cytochrome C in *Macf1* Cre- (left panel) and Cre+ (right panel) mice of 12-month-old mice. Scale Bar = 15 µm. (**H**) Quantification of the percentage of myofibers with irregular (broken/oriented/accumulated) mitochondrial staining in isolated myofibers of *Tibialis Anterior* muscles from three individual *Macf1* Cre- and Cre+ mice at the age of 12 months. Line is set at median. **p<0.01 (Student's t test). (**I**) Representative electron microscopy images of myofibrils and mitochondria organization within *Tibialis Anterior* muscles from 12-month-old *Macf1* Cre- (upper panels) and *Macf1* Cre+ (lower panels) mice. Scale Bar = 1, 0.5, 0.2 µm. (**J**) Confocal immunofluorescence images (63×) presenting the organization of Cytochrome C (green) in primary myofibers treated either with scramble shRNA (upper panel) or with a pool of four distinct shRNAs targeting *Macf1* (lower panel) after 13 days of differentiation. Myonuclei are presented in red. Scale Bar = 10 µm. (**K**) Quantification of mitochondrial content per area in primary myofibers treated either with scramble shRNA or with a pool of four distinct shRNAs targeting *Macf1* after 13 days of differentiation. Line is set at median. **p<0.01 (Student's t test).

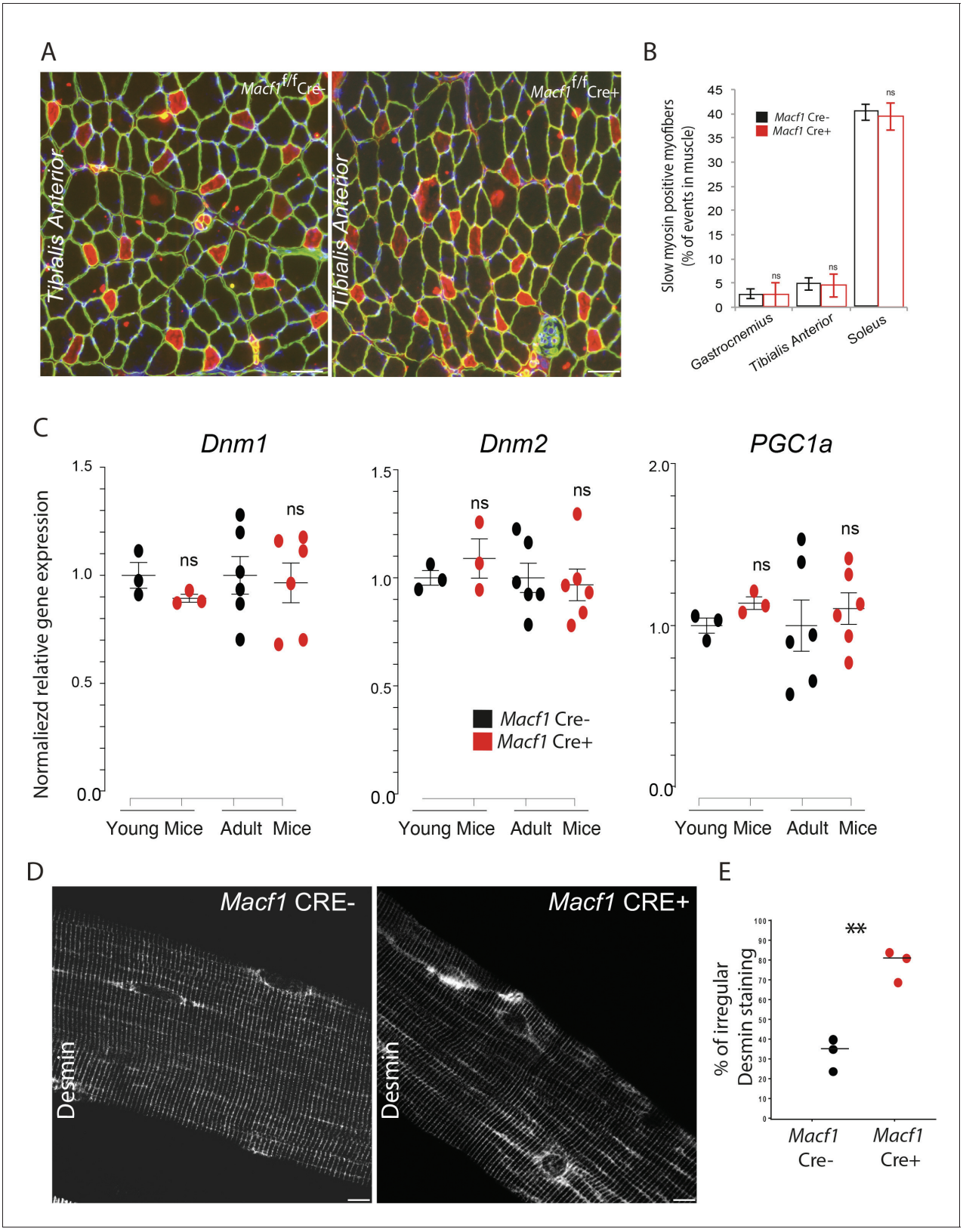

Figure 7—figure supplement 1. MACF1 conditional KO mice present normal distribution of different skeletal muscles types but disorganized Desmin network. (**A**) Representative microscopy images of transverse cross sections from *Tibialis Anterior* muscle of 12-month-old *Macf1* Cre- (left panel) and

Figure 7—figure supplement 1 continued on next page

Figure 7—figure supplement 1 continued

Macf1 Cre+ (right panel) mice stained for slow myosin (red), Laminin (green) and myonuclei (blue). Scale Bar = 150 μm. (**B**) Quantification of the percentage of myofibers with slow myosin expression in *Tibialis Anterior*, *Soleus* and *Gastrocnemius* muscles from 12-month-old *Macf1* Cre- and *Macf1* Cre+ mice. Mean values (with SEM) is presented. Ns stands for not significant (Student's t test). (**C**) QRT-PCR results presenting relative gene expression levels for Dnm1, Dnm2, and PPARGC1A in total mRNA extracts from *Gastrocnemius* of *Macf1* Cre- and Cre+ at each given age. Following the calculation of relative gene expression level with reference to housekeeping genes for each mouse, the mean expression level of each target gene was calculated for the WT mice. Next, the expression level of each WT and KO mouse was normalized to the previously calculated mean value. Line is set at mean (with SEM). Ns stands for not significant (Student's t test). (**D**) Representative confocal images (63×) from isolated myofibers of *Tibialis Anterior* stained for Desmin in *Macf1* Cre- (left panel) and Cre+ (right panel) mice of 12-month-old mice. Scale Bar = 15 μm. (**E**) Quantification of the percentage of myofibers with irregular (broken/oriented/accumulated) Desmin staining in isolated myofibers of *Tibialis Anterior* muscles from three individual *Macf1* Cre- and Cre+ mice at the age of 12 months. Line is set at median. **p<0.01 (Student's t test).

Complementary data 1:

Development and study of inducible skeletal muscle-specific MACF1 KO mouse model

I) Aim of the experiments

For our *in vivo* experiments, we had initially examined adult 12-month-old HSA::Cre; *Macf1*$^{f/f}$ mice to study the role of MACF1 in MT organization and myonuclei positioning within mature myofibers. Indeed, these experiments allowed us to show that MACF1 is an important regulator of MTs and myonuclei organization in skeletal muscle, reflected by observation of disrupted MT gride-like pattern and mispositioned round-shaped myonuclei within MACF1 KO myofibers. However, observation of NMJs fragmentation, mitochondrial accumulation, and sarcomeres disorganization raised the question whether these phenotypes are correlated and appear gradually or are independent. To address these questions, we used inducible HSA::Cre-ERT2; *Macf1*$^{f/f}$ mice which were developed in our lab.

II) Procedure of experiments

7- or 11-month-old female HSA::Cre-ERT2; *Macf1*$^{f/f}$ and WT; *Macf1*$^{f/f}$ mice received five tamoxifen injections (1mg tamoxifen for 20gr of mouse weight) during five consecutive days (Figure 28). 4-month post injections (thus at the age of 11- or 15-month-old), mice tibialis anterior (TA) and gastrocnemius (G) muscles were collected and subjected to qRT-PCR or fluorescent microscopy analysis as already described in the article.

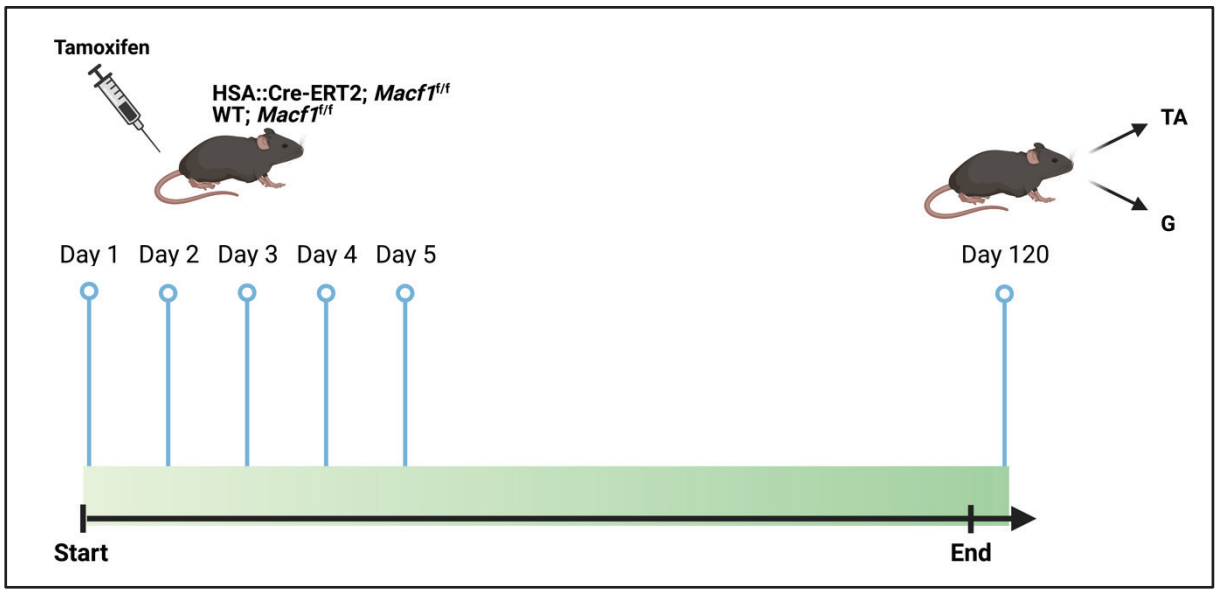

Figure 28: Experimental procedure of HSA::Cre-ERT2; *Macf1*$^{f/f}$ mice treatment.

III) Results

Our qRT-PCR quantification on total mRNA extracts from G muscles revealed a reduction of 40% and 60% in MACF1 mRNA level in 11- and 15-month-old HSA::Cre-ERT2; *Macf1*$^{f/f}$ respectively (Figure 29). Yet, our confocal fluorescent microscopy of individual isolated myofibers from TA of HSA::Cre-ERT2; *Macf1*$^{f/f}$ and WT; *Macf1*$^{f/f}$ mice showed untouched MT gride-like pattern and distance between closest myonuclei at the periphery of myofibers (Figure 30A-C). Interestingly, NMJs fragmentation could be observed in HSA::Cre-ERT2; *Macf1*$^{f/f}$ at both ages, reflected by an increase in the number of AChRs clusters when compared to age-matching controls (Figure 30D). However, NMJs area and synaptic myonuclei number remained stable between HSA::Cre-ERT2; *Macf1*$^{f/f}$ and WT; *Macf1*$^{f/f}$ mice of 11- or 15-month-old (Figure 30E-F).

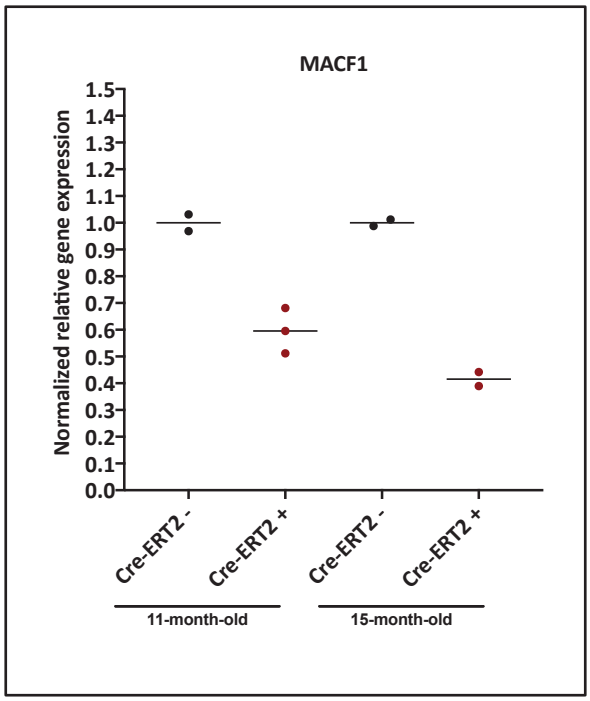

Figure 29: Tamoxifen injection results in reduction of MACF1 mRNA in HSA::Cre-ERT2; *Macf1*$^{f/f}$.
QRT-PCR results presenting relative gene expression level for *Macf1* in total mRNA extracts from G muscles of HSA::Cre-ERT2; *Macf1*$^{f/f}$ and WT; *Macf1*$^{f/f}$ mice of 11- or 15-month-old. Following the calculation of relative target gene expression level in reference to housekeeping genes for each mouse, the mean expression level of MACF1 was calculated for the group of WT mice. Next, the expression level of each WT; *Macf1*$^{f/f}$ and HSA::Cre-ERT2; *Macf1*$^{f/f}$ mouse was normalized to the previously calculated mean value to determine the relative gene expression.

IV) Conclusion

Together, these data confirmed the functionality of the skeletal muscle-specific Cre-ERT2 system in targeting MACF1 expression and suggested that NMJs may be the most sensitive subcellular organizations to the reduction of MACF1 in skeletal myofibers. However, due to the difficulty in the reproducibility of MTs and myonuclei related-phenotypes observed in HSA::Cre; *Macf1*$^{f/f}$ mice, we decided to use HSA::Cre; *Macf1*$^{f/f}$ mice of different ages (as presented in the article) to follow the apparition of each phenotype with time.

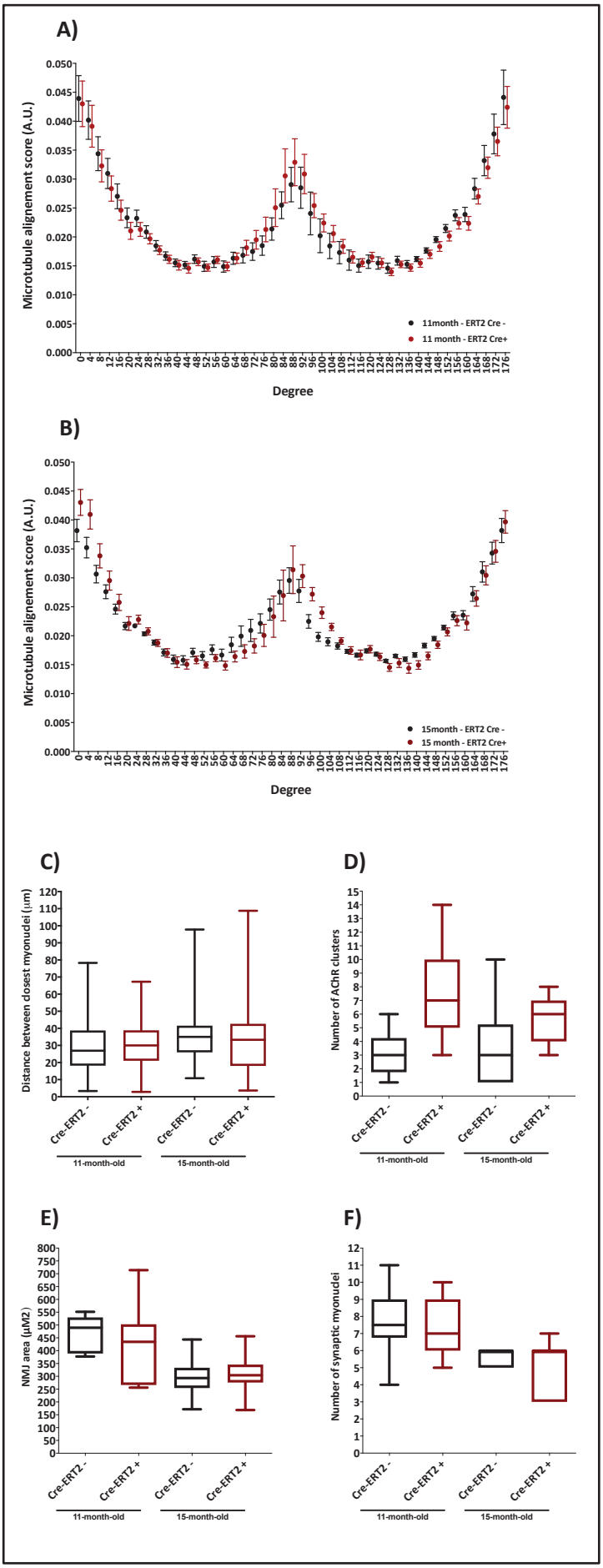

Figure 30: HSA::Cre-ERT2; *Macf1*$^{f/f}$ injection with tamoxifen has no impact on myofibers MTs or myonuclei organization but results in NMJs fragmentation. (A-B) Microtubules network organization analysis by TeDT software on isolated myofibers from TA muscles obtained from HSA::Cre-ERT2; *Macf1*$^{f/f}$ and WT; *Macf1*$^{f/f}$ mice at the age of 11 (A) or 15 (B) month-old. The final generated graph presents a global score for each given degree of microtubules orientation, with 0° and 180° degrees corresponding to the longitudinal microtubules and 90° degrees corresponding to the transverse microtubules. Mean values (with SEM) are presented. (C) Quantification of the distance between neighboring myonuclei measured on isolated myofibers from TA of HSA::Cre-ERT2; *Macf1*$^{f/f}$ and WT; *Macf1*$^{f/f}$ mice of 11- or 15-month-old. (D-F) Quantification of the number of AChR clusters (D), post synaptic NMJs area (E), and the number of post-synaptic myonuclei (F) measured on isolated myofibers from TA of HSA::Cre-ERT2; *Macf1*$^{f/f}$ and WT; *Macf1*$^{f/f}$ mice of 11- or 15-month-old.

Study 2

From MACF1 to SVBP:

Emerging questions and hypotheses

In my first project, we observed that the absence of MACF1 from myofibers results in modified ratio between tyrosinated and detyrosinated α-tubulins, which are associated with dynamic and long-lived-stable MTs respectively. In fact, the reduction of detyrosinated α-tubulins was specific to the perinuclear region and was observed only in 12-month-old KO mice, concomitant to high MT disorganization and increased myonuclei mislocalization.

Therefore, I was wondering whether some of the observed phenotypes in the MACF1 KO myofibers, such as myonuclei positioning, could be related to an imbalanced MT tyrosination/detyrosination ratio.

Interestingly, other studies were suggesting that proper regulation of MT tyrosination/detyrosination levels could be important during myogenesis and could impact myofibers activity. Among these observations are:

1) the high tubulin tyrosine ligase (TTL) activity during skeletal muscle embryonic development in chicken (Deanin et al., 1977),

2) the increasing small vasohibin binding protein (SVBP) mRNA expression (based on RNA sequencing databases) in mouse head and trunk skeletal muscles during embryonic development *in vivo* and hindlimb myoblasts during differentiation *in vitro* (Harel et al., 2012; Porter et al., 2006),

3) the presence of excessive MT detyrosination in myofibers of dystrophic mice and its correlation to stiff disorganized MTs in addition to irregular Ca^{2+} channel activation. This in turn results in myofibers damage due to aberrant contraction (Kerr et al., 2015; Khairallah et al., 2012; Ward et al., 2014),

4) the interaction between detyrosinated MTs and sarcomeric desmin in mouse cardiac muscle to support the contractile units during mechanical stress transduction (Robison et al., 2016).

However, no data were available on the regulation of the balance between this PTM during myogenesis, nor the importance of this balance in organelles organization, such as myonuclei positioning, during myogenesis, and within myofibers.

Therefore, my second goal was to follow the evolution of this PTM during myofibers development and to determine the importance of MTs tyrosinated/detyrosinated balance in skeletal muscle homeostasis.

To address these questions, I launched a collaboration with Dr. Marie-Jo Moutin (Grenoble Institut des Neurosciences) who has recently developed a null mouse model for SVBP characterized by a strong reduction of α-tubulins detyrosination in their system (Pagnamenta et al., 2019). The *Svbp* KO mice developed in the team of Dr. Moutin were generated by the induction of a deletion within the *Svbp* gene using CRISPR/Cas9 technology. These mice

present reduced MTs detyrosination and show abnormal brain morphology associated to behavioral defects such as impaired social interaction, therefore recapitulating the phenotypes observed in patients with mutant SVBP (Pagnamenta et al., 2019).

To address my goals, I started by comparing myofibers from WT and *Svbp* KO mice at two different ages of young 4.5-month-old and old 22-month-old. The choice of age was based on my previous experiments from skeletal muscle specific MACF1 KO model, where younger mice showed disorganized myonuclei but older mice (from 12-month-old) showed disorganized and internalized myonuclei.

First, I validated the model by verifying the reduction of detyrosinated MTs in *Svbp* KO mice. Next, I studied the organization and positioning of myonuclei within myofibers *in vivo* and I observed that the distance between myonuclei at the periphery of *Svbp* KO myofibers is reduced compared to WT myofibers. In addition, both young and old groups of *Svbp* KO mice presented mispositioned myonuclei within some of their myofibers compared to WT mice. In my previous model, I had linked the myonuclei disorganization to increased myonuclei dynamics and the myonuclei internalization to disorganized myofibrils. However, my *in vitro* studies on isolated myoblasts from WT and *Svbp* KO mice showed similar myonuclei dynamics during myofibers formation. In addition, studies of myofibrils ultrastructure via electronic microscopy showed regular myofibrils and sarcomeres organization between WT and *Svbp* KO mice. Thus, I hypothesized that reduced distance of myonuclei at the periphery of *Svbp* KO myofibers may be due to an increase in myonuclei content per myofiber. In collaboration with Dr. Caroline Brun from our team, I showed that MuSCs associated to *Svbp* KO myofibers *ex vivo* are more proliferative and more prone to differentiation compared to WT MuSCs. In line with these results, I observed that SVBP expression and MTs detyrosination level are boosted in WT myoblasts with induction of differentiation, suggesting they could be essential for proper regulation of myogenic differentiation. In search for a source of stress which would induce MuSCs activation *in vivo*, I found that some of the NMJs from *Svbp* KO myofibers are fragmented and denervated compared to WT NMJs. As NMJs denervation have been previously linked to MuSCs activation *in vivo*, these experiments suggest that reduction of detyrosinated MTs in myofibers and MuSCs of *Svbp* KO mice indirectly disrupts myonuclear domains organization due to an increased number of myonuclei per myofiber.

The ensemble of data obtained from these experiments are presented in the following unpublished article (for *in vivo* myofibers analysis of young 4.5-month-old mice, *in vitro* analysis of myoblasts behavior, and *ex vivo* analysis of MuSCs behavior) or in the following “complementary data 2” (for *in vivo* myofibers analysis of old 22-month-old mice and *in vitro* analysis of purified MuSCs behavior).

Publication 2:

Role of SVBP and microtubules detyrosination in skeletal muscle development and homeostasis.

In preparation.

Alireza Ghasemizadeh*, *Caroline Brun, Emilie Christin, Celine Malleval, Edwige Belotti, Julien Gondin, Marie-Jo Moutin, and Vincent Gache

Role of SVBP and microtubules detyrosination in skeletal muscle development and homeostasis

Alireza Ghasemizadeh[1], Caroline Brun[1], Emilie Christin[1], Celine Malleval[1], Edwige Belotti[1], Julien Gondin[1], Marie-Jo Moutin[2], and Vincent Gache[1,3]

1 Physiopathologie et Génétique du Neurone et du Muscle, Institut NeuroMyoGène, UMR CNRS 5261 – INSERM U1315, Université Claude Bernard Lyon 1, 8 Avenue Rockefeller, 69008, Lyon, France

2 Grenoble Institut Neurosciences, Inserm, U1216, CNRS, Université Grenoble Alpes, 38000 Grenoble, France

3 Physiopathologie et Génétique du Neurone et du Muscle, Institut NeuroMyoGène, UMR CNRS 5261 – INSERM U1315, Université Claude Bernard Lyon 1, 8 Avenue Rockefeller, 69008, Lyon, France. vincent.gache@inserm.fr

Abstract

Microtubules (MTs) are highly dynamic members of the cytoskeleton which can go through cycles of polymerization and depolymerization. This MTs dynamic depends greatly on microtubules post-translational modifications (PTMs) and can influence subcellular trafficking. Skeletal myofibers are syncytia where each nucleus transcriptionally supports a theoretical territory of cytoplasm, referred to as myonuclear domains. As progenitor cells fuse to form myofibers, MTs actively participate in myonuclear domains organization by regulating fusing cells nuclei dispersion along the developing syncytia. However, the importance of MTs PTMs in myonuclear domain organization during myogenesis or in myofibers has never been studied. Here, we report MTs detyrosination, a MTs PTM associated with MTs stability, as an important factor in the maintenance of skeletal muscle homeostasis. We show that knock out of SVBP, the co-enzyme necessary for MTs detyrosination, affects muscle stem cells (MuSCs) behavior and result in their increased activation and differentiation following environmental stress. These data are in parallel with the observation of disrupted myonuclear domains in *Svbp* KO mice due to increased myonuclei number per myofiber. Further, we show that neuromuscular junctions (NMJs) of *Svbp* KO mice are denervated, suggesting they may be the main reason behind aberrant MuSCs activation and fusion with myofibers.

Introduction

Skeletal myofibers are syncytia that originate from the fusion of mononuclear muscle progenitor cells known as myoblasts (Buckingham et al., 2003). At the periphery of each myofiber, hundreds of myonuclei are regularly dispersed or clustered under specific zones such as neuromuscular junctions (NMJs) (Bruusgaard et al., 2003). This results in the formation of myonuclear domains to guarantee a homogenous transcriptional activity all along myofibers (Cramer et al., 2020; Hall and Ralston, 1989). This system is challenged in different muscular diseases, such as sarcopenia, centronuclear myopathies, or neuromuscular diseases, where mispositioned myonuclei can be observed along myofibers (Bruusgaard et al., 2006; Folker and Baylies, 2013; Jungbluth et al., 2008; Jungbluth and Gautel, 2014). The myonuclear domain is also challenged during muscle regeneration, where quiescent muscle stem cells (MuSCs) get activated, proliferate, differentiate, and fuse with damaged myofibers, resulting in the accumulation of central myonuclei within myofibers (Forcina et al., 2020; Relaix et al., 2021). However, how myofibers regulate their myonuclear domains remains poorly understood. Interestingly, our previous data from a murine model with disorganized microtubules (MTs) present a correlation between reduced perinuclear MTs detyrosination, a marker of stable MTs, and myonuclei mispositioning within myofibers, suggesting that MTs detyrosination may contribute to myonuclear domains organization (Ghasemizadeh et al., 2021).

MTs are highly dynamic filaments made from α- and β-tubulin dimers which go through cycles of polymerization and depolymerization to support different cellular event (Goodson and Jonasson, 2018). The balance between stable and dynamic MTs is dependent on microtubules post-translational modifications (PTMs), such as detyrosination, and microtubules associates proteins (MAPs) (Gadadhar et al., 2017). During myogenesis, MTs participate in myonuclear domains organization by providing dynamic railways for motor molecules and ordering myonuclei spreading in growing myofibers (Gache et al., 2017). In parallel, we have previously shown that during myogenesis, MTs dynamic is reduced, going toward a more stable MTs network in myofibers (Ghasemizadeh et al., 2021). Yet, the impact of this shift in MTs dynamics in myofibers development remains unclear.

Among MTs PTMs, α-tubulin tyrosination and detyrosination are associated with dynamic and stable MTs respectively (Goodson and Jonasson, 2018). The majority of α-tubulins are expressed with a C-terminal tyrosine, which is a marker of dynamic MTs apt to undergo the polymerization/depolymerization cycles (Valenzuela et al., 1981). This terminal tyrosine can be cleaved from MTs α-tubulin by tubulin carboxypeptidase activity of the newly discovered complexes formed of small vasohibin binding protein (SVBP) and one of its partners, vasohobin1 or 2 (VASH1/VASH2) (Aillaud et al., 2017). Over decades, detyrosinated MTs have been known as long-lived stable MTs since they prevent the installation and activity of Kinesin proteins such as MCAK and Kif2A and thereby protect MTs from depolymerization (Bré et al., 1987; Ferreira et al., 2020; Kreis, 1987; Peris et al., 2009). In the nervous system, perturbation of the balance between tyrosinated and detyrosinated MTs following SVBP down-regulation results in defects in neuronal development *in vitro* and brain malformation *in vivo* (Aillaud et al., 2017; Pagnamenta et al., 2019). In cardiomyocytes, reduced MTs detyrosination disrupts MTs interaction with sarcomeres and results in faster sarcomeres shortening during contraction. In contrast, increased MTs detyrosination can be observed in patients with heart failure who suffer from increased cardiomyocytes stiffness (Robison et al., 2016). In skeletal muscle, increased MTs detyrosination has been associated with increased cytoskeleton stiffness, aberrant Ca^{2+} channels activation, and contraction-induced muscular injury (Kerr et al., 2015). Conversely, skeletal muscle hypotonia is among the clinical manifestations of patients with mutations in the *SVBP* gene (Iqbal et al., 2019). However, how MTs tyrosination/detyrosination

balance is regulated in skeletal muscle and how this contributes to skeletal muscle homeostasis have not been studied.
Here, we report that SVBP expression and MTs detyrosination level are increased with muscle differentiation. Using *Svbp* KO mice, we show that the absence of detyrosinated MTs from myofibers results in smaller myonuclear domains, correlated with increased myonuclei content per myofiber. Interestingly, our studies on *Svbp* KO MuSCs show an increase in their activation and differentiation speed, suggesting that reduced myonuclear domains may be related to stress-induced activation of MuSCs in the absence of MTs detyrosination, independent of muscle regeneration. Finally, we show that NMJs are fragmented and denervated in *Svbp* KO mice, suggesting that they could contribute to MuSCs stress-induced activation and fusion with myofibers.

Results

Svbp KO myofibers present disrupted myonuclear domains

SVBP is necessary for tyrosine carboxypeptidase activity of VASH1 and improves the activity of VASH2 (Figure 1A) (Li et al., 2019; van der Laan et al., 2019). Thus, we checked the level of detyrosinated MTs in *gastrocnemius* (G) muscles of WT and *Svbp* KO mice (Figure 1B). Our western blot data present a huge reduction of detyrosinated α-tubulin in total protein extracts from *Svbp* KO mice compared to WT mice (Figure 1B-C). These data were confirmed by the observation of a twofold reduction in detyrosinated α-tubulin immunofluorescence intensity at the periphery of individually isolated myofibers from *tibialis anterior* (TA) of *Svbp* KO mice (Figure 1D-F).

In cardiomyocytes, detyrosinated MTs mediate MTs interaction with sarcomeres and are essential for MTs support of sarcomeres shortening during contraction (Robison et al., 2016). Therefore, we checked if the reduction of MTs detyrosination in *Svbp* KO myofibers has an impact on sarcomeres structure. To do so, individual myofibers from TA of WT and *Svbp* KO mice were stained for α-actinin, a major component of skeletal myofibers sarcomeres (Roulier et al., 1992). Both WT and *Svbp* KO myofibers showed regular sarcomeres organization with no drastic breaks or disruption in the absence of MTs detyrosination (Figure 1G). However, the distance between adjacent α-actinin sarcomeres was slightly shorter in *Svbp* KO myofibers compared to WT myofibers (Figure 1H). To make sure that myofibrillogenesis is not affected, we used a cell culture technique that allows us to develop myofibers from mouse primary isolated myoblasts *in vitro* (Figure 1I) (Falcone et al., 2014). Our analysis of α-actinin staining confirmed that while sarcomeres formation is not affected in *Svbp* KO myofibers, the distance between adjacent α-actinin sarcomeres of *Svbp* KO primary myofibers is reduced compared to WT myofibers (Figure 1J-K).

Aside from sarcomeres, we immediately noticed that myonuclei are much closer to each other at the periphery of *Svbp* KO myofibers compared to WT myofibers both *in vivo* and *in vitro* (Figure 2A&C). Thus, we quantified the distance between neighboring myonuclei at the periphery myofibers. *In vitro*, we observed a 23% reduction of distance between adjacent myonuclei at the periphery of *Svbp* KO myofibers compared to WT myofibers (Figure 2B). This phenotype was stronger *in vivo*, as stated by a 30% reduction of distance between neighboring myonuclei at the periphery of *Svbp* KO myofibers compared to WT myofibers (Figure 2D). Interestingly, while myonuclei flatten-shape was untouched, the myonuclear domain was altered at the periphery of *Svbp* KO myofibers, as stated by a 24% reduction in the area per myonuclei at the periphery of *Svbp* KO myofibers compared to control myofibers (Figure 2E-H).

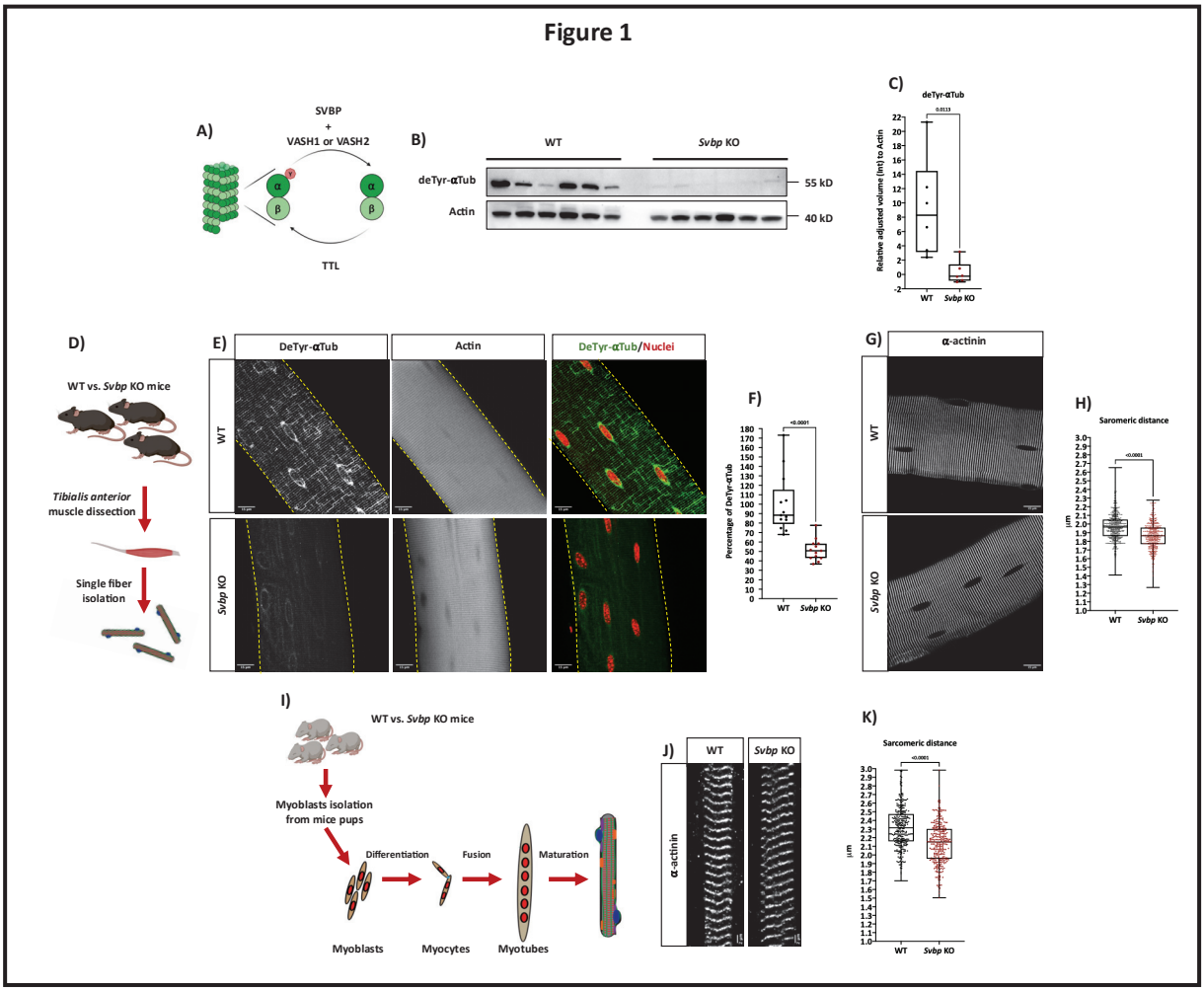

Figure 1: MTs detyrosination is strongly reduced in *Svbp* KO myofibers.
(A) Schema presenting α-tubulin detyrosination process following coupling of SVBP to either of its partners, VASH1 or VASH2. The graph shows the reversibility of this process due to TTLs activity. **(B)** Western blot analysis of detyrosinated α-tubulin in total extracts from *gastrocnemius* muscles of 4.5-month-old WT and *Svbp* KO mice. Actin is used as the loading control. **(C)** Relative adjusted protein volume (Int) of detyrosinated α-tubulin to Actin quantified by western blot (as presented in panel **B**). Each category groups six individual mice. Line is set at median. "ns" stands for not significant; p values are calculated by Student's t test. **(D)** Schema of the strategy used to isolate and study individual myofibers from *tibialis anterior* of adult WT and *Svbp* KO mice. **(E)** Representative confocal images (63X) from *tibialis anterior* isolated myofibers issued from 4.5-month-old WT (upper panels) and *Svbp* KO (lower panels) mice and stained for detyrosinated α-tubulin (green) and myonuclei (red) in the overlay images. Actin was used as control staining to visualize the limits of each myofiber. Scale Bar = 15 µm. **(F)** Quantification of detyrosinated α-tubulin intensity on *tibialis anterior* isolated myofibers issued from 4.5-month-old WT and *Svbp* KO mice (as presented in panel **E**). Following the measurement of detyrosinated α-tubulin fluorescent intensity per myofiber, a mean fluorescence intensity was calculated for the group of WT mice. Next, the measured fluorescence intensity of each WT and *Svbp* KO myofiber was normalized to the previously calculated mean value to determine the percentage of difference between myofibers. Line is set at median. p value is calculated by Student's t test. **(G)** Representative confocal images (63X) of myofibers isolated from *tibialis anterior* of WT (left panel) and *Svbp* KO (right panel) mice of 4.5 months old presenting α-actinin (gray). Scale Bar = 15 µm. **(H)** Quantification of the distance between adjacent sarcomeres measured on isolated myofibers from *tibialis anterior* of WT and *Svbp* KO mice of 4.5 months old (as presented in panel **G**). Nine individual mice (with at least three myofibers per mouse) were studied in each group. Line is set at median. p values are calculated by Student's t test. "ns" stands for not significant. **(I)** Scheme presenting the sequential steps of myoblast isolation from mice pups and their transfection with plasmids in order to further study immature myotubes and/or mature myofibers *in vitro*. **(J)** Representative immunofluorescence microscopy images (63X) of α-actinin (gray) in primary myofibers obtained from isolated myoblasts of WT (left panel) or *Svbp* KO (right panel) mice after 12 days of differentiation *in vitro*. Scale Bar = 2 µm. **(K)** Distance between adjacent sarcomeres measured on mature primary myofibers obtained from isolated myoblasts of WT or *Svbp* KO mice (as presented in panel **J**). Panel was generated from data from two individual experimental mice per group. Line is set median. p values are calculated by Student's t test.

In parallel, our studies on TA muscles cross-sections revealed that while the majority of myonuclei remain at the periphery of myofibers, *Svbp* KO mice have a higher percentage of myofibers with mispositioned myonuclei located within myofiber compared to WT mice (Figure 2I-J).

Altogether, these data confirm that SVBP/VASH complexes are majorly responsible for MTs detyrosination in skeletal muscle. Our data suggest that the absence of SVBP does not affect myofibrillogenesis and the consequent myonuclei push to the periphery of myofibers, but results in altered myonuclear domains at the periphery of myofibers. This could be due to altered myonuclei dynamic or increased myonuclei content per myofiber.

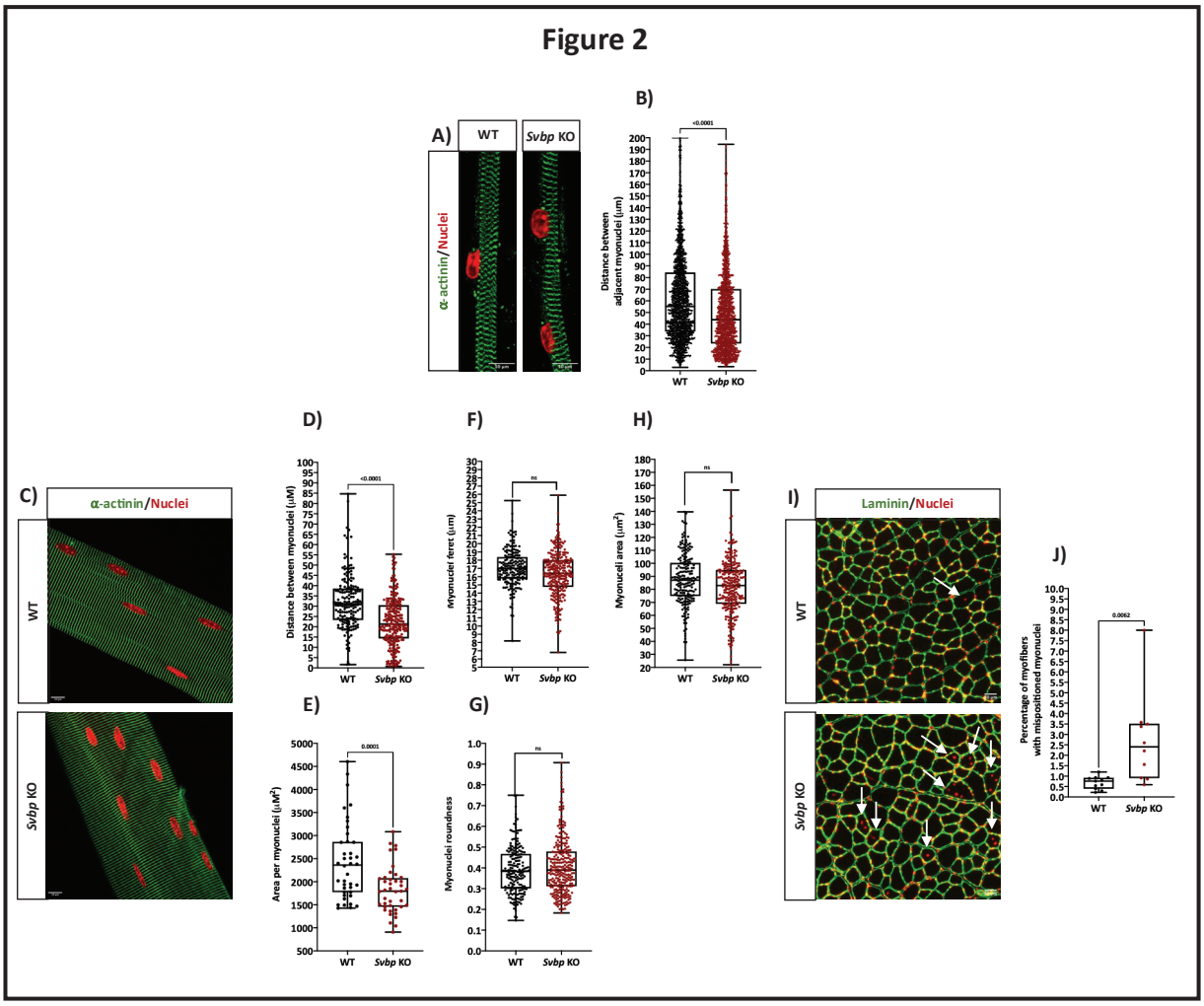

Figure 2: *Svbp* KO mice present reduced myonuclear domain.
(A) Representative immunofluorescence microscopy images (63X) of α-actinin (green) and myonuclei (red) in primary myofibers obtained from isolated myoblasts of WT (left panel) or *Svbp* KO (right panel) mice after 12 days of differentiation *in vitro*. Scale Bar = 10 µm. **(B)** Distance between adjacent myonuclei measured on mature primary myofibers obtained from isolated myoblasts of WT or *Svbp* KO mice (as presented in panel **A**). Panel was generated from data from two individual experimental mice per group. Line is set median. p values are calculated by Student's t test. **(C)** Representative confocal images (63X) of myofibers isolated from *tibialis anterior* of WT (upper panel) and *Svbp* KO (lower panel) mice of 4.5 months old presenting α-actinin (green) and myonuclei (red). Scale Bar = 10 µm. **(D-H)** Quantification of the distance between neighboring myonuclei **(D)**, area per myonuclei **(E)**, myonuclei feret **(F)**, myonuclei roundness **(G)**, and myonuclei area **(H)** measured on isolated myofibers from *tibialis anterior* of WT and *Svbp* KO mice of 4.5 months old (as presented in panel **C**). Nine individual mice (with at least three myofibers per mouse) were studied in each group. Line is set at median. p values are calculated by Student's t test. "ns" stands for not significant. **(I)** Representative images of *tibialis anterior* muscle cross sections from 4.5-month-old WT (upper panel) and *Svbp* KO (lower panel) mice stained for Laminin (green) and myonuclei (red). White arrows point to myofibers with mispositioned myonuclei. Scale Bar = 50 µm. **(J)** Quantification of the percentage of myofibers with mispositioned myonuclei in *tibialis anterior* of WT and *Svbp* KO mice of 4.5 months old (as presented in panel **I**). Ten individual mice were studied in each group. Line is set at median. p value is calculated by Student's t test.

***Svbp* KO does not affect myonuclei dynamics but results in increased myoblasts fusion**

SVBP knock-down and knock-out have been linked to the accumulation of tyrosinated α-tubulin following the reduction of α-tubulin detyrosination in the brain and neurons (Aillaud et al., 2017; Pagnamenta et al., 2019). Therefore, we studied the impact of *Svbp* KO on different tubulin pools in skeletal muscle (Figure 3A). Our western blot results show that while the absence of SVBP does not affect acetylated α-tubulin, total α-tubulin, or β-tubulin protein levels, it results in a twofold increase in tyrosinated α-tubulin level in total protein extracts from G muscles of *Svbp* KO mice compared to WT mice (Figure 3B-E). To study the impact of accumulated tyrosinated MTs on their organization, single isolated myofibers were studied for tyrosinated α-tubulin staining (Figure 3F-G). First, we observed a 47% increase in the mean fluorescence intensity of tyrosinated α-tubulin in *Svbp* KO myofibers when compared to WT myofibers, confirming the accumulation of tyrosinated α-tubulin in *Svbp* KO mice (Figure 3F). Next, we observed the presence of randomly oriented tyrosinated MTs in *Svbp* KO myofibers compared to their gride-like organization within WT myofibers (Figure 3G, zoom panels). Thus, we analyzed the organization of the tyrosinated α-tubulin network along myofibers using a MTs texture detection tool as described before (Liu and Ralston, 2014). While in WT myofibers, the highest scores are given to 0°, 90°, and 180° degrees oriented tyrosinated α-tubulin (forming the longitudinal and transversal gride-like network), in *Svbp* KO myofibers, we observed a strong reduction of 80° to 96° oriented tyrosinated α-tubulin. Concomitantly, we observed an increase in score for randomly oriented tyrosinated α-tubulin, especially between 16° to 24° degrees, in *Svbp* KO myofibers compared to WT myofiber (Figure 3H). These results confirm that the lack of detyrosinated MTs results in the accumulation of disorganized tyrosinated MTs in myofibers.

Over decades, detyrosinated MTs have been linked with long-lived stable MTs while tyrosinated MTs have been linked to dynamic MTs (Sanyal et al., 2021). In addition, we have previously shown that increased MTs dynamic can cause an increase in myonuclei motion during myofiber development and result in a reduction of distance between neighboring myonuclei *in vivo* and *in vitro* (Ghasemizadeh et al., 2021). Therefore, we were wondering whether the reduction of distance between peripheral myonuclei of *Svbp* KO myofibers is due to altered myonuclei dynamics (Figure 2A-C). First, we confirmed the increase in MTs dynamics in *Svbp* KO myofibers during their development *in vitro*. To do so, we transfected our WT or *Svbp* KO mouse primary myoblasts with a plasmid coding for GFP tagged MTs end-binding protein 3 (EB3) just before induction of differentiation and tracked the dynamics of EB3-GFP particles at different time points during maturation of primary myofibers *in vitro* (Figure 3I). Using the same culture system, we have previously shown that myofibers development and maturation are accompanied by reduced MTs dynamics *in vitro* (Ghasemizadeh et al., 2021). In our current study, we confirmed the same reduction of MTs dynamics with the maturation of WT cells marked by a 14% decrease in EB3-comets speed from myotubes to myofibers (Figure 3I). In parallel, the absence of detyrosinated MTs from *Svbp* KO cells resulted in an increase of 13% in EB3-comets speed in both myotubes and myofibers when compared to matching control cells (Figure 3I). Next, we transfected WT and *Svbp* KO myoblasts with RFP-lamin-chromobody just before myoblast fusion, in order to visualize myonuclei and follow their movement during myofiber development. We tracked myonuclei for 3 days differentiating myofibers by tacking time-laps images every 15 minutes during 8 hours as described before (Figure 4A) (Cadot et al., 2014). Our data indicate equal myonuclei speed, time in motion, total coursed distance, or movement persistence between *Svbp* KO and control myonuclei (Figure 4B-E). These results suggest that reduced myonuclei distance in *Svbp* KO myofiber is not due to altered myonuclei dynamics and raised the hypothesis that reduced myonuclear domain at the periphery of *Svbp* KO myofiber may be due to increased myonuclei content per myofiber.

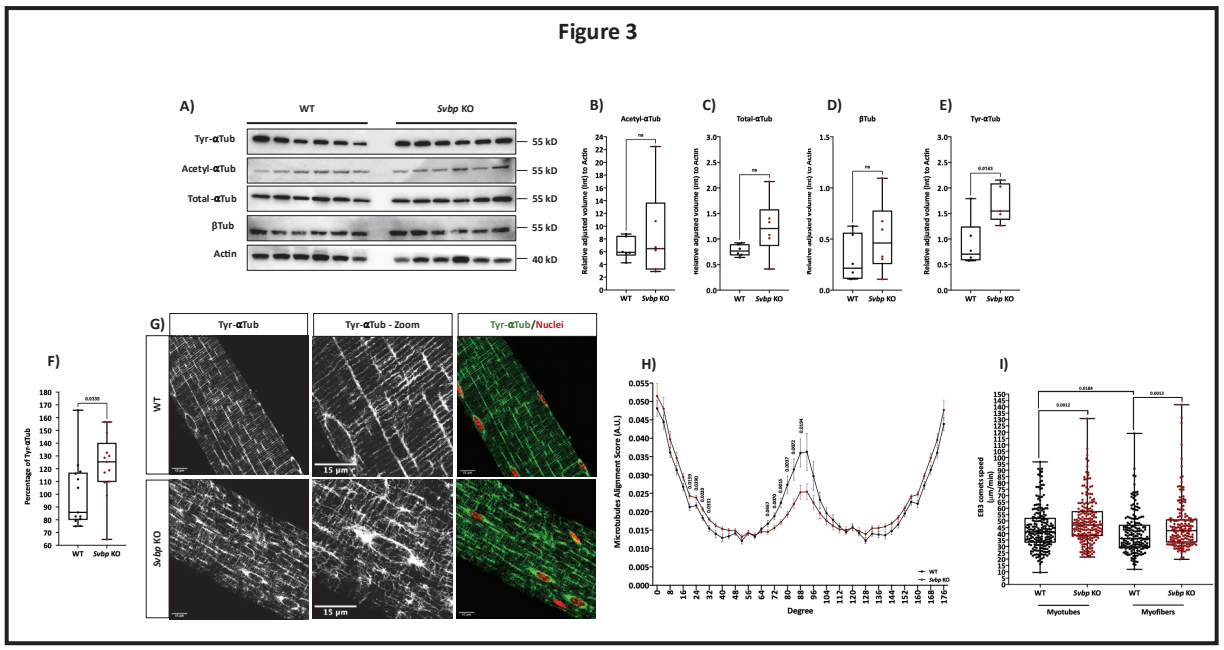

Figure 3: *Svbp* KO affects tyrosinated MTs organization and MTs dynamics.
(A) Western blot analysis of tyrosinated α-tubulin, acetylated α-tubulin, total α-tubulin, and β-tubulin in total extracts from *gastrocnemius* muscles of 4.5-month-old WT and *Svbp* KO mice. Actin is used as the loading control. **(B-E)** Relative adjusted protein volume (Int) of tyrosinated α-tubulin **(B),** acetylated α-tubulin **(C),** total α-tubulin **(D),** and β-tubulin **(E)** to Actin quantified by western blot (as presented in panel **A**). Each category groups six individual mice. Line is set at median. "ns" stands for not significant; p values are calculated by Student's t test. **(F)** Quantification of tyrosinated α-tubulin intensity on *tibialis anterior* isolated myofibers issued from 4.5-month-old WT and *Svbp* KO mice (as presented in panel **G**). Following the measurement of tyrosinated α-tubulin fluorescent intensity per myofiber, a mean fluorescence intensity was calculated for the group of WT mice. Next, the measured fluorescence intensity of each WT and *Svbp* KO myofiber was normalized to the previously calculated mean value to determine the percentage of difference between myofibers. Line is set at median. p value is calculated by Student's t test. **(G)** Representative confocal images (63X) from *tibialis anterior* isolated myofibers issued from 4.5-month-old WT (left panels) and *Svbp* KO (right panels) mice, presenting tyrosinated α-tubulin (green) and myonuclei (red) in the overlay images. A zoom panel is presented to emphasize on the difference in tyrosinated α-tubulin organization between WT and *Svbp* KO myofibers. Scale Bar = 15 µm. **(H)** Microtubules network organization analysis of tyrosinated α-tubulin staining (as presented in panel **G**), using TeDT software, on isolated myofibers obtained from three WT and *Svbp* KO mice of 4.5-month-old. The final generated graph presents a global score for each given degree of microtubules orientation, with 0 and 180 degrees corresponding to the longitudinal microtubules and 90 degrees corresponding to the transverse microtubules. Mean values (with SEM) are presented. p values are calculated by Student's t test. **(I)** Quantification of EB3 comets speed in primary immature myotubes and mature myofibers obtained from isolated myoblasts of WT or *Svbp* KO mice *in vitro*. Panel was generated from data from three individual experimental mice per group with at least 200 EB3 comets mapped per group. Line is set at median. p values are calculated by Student's t test.

To understand how reduced MTs detyrosination can impact myonuclei content per myofibers, we studied the behavior of primary isolated myoblasts pre- and post-differentiation *in vitro.* During myogenesis, myoblasts migration occurs before their fusion and myotube formation (Choi et al., 2020). Interestingly, increased MTs detyrosination has been linked to increased epithelial cells migration (Müller et al., 2021). Thus, we studied WT and *Svbp* KO myoblasts movement by taking bright-field time-laps images every 10 minutes for 8 hours before differentiation (Figure 4F). We observed that in the absence of α-tubulin detyrosination, *Svbp* KO myoblasts spend less time moving, and when they move, their median speed is slightly lower than WT myoblasts (Figure 4G-I). To check if reduced MTs detyrosination and myoblasts migration have an impact on myoblasts fusion, WT and *Svbp* KO primary myoblasts fusion index was compared 24H post differentiation (Figure 4J). Interestingly, our data show a 10% increase in the fusion index of *Svbp* KO myoblasts compared to control WT myoblasts *in vitro* (Figure 4K). To confirm that level of MTs detyrosination can impact myoblasts fusion, WT myoblasts were transfected with plasmids coding for either SVBP/VASH1-GFP or SVBP/VASH2-GFP to induce MTs detyrosination *in vitro*. 24 hours post differentiation,

transfected cells were fixed and their fusion index was compared to control cells transfected with a plasmid coding only for GFP (Figure 4 – Supplementary Figure 1A). In contrast to the increased fusion of *Svbp* KO myoblasts, over-expression of either of SVBP/VASH1 or SVBP/VASH2 complexes resulted in a reduced fusion index of differentiated myoblasts *in vitro* (Figure 4 – Supplementary Figure 1B).

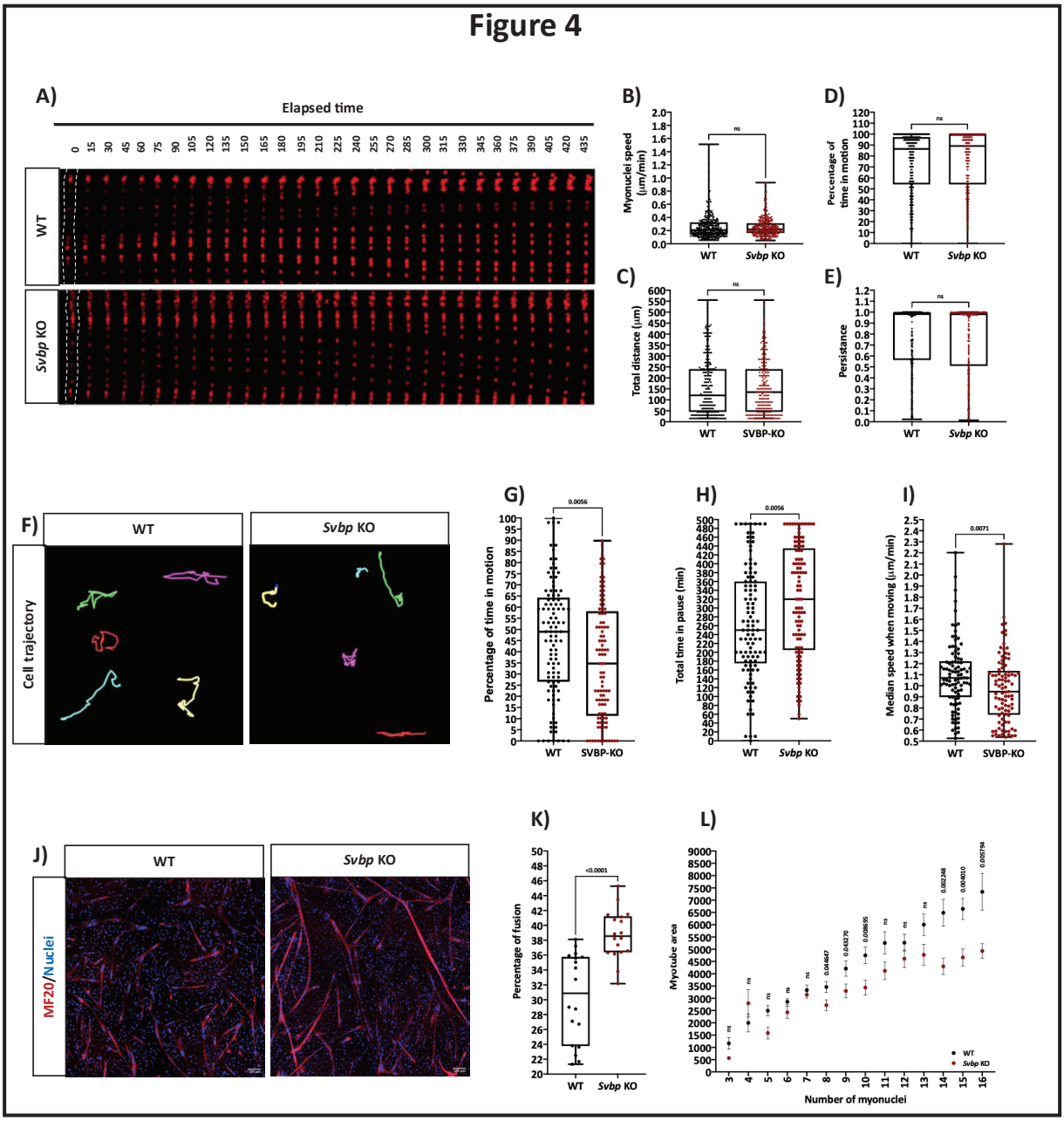

Figure 4: *Svbp* KO results in increased myoblasts fusion *in vitro*.
(A) 7 hours long frames from an 8 hours time-lapse imaging of lamin-chromobody (in red) taken from 3 days differentiated myofibers obtained from isolated myoblasts of WT (upper panel) or *Svbp* KO (lower panel) mice. Myoblasts were transfected with lamin-chromobody plasmid (as described in Figure 2J) before differentiation. In the first frame (on the left), myofibers are selected in white, which corresponds to the region used to create the adjacent kymograph. **(B-E)** Myonuclei speed **(B)**, total distance traveled **(C)**, percentage of time in motion **(D)**, and movement persistence **(E)** were quantified on 300 myonuclei during myotubes maturation obtained from myofibers developed from isolated myoblasts of WT or *Svbp* KO mice. Panels were generated from data from two individual experimental mice per group. Line is set median. "ns" stands for not significant as determined by Student's t test. **(F)** Example cell trajectories of WT and *Svbp* KO myoblasts during a time course of 3 hours from an 8 hours time-lapse imaging. Each colored line represents an individual myoblast isolated from WT (left panel) or *Svbp* KO (right panel). **(G-I)** percentage of time in motion **(G)**, total time in pause during 500 minutes of time-lapse imaging **(H)**, and median of speed when moving **(I)** as quantified on at least 100 myoblasts obtained from WT or *Svbp* KO mice in growth

medium (as presented in panel **F**). Panels were generated from data from three individual experimental mice per group. Line is set median. p values are calculated by Student's t test. **(J)** Immunofluorescence staining (10X) of MF20 (red) and myonuclei (blue) in primary myotubes obtained from isolated myoblasts of WT (left panel) or *Svbp* KO (right panel) mice. Scale Bar = 100 µm. **(K)** Fusion index quantified on primary myotubes obtained from isolated myoblasts of WT or *Svbp* KO mice (as presented in panel **J**). Panel was generated from data from two individual experimental mice. Line is set median. p values are calculated by Student's t test. **(L)** Repartition of mean myotube area based on the number of myonuclei quantified on primary myotubes obtained from isolated myoblasts of WT or *Svbp* KO mice (as presented in panel **J**). Panel was generated from data from two individual experimental mice with at least 150 myotubes analyzed per condition. Mean values with SEM are presented. "ns" stands for not significant; p values are calculated by Student's t test.

In physiological conditions, each fusing myoblast will bring its nucleus and cytoplasm to participate in the growth of the forming myofiber (Lehka and Rędowicz, 2020). Unexpectedly, we observed that *Svbp* KO myotubes have smaller area when compared to WT myotubes with the same number of myonuclei (Figure 4L). This could suggest that in addition to increased myonuclei content, muscular atrophy may participate to reduced myonuclear domain observed at the *Svbp* KO periphery of myofibers. Interestingly, our measurement on primary developed myofibers suggested a reduction in *Svbp* KO myofibers width compared to WT myofibers *in vitro* (Figure 4 – Supplementary Figure 1C). However, TA muscle fibers cross-sections showed similar feret distribution between WT and *Svbp* KO mice in *vivo* (Figure 4 – Supplementary Figure 1D-E). In addition, even though *Svbp* KO mice present a slight reduction of total body mass compared to control mice, we observed no difference between *Svbp* KO and WT mice TA, G, or *extensor digitorum longus* (EDL) muscles weigh normalized to total body weight (Figure 4 – Supplementary Figure 1F-I). Together, these data suggest that *in vivo*, a compensatory mechanism may be contributing to the prevention of myofiber atrophy in *Svbp* KO mice.

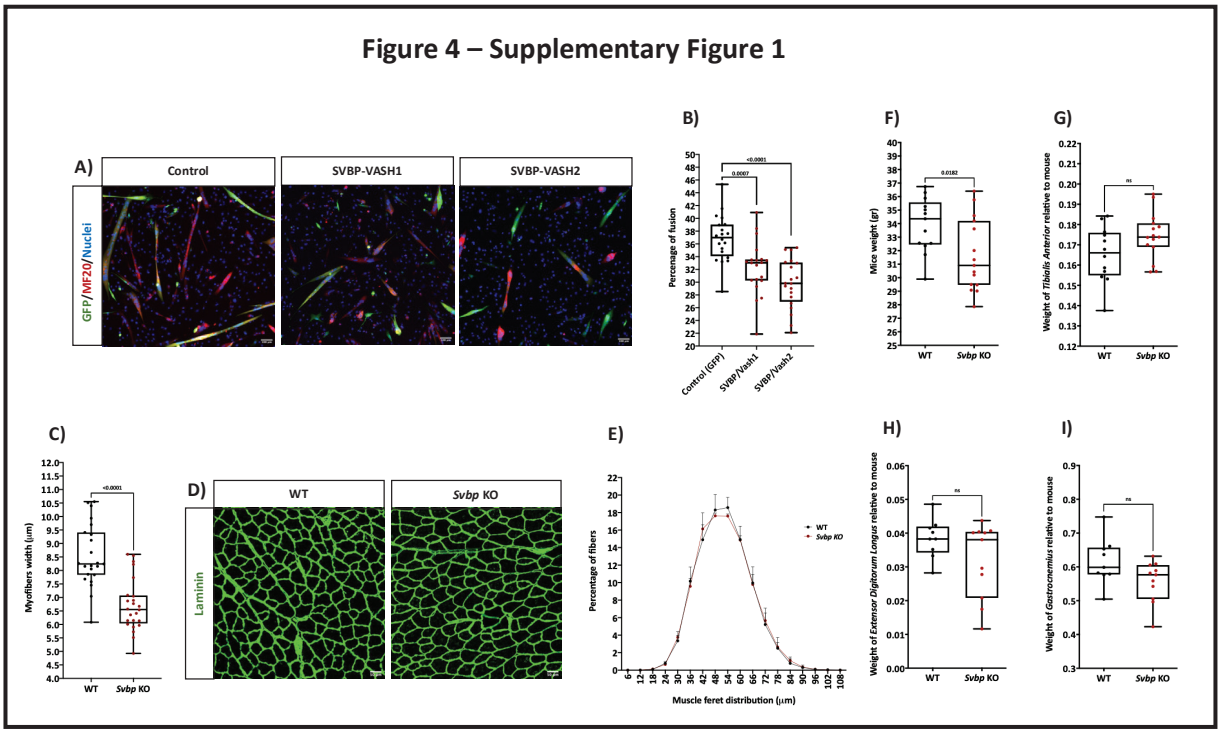

Figure 4 – Supplementary Figure 1: *Svbp* KO affects myofibers size *in vitro* but not *in vivo*.
(A) Representative fluorescence microscopy images (10X) of GFP (green), MF20 (red), and myonuclei (blue) in primary myotubes obtained from isolated myoblasts of WT mice transfected with control GFP plasmid (left panel), SVBP-VASH1-GFP plasmid (middle panel) or SVBP-VASH2-GFP plasmid (right panel). Scale Bar = 100 µm. **(B)** Fusion index quantified on primary myotubes obtained from isolated myoblasts of WT mice transfected with control GFP plasmid, SVBP-VASH1-GFP plasmid, or SVBP-VASH2-GFP plasmid (as presented in panel **A**). Panel was generated from data from four experiments. Line is set median. p values are calculated by Student's t test. **(C)** Myofibers width measured on mature primary myofibers obtained from isolated myoblasts of WT or *Svbp* KO mice. Panel was generated from data from two individual experimental

mice per group. Line is set at median. p value is calculated by Student's t test. **(D)** Representative images of *tibialis anterior* muscle cross sections from 4.5-month-old WT (left panel) and *Svbp* KO (right panel) mice stained for Laminin (green). Scale Bar = 50 µm. **(E)** Distribution of myofibers cross-section feret in *tibialis anterior* from three individual WT and *Svbp* KO mice of 4.5-month-old (as presented in panel **D**). Mean values (with SEM) are showing. **(F-I)** Evaluation of total body weight **(F)** and relative muscle weight to total body weight for *tibialis anterior* **(G)** ***e****xtensor digitorum longus* **(H)** and *gastrocnemius* **(I)** from each mouse studied on a group of at least nine individual WT and *Svbp* KO mice of 4.5-month-old. Line is set median. "ns" stands for not significant; p value is calculated by Student's t test.

MTs detyrosination level can impact MuSCs behavior

Based on our previous data, we were wondering if MTs detyrosination is needed at specific moments during myogenesis and whether MTs PTMs pattern is changed during this process. To address the question, we followed the protein level of cytoskeleton elements including different tubulins pools during early WT myogenesis *in vitro* and myofibers maturation post birth *in vivo*.

Our western blot results show that total, tyrosinated, detyrosinated and acetylated α-tubulins, in addition to β-tubulin and actin proteins level are all increased with primary myoblasts differentiation *in vitro,* side by side with markers of muscle differentiation such as MHC, MyoD and MyoG (Figure 5A). *In vivo*, α- and β-tubulins pools present a slight reduction in their proteins level between 10 to 15 days post birth and remain unchanged further on, while actin remains stable all along myofibers maturation and myogenic markers keep decreasing until they are no longer detectable (Figure 5B).

Based on these results, we questioned if increased α-tubulin detyrosination with primary myoblasts differentiation is accompanied by changes in expression of SVBP, VASH1, and/or VASH2 (Figure 1A). Our western blot results suggested an increase in the protein expression level of SVBP, VASH1, and VASH2 with primary myoblasts differentiation *in vitro* in parallel with α-tubulin detyrosination (Figure 5A). In addition, SVBP protein level was reduced with myofibers maturation post birth (Figure 5B). However, *in vivo* protein level analysis was more complicated for VASH1 and VASH2 due to the presence of several protein bands around the predicted molecular weight (40kD) for both proteins in total muscle extracts (Figure 5B). Thus, we examined their expression by studying their mRNA level. Interestingly, our qRT-PCR results indicated a boost in mRNA level of *Svbp* with primary myoblasts differentiation *in vitro*, which raised as high as *MyoG* mRNA (Figure 5C). Later on, we observed a reduction of *Svbp* gene expression along myofibers maturation both *in vitro* and post birth *in vivo* (Figure 5C-D). *Vash2* mRNA expression pattern was similar to *Svbp* with a less pronounced increase during primary myoblasts differentiation *in vitro* and a stronger decrease during myofibers maturation *in vivo* (Figure 5C-D). However, *Vash1* mRNA level keeps increasing during primary myoblasts differentiation *in vitro,* and, compared to *Vash2*, it is less strongly reduced during myofiber maturation post birth (Figure 5C-D). Since primary myoblasts differentiation is rapidly accompanied by their fusion, we evaluated *Svbp, VASH1,* and *VASH2* mRNA expression levels in the C2C12 myogenic cell line where differentiated myoblasts fuse 4 to 5 days post differentiation. Interestingly, we saw that *VASH1, and VASH2* mRNA expression levels remained stable, while *Svbp* mRNA expression gradually increases with C2C12 myoblasts differentiation and even before fusion (Figure 5 – Supplementary Figure 1A).

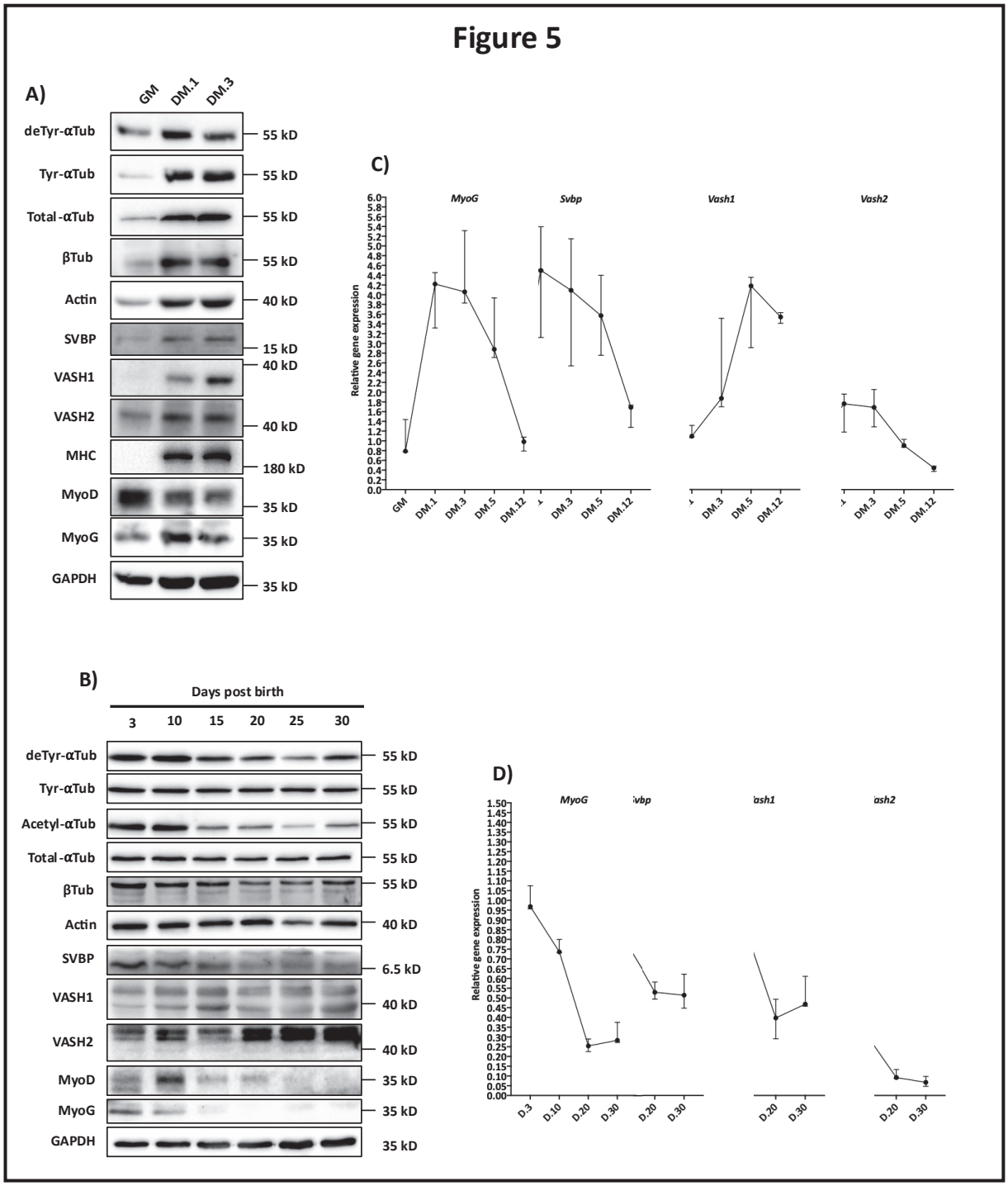

Figure 5: SVBP expression and MTs detyrosination level change during myoblasts differentiation.
(A) Western blot analysis of detyrosinated α-tubulin, tyrosinated α-tubulin, total α-tubulin, β-Tubulin, Actin, SVBP, VASH1, VASH2, MHC, MyoD, and MyoG proteins expression in total extracts from proliferating primary cells (GM) or differentiated cells at day 1 (DM.1) and day 3 (DM.3) post induction of differentiation *in vitro.* Cultures were obtained from isolated WT myoblasts. GAPDH is used as the loading control. **(B)** Western blot analysis of detyrosinated α-tubulin, tyrosinated α-tubulin, acetylated α-tubulin, total α-tubulin, β-Tubulin, Actin, SVBP, VASH1, VASH2, MyoD and MyoG proteins expression in total extracts from *gastrocnemius* of WT mice at different time points post birth during muscle maturation *in vivo*. **(C)** QRT-PCR results presenting relative gene expression levels to housekeeping genes for *MyoG*, *Svbp*, *VASH1,* and *VASH2* in proliferating primary cells (GM) or differentiated cells at day 1 (DM.1), day 3 (DM.3), day 5 (DM5) and day 12 (DM.12) post induction of differentiation *in vitro.* Cultures were obtained from isolated WT myoblasts. Following the calculation of relative target gene expression level in reference to housekeeping genes for each time point, the mean expression level of each target gene was calculated for the GM group. Next, the expression level of each following time point was normalized to the previously calculated mean value to determine the relative gene expression to GM. Median values with interquartile range are showing. **(D)** QRT-PCR results presenting relative gene expression levels to housekeeping genes for *MyoG*, *Svbp*, *VASH1,* and *VASH2* in total mRNA extracts from *gastrocnemius* of WT mice at different time points post birth during muscle maturation *in vivo.*

Following the calculation of relative target gene expression level in reference to housekeeping genes for each time point, the mean expression level of each target gene was calculated for D.3 group. Next, the expression level of each following time point was normalized to the previously calculated mean value to determine the relative gene expression to D.3. Median values with interquartile range are shown.

Collectively, these data suggest that while *Svbp* mRNA expression is induced with myoblasts differentiation, *VASH1* and *VASH2* mRNAs expression are induced with myoblasts fusion and with a stronger and more persistent increase in *VASH1* mRNA expression compared to *VASH2*. In addition, our previous data suggested that manipulation of MTs detyrosination level can impact myoblasts fusion *in vitro*. Thus, we were wondering whether, in the absence of SVBP, MuSCs behavior is affected *in vivo*. To address the consequences of loss of SVBP in MuSCs and their myogenic descendants, we followed a protocol that allows the isolation of single EDL myofibers and preserving their associated MuSCs at their periphery. Myofibers were cultured for 72h in order to analyze MuSCs behavior as they progress through the myogenic lineage or self-renew. At 24h culture in presence of EdU, *Svbp* KO myofibers exhibit a higher proportion of EdU+ MuSCs, suggesting that loss of SVBP increases the ability of MuSCs to enter the cell cycle (Figure 6A-B). As well, this result suggests that *Svbp* KO MuSCs break quiescence faster. At 48h, following 1h-EdU pulse, *Svbp* KO myofibers maintain an increased proportion of EdU+ Ki67+ (marker of proliferating cells) MuSCs compared to WT (Figure 6C-D). This suggests that SVBP controls MuSCs proliferation. Finally, at 72h, when MuSCs exit the cell cycle either to differentiate and express MyoG or to self-renew, we observed that *Svbp* KO myofibers display a higher proportion of MyoG+ cells and a marked decrease in PAX7+EdU- cells (Figure 6E-F).

Figure 5 – Supplementary Figure 1

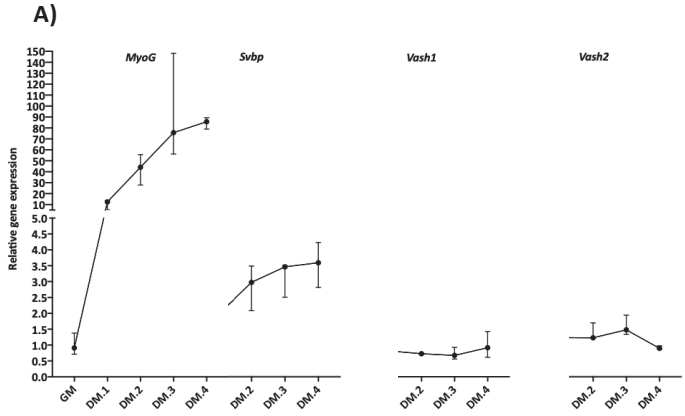

Figure 5 – Supplementary Figure 1: SVBP, VASH1, and VASH2 expression pattern in C2C12 myogenic cell line.
(A) QRT-PCR results presenting relative gene expression levels to housekeeping genes for *MyoG*, *Svbp*, *VASH1,* and *VASH2* in proliferating C2C12 cells (GM) or differentiated cells at day 1 (DM.1), day 2 (DM.2), day 3 (DM3), and day 4 (DM.4) post induction of differentiation *in vitro.* Following the calculation of relative target gene expression level in reference to housekeeping genes for each time point, the mean expression level of each target gene was calculated for the GM group. Next, the expression level of each following time point was normalized to the previously calculated mean value to determine the relative gene expression to GM. Median values with interquartile range are showing.

Together, these results suggest that SVBP is required for self-renewal and its loss disrupts the balance between self-renewal and differentiation, promoting differentiation at the expense of self-renewal.

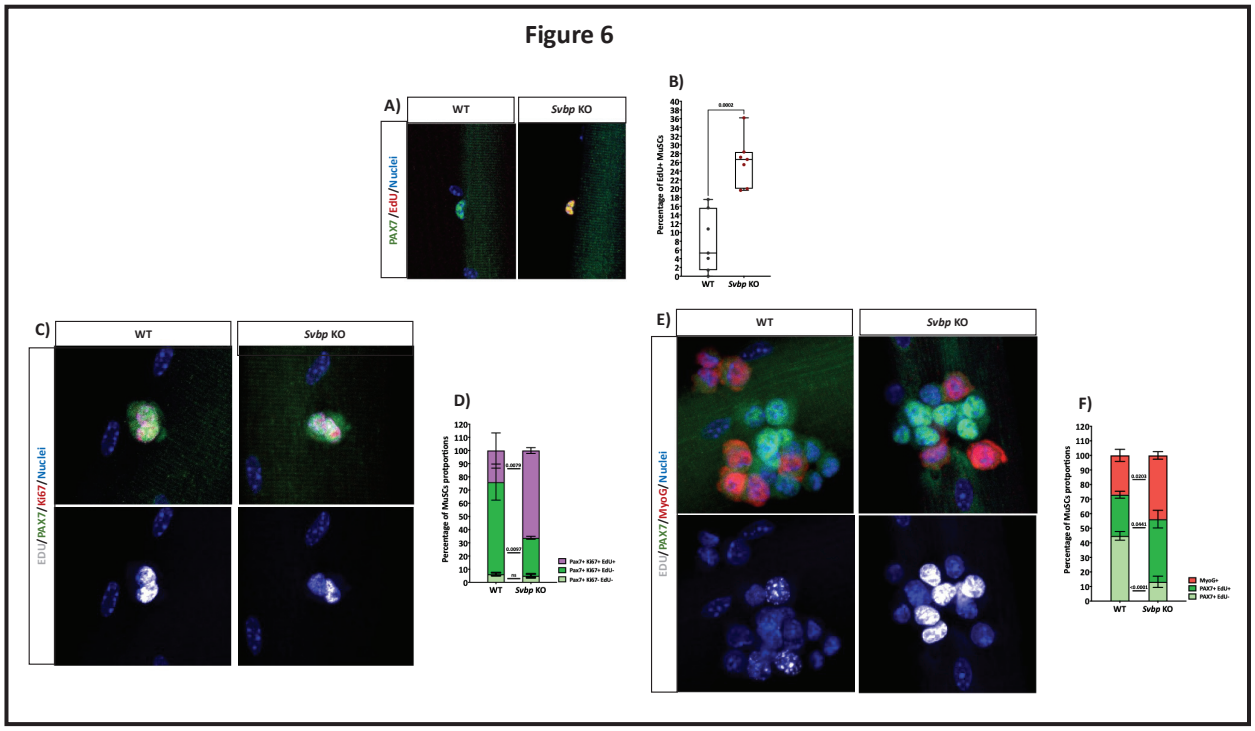

Figure 6: MuSCs from *Svbp* KO mice present aberrant behavior and activity
(A) Representative confocal images of 24 hours cultured MuSCs associated with isolated myofibers from EDL of WT (left panel) and *Svbp* KO (right panel) mice of 4.5-month-old presenting PAX7 (green), EdU (red), and nuclei (bleu). **(B)** percentage of EdU positive MuSCs associated with isolated myofibers from EDL of WT and *Svbp* mice of 4.5-month-old after 24 hours of culture (as presented in panel **A**). **(C)** Representative confocal images of 48 hours cultured MuSCs associated with isolated myofibers from EDL of WT (left panel) and *Svbp* KO (right panel) mice of 4.5-month-old presenting EdU (silver), PAX7 (green), Ki67 (red), and nuclei (bleu). (D) percentage of PAX7, Ki67, and EdU positive or negative MuSCs associated with isolated myofibers from EDL of WT and *Svbp* mice of 4.5-month-old after 48 hours of culture (as presented in panel **C**). **(E)** Representative confocal images of 72 hours cultured MuSCs associated with isolated myofibers from EDL of WT (left panel) and *Svbp* KO (right panel) mice of 4.5-month-old presenting EdU (silver), PAX7 (green), MyoG (red), and nuclei (bleu). **(F)** percentage of PAX7, MyoG, and EdU positive or negative MuSCs associated with isolated myofibers from EDL of WT and *Svbp* mice of 4.5-month-old after 48 hours of culture (as presented in panel **E**).

Denervation may contribute to *Svbp* KO MuSCs activation *in vivo*

Our previous experiments showed that in the absence of SVBP, MuSCs are more sensitive to changes in their environment and are more prone to activation upon stress. Thus, we hypothesized that increased MuSCs activity may be contributing to the presence of mispositioned myonuclei within *Svbp* KO myofibers.

The presence of mispositioned myonuclei is a hallmark of muscle regeneration, which is accompanied by changes in myofiber size, myogenic gene expression, and mitochondrial biogenesis (Beltrà et al., 2021; Duguez et al., 2002; Rahman and Quadrilatero, 2021; Schmidt et al., 2019). Therefore, following the observation of mispositioned myonuclei inside *Svbp* KO myofibers, we investigated whether *Svbp* KO mice undergo spontaneous muscle regeneration. However, immunofluorescence and qRT-PCR experiments show an equal number of myofibers expressing different myosin heavy chain subtypes, equal mitochondrial activity, and equal levels of *MyoG*, *MyoD,* or *PAX7* (markers of myogenesis) in addition to *Sarcolipin* and *PGC1α* (markers of mitochondrial biogenesis) gene expression level between WT and *Svbp* KO mice (Figure 7 – Supplementary Figure 1A-I). Interestingly, it has been previously shown that myofibers denervation can induce MuSCs activation and their fusion with stressed myofibers (Larouche et al., 2021). Thus, we studied NMJs of WT and *Svbp* KO myofibers. At the periphery of mature myofiber, different acetylcholine receptors (AChRs) subunits cluster together to form the post-synaptic NMs (Wanamaker et al., 2003). These specialized zones are dense on different MTs pools such as acetylated, tyrosinated, and detyrosinated MTs, among

which, acetylated MTs have been previously described to be important for AChRs clusters stability (Ghasemizadeh et al., 2021; Jasmin et al., 1990; Osseni et al., 2020). Thus, in order to determine the role of MTs detyrosination at NMJs, isolated myofibers from TA of WT and *Svbp* KO mice were stained with α-Bungarotoxin which specifically binds to AChRs and allows the analysis of AChRs clusters size and morphology as described before (Figure 7A) (Jones et al., 2016). Our confocal microscopy images revealed that AChRs clusters of *Svbp* KO myofibers are fragmented compared to the intact clusters at the periphery of WT myofibers (Figure 7B). Although this fragmentation did not seem to affect NMJs size, post-synaptic myonuclei clustering or expression level of *α* and *ε AChRs* subunits in *Svbp* KO mice, we detected an increase in mRNA level of *AChR β* subunit in *Svbp* KO mice compared to control mice (Figure 7E-G). Interestingly, the AChR β subunit has been shown to be important for AChRs clustering and assembly (Quiram et al., 1999). Following, to study the long-term side effect of apparent NMJs fragmentation in *Svbp* KO mice, isolated myofibers from EDL of WT and *Svbp* KO mice were subjected to Koelle staining, which allows us to detect denervated myofibers due to NMJs instability (Figure 7H) (Koelle and Friedenwald, 1949). Remarkably, our microscopy results showed an increase in the percentage of denervated myofibers in *Svbp* KO compared to WT mice (Figure 7I). Collectively, these results present NMJs instability at the periphery of *Svbp* KO myofibers *in vivo*, which may contribute to increased myonuclei per myofiber by promoting MuSCs activation.

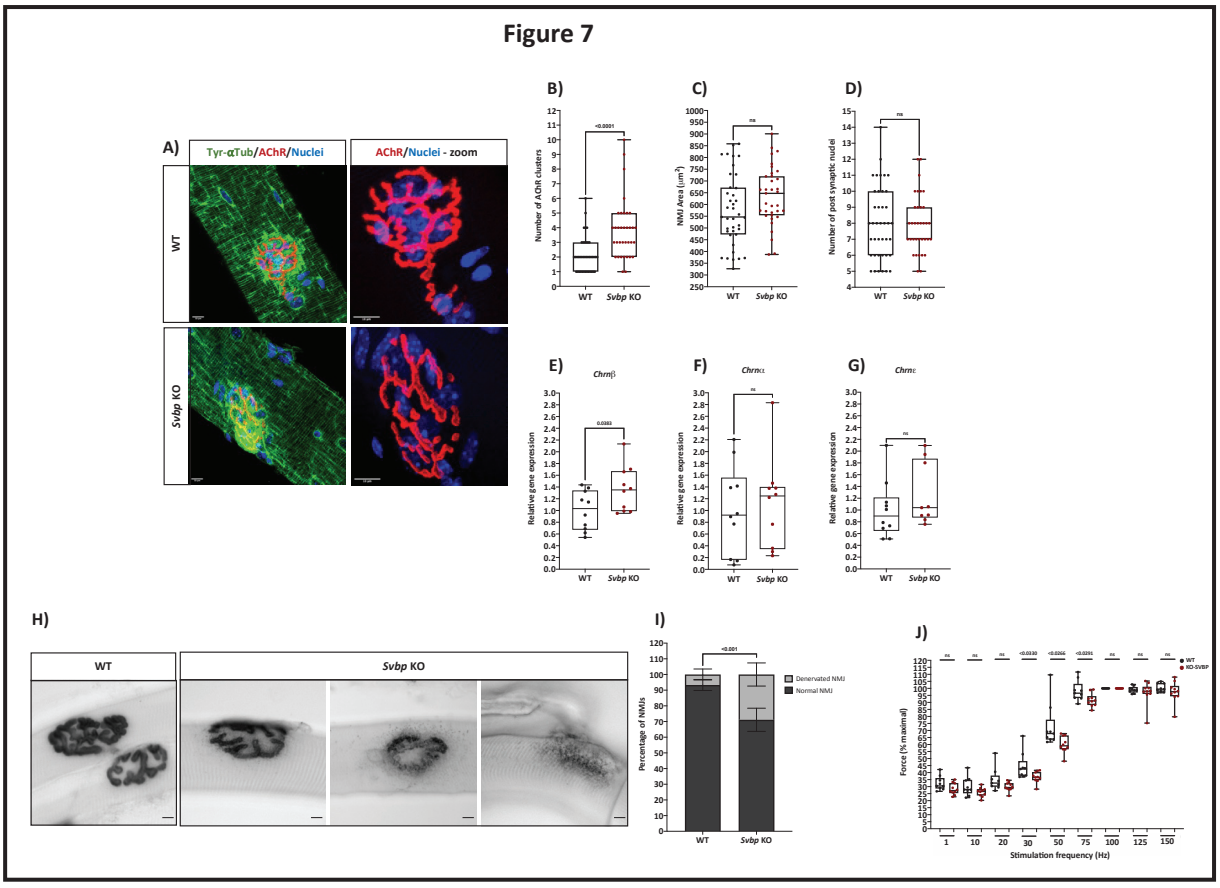

Figure 7: *Svbp* KO mice present NMJs instability.
(A) Representative confocal images (63X) of post-synaptic NMJs within isolated myofibers from *tibialis anterior* WT (upper panels) and *Svbp* KO (lower panels) mice of 4.5-month-old presenting tyrosinated α-tubulin (green), AChRs clusters (red) and myonuclei (blue). A panel of zoom photos is presented to emphasize on AChRs clusters organization. Scale Bar = 10 µm. **(B-D)** Quantification of the number of AChR clusters **(B)**, post synaptic NMJs area **(C),** and the number of post-synaptic myonuclei **(D)** measured on myofibers isolated from *tibialis anterior* of WT and *Svbp* KO mice of 4.5-month-old (as presented in representative images of panel **A**). Nine individual mice (with at least three myofibers per mouse) were studied in each group. Line is set at median. "ns" stands for not significant; p values are calculated by Student's t test. **(E-G)** QRT-PCR results presenting relative gene expression levels for *Chrnβ* **(E)**, *Chrnα* **(F),** and *Chrnε* **(G)** in total mRNA extracts from *gastrocnemius*

of WT and *Svbp* KO mice of 4.5 months old. Following the calculation of relative target gene expression level in reference to housekeeping genes for each mouse, the mean expression level of each target gene was calculated for the group of WT mice. Next, the expression level of each WT and *Svbp* KO mouse was normalized to the previously calculated mean value to determine the relative gene expression. Line is set at median. p value is calculated by Student's t test. "ns" stands for not significant. **(H)** Representative microscopy images of normal NMJ of WT mice (left panel) in addition to normal and two denervated NMJs of *Svbp* KO mice (right panels) represented by the analysis of Acetylcholinesterase activity following Koëlle staining at the age of 4.5month old. Scale bar = 10 µm. **(I)** Percentage of normal (in black) and denervated (in gray) NMJs in WT and *Svbp* KO mice quantified on three mice per group with 50 to 100 junctions per mouse. Mean values (with SEM) are presented. p value is calculated by ANOVA test. **(J)** Force production from the Hindlimb muscles in 4.5-month-old WT and *Svbp* KO mice in response to various incremental stimulation frequencies (from 1 to 150 Hz). Nine individual mice were subjected to study per group. Line is set at median. "ns" stands for not significant; p values are calculated by Student's t test.

Since muscular hypotonia is among the clinical manifestations of patients with a mutation in the *SVBP* gene (Iqbal et al., 2019), we questioned whether the observed denervation among *Svbp* KO myofibers is accompanied by changes in skeletal muscle activity of our *Svbp* KO mouse model. Therefore, we evaluated the muscular performance of WT and *Svbp* KO mice. For this, we used a strictly non-invasive experimental setup offering the possibility to stimulate the hindlimb muscles *in vivo* and record force production. Force was measured in response to incremental stimulation frequencies (from 1 to 150 Hz) to obtain the force-frequency relationship. While there was no significant difference in the values for maximum force produced between the two groups, we observed a rightward shift of the force production capacity in *Svbp* KO mice (Figure 7J). Hence, NMJs instability may also contribute to reduced force production capacity in *Svbp* KO mice. Whether this is true for *SVBP* mutant patients has yet to be determined.

Figure 7 – Supplementary Figure 1

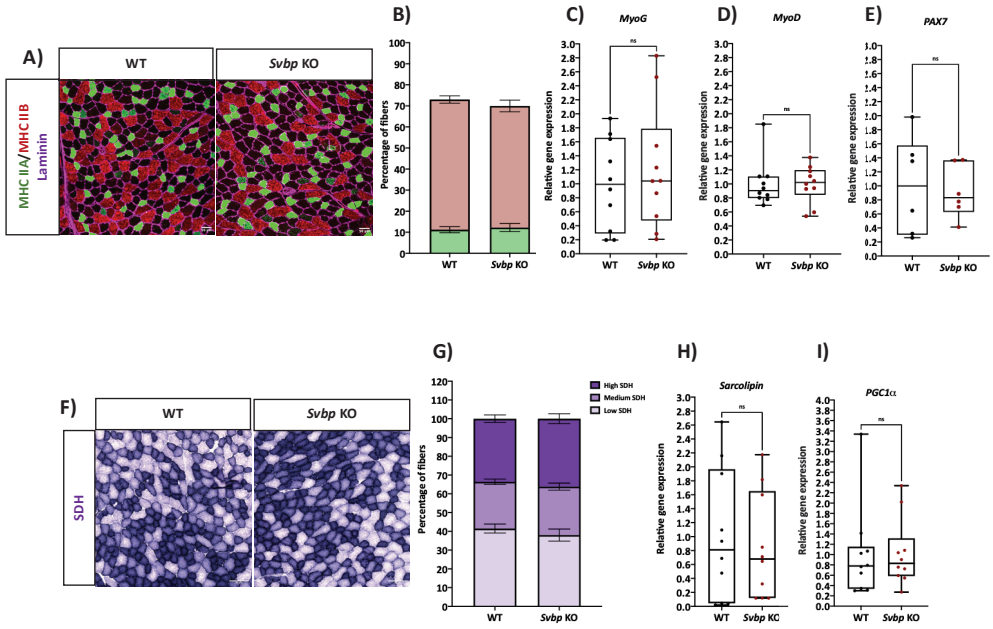

Figure 7 – Supplementary Figure 1: SVBP KO mice show no signs of major muscle regeneration.
(A) Representative microscopy images of cross sections from *tibialis anterior* muscle of WT (left panel) and *Svbp* KO (right panel) mice of 4.5 months old stained for MHC IIA (green), MHC IIB (red), and Laminin (violet). Scale Bar = 50 µm. **(B)** Quantification of the percentage of myofibers positive for MHC IIA (in green) or for MHC IIB (in red) in *tibialis anterior* muscles from 4.5-month-old WT and *Svbp* KO mice (as presented in panel **A**). Three mice per group were studied. Mean values (with SEM) are presented. **(C-E)** QRT-PCR results presenting relative gene expression levels for *MyoG* **(C)**, *MyoD* **(D)**, and *PAX7* **(E)** in total mRNA extracts from *gastrocnemius* of WT and *Svbp* KO mice of 4.5 months old. Following the calculation of relative target gene expression level in reference to housekeeping genes for each mouse, the mean expression level of each target gene was calculated for the group of WT mice. Next, the expression level of each WT and *Svbp* KO mouse was

normalized to the previously calculated mean value to determine the relative gene expression. Line is set at median. p value is calculated by Student's t test. "ns" stands for not significant. **(F)** Representative images of the transversal cross-sections of *tibialis anterior* muscle of WT (left panel) and *Svbp* KO (right panel) mice of 4.5 months old stained for Succinate DeHydrogenase activity. Scale Bar = 50 μm. **(G)** Quantification of the Succinate DeHydrogenase activity relative to myofibers distribution in WT and *Svbp* KO mice of 4.5 months old. Seven mice were studied per group. Mean values (with SEM) are presented. **(H-I)** QRT-PCR results presenting relative gene expression levels for *Sarcolipin* **(H)** and *PGC1α* **(I)** in total mRNA extracts from *gastrocnemius* of WT and *Svbp* KO mice of 4.5 months old. Following the calculation of relative target gene expression level in reference to housekeeping genes for each mouse, the mean expression level of each target gene was calculated for the group of WT mice. Next, the expression level of each WT and *Svbp* KO mouse was normalized to the previously calculated mean value to determine the relative gene expression. Line is set at median. "ns" stands for not significant as determined by Student's t test.

Discussion

At the periphery of myofibers, each myonucleus transcriptionally supports its surrounding cytoplasm, known as myonuclear domains (Hall and Ralston, 1989; Ralston and Hall, 1992). During skeletal muscle development, myonuclear domains are adjusted and adapted to myofibers size as they gain volume and grow following the fusion of active MuSCs (Cardasis and Cooper, 1975). We and others have previously shown that MTs participate in myonuclear domain organization by enabling their MAPs to engage in myonuclei movement during myofibers formation and myonuclei stability at the periphery of mature myofibers (Cadot et al., 2012; Gache et al., 2017; Ghasemizadeh et al., 2021; Metzger et al., 2012; Wang et al., 2015). In addition, MTs ensure the functionality of myonuclear domains by providing a stable network for the transport of nuclear products such as RNA (Denes et al., 2021). However, how MTs stability itself is managed during myofibers formation and how it can impact myofibers functionality remain poorly understood. In this study, we show that myoblasts differentiation is accompanied by an increase in the level of stable detyrosinated MTs hand to hand with an increase of MTs detyrosinating complex members, SVBP, VASH1, and VASH2 (Figure 5). Additionally, we describe how disruption of the balance between detyrosinated-stable and tyrosinated-dynamic MTs affects myonuclear domains organization, not through myonuclei dynamics, but through irregular activation of MuSCs and increased myonuclei per myofiber. We also provide evidences on the importance of stable/dynamic MTs balance for proper myofibers activity.

Our *in vitro* and *in vivo* experiments show that in the absence of SVBP results in increased MTs dynamics and accumulation of disorganized tyrosinated MTs (Figure 3). Indeed, MTs have been previously described to manage Ca^{2+} Chanelle activation and mechanically support myofibers during sarcomeres shortening and contraction (Kerr et al., 2015; Khairallah et al., 2012). In addition, the presence of stable MTs and different MAPs is necessary for NMJs stability (Ghasemizadeh et al., 2021; Osseni et al., 2020; Oury et al., 2019). Interestingly, we observed NMJs fragmentation and muscular denervation for *Svbp* KO myofibers, concomitant with the reduced capacity of skeletal muscles force production (Figure 7). These results can correlate with the presence of muscular hypotonia observed in patients bearing a mutation in the *SVBP* gene (Iqbal et al., 2019). However, we cannot neglect that irregular Ca^{2+} signaling and mechanical stress management may also contribute to the reduced muscle force observed in *Svbp* KO mice.

Interestingly, our cross-section analysis suggests the absence of muscle atrophy, which normally accompanies muscular denervation (Figure 4 – Supplementary Figure 1) (Bongers et al., 2013). Instead, we observed the presence of mispositioned myonuclei within myofibers on cross-sectioned muscles and an increased number of myonuclei at the periphery of isolated myofibers (Figure 2). Interestingly, myofibers denervation has been shown to induce MuSCs activation and their fusion with stressed myofibers (Larouche et al., 2021). This suggests that the stress induced by muscle denervation may be responsible for increased myonuclei number

per myofiber in *Svbp* KO mice. To confirm, it would be interesting to study the MuSCs population and myonuclei number in the vicinity of fragmented NMJs of *Svbp* KO myofibers. In addition, these results were in parallel with an increase in MuSCs activation, proliferation, and differentiation rate at the periphery of live isolated *Svbp* KO myofibers *ex vivo* and increased *Svbp* KO myoblasts fusion *in vitro* (Figures 4&6). These data suggest that *Svbp* KO myofibers NMJs instability may only partially be responsible for aberrant MuSCs activity *in vivo*, as their behavior does not match with WT MuSCs even in the absence of NMJs *ex vivo* and *in vitro*. Within skeletal muscle, MuSCs are highly sensitive to the composition of their niche, which is constructed by themselves, myofibers, and other neighboring cells (Loreti and Sacco, 2022; Relaix et al., 2021). Thus, the increased MuSCs activation at the periphery of *Svbp* KO myofibers may be due to changes in their extracellular matrix composition. If so, the difference of MuSCs extracellular matrix between WT and total *Svbp* KO mice in addition to the cellular sources of this difference have to be further investigated. Nonetheless, while the mechanical role of MTs in MuSCs has never been addressed, previous data from other types of stem cells suggest a determining role of MTs in nuclear mechanotransduction, differentiation, and the fate of the stem cells (Biedzinski et al., 2020; Meka et al., 2017). Therefore, the increased differentiation and fusion of *Svbp* KO MuSCs and myoblasts may be linked to disrupted MTs-dependent mechanotransduction within these cells.

Altogether, our data suggest that the absence of stable-detyrosinated MTs in *Svbp* KO mice results in abnormal MuSCs activity and their increased fusion with myofibers, which most probably compensates the muscular atrophy due to denervation but also disrupts myonuclear domains by increasing myonuclei content per myofiber.

Materials and Methods

Primary myoblasts isolation, culture, and transfection

Primary myoblasts were collected from WT or *Svbp* KO C57BL6 mice as described before (Falcone et al., 2014). Briefly, Hindlimb muscles from 5-6 days pups were extracted and digested with collagenase (Sigma, C9263-1G) and dispase (Roche, 04942078001). After a pre-plating step to discard contaminant cells such as fibroblasts, myoblasts were cultured on 1% matrigel coated-dish (Corning, 356231) in growth media (GM: IMDM (Gibco, 21980-032), 20% fetal bovine serum (Gibco, 10270-106), 10% chicken embryo extract (USBiological, C3999), and 1% penicillin-streptomycin (Gibco, 15140-122)). When reached to 90% of confluence, myocytes were induced to differentiate in myotubes for 2-3 days in differentiation media (DM: IMDM (Gibco, 21980-032), 2% of horse serum (Gibco, 16050-122), and 1% penicillin-streptomycin (Gibco, 15140-122)). Myotubes were then covered by a concentrated layer of matrigel and maintained for up to 10 days in long differentiation culture medium (LDM: IMDM (Gibco, 21980-032), 2% of horse serum (Gibco, 16050-122), 0.1% Agrin + 1% penicillin-streptomycin (Gibco, 15140-122)) until the formation of mature and contracting myofibers. LDM was changed every two days.

For the production of recombinant Agrin, the stably transfected HEK293-EBNA cells were grown to about 80% confluence and were transferred to expression medium without FBS. Conditioned medium containing secreted proteins was collected every 3 days and replaced with fresh expression media for 12 days. Conditioned medium was centrifuged at 2,000RCF for 10 min to pellet the cells before storing at -20°C. After thawing, recombinant proteins were purified from conditioned media by HPLC, on a HiTRAP Imac HP column (GE Healthcare, 17-0920-03), eluted with imidazol and desalted on silica column with PBS (GE Healthcare, HiPrep 26 /10 Desalting) or on a Vivaspin column (Vivaspin Sartorius). The absolute concentration of soluble Agrins was estimated on a coomassie blue stained gel by comparison with a known amount of a commercial purified Agrin.

For primary cells transfection, EB3-GFP (homemade), Lamin-chromobody-RFP (Chromotek), and SVBP/VASH1-GFP or SVBP/VASH2-GFP (gifts from Dr. Marie-Jo Moutin's lab) cDNA were transfected to cells using Lipofectamine 3000 (ThermoFisher Scientifics, L3000-008) following manufacturer instructions, just before differentiation.

Video-Microscopy, time-lapse imaging, and analysis

To analyze the movement of myonuclei, time-lapse 10X images were acquired using Z1-AxioObserver (Zeiss) with intervals of 15 minutes. To analyze the movement of myoblasts, time-lapse 10X images were acquired using Z1-AxioObserver (Zeiss) with intervals of 10 minutes. Final videos were analyzed using Metamorph (Zeiss) and SkyPad plugin as described before (Cadot et al., 2014).

To analyze the dynamic of EB3, 50 stream acquisitions were obtained at 63X with 500ms of intervals using Z1-AxioObserver (Zeiss). The movement and speed of each comet was further analyzed as described before (Sbalzarini and Koumoutsakos, 2005).

Primary cell immunofluorescence staining and analysis

Cells were fixed in 4% PFA-1X PBS for 20 min at 37°C followed by washes with 1X PBS and permeabilization with 0.5% Triton-X100-1X PBS for 5 min at RT. Following washes with 1X PBS, cells were saturated with 1% BSA-1X PBS for 30 min at RT and incubated in primary antibodies overnight at 4°C. After several washes with 0.05% Triton-X100-1X PBS, cells were incubated in secondary antibodies or dyes for 2H at RT and washed with 0.05% Triton-X100-1X PBS before image acquisition. The list of the antibodies used for each staining can be found in table 1.

Following fixation and immunofluorescent staining, the measurement of the distance between adjacent myonuclei was done on 10X mosaic images acquired by Z1-AxioObserver (Zeiss) on myofibers stained for myonuclei and α-actinin.

The distance between adjacent sarcomeres was measured manually on mono Z images of α-actinin staining imaged by confocal LSM880 (Zeiss) microscope.

The width of each myofiber was measured on α-actinin staining in myofibers presenting formed sarcomeres. Confocal 63X images were acquired by LSM880 (Zeiss).

Myotubes fusion index was calculated by normalizing the number of myonuclei within myotubes on the total myonuclei present in each 10X mosaic image acquired by Z1-AxioObserver (Zeiss).

Quantifications in immature myotubes were assessed on 10X mosaic images acquired by Z1-AxioObserver (Zeiss) using an analysis tool developed by our team. An image analysis performed in ImageJ® software is combined with a statistical analysis in RStudio® software. This provides quantifications of parameters, ranked by myonuclei content per myotubes, regarding the phenotype of myotubes (area, length) and their respective myonuclei positioning.

All the quantifications/measurements were done using ImageJ® software.

Mouse model

Previously described WT and *Svbp* KO mice of 4.5-month-old were kindly provided by Dr. Marie-Jo Moutin (Pagnamenta et al., 2019).

Each mouse was weighed prior to experimentation. Following muscle dissection, the weight of each muscle was normalized on total mouse weight in order to calculate the relative muscle to mouse weight.

All of the experiments and procedures were conducted in accordance with the guidelines of the local animal ethics committee of the University Claude Bernard – Lyon 1 and in accordance with French and European legislation on animal experimentation and approved by the ethics committee CECCAPP and the French ministry of research.

In vivo force measurements

Mice were initially anesthetized in an induction chamber using 4% isoflurane. The right Hindlimb was shaved before an electrode cream was applied at the knee and heel regions to optimize electrical stimulation. Each anesthetized mouse was placed supine in a cradle allowing for a strict standardization of the animal positioning. Throughout a typical experiment, anesthesia was maintained by air inhalation through a facemask continuously supplied with 1.5% isoflurane. The cradle also includes an electrical heating blanket in order to maintain the animal at a physiological temperature during anesthesia. Electrical stimuli were delivered through two electrodes located below the knee and the Achille's tendon. The right foot was positioned and firmly immobilized through a rigid slipper on a pedal of an ergometer (NIMPHEA_Research, AII Biomedical SAS) allowing for the measurement of the force produced by the Hindlimb muscles (i.e., mainly the *gastrocnemius* muscle). The right knee was also firmly maintained using a rigid fixation in order to optimize isometric force recordings. Monophasic rectangular pulses of 0.2ms were delivered using a constant-current stimulator (Digitimer DS7AH, maximal voltage: 400V). The force-frequency curves were determined by stepwise increasing stimulation frequency, with resting periods > 30s between stimuli in order to avoid effects due to fatigue. For each stimulation train, isometric peak force was calculated. After a 3-min recovery period, force was assessed during a fatigue protocol consisting of 30Hz stimulation trains of 0.3s delivered once every second for 180s. The peak force of each contraction was measured and averaged every 5 contractions. Force signal was sampled at 1000Hz using a Powerlab system and Labchart software (ADinstruments).

Single EDL myofiber isolation and culture for MuSCs analysis

Single myofibers were isolated from the EDL muscles of 4.5-month-old WT or *Svbp* KO mice, as previously described (Brun et al., 2018). Briefly, EDL muscles were dissected and digested in DMEM containing 2.5 mg/ml collagenase I for 1H. Single myofibers were released by gentle trituration of the muscle. Following several washes, myofibers were cultured in floating condition in DMEM supplemented with 20% fetal bovine serum and 1% penicillin-streptomycin. Before fixation, EdU Click-iT kit (ThermoFisher Scientific, C10340) was used as instructed by the manufacturer. At each time point, a minimum of 20 myofibers per mouse was fixed, stained for by desired primary and secondary antibodies, and analyzed. A list of the antibodies used for immunofluorescence staining can be found in table 1.

Protein extraction, western blot, and analysis

For *in vitro* experiments, cultured cells were collected using a cell scrapper in cold 1X PBS on ice. Collected samples were then centrifuged at 11000RPM for 30 seconds to obtain cell pellets. Each sample was diluted and incubated in the optimal volume of RIPA lysis buffer containing phosphatases inhibitors (Sigma, P5726-5mL) and proteases inhibitors (Sigma, P8340) for 30 min on ice. Following a sonication and a centrifugation at 12000RPM for 10 min at 4°C, protein samples were collected in fresh tubes for further use. The concentration of proteins was determined using BCA protein assay kit (Thermo Fisher Scientifics, 23225) as described by the manufacturer.

To obtain protein extracts from dissected muscles, samples were finely cut onto tubes containing ceramic beads (MP Biomedicals Lysing Matrix D, 6913100) with the optimal volume of RIPA lysis buffer completed with phosphatases inhibitors (Sigma, P5726-5mL) and proteases inhibitors (Sigma, P8340). Tubes were subjected to harsh shaking (6500rpm, 3cycles of 15 seconds with 30 seconds pause intervals at 4°C) and rested at 4°C for 1H. Following a sonication and a centrifugation at 12000RPM for 10 min at 4°C, protein samples were collected to fresh tubes for further uses. The concentration of proteins was determined using BCA protein assay kit (Thermo Fisher Scientifics, 23225) as described by the manufacturer.

Per condition, 30µg of protein was loaded in 12 or 16.5% running acrylamide gels depending on the size of the target proteins. Based on the target size, proteins were transferred to 0.45 µm nitrocellulose (Amersham, GE10600002) or 0.22 µm PVDF (Merck, 2660406) membranes between 45 to 110 mins. Western blot membranes were then saturated in 5% milk in 1X TBS for 1H at RT and were incubated in primary antibodies diluted in 1% milk-1X TBS overnight at 4°C. A list of antibodies used for western blot can be found in table 2. Following washes by 0.1% Tween-20-1X TBS, the membranes were incubated in HRP conjugated secondary antibodies in 5% milk in 0.1% Tween-20-1X TBS for 1H at RT. Following washes by 0.1% Tween-20-1X TBS the detection of the target proteins was carried out using Super Signal West Femto (Thermo Fisher Scientifics, 34095) and ChemiDoc imaging system (BioRad).

BioRad Image Lab software was used to quantify proteins volume.

Koelle staining on EDL

Koelle staining was used as described in to stain AChE activity (Koelle and Friedenwald, 1949). Briefly, EDL muscles were collected and fixed for 15 min in 4% H2O-paraformaldehyde. Samples were preincubated in a substrate-free medium for 10 min before incubation with the Acétylthiocholine iodide substrate (Sigma, A5751) for 15 min at RT. After washing, AchE staining was revealed with 1% ammonium sulfide solution (Sigma, A1952) for 1 minute 40 seconds. Muscles were then fixed in PFA 4% for 1H. After washing, muscles were slowly teased with fine forceps to isolate individual fibers and small fiber bundles and then mounted on a glass slide with Immu-Mount™ (FisherScientific).

Muscle cross-sections histochemical and immunofluorescence staining and analysis

Mice were euthanized and muscles were harvested, embedded in OCT, and frozen in liquid-nitrogen-cooled isopentane. Embedded muscles were transversely sectioned at 10 µm thickness. Sections were fixed in 4% PFA-1XPBS for 10 min at room temperature, permeabilized in 0.1M glycine, 0.1% Triton X100-1X PBS and blocked in 5% goat serum, 2% BSA-1X PBS supplemented with M.O.M. Blocking reagent (Vector laboratories, MKB-2213-1). Then, sections were incubated with primary antibodies diluted in blocking buffer, overnight at 4°C (Table 2). Following PBS washes, sections were incubated with the appropriate secondary antibodies for 1H at room temperature. A list of the antibodies used for immunofluorescent staining can be found in table 1. Finally, sections were washed in PBS and counterstained with DAPI.

SDH staining was performed as previously described (Nachlas et al., 1960). Briefly, transverse sections (8 µm) were cut from the mid-belly of the TA muscles on a cryostat at −20°C and stored at −80°C until SDH staining was performed. The sections were dried at room temperature for 30 min before incubation in a solution made up of 0.2M phosphate buffer (pH 7.4), 0.1M MgCl2, 0.2M Succinic Acid, and 2.4mM NitroBlue Tetrazolium at 37°C in a humidity chamber for 45 min. The sections were then washed in deionized water for 3 min, dehydrated in 50% ethanol for 2 min, and mounted for viewing with DPX mount medium (Electron Microscopy Sciences).

Fluorescence microscopy and transmission microscopy were performed using Axioimager Z1 microscope with CP Achromat 5x/0.12, 10x/0.3 Ph1, or 20x/0.5 Plan NeoFluar objectives (Zeiss). Images were captured using a charge-coupled device monochrome camera (Coolsnap HQ, Photometrics) or color camera (Coolsnap colour) and MetaMorph software. For all imaging, exposure settings were identical between compared samples.

The percentage of myofibers with peripheral or mispositioned myonuclei was quantified manually on whole cross-sections using ImageJ® software.

Muscle cross-sections were analyzed for fiber counting and minimum Feret's diameter using SMASH (Smith and Barton, 2014).

Plugin Protocols of Icy® software was used to generate a graphical environment and create a bioimage analysis workflow which can automatically process images. The protocol consists of multiple elementary blocks that performs sequential steps of fibers segmentation (based on laminin staining) and calculates SDH mean intensity in each fiber. Size and morphology criteria were used to include only correctly delimited fibers.

TA mono-myofibers isolation, immunofluorescence staining, and analysis

Following the dissection of the whole TA muscle from mice, muscle blocks were fixed in 4% PFA-1X PBS for 2H at RT. After several washes, 30 to 50 mono-myofibers were isolated per staining from each muscle. Myofibers were then permeabilized using 1% Triton-X100-1X PBS for 15 min at 37°C and saturated in 1% BSA-1XPBS for 30 min at RT. Based on the experiments, myofibers were incubated in desired primary antibodies at 4°C ON. A list of the antibodies used for immunofluorescent staining can be found in table 1. Following washes with 0.05% Triton-X100-1X PBS, myofibers were incubated in desired secondary antibodies at 4°C ON. On the next day, myofibers were incubated with desired dyes for 2H at RT and washed several times with 0.05% Triton-X100-1X PBS before mounting on slides. Myofibers were mounted on slides using fluromount Aqueous mounting (Sigma, F4680-25mL) and kept at 4°C utile image acquisition.

The fluorescence intensity of detyrosinated or tyrosinated α-tubulin staining were quantified on 2-3μM peripheral Z-stacks of each myofiber. Myofibers were imaged by applying the same imaging setting using confocal LSM880 (Zeiss) microscope.

The distance between each myonucleus and its closest neighbor, area per myonuclei, myonuclei feret, myonuclei area, and myonuclei roundness were quantified on 3μM peripheral Z-stacks of each myofiber acquired by confocal LSM880 (Zeiss) microscope.

The microtubules orientation was assessed on mono Z images, acquired by confocal LSM880 (Zeiss) microscope, of tubulin staining using TeTD directionality tool as described before (Liu and Ralston, 2014).

Each NMJs morphology and characteristics were studied on Z-stack images, acquired by confocal LSM880 (Zeiss) microscope, of bungarotoxin staining as described previously (Jones et al., 2016).

The distance between adjacent sarcomeres was measured manually on mono Z images of α-actinin staining imaged by confocal LSM880 (Zeiss) microscope.

All the quantifications/measurements were done using ImageJ® software.

QRT-PCR and analysis

RNA extraction and RT-PCR: For primary cells, Trizol (Sigma, T9424-200mL) was directly added to each culture well, for dissected muscles, after the addition of Trizol on each sample, lysing matrix D and fast prep system (MPbio, 6913-100) were used for sample digestion and pre-RNA extraction. Following, in order to extract RNA, samples were incubated in chloroform for 5 min at RT, centrifuged for 15 min at 12000RCF at 4°C and incubated in the tubes containing isopropanol (precipitation of RNA) for 10 min at RT. Following a centrifuge of samples for 15 min at 12000RCF at 4°C, samples were washed 2 times with 70% ethanol and the final RNA pellets were diluted in ultra-pure RNase free water (Invitrogen, 10977-035). RNA concentration was calculated using Nanodrop (ThermoFisher Scientifics). GoScript Reverse Transcriptase System (Promega, A5001) was used as described by the manufacturer to produce the cDNA.

q-PCR: Fast Start Universal SYBR Green Master (Rox) (Roche, 04913914001) and CFX Connect™ Real-Time PCR Detection System (BioRad) were used to carry out the

quantitative PCR using the following primer sets. For analysis of genes expression level, The CT of target genes was normalized on 3 control genes. The list of primers used for q-PCR can be found in table 3.

Table 1: List of antibodies used for immunofluorescence staining:

Antibody or Dye	Species and Utility	Dilution Factor	Manufacturer and Reference
Anti-Myosin heavy chain	Mouse-primary	1:10	DSHB MF20 (hybridoma supernatant)
Anti-Laminin	Rabbit - primary	1:2000	Sigma L9393
Anti-MHC IIA	Mouse IgG1 - primary	1:100	DSHB SC-71 (hybridoma supernatant)
Anti-MHC IIB	Mouse IgM - primary	1:100	DSHB BF-F3 (hybridoma supernatant)
Anti- Total-αTub	Mouse - primary	1:1000	Sigma T6074
Anti-Tyr-αTub	Rat - primary	1:1000	Andrieux's Lab gift
Anti-deTyr-αTub	Rabbit - primary	1:1000	Andrieux's Lab gift
Anti-α-actinin	Mouse – primary	1:350	Sigma A7811
Anti-PAX7	Mouse IgG1 - primary	1:2	DSHB PAX7 (hybridoma supernatant)
Anti-MyoG	Rabbit - primary	1:500	Abcam ab124800
Dapi-brilliant blue	Dye	1:50000	Thermo Fisher Scientifics D1306
α-Bungarotoxin-Alexa Flour 555	Dye	1:200	Thermo Fisher Scientifics B35451
Anti-rat-Alexa Flour 488	Donkey - secondary	1:500	Thermo Fisher Scientifics A-21208
Anti-rabbit-Alexa Flour 555	Goat - secondary	1:500	Thermo Fisher Scientifics A-21429
Anti-mouse-Alexa Flour 448	Goat - secondary	1:500	Thermo Fisher Scientifics A-211029

Table 2: List of antibodies used for western blot:

Antibody	Species and Utility	Dilution Factor	Manufacturer and Reference
Anti-deTyr-αTub	Rat - primary	1:5000	Andrieux's Lab gift
Anti-Tyr-αTub	Rabbit - primary	1:5000	Andrieux's Lab gift
Anti-Acetyl-αTub	Mouse - Primary	1:500	Sigma T7451
Anti- Total-αTub	Mouse - primary	1:1000	Sigma T6074
Anti-SVBP	Rabbit - primary	1:500	Human protein atlas HPA008507
Anti-VASH1	Rabbit - primary	1:500	Proteintech 12730-1-AP
Anti-VASH2	Mouse - primary	1:500	Merck MABC536
Anti-βTub	Rabbit - primary	1:1000	ThermoFisher Scientific PA5-21826
Anti-Actin	Mouse - primary	1:5000	Merck MAB1501
Anti-MHC	Mouse - primary	1:1000	Santa Cruz SC53091
Anti-MyoD	Mouse - primary	1:500	Santa Cruz SC32758
Anti-MyoG	Rat - primary	1:250	BD Biosciences BD556358
Anti-GAPDH	Mouse - primary	1/40000	Sigma-Aldrich MAB374
Anti-mouse-HRP	Goat - secondary	1:5000	Invitrogen 62-6520
Anti-rabbit-HRP	Goat - secondary	1:5000	Invitrogen 65-6120
Anti-rat-HRP	Goat - secondary	1:5000	Invitrogen 62-9520

Table 3: List of the primers used for qPCR:

Primers	Sequence
MyoG - F	CAATGCACTGGAGTTCGGTC
MyoG - F	ACAATCTCAGTTGGGCATGG
MyoD - F	AGCACTACAGTGGCGACTCA
MyoD - R	GCTCCACTATGCTGGACAGG
PAX7 - F	GACGACGAGGAAGGAGACAA
PAX7 - R	ACATCTGAGCCCTCATCCAG
Sarcolipin - F	GGTCCTTGGTAGCCTGAGTG
Sarcolipin - R	CGGTGATGAGGACAACTGTG
PGC1α - F	GCAGGTCGAACGAAACTGAC
PGC1α - R	CTTGCTCTTGGTGGAAGCAG
Chrnα - F	TCCCTTCGATGAGCAGAACT
Chrnα - R	GGGCAGCAGGAGTAGAACAC
Chrnβ - F	ATTCTCTCCGCATCACTGCT
Chrnβ - R	GTGCAGTTCTGCCAGTCAAA
Chrnε - F	GCGGAGCGAACTCGTGTTTG
Chrnε - R	ACAGCAGCGGATTTCTGGGG
SVBP - F	AACCAGCCTTCAGAGTGGAGAAGG
SVBP - R	GCTCCGTCATGACTCTGTTGAGAGC
VASH1 - F	TGGCCAAGATCCACCCAGATG
VASH1 - R	TCGTCGGCTGGAAAGTAGGCAC
VASH2 - F	CCACTCTCCAACCCAAGTGAG
VASH2 - R	TCGGTCAGAGCAGGCGATT
RpL4 F	GCCATGAGAGCGAAGTGG
RpL4 R	CTCCTGCAGGCGTCGTAG
GAPDH - F	AACTTTGGCATTGTGGAAGG
GAPDH - R	ACACATTGGGGGTAGGAACA
Cylosporin B - F	GATGGCACAGGAGGAAAGAG
Cylosporin B - R	AACTTTGCCGAAAACCACAT
GusB - F	GAGGATTGCCAACGAAACCG
GusB - R	GTGTCTGGGGACACCTTTGA

References

Aillaud, C., Bosc, C., Peris, L., Bosson, A., Heemeryck, P., Van Dijk, J., Le Friec, J., Boulan, B., Vossier, F., Sanman, L.E., Syed, S., Amara, N., Couté, Y., Lafanechère, L., Denarier, E., Delphin, C., Pelletier, L., Humbert, S., Bogyo, M., Andrieux, A., Rogowski, K., Moutin, M.-J., 2017. Vasohibins/SVBP are tubulin carboxypeptidases (TCPs) that regulate neuron differentiation. Science 358, 1448–1453. https://doi.org/10.1126/science.aao4165

Beltrà, M., Pin, F., Costamagna, D., Duelen, R., Renzini, A., Ballarò, R., Garcia-Castillo, L., Iannuzzi, A., Moresi, V., Coletti, D., Sampaolesi, M., Penna, F., Costelli, P., 2021. PGC-1α in the myofibers regulates the balance between myogenic and adipogenic progenitors affecting muscle regeneration (preprint). Molecular Biology. https://doi.org/10.1101/2021.11.03.466970

Biedzinski, S., Agsu, G., Vianay, B., Delord, M., Blanchoin, L., Larghero, J., Faivre, L., Théry, M., Brunet, S., 2020. Microtubules control nuclear shape and gene expression during early stages of hematopoietic differentiation. EMBO J. 39, e103957. https://doi.org/10.15252/embj.2019103957

Bongers, K.S., Fox, D.K., Ebert, S.M., Kunkel, S.D., Dyle, M.C., Bullard, S.A., Dierdorff, J.M., Adams, C.M., 2013. Skeletal muscle denervation causes skeletal muscle atrophy through a pathway that involves both Gadd45a and HDAC4. Am. J. Physiol. Endocrinol. Metab. 305, E907-915. https://doi.org/10.1152/ajpendo.00380.2013

Bré, M.H., Kreis, T.E., Karsenti, E., 1987. Control of microtubule nucleation and stability in Madin-Darby canine kidney cells: the occurrence of noncentrosomal, stable detyrosinated microtubules. J. Cell Biol. 105, 1283–1296. https://doi.org/10.1083/jcb.105.3.1283

Brun, C.E., Wang, Y.X., Rudnicki, M.A., 2018. Single EDL Myofiber Isolation for Analyses of Quiescent and Activated Muscle Stem Cells, in: Lacorazza, H.D. (Ed.), Cellular Quiescence, Methods in Molecular Biology. Springer New York, New York, NY, pp. 149–159. https://doi.org/10.1007/978-1-4939-7371-2_11

Bruusgaard, J.C., Liestøl, K., Ekmark, M., Kollstad, K., Gundersen, K., 2003. Number and spatial distribution of nuclei in the muscle fibres of normal mice studied *in vivo*. J. Physiol. 551, 467–478. https://doi.org/10.1113/jphysiol.2003.045328

Bruusgaard, J.C., Liestøl, K., Gundersen, K., 2006. Distribution of myonuclei and microtubules in live muscle fibers of young, middle-aged, and old mice. J. Appl. Physiol. 100, 2024–2030. https://doi.org/10.1152/japplphysiol.00913.2005

Buckingham, M., Bajard, L., Chang, T., Daubas, P., Hadchouel, J., Meilhac, S., Montarras, D., Rocancourt, D., Relaix, F., 2003. The formation of skeletal muscle: from somite to limb. J. Anat. 202, 59–68. https://doi.org/10.1046/j.1469-7580.2003.00139.x

Cadot, B., Gache, V., Gomes, E.R., 2014. Fast, Multi-Dimensional and Simultaneous Kymograph-Like Particle Dynamics (SkyPad) Analysis. PLoS ONE 9, e89073. https://doi.org/10.1371/journal.pone.0089073

Cadot, B., Gache, V., Vasyutina, E., Falcone, S., Birchmeier, C., Gomes, E.R., 2012. Nuclear movement during myotube formation is microtubule and dynein dependent and is regulated by Cdc42, Par6 and Par3. EMBO Rep. 13, 741–749. https://doi.org/10.1038/embor.2012.89

Cardasis, C.A., Cooper, G.W., 1975. An analysis of nuclear numbers in individual muscle fibers during differentiation and growth: A satellite cell-muscle fiber growth unit. J. Exp. Zool. 191, 347–357. https://doi.org/10.1002/jez.1401910305

Choi, S., Ferrari, G., Tedesco, F.S., 2020. Cellular dynamics of myogenic cell migration: molecular mechanisms and implications for skeletal muscle cell therapies. EMBO Mol. Med. 12. https://doi.org/10.15252/emmm.202012357

Cramer, A.A.W., Prasad, V., Eftestøl, E., Song, T., Hansson, K.-A., Dugdale, H.F., Sadayappan, S., Ochala, J., Gundersen, K., Millay, D.P., 2020. Nuclear numbers in syncytial muscle fibers promote size but limit the development of larger myonuclear domains. Nat. Commun. 11, 6287. https://doi.org/10.1038/s41467-020-20058-7

Denes, L.T., Kelley, C.P., Wang, E.T., 2021. Microtubule-based transport is essential to distribute RNA and nascent protein in skeletal muscle. Nat. Commun. 12, 6079. https://doi.org/10.1038/s41467-021-26383-9

Duguez, S., Féasson, L., Denis, C., Freyssenet, D., 2002. Mitochondrial biogenesis during skeletal muscle regeneration. Am. J. Physiol.-Endocrinol. Metab. 282, E802–E809. https://doi.org/10.1152/ajpendo.00343.2001

Falcone, S., Roman, W., Hnia, K., Gache, V., Didier, N., Lainé, J., Auradé, F., Marty, I., Nishino, I., Charlet-Berguerand, N., Romero, N.B., Marazzi, G., Sassoon, D., Laporte, J., Gomes, E.R., 2014. N- WASP is required for Amphiphysin-2/ BIN 1-dependent nuclear positioning and triad organization in skeletal muscle and is involved in the pathophysiology of centronuclear myopathy. EMBO Mol. Med. 6, 1455–1475. https://doi.org/10.15252/emmm.201404436

Ferreira, L.T., Orr, B., Rajendraprasad, G., Pereira, A.J., Lemos, C., Lima, J.T., Guasch Boldú, C., Ferreira, J.G., Barisic, M., Maiato, H., 2020. α-Tubulin detyrosination impairs mitotic error correction by suppressing MCAK centromeric activity. J. Cell Biol. 219, e201910064. https://doi.org/10.1083/jcb.201910064

Folker, E.S., Baylies, M.K., 2013. Nuclear positioning in muscle development and disease. Front. Physiol. 4. https://doi.org/10.3389/fphys.2013.00363

Forcina, L., Cosentino, M., Musarò, A., 2020. Mechanisms Regulating Muscle Regeneration: Insights into the Interrelated and Time-Dependent Phases of Tissue Healing. Cells 9, 1297. https://doi.org/10.3390/cells9051297

Gache, V., Gomes, E.R., Cadot, B., 2017. Microtubule motors involved in nuclear movement during skeletal muscle differentiation. Mol. Biol. Cell 28, 865–874. https://doi.org/10.1091/mbc.e16-06-0405

Gadadhar, S., Bodakuntla, S., Natarajan, K., Janke, C., 2017. The tubulin code at a glance. J. Cell Sci. jcs.199471. https://doi.org/10.1242/jcs.199471

Ghasemizadeh, A., Christin, E., Guiraud, A., Couturier, N., Abitbol, M., Risson, V., Girard, E., Jagla, C., Soler, C., Laddada, L., Sanchez, C., Jaque-Fernandez, F.-I., Jacquemond, V., Thomas, J.-L., Lanfranchi, M., Courchet, J., Gondin, J., Schaeffer, L., Gache, V., 2021. MACF1 controls skeletal muscle function through the microtubule-dependent localization of extra-synaptic myonuclei and mitochondria biogenesis. eLife 10, e70490. https://doi.org/10.7554/eLife.70490

Goodson, H.V., Jonasson, E.M., 2018. Microtubules and Microtubule-Associated Proteins. Cold Spring Harb. Perspect. Biol. 10, a022608. https://doi.org/10.1101/cshperspect.a022608

Hall, Z.W., Ralston, E., 1989. Nuclear domains in muscle cells. Cell 59, 771–772. https://doi.org/10.1016/0092-8674(89)90597-7

Iqbal, Z., Tawamie, H., Ba, W., Reis, A., Halak, B.A., Sticht, H., Uebe, S., Kasri, N.N., Riazuddin, S., van Bokhoven, H., Abou Jamra, R., 2019. Loss of function of SVBP leads to autosomal recessive intellectual disability, microcephaly, ataxia, and hypotonia. Genet. Med. 21, 1790–1796. https://doi.org/10.1038/s41436-018-0415-8

Jasmin, B.J., Changeux, J.-P., Cartaud, J., 1990. Compartmentalization of cold-stable and acetylated microtubules in the subsynaptic domain of chick skeletal muscle fibre. Nature 344, 673–675. https://doi.org/10.1038/344673a0

Jones, R.A., Reich, C.D., Dissanayake, K.N., Kristmundsdottir, F., Findlater, G.S., Ribchester, R.R., Simmen, M.W., Gillingwater, T.H., 2016. NMJ-morph reveals principal components of synaptic morphology influencing structure–function relationships at the neuromuscular junction. Open Biol. 6, 160240. https://doi.org/10.1098/rsob.160240

Jungbluth, H., Gautel, M., 2014. Pathogenic Mechanisms in Centronuclear Myopathies. Front. Aging Neurosci. 6. https://doi.org/10.3389/fnagi.2014.00339

Jungbluth, H., Wallgren-Pettersson, C., Laporte, J., 2008. Centronuclear (myotubular) myopathy. Orphanet J. Rare Dis. 3, 26. https://doi.org/10.1186/1750-1172-3-26

Kerr, J.P., Robison, P., Shi, G., Bogush, A.I., Kempema, A.M., Hexum, J.K., Becerra, N., Harki, D.A., Martin, S.S., Raiteri, R., Prosser, B.L., Ward, C.W., 2015. Detyrosinated microtubules modulate mechanotransduction in heart and skeletal muscle. Nat. Commun. 6, 8526. https://doi.org/10.1038/ncomms9526

Khairallah, R.J., Shi, G., Sbrana, F., Prosser, B.L., Borroto, C., Mazaitis, M.J., Hoffman, E.P., Mahurkar, A., Sachs, F., Sun, Y., Chen, Y.-W., Raiteri, R., Lederer, W.J., Dorsey, S.G., Ward, C.W., 2012. Microtubules Underlie Dysfunction in Duchenne Muscular Dystrophy. Sci. Signal. 5. https://doi.org/10.1126/scisignal.2002829

Koelle, G.B., Friedenwald, J.S., 1949. A Histochemical Method for Localizing Cholinesterase Activity. Exp. Biol. Med. 70, 617–622. https://doi.org/10.3181/00379727-70-17013

Kreis, T.E., 1987. Microtubules containing detyrosinated tubulin are less dynamic. EMBO J. 6, 2597–2606. https://doi.org/10.1002/j.1460-2075.1987.tb02550.x

Larouche, J.A., Mohiuddin, M., Choi, J.J., Ulintz, P.J., Fraczek, P., Sabin, K., Pitchiaya, S., Kurpiers, S.J., Castor-Macias, J., Liu, W., Hastings, R.L., Brown, L.A., Markworth, J.F., De Silva, K., Levi, B., Merajver, S.D., Valdez, G., Chakkalakal, J.V., Jang, Y.C., Brooks, S.V., Aguilar, C.A., 2021. Murine muscle stem cell response to perturbations of the neuromuscular junction are attenuated with aging. eLife 10, e66749. https://doi.org/10.7554/eLife.66749

Lehka, L., Rędowicz, M.J., 2020. Mechanisms regulating myoblast fusion: A multilevel interplay. Semin. Cell Dev. Biol. 104, 81–92. https://doi.org/10.1016/j.semcdb.2020.02.004

Li, F., Hu, Y., Qi, S., Luo, X., Yu, H., 2019. Structural basis of tubulin detyrosination by vasohibins. Nat. Struct. Mol. Biol. 26, 583–591. https://doi.org/10.1038/s41594-019-0242-x

Liu, W., Ralston, E., 2014. A new directionality tool for assessing microtubule pattern alterations: Assessing Microtubule Pattern Alterations. Cytoskeleton 71, 230–240. https://doi.org/10.1002/cm.21166

Loreti, M., Sacco, A., 2022. The jam session between muscle stem cells and the extracellular matrix in the tissue microenvironment. NPJ Regen. Med. 7, 16. https://doi.org/10.1038/s41536-022-00204-z

Meka, S.R.K., Chacko, L.A., Ravi, A., Chatterjee, K., Ananthanarayanan, V., 2017. Role of Microtubules in Osteogenic Differentiation of Mesenchymal Stem Cells on 3D Nanofibrous Scaffolds. ACS Biomater. Sci. Eng. 3, 551–559. https://doi.org/10.1021/acsbiomaterials.6b00725

Metzger, T., Gache, V., Xu, M., Cadot, B., Folker, E.S., Richardson, B.E., Gomes, E.R., Baylies, M.K., 2012. MAP and kinesin-dependent nuclear positioning is required for skeletal muscle function. Nature 484, 120–124. https://doi.org/10.1038/nature10914

Müller, M., Ringer, K., Hub, F., Kamm, N., Worzfeld, T., Jacob, R., 2021. TTL-Expression Modulates Epithelial Morphogenesis. Front. Cell Dev. Biol. 9, 635723. https://doi.org/10.3389/fcell.2021.635723

Nachlas, M.M., Margulies, S.I., Seligman, A.M., 1960. A Colorimetric Method for the Estimation of Succinic Dehydrogenase Activity. J. Biol. Chem. 235, 499–503. https://doi.org/10.1016/S0021-9258(18)69554-7

Osseni, A., Ravel-Chapuis, A., Thomas, J.-L., Gache, V., Schaeffer, L., Jasmin, B.J., 2020. HDAC6 regulates microtubule stability and clustering of AChRs at neuromuscular junctions. J. Cell Biol. 219, e201901099. https://doi.org/10.1083/jcb.201901099

Oury, J., Liu, Y., Töpf, A., Todorovic, S., Hoedt, E., Preethish-Kumar, V., Neubert, T.A., Lin, W., Lochmüller, H., Burden, S.J., 2019. MACF1 links Rapsyn to microtubule- and actin-binding proteins to maintain neuromuscular synapses. J. Cell Biol. 218, 1686–1705. https://doi.org/10.1083/jcb.201810023

Pagnamenta, A.T., Heemeryck, P., Martin, H.C., Bosc, C., Peris, L., Uszynski, I., Gory-Fauré, S., Couly, S., Deshpande, C., Siddiqui, A., Elmonairy, A.A., WGS500 Consortium, Genomics England Research Consortium, Jayawant, S., Murthy, S., Walker, I., Loong, L., Bauer, P., Vossier, F., Denarier, E., Maurice, T., Barbier, E.L., Deloulme, J.-C., Taylor, J.C., Blair, E.M., Andrieux, A., Moutin, M.-J., 2019. Defective tubulin detyrosination causes structural brain abnormalities with cognitive deficiency in humans and mice. Hum. Mol. Genet. 28, 3391–3405. https://doi.org/10.1093/hmg/ddz186

Peris, L., Wagenbach, M., Lafanechère, L., Brocard, J., Moore, A.T., Kozielski, F., Job, D., Wordeman, L., Andrieux, A., 2009. Motor-dependent microtubule disassembly driven by tubulin tyrosination. J. Cell Biol. 185, 1159–1166. https://doi.org/10.1083/jcb.200902142

Quiram, P.A., Ohno, K., Milone, M., Patterson, M.C., Pruitt, N.J., Brengman, J.M., Sine, S.M., Engel, A.G., 1999. Mutation causing congenital myasthenia reveals acetylcholine receptor β/δ subunit interaction essential for assembly. J. Clin. Invest. 104, 1403–1410. https://doi.org/10.1172/JCI8179

Rahman, F.A., Quadrilatero, J., 2021. Mitochondrial network remodeling: an important feature of myogenesis and skeletal muscle regeneration. Cell. Mol. Life Sci. 78, 4653–4675. https://doi.org/10.1007/s00018-021-03807-9

Ralston, E., Hall, Z.W., 1992. Restricted distribution of mRNA produced from a single nucleus in hybrid myotubes. J. Cell Biol. 119, 1063–1068. https://doi.org/10.1083/jcb.119.5.1063

Relaix, F., Bencze, M., Borok, M.J., Der Vartanian, A., Gattazzo, F., Mademtzoglou, D., Perez-Diaz, S., Prola, A., Reyes-Fernandez, P.C., Rotini, A., Taglietti, 2021. Perspectives on skeletal muscle stem cells. Nat. Commun. 12, 692. https://doi.org/10.1038/s41467-020-20760-6

Robison, P., Caporizzo, M.A., Ahmadzadeh, H., Bogush, A.I., Chen, C.Y., Margulies, K.B., Shenoy, V.B., Prosser, B.L., 2016. Detyrosinated microtubules buckle and bear load in contracting cardiomyocytes. Science 352, aaf0659. https://doi.org/10.1126/science.aaf0659

Roulier, E.M., Fyrberg, C., Fyrberg, E., 1992. Perturbations of Drosophila alpha-actinin cause muscle paralysis, weakness, and atrophy but do not confer obvious nonmuscle phenotypes. J. Cell Biol. 116, 911–922. https://doi.org/10.1083/jcb.116.4.911

Sanyal, C., Pietsch, N., Ramirez Rios, S., Peris, L., Carrier, L., Moutin, M.-J., 2021. The detyrosination/re-tyrosination cycle of tubulin and its role and dysfunction in neurons and cardiomyocytes. Semin. Cell Dev. Biol. S1084952121003141. https://doi.org/10.1016/j.semcdb.2021.12.006

Sbalzarini, I.F., Koumoutsakos, P., 2005. Feature point tracking and trajectory analysis for video imaging in cell biology. J. Struct. Biol. 151, 182–195. https://doi.org/10.1016/j.jsb.2005.06.002

Schmidt, M., Schüler, S.C., Hüttner, S.S., von Eyss, B., von Maltzahn, J., 2019. Adult stem cells at work: regenerating skeletal muscle. Cell. Mol. Life Sci. 76, 2559–2570. https://doi.org/10.1007/s00018-019-03093-6

Smith, L.R., Barton, E.R., 2014. SMASH – semi-automatic muscle analysis using segmentation of histology: a MATLAB application. Skelet. Muscle 4, 21. https://doi.org/10.1186/2044-5040-4-21

Valenzuela, P., Quiroga, M., Zaldivar, J., Rutter, W.J., Kirschner, M.W., Cleveland, D.W., 1981. Nucleotide and corresponding amino acid sequences encoded by α and β tubulin mRNAs. Nature 289, 650–655. https://doi.org/10.1038/289650a0

van der Laan, S., Lévêque, M.F., Marcellin, G., Vezenkov, L., Lannay, Y., Dubra, G., Bompard, G., Ovejero, S., Urbach, S., Burgess, A., Amblard, M., Sterkers, Y., Bastien, P., Rogowski, K., 2019. Evolutionary Divergence of Enzymatic Mechanisms for Tubulin Detyrosination. Cell Rep. 29, 4159-4171.e6. https://doi.org/10.1016/j.celrep.2019.11.074

Wanamaker, C.P., Christianson, J.C., Green, W.N., 2003. Regulation of Nicotinic Acetylcholine Receptor Assembly. Ann. N. Y. Acad. Sci. 998, 66–80. https://doi.org/10.1196/annals.1254.009

Wang, S., Reuveny, A., Volk, T., 2015. Nesprin provides elastic properties to muscle nuclei by cooperating with spectraplakin and EB1. J. Cell Biol. 209, 529–538. https://doi.org/10.1083/jcb.201408098

Complementary data 2:

From *Svbp* KO MuSCs behaviour *in vitro* to long-term impact of reduced MTs detyrosination in myofibers *in vivo*.

I) Aim of the experiments

Our studies on MuSCs associated with isolated myofibers *ex vivo* showed increased activation, proliferation and differentiation for MuSCs at the periphery *Svbp* KO myofibers compared to MuSCs at the periphery of WT myofibers. To confirm these results, we studied the behavior of MuSCs isolated from 4.5-month-old WT and *Svbp* KO skeletal muscles *in vitro*.

In addition, our previous experiments from MACF1 KO mice suggested that disorganized MTs can cause subcellular changes in skeletal myofibers which appear or engrave slowly with age. Since all of our studies on *Svbp* KO mice were performed on young 4.5-month-old mice, we decided to analyze skeletal muscles of aged 22-month-old WT and *Svbp* KO mice and look for eventual changes in any of the phenotypes concerning MTs, myonuclei, NMJs, or sarcomeres. Moreover, our immunofluorescence microscopy results were indicating a shortening of sarcomeric distance in *Svbp* KO myofibers compared to WT myofibers both *in vitro* and *in vivo*. Since in myofibers, sarcomeres are in tight connection with T-Tubules and sarcoplasmic reticulum, we performed electron microscopy to study and compare the ultrastructure of EDL or TA muscles from 4.5- and 22-month-old WT and *Svbp* KO mice.

II) Procedure of experiments

1) MuSCs isolation, culture and analysis

4.5-month-old WT and *Svbp* KO mice were used to isolated and purify MuSCs from whole hindlimb muscles following the protocol provided for MACS satellite cell isolation kit (Miltenyi Biotec, 130-104-268). Briefly, following hindlimb muscles dissection and digestion, non-target cells were magnetically labeled and depleted using MACS magnetic columns. Following purification, MuSCs were maintained on culture on collagen-coated dishes in proliferation culture medium (Ham's F10 nutrient mix (Gibco, 11550043), 20% FBS (Gibco, 10270-106), 1% penicillin/streptomycin (Gibco, 15140-122), and 5 ng/ml of basic FGF (Miltenyi Biotec, 130-105-786)).

To study MuSCs subpopulations, same number of MuSCs were plated on 1% matrigel coated-dish (Corning, 356231) and maintained in proliferation culture medium. MuSCs were fixed and stained for fluorescence microscopy imaging as previously described in the article.

To study MuSCs proliferation rate, EdU Click-iT kit (ThermoFisher Scientific, C10340) was used as instructed by the manufacturer. MuSCs proliferation rate was quantified either by flow cytometry (for MuSCs plated on collagen) or by analyzing fluorescent microscopy images (for MuSCs plated on matrigel).

2) Electronic microscopy sample preparation and imaging

For electronic microscopy, TA or EDL muscles of 4.5- or 22-month-old WT and *Svbp* KO mice were dissected and fixed in 2% glutaraldehyde for 2H at 4°C. Samples were washed three times

for 1H at 4°C and post-fixed with 2% OsO4 1H at 4°C. Then tissues were dehydrated with an increasing ethanol gradient (5 min in 30%, 50%, 70%, 95%) and tree times for 10 min in absolute ethanol. Impregnation was performed with Epon A (75%) plus Epon B (25%) plus DMP30 (1.7%). Inclusion was obtained by polymerization at 60°C for 72H. Ultrathin sections (approximately 70nm thick) were cut on a UC7 (Leica) ultra-microtome, mounted on 200 mesh copper grids coated with 1:1000 polylysine, and stabilized for 1 day at room temperature and contrasted with uranyl acetate and lead citrate. Sections were acquired with a Jeol 1400JEM (Tokyo, Japan) transmission electron microscope, 80Kv, equipped with a Orius 600 camera and Digital Micrograph.

3) complementary experiments

Western blots, and qRT-PCRs, in addition to myofibers isolation, immunofluorescence stanning, microscopy imaging and analysis were all performed on TA or G muscles of aged 22-month-old WT and *Svbp* KO mice exactly as previously described in the article.

III) Results and conclusions

1) *Svbp* KO MuSCs behavior *in vitro*

To study MuSCs proliferation rate, collagen-seeded MuSCs were incubated with EdU prior to fixation (Figure 31A). Following, MuSCs were collected, fixed and prepared for analysis by flow cytometer as instructed for EdU Click-iT kit. Our results indicated a 12% increase in percentage of proliferating MuSCs isolated from *Svbp* KO mice compared to WT MuSCs, confirming our previous observations on MuSCs associated with myofibers *ex vivo* (Figure 31B).

To further study different MuSCs subpopulations *in vitro*, isolated MuSCs from WT or *Svbp* KO mice were seeded on matrigel-coated dishes. Following EdU treatment, MuSCs were fixed and stained with PAX7 antibody and Dapi (Figure 31C). To our surprise, the percentage of PAX7+ EdU+ MuSCs isolated from *Svbp* KO mice was similar to MuSCs isolated from WT mice (Figure 31D). These results were not in complete accordance with our previous observations, however, since our studies on MuSCs associated with isolated myofibers also indicated an increase in MuSCs differentiation, we questioned whether a premature differentiation is occurring among *Svbp* KO isolated MuSCs *in vitro*. To address the question, isolated matrigel-seeded MuSCs were stained with MyoD and MyoG antibodies in addition to phalloidin and imaged by fluorescent microscopy (Figure 32A). once again, we observed no significant difference in the percentage of MyoD+ MyoG+ MuSCs among *Svbp* KO MuSCs compared to WT MuSCs (Figure 32B). However, we were surprised to observe *that Svbp* KO MyoG+ MuSCs are smaller than WT MuSCs (Figure 32C). This was further confirmed when we used actin staining to visualize the limits of MyoG+ MuSCs and we observed a reduction in *Svbp* KO MyoG+ MuSCs area and feret compared to WT MyoG+ MuSCs (Figure 32D-E).

Collectively, our different results from collagen- or matrigel-seeded MuSCs suggest that *Svbp* KO MuSCs may be smaller and more sensitive to the stiffness of their microenvironment compared to WT MuSCs.

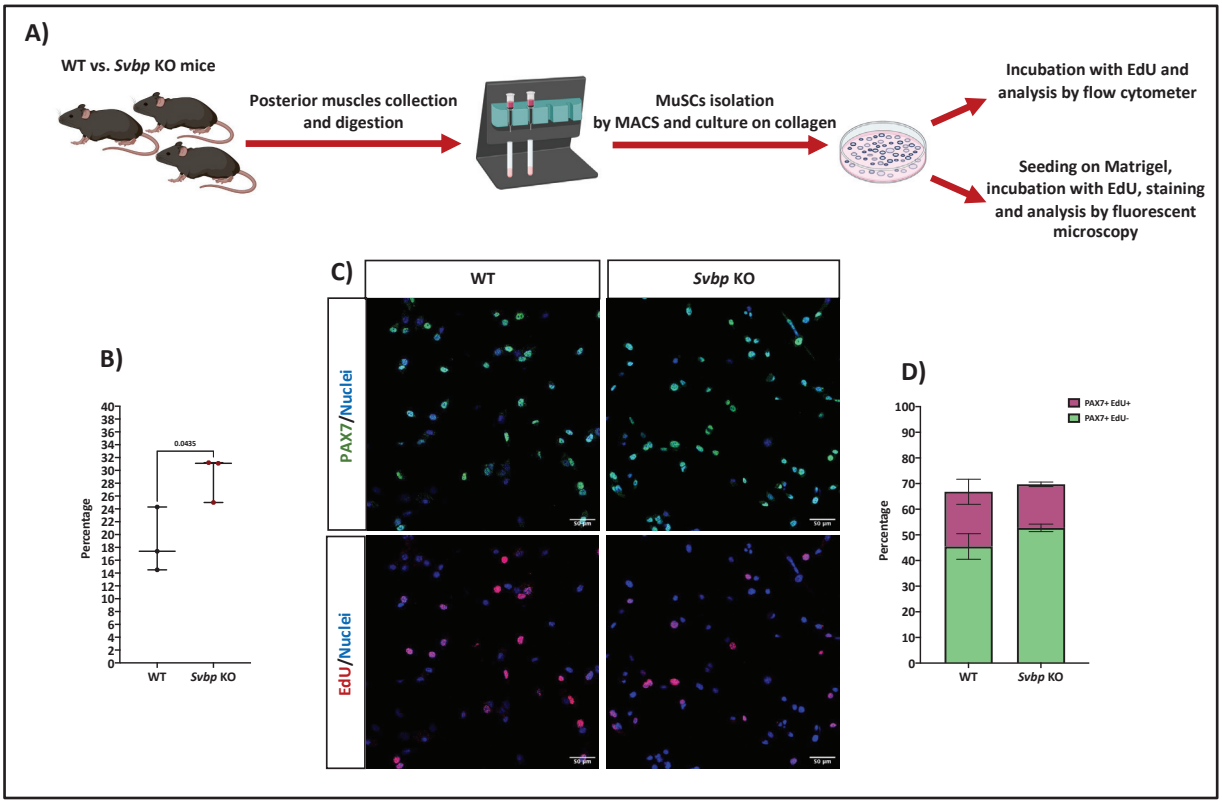

Figure 31: Analysis of *Svbp* KO MuSCs proliferation *in vitro*.
(A) Scheme presenting the sequential steps of adult MuSCs isolation using MACS technique and their culture *in vitro*. (B) Flow cytometry results presenting the percentage of EdU+ proliferating MuSCs detected among WT or *Svbp* KO collagen-seeded MuSCs in proliferation culture medium. Three mice per group were studied. Line is set median. p values are calculated by Student's t test. (C) Immunofluorescence staining (10X) of PAX7 (green) and nuclei (blue) in upper panels, in addition to EdU (red) and nuclei (blue) in lower panels in primary MuSCs isolated from WT (left panels) or *Svbp* KO (right panels) mice. Scale Bar = 50 µm. (D) Quantification of the percentage of MuSCs isolated from WT or *Svbp* KO mice (as presented in panel C) and positive for PAX7 only (in green) or PAX7 and EdU (in purple). At least three mice per group were studied. Mean values (with SEM) are presented.

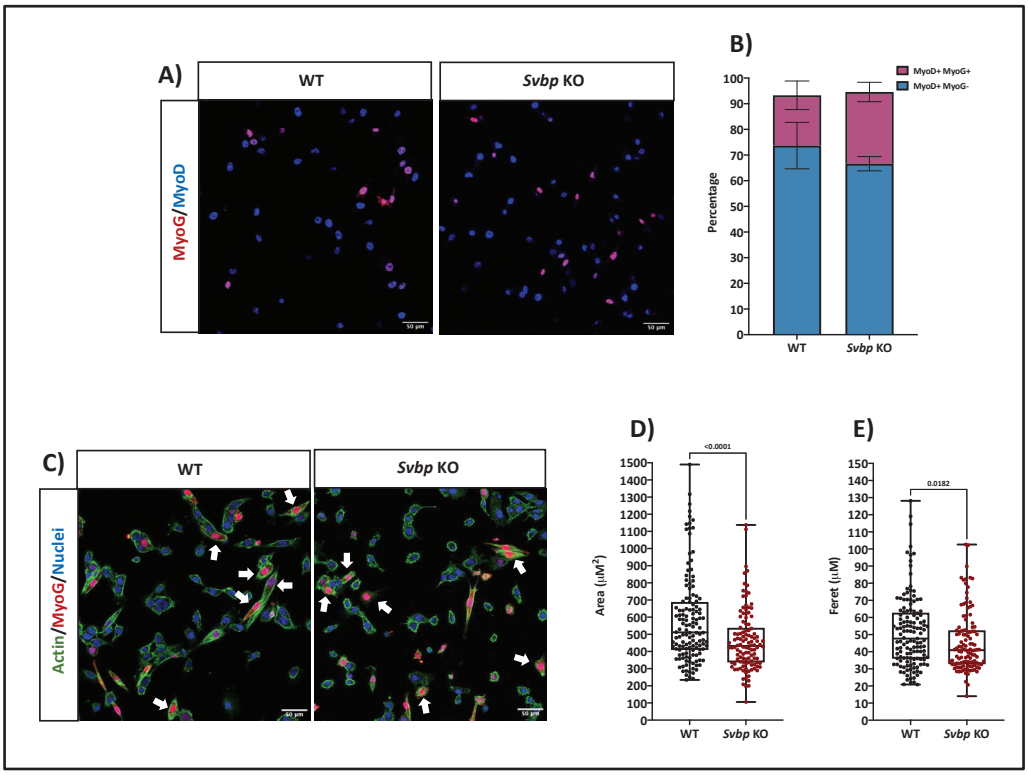

Figure 32: Analysis of *Svbp* KO MuSCs behavior and characteristics *in vitro*.
(A) Immunofluorescence staining (10X) of MyoD (blue) and MyoG (red) in primary MuSCs isolated from WT (left panel) or *Svbp* KO (right panel) mice. Scale Bar = 50 µm. (B) Quantification of the percentage of MuSCs isolated from WT or *Svbp* KO mice (as presented in panel A) and positive for MyoD only (in blue) or MyoD and MyoG (in purple). At least three mice per group were studied. Mean values (with SEM) are presented. (C) Immunofluorescence staining (10X) of Actin (green), MyoG (red) and myonuclei (blue) in primary myoblasts isolated from WT (left panel) or *Svbp* KO (right panel) mice. White arrows point to example MyoG+ cells. Scale Bar = 50 µm. (D-E) Area (D) and feret (E) of MyoG positive cells quantified on primary myoblasts isolated from WT or *Svbp* KO mice (as presented in panel C). Panel was generated from data from at least three individual experimental mice. Line is set median. p values are calculated by Student's t test.

2) long-term impact of reduced MT detyrosination in myofibers *in vivo*

First, we confirmed the reduction of detyrosinated MTs and accumulation of tyrosinated MTs in total protein extracts of G muscles from 22-month-old *Svbp* KO mice compared to control mice (Figure 33A).

Next, we examined muscles weight and organization. We observed that just like 4.5-month-old mice, 22-month-old *Svbp* KO mice have a slight reduction in total body weight compared to control mice, however, TA, EDL, and G muscles weight relative to total body weight showed no significant difference between WT and *Svbp* KO mice (Figure 33B-E). Our studies on cross-sectioned TA muscles showed similar myofibers number, CSA distribution, and feret distribution between 22-month-old WT and *Svbp* KO mice (Figure 34A-C). In addition, our qRT-PCR experiments on total mRNA extracts of G muscles from 22-month-old mice showed similar levels of *MyoG*, *MyoD* or *PAX7* genes expression in WT and *Svbp* KO mice (Figure 34D-F). These data suggested the absence of muscle regeneration in 22-month-old *Svbp* KO mice.

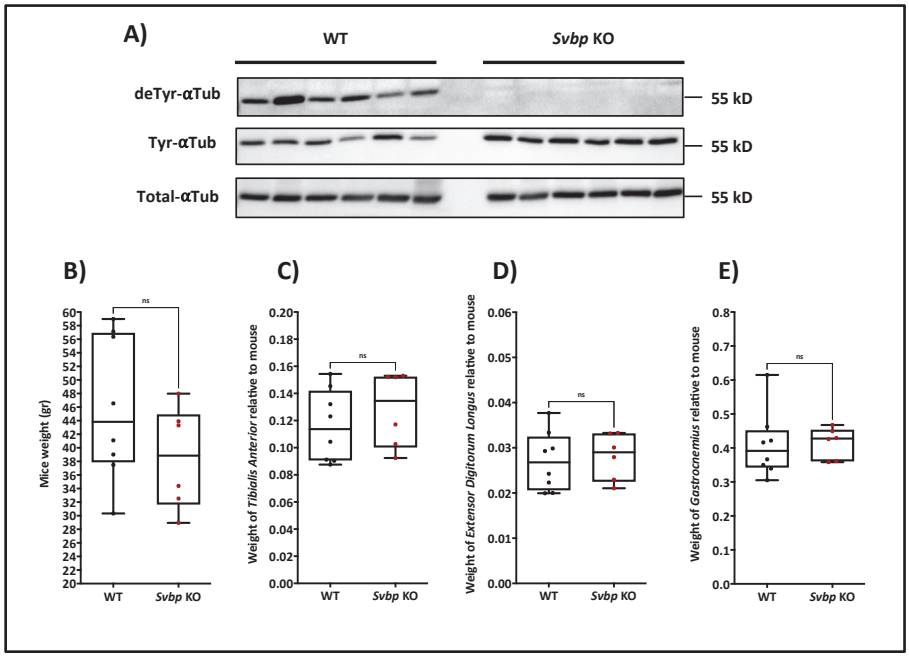

Figure 33: Comparison of muscles weight between 22-month-old WT and *Svbp* KO mice. (A) Western blot analysis of detyrosinated α-tubulin and tyrosinated α-tubulin in total extracts from *gastrocnemius* muscles of 22-month-old WT and *Svbp* KO mice. total α-tubulin is used as loading control. (B-E) Evaluation of total body weight (B) and relative muscle weight to total body weight for *tibialis anterior* (C) *extensor digitorum longus* (D) and *gastrocnemius* (E) from each mouse studied on a group of at least six individual WT and *Svbp* KO mice of 22-month-old. Line is set median. Ns stands for not significant as calculated by Student's t test.

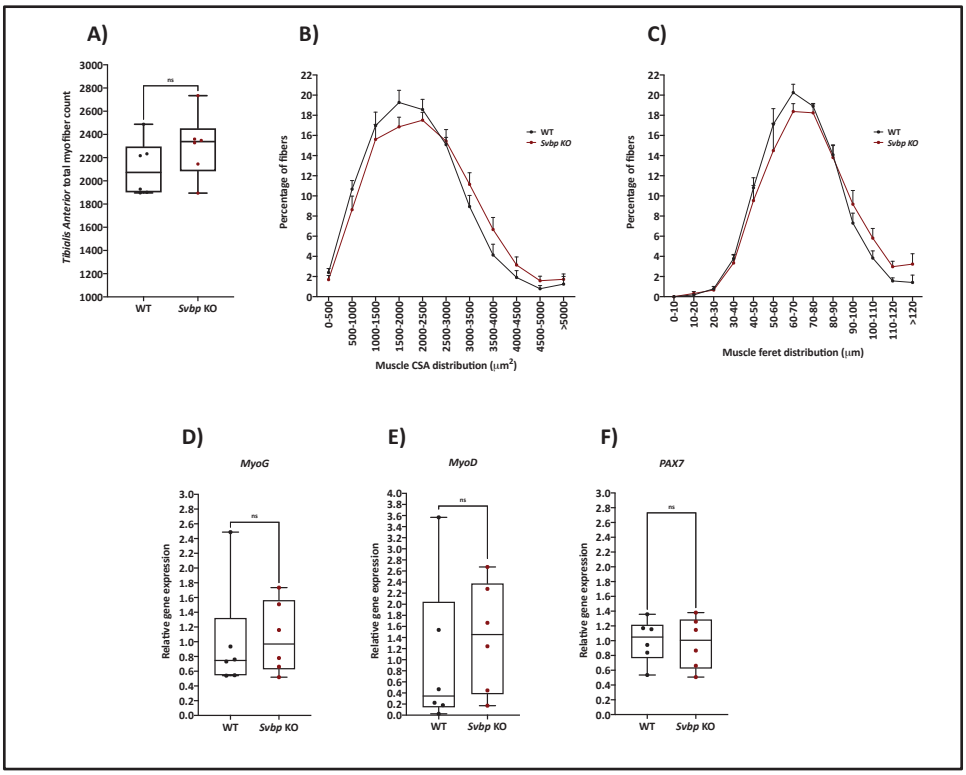

Figure 34: Analysis of 22-month-old *Svbp* KO mice myofibers characteristics and genes expression.

(A) Total number of myofibers per *tibialis anterior* quantified on cross section of muscles from six WT and *Svbp* KO mice of 22-month-old. Line is set median. Ns stands for not significant as determined by Student's t test. (B-C) Distribution of myofibers cross section area (B) and feret (C) in *tibialis anterior* from six individual WT and *Svbp* KO mice of 22-month-old. Mean values (with SEM) are showing. (D-F) QRT-PCR results presenting relative gene expression levels for *MyoG* (D), *MyoD* (E) and *PAX7* (F) in total mRNA extracts from *gastrocnemius* of WT and *Svbp* KO mice of 22-months-old. Following the calculation of relative target gene expression level in reference to housekeeping genes for each mouse, the mean expression level of each target gene was calculated for the group of WT mice. Next, the expression level of each WT and *Svbp* KO mouse was normalized to the previously calculated mean value to determine the relative gene expression. Line is set at median. Ns stands for not significant as determined by Student's t test.

To our surprise, our microscopy analysis of TA cross-sectioned muscles revealed an increase in number of myofibers with strong SDH intensity in 22-month-old *Svbp* KO mice compared to WT mice (Figure 35A). This result was confirmed by the observation of an increase in SDH level in protein extracts from G muscles of 22-month-old *Svbp* KO mice compared to WT mice (Figure 35B). In the absence of muscle regeneration, increased SDH level can be a sign of aberrant mitochondrial activity or increased mitochondrial number, as we had observed in MACF1 KO myofibers. However, our qRT-PCR results from total mRNA of G muscles indicated no difference in genes expression levels of *PGC1α* and *Sarcolipin* (markers of mitochondrial biogenesis) or *DNM1* and *DNM2* (markers of mitochondrial fusion and fission) between 22-month-old WT and *Svbp* KO mice (Figure 35C-F). These data suggest that increased SDH in *Svbp* KO mice may originate from altered mitochondrial activity.

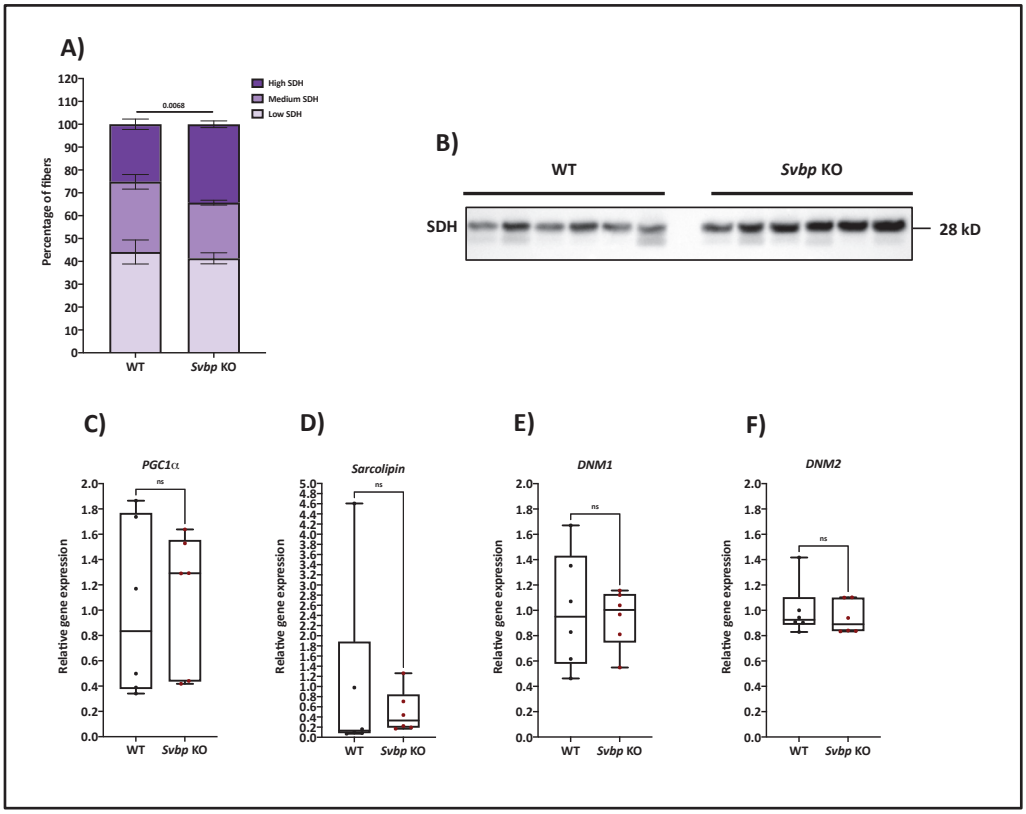

Figure 35: Analysis of mitochondrial activity and mitochondrial-related genes expression in 22-month-old *Svbp* KO mice muscles.
(A) Quantification of the SDH activity relative to myofibers distribution in WT and *Svbp* KO mice of 22-months-old. five mice were studied per each group. Mean values (with SEM) are presented. p value is calculated by Student's t test. (B) Western blot analysis of SDH protein level in total extracts from *gastrocnemius* muscles of 22-month-old WT and *Svbp* KO mice. (C-F) QRT-PCR results presenting relative gene expression levels for *PGC1α* (C), *Sarcolipin* (D), *DNM1* (E), and *DNM2* (F) in total mRNA extracts from G of WT and *Svbp* KO mice of 4.5 months old. Following the calculation of relative target gene expression level in reference to housekeeping genes for each mouse, the mean expression level of each target gene was calculated for the group of WT mice. Next, the expression level of each WT and *Svbp* KO mouse was normalized to the previously calculated mean value to determine the relative gene expression. Line is set at median. Ns stands for not significant as determined by Student's t test.

On myofibers longitudinal axis, we could see that MT disorganization is preserved in TA myofibers of 22-month-old *Svbp* KO mice, reflected by reduction of score for 80° to 96° oriented MTs compared to WT myofibers, measured by TeTD plugin on total α-tubulin staining (Figure 36A). Signs of increased myonuclei per myofibers could still be observed as our measurements indicated reduced distance between adjacent myonuclei and reduced area per myonuclei at the periphery of myofibers in 22-month-old *Svbp* KO mice compared to WT mice (Figure 36B-C). Interestingly, we observed a reduction in area and feret of myonuclei at the periphery of 22-month-old *Svbp* KO myofibers compared to WT myofibers which was not observed in 4.5-month-old mice (Figure 36D-E). However, no difference could be observed in myonuclei roundness between myonuclei at the periphery of 22-month-old WT and *Svbp* KO myofibers (Figure 36F).

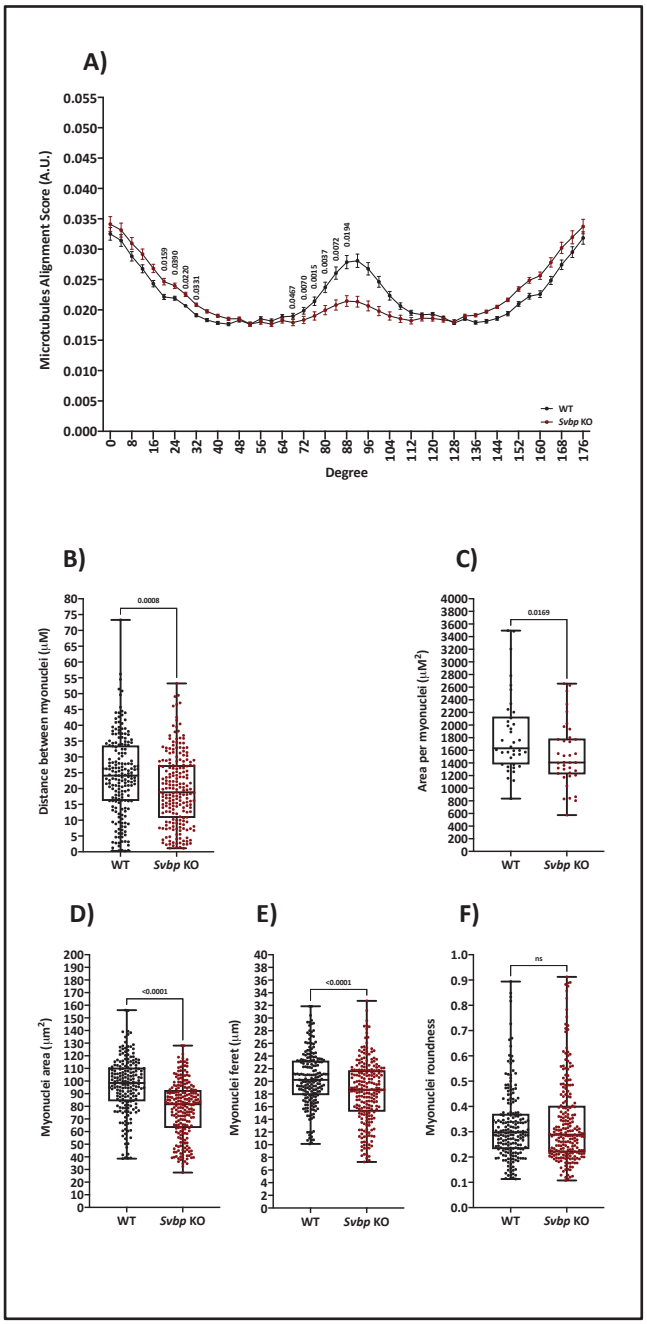

Figure 36: Analysis of MTs and myonuclei at the periphery of 22-month-old *Svbp* KO mice.
(A) Microtubules network organization analysis of total α-tubulin staining using TeDT software on isolated myofibers obtained from six WT and *Svbp* KO mice of 22-month-old. The final generated graph presents a global score for each given degree of microtubules orientation, with 0° and 180° degrees corresponding to the longitudinal microtubules and 90° degrees corresponding to the transverse microtubules. Mean values (with SEM) are presented. p values are calculated by Student's t test. (B-F) Quantification of distance between neighboring myonuclei (B), myonuclei feret (C), myonuclei area (D), myonuclei feret (E), and myonuclei roundness (F) measured on isolated myofibers from *tibialis anterior* of WT and *Svbp* KO mice of 22-months-old. Six individual mice (with at least three myofibers per mouse) were studied in each group. Line is set at median. p values are calculated by Student's t test. Ns stands for not significant.

Concerning NMJs, their area and number of synaptic myonuclei remained indifference between 22-month-old WT and *Svbp* KO myofibers, as it had already been observed in younger 4.5-month-old myofibers (Figure 37A-B). However, while NMJs fragmentation level remained similar between 4.5- and 22-month-old *Svbp* KO myofibers, NMJs from 22-month-old WT showed the same number of fragments as 22-month-old *Svbp* KO, indicating an increase in WT NMJs fragmentation from 4.5- to 22-month-old myofibers, which could be due to NMJs degeneration with aging (Figure 37C) (Rudolf et al., 2014). In parallel, we could no longer detect a difference in expression level of *AChRβ* subunit between *Svbp* KO and WT mice at the age of 22-month-old, which was previously observed between 4.5-month-old mice (Figure 37D). The expression level of *α* and *ε AChRs* subunits remained similar between 22-month-old WT and *Svbp* KO mice, which corelate with our previous results (Figure 37E-F).

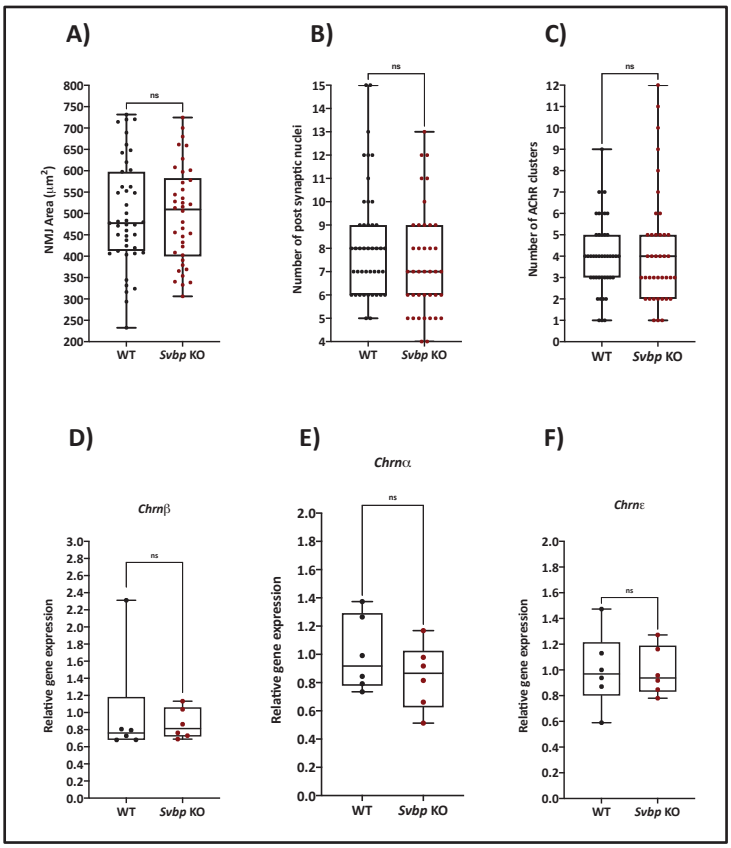

Figure 37: Analysis of NMJs at the periphery of 22-month-old *Svbp* KO mice.
(A-C) Quantification of post synaptic NMJs area (A), number of AChR clusters (B) and number of post synaptic myonuclei (C) measured on myofibers isolated from *tibialis anterior* of WT and *Svbp* KO mice of 22-month-old. Six individual mice (with at least three myofibers per mouse) were studied in each group. Line is set at median. Ns stands for not significant as indicated by Student's t test. (D-F) QRT-PCR results presenting relative gene expression levels for *Chrnβ* (D), *Chrnα* (E) and *Chrnε* (F) in total mRNA extracts from *gastrocnemius* of WT and *Svbp* KO mice of 22-months-old. Following the calculation of relative target gene expression level in reference to housekeeping genes for each mouse, the mean expression level of each target gene was calculated for the group of WT mice. Next, the expression level of each WT and *Svbp* KO mouse was normalized to the previously calculated mean value to determine the relative gene expression. Line is set at median. Ns stands for not significant as indicated by Student's t test.

When it comes to sarcomeres, our measurements indicated the same reduction in the sarcomeric distance in TA myofibers of 22-month-old *Svbp* KO compared to WT myofibers (Figure 38A). However, electronic microscopy images of 22-month-old EDL muscles from WT and *Svbp* KO mice suggested untouched T-Tubules organization in the absence of MT detyrosination in *Svbp* KO mice compared to WT mice (Figure 38B). Surprisingly, our electronic microscopy images suggested the accumulation of glycogen within TA muscles of 4.5-month-old *Svbp* KO mice compared to WT mice (Figure 38C). To dig further, we studied the phosphorylation of glycogen synthase kinase 3 α and β (GSK3α/β). When not phosphorylated, GSK3α and β can themselves phosphorylate glycogen synthase and reduce its activity (Welsh et al., 1996). However, phosphorylation of GSK3α and β, on Ser9 and Ser21 respectively, results in their inactivation and thus increased glycogenesis (Cross et al., 1995; Srivastava and Pandey, 1998). Using a polyclonal antibody that targets both GSK3α Ser9 and GSK3β Ser21, we saw a significant increase in GSK3α Ser9 phosphorylation level and a tendency of increase in GSK3β Ser21 phosphorylation level, while the total GSK3α and β proteins level remained untouched (Figure 38D-H).

Altogether, these experiments confirm that in addition to previously described phenotypes for young *Svbp* KO mice, long-term absence of MT detyrosination can result in surplus subcellular changes in myofibers, such as reduced myonuclei area and increased number of myofibers with high SDH activity. In addition, we discovered that in 4.5-month-old *Svbp* KO mice, glycogenesis is increased, most certainly due to disrupted GSK3 activity.

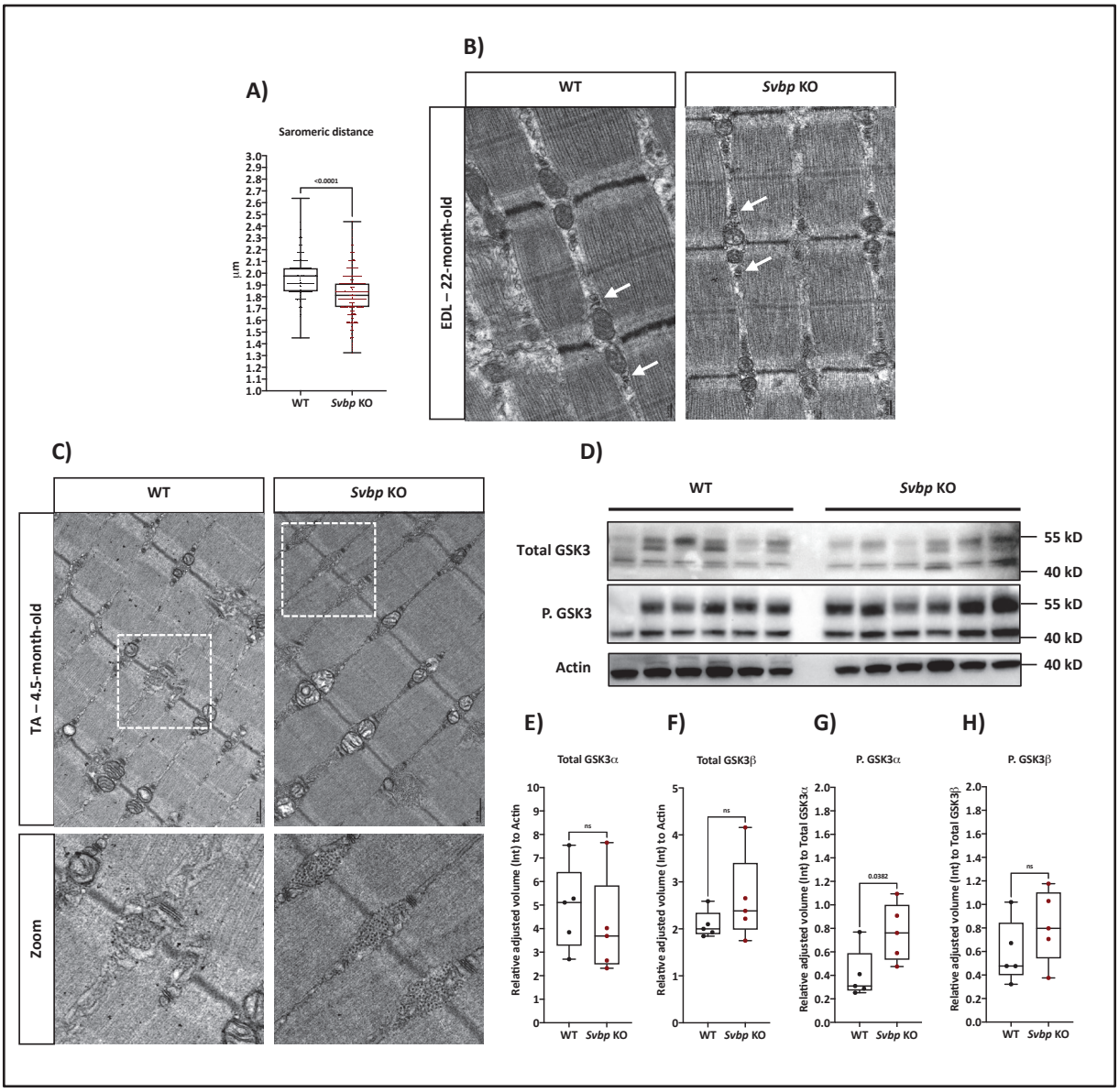

Figure 38: Analysis of young and aged *Svbp* KO muscles by electronic microscopy.
(A) Quantification of distance between adjacent sarcomeres measured on isolated myofibers from *tibialis anterior* of WT and *Svbp* KO mice of 22-month-old. Six individual mice (with at least three myofibers per mouse) were studied in each group. Line is set at median. p values are calculated by Student's t test. (B) Representative electron microscopy images of sarcomeres and T-Tubule organization within EDL muscles from 22-month-old WT (left panel) and *Svbp* KO (right panel) mice. White arrows point to representative T-Tubule. Scale Bar = 0.2 µm. (C) Representative electron microscopy images of myofibrils organization within TA muscles from 4.5-month-old WT (left panels) and *Svbp* KO (right panels) mice. White cages represent the areas showed in zoom panels. Scale Bar = 0.5 µm. (D) Western blot analysis of total and phosphorylated α- (upper bands) or β- (lower bands) GSK3 protein levels in total extracts from *gastrocnemius* muscles of 4.5-month-old WT and *Svbp* KO mice. Actin is used as loading control. (E-H) Adjusted protein volume (Int) of total GSK3α (E) and total GSK3β (F) relative to Actin in addition to adjusted protein volume (Int) of phosphorylated GSK3α (G) and phosphorylated GSK3β (H) relative to the corresponding total protein quantified by western blot. Each category groups six individual mice. Line is set at median. Ns stands for not significant; p values are calculated by Student's t test.

Study 3

Developing a motor neuron/myofiber co-culture to increase myofibers and MTs network maturity *in vitro*.

I) Aim of the experiments

Our *in vitro* mouse primary myoblasts culture is a great experimental source which allows us to develop contractile myofibers and study the evolution of events such as myonuclei positioning with myogenesis. However, this system shows limits in MT network maturation, as MTs form longitudinal chains along myofibers *in vitro* compared to gride-like network within myofibers *in vivo* (Figure 39A-B).

The limit in myofibers maturation is even higher for myofibers developed from human primary myoblasts *in vitro*, stated by the persisting central myonuclei and lack of sarcomeres formation within myofibers in addition to absence of myofibers contraction. In these myofibers, MTs are curly and show longitudinal organization (Figure 39C).

Increasing myofibers and MT maturity could not be achieved by an increase of differentiation duration, as myofibers of mouse origin begin to fatigue and collapse after twelve days of differentiation *in vitro*, and myofibers of human origin do not show any subcellular sign of maturation even 30 days post differentiation *in vitro*.

Since motor neurons arrival and NMJs formation are essential for proper skeletal muscle embryonic development and maturation (Sohal and Holt, 1980), we aimed to increase the maturity of our *in vitro* myofibers by developing a motor neuron/myofibers co-culture system.

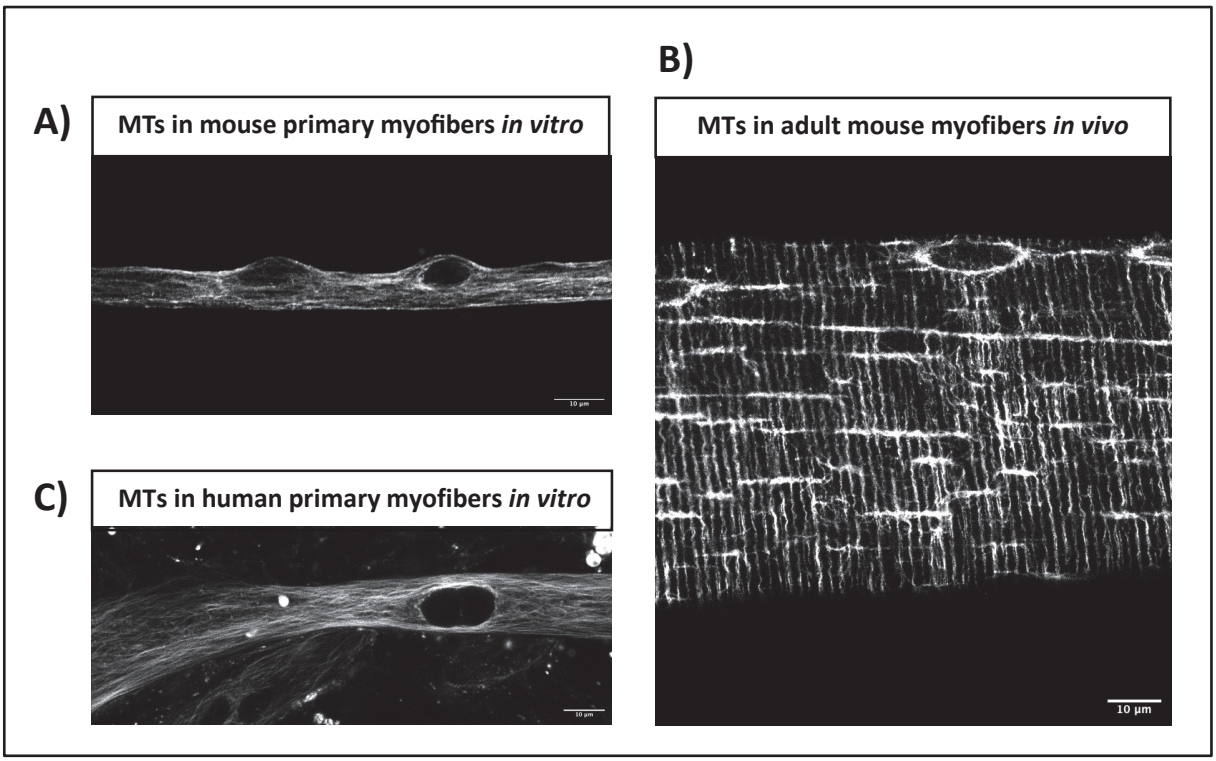

Figure 39: Comparing MT organization between myofibers developed *in vitro* or *in vivo*. (A-C) representative confocal microscopy images of MT organization in mature mouse myofiber in vitro (A), mature mouse *tibialis anterior* myofiber in vivo (B) and human myofiber in vitro (C). Scale Bar = 10 µm.

II) Procedure of experiments

1) Motor neurons isolation

The co-culture experiments were performed in collaboration with Dr. Arnaud Jacquier (Institut NeuroMyoGene, Lyon, France), who is a specialist in motor neurons isolation, from rat embryos, and subsequently their culture (Jacquier et al., 2019). For every experiment, freshly isolated motor neurons were directly used for co-culture development.

2) Mouse primary myoblasts isolation and simple culture

Hindlimb muscles from 6 days pups were extracted and digested with collagenase (Sigma, C9263-1G) and dispase (Roche, 04942078001). After a pre-plating step to discard contaminant cells such as fibroblasts, myoblasts were cultured on 1% matrigel coated-dish (Corning, 356231) in growth media (IMDM (Gibco, 21980-032), 20% fetal bovine serum (Gibco, 10270-106), 10% chicken embryo extract (USBiological, C3999) and 1% penicillin-streptomycin (Gibco, 15140-122)). When reached to 90% of confluence, myocytes were induced to differentiate in myotubes for 2-3 days in differentiation media (IMDM (Gibco, 21980-032), 2% of horse serum (Gibco, 16050-122) and 1% penicillin-streptomycin (Gibco, 15140-122)). Myotubes were then covered by a concentrated layer of matrigel and maintained for up to 10 days in differentiation culture medium. Culture medium was changed every two days.

3) Human primary myoblasts simple culture

Human primary myoblasts were gifted by Dr. Thomas Laumonier (Cell Therapy & Musculoskeletal Disorders, Geneva University, Geneva, Switzerland). Myoblasts were isolated from healthy patients' biopsies and were used for our experiments indifferent to the sex or age of the donners.

myoblasts were cultured on 1% matrigel coated-dish (Corning, 356231) in growth media (Ham's F10 nutrient mix (Gibco, 11550043) completed with 15% FBS (Gibco, 10270-106), 0.5 mg/ml of BSA (Sigma, A9418), 0.5 mg/ml of Fetuin (Sigma, F2379), 0.39 µg/ml of Dexamethasone, 0.04 mg/ml of Insulin (Sigma, I5500), 100 µg/ml of Pyruvate (Sigma, P4562), 50 µg/ml of Uridine (Sigma, U3003), 5 µg/ml of Gentamycin (Gibco, 15710064), and Creatine (Sigma, C3630) at 1mM). When reached to 90% of confluence, myocytes were induced to differentiate in myotubes for 2-3 days in differentiation media (DMEM completed with 0.5 mg/ml of BSA (Sigma, A9418), 0.01 mg/ml of Insulin (Sigma, I5500), 100 µg/ml of Pyruvate (Sigma, P4562), 50 µg/ml of Uridine (Sigma, U3003), 5 µg/ml of Gentamycin (Gibco, 15710064), and Creatine (Sigma, C3630) at 1 mM). Myotubes were then covered by a concentrated layer of matrigel and maintained for up to 30 days in differentiation culture medium. Culture medium was changed every two days.

4) Live MTs labeling and imaging

To visualized MT organization, live cells were labeled by SiR-tubulin as instructed by the manufacturer (Spirochrome, SC002). Briefly, cells were incubated for 1H with fresh culture medium containing SiR-tubulin and Verapamil (pump inhibitor) at 1 µM and 10 µM final concentration respectively. At the end of the incubation time, cells were gently washed by color less (no phenol red) HBSS (Gibco, 14065056) culture medium and kept in HBSS culture medium for live imaging.

To proceed live imaging, cells were stabilized in the live imaging chamber, regulated at 37°C with 5% of CO2. Following, cells were imaged by confocal LSM880 (Zeiss) microscope.

5) Co-culture fixation, immunofluorescence staining and imaging

Due to fragility of motor neurons/myofibers synapses *in vitro*, cells were prefixed by incubating in the culture medium complemented with 16% PFA for 30 min at 37°C. Next, culture medium was collected and cells were fixed by 4% PFA-1X PBS for 15 min at 37°C. Following washes with 1X PBS, cells were permeabilization with 0.5% Triton-X100-1X PBS for 5 min at RT and saturated with 1% BSA-1X PBS for 30 min at RT. Next, cells were incubated in primary antibodies over night at 4°C. After several washes with 0.05% Triton-X100-1X PBS, cells were incubated in secondary antibodies or dyes for 2H at RT and washed with 0.05% Triton-X100-1X PBS before image acquisition. The list of the antibodies used for each staining can be found in the following section. All the images were acquired by confocal LSM880 (Zeiss) microscope. All the quantifications/measurements were done using ImageJ® software.

Antibody	Species and Utility	Dilution Factor	Manufacturer and Reference
Anti-Total-αTub	Mouse - primary	1:1000	Sigma T8203
Anti-Desmin	Rabbit - Primary	1:500	Cell signaling technology 5332
Anti-NF-H (SMI32)	Mouse - primary	1:500	BioLegend 801707
Anti-mouse- Alexa Flour 448	Goat - secondary	1:500	Thermo Fisher Scientifics A-211029
Anti-rabbit- Alexa Flour 448	Goat - secondary	1:500	Thermo Fisher Scientifics A-21245
Dapi-brilliant blue	Dye	1:50000	Thermo Fisher Scientifics D1306
α-Bungarotoxin- Alexa Flour 555	Dye	1:500	Thermo Fisher Scientifics B35451

III) Experimental design and co-culture protocol

To start our experiments, several fundamental questions needed to be addressed. These include:

- Which culture medium should be used? Nor mouse neither human myoblasts do not grow or differentiate in the same culture medium as motor neurons. In addition, freshly isolated motor neurons are highly sensitive to the composition of their culture medium. Thus, we were wondering if following co-culture, we should switch to motor neurons culture medium? Or should we mix motor neurons and myofibers culture medium?

- When should we add motor neurons to myoblasts? Before myoblasts differentiation? Post differentiation but before addition of concentrated matrigel? Or on top of the concentrated matrigel layer?

- How long should we maintain co-cultures in order to obtain a higher maturity within myofibers?

To address these questions, multiple experiments were designed in order to test different culture mediums and different co-culture initiation times, and to find the experimental condition that best suited mouse or human primary myoblasts and rat motor neurons. At last, the following protocol showed promising results for both mouse and human myoblasts co-culture with rat motor neurons (Figure 40):

- Mouse or human myoblasts were plated on 1% matrigel-coated dish in their adapted proliferation medium, for 3 to 5 days, in order to achieve 90% of confluence. During this period, culture medium was changed every 2 days.

- Following, myoblasts were pushed to differentiation by changing from proliferation to their adapted differentiation culture medium.

- 2-3 days post differentiation, a second layer of concentrated matrigel was added on top of the myotubes.

- From this point, myotubes were kept on culture in their adapted differentiation culture medium for 8-10 days, until they would form elongated myofibers. During this period, half of the culture medium was changed every two days.

- At the end of the elongation, cells were washed, and freshly isolated motor neurons were added on top of the concentrated matrigel layer. From this point, co-cultured cells were maintained in motor neurons culture medium for up to 13-15 additional days. Culture medium was not changed for the first two days, allowing motor neurons to install and stabilize. Later on, half of the culture medium was changed every day.

We chose to use motor neurons as the main culture medium for our co-culture since it did not affect myoblasts viability, while utilization of myofibers differentiation medium, either pure or mixed with motor neurons culture medium, greatly reduced motor neurons attachment and differentiation.

In experiments where motor neurons were added before the concentrated matrigel layer, some motor neurons died, and for most of the remaining motor neurons, axons length was shorter compared to experiments where motor neurons were added on top of the concentrated matrigel layer. Actually, motor neurons install and differentiate nicely on the top of the concentrated matrigel layer and project their axons to pass the matrigel and create synapse with myofibers below.

The choice of timing was based on myofibers viability and culture quality. Around 13 to 15 days post co-culture, myofibers contraction frequency could be observed. The high density of large myofibers and motor requires a change of culture medium every 8 to 10 hours to avoid culture medium acidification. In addition, after more than 20 days of culture, the concentrated layer of matrigel begin to get loose and detach from the dish.

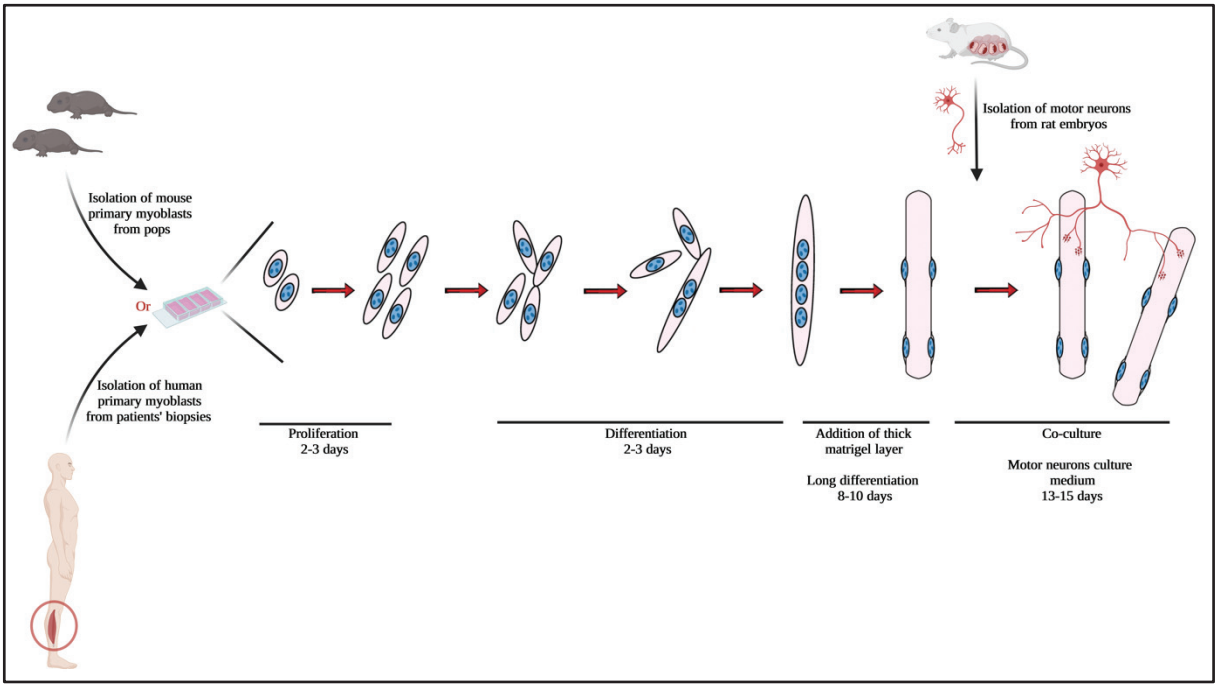

Figure 40: Illustration of sequential steps to develop myofiber/motor neurons co-culture *in vitro*.

IV) Observations, results and conclusions

1) Mouse myofibers co-culture with motor neurons

Our simple culture method already allows us to develop contractile myofibers from primary mouse myoblasts. In control versus co-culture experiments, our control cells begin to shrink and collapse around 3-5 days post passage to motor neurons culture medium. A population of control myofibers always persist on culture, however, a strong reduction in their contraction frequency could be stated. Interestingly, co-cultured myofibers remained stable in size and remained contractile.

Our confocal images suggest the formation of NMJs between motor neurons and myofibers in co-culture experiments, as stated by colocalization of motor neurons NF-H with AChRs clusters at the periphery of co-cultured myofibers (Figure 41A-B). While the presence of motor neurons did not affect the percentage of myofibers expressing AChRs, a slight increase in the size of AChRs clusters in co-cultured myofibers compared to control myofibers could be observed (Figure 41C-D).

Concerning MTs, it was much more difficult to study their organization in co-culture conditions. As presented in Figure 41A, co-culture conditions are dense with an upper layer of motor neurons which contain a rich MT network within them. Motor neurons MT network, in addition to a thick layer of topping matrigel, result in the generation of a high surrounding background and interfere with MTs imaging within fixed myofibers labeled with primary and secondary antibodies. However, our live MTs labeling by SiR-tubulin allowed us to get sharper MT intensity from myofibers with much less background noise (Figure 42A-B). Thanks to this live imaging, we were able to observe the formation of randomly oriented MTs at the periphery of co-cultured myofibers, while MTs from simple cultured myofibers remain longitudinally oriented.

Together, these results suggest the formation of functional NMJs between mouse primary myofibers and motor neurons in our co-culture system. The presence of motor neurons seems to have a positive impact on myofibers viability and maturation and results in a reorganization of MTs toward a more complex network. Experiments have to be repeated in order to valid these observations.

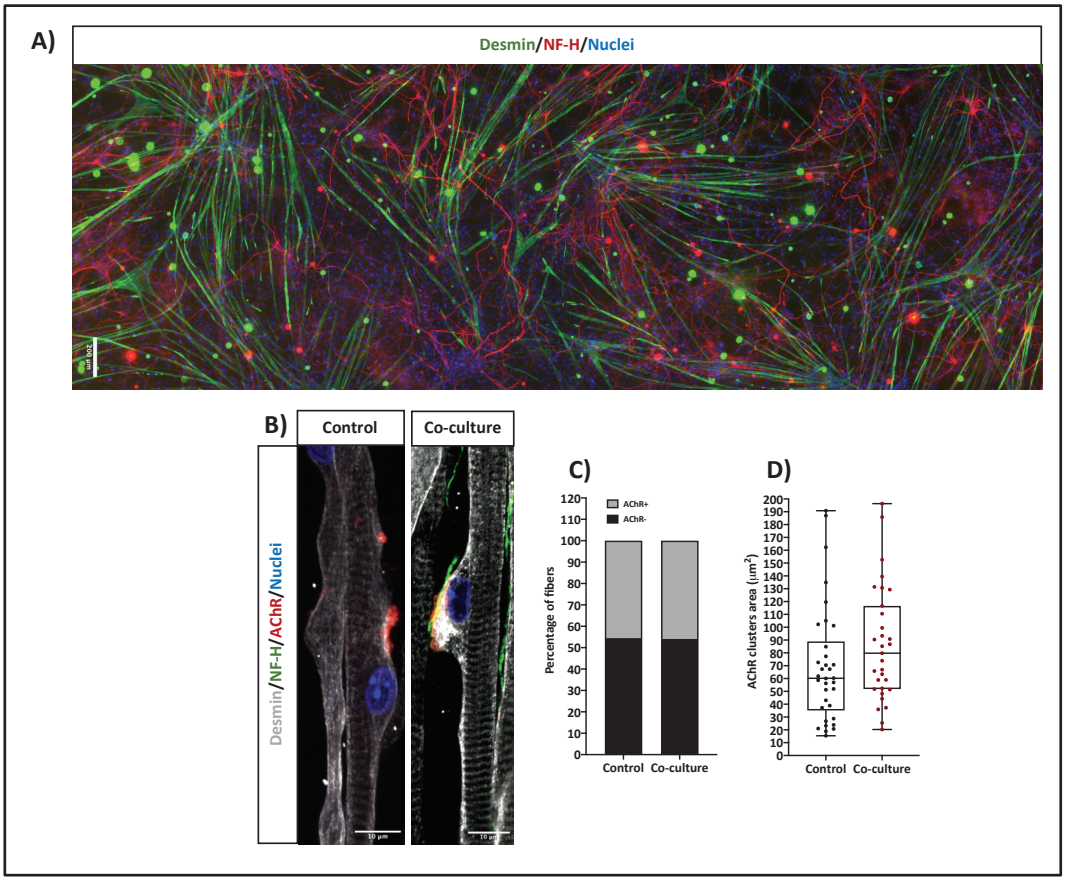

Figure 41: Development of NMJs between mouse myofibers and rat motor neurons *in vitro*.

(A) Representative mosaic immunofluorescence image (10X) of primary mouse myofibers co-cultured with rat motor neurons after 14 days of co-culture, presenting myofibers desmin (green), motor neurons NF-H (red), and nuclei (blue). Scale Bar = 200 µm. (B) Representative confocal images (63X) of control and co-cultured mouse myofibers presenting myofibers desmin (silver), motor neurons NF-H (green), AChRs clusters (red) and myonuclei (blue). Scale Bar = 10 µm. (C) Quantification of percentage of myofibers negative (black) or positive (gray) for AChRs clusters in control and co-cultured mouse primary myofibers. Quantification was performed by analyzing myofibers with immunofluorescence microscopy (63X). Data collected from one experiment. (D) quantification of AChRs clusters area in control and co-cultured mouse primary myofibers. Quantification was performed on confocal immunofluorescence images (63X). Data collected from one experiment.

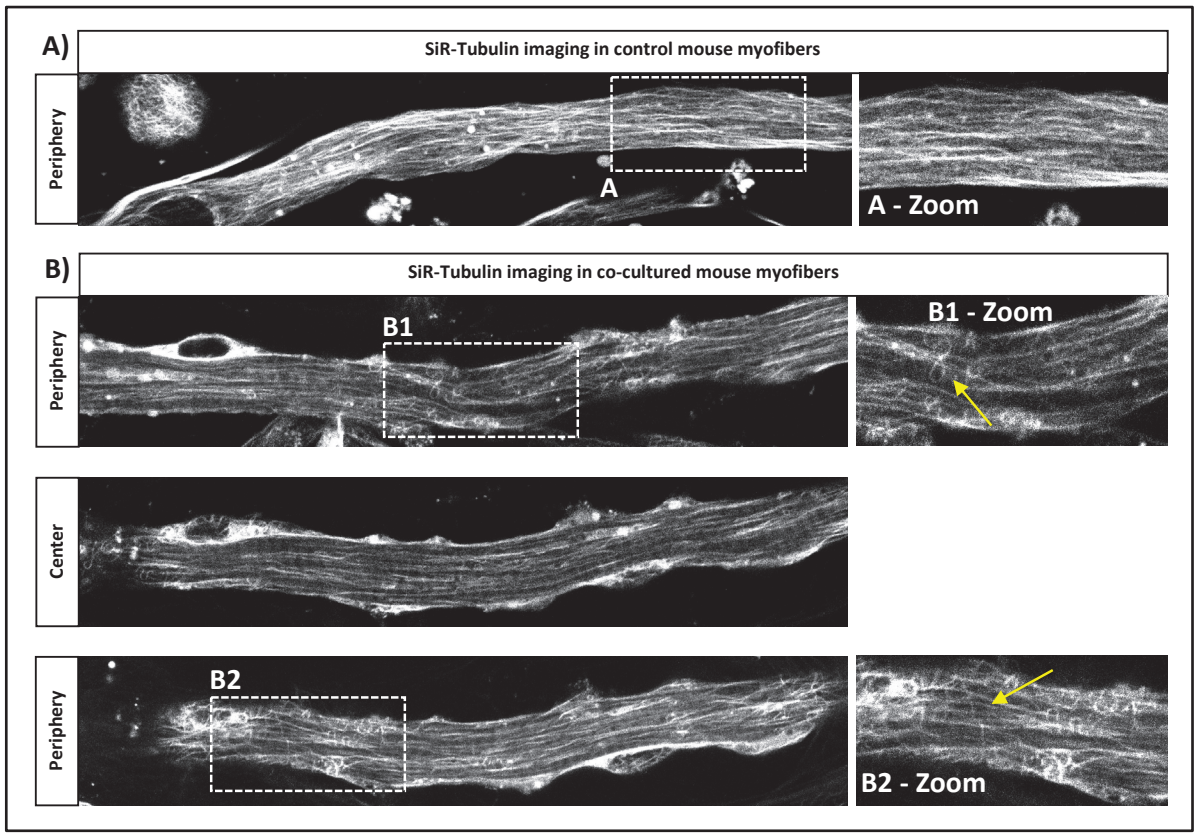

Figure 42: effect of mouse myofibers co-culture with motor neurons on MT network.
(A-B) Representative confocal images (63X) obtained from SiR-tubulin labeling of MTs in control (A) and co-cultured (B) mouse primary myofibers. For each image, white cages surround the area presented in the adjacent zoom panels. White fleshes point to examples of non-longitudinal MTs at the periphery of co-cultured myofibers.

2) Human myofibers co-culture with motor neurons

In vitro myofibers developed from human primary myoblasts can be kept on culture for more that 20 days even in the absence of motor neurons. However, as previously mentioned, these myofibers lack sarcomeres formation, contraction and myonuclei peripherization. Interestingly, our human myofibers begin to contract (at low frequency) around 5 days post co-culture.

Just like our results from mouse myofibers and motor neurons co-culture, our confocal images from human myofibers and motor neurons co-cultures suggest the formation of NMJs between motor neurons and myofibers in co-culture experiments, as we observed the colocalization of motor neurons NF-H and AChRs staining at periphery of co-cultured human myofibers (Figure 43A-B). Another similarity between the two models was that presence of motor neurons had no impact on the percentage of human myofibers expressing AChRs (Figure 43C). However, AChRs clusters size was greatly variable in co-cultured human myofibers with a remarkable increase in the mean area covered by AChRs in co-cultured myofibers compared to control myofibers (Figure 43D). Interestingly, co-cultured myofibers contraction was in parallel with the observation of Desmin sarcomeres formation and myonuclei peripherization (Figure 43E).

As for MT network, our live imaging revealed a regular smooth longitudinal MT network within co-cultured myofibers with peripheral myonuclei compared to wavy MTs in control myofibers with central myonuclei (Figure 44A-B).

In conclusion, our co-culture method has allowed us to increase human myofibers maturity *in vitro*. Further adjustments in the protocol to increase the co-culture duration may help us to get our *in vitro* human myofibers one step closer to their *in vivo* characteristics.

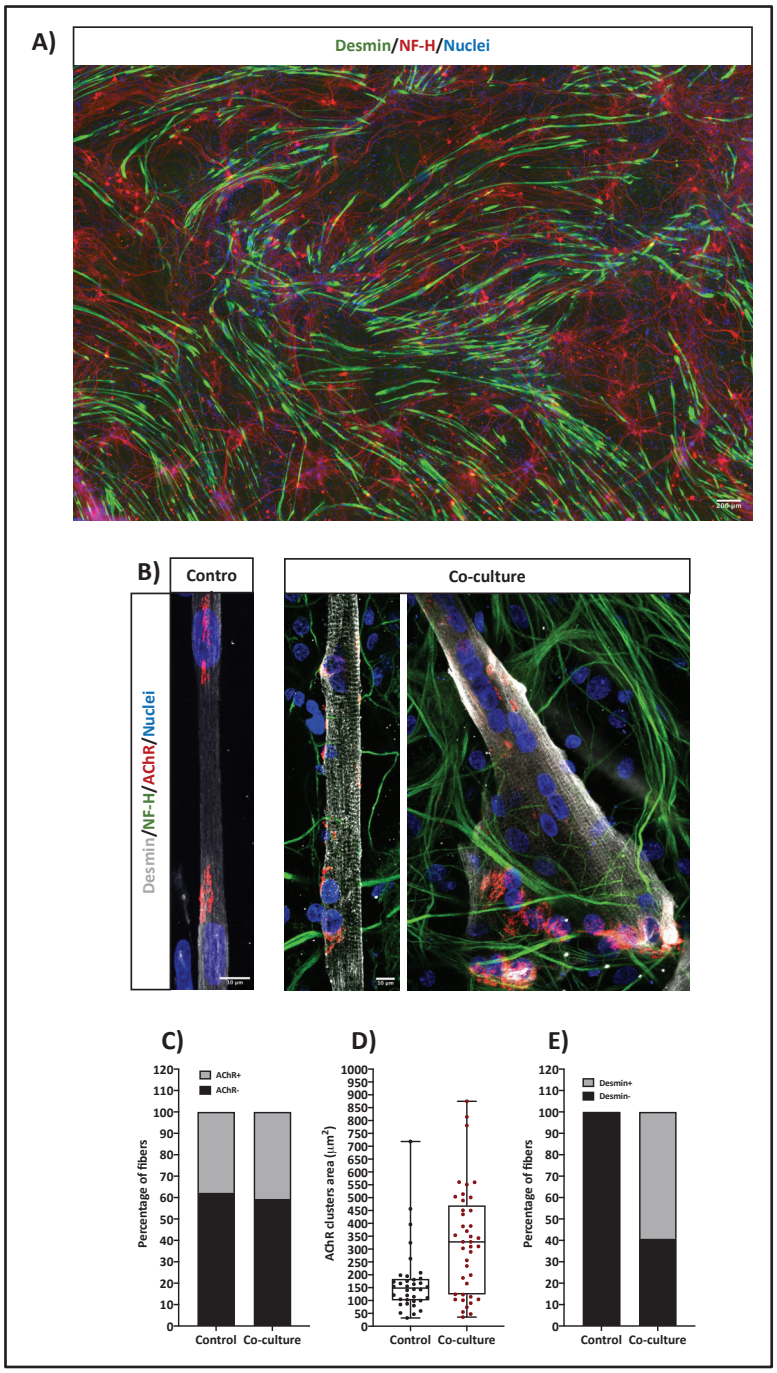

Figure 43: Development of NMJs between human myofibers and rat motor neurons *in vitro*.
(A) Representative mosaic immunofluorescence image (10X) of primary human myofibers co-cultured with rat motor neurons after 14 days of co-culture, presenting myofibers desmin (green), motor neurons NF-H (red), and nuclei (blue). Scale Bar = 200 µm. (B) Representative confocal images (63X) of control and co-cultured human myofibers presenting myofibers desmin (silver), motor neurons NF-H (green), AChRs clusters (red) and myonuclei (blue). Scale Bar = 10 µm. (C) Quantification of percentage of myofibers negative (black) or positive (gray) for AChRs clusters in control and co-cultured human primary myofibers. Quantification was performed by analyzing myofibers with immunofluorescence microscopy (63X). Data collected from one experiment. (D) quantification of AChRs clusters area in control and co-cultured human primary myofibers. Quantification was performed on confocal immunofluorescence images (63X). Data collected from one experiment. (E) Quantification of percentage of myofibers negative (black) or positive (gray) for desmin striation in control and co-cultured human primary myofibers. Quantification was performed on confocal immunofluorescence images (63X). Data collected from one experiment.

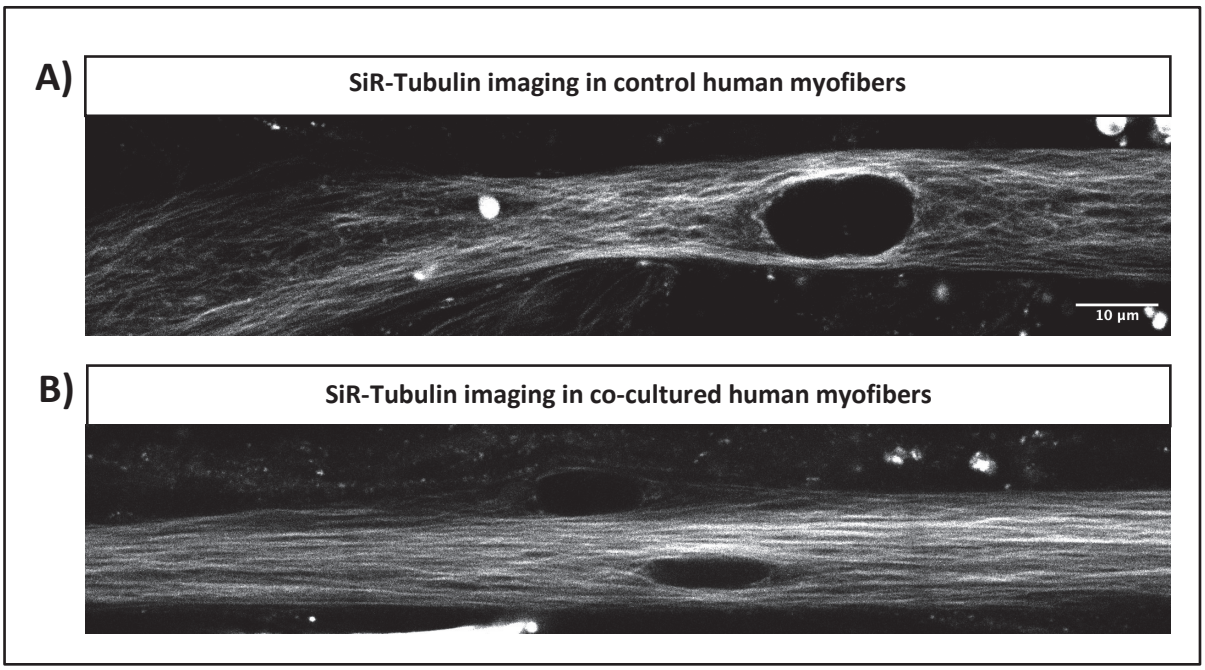

Figure 44: effect of human myofibers co-culture with motor neurons on MT network.
(A-B) Representative confocal images (63X) obtained from SiR-tubulin labeling of MTs in control (A) and co-cultured (B) human primary myofibers. Scale Bar = 10 µm.

Discussion and perspectives

In this thesis, I address the importance of peripheral myonuclei positioning and myonuclear domains organization by challenging MT dynamics. Diverse *in vitro* and *in vivo* models have allowed us to show that increasing MT dynamics perturb myonuclear domains. Importantly, we show that depending on the origin of increased MT dynamics, myonuclei organization is affected differently, which can be due to an increase in myonuclei dynamic or an increase in myonuclei content per myofiber. In both cases, we gather evidences which link the increased MT dynamics and/or disrupted myonuclear domains to lowered myofibers functionality.

I) MTs in skeletal myofibers

1) MT dynamics during myogenesis

MTs go through constant cycles of polymerization and depolymerization, a process that is highly dependent on their binding proteins or post-translational modifications (Janke and Magiera, 2020). Our data suggest that MACF1 protein and MT detyrosination are among the regulators of MT dynamics in skeletal muscle. By tracking MT growth rate *in vitro*, we show for the first time that MT network goes toward a more stable state as myofibers develop. In our experiments, the absence of MACF1 (knock down) or MT detyrosination (*Svbp* KO) both resulted in increased MT dynamics during myofibers development *in vitro* and subsequently MT disorganization *in vivo*.

MACF1 is a member of giant Spectraplakins cytoskeleton linkers family (Conrad L. Leung et al., 1999). In mononuclear cells, MACF1 decorates MT plus-tips and guides MT growth by following actin filaments (Wu et al., 2011, 2008). Plus-tips are critical sites in MT turnover since they can be subjected to depolymerization in the absence of proper stabilizing proteins. At these sites, MACF1 has been shown to partner with different MT plus-tips proteins, such as EB1/Clip170 complex, CLASP2 and ELMO, and help them to promote MT stability (Drabek et al., 2006; Kodama et al., 2003; Margaron et al., 2013). Interestingly, our overexpression experiments have revealed that MACF1 microtubules binding domain also decorates MT plus-tips in multinucleated myotubes. Therefore, it is tempting to imagine that in multinucleated myotubes and myofibers, MACF1 promotes MT stability, by helping different MT plus-tips protectors, as it does in mononuclear cells. As a result, the increased MT dynamics observed in MACF1 depleted myotubes and myofibers could be linked to reduced presence of MACF1 MT plus-tips stabilizing partners at these sites, which could also leave MT plus-tips unprotected and thus accessible to installation and activity of different MT destabilizing factors. Additionally, in epithelial cells, MACF1 binds MT binding protein CAMSAP3 and brings stability to MT minus-ends by crosslinking them to actin (Ning et al., 2016). Interestingly, our confocal images from mature skeletal myofibers present a dense MACF1 decoration along both longitudinal and transversal MT latices. Our data also show that MACF1 forms a strong ring around myonuclei, where MT nucleation center and minus-ends are located. Thus, we can imagine that in large myofibers, MACF1 promotes MT stability by binding to different partners in a site-dependent manner. Hence, the disorganized MT network in MACF1 KO myofibers could reflect the lack of MT-to-actin crosslinking on one hand and the incapacity of MACF1 binding partners to promote MT stability on the other hand.

Surprisingly, in myofibers, we observed that MACF1 KO results in a specific reduction of detyrosinated MTs around myonuclei, where ncMTOCs are located. Detyrosination occurs on MT lattice and is associated with stable MTs since it promotes the installation of MT stabilizing proteins such as KIF17 and reduces the activity of MT destabilizing proteins such as KIF2A (Gundersen et al., 1987; Jaulin and Kreitzer, 2010; Kumar and Flavin, 1981; Peris et al., 2009). Thereby, reduced MT detyrosination in MACF1 KO myofibers opens two hypotheses. One could be the potential reduced recognition/affinity of SVBP/VASH1 and/or SVBP/VASH2 MT detyrosinating complexes for MT lattice when MACF1 is not present. The other hypothesis could be that absence of MACF1 does not affect MT detyrosination rate, but increases the MT depolymerizing rate. In either case, reduced MT detyrosination might also take part in increased MT dynamic in MACF1-depleted myofibers. This hypothesis is consolidated by our *in vitro* observations of increased MT dynamics in *Svbp* KO myotubes and myofibers with a huge reduction of MT detyrosination. In accordance with previous data from cultured neurons, we show that the absence of MT detyrosination results in excessive tyrosinated MTs accumulation in myofibers and correlates with their strong disorganization (Aillaud et al., 2017; Pagnamenta et al., 2019).

Furthermore, our western blot studies revealed an increase in MT detyrosination with myoblasts differentiation *in vitro*, which occurs side by side with an increase in both mRNAs and proteins levels of MACF1, SVBP, VASH1, and VASH2. These data suggest the presence of paralleled regulatory mechanisms that monitor MT dynamics and ensure their stability as myofibers develop (Figure 45).

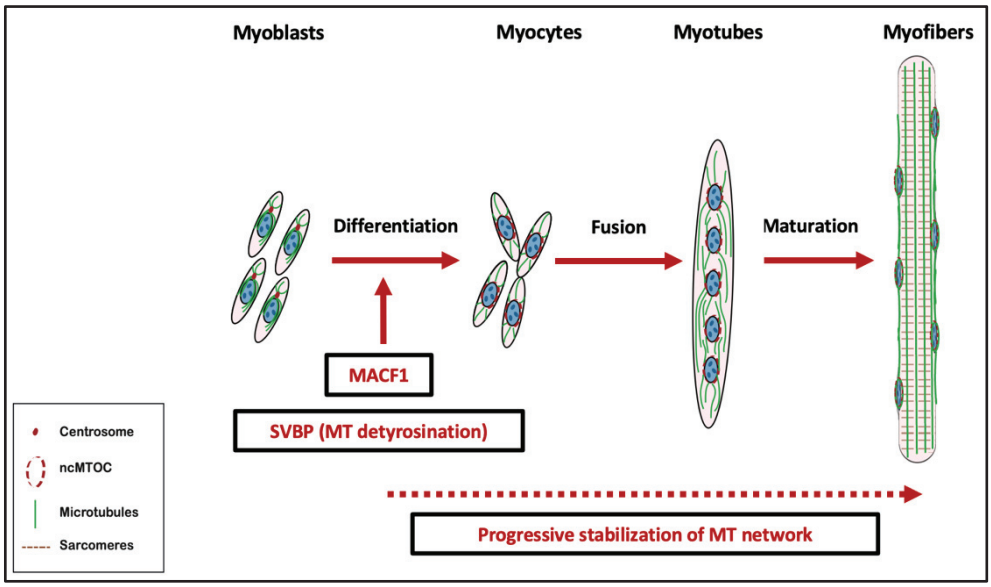

Figure 45: proposed model of progressive MT network stabilization during myofibers formation *in vitro*.
As myoblasts differentiate to myocytes and prepare for fusion, MACF1 expression is upregulated side-by-side with SVBP expression and MT detyrosination level. These elements contribute to the progressive MT network stabilization during myofibers development as stated by our *in vitro* experiments.

2) MT organization during myofibers maturation

Our *in vitro* primary mouse myofiber allows us to study changes in MT dynamics and organization, during early myogenesis and myofibers formation. However, MTs remain longitudinally organized even after 10 days of maturation and do not achieve the gride-like organization observed in mature myofibers *in vivo*. As a result, no data is available on how MTs pass from longitudinal organization in freshly developed myofibers to a gride-like organization in a fully mature myofiber. Thus, we hypothesized that increasing myofibers maturity by forming *in vitro* NMJs would give us the chance to achieve the gride-like MT organization *in vitro* (Sohal and Holt, 1980). Interestingly, we observed that myofibers co-culture with motor neurons increased primary mouse myofibers viability, increased primary human myofibers maturity, and changed MT pattern and organization in both mouse and human primary myofibers *in vitro*. These data suggest that by increasing myofibers maturity we might be able to picture and follow changes in MT network toward their gride-like organization during myofibers maturation. As encouraging as these results are, our co-culture method is limited at two points.

First, our method is based on using freshly isolated motor neurons from rat embryos. This demands a precise retro planning before every experiment to make sure that our myofibers are developed and ready for the co-culture on the day of motor neurons extraction from embryos. In theory, we should be able to use the same planning for every experiment. In practice, this is most likely possible for myofibers developed from primary mouse myoblasts, since myoblasts are always extracted from 5 or 6-day-old mouse pups, offering a reproducible culture quality between experiments. However, human myoblasts isolated from patients' biopsies do not always have the same proliferation and differentiation speed, which makes it difficult to ensure the formation of myofibers before the motor neurons extraction. The second limit of our method is the long-term maintenance of culture. As previously mentioned, our co-cultures medium requires frequent change, which can be 2-3 times per day during the last days. This is most probably due to high cellular (myofibers and motor neurons) density compared to culture wells capacity.

Of interest, different methods have been previously described for myofibers and motor neurons co-culture and NMJs formation *in vitro* (Barbeau et al., 2020). Among these methods, current advances propose the formation of *in vitro* NMJs between induced pluripotent stem cells (iPSCs) derived myofibers and motor neurons. Whether human or mouse iPSCs derived myofibers develop the same maturity and characteristics as primary myofibers has to be verified. Indeed, the use of iPSCs-derived myofibers and motor neurons could give us a great advantage in time management and co-culture development and ensure reproducibility of the experimental model. Once the best experimental model is identified, the suitable cell density can be easily determined by testing different ratios of myofibers versus motor neurons.

Overcoming these limits can help us increase the co-culture duration, increase myofibers maturity, and thereby allow us to study MT network maturity, potentially toward a gride-like organization.

II) MT dynamics and myonuclear domain

Disrupted myonuclear domain due to mispositioned myonuclei is a hallmark of different myopathies, yet, the mechanisms allowing myofibers to control myonuclear number and maintain myonuclei at their periphery remain poorly understood. In our experiments, we show that increased MT dynamics due to the absence of either MACF1 or SVBP affect myonuclear domains, yet through two different mechanisms.

Indeed, myogenesis is a complex process through which both emerging myonuclei from mononuclear cells and MT/actins cytoskeleton are constantly rearranged (Roman and Gomes, 2018). In particular, MT organization center is relocated to the nuclear envelope which creates a two-way-relation between myonuclei and MTs: myonuclei participate in MT nucleation and MTs actively regulate myonuclei movement and dispersion by providing the support for dynein and kinesin motor proteins in developing myofibers (Bugnard et al., 2005; Cadot et al., 2012; Gache et al., 2017; Metzger et al., 2012; Ralston, 1993). At last, the formation of sarcomeres will push myonuclei to myofibers periphery where they are surrounded by a dense MT network (Falcone et al., 2014).

1) MACF1, myonuclei, and myonuclear domain organization

Our experiments have allowed us to show that MACF1 can participate in myonuclei positioning through different processes.

First, we show that MACF1 regulates myonuclei motion during myofibers development through its regulatory role on MT dynamics. Increased MT dynamics in MACF1 depleted cells results in increased myonuclei dynamic within elongated myotubes *in vitro*. This can justify the reduced distance between neighboring myonuclei at the periphery of myofibers both *in vitro* and *in vivo*, yet, does not explain the observation of internalized myonuclei within myofibers of aged MACF1 KO mice *in vivo,* in the absence of muscle regeneration.

It is important to know that mammalian MACF1 has been shown to interact with the LINC complex by binding to perinuclear Nesprin-3 (Wilhelmsen et al., 2005). Interestingly, both our *in vitro* and *in vivo* staining for native MACF1 showed a strong perinuclear MACF1 ring. This also correlates with the previously described perinuclear positioning of *Drosophila* ortholog of MACF1, Shot, where it provides mechanical stability to myonuclei of *Drosophila* larval myofibers by interacting with LINC complex protein MSP300 (the *Drosophila* orthologue of Nesprin) (Wang et al., 2015). In addition, Shot cooperates with EB1 to maintain a stable MT network around myonuclei. As a consequence, the absence of Shot is linked to changes in myonuclei form and disruption of the organization of nuclear lamina, which is in direct contact with chromatin within the nucleus. These data propose a direct role for MACF1 in monitoring nuclear mechanotransduction. Interestingly, *in vitro* and *in vivo* depletion of mouse MACF1 both caused a change in nuclear shape toward rounder myonuclei compared to flatten myonuclei in control myofibers. In our studies, we have correlated the rounder myonuclei shape of MACF1 KO myofibers to loss of MT density, and more specifically detyrosinated MTs

density, around these myonuclei. However, we cannot neglect that the loss of MACF1 may have also affected the organization and rigidity of the LINC complex. Importantly, changes in nucleus-to-chromatin mechanotransduction can be linked to changes in genes expression (Janin and Gache, 2018). In our studies on MACF1 KO myofibers, it was the observation of accumulated mitochondria in between myofibrils that suggested potential alterations of gene expression in MACF1 KO mice, affecting mitochondrial biogenesis. Following these results, we were able to show that myonuclei roundness in MACF1 KO myofibers occurs in parallel with increased mRNA of mitochondrial biogenesis marker and increased mitochondria number with age in parallel with myofibrils disorganization.

In myofibers, mitochondria lie between myofibrils and are in direct contact with sarcomeric protein desmin, which is known to link adjacent myofibrils together (Dayal et al., 2020; Granger and Lazarides, 1979). In addition, recent studies are suggesting a close relation between the spatial organization of mitochondria and myofibrils (Avellaneda et al., 2021; Katti et al., 2022). Therefore, it was not surprising to observe a disorganized Desmin network following mitochondria accumulation in MACF1 KO myofibers. However, it was interesting to see that myonuclei internalization occurs only after myofibrils cohesion disruption within MACF1 KO myofibers. Interestingly, mitochondria can be found disrupted and accumulated in models of desminopathy, a category of myopathies with mispositioned myonuclei (Clemen et al., 2013; Smolina et al., 2020; Winter et al., 2016). Whether a disorganized mitochondrial network is among the origins of mispositioned myonuclei in these myopathic myofibers remains an open question.

In addition, we can imagine that the mitochondrial biogenesis marker is not the only gene affected by myonuclei roundness in MACF1 KO myofibers. Indeed, other genes expression could be altered in MACF1 KO myofibers. The product of these genes and the consequence of their abnormal expression remain to be discovered.

Altogether, our data suggest that MACF1 controls myonuclear domain distribution and functionality through two processes, which are regulating MT dynamics and maintaining myonuclei shape (Figure 46).

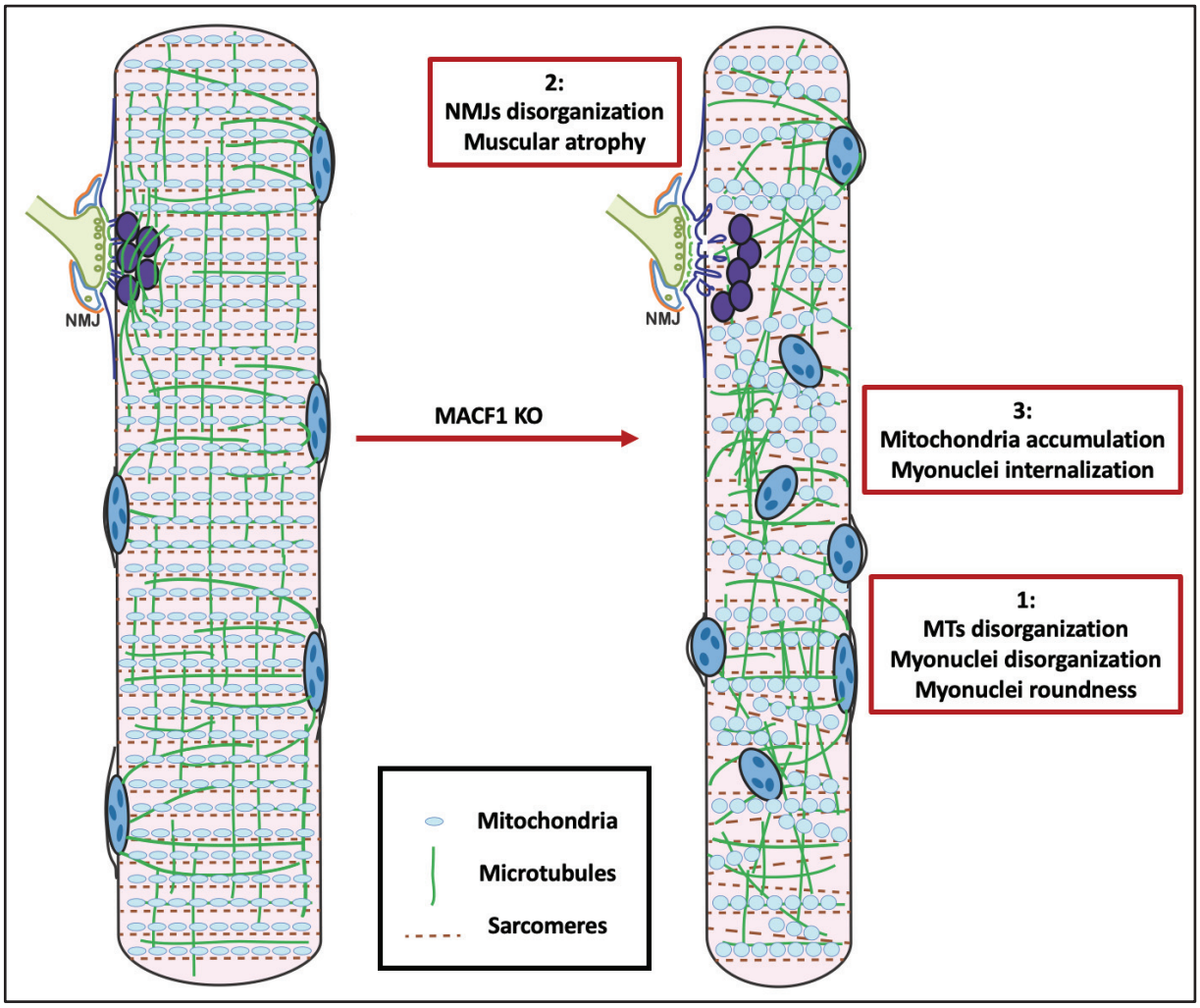

Figure 46: proposed model of the role of MACF1 in skeletal muscle.
In healthy myofibers (left), MACF1 contributes to MT network organization, myonuclei shape and positioning maintenance and NMJs stability. Following MACF1 KO specifically in skeletal muscles, first MT get disorganized and promote a disorganization of myonuclei at the periphery of myofibers concomitant with an alteration in myonuclei shape. The change of myonuclei shape will progressively alter genes expression, among which our experiments revealed an increase in the expression level of marker of mitochondrial biogenesis. Following, we can observe a fragmentation of NMJs which results in muscular atrophy in long term. At last, the long-term accumulation of mitochondria due to excessive mitochondrial biogenesis will break the cohesion between myofibrils and result in loss of peripheral myonuclei and myonuclei internalization.

2) SVBP, MT detyrosination, myonuclei, and myonuclear domains

As previously mentioned, the absence of MT detyrosination also results in increased myofibers dynamics and disorganized tyrosinated MTs in *Svbp* KO myofibers. Surprisingly, our *in vitro* myonuclei tracking in developing myofibers showed no changes in myonuclei displacement parameters between WT and *Svbp* KO myofibers. However, our observations from *Svbp* KO myofibers showed the reduced distance between neighboring myonuclei at the periphery of myofibers both *in vitro* and *in vivo*. Interestingly, the reduced distance between myonuclei was paralleled to increased myonuclei number per area at the periphery of myofibers and the presence of internal myonuclei within myofibers. Yet, compared to our previous model, the absence of MT detyrosination did not affect peripheral myonuclei form in young *Svbp* KO, suggesting untouched nuclear mechanotransduction in young *Svbp* KO myofibers, nor did it affect myofibrils organization, suggesting that internalized myonuclei may come from *de novo* fusion events. Accordingly, our *in vitro* experiments on *Svbp* KO myocytes showed an increased fusion rate compared to control myocytes.

One of the pioneer studies on detyrosinated MTs has described their enrichment toward the leading edge of migrating fibroblasts (Gundersen and Bulinski, 1988). Additionally, one of the most recent studies on the balance between tyrosinated and detyrosinated MTs during epithelial cell migration has described the same detyrosinated MT enrichment at the cells leading edge, and has shown that increased MT detyrosination results in the formation of more stable focal adhesion, helps MT elongation, and increases epithelial cells migration (Müller et al., 2022). Our results from *Svbp* KO myoblasts are consistent with these data. Our time-lapse imaging of isolated myoblasts from WT or *Svbp* KO mice show that in the absence of MT detyrosination, myoblasts migrate slower and less frequently. Thus, we can speculate that reduced *Svbp* KO myoblasts migration is due to less organized focal adhesion at the leading edge of migrating cells. *In vitro*, the reduced myoblasts migration may increase their chance to get stuck with one another and thereby increase the chance of myocytes fusion. However, reduced myocytes migration does not explain the presence of *de novo* fusion and increased myonuclei per myofibers *in vivo.*

Interestingly, our *ex vivo* studies on MuSCs associated to live isolated myofibers have revealed that *Svbp* KO MuSCs get activated faster, proliferate more, and enter differentiation quicker than WT MuSCs.

Several factors may be responsible for *Svbp* KO MuSCs activation. To begin with, we cannot neglect the fact that the studied SVBP mouse strain is a total KO model, lacking MT detyrosination in every cell and organ. This is important since MuSCs are constantly interacting with different neighboring cell types such as endothelial cells, fibro-adipogenic progenitors, macrophages, and especially myofibers, in addition to their ECM (Relaix et al., 2021). Changes in extracellular matrix composition/stiffness, in cell-cell contacts, or in secretory factors received from neighboring cells can be considered as an activating alert by MuSCs and result in their proliferation and subsequent differentiation. Therefore, we can speculate that in the absence of MT detyrosination, changes in MuSCs neighboring cells behavior may be triggering

MuSCs activation. What are the consequences of absent MT detyrosination for each neighboring cell type remains open questions, however, our data suggest that unstable NMJs and disorganized MTs cytoskeleton of *Svbp* KO myofibers may be great players in *Svbp* KO MuSCs activation. Indeed, it has been previously shown that myofibers denervation alerts quiescent MuSCs and results in their proliferation and fusion with myofiber (Larouche et al., 2021; Wong et al., 2021). Therefore, fragmented and denervated NMJs of *Svbp* KO mice could contribute to induced MuSCs fusion with myofiber and increased myonuclei per myofibers. In addition, MTs, and more precisely detyrosinated MTs, have been described as essential regulators of Ca^{2+} signaling and mechanical stress management during myofibers contraction (Kerr et al., 2015; Khairallah et al., 2012; Ward et al., 2014). Even though the status of Ca^{2+} signaling has not been checked in *Svbp* KO myofibers, we can imagine that in the absence of SVBP, the stress induced by irregular Ca^{2+} signaling within myofibers may be another contributor to myofiber-dependent MuSCs alert and activation. Nonetheless, the MT network is known to participate in cell shape and stiffness in various cell types (Goldman, 1971; Kopf et al., 2020; Rodionov et al., 1993). While MuSCs mechanical properties have never been studied, we cannot exclude that absence of MT detyrosination can affect MuSCs stiffness and mechanosensitivity. Notably, our complementary experiments on isolated MuSCs *in vitro* show that *Svbp* KO MuSCs are more sensitive to the stiffness of their culture support compared to WT MuSCs, as stated by increased *Svbp* KO MuSCs proliferation only when cultured on collagen and not matrigel. This suggests a disrupted mechanotransduction in *Svbp* KO MuSCs in the absence of stable detyrosinated MTs. Whether *in vivo*, MuSCs ECM composition or stiffness is altered in *Svbp* KO mice remains an open question for the moment. In addition, we can speculate that changes in MuSCs shape and stiffness may affect its cell-cell interaction and the active/inactive status of signaling pathways, such as Notch and Wnt, which are essential for MuSCs quiescence maintenance (Baghdadi et al., 2018; Eliazer et al., 2019; Mourikis et al., 2012). On the other hand, MTs have been shown to participate in Wnt signaling transduction by promoting the nuclear translocation of the Wnt signaling actor, β-catenin (Kumari et al., 2021). Therefore, we can hypothesis that increased MT dynamic within MuSCs may also affect the subcellular translocation rate of essential signaling pathways actors and thus affect MuSCs quiescence.

When it comes to cell division and proliferation, MTs are known to orchestrate chromosome segregation and orient mitotic spindle (Meunier and Vernos, 2012). Of interest, it has been shown that detyrosinated MTs are one of the main components of spindle MTs and are specifically used by Kinesins to move chromosomes to spindle equators (Barisic et al., 2015; G G Gundersen and Bulinski, 1986). Reduced MT detyrosination either by TTL overexpression or VASH1/VASH2 downregulation, results in the mispositioned mitotic spindle and delayed mitosis in osteosarcoma U2OS and fibroblastic MEF cell lines (Barisic et al., 2015; Liao et al., 2019; Peris et al., 2006). Yet, controversial data suggest that increased or decreased MT detyrosination can affect cell division in a cell-type-dependent manner. For example, increased MT detyrosination has been described for more aggressive breast cancer cells and reduced TTL (thereby indirect increased MTs detyrosination) has been shown to promote tumor growth (Lafanechère et al., 1998; Mialhe et al., 2001). However, reduced TTL in epithelial cells has been linked to reduced cell proliferation (Müller et al., 2021). In addition, overexpression of

VASH1 (thereby increased MTs detyrosination) specifically reduce fibroblasts growth without affecting keratinocytes and VASH1 KD (thereby reduced MT detyrosination) results in increased leukemia cells proliferation rate (Kern et al., 2008; Naito et al., 2009). These data suggest that increased *Svbp* KO MuSCs proliferation could be linked to defeated mitosis and cell division in the absence of MT detyrosination, however, the altered molecular mechanism is yet to be discovered.

At last, *Svbp* KO MuSCs associated with isolated myofibers *ex vivo* present a higher speed in entering differentiation. In addition, isolated myoblasts from *Svbp* KO mice show a higher fusion index *in vitro* compared to myoblasts from WT mice. This could be simply due to faster *Svbp* KO MuSCs activation and proliferation, which in a cascade of events, would result in their faster entry in differentiation. Furthermore, *Svbp* KO MuSCs may present faster differentiation due to changes in their cytoskeleton stiffness and nuclear mechanotransduction following modifications in their MT network organization. This hypothesis is supported by previous studies pointing to MT-dependent regulation of lineage differentiation. For example, in osteoblasts 3D cultures MTs control cells differentiation by maintaining cell and nuclear shape, and in hematopoietic progenitor cells MT density around the nucleus determines their myeloid differentiation by affecting chromatin organization and genes expression (Biedzinski et al., 2020; Meka et al., 2017). Finally, we know that MuSCs differentiation is accompanied by a switch from MTOC to ncMTOC (Tassin et al., 1985). In our experiments, we show that myoblasts differentiation occurs in parallel with a burst in SVBP expression and increased MT detyrosination. Thus, it is tempting to imagine that due to increased MT dynamics in the *Svbp* KO cells, the MTOC to ncMTOC redistribution occurs faster, resulting in a higher differentiation speed of *Svbp* KO MuSCs.

Altogether, these data suggest that increased MT dynamics due to the absence of MT detyrosination is the source of increased myonuclei number per myofiber. Normally, the increased myonuclei number is accompanied by increased myofibers volume and adaptation of myonuclear domain (Kadi et al., 1999; Rosenblatt et al., 1994). However, *Svbp* KO myofibers have similar size as WT myofibers and thus present a reduced myonuclear domain. One probable reason behind this phenomenon is the existing NMJs instability and denervation in the *Svbp* KO mice. Indeed, muscle denervation is generally followed by a global muscular atrophy in the affected skeletal muscle (Bongers et al., 2013). In addition, our *in vitro* experiments on long-term differentiated myoblasts show that in the absence of new fusion events, *Svbp* KO myofibers have smaller myofibers width compared to WT myofibers, suggesting the potential presence of another source of muscular atrophy in *Svbp* KO mice independent to muscular denervation, which remains to be identified. As a whole, these results propose a model in which muscular atrophy is compensated by MuSCs activation and fusion-induced muscular hypertrophy (Figure 47).

Interestingly, our complementary data from aged *Svbp* KO mice suggest that in addition to myonuclear domains, myonuclei shape can also be influenced by the long-term absence of stable detyrosinated MTs. Indeed, while myonuclei from young *Svbp* KO myofibers have the same morphology as myonuclei from WT myofibers, myonuclei from aged *Svbp* KO myofibers

present reduced area and feret compared to myonuclei from WT myofibers. This phenotype is observed much more delayed for myonuclei at the periphery of *Svbp* KO myofibers compared to MACF1 KO myofibers. However, we can imagine that just like in MACF1 KO mice, altered myonuclei shape may have resulted in altered gene expression in aged *Svbp* KO mice. If so, the expression of which gene is affected and what are the consequences for *Svbp* KO myofibers remain to be discovered.

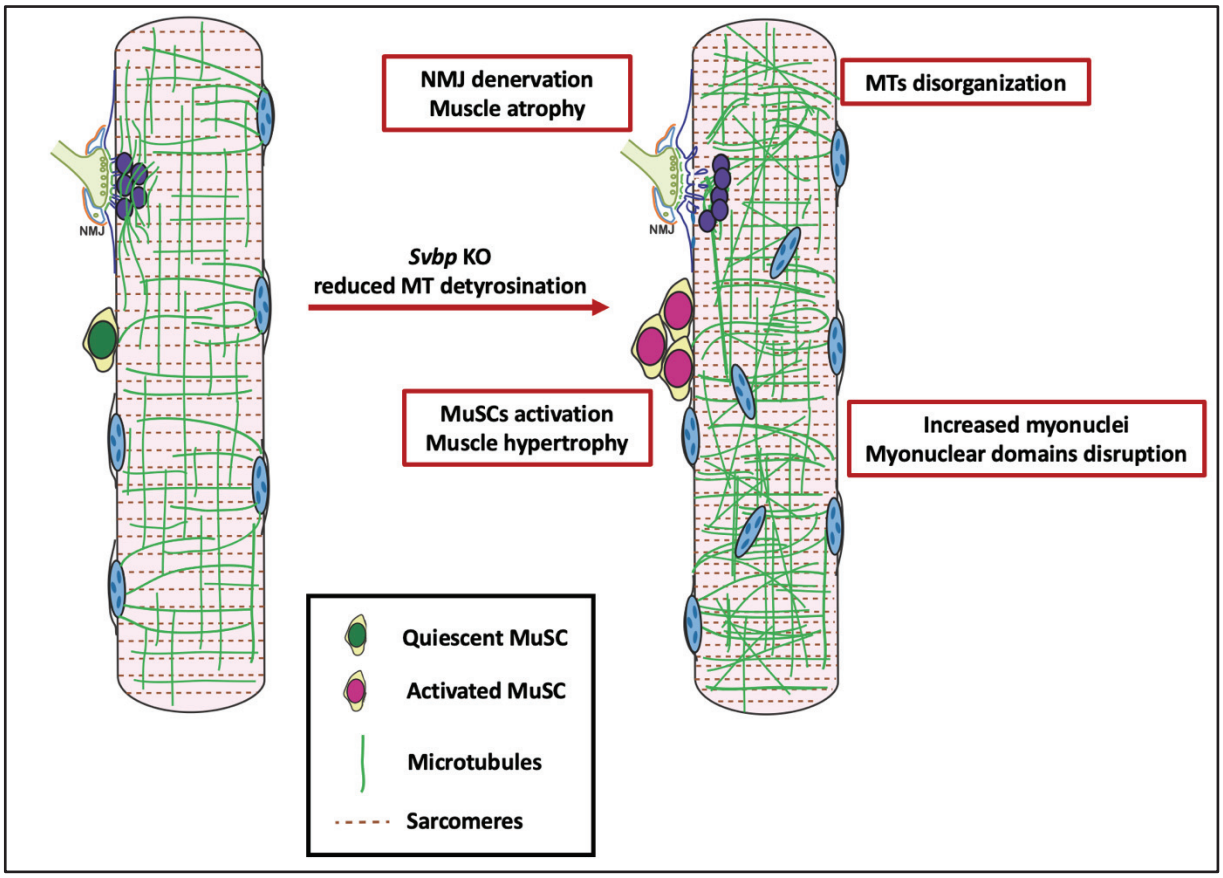

Figure 47: proposed model of the importance of SVBP and MT detyrosination in skeletal muscle homeostasis.

In healthy myofibers (left), SVBP promotes MT detyrosination in myofibers, their innervating motor neuron and their associated MuSCs. This creates a balance between dynamic tyrosinated and stable detyrosinated MTs and contributes to tissues homeostasis. Following a total abolishment of SVBP and high reduction of MT detyrosination, we can observe a disorganization of MTs within myofibers. In parallel we can observe a fragmentation and loss of NMJs, which could be due to NMJs instability at both pre- and post-synaptic regions. This NMJs denervation can be one of the contributes to MuSCs activation, which themselves have higher sensitivity to stress, higher proliferation, and higher differentiation rate in the absence of SVBP. In this proposed model, the fusion of MuSCs with adjacent myofibers compensates the muscular atrophy which should be present due to denervation and contributes to myonuclear domains disruption by increasing myonuclei content per myofibers.

III) MT network and myofibers functionality

1) Importance of MTs for NMJs and sarcomeres activity

Both MACF1 and SVBP KO mice present reduced muscle force production in response to stimulation when compared to matching-controls. These results correlate with muscular hypotonia observed in patients bearing mutations in either MACF1 or SVBP genes (Iqbal et al., 2019; Jørgensen et al., 2015; Oury et al., 2019). Interestingly, our complementary experiments suggest that reduced muscular force production could be mostly linked to NMJs disorganization in both models.

Our data from WT mice show that NMJs size is increased with myofibers maturation. In line with previously published data, we show that in healthy myofibers AChRs clusters at NMJs remain intact and hold on to their synaptic myonuclei which also increase in number as NMJs grow. Additionally, we observe rich tyrosinated and detyrosinated MT pools at the post-synaptic side of NMJs, suggesting that not all MTs at NMJs are detyrosinated and that both could participate in NMJs organization. Indeed, NMJs are known to be dense with MTs and MT-associated proteins such as Dynein, CLASP2, Clip170, and EB3, which are described important for NMJs stability (Basu et al., 2015, 2014; Ralston et al., 1999; Schmidt et al., 2012; Vilmont et al., 2016).

As a MAP, MACF1 has been described to support NMJs structure by linking MTs to AChRs through interaction with EB1 and MAP1b (Oury et al., 2019). In our experiments, we were able to show that in the absence of MACF1, AChRs do not cluster *in vitro.* In addition, our data from the skeletal muscle-specific inducible MACF1 KO mouse model confirms that MACF1 plays an essential role in NMJs stability as post-synaptic NMJs fragmentation precedes MTs and myonuclei disorganization in myofibers. In line with these results, we could observe a progressive NMJs fragmentation in MACF1 KO myofibers with age. Accordingly, MACF1 KO myofibers NMJs area do not grow with age *in vivo* and NMJs fail to recruit synaptic myonuclei. As previously discussed, MT disorganization and loss of MT density around myonuclei of MACF1 KO myofibers also results in long-term myofibrils disorganization due to mitochondrial accumulation in adult mice. In addition, MT disorganization have been linked to disrupted Ca^{2+} signaling within myofibers and thus irregular myofibers contractility (Khairallah et al., 2012). However, our data show no difference between Ca^{2+} release from SR of WT and MACF1 KO myofibers. In addition, reduced muscle force can be detected even in young MACF1 KO mice in advance to myofibrils disorganization in older mice. Together, these data suggest that lack of post-synaptic MT organization and NMJs fragmentation could be the main reasons behind reduced muscle force of MACF1 KO mice (Figure 46).

As a regulator of MT dynamics, we show that SVBP also participates in NMJs organization by stabilizing MTs through detyrosination. However, the NMJs fragmentation and denervation of *Svbp* KO myofibers can be looked at from different angles. On the fiber side, increased tyrosinated MTs in *Svbp* KO myofibers can affect the pool of MAPs at NMJs and result in NMJs instability and fragmentation. An example could be EB1, which has been previously

described at NMJs and has a preference for tyrosinated MTs (Chen et al., 2021; Oury et al., 2019). However, further studies are needed to uncover which of the post-synaptic MAPs are really affected by the absence of MT detyrosination and how this contributes to NMJs fragmentation. On the neurons side, reduced MT detyrosination has been shown to delay neurons axonal differentiation *in vitro* and reduce neuronal migration in the brain cortex *in vivo* (Aillaud et al., 2017). Thus, in our total *Svbp* KO model, we can imagine that myofibers denervation may be due to a mix of structural disorganization from the myofibers interior and neuronal instability from the exterior. Interestingly, in *Svbp* KO myofibers, number of synaptic myonuclei under fragmented NMJs remains equal to WT NMJs. One way to explain this is by imagining a compensatory myonuclei replacement due to MuSCs activation. As previously mentioned, instability of NMJs has been linked to the fusion of nearest MuSCs with myofibers and recruitment of accreted myonuclei to NMJs (Larouche et al., 2021). Therefore, we can speculate that following NMJs fragmentation in *Svbp* KO myofibers, synaptic myonuclei are lost and are subsequently replaced by newly added myonuclei. Nonetheless, dysfunctional NMJs may not be the only reasons behind reduced skeletal muscle force of *Svbp* KO mice, since *Svbp* KO myofibers also present shorter sarcomeric distance. This may be due to the disrupted MT interaction with sarcomeric Dystrophin, which is shown to be mainly mediated by detyrosinated MTs (Prins et al., 2009). Interestingly, increased MT detyrosination in MDX mice has been linked to increased myofibers stiffness, increased Ca^{2+} channels activation, and subsequently an increased myofibers contraction speed (Kerr et al., 2015). Whether the reverse is true for *Svbp* KO mice with reduced MT detyrosination remains to be explored. Yet, one can imagine that in addition to NMJs disorganization, disrupted Ca^{2+} signaling may also be a contributor to reduced myofibers force in *Svbp* KO mice.

2) Importance of MTs in other subcellular processes

In addition to structural and mechanical support, our data suggest that a stable MT organization can ensure the proper functionality of different subcellular processes within myofibers.

Our electronic microscopy images suggest an accumulation of glycogen within young *Svbp* KO myofibers. Remarkably, accumulated glycogen has been previously linked to altered myofibers metabolism and functionality (Testoni et al., 2017). What are the consequences of this increased glycogen accumulation for *Svbp* KO myofibers metabolism are unknown for the moment. However, this glycogen accumulation could partially participate to reduced *Svbp* KO mice muscle functionality. These data are consistent with the observation of GSK3 phosphorylation in whole protein extracts from young *Svbp* KO skeletal muscles. Indeed, GSK3 phosphorylation results in its inactivation and subsequently increased activity of glycogen synthesis (Cross et al., 1995; Srivastava and Pandey, 1998; Welsh et al., 1996). These data suggest that the accumulation of glycogen within *Svbp* KO myofibers may be due to aberrant GSK3 activity. Yet, which upstream regulator of GSK3 phosphorylation is disrupted by imbalanced MT tyrosination/detyrosination in young *Svbp* KO myofibers remains to be discovered.

Interestingly, our complementary data suggest that glycogenesis is not the only metabolic pathways which is altered in *Svbp* KO mice. Our histological and protein analysis on aged *Svbp*

KO muscles suggest an increased mitochondrial activity compared to WT muscles. Yet, compared to MACF1 KO mice, we could not detect an increase in markers of mitochondrial biogenesis to explain the increased mitochondrial activity in *Svbp* KO mice myofibers. Indeed, MTs can participate in mitochondria dynamics and disruption of MT network can directly affect mitochondrial activity (Maldonado et al., 2010; Melkov et al., 2015). Thus, the dysregulated mechanism behind increased mitochondrial due to MT disorganization in aged *Svbp* KO muscles has to be further investigated.

At last, another example of MT-dependent subcellular processes could be the distribution of subcellular cargoes, such as mRNAs, which are moved on MT railways to travel within large myofibers (Denes et al., 2021; Ralston and Hall, 1992). Therefore, we can imagine that increased MT dynamics and MT network disorganization in MACF1 and SVBP KO myofibers may also disrupt proper mRNA transport and homogenous genes expression within myofibers.

Conclusion

Altogether, this thesis has allowed us to highlight the importance of a regulated MT dynamics in skeletal muscle, from development to function. While this project was initially concentrated on the role of the microtubule-associated protein MACF1 in myonuclei positioning, the complexity of myofibers interior architecture guided us to reveal how regulation of MT dynamics, either through associated proteins such as MACF1, or through its PTMs such as detyrosination, can impact myonuclear domain distribution, NMJs stability, sarcomeres organization, and altogether, myofibers functionality.

References

A

Abou Sawan, S., Hodson, N., Babits, P., Malowany, J.M., Kumbhare, D., Moore, D.R., 2021. Satellite cell and myonuclear accretion is related to training-induced skeletal muscle fiber hypertrophy in young males and females. J. Appl. Physiol. 131, 871–880. https://doi.org/10.1152/japplphysiol.00424.2021

Adames, N.R., Cooper, J.A., 2000. Microtubule Interactions with the Cell Cortex Causing Nuclear Movements in Saccharomyces cerevisiae. J. Cell Biol. 149, 863–874. https://doi.org/10.1083/jcb.149.4.863

Adhihetty, P.J., O'Leary, M.F.N., Chabi, B., Wicks, K.L., Hood, D.A., 2007. Effect of denervation on mitochondrially mediated apoptosis in skeletal muscle. J. Appl. Physiol. 102, 1143–1151. https://doi.org/10.1152/japplphysiol.00768.2006

Ahuja, A.S., 2018. Understanding mitochondrial myopathies: a review. PeerJ 6, e4790. https://doi.org/10.7717/peerj.4790

Aillaud, C., Bosc, C., Peris, L., Bosson, A., Heemeryck, P., Van Dijk, J., Le Friec, J., Boulan, B., Vossier, F., Sanman, L.E., Syed, S., Amara, N., Couté, Y., Lafanechère, L., Denarier, E., Delphin, C., Pelletier, L., Humbert, S., Bogyo, M., Andrieux, A., Rogowski, K., Moutin, M.-J., 2017. Vasohibins/SVBP are tubulin carboxypeptidases (TCPs) that regulate neuron differentiation. Science 358, 1448–1453. https://doi.org/10.1126/science.aao4165

Akella, J.S., Wloga, D., Kim, J., Starostina, N.G., Lyons-Abbott, S., Morrissette, N.S., Dougan, S.T., Kipreos, E.T., Gaertig, J., 2010. MEC-17 is an α-tubulin acetyltransferase. Nature 467, 218–222. https://doi.org/10.1038/nature09324

Akhmanova, A., Steinmetz, M.O., 2010. Microtubule +TIPs at a glance. J. Cell Sci. 123, 3415–3419. https://doi.org/10.1242/jcs.062414

Alberts, B., 2019. Essential cell biology, Fifth edition. ed. W.W. Norton & Company, New York.

Allen, D.L., Linderman, J.K., Roy, R.R., Bigbee, A.J., Grindeland, R.E., Mukku, V., Edgerton, V.R., 1997. Apoptosis: a mechanism contributing to remodeling of skeletal muscle in response to hindlimb unweighting. Am. J. Physiol.-Cell Physiol. 273, C579–C587. https://doi.org/10.1152/ajpcell.1997.273.2.C579

Allen, D.L., Yasui, W., Tanaka, T., Ohira, Y., Nagaoka, S., Sekiguchi, C., Hinds, W.E., Roy, R.R., Edgerton, V.R., 1996. Myonuclear number and myosin heavy chain expression in rat soleus single muscle fibers after spaceflight. J. Appl. Physiol. 81, 145–151. https://doi.org/10.1152/jappl.1996.81.1.145

Almada, A.E., Wagers, A.J., 2016. Molecular circuitry of stem cell fate in skeletal muscle regeneration, ageing and disease. Nat. Rev. Mol. Cell Biol. 17, 267–279. https://doi.org/10.1038/nrm.2016.7

Al-Qusairi, L., Laporte, J., 2011. T-tubule biogenesis and triad formation in skeletal muscle and implication in human diseases. Skelet. Muscle 1, 26. https://doi.org/10.1186/2044-5040-1-26

Al-Qusairi, L., Weiss, N., Toussaint, A., Berbey, C., Messaddeq, N., Kretz, C., Sanoudou, D., Beggs, A.H., Allard, B., Mandel, J.-L., Laporte, J., Jacquemond, V., Buj-Bello, A., 2009. T-tubule disorganization and defective excitation-contraction coupling in muscle fibers lacking myotubularin lipid phosphatase. Proc. Natl. Acad. Sci. U. S. A. 106, 18763–18768. https://doi.org/10.1073/pnas.0900705106

Alway, S.E., Degens, H., Krishnamurthy, G., Chaudhrai, A., 2003. Denervation Stimulates Apoptosis But Not Id2 Expression in Hindlimb Muscles of Aged Rats. J. Gerontol. A. Biol. Sci. Med. Sci. 58, B687–B697. https://doi.org/10.1093/gerona/58.8.B687

Amthor, H., Christ, B., Weil, M., Patel, K., 1998. The importance of timing differentiation during limb muscle development. Curr. Biol. 8, 642–652. https://doi.org/10.1016/S0960-9822(98)70251-9

Antin, P.B., Forry-Schaudies, S., Friedman, T.M., Tapscott, S.J., Holtzer, H., 1981. Taxol induces postmitotic myoblasts to assemble interdigitating microtubule-myosin arrays that exclude actin filaments. J. Cell Biol. 90, 300–308. https://doi.org/10.1083/jcb.90.2.300

Aouizerate, J., De Antonio, M., Bader-Meunier, B., Barnerias, C., Bodemer, C., Isapof, A., Quartier, P., Melki, I., Charuel, J.-L., Bassez, G., Desguerre, I., Gherardi, R.K., Authier, F.-J., Gitiaux, C., 2018. Muscle ischaemia associated with NXP2 autoantibodies: a severe subtype of juvenile dermatomyositis. Rheumatology 57, 873–879. https://doi.org/10.1093/rheumatology/kex516

Arce, C.A., Hallak, M.E., Rodriguez, J.A., Barra, H.S., Caputio, R., 1978. CAPABILITY OF TUBULIN AND MICROTUBULES TO INCORPORATE AND TO RELEASE TYROSINE AND PHENYLALANINE AND THE EFFECT OF THE INCORPORATION OF THESE AMINO ACIDS ON TUBULIN ASSEMBLY. J. Neurochem. 31, 205–210. https://doi.org/10.1111/j.1471-4159.1978.tb12449.x

Arce, C.A., Rodriguez, J.A., Barra, H.S., Caputto, R., 1975. Incorporation of l-Tyrosine, l-Phenylalanine and l-3,4-Dihydroxyphenylalanine as Single Units into Rat Brain Tubulin. Eur. J. Biochem. 59, 145–149. https://doi.org/10.1111/j.1432-1033.1975.tb02435.x

Auld, A.L., Folker, E.S., 2016. Nucleus-dependent sarcomere assembly is mediated by the LINC complex. Mol. Biol. Cell 27, 2351–2359. https://doi.org/10.1091/mbc.E16-01-0021

Avellaneda, J., Rodier, C., Daian, F., Brouilly, N., Rival, T., Luis, N.M., Schnorrer, F., 2021. Myofibril and mitochondria morphogenesis are coordinated by a mechanical feedback mechanism in muscle. Nat. Commun. 12, 2091. https://doi.org/10.1038/s41467-021-22058-7

Aziz, A., Sebastian, S., Dilworth, F.J., 2012. The Origin and Fate of Muscle Satellite Cells. Stem Cell Rev. Rep. 8, 609–622. https://doi.org/10.1007/s12015-012-9352-0

B

Baas, P.W., Deitch, J.S., Black, M.M., Banker, G.A., 1988. Polarity orientation of microtubules in hippocampal neurons: uniformity in the axon and nonuniformity in the dendrite. Proc. Natl. Acad. Sci. U. S. A. 85, 8335–8339. https://doi.org/10.1073/pnas.85.21.8335

Baghdadi, M.B., Castel, D., Machado, L., Fukada, S.-I., Birk, D.E., Relaix, F., Tajbakhsh, S., Mourikis, P., 2018. Reciprocal signalling by Notch-Collagen V-CALCR retains muscle stem cells in their niche. Nature 557, 714–718. https://doi.org/10.1038/s41586-018-0144-9

Barbeau, S., Tahraoui-Bories, J., Legay, C., Martinat, C., 2020. Building neuromuscular junctions *in vitro*. Development 147, dev193920. https://doi.org/10.1242/dev.193920

Barik, A., Li, L., Sathyamurthy, A., Xiong, W.-C., Mei, L., 2016. Schwann Cells in Neuromuscular Junction Formation and Maintenance. J. Neurosci. 36, 9770–9781. https://doi.org/10.1523/JNEUROSCI.0174-16.2016

Barisic, M., Silva e Sousa, R., Tripathy, S.K., Magiera, M.M., Zaytsev, A.V., Pereira, A.L., Janke, C., Grishchuk, E.L., Maiato, H., 2015. Microtubule detyrosination guides chromosomes during mitosis. Science 348, 799–803. https://doi.org/10.1126/science.aaa5175

Basu, S., Sladecek, S., Martinez de la Peña y Valenzuela, I., Akaaboune, M., Smal, I., Martin, K., Galjart, N., Brenner, H.R., 2015. CLASP2-dependent microtubule capture at the neuromuscular junction membrane requires LL5β and actin for focal delivery of acetylcholine receptor vesicles. Mol. Biol. Cell 26, 938–951. https://doi.org/10.1091/mbc.E14-06-1158

Basu, S., Sladecek, S., Pemble, H., Wittmann, T., Slotman, J.A., van Cappellen, W., Brenner, H.-R., Galjart, N., 2014. Acetylcholine Receptor (AChR) Clustering Is Regulated Both by Glycogen Synthase Kinase 3β (GSK3β)-dependent Phosphorylation and the Level of CLIP-associated Protein 2 (CLASP2) Mediating the Capture of Microtubule Plus-ends. J. Biol. Chem. 289, 30857–30867. https://doi.org/10.1074/jbc.M114.589457

Baye, L.M., Link, B.A., 2008. Nuclear migration during retinal development. Brain Res. 1192, 29–36. https://doi.org/10.1016/j.brainres.2007.05.021

Belanto, J.J., Mader, T.L., Eckhoff, M.D., Strandjord, D.M., Banks, G.B., Gardner, M.K., Lowe, D.A., Ervasti, J.M., 2014. Microtubule binding distinguishes dystrophin from utrophin. Proc. Natl. Acad. Sci. 111, 5723–5728. https://doi.org/10.1073/pnas.1323842111

Berbari, N.F., Bishop, G.A., Askwith, C.C., Lewis, J.S., Mykytyn, K., 2007. Hippocampal neurons possess primary cilia in culture. J. Neurosci. Res. 85, 1095–1100. https://doi.org/10.1002/jnr.21209

Bernier, G., Mathieu, M., De Repentigny, Y., Vidal, S.M., Kothary, R., 1996. Cloning and characterization of mouse ACF7, a novel member of the dystonin subfamily of actin binding proteins. Genomics 38, 19–29. https://doi.org/10.1006/geno.1996.0587

Biedzinski, S., Agsu, G., Vianay, B., Delord, M., Blanchoin, L., Larghero, J., Faivre, L., Théry, M., Brunet, S., 2020. Microtubules control nuclear shape and gene expression during early stages of hematopoietic differentiation. EMBO J. 39. https://doi.org/10.15252/embj.2019103957

Birchmeier, C., Brohmann, H., 2000. Genes that control the development of migrating muscle precursor cells. Curr. Opin. Cell Biol. 12, 725–730. https://doi.org/10.1016/S0955-0674(00)00159-9

Bongers, K.S., Fox, D.K., Ebert, S.M., Kunkel, S.D., Dyle, M.C., Bullard, S.A., Dierdorff, J.M., Adams, C.M., 2013. Skeletal muscle denervation causes skeletal muscle atrophy through a pathway that involves both Gadd45a and HDAC4. Am. J. Physiol. Endocrinol. Metab. 305, E907-915. https://doi.org/10.1152/ajpendo.00380.2013

Bornens, M., 2012. The Centrosome in Cells and Organisms. Science 335, 422–426. https://doi.org/10.1126/science.1209037

Boyer, J.G., Bhanot, K., Kothary, R., Boudreau-Larivière, C., 2010. Hearts of Dystonia musculorum Mice Display Normal Morphological and Histological Features but Show Signs of Cardiac Stress. PLoS ONE 5, e9465. https://doi.org/10.1371/journal.pone.0009465

Brodu, V., Baffet, A.D., Le Droguen, P.-M., Casanova, J., Guichet, A., 2010. A Developmentally Regulated Two-Step Process Generates a Noncentrosomal Microtubule Network in Drosophila Tracheal Cells. Dev. Cell 18, 790–801. https://doi.org/10.1016/j.devcel.2010.03.015

Bruusgaard, J.C., Gundersen, K., 2008. In vivo time-lapse microscopy reveals no loss of murine myonuclei during weeks of muscle atrophy. J. Clin. Invest. 118, 1450–1457. https://doi.org/10.1172/JCI34022

Bruusgaard, J.C., Liestøl, K., Ekmark, M., Kollstad, K., Gundersen, K., 2003. Number and spatial distribution of nuclei in the muscle fibres of normal mice studied *in vivo*. J. Physiol. 551, 467–478. https://doi.org/10.1113/jphysiol.2003.045328

Buckingham, M., Bajard, L., Chang, T., Daubas, P., Hadchouel, J., Meilhac, S., Montarras, D., Rocancourt, D., Relaix, F., 2003. The formation of skeletal muscle: from somite to limb. J. Anat. 202, 59–68. https://doi.org/10.1046/j.1469-7580.2003.00139.x

Buckingham, M., Relaix, F., 2015. PAX3 and PAX7 as upstream regulators of myogenesis. Semin. Cell Dev. Biol. 44, 115–125. https://doi.org/10.1016/j.semcdb.2015.09.017

Bugnard, E., Zaal, K.J.M., Ralston, E., 2005. Reorganization of microtubule nucleation during muscle differentiation. Cell Motil. Cytoskeleton 60, 1–13. https://doi.org/10.1002/cm.20042

Burleigh, I.G., 1977. Observations on the number of nuclei within the fibres of some red and white muscles. J. Cell Sci. 23, 269–284. https://doi.org/10.1242/jcs.23.1.269

Buxboim, A., Swift, J., Irianto, J., Spinler, K.R., Dingal, P.C.D.P., Athirasala, A., Kao, Y.-R.C., Cho, S., Harada, T., Shin, J.-W., Discher, D.E., 2014. Matrix elasticity regulates lamin-A,C phosphorylation and turnover with feedback to actomyosin. Curr. Biol. CB 24, 1909–1917. https://doi.org/10.1016/j.cub.2014.07.001

Byers, T.J., Beggs, A.H., McNally, E.M., Kunkel, L.M., 1995. Novel actin crosslinker superfamily member identified by a two step degenerate PCR procedure. FEBS Lett. 368, 500–504. https://doi.org/10.1016/0014-5793(95)00722-l

C

Cadot, B., Gache, V., Gomes, E.R., 2015. Moving and positioning the nucleus in skeletal muscle – one step at a time. Nucleus 6, 373–381. https://doi.org/10.1080/19491034.2015.1090073

Cadot, B., Gache, V., Vasyutina, E., Falcone, S., Birchmeier, C., Gomes, E.R., 2012. Nuclear movement during myotube formation is microtubule and dynein dependent and is regulated by Cdc42, Par6 and Par3. EMBO Rep. 13, 741–749. https://doi.org/10.1038/embor.2012.89

Caplow, M., 1992. Microtubule dynamics. Curr. Opin. Cell Biol. 4, 58–65. https://doi.org/10.1016/0955-0674(92)90059-L

Caplow, M., Shanks, J., 1996. Evidence that a single monolayer tubulin-GTP cap is both necessary and sufficient to stabilize microtubules. Mol. Biol. Cell 7, 663–675. https://doi.org/10.1091/mbc.7.4.663

Caplow, M., Shanks, J., 1990. Mechanism of the microtubule GTPase reaction. J. Biol. Chem. 265, 8935–8941. https://doi.org/10.1016/S0021-9258(19)38978-1

Caporizzo, M.A., Chen, C.Y., Salomon, A.K., Margulies, K.B., Prosser, B.L., 2018. Microtubules Provide a Viscoelastic Resistance to Myocyte Motion. Biophys. J. 115, 1796–1807. https://doi.org/10.1016/j.bpj.2018.09.019

Cardasis, C.A., Cooper, G.W., 1975. An analysis of nuclear numbers in individual muscle fibers during differentiation and growth: A satellite cell-muscle fiber growth unit. J. Exp. Zool. 191, 347–357. https://doi.org/10.1002/jez.1401910305

Caudron, N., Arnal, I., Buhler, E., Job, D., Valiron, O., 2002. Microtubule Nucleation from Stable Tubulin Oligomers. J. Biol. Chem. 277, 50973–50979. https://doi.org/10.1074/jbc.M209753200

Cetin, H., Beeson, D., Vincent, A., Webster, R., 2020. The Structure, Function, and Physiology of the Fetal and Adult Acetylcholine Receptor in Muscle. Front. Mol. Neurosci. 13, 581097. https://doi.org/10.3389/fnmol.2020.581097

Chal, J., Pourquié, O., 2017. Making muscle: skeletal myogenesis *in vivo* and *in vitro*. Development 144, 2104–2122. https://doi.org/10.1242/dev.151035

Chapman, M.A., Zhang, J., Banerjee, I., Guo, L.T., Zhang, Z., Shelton, G.D., Ouyang, K., Lieber, R.L., Chen, J., 2014. Disruption of both nesprin 1 and desmin results in nuclear anchorage defects and fibrosis in skeletal muscle. Hum. Mol. Genet. 23, 5879–5892. https://doi.org/10.1093/hmg/ddu310

Charvet, B., Ruggiero, F., Le Guellec, D., 2012. The development of the myotendinous junction. A review. Muscles Ligaments Tendons J. 2, 53–63.

Chen, C.Y., Caporizzo, M.A., Bedi, K., Vite, A., Bogush, A.I., Robison, P., Heffler, J.G., Salomon, A.K., Kelly, N.A., Babu, A., Morley, M.P., Margulies, K.B., Prosser, B.L., 2018. Suppression of detyrosinated microtubules improves cardiomyocyte function in human heart failure. Nat. Med. 24, 1225–1233. https://doi.org/10.1038/s41591-018-0046-2

Chen, C.Y., Salomon, A.K., Caporizzo, M.A., Curry, S., Kelly, N.A., Bedi, K., Bogush, A.I., Krämer, E., Schlossarek, S., Janiak, P., Moutin, M.-J., Carrier, L., Margulies, K.B., Prosser, B.L., 2020. Depletion of Vasohibin 1 Speeds Contraction and Relaxation in Failing Human Cardiomyocytes. Circ. Res. 127. https://doi.org/10.1161/CIRCRESAHA.119.315947

Chen, H.-J., Lin, C.-M., Lin, C.-S., Perez-Olle, R., Leung, C.L., Liem, R.K.H., 2006. The role of microtubule actin cross-linking factor 1 (MACF1) in the Wnt signaling pathway. Genes Dev. 20, 1933–1945. https://doi.org/10.1101/gad.1411206

Chen, J., Kholina, E., Szyk, A., Fedorov, V.A., Kovalenko, I., Gudimchuk, N., Roll-Mecak, A., 2021. α-tubulin tail modifications regulate microtubule stability through selective effector recruitment, not changes in intrinsic polymer dynamics. Dev. Cell 56, 2016-2028.e4. https://doi.org/10.1016/j.devcel.2021.05.005

Choi, Y.-K., Liu, P., Sze, S.K., Dai, C., Qi, R.Z., 2010. CDK5RAP2 stimulates microtubule nucleation by the γ-tubulin ring complex. J. Cell Biol. 191, 1089–1095. https://doi.org/10.1083/jcb.201007030

Chrétien, D., Fuller, S.D., Karsenti, E., 1995. Structure of growing microtubule ends: two-dimensional sheets close into tubes at variable rates. J. Cell Biol. 129, 1311–1328. https://doi.org/10.1083/jcb.129.5.1311

Clemen, C.S., Herrmann, H., Strelkov, S.V., Schröder, R., 2013. Desminopathies: pathology and mechanisms. Acta Neuropathol. (Berl.) 125, 47–75. https://doi.org/10.1007/s00401-012-1057-6

Coleman, A.K., Joca, H.C., Shi, G., Lederer, W.J., Ward, C.W., 2021. Tubulin acetylation increases cytoskeletal stiffness to regulate mechanotransduction in striated muscle. J. Gen. Physiol. 153, e202012743. https://doi.org/10.1085/jgp.202012743

Collins, M.A., Mandigo, T.R., Camuglia, J.M., Vazquez, G.A., Anderson, A.J., Hudson, C.H., Hanron, J.L., Folker, E.S., 2017. Emery–Dreifuss muscular dystrophy–linked genes and centronuclear myopathy–linked genes regulate myonuclear movement by distinct mechanisms. Mol. Biol. Cell 28, 2303–2317. https://doi.org/10.1091/mbc.e16-10-0721

Connolly, J.A., Kiosses, B.W., Kalnins, V.I., 1986. Centrioles are lost as embryonic myoblasts fuse into myotubes in vitro. Eur. J. Cell Biol. 39, 341–345.

Coombes, C.E., Yamamoto, A., Kenzie, M.R., Odde, D.J., Gardner, M.K., 2013. Evolving Tip Structures Can Explain Age-Dependent Microtubule Catastrophe. Curr. Biol. 23, 1342–1348. https://doi.org/10.1016/j.cub.2013.05.059

Cota, R.R., Teixidó-Travesa, N., Ezquerra, A., Eibes, S., Lacasa, C., Roig, J., Lüders, J., 2016. MZT1 regulates microtubule nucleation by linking γTuRC assembly to adapter-mediated targeting and activation. J. Cell Sci. jcs.195321. https://doi.org/10.1242/jcs.195321

Couturier, N., Gache, V., 2017. Prix Master 2016 de la SFM: Domaine nucléaire et protéome microtubulaire au cours de la maturation des fibres musculaires. médecine/sciences 33, 63–66. https://doi.org/10.1051/medsci/201733s115

Cowling, B.S., Toussaint, A., Amoasii, L., Koebel, P., Ferry, A., Davignon, L., Nishino, I., Mandel, J.-L., Laporte, J., 2011. Increased Expression of Wild-Type or a Centronuclear Myopathy Mutant of Dynamin 2 in Skeletal Muscle of Adult Mice Leads to Structural Defects and Muscle Weakness. Am. J. Pathol. 178, 2224–2235. https://doi.org/10.1016/j.ajpath.2011.01.054

Cramer, A.A.W., Prasad, V., Eftestøl, E., Song, T., Hansson, K.-A., Dugdale, H.F., Sadayappan, S., Ochala, J., Gundersen, K., Millay, D.P., 2020. Nuclear numbers in syncytial muscle fibers promote size but limit the development of larger myonuclear domains. Nat. Commun. 11, 6287. https://doi.org/10.1038/s41467-020-20058-7

Crameri, R.M., Aagaard, P., Qvortrup, K., Langberg, H., Olesen, J., Kjaer, M., 2007. Myofibre damage in human skeletal muscle: effects of electrical stimulation *versus* voluntary contraction: Uniform *versus* heterogenic activation of muscle fibres. J. Physiol. 583, 365–380. https://doi.org/10.1113/jphysiol.2007.128827

Crawford, K., Flick, R., Close, L., Shelly, D., Paul, R., Bove, K., Kumar, A., Lessard, J., 2002. Mice lacking skeletal muscle actin show reduced muscle strength and growth deficits and die during the neonatal period. Mol. Cell. Biol. 22, 5887–5896. https://doi.org/10.1128/MCB.22.16.5887-5896.2002

Cross, D.A.E., Alessi, D.R., Cohen, P., Andjelkovich, M., Hemmings, B.A., 1995. Inhibition of glycogen synthase kinase-3 by insulin mediated by protein kinase B. Nature 378, 785–789. https://doi.org/10.1038/378785a0

Cusseddu, R., Robert, A., Côté, J.-F., 2021. Strength Through Unity: The Power of the Mega-Scaffold MACF1. Front. Cell Dev. Biol. 9, 641727. https://doi.org/10.3389/fcell.2021.641727
Dahl, K.N., Ribeiro, A.J.S., Lammerding, J., 2008. Nuclear Shape, Mechanics, and Mechanotransduction. Circ. Res. 102, 1307–1318. https://doi.org/10.1161/CIRCRESAHA.108.173989

D

Dalpé, G., Mathieu, M., Comtois, A., Zhu, E., Wasiak, S., De Repentigny, Y., Leclerc, N., Kothary, R., 1999. Dystonin-Deficient Mice Exhibit an Intrinsic Muscle Weakness and an Instability of Skeletal Muscle Cytoarchitecture. Dev. Biol. 210, 367–380. https://doi.org/10.1006/dbio.1999.9263

Darr, K.C., Schultz, E., 1989. Hindlimb suspension suppresses muscle growth and satellite cell proliferation. J. Appl. Physiol. 67, 1827–1834. https://doi.org/10.1152/jappl.1989.67.5.1827

Davidson, P.M., Cadot, B., 2021. Actin on and around the Nucleus. Trends Cell Biol. 31, 211–223. https://doi.org/10.1016/j.tcb.2020.11.009

Dayal, A.A., Medvedeva, N.V., Nekrasova, T.M., Duhalin, S.D., Surin, A.K., Minin, A.A., 2020. Desmin Interacts Directly with Mitochondria. Int. J. Mol. Sci. 21, 8122. https://doi.org/10.3390/ijms21218122

de Castro Rodrigues, A., Schmalbruch, H., 1995. Satellite cells and myonuclei in long-term denervated rat muscles. Anat. Rec. 243, 430–437. https://doi.org/10.1002/ar.1092430405

De Magistris, P., Antonin, W., 2018. The Dynamic Nature of the Nuclear Envelope. Curr. Biol. 28, R487–R497. https://doi.org/10.1016/j.cub.2018.01.073

Deanin, G.G., Gordon, M.W., 1976. The distribution of tyrosyltubulin ligase in brain and other tissues. Biochem. Biophys. Res. Commun. 71, 676–683. https://doi.org/10.1016/0006-291X(76)90841-X

Deanin, G.G., Thompson, W.C., Gordon, M.W., 1977. Tyrosyltubulin ligase activity in brain, skeletal muscle, and liver of the developing chick. Dev. Biol. 57, 230–233. https://doi.org/10.1016/0012-1606(77)90370-0

Denes, L.T., Kelley, C.P., Wang, E.T., 2021. Microtubule-based transport is essential to distribute RNA and nascent protein in skeletal muscle. Nat. Commun. 12, 6079. https://doi.org/10.1038/s41467-021-26383-9

Dimitrov, A., Quesnoit, M., Moutel, S., Cantaloube, I., Poüs, C., Perez, F., 2008. Detection of GTP-Tubulin Conformation in Vivo Reveals a Role for GTP Remnants in Microtubule Rescues. Science 322, 1353–1356. https://doi.org/10.1126/science.1165401

Dobrowolny, G., Barbiera, A., Sica, G., Scicchitano, B.M., 2021. Age-Related Alterations at Neuromuscular Junction: Role of Oxidative Stress and Epigenetic Modifications. Cells 10, 1307. https://doi.org/10.3390/cells10061307

Dowling, J.J., Vreede, A.P., Low, S.E., Gibbs, E.M., Kuwada, J.Y., Bonnemann, C.G., Feldman, E.L., 2009. Loss of myotubularin function results in T-tubule disorganization in zebrafish and human myotubular myopathy. PLoS Genet. 5, e1000372. https://doi.org/10.1371/journal.pgen.1000372

Doxsey, S., 2001. Re-evaluating centrosome function. Nat. Rev. Mol. Cell Biol. 2, 688–698. https://doi.org/10.1038/35089575

Drabek, K., van Ham, M., Stepanova, T., Draegestein, K., van Horssen, R., Sayas, C.L., Akhmanova, A., ten Hagen, T., Smits, R., Fodde, R., Grosveld, F., Galjart, N., 2006. Role of CLASP2 in Microtubule Stabilization and the Regulation of Persistent Motility. Curr. Biol. 16, 2259–2264. https://doi.org/10.1016/j.cub.2006.09.065

Drechsel, D.N., Kirschner, M.W., 1994. The minimum GTP cap required to stabilize microtubules. Curr. Biol. CB 4, 1053–1061. https://doi.org/10.1016/s0960-9822(00)00243-8

Duan, D., Goemans, N., Takeda, S., Mercuri, E., Aartsma-Rus, A., 2021. Duchenne muscular dystrophy. Nat. Rev. Dis. Primer 7, 13. https://doi.org/10.1038/s41572-021-00248-3

Dungan, C.M., Murach, K.A., Frick, K.K., Jones, S.R., Crow, S.E., Englund, D.A., Vechetti, I.J., Figueiredo, V.C., Levitan, B.M., Satin, J., McCarthy, J.J., Peterson, C.A., 2019. Elevated myonuclear density during skeletal muscle hypertrophy in response to training is reversed during detraining. Am. J. Physiol.-Cell Physiol. 316, C649–C654. https://doi.org/10.1152/ajpcell.00050.2019

E

Efimov, A., Kharitonov, A., Efimova, N., Loncarek, J., Miller, P.M., Andreyeva, N., Gleeson, P., Galjart, N., Maia, A.R.R., McLeod, I.X., Yates, J.R., Maiato, H., Khodjakov, A., Akhmanova, A., Kaverina, I., 2007. Asymmetric CLASP-Dependent Nucleation of Noncentrosomal Microtubules at the trans-Golgi Network. Dev. Cell 12, 917–930. https://doi.org/10.1016/j.devcel.2007.04.002

Eliazer, S., Muncie, J.M., Christensen, J., Sun, X., D'Urso, R.S., Weaver, V.M., Brack, A.S., 2019. Wnt4 from the Niche Controls the Mechano-Properties and Quiescent State of Muscle Stem Cells. Cell Stem Cell 25, 654-665.e4. https://doi.org/10.1016/j.stem.2019.08.007

Elosegui-Artola, A., Andreu, I., Beedle, A.E.M., Lezamiz, A., Uroz, M., Kosmalska, A.J., Oria, R., Kechagia, J.Z., Rico-Lastres, P., Le Roux, A.-L., Shanahan, C.M., Trepat, X., Navajas, D., Garcia-Manyes, S., Roca-Cusachs, P., 2017. Force Triggers YAP Nuclear Entry by Regulating Transport across Nuclear Pores. Cell 171, 1397-1410.e14. https://doi.org/10.1016/j.cell.2017.10.008

Enyedi, B., Niethammer, P., 2017. Nuclear membrane stretch and its role in mechanotransduction. Nucleus 8, 156–161. https://doi.org/10.1080/19491034.2016.1263411

Erickson, H.P., O'Brien, E.T., 1992. Microtubule Dynamic Instability and GTP Hydrolysis. Annu. Rev. Biophys. Biomol. Struct. 21, 145–166. https://doi.org/10.1146/annurev.bb.21.060192.001045

Ersfeld, K., Wehland, J., Plessmann, U., Dodemont, H., Gerke, V., Weber, K., 1993. Characterization of the tubulin-tyrosine ligase. J. Cell Biol. 120, 725–732. https://doi.org/10.1083/jcb.120.3.725

Espigat-Georger, A., Dyachuk, V., Chemin, C., Emorine, L., Merdes, A., 2016. Nuclear alignment in myotubes requires centrosome proteins recruited by nesprin-1. J. Cell Sci. jcs.191767. https://doi.org/10.1242/jcs.191767

Esteves de Lima, J., Bonnin, M.-A., Birchmeier, C., Duprez, D., 2016. Muscle contraction is required to maintain the pool of muscle progenitors via YAP and NOTCH during fetal myogenesis. eLife 5, e15593. https://doi.org/10.7554/eLife.15593

F

Falcone, S., Roman, W., Hnia, K., Gache, V., Didier, N., Lainé, J., Auradé, F., Marty, I., Nishino, I., Charlet-Berguerand, N., Romero, N.B., Marazzi, G., Sassoon, D., Laporte, J., Gomes, E.R., 2014. N- WASP is required for Amphiphysin-2/ BIN 1-dependent nuclear positioning and triad organization in skeletal muscle and is involved in the pathophysiology of centronuclear myopathy. EMBO Mol. Med. 6, 1455–1475. https://doi.org/10.15252/emmm.201404436

Fant, X., Srsen, V., Espigat-Georger, A., Merdes, A., 2009. Nuclei of Non-Muscle Cells Bind Centrosome Proteins upon Fusion with Differentiating Myoblasts. PLoS ONE 4, e8303. https://doi.org/10.1371/journal.pone.0008303

Farache, D., Emorine, L., Haren, L., Merdes, A., 2018. Assembly and regulation of γ-tubulin complexes. Open Biol. 8, 170266. https://doi.org/10.1098/rsob.170266

Ferreira, L.T., Orr, B., Rajendraprasad, G., Pereira, A.J., Lemos, C., Lima, J.T., Guasch Boldú, C., Ferreira, J.G., Barisic, M., Maiato, H., 2020. α-Tubulin detyrosination impairs mitotic error correction by suppressing MCAK centromeric activity. J. Cell Biol. 219, e201910064. https://doi.org/10.1083/jcb.201910064

Findeisen, P., Mühlhausen, S., Dempewolf, S., Hertzog, J., Zietlow, A., Carlomagno, T., Kollmar, M., 2014. Six Subgroups and Extensive Recent Duplications Characterize the Evolution of the Eukaryotic Tubulin Protein Family. Genome Biol. Evol. 6, 2274–2288. https://doi.org/10.1093/gbe/evu187

Folker, E.S., Baylies, M.K., 2013. Nuclear positioning in muscle development and disease. Front. Physiol. 4. https://doi.org/10.3389/fphys.2013.00363

Forcina, L., Cosentino, M., Musarò, A., 2020. Mechanisms Regulating Muscle Regeneration: Insights into the Interrelated and Time-Dependent Phases of Tissue Healing. Cells 9, 1297. https://doi.org/10.3390/cells9051297

Frontera, W.R., Ochala, J., 2015. Skeletal Muscle: A Brief Review of Structure and Function. Calcif. Tissue Int. 96, 183–195. https://doi.org/10.1007/s00223-014-9915-y

Fukada, S., Higashimoto, T., Kaneshige, A., 2022. Differences in muscle satellite cell dynamics during muscle hypertrophy and regeneration. Skelet. Muscle 12, 17. https://doi.org/10.1186/s13395-022-00300-0

G

Gache, V., Gomes, E.R., Cadot, B., 2017. Microtubule motors involved in nuclear movement during skeletal muscle differentiation. Mol. Biol. Cell 28, 865–874. https://doi.org/10.1091/mbc.e16-06-0405

Gache, V., Waridel, P., Luche, S., Shevchenko, A., Popov, A.V., 2007. Purification and Mass-Spectrometry Identification of Microtubule-Binding Proteins from Xenopus Egg Extracts, in: Zhou, J. (Ed.), Microtubule Protocols, Methods in Molecular Medicine™. Humana Press, Totowa, NJ, pp. 29–43. https://doi.org/10.1007/978-1-59745-442-1_3

Gadadhar, S., Bodakuntla, S., Natarajan, K., Janke, C., 2017. The tubulin code at a glance. J. Cell Sci. jcs.199471. https://doi.org/10.1242/jcs.199471

Gasic, I., 2022. Regulation of Tubulin Gene Expression: From Isotype Identity to Functional Specialization. Front. Cell Dev. Biol. 10, 9.

Gimpel, P., Lee, Y.L., Sobota, R.M., Calvi, A., Koullourou, V., Patel, R., Mamchaoui, K., Nédélec, F., Shackleton, S., Schmoranzer, J., Burke, B., Cadot, B., Gomes, E.R., 2017. Nesprin-1α-Dependent Microtubule Nucleation from the Nuclear Envelope via Akap450 Is Necessary for Nuclear Positioning in Muscle Cells. Curr. Biol. 27, 2999-3009.e9. https://doi.org/10.1016/j.cub.2017.08.031

Giordani, J., Bajard, L., Demignon, J., Daubas, P., Buckingham, M., Maire, P., 2007. Six proteins regulate the activation of *Myf5* expression in embryonic mouse limbs. Proc. Natl. Acad. Sci. 104, 11310–11315. https://doi.org/10.1073/pnas.0611299104

Goh, Q., Song, T., Petrany, M.J., Cramer, A.A., Sun, C., Sadayappan, S., Lee, S.-J., Millay, D.P., 2019. Myonuclear accretion is a determinant of exercise-induced remodeling in skeletal muscle. eLife 8, e44876. https://doi.org/10.7554/eLife.44876

Goldman, R.D., 1971. THE ROLE OF THREE CYTOPLASMIC FIBERS IN BHK-21 CELL MOTILITY. J. Cell Biol. 51, 752–762. https://doi.org/10.1083/jcb.51.3.752

Goldmann, W.H., 2018. Intermediate filaments and cellular mechanics: Intermediate filaments influence cell mechanics. Cell Biol. Int. 42, 132–138. https://doi.org/10.1002/cbin.10879

Gong, T.W., Besirli, C.G., Lomax, M.I., 2001. MACF1 gene structure: a hybrid of plectin and dystrophin. Mamm. Genome Off. J. Int. Mamm. Genome Soc. 12, 852–861. https://doi.org/10.1007/s00335-001-3037-3

Goodson, H.V., Jonasson, E.M., 2018. Microtubules and Microtubule-Associated Proteins. Cold Spring Harb. Perspect. Biol. 10, a022608. https://doi.org/10.1101/cshperspect.a022608

Goryunov, D., He, C.-Z., Lin, C.-S., Leung, C.L., Liem, R.K.H., 2010. Nervous-tissue-specific elimination of microtubule-actin crosslinking factor 1a results in multiple developmental defects in the mouse brain. Mol. Cell. Neurosci. 44, 1–14. https://doi.org/10.1016/j.mcn.2010.01.010

Granger, B.L., Lazarides, E., 1979. Desmin and vimentin coexist at the periphery of the myofibril Z disc. Cell 18, 1053–1063. https://doi.org/10.1016/0092-8674(79)90218-6

Grifone, R., Demignon, J., Houbron, C., Souil, E., Niro, C., Seller, M.J., Hamard, G., Maire, P., 2005. Six1 and Six4 homeoproteins are required for Pax3 and Mrf expression during myogenesis in the mouse embryo. Development 132, 2235–2249. https://doi.org/10.1242/dev.01773

Guillet, V., Knibiehler, M., Gregory-Pauron, L., Remy, M.-H., Chemin, C., Raynaud-Messina, B., Bon, C., Kollman, J.M., Agard, D.A., Merdes, A., Mourey, L., 2011. Crystal structure of γ-tubulin complex protein GCP4 provides insight into microtubule nucleation. Nat. Struct. Mol. Biol. 18, 915–919. https://doi.org/10.1038/nsmb.2083

Guilluy, C., Burridge, K., 2015. Nuclear mechanotransduction: Forcing the nucleus to respond. Nucleus 6, 19–22. https://doi.org/10.1080/19491034.2014.1001705

Gumy, L.F., Chew, D.J., Tortosa, E., Katrukha, E.A., Kapitein, L.C., Tolkovsky, A.M., Hoogenraad, C.C., Fawcett, J.W., 2013. The Kinesin-2 Family Member KIF3C Regulates Microtubule Dynamics and Is Required for Axon Growth and Regeneration. J. Neurosci. 33, 11329–11345. https://doi.org/10.1523/JNEUROSCI.5221-12.2013

Gundersen, G.G., Bulinski, J.C., 1988. Selective stabilization of microtubules oriented toward the direction of cell migration. Proc. Natl. Acad. Sci. 85, 5946–5950. https://doi.org/10.1073/pnas.85.16.5946

Gundersen, G. G., Bulinski, J.C., 1986. Microtubule arrays in differentiated cells contain elevated levels of a post-translationally modified form of tubulin. Eur. J. Cell Biol. 42, 288–294.

Gundersen, G G, Bulinski, J.C., 1986. Distribution of tyrosinated and nontyrosinated alpha-tubulin during mitosis. J. Cell Biol. 102, 1118–1126. https://doi.org/10.1083/jcb.102.3.1118

Gundersen, G.G., Khawaja, S., Bulinski, J.C., 1987. Postpolymerization detyrosination of alpha-tubulin: a mechanism for subcellular differentiation of microtubules. J. Cell Biol. 105, 251–264. https://doi.org/10.1083/jcb.105.1.251

Gundersen, G.G., Worman, H.J., 2013. Nuclear Positioning. Cell 152, 1376–1389. https://doi.org/10.1016/j.cell.2013.02.031

Gunning, P.W., Ghoshdastider, U., Whitaker, S., Popp, D., Robinson, R.C., 2015. The evolution of compositionally and functionally distinct actin filaments. J. Cell Sci. 128, 2009–2019. https://doi.org/10.1242/jcs.165563

H

Hall, Z.W., Ralston, E., 1989. Nuclear domains in muscle cells. Cell 59, 771–772. https://doi.org/10.1016/0092-8674(89)90597-7

Hallak, M.E., Rodriguez, J.A., Barra, H.S., Caputto, R., 1977. Release of tyrosine from tyrosinated tubulin. Some common factors that affect this process and the assembly of tubulin. FEBS Lett. 73, 147–150. https://doi.org/10.1016/0014-5793(77)80968-X

Hansson, K.-A., Eftestøl, E., Bruusgaard, J.C., Juvkam, I., Cramer, A.W., Malthe-Sørenssen, A., Millay, D.P., Gundersen, K., 2020. Myonuclear content regulates cell size with similar scaling properties in mice and humans. Nat. Commun. 11, 6288. https://doi.org/10.1038/s41467-020-20057-8

Hao, H., Starr, D.A., 2019. SUN/KASH interactions facilitate force transmission across the nuclear envelope. Nucleus 10, 73–80. https://doi.org/10.1080/19491034.2019.1595313

Harel, I., Maezawa, Y., Avraham, R., Rinon, A., Ma, H.-Y., Cross, J.W., Leviatan, N., Hegesh, J., Roy, A., Jacob-Hirsch, J., Rechavi, G., Carvajal, J., Tole, S., Kioussi, C., Quaggin, S., Tzahor, E., 2012. Pharyngeal mesoderm regulatory network controls cardiac and head muscle morphogenesis. Proc. Natl. Acad. Sci. U. S. A. 109, 18839–18844. https://doi.org/10.1073/pnas.1208690109

Haren, L., Remy, M.-H., Bazin, I., Callebaut, I., Wright, M., Merdes, A., 2006. NEDD1-dependent recruitment of the γ-tubulin ring complex to the centrosome is necessary for centriole duplication and spindle assembly. J. Cell Biol. 172, 505–515. https://doi.org/10.1083/jcb.200510028

Heller, S.A., Shih, R., Kalra, R., Kang, P.B., 2020. Emery-Dreifuss muscular dystrophy. Muscle Nerve 61, 436–448. https://doi.org/10.1002/mus.26782

Hernández-Hernández, J.M., García-González, E.G., Brun, C.E., Rudnicki, M.A., 2017. The myogenic regulatory factors, determinants of muscle development, cell identity and regeneration. Semin. Cell Dev. Biol. 72, 10–18. https://doi.org/10.1016/j.semcdb.2017.11.010

Hetzer, M.W., 2010. The Nuclear Envelope. Cold Spring Harb. Perspect. Biol. 2, a000539–a000539. https://doi.org/10.1101/cshperspect.a000539

Hnia, K., Tronchère, H., Tomczak, K.K., Amoasii, L., Schultz, P., Beggs, A.H., Payrastre, B., Mandel, J.L., Laporte, J., 2011. Myotubularin controls desmin intermediate filament architecture and mitochondrial dynamics in human and mouse skeletal muscle. J. Clin. Invest. 121, 70–85. https://doi.org/10.1172/JCI44021

Holaska, J.M., 2016. Diseases of the Nucleoskeleton. Compr. Physiol. 6, 1655–1674. https://doi.org/10.1002/cphy.c150039

Honnappa, S., Gouveia, S.M., Weisbrich, A., Damberger, F.F., Bhavesh, N.S., Jawhari, H., Grigoriev, I., van Rijssel, F.J.A., Buey, R.M., Lawera, A., Jelesarov, I., Winkler, F.K., Wüthrich, K., Akhmanova, A., Steinmetz, M.O., 2009. An EB1-Binding Motif Acts as a Microtubule Tip Localization Signal. Cell 138, 366–376. https://doi.org/10.1016/j.cell.2009.04.065

Hotta, T., Haynes, S.E., Blasius, T.L., Gebbie, M., Eberhardt, E.L., Sept, D., Cianfrocco, M., Verhey, K.J., Nesvizhskii, A.I., Ohi, R., 2021. Parthenolide Destabilizes Microtubules by Covalently Modifying Tubulin. Curr. Biol. 31, 900-907.e6. https://doi.org/10.1016/j.cub.2020.11.055

Howes, S.C., Alushin, G.M., Shida, T., Nachury, M.V., Nogales, E., 2014. Effects of tubulin acetylation and tubulin acetyltransferase binding on microtubule structure. Mol. Biol. Cell 25, 257–266. https://doi.org/10.1091/mbc.E13-07-0387

Hu, L., Huang, Z., Wu, Z., Ali, A., Qian, A., 2018. Mammalian Plakins, Giant Cytolinkers: Versatile Biological Functions and Roles in Cancer. Int. J. Mol. Sci. 19, 974. https://doi.org/10.3390/ijms19040974

Hubbert, C., Guardiola, A., Shao, R., Kawaguchi, Y., Ito, A., Nixon, A., Yoshida, M., Wang, X.-F., Yao, T.-P., 2002. HDAC6 is a microtubule-associated deacetylase. Nature 417, 455–458. https://doi.org/10.1038/417455a

Hutcheson, D.A., Zhao, J., Merrell, A., Haldar, M., Kardon, G., 2009. Embryonic and fetal limb myogenic cells are derived from developmentally distinct progenitors and have different requirements for β-catenin. Genes Dev. 23, 997–1013. https://doi.org/10.1101/gad.1769009

Hyldahl, R.D., Olson, T., Welling, T., Groscost, L., Parcell, A.C., 2014. Satellite cell activity is differentially affected by contraction mode in human muscle following a work-matched bout of exercise. Front. Physiol. 5. https://doi.org/10.3389/fphys.2014.00485

I

Iqbal, Z., Tawamie, H., Ba, W., Reis, A., Halak, B.A., Sticht, H., Uebe, S., Kasri, N.N., Riazuddin, S., van Bokhoven, H., Abou Jamra, R., 2019. Loss of function of SVBP leads to autosomal recessive intellectual disability, microcephaly, ataxia, and hypotonia. Genet. Med. 21, 1790–1796. https://doi.org/10.1038/s41436-018-0415-8

Iyer, K.V., Pulford, S., Mogilner, A., Shivashankar, G.V., 2012. Mechanical Activation of Cells Induces Chromatin Remodeling Preceding MKL Nuclear Transport. Biophys. J. 103, 1416–1428. https://doi.org/10.1016/j.bpj.2012.08.041

Iyer, S.R., Shah, S.B., Valencia, A.P., Schneider, M.F., Hernández-Ochoa, E.O., Stains, J.P., Blemker, S.S., Lovering, R.M., 2017. Altered nuclear dynamics in MDX myofibers. J. Appl. Physiol. 122, 470–481. https://doi.org/10.1152/japplphysiol.00857.2016

J

Jacquier, A., Risson, V., Schaeffer, L., 2019. Modeling Charcot-Marie-Tooth Disease In Vitro by Transfecting Mouse Primary Motoneurons. J. Vis. Exp. 57988. https://doi.org/10.3791/57988

Janin, A., Gache, V., 2018. Nesprins and Lamins in Health and Diseases of Cardiac and Skeletal Muscles. Front. Physiol. 9, 1277. https://doi.org/10.3389/fphys.2018.01277

Janke, C., Magiera, M.M., 2020. The tubulin code and its role in controlling microtubule properties and functions. Nat. Rev. Mol. Cell Biol. 21, 307–326. https://doi.org/10.1038/s41580-020-0214-3

Jasmin, B.J., Changeux, J.-P., Cartaud, J., 1990. Compartmentalization of cold-stable and acetylated microtubules in the subsynaptic domain of chick skeletal muscle fibre. Nature 344, 673–675. https://doi.org/10.1038/344673a0

Jaulin, F., Kreitzer, G., 2010. KIF17 stabilizes microtubules and contributes to epithelial morphogenesis by acting at MT plus ends with EB1 and APC. J. Cell Biol. 190, 443–460. https://doi.org/10.1083/jcb.201006044

Jørgensen, L.H., Mosbech, M.-B., Færgeman, N.J., Graakjaer, J., Jacobsen, S.V., Schrøder, H.D., 2015. Duplication in the Microtubule-Actin Cross-linking Factor 1 gene causes a novel neuromuscular condition. Sci. Rep. 4, 5180. https://doi.org/10.1038/srep05180

Jungbluth, H., Wallgren-Pettersson, C., Laporte, J., 2008. Centronuclear (myotubular) myopathy. Orphanet J. Rare Dis. 3, 26. https://doi.org/10.1186/1750-1172-3-26

K

Kadi, F., Eriksson, A., Holmner, S., Butler-Browne, G.S., Thornell, L.-E., 1999. Cellular adaptation of the trapezius muscle in strength-trained athletes. Histochem. Cell Biol. 111, 189–195. https://doi.org/10.1007/s004180050348

Kakinuma, T., Ichikawa, H., Tsukada, Y., Nakamura, T., Toh, B.-H., 2004. Interaction between p230 and MACF1 is associated with transport of a glycosyl phosphatidyl inositol-anchored protein from the Golgi to the cell periphery. Exp. Cell Res. 298, 388–398. https://doi.org/10.1016/j.yexcr.2004.04.047

Kang, L., Liu, Y., Jin, Y., Li, M., Song, J., Zhang, Yi, Zhang, Yao, Yang, Y., 2020. Mutations of MACF1, Encoding Microtubule-Actin Crosslinking-Factor 1, Cause Spectraplakinopathy. Front. Neurol. 10, 1335. https://doi.org/10.3389/fneur.2019.01335

Kapitein, L.C., Hoogenraad, C.C., 2015. Building the Neuronal Microtubule Cytoskeleton. Neuron 87, 492–506. https://doi.org/10.1016/j.neuron.2015.05.046

Kastenschmidt, J.M., Ellefsen, K.L., Mannaa, A.H., Giebel, J.J., Yahia, R., Ayer, R.E., Pham, P., Rios, R., Vetrone, S.A., Mozaffar, T., Villalta, S.A., 2019. QuantiMus: A Machine Learning-Based Approach for High Precision Analysis of Skeletal Muscle Morphology. Front. Physiol. 10, 1416. https://doi.org/10.3389/fphys.2019.01416

Katti, P., Hall, A.S., Ajayi, P.T., Kim, Y., Willingham, T.B., Bleck, C.K.E., Wen, H., Glancy, B., 2022. Mitochondrial Network Configuration Influences Sarcomere and Myosin Filament Structure in Striated Muscles (preprint). Cell Biology. https://doi.org/10.1101/2022.01.14.476070

Kern, J., Bauer, M., Rychli, K., Wojta, J., Ritsch, A., Gastl, G., Gunsilius, E., Untergasser, G., 2008. Alternative Splicing of Vasohibin-1 Generates an Inhibitor of Endothelial Cell Proliferation, Migration, and Capillary Tube Formation. Arterioscler. Thromb. Vasc. Biol. 28, 478–484. https://doi.org/10.1161/ATVBAHA.107.160432

Kerr, J.P., Robison, P., Shi, G., Bogush, A.I., Kempema, A.M., Hexum, J.K., Becerra, N., Harki, D.A., Martin, S.S., Raiteri, R., Prosser, B.L., Ward, C.W., 2015. Detyrosinated microtubules modulate mechanotransduction in heart and skeletal muscle. Nat. Commun. 6, 8526. https://doi.org/10.1038/ncomms9526

Khairallah, R.J., Shi, G., Sbrana, F., Prosser, B.L., Borroto, C., Mazaitis, M.J., Hoffman, E.P., Mahurkar, A., Sachs, F., Sun, Y., Chen, Y.-W., Raiteri, R., Lederer, W.J., Dorsey, S.G., Ward, C.W., 2012. Microtubules underlie dysfunction in duchenne muscular dystrophy. Sci. Signal. 5, ra56. https://doi.org/10.1126/scisignal.2002829

Kim, D.-H., Wirtz, D., 2015. Cytoskeletal tension induces the polarized architecture of the nucleus. Biomaterials 48, 161–172. https://doi.org/10.1016/j.biomaterials.2015.01.023

Kimura, H., Miyashita, H., Suzuki, Y., Kobayashi, M., Watanabe, K., Sonoda, H., Ohta, H., Fujiwara, T., Shimosegawa, T., Sato, Y., 2009. Distinctive localization and opposed roles of vasohibin-1 and vasohibin-2 in the regulation of angiogenesis. Blood 113, 4810–4818. https://doi.org/10.1182/blood-2008-07-170316

Kodama, A., Karakesisoglou, I., Wong, E., Vaezi, A., Fuchs, E., 2003. ACF7: an essential integrator of microtubule dynamics. Cell 115, 343–354. https://doi.org/10.1016/s0092-8674(03)00813-4

Kollman, J.M., Polka, J.K., Zelter, A., Davis, T.N., Agard, D.A., 2010. Microtubule nucleating γ-TuSC assembles structures with 13-fold microtubule-like symmetry. Nature 466, 879–882. https://doi.org/10.1038/nature09207

Komarova, Y., De Groot, C.O., Grigoriev, I., Gouveia, S.M., Munteanu, E.L., Schober, J.M., Honnappa, S., Buey, R.M., Hoogenraad, C.C., Dogterom, M., Borisy, G.G., Steinmetz, M.O., Akhmanova, A., 2009. Mammalian end binding proteins control persistent microtubule growth. J. Cell Biol. 184, 691–706. https://doi.org/10.1083/jcb.200807179

Konieczny, P., Fuchs, P., Reipert, S., Kunz, W.S., Zeöld, A., Fischer, I., Paulin, D., Schröder, R., Wiche, G., 2008. Myofiber integrity depends on desmin network targeting to Z-disks and costameres via distinct plectin isoforms. J. Cell Biol. 181, 667–681. https://doi.org/10.1083/jcb.200711058

Kopf, A., Renkawitz, J., Hauschild, R., Girkontaite, I., Tedford, K., Merrin, J., Thorn-Seshold, O., Trauner, D., Häcker, H., Fischer, K.-D., Kiermaier, E., Sixt, M., 2020. Microtubules control cellular shape and coherence in amoeboid migrating cells. J. Cell Biol. 219, e201907154. https://doi.org/10.1083/jcb.201907154

Kumar, N., Flavin, M., 1981. Preferential action of a brain detyrosinolating carboxypeptidase on polymerized tubulin. J. Biol. Chem. 256, 7678–7686.

Kumari, A., Shriwas, O., Sisodiya, S., Santra, M.K., Guchhait, S.K., Dash, R., Panda, D., 2021. Microtubule-targeting agents impair kinesin-2-dependent nuclear transport of β-catenin: Evidence of inhibition of Wnt/β-catenin signaling as an important antitumor mechanism of microtubule-targeting agents. FASEB J. 35. https://doi.org/10.1096/fj.202002594R

L

Lafanechère, L., Courtay-Cahen, C., Kawakami, T., Jacrot, M., Rüdiger, M., Wehland, J., Job, D., Margolis, R.L., 1998. Suppression of tubulin tyrosine ligase during tumor growth. J. Cell Sci. 111 (Pt 2), 171–181. https://doi.org/10.1242/jcs.111.2.171

Lahmann, I., Bröhl, D., Zyrianova, T., Isomura, A., Czajkowski, M.T., Kapoor, V., Griger, J., Ruffault, P.-L., Mademtzoglou, D., Zammit, P.S., Wunderlich, T., Spuler, S., Kühn, R., Preibisch, S., Wolf, J., Kageyama, R., Birchmeier, C., 2019. Oscillations of MyoD and Hes1 proteins regulate the maintenance of activated muscle stem cells. Genes Dev. 33, 524–535. https://doi.org/10.1101/gad.322818.118

Lane, T.R., Fuchs, E., Slep, K.C., 2017. Structure of the ACF7 EF-Hand-GAR Module and Delineation of Microtubule Binding Determinants. Struct. Lond. Engl. 1993 25, 1130-1138.e6. https://doi.org/10.1016/j.str.2017.05.006

Larouche, J.A., Mohiuddin, M., Choi, J.J., Ulintz, P.J., Fraczek, P., Sabin, K., Pitchiaya, S., Kurpiers, S.J., Castor-Macias, J., Liu, W., Hastings, R.L., Brown, L.A., Markworth, J.F., De Silva, K., Levi, B., Merajver, S.D., Valdez, G., Chakkalakal, J.V., Jang, Y.C., Brooks, S.V., Aguilar, C.A., 2021. Murine muscle stem cell response to perturbations of the neuromuscular junction are attenuated with aging. eLife 10, e66749. https://doi.org/10.7554/eLife.66749

Latroche, C., Gitiaux, C., Chrétien, F., Desguerre, I., Mounier, R., Chazaud, B., 2015. Skeletal Muscle Microvasculature: A Highly Dynamic Lifeline. Physiology 30, 417–427. https://doi.org/10.1152/physiol.00026.2015

Lawo, S., Hasegan, M., Gupta, G.D., Pelletier, L., 2012. Subdiffraction imaging of centrosomes reveals higher-order organizational features of pericentriolar material. Nat. Cell Biol. 14, 1148–1158. https://doi.org/10.1038/ncb2591

Lee, E., Marcucci, M., Daniell, L., Pypaert, M., Weisz, O.A., Ochoa, G.-C., Farsad, K., Wenk, M.R., De Camilli, P., 2002. Amphiphysin 2 (Bin1) and T-Tubule Biogenesis in Muscle. Science 297, 1193–1196. https://doi.org/10.1126/science.1071362

Lei, K., Zhang, X., Ding, X., Guo, X., Chen, M., Zhu, B., Xu, T., Zhuang, Y., Xu, R., Han, M., 2009. SUN1 and SUN2 play critical but partially redundant roles in anchoring nuclei in skeletal muscle cells in mice. Proc. Natl. Acad. Sci. 106, 10207–10212. https://doi.org/10.1073/pnas.0812037106

Leung, C. L., Sun, D., Zheng, M., Knowles, D.R., Liem, R.K., 1999. Microtubule actin cross-linking factor (MACF): a hybrid of dystonin and dystrophin that can interact with the actin and microtubule cytoskeletons. J. Cell Biol. 147, 1275–1286. https://doi.org/10.1083/jcb.147.6.1275

Leung, Conrad L., Sun, D., Zheng, M., Knowles, D.R., Liem, R.K.H., 1999. Microtubule Actin Cross-Linking Factor (Macf). J. Cell Biol. 147, 1275–1286. https://doi.org/10.1083/jcb.147.6.1275

L'Hernault, S.W., Rosenbaum, J.L., 1985. Chlamydomonas .alpha.-tubulin is posttranslationally modified by acetylation on the .epsilon.-amino group of a lysine. Biochemistry 24, 473–478. https://doi.org/10.1021/bi00323a034

Li, F., Hu, Y., Qi, S., Luo, X., Yu, H., 2019. Structural basis of tubulin detyrosination by vasohibins. Nat. Struct. Mol. Biol. 26, 583–591. https://doi.org/10.1038/s41594-019-0242-x

Li, L., Xiong, W.-C., Mei, L., 2018. Neuromuscular Junction Formation, Aging, and Disorders. Annu. Rev. Physiol. 80, 159–188. https://doi.org/10.1146/annurev-physiol-022516-034255

Liao, S., Rajendraprasad, G., Wang, N., Eibes, S., Gao, J., Yu, H., Wu, G., Tu, X., Huang, H., Barisic, M., Xu, C., 2019. Molecular basis of vasohibins-mediated detyrosination and its impact on spindle function and mitosis. Cell Res. 29, 533–547. https://doi.org/10.1038/s41422-019-0187-y

Liem, R.K.H., 2016. Cytoskeletal Integrators: The Spectrin Superfamily. Cold Spring Harb. Perspect. Biol. 8, a018259. https://doi.org/10.1101/cshperspect.a018259

Lin, C.-M., Chen, H.-J., Leung, C.L., Parry, D.A.D., Liem, R.K.H., 2005. Microtubule actin crosslinking factor 1b: a novel plakin that localizes to the Golgi complex. J. Cell Sci. 118, 3727–3738. https://doi.org/10.1242/jcs.02510

Lin, T., Neuner, A., Flemming, D., Liu, P., Chinen, T., Jäkle, U., Arkowitz, R., Schiebel, E., 2016. MOZART1 and γ-tubulin complex receptors are both required to turn γ-TuSC into an active microtubule nucleation template. J. Cell Biol. 215, 823–840. https://doi.org/10.1083/jcb.201606092

Liu, Q., Pante, N., Misteli, T., Elsagga, M., Crisp, M., Hodzic, D., Burke, B., Roux, K.J., 2007. Functional association of Sun1 with nuclear pore complexes. J. Cell Biol. 178, 785–798. https://doi.org/10.1083/jcb.200704108

Loreti, M., Sacco, A., 2022. The jam session between muscle stem cells and the extracellular matrix in the tissue microenvironment. Npj Regen. Med. 7, 16. https://doi.org/10.1038/s41536-022-00204-z

Lu, Y., Roy, R., 2014. Centrosome/Cell Cycle Uncoupling and Elimination in the Endoreduplicating Intestinal Cells of C. elegans. PLoS ONE 9, e110958. https://doi.org/10.1371/journal.pone.0110958

Lu, Z., Joseph, D., Bugnard, E., Zaal, K.J., Ralston, E., 2001. Golgi complex reorganization during muscle differentiation: visualization in living cells and mechanism. Mol. Biol. Cell 12, 795–808. https://doi.org/10.1091/mbc.12.4.795

Ludueña, R.F., Banerjee, A., 2008. The Isotypes of Tubulin, in: Fojo, T. (Ed.), The Role of Microtubules in Cell Biology, Neurobiology, and Oncology. Humana Press, Totowa, NJ, pp. 123–175. https://doi.org/10.1007/978-1-59745-336-3_6

Luis, N.M., Schnorrer, F., 2021. Mechanobiology of muscle and myofibril morphogenesis. Cells Dev. 168, 203760. https://doi.org/10.1016/j.cdev.2021.203760

Luxton, G.W.G., Gomes, E.R., Folker, E.S., Vintinner, E., Gundersen, G.G., 2010. Linear Arrays of Nuclear Envelope Proteins Harness Retrograde Actin Flow for Nuclear Movement. Science 329, 956–959. https://doi.org/10.1126/science.1189072

M

Ma, Y., Yue, J., Zhang, Y., Shi, C., Odenwald, M., Liang, W.G., Wei, Q., Goel, A., Gou, X., Zhang, J., Chen, S.-Y., Tang, W.-J., Turner, J.R., Yang, F., Liang, H., Qin, H., Wu, X., 2017. Erratum: ACF7 regulates inflammatory colitis and intestinal wound response by orchestrating tight junction dynamics. Nat. Commun. 8, 16121. https://doi.org/10.1038/ncomms16121

Maire, P., Dos Santos, M., Madani, R., Sakakibara, I., Viaut, C., Wurmser, M., 2020. Myogenesis control by SIX transcriptional complexes. Semin. Cell Dev. Biol. 104, 51–64. https://doi.org/10.1016/j.semcdb.2020.03.003

Maldonado, E.N., Patnaik, J., Mullins, M.R., Lemasters, J.J., 2010. Free tubulin modulates mitochondrial membrane potential in cancer cells. Cancer Res. 70, 10192–10201. https://doi.org/10.1158/0008-5472.CAN-10-2429

Manning, J.A., Shalini, S., Risk, J.M., Day, C.L., Kumar, S., 2010. A Direct Interaction with NEDD1 Regulates γ-Tubulin Recruitment to the Centrosome. PLoS ONE 5, e9618. https://doi.org/10.1371/journal.pone.0009618

Manta, P., Vassilopoulos, D., Spengos, M., 1987. Nucleo-cytoplasmic ratio in ageing skeletal muscle. Eur. Arch. Psychiatry Neurol. Sci. 236, 235–236. https://doi.org/10.1007/BF00383854
Margaron, Y., Fradet, N., Côté, J.-F., 2013. ELMO Recruits Actin Cross-linking Family 7 (ACF7) at the Cell Membrane for Microtubule Capture and Stabilization of Cellular Protrusions. J. Biol. Chem. 288, 1184–1199. https://doi.org/10.1074/jbc.M112.431825

Margolis, R.L., Wilson, L., 1978. Opposite end assembly and disassembly of microtubules at steady state in vitro. Cell 13, 1–8. https://doi.org/10.1016/0092-8674(78)90132-0

Marieb, E.N., 2001. Human anatomy & physiology, 5th ed. ed. Benjamin Cummings, San Francisco.

Marks, P.C., Petrie, R.J., 2022. Push or pull: how cytoskeletal crosstalk facilitates nuclear movement through 3D environments. Phys. Biol. 19, 021003. https://doi.org/10.1088/1478-3975/ac45e3

Mashinchian, O., Pisconti, A., Le Moal, E., Bentzinger, C.F., 2018. The Muscle Stem Cell Niche in Health and Disease, in: Current Topics in Developmental Biology. Elsevier, pp. 23–65. https://doi.org/10.1016/bs.ctdb.2017.08.003

Masschelein, E., D'Hulst, G., Zvick, J., Hinte, L., Soro-Arnaiz, I., Gorski, T., von Meyenn, F., Bar-Nur, O., De Bock, K., 2020. Exercise promotes satellite cell contribution to myofibers in a load-dependent manner. Skelet. Muscle 10, 21. https://doi.org/10.1186/s13395-020-00237-2

Mayran, A., 2015. Pax factors in transcription and epigenetic remodelling. Dev. Biol. 10.

McIntosh, J.R., Morphew, M.K., Grissom, P.M., Gilbert, S.P., Hoenger, A., 2009. Lattice Structure of Cytoplasmic Microtubules in a Cultured Mammalian Cell. J. Mol. Biol. 394, 177–182. https://doi.org/10.1016/j.jmb.2009.09.033

Meads, T., Schroer, T.A., 1995. Polarity and nucleation of microtubules in polarized epithelial cells. Cell Motil. Cytoskeleton 32, 273–288. https://doi.org/10.1002/cm.970320404

Meka, S.R.K., Chacko, L.A., Ravi, A., Chatterjee, K., Ananthanarayanan, V., 2017. Role of Microtubules in Osteogenic Differentiation of Mesenchymal Stem Cells on 3D Nanofibrous Scaffolds. ACS Biomater. Sci. Eng. 3, 551–559. https://doi.org/10.1021/acsbiomaterials.6b00725

Melkov, A., Simchoni, Y., Alcalay, Y., Abdu, U., 2015. Dynamic microtubule organization and mitochondrial transport are regulated by distinct Kinesin-1 pathways. Biol. Open 4, 1696–1706. https://doi.org/10.1242/bio.015206

Metoz, F., Arnal, I., Wade, R.H., 1997. Tomography without Tilt: Three-Dimensional Imaging of Microtubule/Motor Complexes. J. Struct. Biol. 118, 159–168. https://doi.org/10.1006/jsbi.1997.3850

Metzger, T., Gache, V., Xu, M., Cadot, B., Folker, E.S., Richardson, B.E., Gomes, E.R., Baylies, M.K., 2012. MAP and kinesin-dependent nuclear positioning is required for skeletal muscle function. Nature 484, 120–124. https://doi.org/10.1038/nature10914

Meunier, S., Vernos, I., 2012. Microtubule assembly during mitosis – from distinct origins to distinct functions? J. Cell Sci. jcs.092429. https://doi.org/10.1242/jcs.092429

Mialhe, A., Lafanechère, L., Treilleux, I., Peloux, N., Dumontet, C., Brémond, A., Panh, M.-H., Payan, R., Wehland, J., Margolis, R.-L., Job, D., 2001. Tubulin Detyrosination Is a Frequent Occurrence in Breast Cancers of Poor Prognosis1. Cancer Res. 61, 5024–5027.

Michiels, F., Gasch, A., Kaltschmidt, B., Renkawitz-Pohl, R., 1989. A 14 bp promoter element directs the testis specificity of the Drosophila beta 2 tubulin gene. EMBO J. 8, 1559–1565. https://doi.org/10.1002/j.1460-2075.1989.tb03540.x

Millay, D.P., 2022. Regulation of the myoblast fusion reaction for muscle development, regeneration, and adaptations. Exp. Cell Res. 415, 113134. https://doi.org/10.1016/j.yexcr.2022.113134

Milner, D.J., Mavroidis, M., Weisleder, N., Capetanaki, Y., 2000. Desmin Cytoskeleton Linked to Muscle Mitochondrial Distribution and Respiratory Function. J. Cell Biol. 150, 1283–1298. https://doi.org/10.1083/jcb.150.6.1283

Mitchison, T., Kirschner, M., 1984. Dynamic instability of microtubule growth. Nature 312, 237–242. https://doi.org/10.1038/312237a0

Mogensen, M.M., Malik, A., Piel, M., Bouckson-Castaing, V., Bornens, M., 2000. Microtubule minus-end anchorage at centrosomal and non-centrosomal sites: the role of ninein. J. Cell Sci. 113, 3013–3023. https://doi.org/10.1242/jcs.113.17.3013

Mogessie, B., Roth, D., Rahil, Z., Straube, A., 2015. A novel isoform of MAP4 organises the paraxial microtubule array required for muscle cell differentiation. eLife 4, e05697. https://doi.org/10.7554/eLife.05697

Morito, Y., Terada, Y., Nakamura, S., Morita, J., Yoshimoto, T., Murakami, T., Yaegashi, N., Okamura, K., 2005. Dynamics of Microtubules and Positioning of Female Pronucleus During Bovine Parthenogenesis. Biol. Reprod. 73, 935–941. https://doi.org/10.1095/biolreprod.105.042366

Morrison, B., 2016. Neuromuscular Diseases. Semin. Neurol. 36, 409–418. https://doi.org/10.1055/s-0036-1586263

Moss, F.P., 1968. The relationship between the dimensions of the fibres and the number of nuclei during normal growth of skeletal muscle in the domestic fowl. Am. J. Anat. 122, 555–563. https://doi.org/10.1002/aja.1001220308

Mourikis, P., Sambasivan, R., Castel, D., Rocheteau, P., Bizzarro, V., Tajbakhsh, S., 2012. A Critical Requirement for Notch Signaling in Maintenance of the Quiescent Skeletal Muscle Stem Cell State. Stem Cells 30, 243–252. https://doi.org/10.1002/stem.775

Mukund, K., Subramaniam, S., 2020. Skeletal muscle: A review of molecular structure and function, in health and disease. WIREs Syst. Biol. Med. 12. https://doi.org/10.1002/wsbm.1462

Müller, M., Gorek, L., Kamm, N., Jacob, R., 2022. Manipulation of the Tubulin Code Alters Directional Cell Migration and Ciliogenesis. Front. Cell Dev. Biol. 10, 901999. https://doi.org/10.3389/fcell.2022.901999

Müller, M., Ringer, K., Hub, F., Kamm, N., Worzfeld, T., Jacob, R., 2021. TTL-Expression Modulates Epithelial Morphogenesis. Front. Cell Dev. Biol. 9, 635723. https://doi.org/10.3389/fcell.2021.635723

Murach, K.A., White, S.H., Wen, Y., Ho, A., Dupont-Versteegden, E.E., McCarthy, J.J., Peterson, C.A., 2017. Differential requirement for satellite cells during overload-induced muscle hypertrophy in growing versus mature mice. Skelet. Muscle 7, 14. https://doi.org/10.1186/s13395-017-0132-z

Muroyama, A., Seldin, L., Lechler, T., 2016. Divergent regulation of functionally distinct γ-tubulin complexes during differentiation. J. Cell Biol. 213, 679–692. https://doi.org/10.1083/jcb.201601099

N

Naito, H., Kidoya, H., Sato, Y., Takakura, N., 2009. Induction and Expression of Anti-Angiogenic Vasohibins in the Hematopoietic Stem/Progenitor Cell Population. J Biochem 145, 7.

Nakazawa, N., Kengaku, M., 2020. Mechanical Regulation of Nuclear Translocation in Migratory Neurons. Front. Cell Dev. Biol. 8, 150. https://doi.org/10.3389/fcell.2020.00150

Nieuwenhuis, J., Adamopoulos, A., Bleijerveld, O.B., Mazouzi, A., Stickel, E., Celie, P., Altelaar, M., Knipscheer, P., Perrakis, A., Blomen, V.A., Brummelkamp, T.R., 2017. Vasohibins encode tubulin detyrosinating activity. Science 358, 1453–1456. https://doi.org/10.1126/science.aao5676

Ning, W., Yu, Y., Xu, H., Liu, X., Wang, D., Wang, J., Wang, Y., Meng, W., 2016. The CAMSAP3-ACF7 Complex Couples Noncentrosomal Microtubules with Actin Filaments to Coordinate Their Dynamics. Dev. Cell 39, 61–74. https://doi.org/10.1016/j.devcel.2016.09.003

Norden, C., Young, S., Link, B.A., Harris, W.A., 2009. Actomyosin Is the Main Driver of Interkinetic Nuclear Migration in the Retina. Cell 138, 1195–1208. https://doi.org/10.1016/j.cell.2009.06.032

North, B.J., Marshall, B.L., Borra, M.T., Denu, J.M., Verdin, E., 2003. The Human Sir2 Ortholog, SIRT2, Is an NAD+-Dependent Tubulin Deacetylase. Mol. Cell 11, 437–444. https://doi.org/10.1016/S1097-2765(03)00038-8

Nowak, S.J., Nahirney, P.C., Hadjantonakis, A.-K., Baylies, M.K., 2009. Nap1-mediated actin remodeling is essential for mammalian myoblast fusion. J. Cell Sci. 122, 3282–3293. https://doi.org/10.1242/jcs.047597

O

Odde, D.J., Cassimeris, L., Buettner, H.M., 1995. Kinetics of microtubule catastrophe assessed by probabilistic analysis. Biophys. J. 69, 796–802. https://doi.org/10.1016/S0006-3495(95)79953-2

Oddoux, S., Randazzo, D., Kenea, A., Alonso, B., Zaal, K.J.M., Ralston, E., 2019. Misplaced Golgi Elements Produce Randomly Oriented Microtubules and Aberrant Cortical Arrays of Microtubules in Dystrophic Skeletal Muscle Fibers. Front. Cell Dev. Biol. 7, 176. https://doi.org/10.3389/fcell.2019.00176

Oddoux, S., Zaal, K.J., Tate, V., Kenea, A., Nandkeolyar, S.A., Reid, E., Liu, W., Ralston, E., 2013. Microtubules that form the stationary lattice of muscle fibers are dynamic and nucleated at Golgi elements. J. Cell Biol. 203, 205–213. https://doi.org/10.1083/jcb.201304063

Ono, Y., Calhabeu, F., Morgan, J.E., Katagiri, T., Amthor, H., Zammit, P.S., 2011. BMP signalling permits population expansion by preventing premature myogenic differentiation in muscle satellite cells. Cell Death Differ. 18, 222–234. https://doi.org/10.1038/cdd.2010.95

Osseni, A., Ravel-Chapuis, A., Thomas, J.-L., Gache, V., Schaeffer, L., Jasmin, B.J., 2020. HDAC6 regulates microtubule stability and clustering of AChRs at neuromuscular junctions. J. Cell Biol. 219, e201901099. https://doi.org/10.1083/jcb.201901099

Oury, J., Liu, Y., Töpf, A., Todorovic, S., Hoedt, E., Preethish-Kumar, V., Neubert, T.A., Lin, W., Lochmüller, H., Burden, S.J., 2019. MACF1 links Rapsyn to microtubule- and actin-binding proteins to maintain neuromuscular synapses. J. Cell Biol. 218, 1686–1705. https://doi.org/10.1083/jcb.201810023

Ozer, R.S., Halpain, S., 2000. Phosphorylation-dependent localization of microtubule-associated protein MAP2c to the actin cytoskeleton. Mol. Biol. Cell 11, 3573–3587. https://doi.org/10.1091/mbc.11.10.3573

P

Pagnamenta, A.T., Heemeryck, P., Martin, H.C., Bosc, C., Peris, L., Uszynski, I., Gory-Fauré, S., Couly, S., Deshpande, C., Siddiqui, A., Elmonairy, A.A., WGS500 Consortium, Genomics England Research Consortium, Jayawant, S., Murthy, S., Walker, I., Loong, L., Bauer, P., Vossier, F., Denarier, E., Maurice, T., Barbier, E.L., Deloulme, J.-C., Taylor, J.C., Blair, E.M., Andrieux, A., Moutin, M.-J., 2019. Defective tubulin detyrosination causes structural brain abnormalities with cognitive deficiency in humans and mice. Hum. Mol. Genet. 28, 3391–3405. https://doi.org/10.1093/hmg/ddz186

Pavlath, G.K., Rich, K., Webster, S.G., Blau, H.M., 1989. Localization of muscle gene products in nuclear domains. Nature 337, 570–573. https://doi.org/10.1038/337570a0

Pederson, T., 2011. The Nucleus Introduced. Cold Spring Harb. Perspect. Biol. 3, a000521–a000521. https://doi.org/10.1101/cshperspect.a000521

Pegoraro, A.F., Janmey, P., Weitz, D.A., 2017. Mechanical Properties of the Cytoskeleton and Cells. Cold Spring Harb. Perspect. Biol. 9, a022038. https://doi.org/10.1101/cshperspect.a022038

Perillo, M., Folker, E.S., 2018. Specialized Positioning of Myonuclei Near Cell-Cell Junctions. Front. Physiol. 9, 1531. https://doi.org/10.3389/fphys.2018.01531

Peris, L., Thery, M., Fauré, J., Saoudi, Y., Lafanechère, L., Chilton, J.K., Gordon-Weeks, P., Galjart, N., Bornens, M., Wordeman, L., Wehland, J., Andrieux, A., Job, D., 2006. Tubulin tyrosination is a major factor affecting the recruitment of CAP-Gly proteins at microtubule plus ends. J. Cell Biol. 174, 839–849. https://doi.org/10.1083/jcb.200512058

Peris, L., Wagenbach, M., Lafanechère, L., Brocard, J., Moore, A.T., Kozielski, F., Job, D., Wordeman, L., Andrieux, A., 2009. Motor-dependent microtubule disassembly driven by tubulin tyrosination. J. Cell Biol. 185, 1159–1166. https://doi.org/10.1083/jcb.200902142

Pizon, V., Gerbal, F., Diaz, C.C., Karsenti, E., 2005. Microtubule-dependent transport and organization of sarcomeric myosin during skeletal muscle differentiation. EMBO J. 24, 3781–3792. https://doi.org/10.1038/sj.emboj.7600842

Pollard, T.D., 2016. Actin and Actin-Binding Proteins. Cold Spring Harb. Perspect. Biol. 8, a018226. https://doi.org/10.1101/cshperspect.a018226

Pollard, T.D., Goldman, R.D., 2018. Overview of the Cytoskeleton from an Evolutionary Perspective. Cold Spring Harb. Perspect. Biol. 10, a030288. https://doi.org/10.1101/cshperspect.a030288

Porter, J.D., Israel, S., Gong, B., Merriam, A.P., Feuerman, J., Khanna, S., Kaminski, H.J., 2006. Distinctive morphological and gene/protein expression signatures during myogenesis in novel cell lines from extraocular and hindlimb muscle. Physiol. Genomics 24, 264–275. https://doi.org/10.1152/physiolgenomics.00234.2004

Portran, D., Schaedel, L., Xu, Z., Théry, M., Nachury, M.V., 2017. Tubulin acetylation protects long-lived microtubules against mechanical ageing. Nat. Cell Biol. 19, 391–398. https://doi.org/10.1038/ncb3481

Prins, K.W., Humston, J.L., Mehta, A., Tate, V., Ralston, E., Ervasti, J.M., 2009. Dystrophin is a microtubule-associated protein. J. Cell Biol. 186, 363–369. https://doi.org/10.1083/jcb.200905048

Prokic, I., Cowling, B.S., Kutchukian, C., Kretz, C., Tasfaout, H., Gache, V., Hergueux, J., Wendling, O., Ferry, A., Toussaint, A., Gavriilidis, C., Nattarayan, V., Koch, C., Lainé, J., Combe, R., Tiret, L., Jacquemond, V., Pilot-Storck, F., Laporte, J., 2020. Differential physiological role of BIN1 isoforms in skeletal muscle development, function and regeneration. Dis. Model. Mech. dmm.044354. https://doi.org/10.1242/dmm.044354

Prota, A.E., Magiera, M.M., Kuijpers, M., Bargsten, K., Frey, D., Wieser, M., Jaussi, R., Hoogenraad, C.C., Kammerer, R.A., Janke, C., Steinmetz, M.O., 2013. Structural basis of tubulin tyrosination by tubulin tyrosine ligase. J. Cell Biol. 200, 259–270. https://doi.org/10.1083/jcb.201211017

Przybylski, R.J., 1971. OCCURRENCE OF CENTRIOLES DURING SKELETAL AND CARDIAC MYOGENESIS. J. Cell Biol. 49, 214–221. https://doi.org/10.1083/jcb.49.1.214

Puckelwartz, M.J., Kessler, E., Zhang, Y., Hodzic, D., Randles, K.N., Morris, G., Earley, J.U., Hadhazy, M., Holaska, J.M., Mewborn, S.K., Pytel, P., McNally, E.M., 2009. Disruption of nesprin-1 produces an Emery Dreifuss muscular dystrophy-like phenotype in mice. Hum. Mol. Genet. 18, 607–620. https://doi.org/10.1093/hmg/ddn386

Purslow, P.P., 2020. The Structure and Role of Intramuscular Connective Tissue in Muscle Function. Front. Physiol. 11, 495. https://doi.org/10.3389/fphys.2020.00495

Purslow, P.P., 1989. Strain-induced reorientation of an intramuscular connective tissue network: Implications for passive muscle elasticity. J. Biomech. 22, 21–31. https://doi.org/10.1016/0021-9290(89)90181-4

R

Ralston, E., 1993. Changes in architecture of the Golgi complex and other subcellular organelles during myogenesis. J. Cell Biol. 120, 399–409. https://doi.org/10.1083/jcb.120.2.399

Ralston, E., Hall, Z.W., 1992. Restricted distribution of mRNA produced from a single nucleus in hybrid myotubes. J. Cell Biol. 119, 1063–1068. https://doi.org/10.1083/jcb.119.5.1063

Ralston, E., Lu, Z., Biscocho, N., Soumaka, E., Mavroidis, M., Prats, C., Lømo, T., Capetanaki, Y., Ploug, T., 2006. Blood vessels and desmin control the positioning of nuclei in skeletal muscle fibers. J. Cell. Physiol. 209, 874–882. https://doi.org/10.1002/jcp.20780

Ralston, E., Lu, Z., Ploug, T., 1999. The Organization of the Golgi Complex and Microtubules in Skeletal Muscle Is Fiber Type-Dependent. J. Neurosci. 19, 10694–10705. https://doi.org/10.1523/JNEUROSCI.19-24-10694.1999

Randazzo, D., Khalique, U., Belanto, J.J., Kenea, A., Talsness, D.M., Olthoff, J.T., Tran, M.D., Zaal, K.J., Pak, K., Pinal-Fernandez, I., Mammen, A.L., Sackett, D., Ervasti, J.M., Ralston, E., 2019. Persistent upregulation of the β-tubulin tubb6, linked to muscle regeneration, is a source of microtubule disorganization in dystrophic muscle. Hum. Mol. Genet. 28, 1117–1135. https://doi.org/10.1093/hmg/ddy418

Raybin, D., Flavin, M., 1977. Enzyme which specifically adds tyrosine to the α chain of tubulin. Biochemistry 16, 2189–2194. https://doi.org/10.1021/bi00629a023

Razzaq, A., Robinson, I.M., McMahon, H.T., Skepper, J.N., Su, Y., Zelhof, A.C., Jackson, A.P., Gay, N.J., O'Kane, C.J., 2001. Amphiphysin is necessary for organization of the excitation-contraction coupling machinery of muscles, but not for synaptic vesicle endocytosis in Drosophila. Genes Dev. 15, 2967–2979. https://doi.org/10.1101/gad.207801

Reinsch, S., Gonczy, P., 1998. Mechanisms of nuclear positioning. J. Cell Sci. 111, 2283–2295. https://doi.org/10.1242/jcs.111.16.2283

Relaix, F., Bencze, M., Borok, M.J., Der Vartanian, A., Gattazzo, F., Mademtzoglou, D., Perez-Diaz, S., Prola, A., Reyes-Fernandez, P.C., Rotini, A., Taglietti, 2021. Perspectives on skeletal muscle stem cells. Nat. Commun. 12, 692. https://doi.org/10.1038/s41467-020-20760-6

Relaix, F., Demignon, J., Laclef, C., Pujol, J., Santolini, M., Niro, C., Lagha, M., Rocancourt, D., Buckingham, M., Maire, P., 2013. Six Homeoproteins Directly Activate Myod Expression in the Gene Regulatory Networks That Control Early Myogenesis. PLoS Genet. 9, e1003425. https://doi.org/10.1371/journal.pgen.1003425

Remels, A.H.V., Langen, R.C.J., Schrauwen, P., Schaart, G., Schols, A.M.W.J., Gosker, H.R., 2010. Regulation of mitochondrial biogenesis during myogenesis. Mol. Cell. Endocrinol. 315, 113–120. https://doi.org/10.1016/j.mce.2009.09.029

Robison, P., Caporizzo, M.A., Ahmadzadeh, H., Bogush, A.I., Chen, C.Y., Margulies, K.B., Shenoy, V.B., Prosser, B.L., 2016. Detyrosinated microtubules buckle and bear load in contracting cardiomyocytes. Science 352, aaf0659. https://doi.org/10.1126/science.aaf0659

Rodionov, V.I., Gyoeva, F.K., Tanaka, E., Bershadsky, A.D., Vasiliev, J.M., Gelfand, V.I., 1993. Microtubule-dependent control of cell shape and pseudopodial activity is inhibited by the antibody to kinesin motor domain. J. Cell Biol. 123, 1811–1820. https://doi.org/10.1083/jcb.123.6.1811

Roman, W., Gomes, E.R., 2018. Nuclear positioning in skeletal muscle. Semin. Cell Dev. Biol. 82, 51–56. https://doi.org/10.1016/j.semcdb.2017.11.005

Roman, W., Martins, J.P., Carvalho, F.A., Voituriez, R., Abella, J.V.G., Santos, N.C., Cadot, B., Way, M., Gomes, E.R., 2017. Myofibril contraction and crosslinking drive nuclear movement to the periphery of skeletal muscle. Nat. Cell Biol. 19, 1189–1201. https://doi.org/10.1038/ncb3605

Roman, W., Martins, J.P., Gomes, E.R., 2018. Local Arrangement of Fibronectin by Myofibroblasts Governs Peripheral Nuclear Positioning in Muscle Cells. Dev. Cell 46, 102-111.e6. https://doi.org/10.1016/j.devcel.2018.05.031

Roman, W., Pinheiro, H., Pimentel, M.R., Segalés, J., Oliveira, L.M., García-Domínguez, E., Gómez-Cabrera, M.C., Serrano, A.L., Gomes, E.R., Muñoz-Cánoves, P., 2021. Muscle repair after physiological damage relies on nuclear migration for cellular reconstruction. Science 374, 355–359. https://doi.org/10.1126/science.abe5620

Romero, N.B., Bitoun, M., 2011. Centronuclear Myopathies. Semin. Pediatr. Neurol. 18, 250–256. https://doi.org/10.1016/j.spen.2011.10.006

Rosenblatt, J.D., Yong, D., Parry, D.J., 1994. Satellite cell activity is required for hypertrophy of overloaded adult rat muscle. Muscle Nerve 17, 608–613. https://doi.org/10.1002/mus.880170607

Roy, R.R., Baldwin, K.M., Edgerton, V.R., 1991. The plasticity of skeletal muscle: effects of neuromuscular activity. Exerc. Sport Sci. Rev. 19, 269–312.

Rudolf, R., Khan, M.M., Labeit, S., Deschenes, M.R., 2014. Degeneration of Neuromuscular Junction in Age and Dystrophy. Front. Aging Neurosci. 6. https://doi.org/10.3389/fnagi.2014.00099

S

Sabourin, L.A., Rudnicki, M.A., 2000. The molecular regulation of myogenesis: The molecular regulation of myogenesis. Clin. Genet. 57, 16–25. https://doi.org/10.1034/j.1399-0004.2000.570103.x

Saitoh, O., Arai, T., Obinata, T., 1988. Distribution of microtubules and other cytoskeletal filaments during myotube elongation as revealed by fluorescence microscopy. Cell Tissue Res. 252. https://doi.org/10.1007/BF00214368

Sambasivan, R., Pavlath, G.K., Dhawan, J., 2008. A gene-trap strategy identifies quiescence-induced genes in synchronized myoblasts. J. Biosci. 33, 27–44. https://doi.org/10.1007/s12038-008-0019-6

Sanchez, A.D., Feldman, J.L., 2017. Microtubule-organizing centers: from the centrosome to non-centrosomal sites. Curr. Opin. Cell Biol. 44, 93–101. https://doi.org/10.1016/j.ceb.2016.09.003

Sanger, J.W., Wang, J., Fan, Y., White, J., Sanger, J.M., 2010. Assembly and Dynamics of Myofibrils. J. Biomed. Biotechnol. 2010, 1–8. https://doi.org/10.1155/2010/858606

Schaar, B.T., McConnell, S.K., 2005. Cytoskeletal coordination during neuronal migration. Proc. Natl. Acad. Sci. 102, 13652–13657. https://doi.org/10.1073/pnas.0506008102

Schiaffino, S., Reggiani, C., 2011. Fiber Types in Mammalian Skeletal Muscles. Physiol. Rev. 91, 1447–1531. https://doi.org/10.1152/physrev.00031.2010

Schmidt, N., Basu, S., Sladecek, S., Gatti, S., van Haren, J., Treves, S., Pielage, J., Galjart, N., Brenner, H.R., 2012. Agrin regulates CLASP2-mediated capture of microtubules at the neuromuscular junction synaptic membrane. J. Cell Biol. 198, 421–437. https://doi.org/10.1083/jcb.201111130

Sébastien, M., Giannesini, B., Aubin, P., Brocard, Julie, Chivet, M., Pietrangelo, L., Boncompagni, S., Bosc, C., Brocard, Jacques, Rendu, J., Gory-Fauré, S., Andrieux, A., Fourest-Lieuvin, A., Fauré, J., Marty, I., 2018. Deletion of the microtubule-associated protein 6 (MAP6) results in skeletal muscle dysfunction. Skelet. Muscle 8, 30. https://doi.org/10.1186/s13395-018-0176-8

Slep, K.C., Rogers, S.L., Elliott, S.L., Ohkura, H., Kolodziej, P.A., Vale, R.D., 2005. Structural determinants for EB1-mediated recruitment of APC and spectraplakins to the microtubule plus end. J. Cell Biol. 168, 587–598. https://doi.org/10.1083/jcb.200410114

Smolina, N., Khudiakov, A., Knyazeva, A., Zlotina, A., Sukhareva, K., Kondratov, K., Gogvadze, V., Zhivotovsky, B., Sejersen, T., Kostareva, A., 2020. Desmin mutations result in mitochondrial dysfunction regardless of their aggregation properties. Biochim. Biophys. Acta BBA - Mol. Basis Dis. 1866, 165745. https://doi.org/10.1016/j.bbadis.2020.165745

Sohal, G.S., Holt, R.K., 1980. Role of innervation on the embryonic development of skeletal muscle. Cell Tissue Res. 210. https://doi.org/10.1007/BF00220196

Srivastava, A.K., Pandey, S.K., 1998. Potential mechanism(s) involved in the regulation of glycogen synthesis by insulin. Mol. Cell. Biochem. 182, 135–141.

Srsen, V., Fant, X., Heald, R., Rabouille, C., Merdes, A., 2009. Centrosome proteins form an insoluble perinuclear matrix during muscle cell differentiation. BMC Cell Biol. 10, 28. https://doi.org/10.1186/1471-2121-10-28

Starr, D.A., Fischer, J.A., 2005. KASH 'n Karry: The KASH domain family of cargo-specific cytoskeletal adaptor proteins. BioEssays 27, 1136–1146. https://doi.org/10.1002/bies.20312

Steiner-Champliaud, M.-F., Schneider, Y., Favre, B., Paulhe, F., Praetzel-Wunder, S., Faulkner, G., Konieczny, P., Raith, M., Wiche, G., Adebola, A., Liem, R.K., Langbein, L., Sonnenberg, A., Fontao, L., Borradori, L., 2010. BPAG1 isoform-b: Complex distribution pattern in striated and heart muscle and association with plectin and α-actinin. Exp. Cell Res. 316, 297–313. https://doi.org/10.1016/j.yexcr.2009.11.010

Stepanova, T., Slemmer, J., Hoogenraad, C.C., Lansbergen, G., Dortland, B., De Zeeuw, C.I., Grosveld, F., van Cappellen, G., Akhmanova, A., Galjart, N., 2003. Visualization of Microtubule Growth in Cultured Neurons via the Use of EB3-GFP (End-Binding Protein 3-Green Fluorescent Protein). J. Neurosci. 23, 2655–2664. https://doi.org/10.1523/JNEUROSCI.23-07-02655.2003

Straube, A., Merdes, A., 2007. EB3 regulates microtubule dynamics at the cell cortex and is required for myoblast elongation and fusion. Curr. Biol. CB 17, 1318–1325. https://doi.org/10.1016/j.cub.2007.06.058

Stroud, M.J., Feng, W., Zhang, J., Veevers, J., Fang, X., Gerace, L., Chen, J., 2017. Nesprin 1α2 is essential for mouse postnatal viability and nuclear positioning in skeletal muscle. J. Cell Biol. 216, 1915–1924. https://doi.org/10.1083/jcb.201612128

Sullivan, K.F., 1988. Structure and Utilization of Tubulin Isotypes. Annu. Rev. Cell Biol. 4, 687–716. https://doi.org/10.1146/annurev.cb.04.110188.003351

Sun, Y., Zhang, J., Kraeft, S.-K., Auclair, D., Chang, M.-S., Liu, Y., Sutherland, R., Salgia, R., Griffin, J.D., Ferland, L.H., Chen, L.B., 1999. Molecular Cloning and Characterization of Human Trabeculin-α, a Giant Protein Defining a New Family of Actin-binding Proteins. J. Biol. Chem. 274, 33522–33530. https://doi.org/10.1074/jbc.274.47.33522

Suzuki, Y., Kobayashi, M., Miyashita, H., Ohta, H., Sonoda, H., Sato, Y., 2010. Isolation of a small vasohibin-binding protein (SVBP) and its role in vasohibin secretion. J. Cell Sci. 123, 3094–3101. https://doi.org/10.1242/jcs.067538

Swift, J., Ivanovska, I.L., Buxboim, A., Harada, T., Dingal, P.C.D.P., Pinter, J., Pajerowski, J.D., Spinler, K.R., Shin, J.-W., Tewari, M., Rehfeldt, F., Speicher, D.W., Discher, D.E., 2013. Nuclear lamin-A scales with tissue stiffness and enhances matrix-directed differentiation. Science 341, 1240104. https://doi.org/10.1126/science.1240104

Szebenyi, G., Bollati, F., Bisbal, M., Sheridan, S., Faas, L., Wray, R., Haferkamp, S., Nguyen, S., Caceres, A., Brady, S.T., 2005. Activity-Driven Dendritic Remodeling Requires Microtubule-Associated Protein 1A. Curr. Biol. 15, 1820–1826. https://doi.org/10.1016/j.cub.2005.08.069

T

Tajbakhsh, S., 2009. Skeletal muscle stem cells in developmental versus regenerative myogenesis. J. Intern. Med. 266, 372–389. https://doi.org/10.1111/j.1365-2796.2009.02158.x

Tajbakhsh, S., Borello, U., Vivarelli, E., Kelly, R., Papkoff, J., Duprez, D., Buckingham, M., Cossu, G., 1998. Differential activation of Myf5 and MyoD by different Wnts in explants of mouse paraxial mesoderm and the later activation of myogenesis in the absence of Myf5. Development 125, 4155–4162. https://doi.org/10.1242/dev.125.21.4155

Tajbakhsh, S., Cossu, G., 1997. Establishing myogenic identity during somitogenesis. Curr. Opin. Genet. Dev. 7, 634–641. https://doi.org/10.1016/S0959-437X(97)80011-1

Takahashi, M., Yamagiwa, A., Nishimura, T., Mukai, H., Ono, Y., 2002. Centrosomal Proteins CG-NAP and Kendrin Provide Microtubule Nucleation Sites by Anchoring γ-Tubulin Ring Complex. Mol. Biol. Cell 13, 3235–3245. https://doi.org/10.1091/mbc.e02-02-0112

Talamas, J.A., Hetzer, M.W., 2011. POM121 and Sun1 play a role in early steps of interphase NPC assembly. J. Cell Biol. 194, 27–37. https://doi.org/10.1083/jcb.201012154

Tassin, A.M., Maro, B., Bornens, M., 1985. Fate of microtubule-organizing centers during myogenesis in vitro. J. Cell Biol. 100, 35–46. https://doi.org/10.1083/jcb.100.1.35

Taverna, E., Huttner, W.B., 2010. Neural Progenitor Nuclei IN Motion. Neuron 67, 906–914. https://doi.org/10.1016/j.neuron.2010.08.027

Teixidó-Travesa, N., Roig, J., Lüders, J., 2012. The where, when and how of microtubule nucleation – one ring to rule them all. J. Cell Sci. jcs.106971. https://doi.org/10.1242/jcs.106971

Testoni, G., Duran, J., García-Rocha, M., Vilaplana, F., Serrano, A.L., Sebastián, D., López-Soldado, I., Sullivan, M.A., Slebe, F., Vilaseca, M., Muñoz-Cánoves, P., Guinovart, J.J., 2017. Lack of Glycogenin Causes Glycogen Accumulation and Muscle Function Impairment. Cell Metab. 26, 256-266.e4. https://doi.org/10.1016/j.cmet.2017.06.008

Thompson, W.C., Deanin, G.G., Gordon, M.W., 1979. Intact microtubules are required for rapid turnover of carboxyl-terminal tyrosine of alpha-tubulin in cell cultures. Proc. Natl. Acad. Sci. 76, 1318–1322. https://doi.org/10.1073/pnas.76.3.1318

Thorpe, S.D., Charpentier, M., 2017. Highlight on the dynamic organization of the nucleus. Nucleus 8, 2–10. https://doi.org/10.1080/19491034.2016.1243634

Timson, B.F., 1990. Evaluation of animal models for the study of exercise-induced muscle enlargement. J. Appl. Physiol. 69, 1935–1945. https://doi.org/10.1152/jappl.1990.69.6.1935

Tirnauer, J.S., Grego, S., Salmon, E.D., Mitchison, T.J., 2002. EB1-microtubule interactions in Xenopus egg extracts: role of EB1 in microtubule stabilization and mechanisms of targeting to microtubules. Mol. Biol. Cell 13, 3614–3626. https://doi.org/10.1091/mbc.02-04-0210

Tolkatchev, D., Smith, G.E., Kostyukova, A.S., 2019. Role of intrinsic disorder in muscle sarcomeres, in: Progress in Molecular Biology and Translational Science. Elsevier, pp. 311–340. https://doi.org/10.1016/bs.pmbts.2019.03.014

Toussaint, A., Cowling, B.S., Hnia, K., Mohr, M., Oldfors, A., Schwab, Y., Yis, U., Maisonobe, T., Stojkovic, T., Wallgren-Pettersson, C., Laugel, V., Echaniz-Laguna, A., Mandel, J.-L., Nishino, I., Laporte, J., 2011. Defects in amphiphysin 2 (BIN1) and triads in several forms of centronuclear myopathies. Acta Neuropathol. (Berl.) 121, 253–266. https://doi.org/10.1007/s00401-010-0754-2

Tovey, C.A., Conduit, P.T., 2018. Microtubule nucleation by γ-tubulin complexes and beyond. Essays Biochem. 62, 765–780. https://doi.org/10.1042/EBC20180028

Toya, M., Kobayashi, S., Kawasaki, M., Shioi, G., Kaneko, M., Ishiuchi, T., Misaki, K., Meng, W., Takeichi, M., 2016. CAMSAP3 orients the apical-to-basal polarity of microtubule arrays in epithelial cells. Proc. Natl. Acad. Sci. 113, 332–337. https://doi.org/10.1073/pnas.1520638113

Tran, P.T., Marsh, L., Doye, V., Inoué, S., Chang, F., 2001. A Mechanism for Nuclear Positioning in Fission Yeast Based on Microtubule Pushing. J. Cell Biol. 153, 397–412. https://doi.org/10.1083/jcb.153.2.397

Triclin, S., Inoue, D., Gaillard, J., Htet, Z.M., DeSantis, M.E., Portran, D., Derivery, E., Aumeier, C., Schaedel, L., John, K., Leterrier, C., Reck-Peterson, S.L., Blanchoin, L., Théry, M., 2021. Self-repair protects microtubules from destruction by molecular motors. Nat. Mater. 20, 883–891. https://doi.org/10.1038/s41563-020-00905-0

Trotter, J.A., Purslow, P.P., 1992. Functional morphology of the endomysium in series fibered muscles. J. Morphol. 212, 109–122. https://doi.org/10.1002/jmor.1052120203

Tucker, J.B., Paton, C.C., Richardson, G.P., Mogensen, M.M., Russell, I.J., 1992. A cell surface-associated centrosomal layer of microtubule-organizing material in the inner pillar cell of the mouse cochlea. J. Cell Sci. 102, 215–226. https://doi.org/10.1242/jcs.102.2.215

V

Valenzuela, P., Quiroga, M., Zaldivar, J., Rutter, W.J., Kirschner, M.W., Cleveland, D.W., 1981. Nucleotide and corresponding amino acid sequences encoded by α and β tubulin mRNAs. Nature 289, 650–655. https://doi.org/10.1038/289650a0

van der Laan, S., Lévêque, M.F., Marcellin, G., Vezenkov, L., Lannay, Y., Dubra, G., Bompard, G., Ovejero, S., Urbach, S., Burgess, A., Amblard, M., Sterkers, Y., Bastien, P., Rogowski, K., 2019. Evolutionary Divergence of Enzymatic Mechanisms for Tubulin Detyrosination. Cell Rep. 29, 4159-4171.e6. https://doi.org/10.1016/j.celrep.2019.11.074

Varga, V., Leduc, C., Bormuth, V., Diez, S., Howard, J., 2009. Kinesin-8 motors act cooperatively to mediate length-dependent microtubule depolymerization. Cell 138, 1174–1183. https://doi.org/10.1016/j.cell.2009.07.032

Vasyutina, E., Lenhard, D.C., Wende, H., Erdmann, B., Epstein, J.A., Birchmeier, C., 2007. *RBP-J* (*Rbpsuh*) is essential to maintain muscle progenitor cells and to generate satellite cells. Proc. Natl. Acad. Sci. 104, 4443–4448. https://doi.org/10.1073/pnas.0610647104

Viguie, C.A., Lu, D.-X., Huang, S.-K., Rengen, H., Carlson, B.M., 1997. Quantitative study of the effects of long-term denervation on the extensor digitorum longus muscle of the rat. Anat. Rec. 248, 346–354. https://doi.org/10.1002/(SICI)1097-0185(199707)248:3<346::AID-AR7>3.0.CO;2-N

Vilmont, V., Cadot, B., Vezin, E., Le Grand, F., Gomes, E.R., 2016. Dynein disruption perturbs post-synaptic components and contributes to impaired MuSK clustering at the NMJ: implication in ALS. Sci. Rep. 6, 27804. https://doi.org/10.1038/srep27804

W

Walker, R.A., O'Brien, E.T., Pryer, N.K., Soboeiro, M.F., Voter, W.A., Erickson, H.P., Salmon, E.D., 1988. Dynamic instability of individual microtubules analyzed by video light microscopy: rate constants and transition frequencies. J. Cell Biol. 107, 1437–1448. https://doi.org/10.1083/jcb.107.4.1437

Wang, S., Reuveny, A., Volk, T., 2015. Nesprin provides elastic properties to muscle nuclei by cooperating with spectraplakin and EB1. J. Cell Biol. 209, 529–538. https://doi.org/10.1083/jcb.201408098

Wang, Z., Cui, J., Wong, W.M., Li, X., Xue, W., Lin, R., Wang, J., Wang, P., Tanner, J.A., Cheah, K.S.E., Wu, W., Huang, J.-D., 2013. Kif5b controls the localization of myofibril components for their assembly and linkage to the myotendinous junctions. Development 140, 617–626. https://doi.org/10.1242/dev.085969

Ward, C.W., Prosser, B.L., Lederer, W.J., 2014. Mechanical Stretch-Induced Activation of ROS/RNS Signaling in Striated Muscle. Antioxid. Redox Signal. 20, 929–936. https://doi.org/10.1089/ars.2013.5517

Warren, R.H., 1974. MICROTUBULAR ORGANIZATION IN ELONGATING MYOGENIC CELLS. J. Cell Biol. 63, 550–566. https://doi.org/10.1083/jcb.63.2.550

Welsh, G.I., Wilson, C., Proud, C.G., 1996. GSK3: a SHAGGY frog story. Trends Cell Biol. 6, 274–279. https://doi.org/10.1016/0962-8924(96)10023-4

Wilhelmsen, K., Litjens, S.H.M., Kuikman, I., Tshimbalanga, N., Janssen, H., van den Bout, I., Raymond, K., Sonnenberg, A., 2005. Nesprin-3, a novel outer nuclear membrane protein, associates with the cytoskeletal linker protein plectin. J. Cell Biol. 171, 799–810. https://doi.org/10.1083/jcb.200506083

Willingham, T.B., Ajayi, P.T., Glancy, B., 2021. Subcellular Specialization of Mitochondrial Form and Function in Skeletal Muscle Cells. Front. Cell Dev. Biol. 9, 757305. https://doi.org/10.3389/fcell.2021.757305

Wilson, M.H., Holzbaur, E.L.F., 2015. Nesprins anchor kinesin-1 motors to the nucleus to drive nuclear distribution in muscle cells. Development 142, 218–228. https://doi.org/10.1242/dev.114769

Wilson, M.H., Holzbaur, E.L.F., 2012. Opposing microtubule motors drive robust nuclear dynamics in developing muscle cells. J. Cell Sci. jcs.108688. https://doi.org/10.1242/jcs.108688

Winter, L., Wittig, I., Peeva, V., Eggers, B., Heidler, J., Chevessier, F., Kley, R.A., Barkovits, K., Strecker, V., Berwanger, C., Herrmann, H., Marcus, K., Kornblum, C., Kunz, W.S., Schröder, R., Clemen, C.S., 2016. Mutant desmin substantially perturbs mitochondrial morphology, function and maintenance in skeletal muscle tissue. Acta Neuropathol. (Berl.) 132, 453–473. https://doi.org/10.1007/s00401-016-1592-7

Witzemann, V., 2006. Development of the neuromuscular junction. Cell Tissue Res. 326, 263–271. https://doi.org/10.1007/s00441-006-0237-x

Wong, A., Garcia, S.M., Tamaki, S., Striedinger, K., Barruet, E., Hansen, S.L., Young, D.M., Pomerantz, J.H., 2021. Satellite cell activation and retention of muscle regenerative potential after long-term denervation. Stem Cells 39, 331–344. https://doi.org/10.1002/stem.3316

Wu, H.-Y., Nazockdast, E., Shelley, M.J., Needleman, D.J., 2017. Forces positioning the mitotic spindle: Theories, and now experiments. BioEssays 39, 1600212. https://doi.org/10.1002/bies.201600212

Wu, X., Kodama, A., Fuchs, E., 2008. ACF7 regulates cytoskeletal-focal adhesion dynamics and migration and has ATPase activity. Cell 135, 137–148. https://doi.org/10.1016/j.cell.2008.07.045

Wu, X., Shen, Q.-T., Oristian, D.S., Lu, C.P., Zheng, Q., Wang, H.-W., Fuchs, E., 2011. Skin Stem Cells Orchestrate Directional Migration by Regulating Microtubule-ACF7 Connections through GSK3β. Cell 144, 341–352. https://doi.org/10.1016/j.cell.2010.12.033

X

Xu, Z., Schaedel, L., Portran, D., Aguilar, A., Gaillard, J., Marinkovich, M.P., Théry, M., Nachury, M.V., 2017. Microtubules acquire resistance from mechanical breakage through intralumenal acetylation. Science 356, 328–332. https://doi.org/10.1126/science.aai8764

Xue, X., Gao, W., Sun, B., Xu, Y., Han, B., Wang, F., Zhang, Y., Sun, J., Wei, J., Lu, Z., Zhu, Y., Sato, Y., Sekido, Y., Miao, Y., Kondo, Y., 2013. Vasohibin 2 is transcriptionally activated and promotes angiogenesis in hepatocellular carcinoma. Oncogene 32, 1724–1734. https://doi.org/10.1038/onc.2012.177

Z

Zhang, J., Yue, J., Wu, X., 2017. Spectraplakin family proteins – cytoskeletal crosslinkers with versatile roles. J. Cell Sci. jcs.196154. https://doi.org/10.1242/jcs.196154

Zhang, X., Xu, R., Zhu, B., Yang, X., Ding, X., Duan, S., Xu, T., Zhuang, Y., Han, M., 2007. *Syne-1* and *Syne-2* play crucial roles in myonuclear anchorage and motor neuron innervation. Development 134, 901–908. https://doi.org/10.1242/dev.02783

Zhu, H., Lin, X., Diao, Y., 2021. Function and regulation of muscle stem cells in skeletal muscle development and regeneration: a narrative review. J. Bio-X Res. 4, 89–96. https://doi.org/10.1097/JBR.0000000000000105

Zimmerman, W.C., Sillibourne, J., Rosa, J., Doxsey, S.J., 2004. Mitosis-specific Anchoring of γ Tubulin Complexes by Pericentrin Controls Spindle Organization and Mitotic Entry. Mol. Biol. Cell 15, 3642–3657. https://doi.org/10.1091/mbc.e03-11-0796

Zou, S., Pan, B.-X., 2022. Post-synaptic specialization of the neuromuscular junction: junctional folds formation, function, and disorders. Cell Biosci. 12, 93. https://doi.org/10.1186/s13578-022-00829-z

Annex:
Other publications

During my thesis, I had the opportunity to participated in the development of different projects in the team or within the institute.

Following my first publication on the importance of MACF1 in skeletal muscle, we were proposed to describe and publish our experimental method for mice skeletal muscle denervation. As this technique was initially performed by our collaborator Dr. Jean-Luc Thomas, we continued this collaboration with him and his collogue Dr. Alexi Osseni to proceed the data and article preparation. This experimental protocol is recently published in Bio-protocol journal and is presented as “publication 3” in the following section.

I also participated in the study on the role of microtubule binding protein NuMA1 in MTs and myonuclei organization in skeletal muscle. In this study, which is presented as “publication 4”, I analyzed MTs and NMJs organization of isolated myofibers from control and NuMA1 depleted myofibers.

At last, I contributed to the preparation of another ongoing project within the team concentrated on the role of adaptor protein SH3KBP1 in myonuclei organization in skeletal muscle. In this study, I studied T-tubules and DHPR organization by isolating, staining, imaging, and analyzing isolated myofibers from control and SH3KBP1 depleted myofibers. the ensemble of data related to this project are presented as “publication 5”.

Publication 3:

Simple Methods for Permanent or Transient Denervation in Mouse Sciatic Nerve Injury Models.

Bio-protocol, 2022

Alexis Osseni, Jean-Luc Thomas, Alireza Ghasemizadeh, Laurent Schaeffer and Vincent Gache

bio-protocol

Published: Jun 05, 2022

Simple Methods for Permanent or Transient Denervation in Mouse Sciatic Nerve Injury Models

Alexis Osseni[#], Jean-Luc Thomas[#], Alireza Ghasemizadeh, Laurent Schaeffer and Vincent Gache*

INSERM U1315 - CNRS/UCBL1 UMR 5261/ INMG-PGNM (NeuroMyoGene Institute – Dpt. of Physiopathology and Genetics of Neurons and Muscles), Lyon, France
[#]Contributed equally to this work
*For correspondence: vincent.gache@inserm.fr

Abstract

Our ability to move and breathe requires an efficient communication between nerve and muscle that mainly takes place at the neuromuscular junctions (NMJs), a highly specialized synapse that links the axon of a motor neuron to a muscle fiber. When NMJs or axons are disrupted, the control of muscle fiber contraction is lost and muscle are paralyzed. Understanding the adaptation of the neuromuscular system to permanent or transient denervation is a challenge to understand the pathophysiology of many neuromuscular diseases. There is still a lack of *in vitro* models that fully recapitulate the *in vivo* situation, and *in vivo* denervation, carried out by transiently or permanently severing the nerve afferent to a muscle, remains a method of choice to evaluate reinnervation and/or the consequences of the loss of innervation. We describe here a simple surgical intervention performed at the hip zone to expose the sciatic nerve in order to obtain either permanent denervation (nerve-cut) or transient and reversible denervation (nerve-crush). These two methods provide a convenient *in vivo* model to study adaptation to denervation.

Keywords: Muscle, Denervation, Nerve crush, Neuromuscular junction, Acetylcholine receptor, synaptic vesicle glycoprotein 2B

This protocol was validated in: eLife (2021), DOI: 10.7554/eLife.70490

Published: Jun 05, 2022

Graphical abstract:

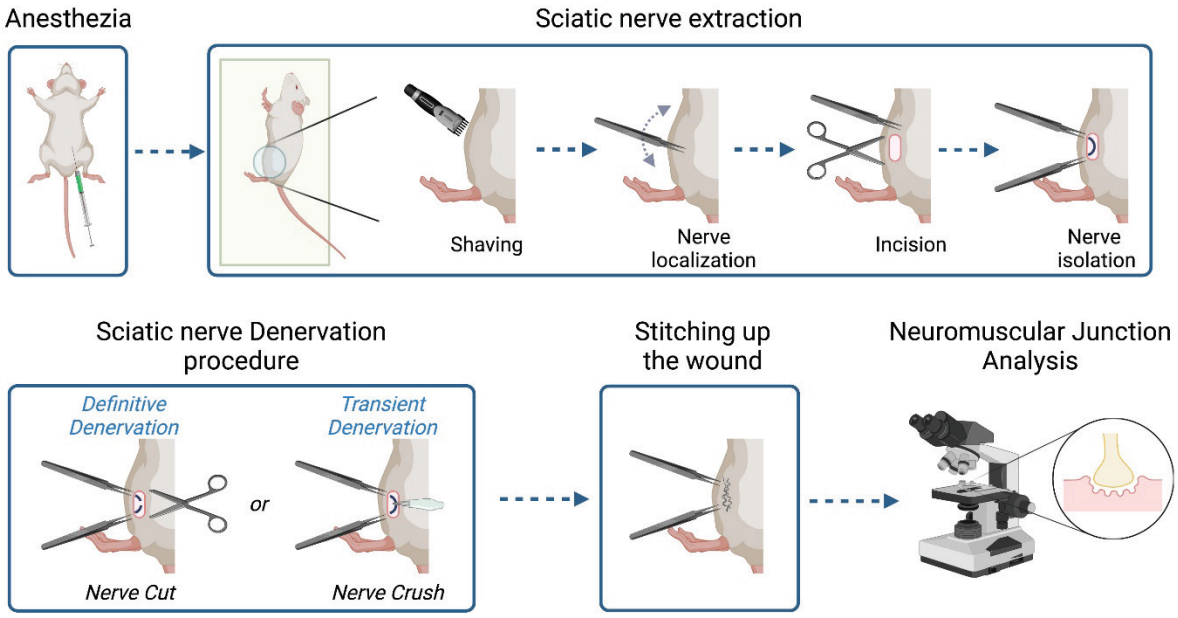

Background

Neuromuscular disorders constitute a heterogeneous group of more than 200 diseases that present impaired motor function and are often debilitating and prematurely fatal. In vertebrates, the neuromuscular junction (NMJ) is a specialized cholinergic synapse with a complex molecular architecture that ensures reliable conversion of the nerve influx into muscle contraction. In various neuromuscular disorders, genetic alterations result in the failure of the neurotransmission caused by the loss of NMJs, characterized by skeletal muscle weakness and fatigue as observed in Congenital Myasthenic Syndromes, Amyotrophic Lateral Sclerosis, or Spinal Muscular Atrophy.

NMJ integrity requires both healthy presynaptic (motoneuronal) and healthy postsynaptic (muscular) compartments. The organization of the postsynaptic region relies on the heparan sulfate proteoglycan agrin secreted by motoneurons at the NMJ (Huzé *et al.*, 2009 and references therein). Agrin binding to the LRP4/MusK complex induces Acetylcholine Receptors (AchR) clustering at the NMJs, as well as the recruitment of approximately 5 myonuclei that specialize in the expression of the genes coding for NMJs components (Simon *et al.*, 1992; Vaittinen *et al.*, 1999; Méjat *et al.*, 2003; Ravel-Chapuis *et al.*, 2007). Besides the control of postsynaptic gene expression, NMJ structural integrity require a meshwork of intermediate filaments (Mihailovska *et al.*, 2014), linkers of the actin network such as the dystrophin glycoprotein complex (Belhasan and Akaaboune, 2020) and a precise patterning of the microtubule network (Osseni *et al.*, 2020; Ghasemizadeh *et al.*, 2021) that contribute to AChR addressing and clustering at the postsynaptic membrane of myofibers.

Here, we describe how to perform an efficient and rapid intervention on the sciatic nerve to create a permanent or a transient denervation. This method is adapted from standard protocols (Méjat *et al*., 2005; Bauder and Ferguson, 2012; Morano *et al*., 2018; Ghasemizadeh *et al*., 2021). We explain how to track efficiently the sciatic nerve allowing a simple surgical gesture involving a small incision through the skin and muscle. We propose two alternative methods for sciatic nerve injury: i) a permanent denervation (Nerve-cut), ii) a transient and reversible denervation (Nerve-crush). Each method provides specific advantages to evaluate the effects of denervation and/or monitor axon and NMJs regeneration (Morano *et al.*, 2018; Ghasemizadeh *et al.*, 2021).

These methods are very simple and permit the *in vivo* study of the neuromuscular integrity along with regeneration processes.

Materials and Reagents

1. Metacam®, 1.5 mg/mL oral suspension for dogs (Boehringer Ingelheim)
2. Ketamine, Imalgène® 1000 solution for injection (Boehringer Ingelheim)
3. Buprenorphine, Buprecare® 0.3 mg/mL solution for dog and cat (Axience)
4. Xylazine, Rompun® 2% (Bayer)
5. Lurocaine, solution for injection/parenteral route (Vetoquinol®)
6. Ocry-gel®, TVM-UK Company
7. PBS (Sigma-Aldrich, catalog number: D1408-500mL)

Equipment

Surgical tools

1. Tool box (Moria, catalog number: 11210)
2. One pair of scissors straight pointed 10 cm long (Moria, catalog number: 4877)
3. Two pairs of Dumont forceps N°5 Swiss model (Moria, catalog number: MC40)
4. One pair of needle holder clamps (Securimed, catalog number: 100AAA100)
5. One pair of Dauphin's scissors (Securimed, catalog number: 2117)
6. Suture thread (Ethicon, catalog number: JV390)
7. Hemostatic clip 1,7 cm Glolink Tool (Vetolabo, catalog number: VT-004-413-13)
8. Syringe 0.3 mL (BD Micro-Fine+)

Equipment

1. Heating Mat (Acculux Thermolux, catalog number: 461265)
2. Heating cabinet (ONO V.B., catalog number: RS5)
3. Isoflurane anesthesia (Ref VI-1586) device (TEM SEGA, MiniTag V1/Evaporator Tec7)
4. Fur trimmer (Moser, catalog number: VI-1586)

Procedure

1. Turn on the heating cabinet to allow anesthetized mice to recover properly after the procedure.
2. Anesthetize mouse with Isoflurane. For this purpose, place the mouse in a clean induction chamber connected to the anesthesia device (Figure 1). Adjust the isoflurane to 3–4% and the oxygen flow to 0.8–1.5 L/min. Once anesthetized the mouse loses all its tonus [For a more detailed procedure, please refer to previously described protocols (Davis, 2008)].

Figure 1. Isoflurane anesthesia set-up.

3. Cover Mouse cornea with a drop of Ocrygel® to prevent eyes from drying-up during the procedure.
4. Anesthetize mouse using an intraperitoneal injection of Ketamine/xylazine mix (100 mg Ketamine/kg weight and 10 mg xylazine/ kg weight) previously diluted in a 10 mM phosphate buffered saline solution. Use a 25 G needle mounted on a 3 mL syringe.
5. To prevent pain due to the surgical procedure, perform a subcutaneous injection of buprenorphine at the site of incision (0.1 mg/kg weight). Use a 25 G needle mounted on a 3 mL syringe.
6. Place the mouse on the heating mat during the whole procedure to avoid any hypothermia.
7. Shave the mouse at the hip (see **Video 1** for the zone to shave).

Video 1. Mouse Hair shaving process.

8. Make a 3 mm incision in the skin over the trochanter (Figure 2A–2C) (see **Video 2** to observe the approach to correctly identify the area to be incised).

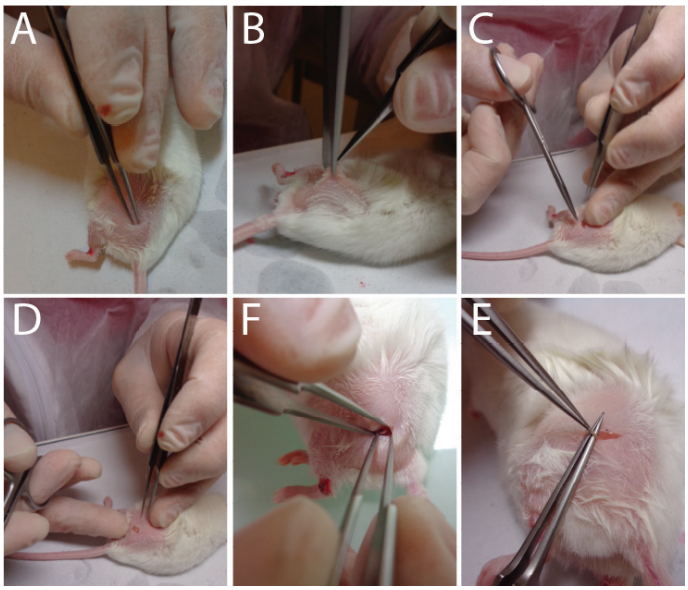

Figure 2. Sequential approaches to reach the sciatic nerve.

Video 2. Localization of the skin incision to correctly reach the sciatic nerve.

9. Incise the conjunctive tissue just on the right of the hip to open a small breach through the conjunctive tissue (Figure 2D) (see **Video 3** to observe the size area incised).

Video 3. Skin incision surgery.

10. Push aside the muscular fascia in order to clearly visualize the nerve (see **Video 4** to observe the extracted nerve) (Figure 2F–2E) (Caution: this must be done without any bleeding).

Video 4. Sciatic nerve isolation.

11. Apply drops (2–3) of lurocaïne directly on the incised zone to perform a local anesthesia of the nerve. Wait at least 2 min to continue the procedure.

For definitive denervation procedure

12. Using a fine forceps (Moria N°5 or equivalent) in order to cut a small part of the nerve (1–3 mm) (Figure 3A) (see **Video 5**).

Video 5. Sciatic nerve section surgery.

For a transient denervation (nerve crush procedure)

13. Pinch for 30 s the exposed sciatic nerve with a hemostatic clip (Figure 3B) (see **Video 6**).

Video 6. Sciatic nerve crush surgery.

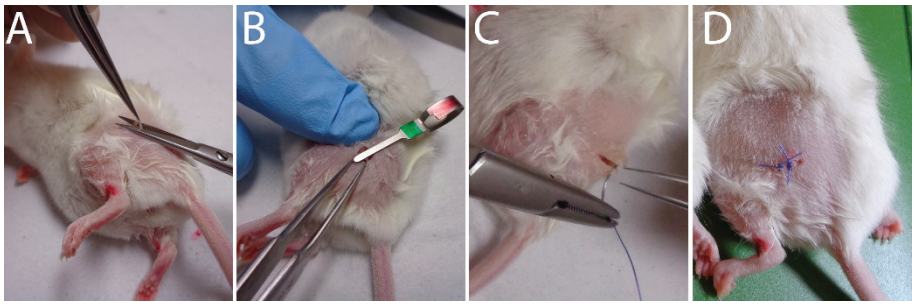

Figure 3. Sequential approaches to reach the sciatic nerve.

14. Stitch the skin with one or two sutures (Figure 3C–3D) (see **Video 7**).

Video 7. Skin stitching surgery.

15. Allow the mice to recover gently from anesthesia in the heating cabinet (25°C).
16. **Analysis of denervation effects** can be appreciated by following NMJs structural changes on *Tibialis anterior* isolated muscle fibers. Using immunofluorescence approaches, 3 days post-surgery you will observe the absence of SV2B labeling on isolated fibers (Figure 4A–4B). Likewise, for the nerve crush procedure, you will observe the reinnervation after 15 days as SV2B staining's begins to progressively reappear (Figure 4C–4D). Note that the overall cross section area (CSA) of muscle fibers will decreased rapidly in the course of denervation/regeneration (Ghasemizadeh *et al.*, 2021). Alterations of the NMJs structure such as fragmentation of AchRs, disruption of NMJs area and/or decrease of synaptic myonuclei number above the NMJs can be tracked as previously described (Jones *et al.*, 2016; Osseni *et al.*, 2020; Ghasemizadeh *et al.*, 2021). Analysis of transcriptional changes by monitoring gene expression along the regeneration processes also allow characterization of the time course of NMJs alterations. mRNA or proteins encoded by genes such as *MyoD* (Myoblast determination protein1), *Myog* (Myogenin), *AchR-α,β,γ,δ,ε* (Acetylcholine Receptor *α,β,γ,δ,ε* subunits), *MITR* (MEF2 interacting Transcription Repressor), *NRG1-α,β* (Neuregulin-*α,β*) and *MusK* (Muscle skeletal receptor tyrosine-protein kinase) will be key to determine the correct time course of denervation/reinnervation (Méjat *et al.*, 2005; Thomas *et al.*, 2015; Morano *et al.*, 2018).

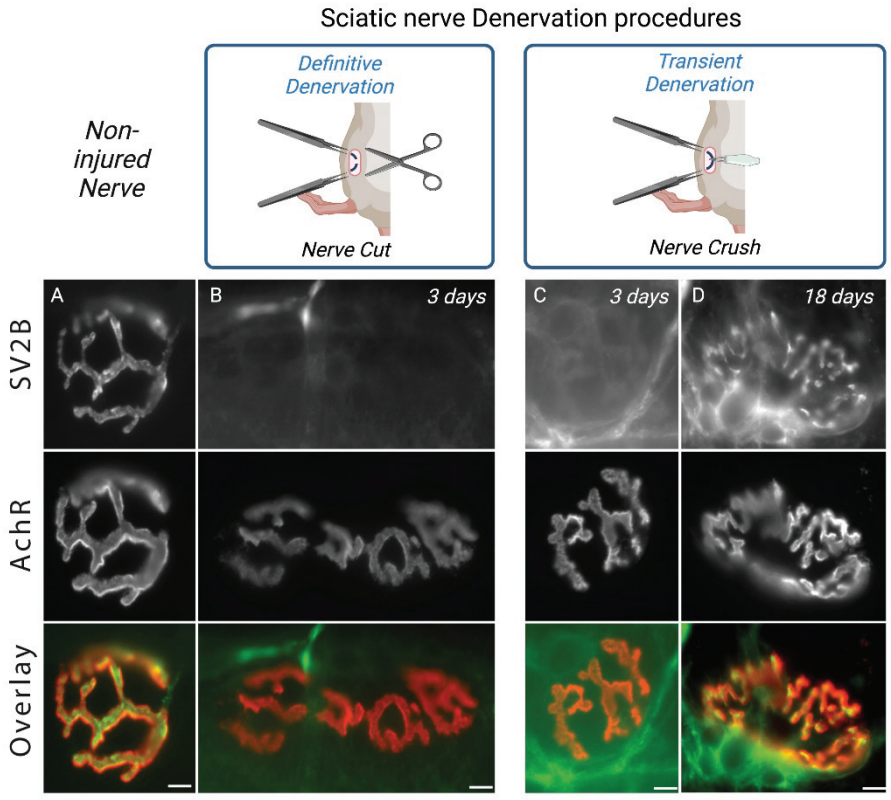

Figure 4. Sciatic nerve denervation procedure effects.
Isolated fibers of *tibialis anterior* muscle from 2-months-old WT double-stained with an antibody against synaptic vesicle glycoprotein 2B (SV2B, in green) to label the presynaptic domain of NMJs and with α-bungarotoxin–A594 (in red) to label the postsynaptic domain of NMJs. Representative immunofluorescence images of non-injured nerve (A), definitive denervation procedure (B) after 3 days and transient denervation procedure after 3 days (C) or 18 days (D). Scale bars, 10 µm.

Notes

1. The main difficulty lay in the precision to locate the area for skin incision (Figure 2A). You must not be too much towards the spine or the knee or both too much above the hip or buttock at the same time; otherwise, it will be very difficult to find the nerve. In fact, the nerve comes to the surface close to the skin just behind the hip as it does for you. Outside of this location, the nerve goes deep into the muscle fascia and becomes very difficult to visualize and grasp.
2. Note that the efficiency of the procedures is not easily visible as mice show a quasi-normal behavior after the procedure (see **Video 8**). Nevertheless, as a consequence of the completed procedure (Nerve-cut or Nerve-crush), after waking up, mice drag the denervated leg, as can be seen in **Video 8**. This situation is definitive for the Nerve-cut procedure whereas, in the case of nerve crush procedure, mice recover gradually the movement of the paw, which appears completely normal 3 weeks after the Nerve-crush procedure.

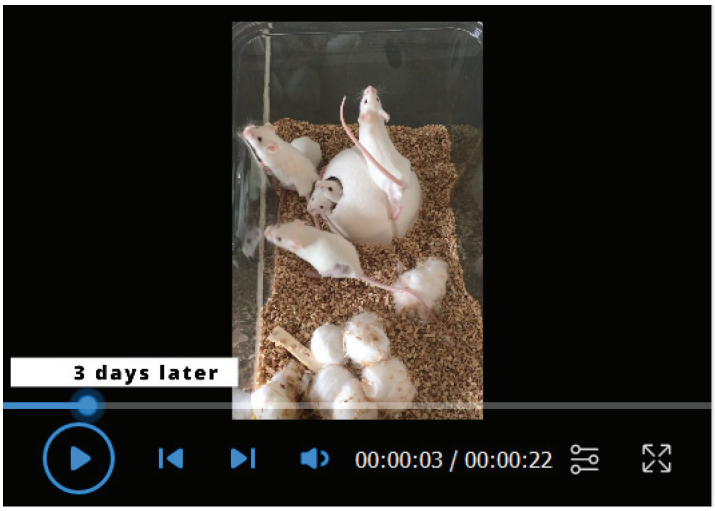

Video 8. Behaviors of mice after the procedure.

Acknowledgments

This work was supported by grants from ATIP-Avenir and AFM via the MyoNeurAlp Alliance. We acknowledge contributions of the CELPHEDIA Infrastructure (http://www.celphedia.eu/), and especially the center AniRA of Lyon "Plateau de Biologie Expérimentale de la Souris". We thank Tiphaine Dorel and members of CIQLE imaging center (Faculté de Médecine Rockefeller, Lyon-Est). All graphic abstracts were created with BioRender.com. These methods were derived from Méjat *et al.* (2005). This protocol was adapted from our recent work (Ghasemizadeh *et al*, 2021; DOI: 10.7554/eLife.70490).

Competing interests

The authors declare no competing financial interests.

Ethics

Animal experimentation: Experiments and procedures were performed in accordance with both the guidelines of the local animal ethics committee of the University Claude Bernard - Lyon 1 and French / European legislation on animal experimentation (Directive 2010/63 from European Union) approved by the ethics committee CECCAPP (agreement number D691230303 delivered by the French Ministry of Research).

References

Bauder, A. R. and Ferguson, T. A. (2012). Reproducible mouse sciatic nerve crush and subsequent assessment of regeneration by whole mount muscle analysis. *J Vis Exp* (60).

Belhasan, D. C. and Akaaboune, M. (2020). The role of the dystrophin glycoprotein complex on the neuromuscular system. *Neurosci Lett* 722: 134833.

Davis, J. A. (2008). Mouse and rat anesthesia and analgesia. *Curr Protoc Neurosci* Appendix 4: Appendix 4B.

Ghasemizadeh, A., Christin, E., Guiraud, A., Couturier, N., Abitbol, M., Risson, V., Girard, E., Jagla, C., Soler, C., Laddada, L., *et al.* (2021). MACF1 controls skeletal muscle function through the microtubule-dependent

localization of extra-synaptic myonuclei and mitochondria biogenesis. *Elife* 10: e70490.

Huzé, C., Bauche, S., Richard, P., Chevessier, F., Goillot, E., Gaudon, K., Ben Ammar, A., Chaboud, A., Grosjean, I., Lecuyer, H. A., *et al*. (2009). Identification of an agrin mutation that causes congenital myasthenia and affects synapse function. *Am J Hum Genet* 85(2): 155-167.

Jones, R. A., Reich, C. D., Dissanayake, K. N., Kristmundsdottir, F., Findlater, G. S., Ribchester, R. R., Simmen, M. W. and Gillingwater, T. H. (2016). NMJ-morph reveals principal components of synaptic morphology influencing structure-function relationships at the neuromuscular junction. *Open Biol* 6(12).

Méjat, A., Ramond, F., Bassel-Duby, R., Khochbin, S., Olson, E. N. and Schaeffer, L. (2005). Histone deacetylase 9 couples neuronal activity to muscle chromatin acetylation and gene expression. *Nat Neurosci* 8(3): 313-321.

Méjat, A., Ravel-Chapuis, A., Vandromme, M. and Schaeffer, L. (2003). Synapse-specific gene expression at the neuromuscular junction. *Ann N Y Acad Sci* 998: 53-65.

Mihailovska, E., Raith, M., Valencia, R. G., Fischer, I., Al Banchaabouchi, M., Herbst, R. and Wiche, G. (2014). Neuromuscular synapse integrity requires linkage of acetylcholine receptors to postsynaptic intermediate filament networks via rapsyn-plectin 1f complexes. *Mol Biol Cell* 25(25): 4130-4149.

Morano, M., Ronchi, G., Nicolò, V., Fornasari, B. E., Crosio, A., Perroteau, I., Geuna, S., Gambarotta, G. and Raimondo, S. (2018). Modulation of the Neuregulin 1/ErbB system after skeletal muscle denervation and reinnervation. *Scientific Reports* 8(1): 5047.

Osseni, A., Ravel-Chapuis, A., Thomas, J. L., Gache, V., Schaeffer, L. and Jasmin, B. J. (2020). HDAC6 regulates microtubule stability and clustering of AChRs at neuromuscular junctions. *J Cell Biol* 219(8).

Ravel-Chapuis, A., Vandromme, M., Thomas, J. L. and Schaeffer, L. (2007). Postsynaptic chromatin is under neural control at the neuromuscular junction. *EMBO J* 26(4): 1117-1128.

Simon, A. M., Hoppe, P. and Burden, S. J. (1992). Spatial restriction of AChR gene expression to subsynaptic nuclei. *Development* 114(3): 545-553.

Thomas, J. L., Moncollin, V., Ravel-Chapuis, A., Valente, C., Corda, D., Mejat, A. and Schaeffer, L. (2015). PAK1 and CtBP1 Regulate the Coupling of Neuronal Activity to Muscle Chromatin and Gene Expression. *Mol Cell Biol* 35(24): 4110-4120.

Vaittinen, S., Lukka, R., Sahlgren, C., Rantanen, J., Hurme, T., Lendahl, U., Eriksson, J. E. and Kalimo, H. (1999). Specific and innervation-regulated expression of the intermediate filament protein nestin at neuromuscular and myotendinous junctions in skeletal muscle. *Am J Pathol* 154(2): 591-600.

Publication 4:

Cytoplasmic NuMA1 promotes microtubule stabilization and controls myonuclear spreading and dynamics in skeletal muscle.

In preparation.

N. Couturier, L. Castellano, A. Ghasemizadeh, E. Christin, A. Janin, A. Osseni, J.L. Thomas, L. Schaeffer, St. Konig, J. Brunetti, M. Frieden, Y. Couté, A. Kraut, J. Courchet and V. Gache

Note: following revisions, the photos presented in Figure 6A will be replaced by new photos obtained from a new commercialized antibody for which the staining and results adapt to the photos presented in Figure 6D. A new version of the manuscript is currently under preparation.

Cytoplasmic NuMA1 promotes microtubule stabilization and controls myonuclear spreading and dynamics in skeletal muscle

Nathalie Couturier[1], Alireza Ghasemizadeh[1], Emilie Christin[1], Alexandre Janin[1], Alexis Osseni[1], Jean-Luc Thomas[1], Laurent Schaeffer[1], Stéphane Konig[2], Jessica Brunetti[2], Maud Frieden[2], Yohann Couté[3], Alexandra Kraut[3], Julien Courchet[1] and Vincent Gache[1,4].

1 Institut NeuroMyoGène, CNRS UMR5310, INSERM U1217, Faculté de Médecine, Rockefeller, Université Claude Bernard Lyon I, 8 Avenue Rockefeller, 69373, Lyon Cedex 08, France.
2 Department of Basic Neurosciences, Geneva Medical Center, 1, Rue Michel Servet, 1211 Geneva 4, Switzerland.
3 University Grenoble Alpes, CEA, INSERM, IRIG, BGE, F-38000 Grenoble, France.
4 Institut NeuroMyoGène, CNRS UMR5310, INSERM U1217, Faculté de Médecine, Rockefeller, Université Claude Bernard Lyon I, 8 Avenue Rockefeller, 69373, Lyon Cedex 08, France. vincent.gache@inserm.fr

Abstract

Skeletal muscle consists in a bundle of thousands of post-mitotic multinucleated cells, called myofibers, in which myonuclei are evenly spaced and positioned at the periphery. This myonuclear positioning is driven by cytoskeleton and associated proteins and is required for proper myofiber function. In numbers of muscle diseases (*i.e.* myopathies), internalized and mispositioned myonuclei impair myofiber function, supporting the need to better understand the fundamental mechanisms that regulates myonuclei dynamics. Here we identify the microtubule-associated protein NuMA1 as an essential regulator of microtubule architecture and myonuclear spreading/positioning. Strikingly, loss of NuMA1 disrupts myonuclear organization in both *in vitro* and *in vivo* muscle fibers. While NuMA1 is expressed in nuclei of undifferentiated cells, it progressively transits in the cytoplasm during muscle cell differentiation to regulate the nucleus-microtubule-organizing-center (nMTOC) integrity. Furthermore, we show that during muscle fiber formation, NuMA1 associates with the Dynein-1 Heavy Chain-1 to shape microtubule orientation. Therefore, our results show that NuMA1 localization (nucleus *versus* cytoplasmic) controls myonuclei motion and is a marker of dynamic myonuclei inside myofibers. Altogether, our data identify a novel mechanism by which nuclear sequestration of a microtubule-associated protein allows to couple nuclear positioning and motion.

Introduction

The building block of skeletal muscle is the post-mitotic muscle fiber (*i.e.* myofibers). Myofiber is formed by the fusion of hundreds of specialized mononucleated cells, namely myoblasts, which shape syncytial cells, called myotubes. Myotubes are immature myofibers in which positioning of nuclei (*i.e.* myonuclei) is finely regulated [1]. In the normal course of muscle development, myonuclei are actively spreading within myotubes/myofibers. Myonuclei finally adopt a specific location in the mature myofiber, regularly spaced at its periphery. The peripheral location of myonuclei induces drastic changes in their shape, mainly due to forces applied on their nuclear envelope, as myonuclei are stuck between the plasma membrane of myofibers and myofibril structures [2]. This conformational adaptation of myonuclei is believed to stabilize internal and external mechanical forces and consequently, constrain chromatin organization and gene expression [3,4]. Thus, this myonuclei organization guaranties a spatial coordinated activity that contribute to myofiber functional integrity [5]. Nonetheless, this apparent myonuclei homogeneity along myofibers is reconsidered in specific areas such as the neuromuscular junction (NMJ) or the myotendinous junction (MTJ) where different characteristics such nuclear protein importation or transcriptional activity are modified/specified [6-8].

Numerous muscle diseases are characterized by myonuclei shape and positioning alterations. In Duchenne muscular dystrophy (DMD), the most common and fatal form of muscular dystrophies, skeletal muscles undergo rapid degeneration followed by regeneration and these chronic cycles progressively lead to the accumulation of damaged myofibers with internalized myonuclei [9]. In a heterogeneous group of inherited muscle diseases, centronuclear myopathies (CNMs) are defined pathologically by an abnormal localization of myonuclei in the center of muscle fibers. We previously show that nuclear positioning within myofibers is required for proper muscle function[10], suggesting that in mature myofibers, the peripheral myonuclei maintenance is key to adjust optimal muscle behavior.

We and others showed that microtubule-related molecular motors, Microtubule-Associated Proteins (MAPs), and the interplay between actin, microtubule and intermediate filament networks, are involved in different steps of myonuclei localization during myofiber formation and maturation [10-13]. Additionally, previous studies highlighted critical roles for proteins localized inside myonuclei, such as Lamin A/C, the Nuclear Envelope Proteins (NEPs) that link nuclear lamina to cytoskeleton through the “Linker of Nucleoskeleton and Cytoskeleton” (LINC) complex, or the SUN proteins that anchor myonuclei inside myofibers [14-16]. Delocalization of microtubule nucleation center at

myonuclei membrane during myogenesis leads to the accumulation of a meshwork of proteins such as γ-tubulin, AKAP9 or MACF1, that regulate myonuclei availability to different cytoskeleton networks [13,17-21]. Mature muscle fibers are long (centimeter scale) and contain hundreds of myonuclei. How myonuclei position is maintained along myofiber length and the ability of each myonucleus to control its own motion is still pending.

Here we report that the Nuclear Mitotic Apparatus 1 protein (NuMA1) is progressively transferred, during myofiber development and maturation, from the nucleus to the cytoplasm compartment where it accumulates and stabilizes microtubule network. Cytoplasmic NuMA1, in association with Dynein-1 Heavy Chain-1, sets the distance between adjacent myonuclei and is crucial for peripheral myonuclei maintenance along myofibers. Moreover, this study shows that the capacity of myonuclei to retain NuMA1 is correlated with their dynamics in myofibers. Thus, we show that NuMA1 is an essential microtubule-associated protein in myofibers that controls physiological roles in muscle fibers through the regulation of nuclear dynamics.

Results

NuMA1 is required for myonuclear positioning and shape during myofiber formation and maintenance.

To identify new factors that regulate microtubule network architecture and consequently, contribute to the establishment of myonuclear domain during myofiber formation, we purified microtubule-associated proteins from 3 days differentiated mouse primary myotubes (immature myofibers) as previously described [13]. Surprisingly, mass-spectrometry analysis revealed the significant presence of the Microtubule-Associated Protein NuMA1 (Nuclear mitotic apparatus protein 1) in equivalent amount to proteins known to participate in microtubules remodeling during myotube formation, such as MAP4 or AKAP9 [18,22] (Extended Data Fig.1a). While NuMA1 was previously reported to play important roles in cell division [23,24], its function in postmitotic myofibers remained unknown. Therefore, we first addressed the role of NuMA1 in the early steps of myotube formation (Fig.1a-d). Primary mouse myoblasts were treated with siRNAs targeting either a scrambled sequence or *Numa1* mRNA, before being induced to fuse and form myotubes for 3 days (Fig.1a-c). At this stage, myonuclei are aligned in the center of myotubes mainly due to an interplay between MAPs and microtubules network [10,11,22]. Interestingly, efficient *Numa1* down-regulation (Extended Data Fig.1b-c) resulted in the formation of myotubes that exhibit strong myonuclei aggregation (Fig.1c). To analyze precisely parameters regarding myotube phenotype and localization of their respective

myonuclei, we developed an ImageJ® plugin, allowing to classify myotubes according to their myonuclei content using a homemade program in RStudio® software (Fig.1d, Extended Data Fig.1d-f). In control condition, we clearly observed a nearly linear relationship between myonuclei addition into myotubes and myonuclei spreading, reflected by the increase of the mean **D**istance between **M**yotubes **c**entroid and **M**yonuclei (DMcM) (Fig.1d, Extended Data Fig.1d). Interestingly, NuMA1 depletion correlates with a failure in myonuclei spreading during myotube expansion, occurring precociously as myotubes containing 5 myonuclei already fail to correctly spread myonuclei (Fig.1d).

As myonuclei spreading and alignment directly influences elongation and shape of myotubes through microtubules network parallelization [25,26], we investigated evolution of myotube length and area according to myonuclei content. Each additional myonucleus is associated with a gradual raise of myotube length (+9,6% ± 4,13) and area (+11% ± 3,51) (Extended Data Fig.1e-f). However, in NuMA1-depleted conditions, length is slightly decreased in myotubes containing 5 to 8 myonuclei and reaches a plateau in myotubes with 9 to 14 myonuclei (Extended Data Fig.1e). Thus, 8-9 myonuclei constitutes a "breaking point" where myotubes fail to complete the myotube elongation step. Interestingly, NuMA1 depletion impairs myotube elongation while emphasizing myotube expansion, as reflected by a constant increase in myotubes area independently of their myonuclei content (Extended Data Fig.1f). Of note, NuMA1 depletion in C2C12 myotubes also leads to an accumulation of myotubes with aggregated myonuclei (Extended Data Fig.2). Altogether, these data support the idea that NuMA1 is involved in the myonuclear positioning during the first steps of differentiation.

To investigate the potential role of NuMA1 in later steps of muscle differentiation, myotubes were induced into a long-termed maturation process [27]. This method allows formation of *in vitro* mature myofibers with regularly spread and peripherized myonuclei (Fig.1e). Using short hairpin RNA (shRNA) tagged with GFP, we addressed the consequences of NuMA1 depletion on long-term muscle maturation (Fig.1e-i). NuMA1 depletion induces a significant increase of aggregated myonuclei (10,3% ± 0,24 in control myofibers *versus* 37,5% ± 3,23 in NuMA1-depleted myofibers) (Fig.1h) concomitantly with a drop from half in peripheral myonuclei localization (Fig.1i). Interestingly, peripheral myonuclei localization was observed in control myofibers that display myofibril structures (Fig.1e-g, asterix), while NuMA1-depleted myofibers with impaired myofibril formation show centralized myonuclei (Fig.1f, arrows). Together, this suggests that NuMA1 regulates myofiber maturation.

To further understand how NuMA1 impacts the integrity of mature myofibers, we depleted NuMA1

in vivo, in *Tibialis Anterior* (TA) muscles from 8-week old wild-type mice for two weeks (Fig.1j-m). Transversal cross-sections of control TA muscles showed that myonuclei are all localized at the periphery of each myofiber where they adopt a flat conformation (Fig.1k, arrows). In NuMA1-depleted myofibers, we observed two major changes: (1) some myonuclei switch orientation/shape resulting in an apparent pointing towards myofiber center (Fig.1l, orange arrows) and (2) some are detached, rounded and localize inside muscle fibers (Fig.1l, white arrow). Mislocalized myonuclei are nearly 8-fold more present in NuMA1-depleted muscle fibers compared to control (Fig.1m). Therefore, our data demonstrate that NuMA1 controls myonuclei localization during early myofiber elongation and late maturation.

NuMA1 is required to maintain myonuclear shape and motion in muscle fibers

Besides myonuclei mislocalization, NuMA1-depleted myofibers also exhibit a strong alteration of the shape of myonuclei that appear much bigger than the ones in control condition (Fig.1). NuMA has recently been shown to serve as a structural component of the "nuclear matrix" [28]. Indeed, analysis of myonuclei shape parameters in NuMA1-depleted myotubes revealed that both myonuclei area and circularity are significantly increased compared to control (Fig.2a-d). Nuclei are physically connected to the cell surface by an interplay between cytoskeleton and proteins from the LINC-complex, which contributes to the transmission of mechanical forces that influence many aspects of cell behavior such as myoblast fusion [29]. However, these forces are not restricted to cell surface receptors and adhesions and can occur inside nucleus through other component of the "nuclear matrix" such as nuclear Lamins and Emerin [30]. We thus hypothesized that NuMA1 influences the content of proteins required for nuclear structure maintenance and function (Fig.2e). Although NuMA1 depletion in myofibers does not impact mRNA expression of both *LaminA/C* and *LaminB*, it significantly increases *Emerin* mRNA expression (Fig.2e). Thus, NuMA1 depletion in myofibers triggers potential to alteration in membrane myonuclei rigidity.

As we previously showed that myonuclei aggregation could be a consequence of myonuclei motion alteration[11], we then tested whether loss of NuMA1 impairs myonuclei movements in myofibers (Fig.3). Myoblasts were co-transfected with RFP-lamin-chromobody®, allowing the visualization of myonuclei, with either siRNA or shRNA targeting scramble or *Numa1* mRNA tagged with a GFP reporter (Fig.3a, Supplementary movie 1-2). In 5-day differentiated myofibers, myonuclei displacement parameters were extracted and analyzed using SkyPad [31]. In control condition, myonuclei are in motion 90% of the time at a median speed of 0.25 ± 0.02 μm/min which leads to a diffusion coefficient value of 2.4 ± 0.4 and 3.1 ± 0.6 μm^2/min in siRNA and shRNA conditions,

respectively (Fig.3-b-d). NuMA1 depletion in myofibers does not affect myonuclei percentage of time in motion compared to control condition (Fig.3b). However, myonuclei speed in NuMA1-depleted myofibers decreases by 30% to 40% using either siRNA or shRNA techniques (Fig.3c). This drop of myonuclei speed is concomitant with a drastic inhibition of myonuclei diffusion coefficient that fall from 50% to more than 70% in siRNA and shRNA conditions, respectively (Fig.3d). Thus, myonuclei aggregation in the absence of NuMA1 is a consequence of a dramatic decrease of both myonuclei speed and diffusion inside myotubes.

Altogether, NuMA1 depletion in myofibers leads to myonuclei mis-organization through the control of myonuclei motion.

NuMA1 governs microtubule orientation at the vicinity of myonuclei

As NuMA1 contains tubulin-binding-domain (Extended Data Fig.3a) that regulates microtubule nucleation during mitosis [32,33], we investigated the role of NuMA1 in controlling the microtubule network architecture during muscle differentiation/maturation (Fig.4). In control myotubes (scramble siRNA), microtubules mainly emanate from myonuclei membrane (*i.e*. nMTOC for nuclear Microtubule Organizing Center) as well as membranes associated nuclear Golgi elements [34,35], resulting in the formation of a parallel network of microtubules along myotube length [10] (Fig.4a). Even though microtubule network parallelization appears at the tip of myotubes, NuMA1-depleted myotubes exhibit an apparent disorganized network at the vicinity of myonuclei aggregates (Fig.4a-b, zooms). This result suggests that NuMA1 participates to microtubule orientation, especially at the myonuclei vicinity. This observation was further confirmed using 3-days differentiated primary myoblasts that were co-transfected with GFP-tagged EB1 and either scramble or *Numa1* siRNA. EB1 comets allow to assess both microtubule polymerization dynamics and orientation [36]. NuMA1 depletion in myotubes does not affect EB1-GFP comets velocity (Extended Data Fig.3b-d, Supplementary movie 3-4), suggesting that NuMA1 is not involved in the global microtubule polymerization rate. The organization of microtubule network was examined in specific areas of the myotubes (Fig.4c-e). In myotube areas devoid of myonuclei, NuMA1 depletion does not affect microtubule growth orientation. Indeed, EB1-GFP comet trajectories are mainly tangential compared to the longitudinal axis of myotubes (56,1% ± 6,62 of EB1-GFP comets orientate in the horizontal axis from -10° to 10° in control compared to 49,5% ± 6,61 in NuMA1-depleted condition) (Fig.4f). However, in myotube areas enriched for myonuclei, EB1-GFP comet trajectories are dramatically disrupted upon NuMA1 depletion. While EB1-GFP comet trajectories are mostly in the horizontal axis in control myotubes (47,5% ± 2,73), we observed a 50% drop of longitudinal EB1-GFP comet

197 trajectories that shift to more randomized orientations in NuMA1 depleted myotubes (Fig.4g).

198 Microtubule nucleation from the nucleus in myotubes requires the relocalization of microtubule
199 nucleator proteins near the membrane of myoncleus[18,21]. We thus examined the nMTOC organization
200 in NuMA1-depleted myotubes by analyzing both the centrosomal protein Pericentrin and the Golgi
201 complex localization (Fig.4h-l). In control, Pericentrin and Golgi elements are highly concentrated at
202 the vicinity of myonuclei membranes (Fig.4h, j, l). However, in NuMA1-depleted myotubes, nuclear
203 Pericentrin accumulation is highly reduced and dispersed within the cytoplasm (Fig.4i). This
204 phenotype is also associated with a substantial Golgi apparatus fragmentation from the vicinity of
205 myonuclei (Fig.4k-l). These results suggest that NuMA1, through the maintenance of nMTOC at the
206 vicinity of myonuclei, constrains microtubule growth orientation in the longitudinal axis of
207 myotubes. Finally, we assessed the consequences of NuMA1 depletion on microtubule organization
208 in mature myofibers (Fig.4m-k). We conducted *in vivo* NuMA1 depletion in TA muscle, extracted
209 and isolated individual myofibers (Fig.4m). As expected, microtubule network architecture is highly
210 impacted with an apparent loss of transversally oriented microtubules compared to longitudinally
211 oriented microtubules observed in controls (Fig.4n-k). These results further confirmed that NuMA1
212 is required to guide and organize microtubule network in mature myofibers.

213 Altogether, our data show that NuMA1 in myofibers sets myonuclei positioning and shape through
214 the control of microtubules anchoring point at the vicinity of myonuclei.

215 **NuMA1 associates with dynein-heavy-chain to control myonuclei positioning**

216 Numerous studies have raised the interaction of NuMA1 and the Dynein/Dynactin complex to
217 regulate mitotic spindle orientation [37-39]. We previously edshow that Dynein in muscle is essential for
218 myonuclei position[11,36]. Interestingly, the mass-spectrometry analysis performed on purified
219 microtubule-binding proteins revealed the presence of four components of the Dynein/Dynactin
220 complex, namely the cytoplasmic Dynein-1 Heavy Chain-1 (Dnchc1, most represented), the
221 cytoplasmic Dynein-1 Intermediate Chain-1 and -2 (Dncic1 and Dncic2) and the Dynactin subunit-1
222 (Dctn1) (Extended Data Fig.4a). When we down-regulated these specific Dynein/Dynactin protein
223 subunits using siRNA and analyzed myonuclei positioning (DMcM & Myonuclei Spreading Graph)
224 and specific myotube parameters (area and length) (Fig.5a, Extended Data Fig.4b), only the *Dnchc1*
225 knockdown recapitulates the aggregation phenotype observed in *Numa1*-depleted myotubes (Fig.5b-
226 d). Therefore, we analyzed the localization of Dynein Heavy Chain in both immature myotubes and
227 mature myofibers (Fig.5e-f). NuMA1 and Dynein co-localize at the vicinity of myonuclei in

myotubes and myofibers (Fig.5e, arrows). As well, there was also a co-localization of NuMA1 and Dynein Heavy Chain along the myofiber length (Fig.5f). Altogether, these results indicate that NuMA1, in association with the cytoplasmic Dynein-1 Heavy Chain-1, contribute to the myonuclei positioning in muscle fibers.

NuMA1 is Progressively excluded from myonuclei during myofiber development.

NuMA1 is a nuclear protein that controls microtubules anchoring specifically during mitosis[23]. This microtubule-related activity is allowed by the fragmentation of nuclear membrane at the beginning of mitosis, leading to the accumulation of cytoplasmic NumMA1. At the end of mitosis, cytoplasmic NuMA1 is "repumped" and sequestered into the nucleus thanks to NLS sequence [40]. In this context, we investigated subcellular localization in post-mitotic muscle cells throughout myogenesis (Fig.6). Our data show that NuMA1 is present in the cytoplasm of myotubes/myofibers and appear excluded from myonuclei (Fig.5e-f). To analyze the localization of NuMA1, we performed immunostaining on individual myofibers isolated from TA muscle. We found that in mature myofibers, NuMA1 co-localizes partially with the stable microtubule network (*i.e.* detyrosinated/acetylated tubulin) and preferentially at the vicinity of myonuclei (Fig.6a, white arrows; Extended Data Fig.5a). The preferential accumulation of NuMA1 in the cytoplasmic compartment of muscle fibers was also confirmed using subcellular fractionation assays on TA myofibers (Fig.6b).

We then investigated the expression/localization of NuMA1 during muscle fiber formation. Although we found a net decrease of NuMA1 protein during early steps of C2C12 myotubes formation by western blot, *NuMA1* mRNA is slightly increased in mouse primary myofibers compared to myotubes (Extended Data Fig.5b-c). To explore the dynamic accumulation of NuMA1 in the cytoplasmic compartment of muscle fibers, we performed a subcellular fractionation assay on human primary myoblasts during a differentiation time course (Fig.6c). Clearly, we showed that a part of NuMA1 pool is present into the cytoplasmic compartment in both myoblasts and myotubes (Fig.6c). Similarly, the presence of a cytoplasmic form of NuMA1 was observed in C2C12 myoblasts and myotubes (Extended Data Fig.5d). Immunostaining on differentiated human primary myoblasts showed a progressive accumulation of NuMA1 in the cytoplasmic compartment during muscle fiber differentiation whereas myonuclei progressively lose NuMA1 staining (Fig.6d-e). Indeed, while NuMA1 is highly expressed in nuclei of non-fused myoblasts (Fig.6d, asterix), myonuclei within myotubes show a mosaic of NuMA1 staining, with some strongly stained myonuclei. Following longer maturation (16 days of differentiation), NuMA1 staining into myonuclei is very weak while there is a clear accumulation into myotube cytoplasm (Fig.6e). Therefore, our results indicate that

NuMA1 is directly present in the cytoplasm of growing myoblast and then transits from the nucleus to the cytoplasm as myotubes differentiate.

To analyze NuMA1 localization in mature myofibers, we used primary myoblast cultures that were differentiated onto micro-patterns to form functional myofibrils, reflected by the typical staining of the F-actin cross-linker protein, alpha-actinin (Fig.6f). Under this condition, we still observed NuMA1 accumulation in the cytoplasm and weaker NuMA1 myonuclei staining compared to immature human myotubes (Fig. 6d-f). Interestingly, a few myonuclei still contains high concentration of NuMA1 inside the same myofibers, suggesting different capacities for myonuclei to constrain NuMA1 (Fig.6f, asterix).

Together, our experiments demonstrate that NuMA1 is in both compartment (nucleus and cytoplasm) in proliferating myoblasts. Once fusion occurs, NuMA1 is progressively cleared out from myonuclei and accumulates subsequently in the cytoplasm, on stable microtubule lattice, thus controlling the microtubule network organization and consequently, myonuclei positioning.

NuMA1 is a marker of myonuclei dynamics in myofibers.

As we observed that immature myotubes contain a mixed population of myonuclei with high and low content of NuMA1 (Fig.6d), we hypothesized that these two populations have distinct motion behavior inside myofibers. To address this question, primary mouse myoblasts were transfected with full-length human NuMA1 tagged with GFP (h-FL-NuMA1, Fig7a). As expected, NuMA1 localizes in the nucleus compartment and partially accumulates on microtubules at the vicinity of myonuclei (Fig7a, Arrows). h-FL-NuMA1-expressing cells were induced to form immature myofibers (myotubes) during 3 days (Fig.7b). Interestingly, we observed a mosaic of myonuclei according to NuMA1 content, suggesting that all myonuclei do not share the same status concerning NuMA1 protein uptake (Fig.7b). In this condition, cytoplasmic-NuMA1 accumulation on microtubule network was visible only in some myotubes with apparent microtubules bundles (Extended Data Fig.6a). Of note, the mosaic pattern was also observed *in vivo* in NuMA1-electroporated TA muscles from 8-week old wild-type mice (Extended Data Fig.6b). Tracking the motion of NuMA1-positive and -negative myonuclei by time-lapse video-microscopy confirmed that myonuclei are in motion 90% of the time independently of NumMA1 expression (Fig.7b). However, NuMA1-positive myonuclei move with a median speed of 0,149 ± 0,01 μm/min leading to a diffusion coefficient value of 0,7 ± 0,2 μm^2/min, while NuMA1-negative myonuclei move 40% slower with a speed of 0,094 ± 0,007 μm/min that leads to a 60% drop of the diffusion coefficient value (0,28 ± 0,08 μm^2/min)

(Fig.7c-d). These data suggest that myonuclei motion relies on their capacity to restrain NuMA1. In other words, myofibers with dynamic myonuclei exhibit more NuMA1-positive myonuclei along their length.

Interestingly, in Duchenne muscular dystrophy (DMD), it was shown that myonuclei within the myofibers display increased mobility [41]. This led us to hypothesize that NuMA1 expression is increased in DMD myonuclei. To address this question, we isolated individual myofibers from TA muscles of 8-week old MDX mice, a mouse model of human DMD, and analyzed NuMA1 localization (Fig7e, Extended Data Fig.6c). Strikingly, we observed that myofibers present: (1) a higher number of NuMA1-positive myonuclei (Fig7e, red arrows), and (2) several areas where NuMA1 accumulates in the microtubule lattice (Fig7e, blue arrows), consistent with a microtubule disorganization (Extended Data Fig.6c).

Altogether, our data show that NuMA1 is progressively cleared out from myonuclei during muscle fiber maturation and transits to stable microtubules in order to control microtubule network organization and myonuclei motion (Fig.8).

Discussion

Nuclear spreading at the periphery of muscle fibers is a prerequisite to obtain fully functional mature myofibers. Diverse motions controlled by a succession of mechanisms allow the spacing of adjacent myonuclei, initially during immature myofiber formation (myotubes) and subsequently in mature myofibers. These processes are affected in many muscle disorders, leading to aberrant myonuclei localization and shape that ultimately impact myonuclei integrity through changes in mechano-transduction processes [3,42,43]. Here, we elucidate the mechanism by which myofibers control both myonuclei spreading and motion during muscle fiber formation and maintenance. We demonstrate that the microtubule binding protein NuMA1 is present in the cytoplasm of developing post-mitotic muscle fibers where it controls myonuclei positioning through the establishment of a specific microtubule architecture at the vicinity of myonuclei in relation with Dynein-1 Heavy Chain-1 (Fig1-5). Furthermore, cytoplasmic NuMA1 remains present in mature myofibers where it is essential for the maintenance of peripheral myonuclei. Finally, we show that NuMA1 accumulation inside myonucleus is a marker of myonuclei dynamics and is highly expressed in myofibers of Duchenne muscular dystrophy (DMD) mouse model (Fig. 5-6).

A cytoplasmic form of NuMA1 controls myonuclei positioning and motion through microtubules network integrity.

Nuclear movements within immature myofibers have been described to depend mainly on microtubule associated proteins and molecular motors[11,44,45]. During myofiber maturation, myofibril formation and bundling contribute to push myonuclei at the periphery of the fibers[12]. Once at the periphery, myonuclei are thought to be anchored at the plasma membrane by a protein meshwork that contributes to stabilize their localization[46]. Recent studies have shown that, although myonuclei stick to the periphery of mature myofibers, they still possess the ability to move between the plasma membrane and myofibrils[13,47]. According to our experimental data, myonuclei motion in mature myofibers results from an interplay between (1) the ability to maintain a polarized architecture of microtubules in the vicinity of each myonuclei and (2) a suitable myonuclei shape that depends on both nuclear stiffness and forces exerted by other structures than microtubules around myonuclei.

Microtubule structures are dynamic networks that constitute a central node with multiple cytoskeleton networks[48,49] to control muscle fibers homeostasis. In mature myofibers, accumulating posttranslational modifications of tubulin contributes to increase microtubule stability, that allows maintenance of functional muscles [13,50,51]. Our results suggest that cytoplasmic NuMA1 specifically targets stable microtubules in mature myofibers. Thus, NuMA1 depletion affects the topology of microtubules dynamics, resulting in mis-orientation of microtubules network in combination with nMTOC components instability. Our data show that depending on the ability of myonucleus to exclude NuMA1, it directly impact myonucleus motion. Future work should address the contribution of both cytoplasmic and nuclear NuMA1 on myonucleus maturation during muscle fiber formation.

A new way to control microtubule network in cells through myonuclei exclusion of NuMA1.

Our experiments suggest that right after the fusion, new nuclei entering myotubes are loaded with NuMA1 protein in both the nuclear and cytoplasm compartments. During muscle fiber formation, cytoplasmic NuMA1 uptake inside myonuclei is progressively blocked. This leads to a complete and exclusive relocalization of NuMA1 in the cytoplasm compartment of mature myofibers, where it orients microtubule lattice and controls myonuclei motion. Cytoplasmic sequestration of nuclear proteins is a common mechanism that regulates the activity of transcription factors. For example, in muscle, such mechanisms apply to proteins such as NF-kappaB [52] and FOXO [53] that control the expression of genes involved in muscle atrophy, or NFAT that controls fiber type [54]. Our results show that muscle cells can also use nuclear sequestration to regulate the cytoplasmic activity of a protein controlling microtubule dynamics. By restraining NuMA1, myonucleus prevents the organization of a stable microtubule network that will be incompatible with their motility required for myonuclei alignment in immature myotubes. During myotube maturation, myonuclei progressively release NuMA1 (or block its uptake) so that it can organize and stabilize the microtubule network

adapted to the postmitotic functions of muscle cells. In the future, it will be interesting to investigate the signals that trigger and control the balance between cytoplasmic and nuclear fraction of NuMA1 in these post-mitotic cells.

Nuclear mis-positioning and myopathies

Numerous muscles diseases are characterized by alterations of myonuclei shape and myonuclear domain alterations. In Duchenne muscular dystrophy (DMD), the absence of Dystrophin leads to the most frequent form of muscular dystrophy. Repetitive degeneration/regeneration cycles progressively trigger accumulation of damaged myofibers with aberrant myonuclei positioning [9]. Dystrophin is a microtubule associated protein and in DMD animal models, alteration of microtubules network and myonuclei motion has been observed [47,55]. Our experiments suggest that NuMA1 positive myonuclei is a marker of both dynamics myonuclei inside myofibers and local alterations of microtubule network integrity. Cortical NuMA1 has been shown to assemble specialized focal structures, containing Dynein, Dynactin and LGN, thereby generating cooperative spindle-pulling forces to organize mitotic spindles [38]. Such type of action could participate to myonuclei mis-positioning and could be perturbed in myopathies associated with aberrant myonuclei positioning. Future work should address how cytoplasmic NuMA1 activity is spatially regulated along muscle fibers and contributes to the loss of peripheral anchorage of myonuclei in these myopathies. Indeed, altogether our findings indicate that cytoplasmic accumulation of NuMA1 is associated with the stabilization of the microtubule network and allows a dynamic control of myonuclei motion and localization during muscle fiber formation, thereby providing a novel avenue of investigation to understand aberrant myonuclei localization in myopathies.

Figures legends

Figure 1: NuMA1 regulates myonuclei positioning throughout myogenesis. a. Scheme of experimental procedure followed for *in vitro* formation of primary myotubes and myofibers. **b-c**. Representative immunofluorescence images of 3-days knocked-down myotubes for scrambled or *Numa1* and stained for myosin heavy chain (MHC, green) and nuclei (blue). Scale bar: 15µm. **d**. Quantification of the mean Distance between Myotubes centroid and Myonuclei (DMcM) according to myonuclei content in 3-days knocked-down myotubes with scrambled or *Numa1* siRNAs. Data from 6 independent experiments were combined. n(Scramble siRNA=618); n(*Numa1* siRNA=687). Unpaired t-test, ***p < 0.001, **p < 0.01, *p < 0.05. Source data are available in Supplementary Table 1. **e-g.** Representative immunofluorescence images of 10-days knocked-down myotubes for

scrambled or *Numa1* shRNA and stained for shRNA plasmid expression (green), actin (red) and nuclei (blue). Asterisks (peripheral myonuclei), Arrows (non-peripheral myonuclei). Scale bar: 15µm. **h**. Quantifications of myonuclei position phenotype in 10-days knocked-down myofibers with either a scrambled or a *Numa1* shRNA. Data from 3 independent experiments were combined. Unpaired t-test, **p < 0.01. n(Scramble shRNA=1452); n(*Numa1* shRNA=2009). **i**. Quantifications of peripheral myonuclei frequency in 10-days scrambled and *Numa1* shRNA transfected myofibers. Unpaired t-test, **p < 0.01. n(Scramble shRNA=966); n(*Numa1* shRNA=760). Data from 4 independent experiments were combined. Center lines show the medians; box limits indicate the 25th and 75th percentiles as determined by R software; whiskers extend 1.5 times the interquartile range from the 25th and 75th percentiles, outliers are represented by dots. Source data are available in Supplementary Table 1. **j.** Schematic protocol of *Tibialis anterior* (TA) electroporation and representative picture of electroporated myofibers with shRNA (green). **k-l**. Representative images of transversal cross-sections of TA myofibers electroporated with scramble or *Numa1* shRNA and stained for GFP (shRNA, green), laminin (red) and myonuclei (blue) Scale bar: 50µm. White arrows indicate peripheral myonuclei, grey arrows indicate internalized myonuclei and orange arrows mis-oriented peripheral myonuclei. **m.** Quantification of mis-oriented myonuclei in TA myofibers electroporated with scramble or *Numa1* shRNAs. Data from 4 independent experiments were combined. n(Scramble shRNA=1258); n(*Numa1* shRNA= 1915). Unpaired t-test, ***p < 0.001. Source data are available in Supplementary Table 1.

Figure 2: NuMA1 regulates myonuclei shape and composition. a-b. Representative immunofluorescence images of 3-days knocked-down myotubes with either scrambled or *Numa1* siRNA and stained for myonuclei (Dapi). Scale bar: 15µm. **c-d.** Quantification of myonuclei area (c) and circularity (d) of 3-days knocked down myotubes with a scrambled or a *Numa1* siRNA. Data from three independent experiments were combined. n(Scramble siRNA=771); n(*Numa1* siRNA=552). Unpaired t-test, **p < 0.01, *p < 0.05. **e**. Bar chart plotting *LaminA/C, LaminB* and *Emerin* mRNA levels in 3-day knocked-down primary myotubes treated with either scrambled or *Numa1* siRNA. Data from 3 independent experiments were combined. Center lines show the medians; box limits indicate the 25th and 75th percentiles as determined by R software; whiskers extend 1.5 times the interquartile range from the 25th and 75th percentiles, outliers are represented by dots. Source data are available in Supplementary Table 2.

Figure 3: NuMA1 regulates myonuclei motion. a. Kymograph extracted from time-lapse video experiments of 5-day knocked-down primary myotubes for scrambled or *Numa1* siRNA and shRNA

and transfected with a Lamin-Chromobody®-RFP plasmid. The first frame of each representative 16h-movie shows a myotubes. Myotubes were tracked during 16hrs with a picture every 20 min. Time-lapse movies data are available in Supplementary Video 1 & 2. **b-d.** Quantifications of percentage of time in motion (b), myonuclei speed (c) and diffusion coefficient (d) of 5-day knocked-down primary myotubes with scrambled or *Numa1* using either siRNA or shRNA methods from 3 independent experiments. n(Scramble siRNA=207); n(*Numa1* siRNA=198); n(Scramble shRNA=203); n(*Numa1* shRNA=203). Unpaired t-test, ***$p < 0.001$, **$p < 0.01$. Center lines show the medians; box limits indicate the 25th and 75th percentiles as determined by R software; whiskers extend 1.5 times the interquartile range from the 25th and 75th percentiles, outliers are represented by dots. Source data are available in Supplementary Table 3.

Figure 4: NuMA1 shapes microtubule network architecture and the nMTOC in myofibers. a-b. Representative immunofluorescence images of 3-days knocked-down myotubes transfected with scrambled or *Numa1* siRNA and stained for α-tubulin (green) and nuclei (red). Scale bar: 10µm. **c-d**. Maximal Z-projection of EB1-GFP comets in 3-days knocked-down myotubes with scrambled or *Numa1* siRNA where six continuous frames of a time-lapse movie were overlapped, the first three are color-coded in green and the last three are color-coded in red. Scale bar=9µm. White asterix show examples of EB1-GFP comets orientation in control (1 & 2) and in *Numa1* knocked down condition (3 & 4). Source data are available in Supplementary Video 3 & 4. **e**. Scheme of myotubes areas analyzed in sections f & g. **f-g**. Quantifications of comet orientation along myotubes axis in different zones of myotubes in 3-days knocked-down myotubes transfected with either scrambled or *Numa1* siRNA. Analyzed myotubes contain at least 6 myonuclei. Data from three independent experiments were combined. n(Scramble siRNA; free myonuclei zone)=175; n(*Numa1* siRNA; free myonuclei zone)=260; n(Scramble siRNA; myonuclei zone)=284; n(*Numa1* siRNA; myonuclei zone)=376. Source data are available in Supplementary Table 4. **h-k.** Representative immunofluorescence images of 3-days knocked-down myotubes with scrambled or *Numa1* siRNA and stained for Pericentrin (green, h-i) and Golgi apparatus (green, j-k). **l.** Quantifications of Golgi apparatus patches number (GM130 staining) by myonuclei in 3-days knocked-down myotubes in scrambled or *Numa1* siRNA condition. Data from 3 independent experiments were combined. Unpaired t-test, *$p < 0.05$. n(Scramble siRNA=177); n(*Numa1* siRNA =177). Source data are available in Supplementary Table 4. **m.** Scheme of *in vivo* protocol to obtain single myofibers of Scramble or *Numa1* shRNA electroporated. **n-o**. Representative immunofluorescence images of 2-months old mice extracted TA myofibers down-regulated during 2 weeks with scrambled or *Numa1* shRNA and stained for α-tubulin (green) and nuclei (red). Scale bar: 10µm. **p-q**. Microtubules network organization analysis of

myofibers down-regulated during 2 weeks with scrambled or *Numa1* shRNA using TeDT software. Data from 5 independent experiments were combined. Source data are available in Supplementary Table 4.

Figure 5: Dynein-1 Heavy Chain-1 is involved in myonuclei positioning and associated with NuMA1. a. Representation of the mean distance from myotubes centroid to each myonuclei (DMcM), Myonuclei Spreading Graphic (MSG), myotubes area and length in 3-days knocked down myotubes with scrambled or *NuMA1, Dncic1, Dncic2, Dctn1 and Dnchc1* siRNAs. Colors are representative of the mean percentage of decrease for red and yellow colors, and increase for green colors compared to control. Source data are available in Supplementary Table 5. **b-c**. Representative immunofluorescence images of 3-days knocked-down myotubes for scrambled or *Dnchc1* (*Dynein-1 heavy chain-1*) and stained for myosin heavy chain (MHC, green) and nuclei (blue). Scale bar: 10µm. **d.** Quantification of mean distances from myotubes centroid to each myonuclei (DMcM) according to their myonuclei content in 3-days knocked-down myotubes transfected with either scrambled or *Numa1* siRNA. n(Scramble siRNA=580); n(*Dnchc1* siRNA=319); n(*Numa1* siRNA=674). Unpaired t-test, ***p < 0.001, **p < 0.01, *p < 0.05. Data from 3 independent experiments were combined. Center lines show the medians; box limits indicate the 25th and 75th percentiles as determined by R software; whiskers extend 1.5 times the interquartile range from the 25th and 75th percentiles, outliers are represented by dots. Source data are available in Supplementary Table 5. **e-f.** Representative immunofluorescence images of 3-days human primary myotubes (e) and extracted TA myofibers stained for NuMA1, Dynein Heavy Chain, Actin and nuclei. Scale bar: 10µm.

Figure 6: NuMA1 localization throughout myofibers development. a. Representative immunofluorescence images of 2-months extracted TA wild-type muscles fibers stained for NuMA1 (red), Detyrosinated-Tubulin (green) and nuclei (blue). Scale bar: 10µm. **b.** Representative subcellular fractionation assay of NuMA1 from *Tibialis Anterior* muscles. HSP90 and Histone H3 are loading controls for the cytoplasm and nuclear compartments, respectively. **c.** Representative subcellular fractionation assay of NuMA1 from human myoblasts and 10 day-differentiated human myotubes. HSP90 and Histone H3 are loading controls for the cytoplasm and nuclear compartments, respectively. Blots were repeated more than 3 times. **d-e.** Representative immunofluorescence images of 8-days (d) and 16-days (e) human primary myotubes stained for NuMA1 (red), α-tubulin (green) and nuclei (blue). Scale bar: 10µm. **f.** Representative immunofluorescence images of 8-days human primary myotubes cultured on micro-patterned and stained for NuMA1 (red), α-actinin (green) and nuclei (blue). Scale bar: 20µm.

Figure 7: NuMA1 is a marker of dynamic myonuclei in myofibers. a-b. Representative immunofluorescence images of primary myoblasts (a) and 3-days mouse primary myotubes (b) transfected with a construct inducing the overexpression of human full-length NuMA1 tagged with GFP (h-FL-NuMA1) and stained for (a) tubulin (red), NuMA1-GFP (green) and nuclei (blue) and (b) nuclei (red) and NuMa1-GFP (green). Scale bar: 10µm. **c-e.** Quantifications of percentage of time in motion (c), myonuclei speed (d) and myonuclei diffusion coefficient (e) of 5-day primary myotubes overexpressing human full length NuMA1 localized in the nucleus (h-NuMA1 positive) or not localized in the nucleus (h-NuMA1 negative). n(GFP-positive=150); n(GFP-negative=150). Unpaired t-test, ***$p < 0.001$. Data from 3 independent experiments were combined. Center lines show the medians; box limits indicate the 25th and 75th percentiles as determined by R software; whiskers extend 1.5 times the interquartile range from the 25th and 75th percentiles, outliers are represented by dots. Source data are available in Supplementary Table 6. **f.** Representative immunofluorescence images of TA myofibers from 2-months old MDX mice, stained for NuMA1 (green) and nuclei (red). Red arrows point NuMA1 positive myonuclei, blue arrows point accumulation cytoplasmic aggregation of NuMA1 Scale bar: 10µm.

Figure 8: Proposed model of NuMA1 activity during muscle differentiation.

Extended figure 1: NuMA1 is present in the microtubule-associated proteome in myotubes and controls myonuclei positioning. a. Table showing details of mass-spectrometry analysis of purified proteins able to bind microtubules from 3 days differentiated mouse primary myotubes as previously described [13]. Pep is the number of peptides; SC is the spectral counting, SSC is the spectral counting specific to the protein and WSC is the weighted spectral counting. **b.** Western blot of 3-days myotubes knocked-down for scrambled or *Numa1* using siRNA technique. Blots were repeated more than 3 times. **c.** Bar chart plotting of *Numa1* mRNA level in 3-day knocked down primary myotubes treated with either scrambled or *Numa1* siRNA. Data from 4 independent experiments were combined. Values are means ± standard deviation. **d.** Myonuclei spreading graphic (MSG) representing statistical frequency of all myonuclei positioning along all analyzed myotubes. **e-f** Quantification of myotubes length (e) and myotubes area (f) in 3-days knocked down myotubes with scrambled or *Numa1* siRNA. Data from six independent experiments were combined. n (Scramble siRNA=618); (*Numa1* siRNA=687). Unpaired t-test, ***$p < 0.001$, **$p < 0.01$, *$p < 0.05$. Source data are available in Supplementary Table 7.

Extended figure 2: NuMA1 controls myonuclei positioning in C2C12 myotubes. **a-b.** Representative immunofluorescence images of 6-days knocked-down C2C12 myotubes with scrambled or *Numa1* siRNA and stained for myosin heavy chain (MHC, green) and nuclei (red). Scale bar: 50 µm. **c.** Quantifications of myonuclei positioning phenotypes in 6-days differentiated mouse C2C12 myotubes knocked down with scrambled or *Numa1* siRNA as described [11,43]. Data from three independent experiments were combined. Center lines show the medians; box limits indicate the 25th and 75th percentiles as determined by R software; whiskers extend 1.5 times the interquartile range from the 25th and 75th percentiles, outliers are represented by dots. Source data are available in Supplementary Table 8.

Extended figure 3: NuMA1 controls microtubule network organization. a. Scheme of NuMA1 protein domains. **b.** Representative images of time-lapse experiments of primary myoblasts co-transfected with EB1-GFP plasmids and with either Scramble-siRNA (top) or *Numa*1-siRNA (bottom). Scale bar: 9µm. **c-d**. Quantification of EB1-GFP comets velocity measured with Particle Tracker [56] in 3-days knocked down myotubes treated with either a scrambled or a *Numa1* siRNA represented as the median of all EB1-GFP comets velocity (c) or through categories (d). n(Scramble siRNA=1183); n(*Numa1* siRNA=2154). Data from three independent experiments were combined. Center lines show the medians; box limits indicate the 25th and 75th percentiles as determined by R software; whiskers extend 1.5 times the interquartile range from the 25th and 75th percentiles, outliers are represented by dots. Source data are available in Supplementary Table 9.

Extended figure 4: NuMA1 controls myonuclei positioning independently of *Dctn1, Dncic1, Dncic2* but probably through *Dnchc1.* a. Table showing details of mass-spectrometry analysis of purified proteins able to bind microtubules from 3 days differentiated mouse primary myotubes and from the dynein complex proteome. Pep is the number of peptides; SC is the spectral counting, SSC is the spectral counting specific to the protein and WSC is the weighted spectral counting. **b**. Myonuclei Spreading Graphic (MSG) representing statistical frequency median of all myonuclei positioning along all analyzed myotubes in knocked-down myotubes with *scramble*, *Numa1, Dctn1, Dncic1, Dncic2* and *Dnchc1* using each time a pool of three siRNAs. n(Scramble siRNA=618); n(*Numa1* siRNA =687); n(*Dctn1* siRNA =50); n(*Dncic1* siRNA = 91); n(*Dncic2* siRNA =106); n(*Dnchc1* siRNA =336). Data from 3 independent experiments were combined. Source data are available in Supplementary Table 10.

Extended figure 5: Localization and expression kinetic of NuMA1 along muscle differentiation. **a.** Representative immunofluorescence images of 2-months TA myofibers stained for NuMA1 (red), Acetylated-Tubulin (green) and nuclei (blue). Scale bar: 10µm. **b**. Western blot analysis of NuMA1 protein expression in total protein extracts from proliferating (GM) or differentiating C2C12 cells up to 5 days. C2C12 differentiation is assessed by Myogenin expression and Actin is used as loading control. Blots were repeated more than 3 times. **c**. RT-qPCR analysis of *Numa1* and *Myh4* gene expression level relative to *Gapdh; GusB* and *Rpl41* genes in primary myotubes cells (3 days) or mature myofibers (10 days of differentiation). Data from 3 independent experiments were combined. Source data are available in Supplementary Table 11. **d**. Representative subcellular fractionation assay of C2C12 mouse myoblasts and 6 days-differentiated C2C12 myotubes. HSP90 and Histone H3 are loading controls for the cytoplasm and nuclear compartments, respectively. Blots were repeated more than 3 times.

Extended figure 6: NuMA1 overexpression along muscle differentiation and in MDX myofibers. **a-b.** Representative images of human full length NuMA1 tagged with the GFP (h-FL-NuMA1) expression in (a) 3-day differentiated myotubes transfected with h-FL-NuMA1 (GFP, green) and detyrosinated-tubulin (red) and in (b) 2-months TA myofibers electroporated with h-FL-NuMA1 (GFP, green) and stained for nuclei (red). **c**. Representative immunofluorescence images of 2-months old MDX mice TA myofibers stained for NuMA1 (red), microtubules (green) and nuclei (blue). Scale bar: 10µm.

Video legend

Supplementary video 1 & 2: Time-lapse experiments of primary myoblasts co-transfected with Lamin-Chromobody-RFP plasmids and with either Scramble siRNA (Supplementary video-1), *Numa1* siRNA (Supplementary video-2) and induced to form myotubes during 5 days after starting differentiation process. Primary myotubes were recorded every 20 minutes for a period of time of 16 hours.

Supplementary video 3 & 4: Time-lapse experiments of primary myoblasts co-transfected with EB1-GFP plasmids and with either Scramble-siRNA (Supplementary video-3) or *NuMA1*- siRNA (Supplementary video-4) and induced to differentiate into myotubes for 3 days. EB1-GFP comets were recorded in primary myotubes every 150 milliseconds for a period of time of 15 seconds.

Materials and methods

Cell culture

Primary mouse myoblasts were purified from wild type C57BL6 newborn mice as described before [27,57]. Myoblasts were cultured on 1% growth factor reduced Matrigel®/IMDM coated-dish (Corning, 356231; ibidi µ-Slide 4 Well, 80426) and induced to differentiate in myotubes for 2 to 3 days in differentiation media (IMDM (Gibco, 21980-032) + 2% of horse serum (Gibco, 16050-122) + 1% penicillin-streptomycin (Gibco, 15140-122)). Myotubes were then covered by a layer of 50% growth factor reduced Matrigel®/IMDM and maintain in culture up to 10 days (IMDM (Gibco, 21980-032) + 2% of horse serum (Gibco, 16050-122) + 0.1% Agrin + 1% penicillin-streptomycin (Gibco, 15140-122)). Half of medium volume was changed every other day.

Mouse myoblast C2C12 cells were cultured in Dulbecco's modified Eagle's medium (DMEM (Gibco, 41966029) + 15% fetal bovine serum (Gibco, 10270-106) + 1% penicillin-streptomycin (Gibco, 15140-122)) and were plated on 1% matrigel-coated dishes for 1-2 days before induction of differentiation by a switching into differentiation media (DMEM + 1% horse serum).

Primary human myoblasts were plated on 1% Matrigel-coated dishes and cultured in a proliferative medium containing 40% Skeletal Muscle cell Growth Medium with supplemented Mix (Promocell, C-23060), 30% DMEM, High Glucose, Pyruvate (Gibco, 41966029), 20% decomplemented FBS (Gibco, 10270-106), 9% Medium 199, GlutaMAX Supplement (Gibco, 41150-020), 1% penicilline – streptomycine (Gibco, 15140-122), 0.005% Puromycin et 0.003% Dexamethasone. Differentiation was induced by a switch into differentiation media (Skeletal Muscle Cell Growth Medium, Promocell, C-23060). Differentiation medium was changed every other day.

Cell transfection

C2C12 and primary myoblasts cell were transfected with either Lipofectamine RNAiMAX (ThermoFisher Scientifics, 13778-150) for siRNA transfection or with Lipofectamine 3000 (ThermoFisher Scientifics, 11668-019) for shRNA transfection, in accordance with manufacturer instructions. Co-transfection experiments (*i.e.* plasmids and siRNA) were performed using Lipofectamine 2000 (ThermoFisher Scientifics, 11668-019) in accordance with manufacturer instructions. The list of siRNA and shRNA used is described in supplementary table 1.

Video-Microscopy

Myonuclei tracking: timelapse images were acquired every 20 min using Z1-AxioObserver (Zeiss). Myonuclei were manually tracked using Metamorph (Zeiss) and analyzed using SkyPad® plugin as described before [31].

EB1 tracking: timelapse images were acquired every 150 milliseconds using Ti Eclipse (Nikon) microscope 60X oil objective, Plan Apo, NA: 1.4, WD: 0.13, coverglass thickness: 0.17. EB1 comets trajectory were extracted using ImageJ®. To determine EB1 comets orientation, Six continuous frame of a time-lapse movie of EB1-GFP were overlapped, the first three are color-coded in green and the last three are color-coded in red as described before[36]. EB1 comets velocity was measured using Particle Tracker in ImageJ® [56].

Primary cells immunofluorescence staining

Cells were fixed in 4% Paraformaldehyde – 4% sucrose in PBS for 20 min at 37°C followed by washes with PBS and membrane permeabilization with 0.5% Triton-X100 in PBS for 5 min at Room Temperature (RT). Following washes with PBS, cells were saturated with 1% BSA in PBS for 30 min at RT and incubated in primary antibodies overnight at 4°C. Following washes with 0.05% Triton-X100 in PBS, cells were incubated in secondary antibodies or dyes for 2h at RT followed by washes with 0.05% Triton-X100 in PBS and a last wash in PBS. Cultured myofibers were imaged using Z1-AxioObserver (Zeiss) with a 10X objective N-Achroplan, 0.25 Ph1, N.A 0.25 or confocal LSM880 microscope (Zeiss). The list of antibodies used for immunostaining is described in supplementary table 2.

Protein sample preparation

Cells were harvested using trypsin (Gibco, 15400054) for 5min at 37°C and centrifuged at 1500RPM for 5 min at 4°C. Cell pellets were diluted and incubated in the optimal volume of RIPA lysis buffer containing phosphatases inhibitors (Sigma, P5726) and proteases inhibitors (Sigma, P8340) for 10 min at 4°C. Following a sonication at 4°C, protein samples were collected for further uses. The concentration of proteins was determined using BCA protein assay kit (Thermo Fisher Scientifics, 23225) as described by the manufacturer.

Subcellular fractionation assays

- On cell cultures

Cells were harvested, using Trypsin for 5min at 37°C and centrifuged at 1500RPM for 5min at 4°C. Cell pellet was washed in PBS at 4°C, diluted into TSE containing 10mM Tris pH 7.4,

250mM sucrose, 1mM EDTA, phosphatases inhibitors (Sigma, P5726) and proteases inhibitors (Sigma, P8340), and then passed 40 times through a 27G needle (Dutscher, 050100B). Cell lysates were centrifuged at 1500 RPM, for 5 min at 4°C. Supernatants containing cytoplasmic fractions were collected and stored at -80°C for further use. Nuclear pellets were washed in TSE 1X, passed 10 times through a 27G needle and centrifuged at 1500RPM for 10 min at 4°C. This step was repeated 3 times. Purified nuclear pellets were diluted in 1% NP40 – TSE 1X and incubated at 4°C for 1h before being stored at -80°C for further use.

- On *Tibialis Anterior* muscles

Total extract of *Tibialis Anterior* were obtained by cutting the muscles into small pieces and were resuspended into SDC buffer containing 600mM NaCl, 1% NP-40, 0.5% sodium deoxycholate, 0.1% SDS, 50mM Tris-HCl pH 8, protease and phosphatase inhibitors. Using ophthalmic scissors, small pieces of muscles are cut until muscle pieces are no more visible.

To obtain nuclear and cytoplasmic fractions, muscle mash was resuspended into 5 volumes of E1 lysis buffer containing 50mM HEPES-KOH, 140mM NaCl, 1mM EDTA, 10% glycerol, 0.5% NP-40, 0.25% Triton X-100, 1mM DTT and protease inhibitor cocktail. Muscle pieces size was reduced by using ophthalmic scissors and then a loose Dounce homogenizer pestle. Muscle lysates were centrifuged at 1100g, for 2min at 4°C. Supernatants containing cytoplasmic fractions were collected. Nuclear pellet was washed in E1 lysis buffer and centrifuged at 1100g, for 2min at 4°C. This step was repeated once. Supernatant was discarded and purified nuclear pellet was resuspended into 2 volumes of SDC buffer. Cytoplasmic and nuclear fractions were sonicated and a centrifugation at 6000g, for 10 min at 4°C was performed to remove cell debris. Extracts were then stored at -80°C for further use.

Western blot analysis

Samples were loaded onto 6% acrylamide gels and migrated at 130V for 10 min followed by 90min at 160V. Wet blotting system (BioRad) was used to transfer proteins to PVDF membranes (Millipore, Immobilon-P, IPVH00010). Membranes were then saturated in 5% milk in 0.1% Tween20 – 1X TBS for 1hr at RT and were incubated in primary antibodies in 1% milk in TBS overnight at 4°C. Following washes by 0.1% Tween20 – 1X TBS, membranes were incubated in HRP conjugated secondary antibodies in 1% milk in TBST for 1hr at RT. Following washes in 0.1% Tween20 – 1X TBS, detections of target proteins were carried out using clarity Western ECL substrate (BioRad, 1705060) and ChemiDoc imaging system (BioRad). The list of antibodies used for western blotting is described in supplementary table 2.

692 **RNA extraction**

693 After addition of Trizol (Sigma, T9424), samples were incubated in chloroform for 5min at RT,
694 centrifuged for 15 min at 12000g at 4°C and incubated in tubes containing isopropanol for 10
695 min at RT. Samples were then centrifuge for 15 min at 12000 g at 4°C, washed two times with
696 70% ethanol and RNA pellets were diluted into ultra-pure RNase free water (Invitrogen, 10977-
697 035). RNA concentration was analyzed using Nanodrop® (ThermoFisher Scientifics).

698 **RT-q-PCR**

699 Goscript Reverse Transcriptase System (Promega, A5001) was used as described by the
700 manufacturer to produce the cDNAs. Fast Start Universal SYBR Green Master (Rox) (Roche,
701 04913914001) and CFX Connect™ Real-Time PCR Detection System (BioRad) were used to
702 carry out quantitative PCR using primer described in supplementary table 3. Normalization was
703 performed using three housekeeping genes (*Gapdh; GusB* and *Rpl41*).

704 **Mice electroporation**
705 8 weeks old male C57BL/6 WT mice were anesthetized with intraperitoneal injection of Ketamin
706 (100mg/kg) - Xylazin (10mg/kg). Hind legs were shaved and 20µg of plasmid DNA diluted into
707 0.9% NaCl were injected in both contralateral *Tibialis Anterior* muscles. Injected muscles
708 received a short massage and a thin layer of ultrasound gel was applied. Electrodes were
709 positioned on both side of muscles and an electrical field was applied characterized by 8 pulses
710 of 20ms spaced 500ms apart, at 200V/cm of thickness of muscle (i.e. 80V). Two weeks post-
711 electroporation, mice were sacrificed and muscles were harvested. The whole experiment
712 procedure is in accordance with the guidelines of the local animal ethics committee of the
713 University Claude Bernard – Lyon 1 and in accordance with French and European legislation on
714 animal experimentation and approved by the ethics committee CECCAPP and the French
715 ministry of research.
716
717 **Isolation of mono-myofibers, immunofluorescence staining**
718 Following dissection of the whole muscle from the mice, *Tibialis Anterior* muscles were fixed in
719 4% PFA in PBS for 30 min at RT. After washes, 30 to 50 mono-myofibers were isolated per
720 condition from each muscle. Myofibers were permeabilized using 1% Triton-X100 in PBS for 15
721 min at RT and saturated in 1% BSA in PBS for 30 min at RT. Myofibers were then incubated in
722 primary antibodies at 4°C for 2 nights. Following 0.05% Triton-X100 in PBS washes, myofibers

were incubated in secondary antibodies or dyes overnight at 4°C. Then, washes with 0.05% Triton-X100 in PBS and a last wash in PBS were carried. Myofibers were mounted on slides using Fluromount Aqueous mounting (Sigma, F4680) and kept at 4°C. Analysis were conducted using confocal LSM880 microscope (Zeiss). Microtubule architecture organization was analyzed using TeDT software described [58]

Microtubule architecture organization

Microtubule architecture organization was analyzed using TeDT software as previously described [58]

Transversal muscles immunostaining and analysis

Tibialis anterior, muscles were collected, embedded in tragacanth gum, and quickly frozen in isopentane cooled in liquid nitrogen. Cross-sections (10µm thick) were obtained from the middle portion of frozen muscles and processed for immunostaining. Images were acquired using Z1-AxioObserver (Zeiss). The myofiber cross-sectional area and the number of centrally nucleated fibers were determined using Laminin and DAPI-stained sections. Cross-sectional areas and myonuclei misorientation within electroporated myofibers were measured and quantified manually using ImageJ® software.

Quantification methods for myonuclei spreading in myotubes

Quantifications in immature myotubes were assessed using an analysis tool developed in our team. An image analysis performed in ImageJ® software is combined with a statistical analysis in RStudio® software. This provides quantifications of parameters, ranked by myonuclei content per myotubes, regarding phenotype of myotubes (area, length) and their respective myonuclei positioning compare to centroid of myotubes (DMcM).

MSG diagrams were obtained through the normalization of lengths of all analyzed myotubes (independently to their myonuclei content) to 100%. White lines represent myonuclei density curves assessing the statistical frequency for myonuclei positioning along myotubes. Each color group reflects statistical estimation of myonuclei clustering along myotubes.

Statistical analysis

The statistical analyses were performed using Student's t test according to samples amount and distribution.

Acknowledgment

We thank C. Brun for comments on the manuscript. We thanks A. Merdes, for the long term following. We thank the Gache Laboratory for discussions. This work was supported by ATIP-Avenir Program & MyoNeurAlp Alliance program.

COMPETING FINANCIAL INTERESTS

The authors declare no competing financial interests.

References

1. Roman, W. & Gomes, E. R. Nuclear positioning in skeletal muscle. *Seminars in Cell and Developmental Biology* (2017). doi:10.1016/j.semcdb.2017.11.005
2. Sanger, J. W., Wang, J., Fan, Y., White, J. & Sanger, J. M. Assembly and dynamics of myofibrils. *Journal of biomedicine \& biotechnology* **2010,** 858606–8 (2010).
3. Cho, S., Irianto, J. & Discher, D. E. Mechanosensing by the nucleus: From pathways to scaling relationships. *J. Cell Biol.* **216,** 305–315 (2017).
4. Lele, T. P., Dickinson, R. B. & Gundersen, G. G. Mechanical principles of nuclear shaping and positioning. *J. Cell Biol.* **109,** jcb.201804052 (2018).
5. Santos, Dos, M. *et al.* Single-nucleus RNA-seq and FISH identify coordinated transcriptional activity in mammalian myofibers. *Nat Commun* **11,** 5102 (2020).
6. Newlands, S. *et al.* Transcription occurs in pulses in muscle fibers. *Genes \& development* **12,** 2748–2758 (1998).
7. Carlsson, L., Li, Z., Paulin, D. & Thornell, L. E. Nestin is expressed during development and in myotendinous and neuromuscular junctions in wild type and desmin knock-out mice. *Experimental Cell Research* **251,** 213–223 (1999).
8. Cutler, A. A., Jackson, J. B., Corbett, A. H. & Pavlath, G. K. Non-equivalence of nuclear import among nuclei in multinucleated skeletal muscle cells. *J. Cell. Sci.* **131,** jcs207670 (2018).
9. Rodrigues, M., Echigoya, Y., Fukada, S.-I. & Yokota, T. Current Translational Research and Murine Models For Duchenne Muscular Dystrophy. *J Neuromuscul Dis* **3,** 29–48 (2016).
10. Metzger, T. *et al.* MAP and kinesin-dependent nuclear positioning is required for skeletal muscle function. *Nature* **484,** 120–124 (2012).
11. Gache, V., Gomes, E. R. & Cadot, B. Microtubule motors involved in nuclear movement during skeletal muscle differentiation. *Mol. Biol. Cell* mbc.E16–06–0405 (2017). doi:10.1091/mbc.E16-06-0405
12. Roman, W. *et al.* Myofibril contraction and crosslinking drive nuclear movement to the periphery of skeletal muscle. *Nat. Cell Biol.* **152,** 1376–33 (2017).
13. Ghasemizadeh, A. *et al.* Skeletal muscle MACF1 maintains myonuclei and mitochondria localization through microtubules to control muscle functionalities. *bioRxiv* **12,** 636464 (2019).
14. Lei, K. *et al.* SUN1 and SUN2 play critical but partially redundant roles in anchoring nuclei in skeletal muscle cells in mice. *Proc. Natl. Acad. Sci. U.S.A.* **106,** 10207–10212 (2009).
15. Méjat, A. *et al.* Lamin A/C-mediated neuromuscular junction defects in Emery-Dreifuss muscular dystrophy. *J. Cell Biol.* **184,** 31–44 (2009).
16. Lee, Y. L. & Burke, B. LINC complexes and nuclear positioning. *Seminars in Cell and Developmental Biology* (2017). doi:10.1016/j.semcdb.2017.11.008
17. Karolczak, J., Sobczak, M., Skowronek, K. & R x119 dowicz, M. J. A Kinase Anchoring Protein 9 Is a Novel Myosin VI Binding Partner That Links Myosin VI with the PKA Pathway in Myogenic Cells. *Biomed Res Int* 1–12 (2015). doi:10.1155/2015/816019
18. Gimpel, P. *et al.* Nesprin-1α-Dependent Microtubule Nucleation from the Nuclear Envelope via Akap450 Is Necessary for Nuclear Positioning in Muscle Cells. *Current biology: CB* (2017). doi:10.1016/j.cub.2017.08.031
19. Zhang, T. *et al.* Microtubule plus-end binding protein EB1 is necessary for muscle cell

differentiation, elongation and fusion. *J. Cell. Sci.* **122,** 1401–1409 (2009).
20. Wang, S., Reuveny, A. & Volk, T. Nesprin provides elastic properties to muscle nuclei by cooperating with spectraplakin and EB1. *J. Cell Biol.* **209,** 529–538 (2015).
21. Bugnard, E., Zaal, K. J. M. & Ralston, E. Reorganization of microtubule nucleation during muscle differentiation. *Cell Motil. Cytoskeleton* **60,** 1–13 (2005).
22. Mogessie, B., Roth, D., Rahil, Z. & Straube, A. A novel isoform of MAP4 organises the paraxial microtubule array required for muscle cell differentiation. *Elife* **4,** e05697 (2015).
23. Silk, A. D., Holland, A. J. & Cleveland, D. W. Requirements for NuMA in maintenance and establishment of mammalian spindle poles. *J. Cell Biol.* **184,** 677–690 (2009).
24. Gallini, S. *et al.* NuMA Phosphorylation by Aurora-A Orchestrates Spindle Orientation. *Current biology: CB* **26,** 458–469 (2016).
25. Bugnard, E., Zaal, K. J. M. & Ralston, E. Reorganization of microtubule nucleation during muscle differentiation. *Cell Motil. Cytoskeleton* **60,** 1–13 (2004).
26. Wilson, M. H. & Holzbaur, E. L. F. Opposing microtubule motors drive robust nuclear dynamics in developing muscle cells. *J. Cell. Sci.* **125,** 4158–4169 (2012).
27. Pimentel, M. R., Falcone, S., Cadot, B. & Gomes, E. R. In Vitro Differentiation of Mature Myofibers for Live Imaging. *Journal of visualized experiments: JoVE* e55141–e55141 (2017). doi:10.3791/55141
28. Serra-Marques, A. *et al.* The mitotic protein NuMA plays a spindle-independent role in nuclear formation and mechanics. *J. Cell Biol.* **219,** 348 (2020).
29. Robson, M. I. *et al.* Tissue-Specific Gene Repositioning by Muscle Nuclear Membrane Proteins Enhances Repression of Critical Developmental Genes during Myogenesis. *Mol. Cell* **62,** 834–847 (2016).
30. Guilluy, C. *et al.* Isolated nuclei adapt to force and reveal a mechanotransduction pathway in the nucleus. *Nat. Cell Biol.* **16,** 376–381 (2014).
31. Cadot, B., Gache, V. & Gomes, E. R. Fast, multi-dimensional and simultaneous kymograph-like particle dynamics (SkyPad) analysis. *PLoS ONE* **9,** e89073 (2014).
32. Haren, L. & Merdes, A. Direct binding of NuMA to tubulin is mediated by a novel sequence motif in the tail domain that bundles and stabilizes microtubules. 1–10 (2002).
33. Gache, V. *et al.* Identification of proteins binding the native tubulin dimer. *Biochem. Biophys. Res. Commun.* **327,** 35–42 (2005).
34. Ralston, E., Ploug, T., Kalhovde, J. & Lømo, T. Golgi complex, endoplasmic reticulum exit sites, and microtubules in skeletal muscle fibers are organized by patterned activity. *J. Neurosci.* **21,** 875–883 (2001).
35. Tassin, A. M., Maro, B. & Bornens, M. Fate of microtubule-organizing centers during myogenesis in vitro. *J. Cell Biol.* **100,** 35–46 (1985).
36. Cadot, B. *et al.* Nuclear movement during myotube formation is microtubule and dynein dependent and is regulated by Cdc42, Par6 and Par3. *EMBO Rep.* **13,** 741–749 (2012).
37. Hueschen, C. L., Kenny, S. J., Xu, K. & Dumont, S. NuMA recruits dynein activity to microtubule minus-ends at mitosis. *Elife* **6,** e29328 (2017).
38. Okumura, M., Natsume, T., Kanemaki, M. T. & Kiyomitsu, T. Dynein-Dynactin-NuMA clusters generate cortical spindle-pulling forces as a multi-arm ensemble. *Elife* **7,** 3453 (2018).
39. Merdes, A., Ramyar, K., Vechio, J. D. & Cleveland, D. W. A complex of NuMA and cytoplasmic dynein is essential for mitotic spindle assembly. *Cell* **87,** 447–458 (1996).
40. Radulescu, A. E. & Cleveland, D. W. NuMA after 30 years: the matrix revisited. *Trends in Cell Biology* **20,** 214–222 (2010).
41. Iyer, S. R. *et al.* Altered nuclear dynamics in MDX myofibers. *Journal of Applied Physiology* **122,** 470–481 (2017).
42. Aureille, J., Belaadi, N. & Guilluy, C. Mechanotransduction via the nuclear envelope: a distant reflection of the cell surface. *Current opinion in cell biology* (2016). doi:10.1016/j.ceb.2016.10.003
43. Metzger, T. *et al.* MAP and kinesin-dependent nuclear positioning is required for skeletal muscle function. *Nature* **484,** 120–124 (2012).
44. Metzger, T. *et al.* MAP and kinesin-dependent nuclear positioning is required for skeletal muscle function. *Nature* **484,** 120–124 (2012).
45. Bruusgaard, J. C., Liestøl, K. & Gundersen, K. Distribution of myonuclei and microtubules in live

muscle fibers of young, middle-aged, and old mice. *Journal of Applied Physiology* **100,** 2024–2030 (2006).
46. Wang, S., Reuveny, A. & Volk, T. Nesprin provides elastic properties to muscle nuclei by cooperating with spectraplakin and EB1. *J. Cell Biol.* **209,** 529–538 (2015).
47. Iyer, S. R. *et al.* Altered nuclear dynamics in MDX myofibers. *Journal of Applied Physiology* jap.00857.2016–34 (2016). doi:10.1152/japplphysiol.00857.2016
48. Oddoux, S. *et al.* Microtubules that form the stationary lattice of muscle fibers are dynamic and nucleated at Golgi elements. *J. Cell Biol.* **203,** 205–213 (2013).
49. Osseni, A. *et al.* Triadin and CLIMP-63 form a link between triads and microtubules in muscle cells. *J. Cell. Sci.* **129,** 3744–3755 (2016).
50. Robison, P. *et al.* Detyrosinated microtubules buckle and bear load in contracting cardiomyocytes. *Science* **352,** aaf0659 (2016).
51. Kerr, J. P. *et al.* Detyrosinated microtubules modulate mechanotransduction in heart and skeletal muscle. *Nat Commun* **6,** 1–14 (2015).
52. Guttridge, D. C., Albanese, C., Reuther, J. Y., Pestell, R. G. & Baldwin, A. S. NF-kappaB controls cell growth and differentiation through transcriptional regulation of cyclin D1. *Molecular and cellular biology* **19,** 5785–5799 (1999).
53. Sandri, M. FOXOphagy path to inducing stress resistance and cell survival. *Nat. Cell Biol.* **14,** 786–788 (2012).
54. Calabria, E. *et al.* NFAT isoforms control activity-dependent muscle fiber type specification. *Proc. Natl. Acad. Sci. U.S.A.* **106,** 13335–13340 (2009).
55. Prins, K. W. *et al.* Dystrophin is a microtubule-associated protein. *J. Cell Biol.* **186,** 363–369 (2009).
56. Sbalzarini, I. F. & Koumoutsakos, P. Feature point tracking and trajectory analysis for video imaging in cell biology. *J. Struct. Biol.* **151,** 182–195 (2005).
57. Falcone, S. *et al.* N-WASP is required for Amphiphysin-2/BIN1-dependent nuclear positioning and triad organization in skeletal muscle and is involved in the pathophysiology of centronuclear myopathy. *EMBO Mol Med* **6,** 1455–1475 (2014).
58. Liu, W. & Ralston, E. A new directionality tool for assessing microtubule pattern alterations. *Cytoskeleton (Hoboken)* **71,** 230–240 (2014).

Figure 1

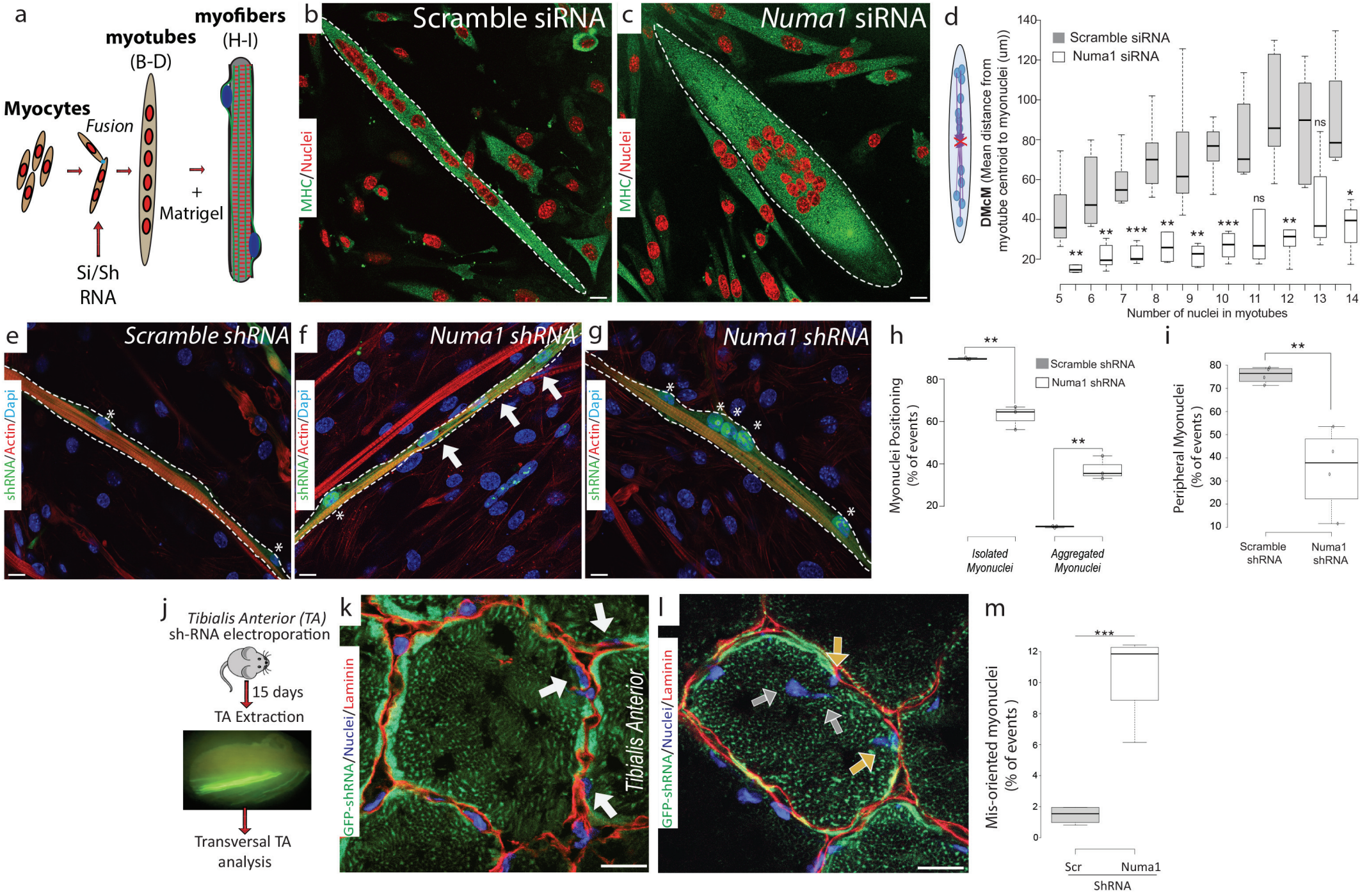
a
myofibers
(H-I)
myotubes
(B-D)
Myocytes
Fusion
+
Matrigel
Si/Sh
RNA
b
Scramble siRNA
MHC/Nuclei
c
Numa1 siRNA
MHC/Nuclei
d
DMcM (Mean distance from myotube centroid to myonuclei (um))
Scramble siRNA
Numa1 siRNA
Number of nuclei in myotubes
e
Scramble shRNA
shRNA/Actin/Dapi
f
Numa1 shRNA
shRNA/Actin/Dapi
g
Numa1 shRNA
shRNA/Actin/Dapi
h
Myonuclei Positioning (% of events)
Scramble shRNA
Numa1 shRNA
Isolated Myonuclei
Aggregated Myonuclei
i
Peripheral Myonuclei (% of events)
Scramble shRNA
Numa1 shRNA
j
Tibialis Anterior (TA)
sh-RNA electroporation
15 days
TA Extraction
Transversal TA analysis
k
GFP-shRNA/Nuclei/Laminin
Tibialis Anterior
l
GFP-shRNA/Nuclei/Laminin
m
Mis-oriented myonuclei (% of events)
Scr
Numa1
ShRNA

Figure 2

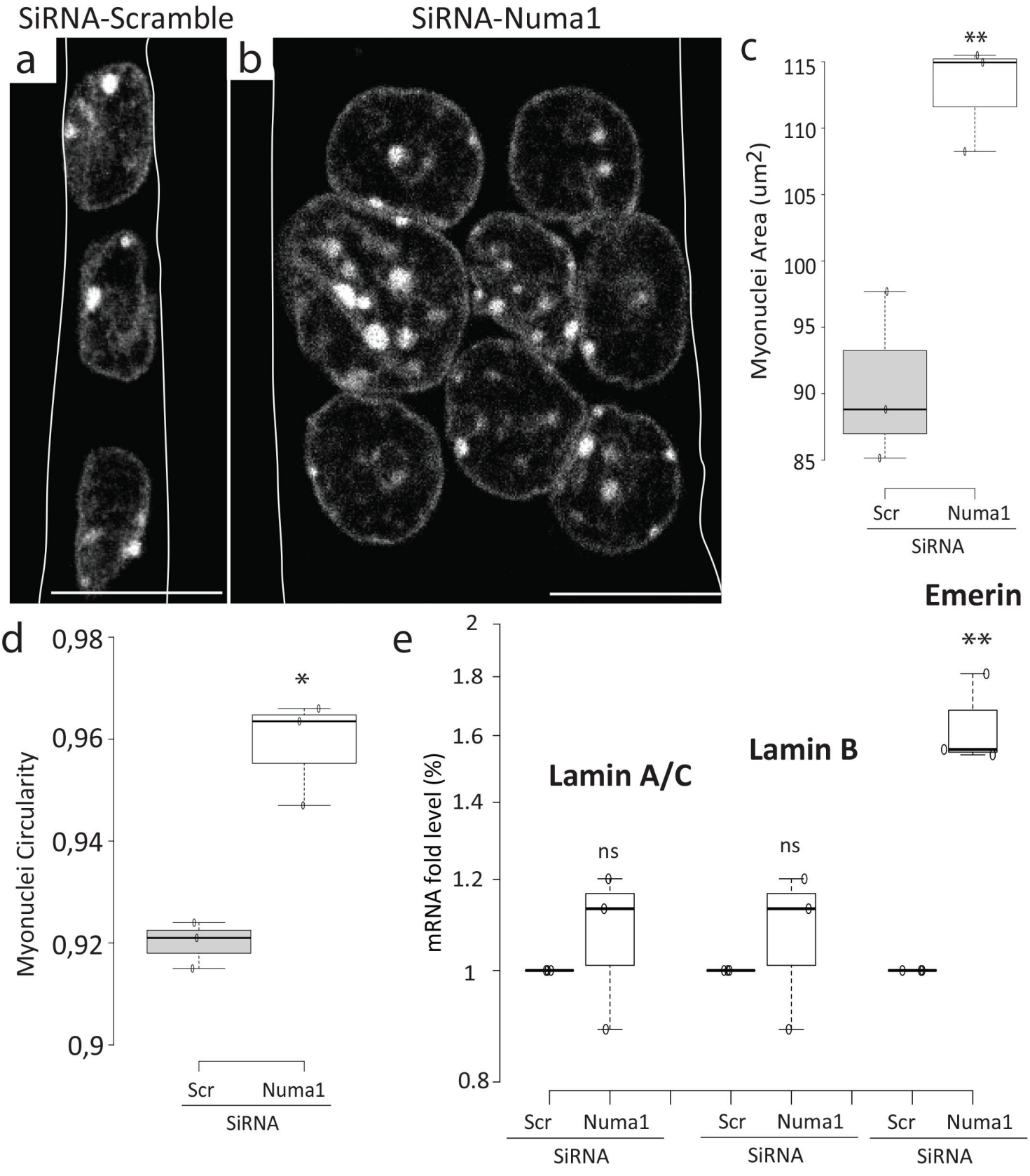
SiRNA-Scramble
SiRNA-Numa1
a
b
c
Myonuclei Area (um2)
115
110
105
100
95
90
85
**
Scr
Numa1
SiRNA
d
Myonuclei Circularity
0,98
0,96
0,94
0,92
0,9
*
Scr
Numa1
SiRNA
e
mRNA fold level (%)
2
1.8
1.6
1.4
1.2
1
0.8
Lamin A/C
Lamin B
Emerin
ns
ns
**
Scr
Numa1
SiRNA

Figure 3

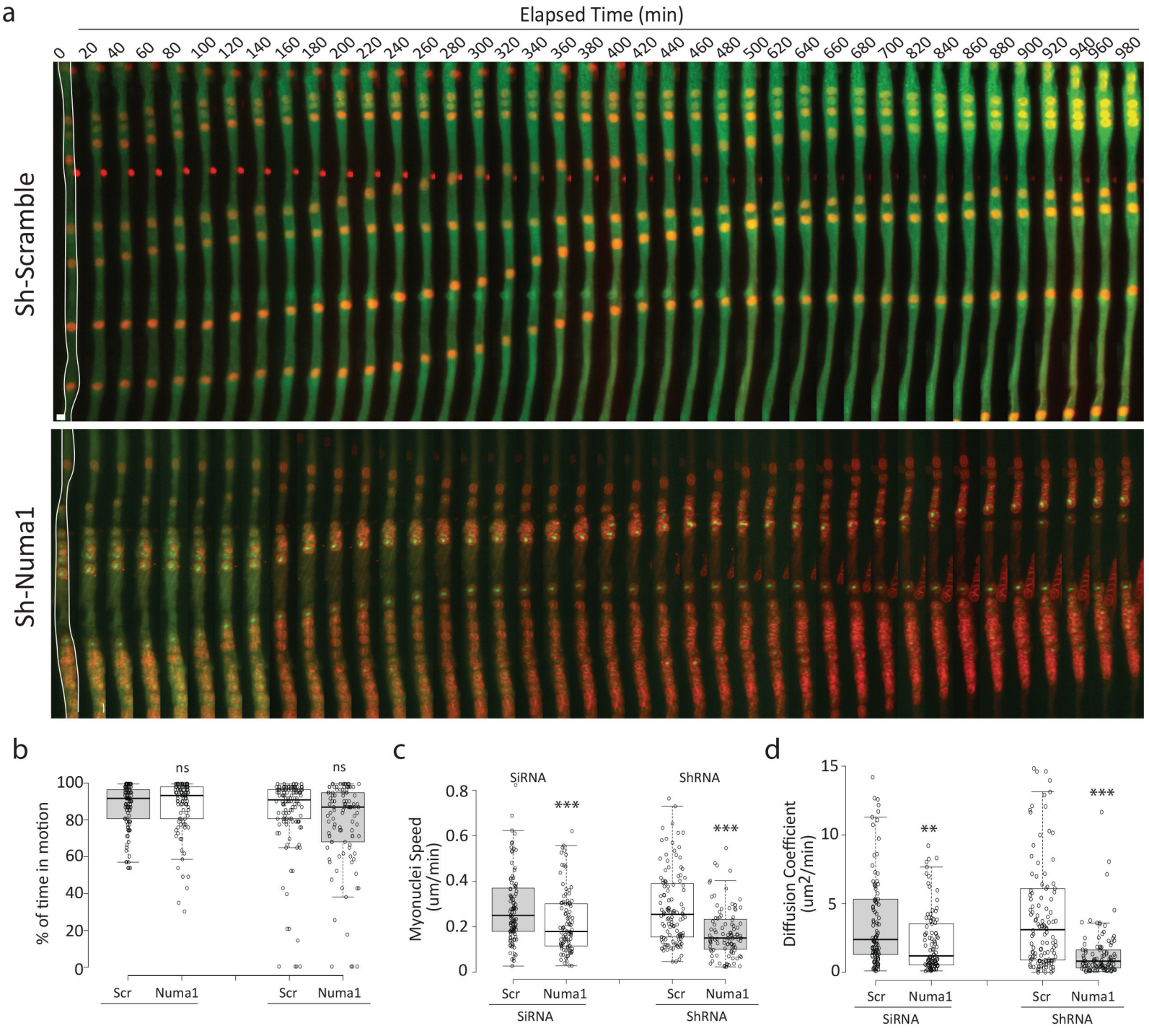
a
Elapsed Time (min)
0 20 40 60 80 100 120 140 160 180 200 220 240 260 280 300 320 340 360 380 400 420 440 460 480 500 620 640 660 680 700 820 840 860 880 900 920 940 960 980
Sh-Scramble
Sh-Numa1
b
% of time in motion
ns
ns
Scr
Numa1
Scr
Numa1
c
Myonuclei Speed (um/min)
SiRNA
ShRNA
***
***
Scr
Numa1
Scr
Numa1
SiRNA
ShRNA
d
Diffusion Coefficient (um2/min)
**
***
Scr
Numa1
Scr
Numa1
SiRNA
ShRNA

Figure 4

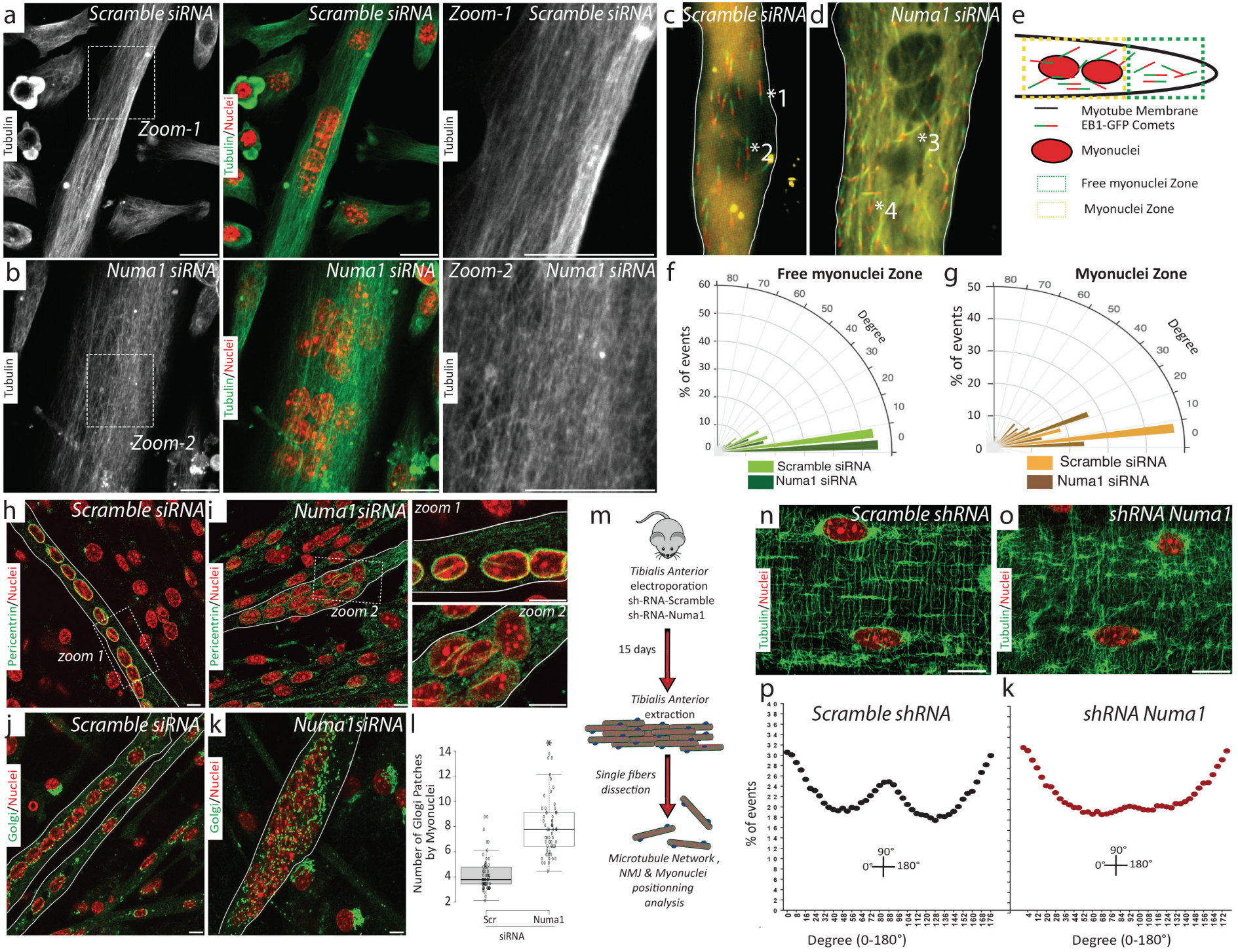
a
Scramble siRNA
Zoom-1
Tubulin
Tubulin/Nuclei
b
Numa1 siRNA
Zoom-2
c
*1
*2
d
*3
*4
e
Myotube Membrane
EB1-GFP Comets
Myonuclei
Free myonuclei Zone
Myonuclei Zone
f
Free myonuclei Zone
% of events
Degree
Scramble siRNA
Numa1 siRNA
g
Myonuclei Zone
h
Pericentrin/Nuclei
zoom 1
i
Numa1siRNA
zoom 2
j
Golgi/Nuclei
k
l
Number of Glogi Patches by Myonuclei
Scr
Numa1
siRNA
m
Tibialis Anterior
electroporation
sh-RNA-Scramble
sh-RNA-Numa1
15 days
Tibialis Anterior
extraction
Single fibers
dissection
Microtubule Network ,
NMJ & Myonuclei
positionning
analysis
n
Scramble shRNA
o
shRNA Numa1
p
90°
0°
180°
Degree (0-180°)

Figure 5

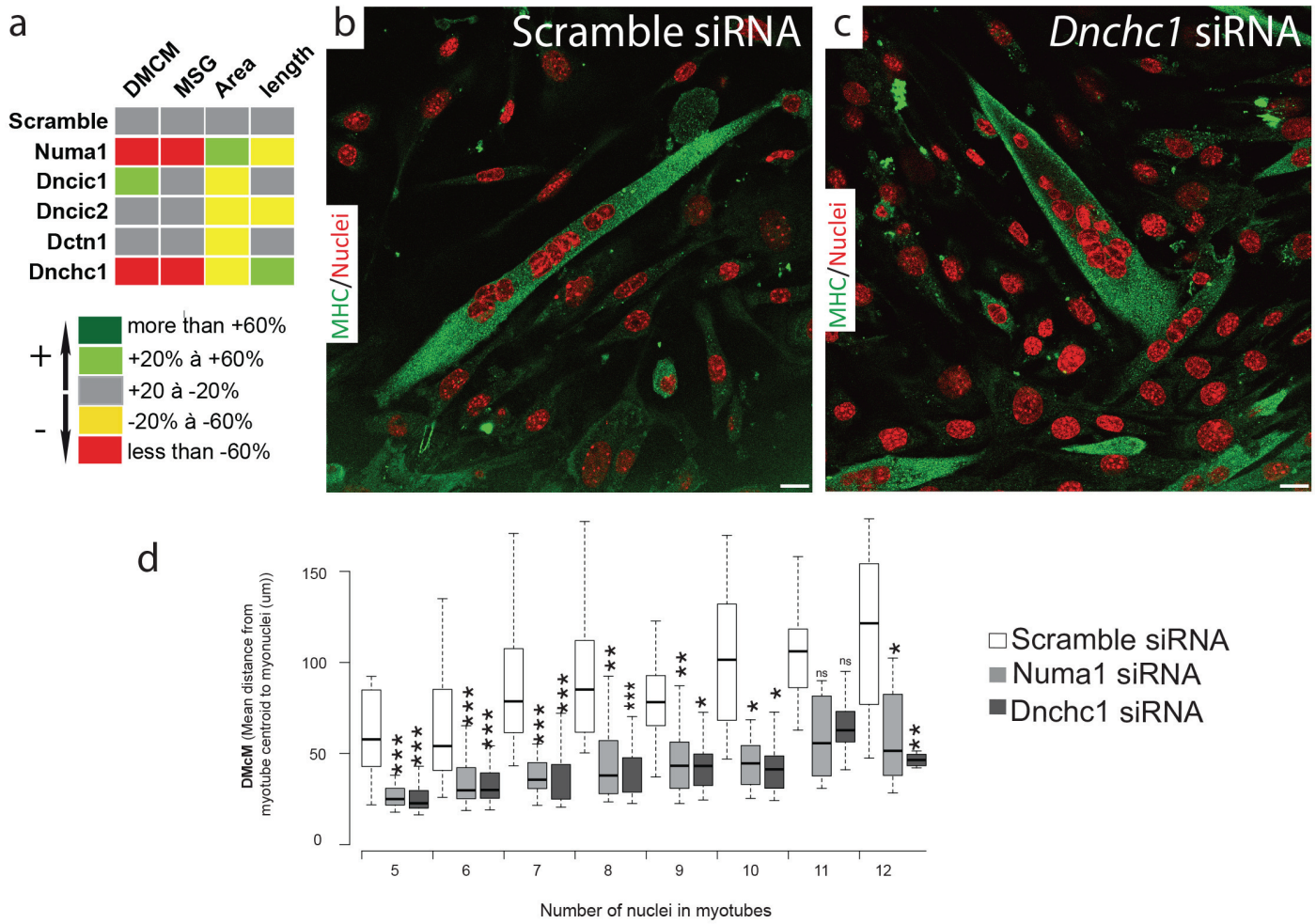
a
DMCM
MSG
Area
length
Scramble
Numa1
Dncic1
Dncic2
Dctn1
Dnchc1
+
-
more than +60%
+20% à +60%
+20 à -20%
-20% à -60%
less than -60%
b
Scramble siRNA
MHC/Nuclei
c
Dnchc1 siRNA
MHC/Nuclei

d
DMcM (Mean distance from myotube centroid to myonuclei (um))
150
100
50
0
5
6
7
8
9
10
11
12
Number of nuclei in myotubes
Scramble siRNA
Numa1 siRNA
Dnchc1 siRNA

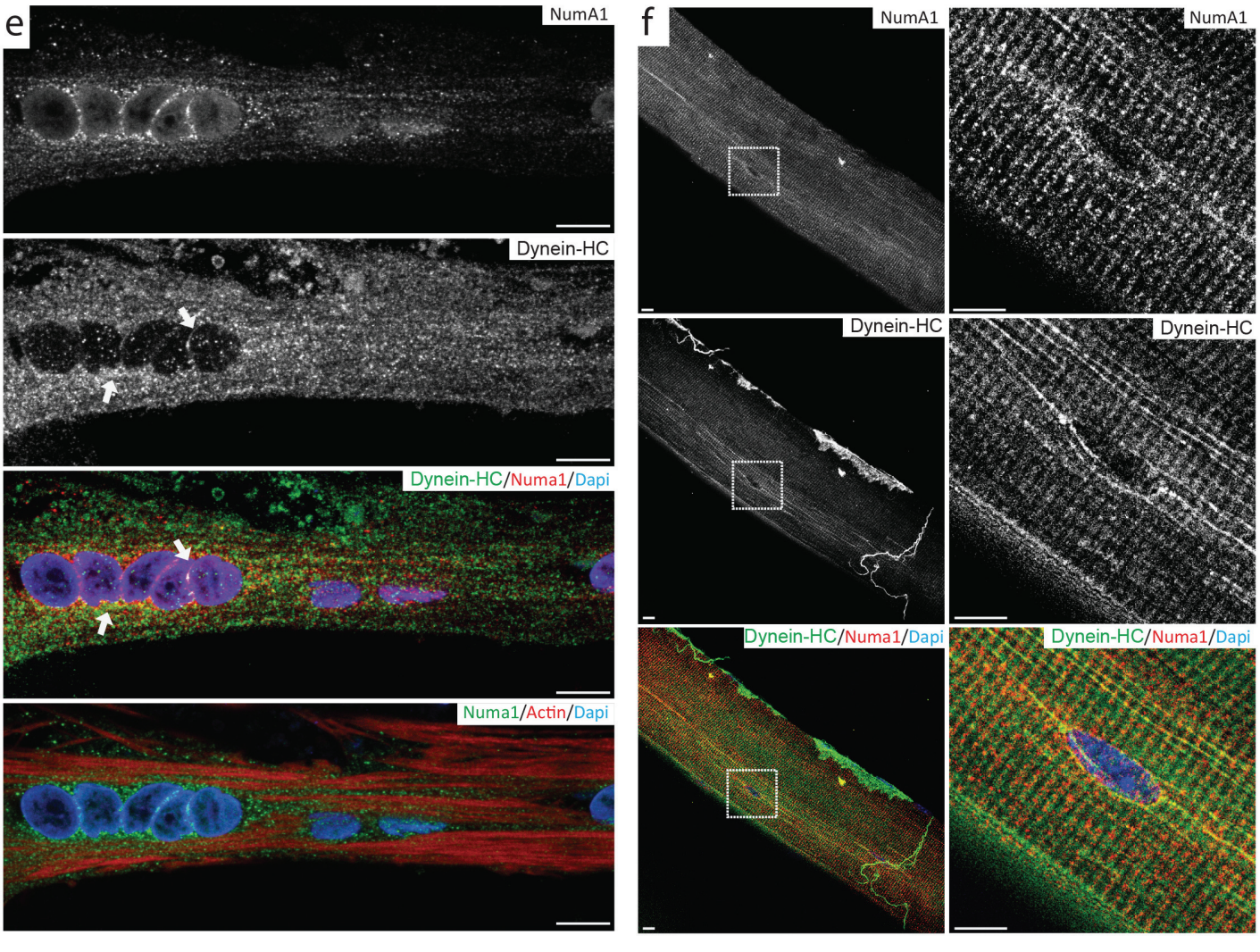
e
NumA1
Dynein-HC
Dynein-HC/Numa1/Dapi
Numa1/Actin/Dapi
f
NumA1
NumA1
Dynein-HC
Dynein-HC
Dynein-HC/Numa1/Dapi
Dynein-HC/Numa1/Dapi

Figure 6

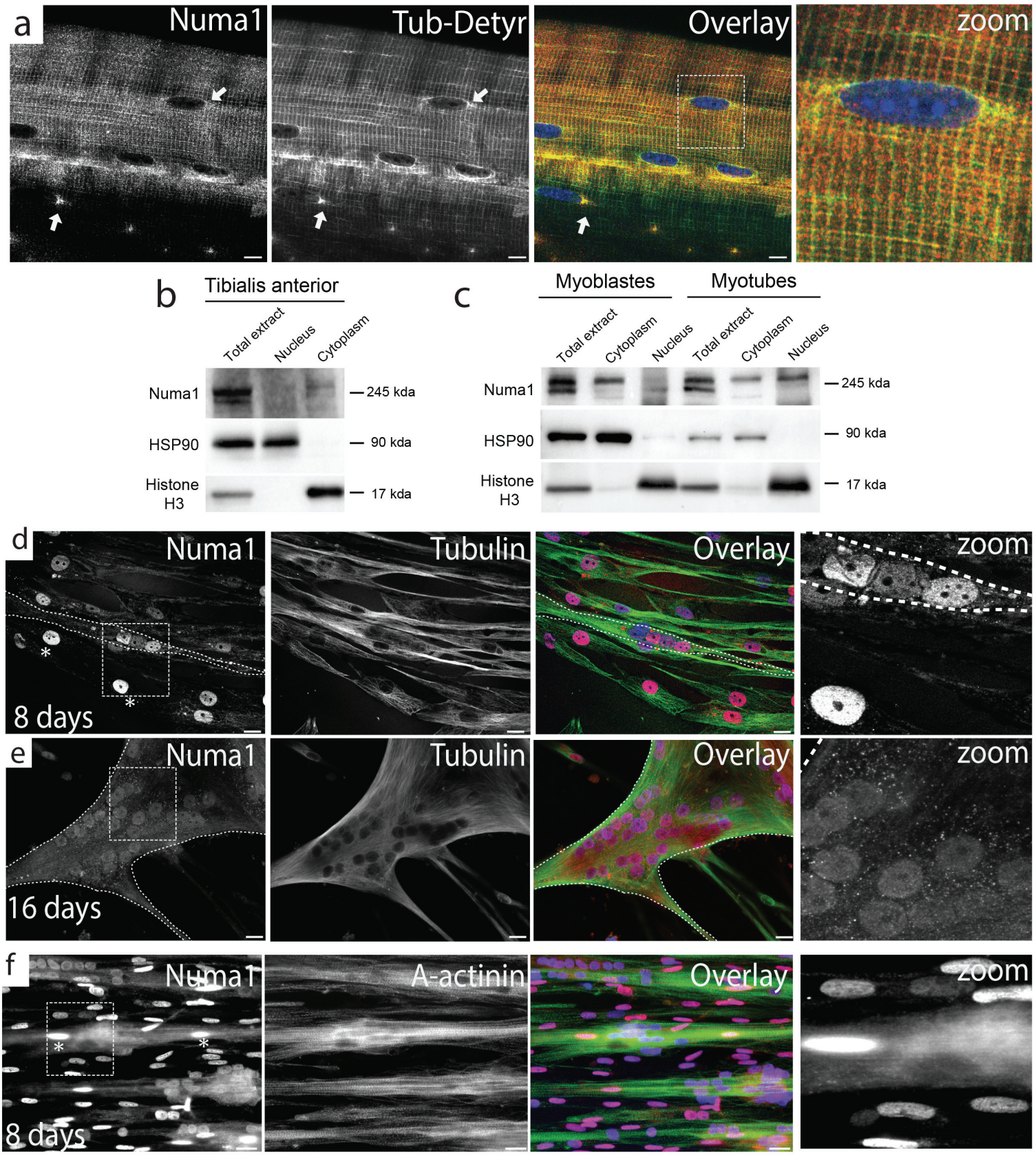
a
Numa1
Tub-Detyr
Overlay
zoom
b
Tibialis anterior
Total extract
Nucleus
Cytoplasm
Numa1
245 kda
HSP90
90 kda
Histone H3
17 kda
c
Myoblastes
Myotubes
Total extract
Cytoplasm
Nucleus
Total extract
Cytoplasm
Nucleus
Numa1
245 kda
HSP90
90 kda
Histone H3
17 kda
d
Numa1
Tubulin
Overlay
zoom
8 days
e
Numa1
Tubulin
Overlay
zoom
16 days
f
Numa1
A-actinin
Overlay
zoom
8 days

Figure 7

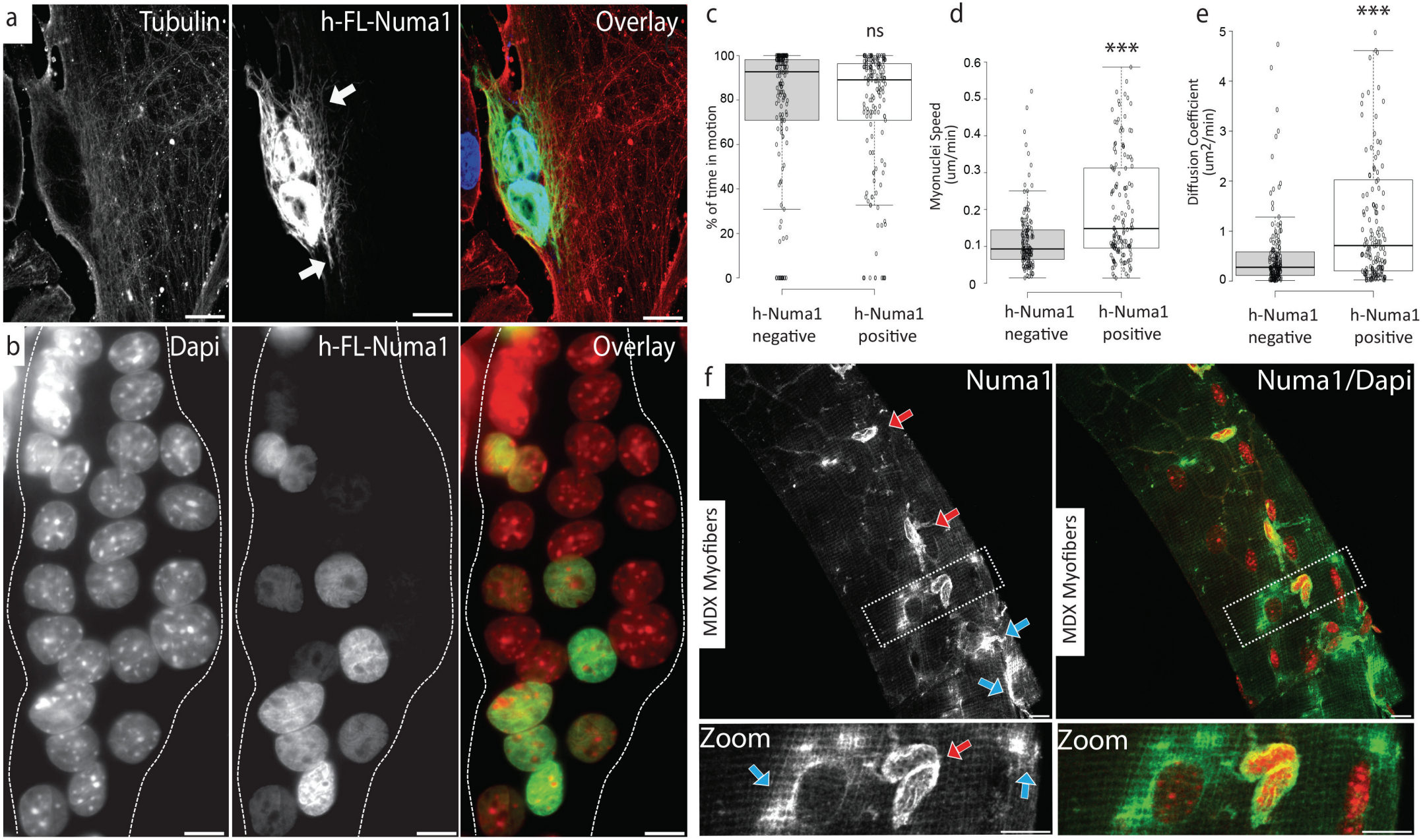
a
Tubulin
h-FL-Numa1
Overlay
b
Dapi
h-FL-Numa1
Overlay
c
ns
% of time in motion
h-Numa1 negative
h-Numa1 positive
d
***
Myonuclei Speed (um/min)
h-Numa1 negative
h-Numa1 positive
e
***
Diffusion Coefficient (um2/min)
h-Numa1 negative
h-Numa1 positive
f
Numa1
Numa1/Dapi
MDX Myofibers
MDX Myofibers
Zoom
Zoom

Figure 8

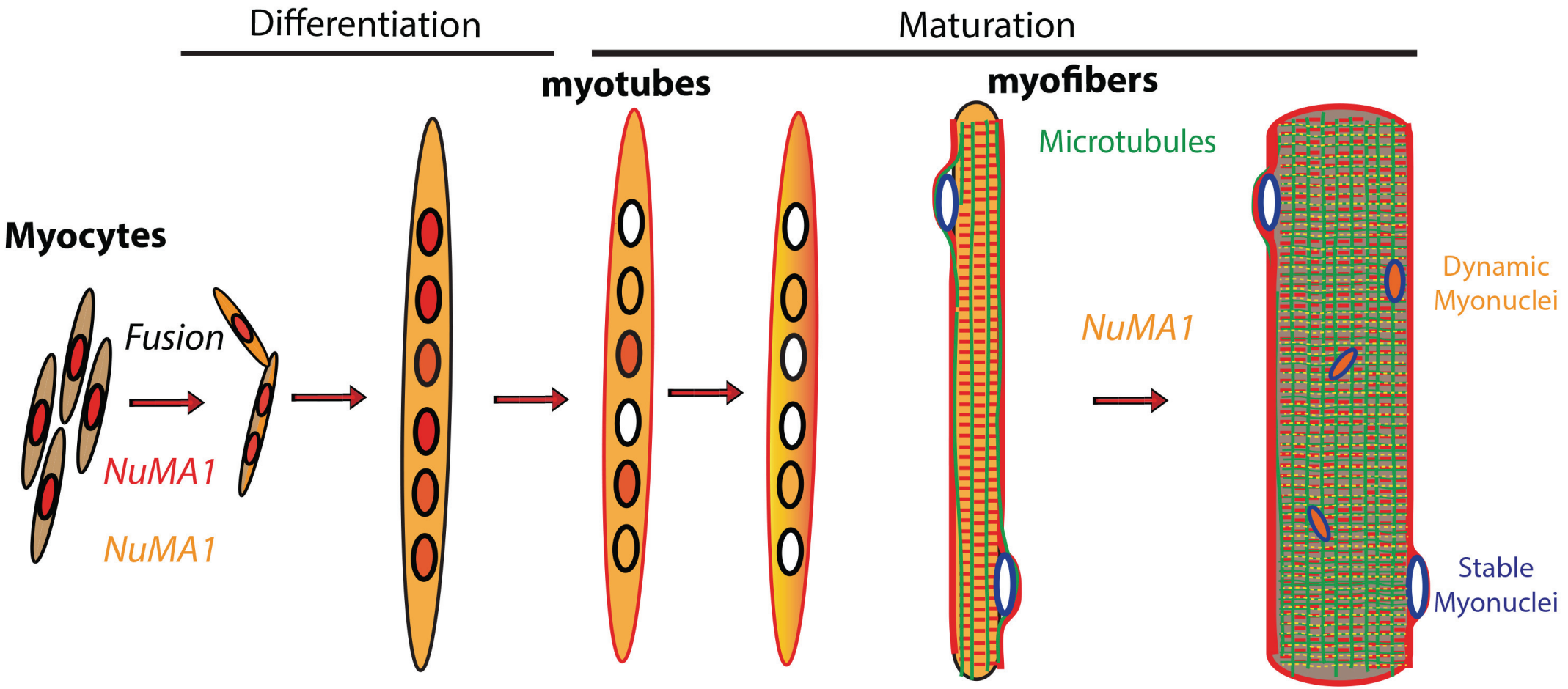
Differentiation
Maturation
myotubes
myofibers
Myocytes
Fusion
NuMA1
NuMA1
Microtubules
NuMA1
Dynamic
Myonuclei
Stable
Myonuclei

Extended Data Figure 1

a

Protein	Entry	Protein names	Gene	Pep	WSC
E9Q7G0_MOUSE	E9Q7G0	Protein Numa1	Numa1	6	6
KINH_MOUSE	Q61768	Kinesin-1 heavy chain	Kif5b	15	16
MAP4_MOUSE	P27546	Microtubule-associated protein4	MAP4	11	13
AKAP9_MOUSE	Q70FJ1	A-kinase anchor protein 9	AKAP9	2	2

b

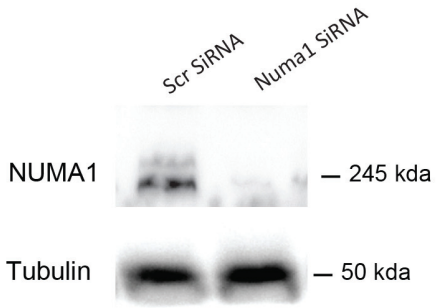

c

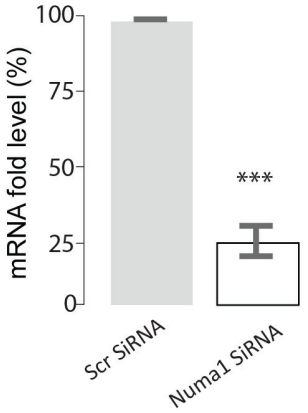

d

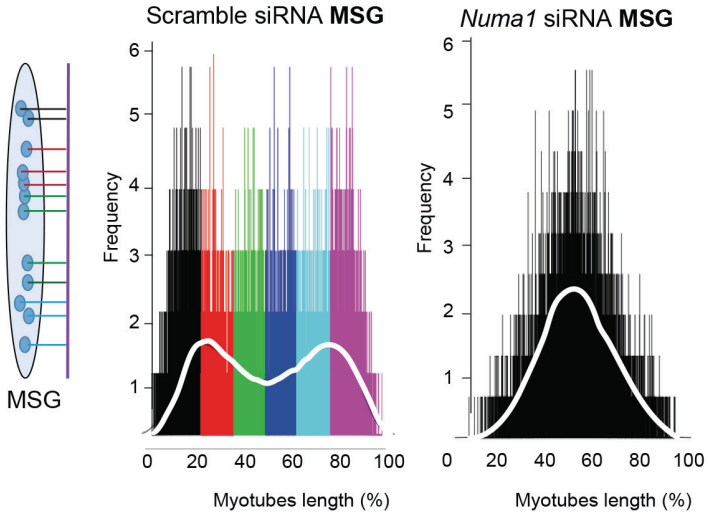

e

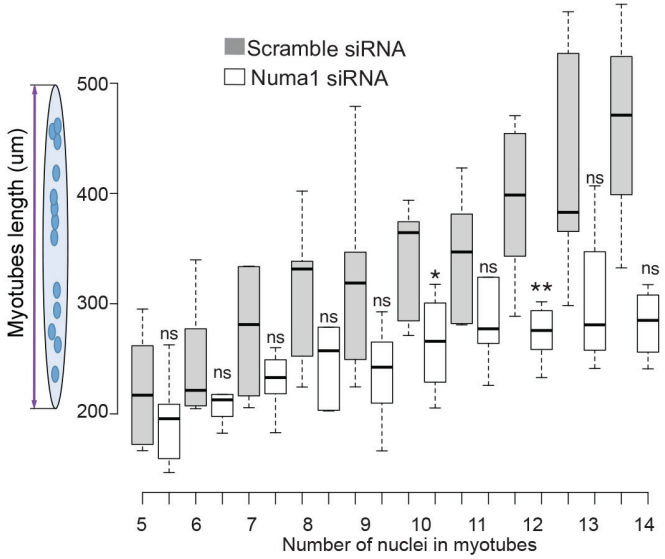

f

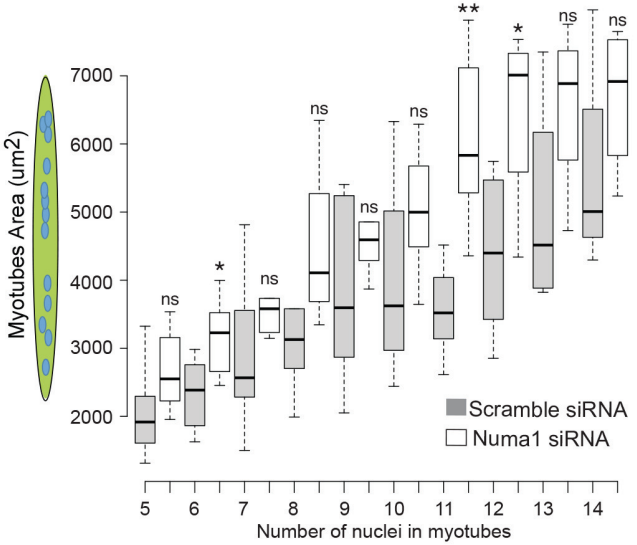

Extended Data Figure 2

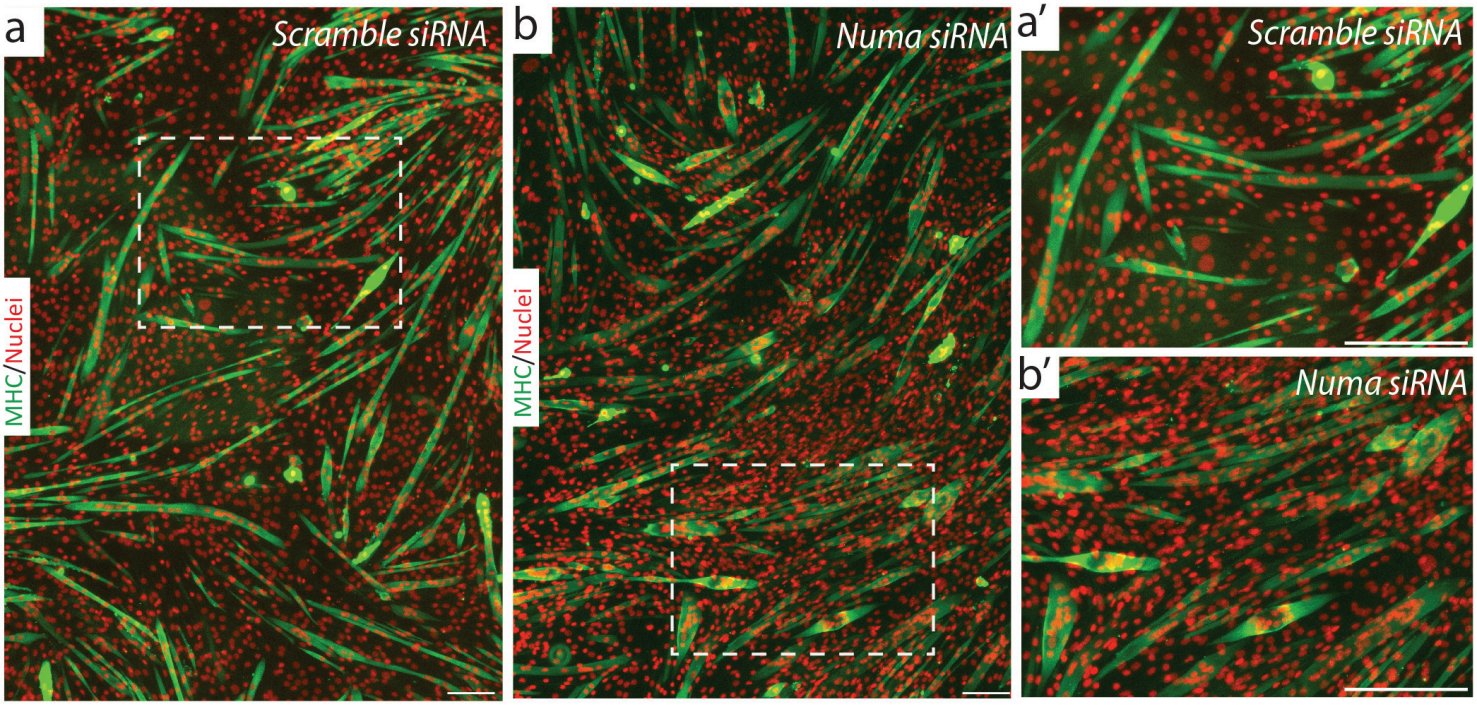

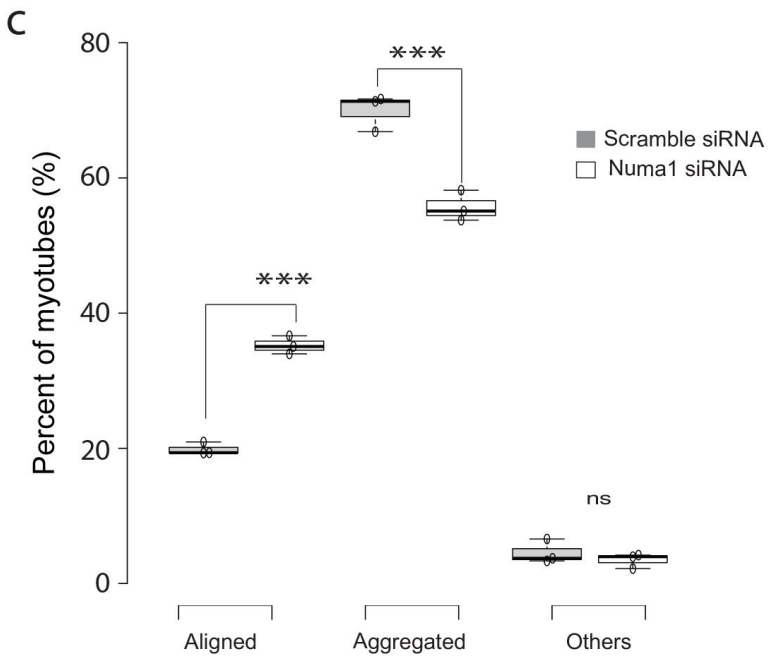

Extended Data Figure 3

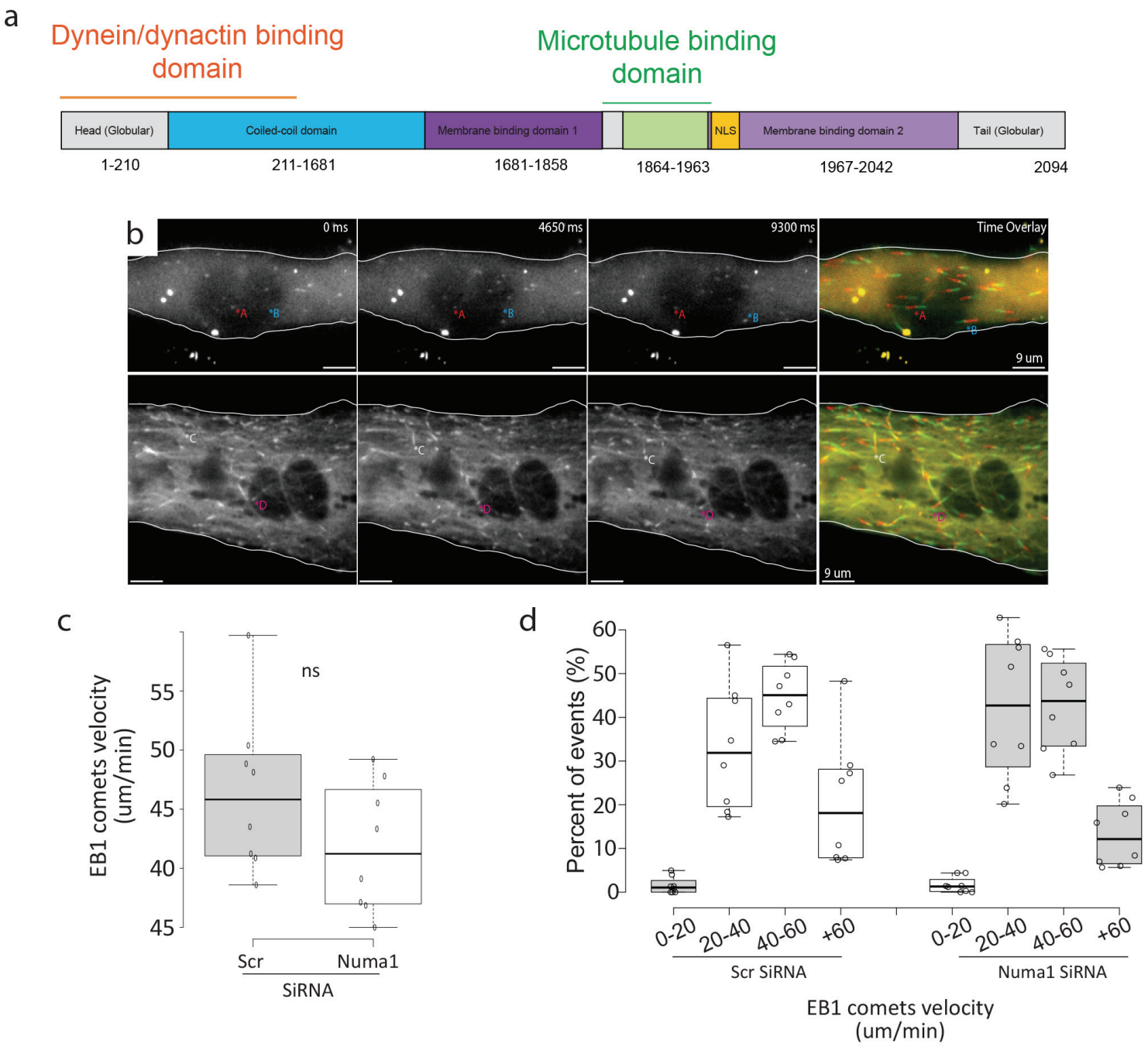

Extended Data Figure 4

a

Protein	Entry	Protein names	Gene	Pep	SC	SSC	WSC
DYHC1_MOUSE	Q8R1Q8	Cytoplasmic dynein 1 heavy chain 1	Dnchc1	89	111	11	111
D3YX34_MOUSE	D3YX34	Dynactin subunit 1	Dctn1	8	11	11	11
DC1L1_MOUSE	Q8R1Q8	Cytoplasmic dynein 1 intermediate chain 1	Dncic1	9	10	9	9,8
A2BFF5_MOUSE	A2BFF5	Cytoplasmic dynein 1 intermediate chain 2	Dncic2	5	5	5	5

b

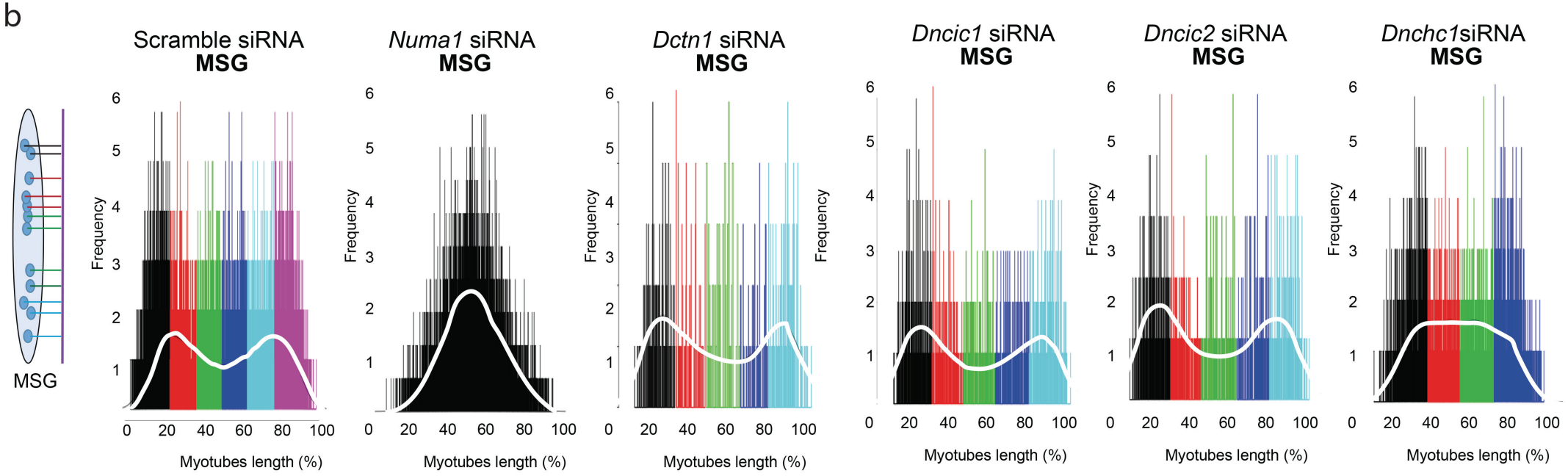

Extended Data Figure 5

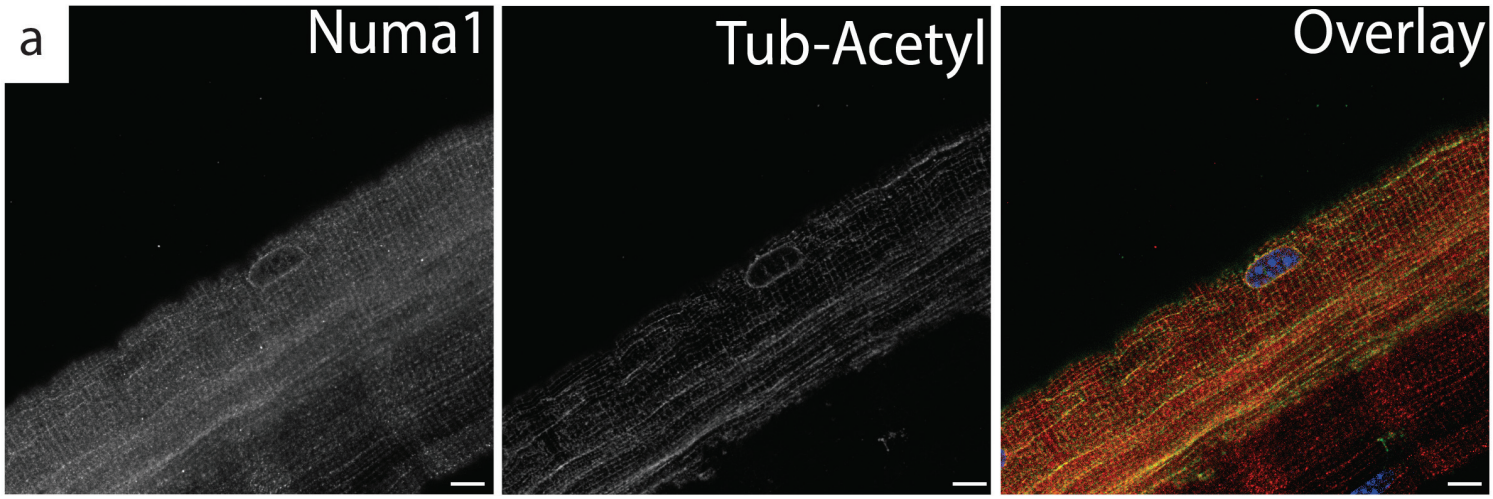

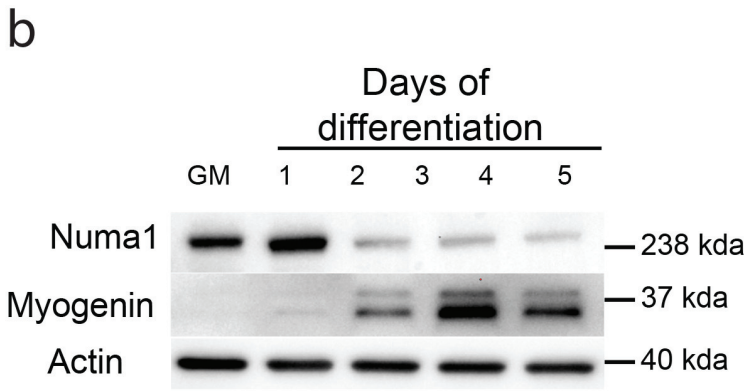

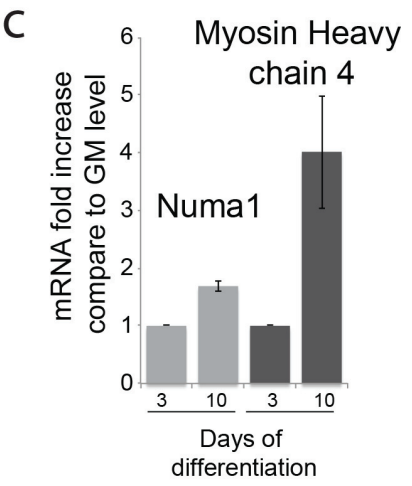

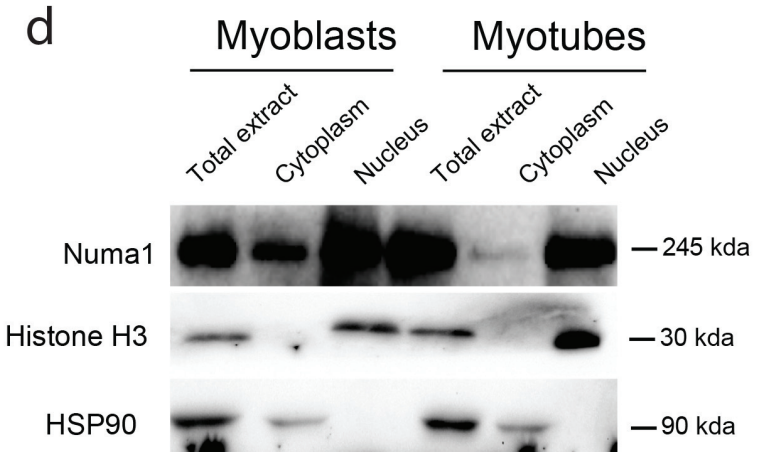

Extended Data Figure 6

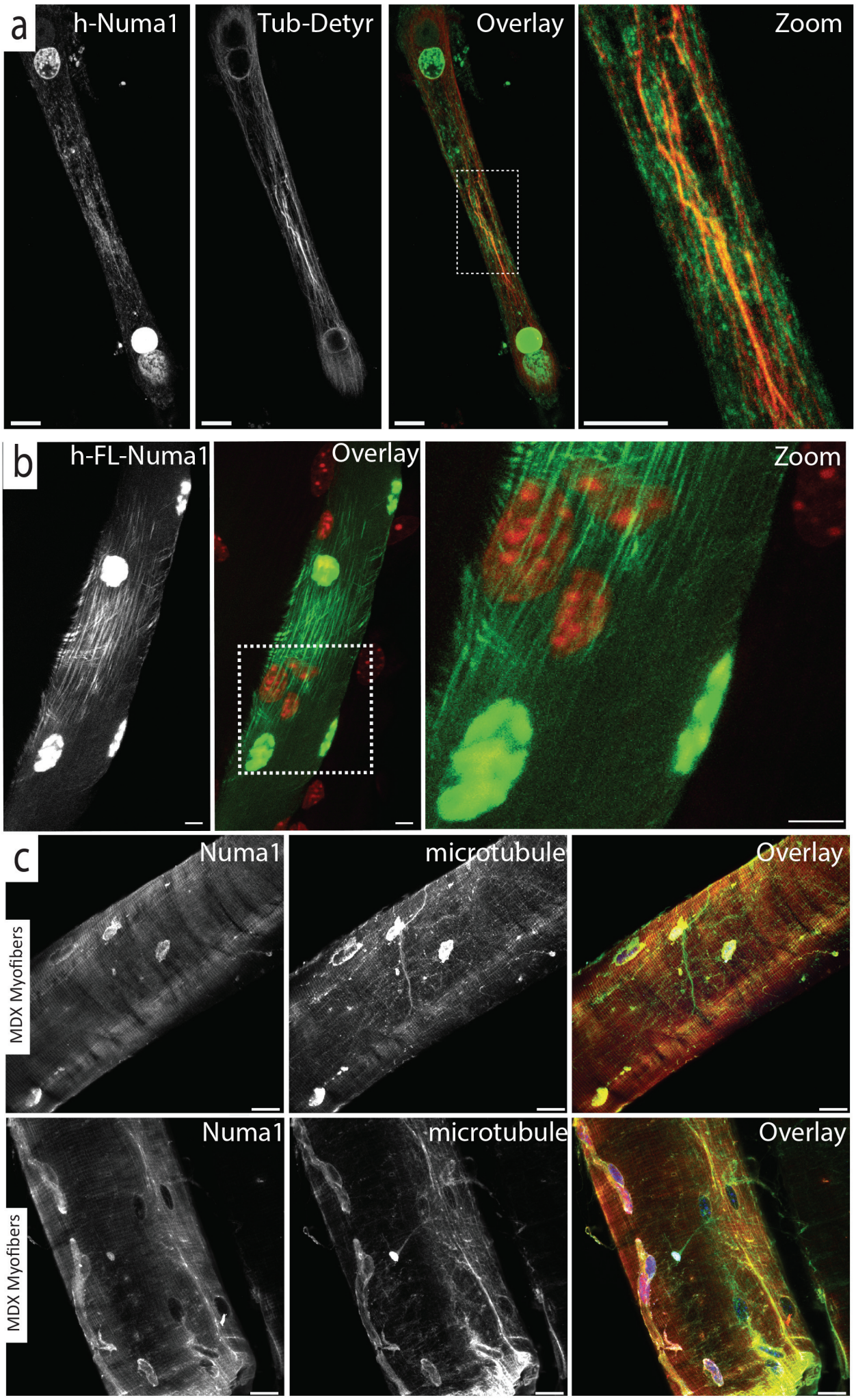

Supplementary Table 1

Immunofluorescence

Antibody or Dye	Species	Dilution Factor	Reference
α-Tubulin	Mouse	1/100	Sigma T6074
Acetylated-Tubulin	Mouse	1/100	Sigma T7451
Detyrosinated Tubulin	Mouse	1/100	US Biological T9154-05H
Laminin-2	Rat	1/200	Sigma L0663
GM130	Mouse	1/100	BD Biosciences 610823
NuMA1	Rabbit	1/100	Thermofisher scientific PA316829
MF20	Mouse	1/10	DSHB
DAPI	Dye	1/50000	Thermofisher scientific D1306
α-bungarotoxin Alexa Fluor 647	Dye	1/100	Thermofisher scientific B35450
Anti-Mouse Alexa Fluor A488	Goat	1/500	Thermofisher scientific A32723
Anti-Mouse Alexa Fluor A555	Goat	1/500	Thermofisher scientific A21424
Anti-Rabbit Alexa Fluor A488	Goat	1/500	Thermofisher scientific A32731
Anti-Rat Alexa Fluor A594	Donkey	1/500	Thermofisher scientific A21209
Pericentrin	Mouse	1/100	BD Biosciences 611815
Phalloïdin Alexa Fluor 555	Dye	1/100	Invitrogen A34055

Western Blotting

Antibody or Dye	Species	Dilution Factor	Reference
α-Tubulin	Mouse	1/1000	Sigma T6074-
Histone H3	Rabbit	1/2000	Abcam 1791
HSP90	Mouse	1/1000	Enzo life SPA830
Myogenin	Mouse	1/500	Santa Cruz sc-12732
NuMA1	Rabbit	1/800	Thermofisher scientific PA316829
Anti-Mouse-HRP	Goat	1/5000	Invitrogen 62-6520
Anti-Rabbit-HRP	Goat	1/5000	Invitrogen 65-6120

Supplementary Table 2

siRNA	Sense oligonucleotide sequence	Anti-Sense oligonucleotide sequence
Scramble	**Ambion, AM4641**	
NuMA1	GGGCAAGGUGAAGCAUUAA	UUAAUGCUUCACCUUGCCC
Dnclc1 n°1	GGAGUUUGACAAGAAGUAC	GUACUUCUUGUCAAACUCC
Dnclc1 n°2	GGUGGCCAUUCUUCUGUUC	GAACAGAAGAAUGGCCACC
Dnclc1 n°3	GGACUGCAUCCAAAUUCCA	UGGAAUUUGGAUGCAGUCC
Dncic1 n°1	GGAAGAGGAGAGGAAGAAG	CUUCUUCCUCUCCUCUUCC
Dncic1 n°2	GGAAGAAAAACAGCAGAUC	GAUCUGCUGUUUUUCUUCC
Dncic1 n°3	CCCAAAAUUGGUCAUGAUU	AAUCAUGACCAAUUUUGGG
Dncic2 n°1	GGAAAGGAAAAAAAAGGAA	UUCCUUUUUUUUCCUUUCC
Dncic2 n°2	GCAGAUUAACAUCUUCUUU	AAAGAAGAUGUUAAUCUGC
Dncic2 n°3	CCAUUCUACGAGAAUUGUA	UACAAUUCUCGUAGAAUGG
Dctn1 n°1	GGAAGUAUUUCACAUGUGA	UCACAUGUGAAAUACUUCC
Dctn1 n°2	CCUGGAAACAUCAUGUAGU	ACUACAUGAUGUUUCCAGG
Dctn1 n°3	CCACAUCAAGUUCACCCAG	CUGGGUGAACUUGAUGUGG
Dnchc1 n°1	GGAGAAAGAAUUCAUUUCC	GGAAAUGAAUUCUUUCUCC
Dnchc1 n°2	GGAGGUUAUGUUUAAAACU	AGUUUUA AACAUAACCUCC
Dnchc1 n°3	GCUCCUGUGAUUGAUGCAG	CUGCAUCAAUCACAGGAGC

shRNA	Clone ID	Target sequence
Scramble		
NuMA1	TRCN0000072130 (Sigma)	GCCAGATGGATCGAAAGATTA

Supplementary Table 3

Primers	Sequence
Emerin_F	CCAAGGAAGCAGCAAATGTT
Emerin_R	ACTGCCACCACCAAGTTTTC
GAPDH_F	AACTTTGGCATTGTGGAAGG
GAPDH_R	ACACATTGGGGGTAGGAACA
GusB_F	GAGGATTGCCAACGAAACCG
GusB_R	GTGTCTGGGGACCACCTTTGA
LaminA/C_F	GGCTACAGACGCTGAAGGAG
LaminA/C_R	CTGTTCCACCTGGTCCTCAT
Lamin B_F	GGGAACCTTTCAAGTGACCA
Lamin B_R	GGTGGAAGAGAGCTTGAACG
Myh4_F	CAAGTCATCGGTGTTTGTGG
Myh4_R	TGTCGTACTTGGGAGGGTTC
NuMA1_F	AAGTATTGACAGCCTGGATCTGA
NuMA1_R	GGTACGAGGCAGCTTGCTA
Rpl41_F	GCCATGAGAGCGAAGTGG
Rpl41_R	CTCCTGCAGGCGTCGTAG

Publication 5:

SH3KBP1 scaffolds endoplasmic reticulum and controls skeletal myofibers architecture and integrity.

In preparation.

A. Guiraud, E. Christin, N. Couturier, C. Kretz-Remy, A. Janin, A. Ghasemizadeh, A.C. Durieux, D. Arnould, N.B. Romero, M.T. Bui, V.L. Buchman, L. Julien, M. Bitoun and V. Gache

SH3KBP1 scaffolds endoplasmic reticulum and controls skeletal myofibers architecture and integrity

Alexandre Guiraud[1*], Emilie Christin[1*], Nathalie Couturier[1*], Carole Kretz-Remy[1], Alexandre Janin[1], Alireza Ghasemizadeh[1], Anne-Cécile Durieux[2], David Arnould[2], Norma Beatriz Romero[3], Mai Thao Bui[3], Vladimir L. Buchman [4], Laura Julien[5], Marc Bitoun[5] and Vincent Gache[1]

* Contribute equally

1-U1217, UMR 5310, INMG, INSERM, CNRS, Claude Bernard University Lyon 1, France.

2- Laboratoire Interuniversitaire de Biologie de la Motricité, Université de Lyon, Université Jean Monnet, Saint Etienne, France.

3- Unité de Morphologie Neuromusculaire, Institut de Myologie, Groupe Hospitalier Universitaire La Pitié-Salpêtrière, Paris, France.

4- School of Biosciences, Cardiff University, Museum Avenue, Cardiff, CF10 3AX, UK.

5- Sorbonne Université, INSERM, , Institute of Myology, Centre of Research in Myology, UMRS 974, F-75013, Paris, France.

Summary

Myonuclei are actively positioned throughout muscular development. Guiraud, Christin, Couturier *et al* show that SH3KBP1 scaffolds the ER through Calnexin interaction and controls myonuclei motion during early steps of muscle fibers formation. Besides SH3KBP1 participates in cell fusion and T-tubules formation/maintenance in mature skeletal muscle fibers and contributes to slow-down CNM-like phenotypes.

Abstract

The building block of skeletal muscle is the multinucleated muscle fiber, formed by the fusion of hundreds of mononucleated precursor cells, myoblasts. In the normal course of muscle fiber development or regeneration,

myonuclei are actively positioned throughout muscular development and adopt special localization in mature fibers: regular spacing along muscle fibers periphery, raising the notion of MyoNuclear Domains (MNDs). There is now growing support for a direct connection between myonuclear positioning and normal function of muscles, but how myonuclei affects muscle function remains poorly characterized.

To identify new factors regulating forces applied on myonuclei in muscles fibers, we performed a siRNA screen and identified SH3KBP1 as a new factor controlling myonuclear positioning in early phases of myofibers formation. Depletion of SH3KBP1 induces a reset of MNDs establishment in mature fibers reflected by a dramatic reduction in pairwise distance between myonuclei. We show that SH3KBP1 scaffolds Endoplasmic Reticulum (ER) in myotubes that in turn controls myonuclei velocity and localization and thus myonuclear domains settings. Additionally, we show that in later phases of muscle maturation, SH3KBP1 contributes to the formation and maintenance of Sarcoplasmic Reticulum (SR) and Transverse-tubules (T-tubules). We also demonstrate that in muscle fibers, GTPase dynamin-2 (DNM2) binds to SH3 domains of SH3KBP1. Interestingly, we observed that *Sh3kbp1* mRNA is up regulated in a mouse model harboring the most frequent mutation for Autosomal Dominant CentroNuclear Myopathy (AD-CNM): *Dnm2*$^{+/R465W}$. SH3KBP1 thus appears as a compensation mechanism in this CNM model since its depletion contributes to an increase of CNM-like phenotypes (reduction of muscle fibers Cross-section Areas (CSA) and increase in slow fibers content).

Altogether our results identify SH3KBP1 as a new regulator of myonuclear domains establishment in the early phase of muscle fibers formation through ER scaffolding and later in myofibers integrity through T-tubules scaffolding/maintenance.

Introduction

The building block of skeletal muscle is the multinucleated muscle fiber, formed by the fusion of hundreds of specialized cells, myoblasts, and in which positioning of nuclei ("myonuclei") is finely regulated. In the normal course of muscle development or regeneration, myonuclei actively localize themselves and adopt specific position in mature myofibers in which they are regularly spaced at the periphery of myofibers (Bruusgaard et al., 2003). This precise myonuclei spatial organization gives rise to the notion of MyoNuclear Domains (MNDs) in which each myonucleus controls genes expression in its surrounding cytoplasm and guaranties muscle function (Gundersen, 2016). MNDs settings mainly depend on muscle fibers ability to maintain a defined distance between myonuclei in a cytoplasmic-adapted context related to myofibers type, size and age (Bruusgaard et al., 2006; Qaisar and Larsson, 2014; Liu et al., 2009). During the first steps of muscle fibers formation, myonuclei have been shown to move and position using mainly microtubule network reorganization (Tassin et al., 1985; Gimpel et al., 2017) and an interplay between microtubule associated proteins (MAPs) such as MAP7 (Metzger et al., 2012) and molecular motors, including dynein and kinesins (Gache et al., 2017). This dynamic of myonuclei contributes to precocious alignment of myonuclei in immature fibers. Although comprehension of mechanisms involved in myonuclear positioning during myofibers formation has recently progressed, how mispositioning of myonuclei affects muscle function still remains an open question.

Abnormal myonuclei internalization in muscle fibers that are not directly linked to excessive regenerative process is the hallmark of a group of humans myopathies called Centronuclear Myopathies (CNMs)(Romero and

Bitoun, 2011; Jungbluth et al., 2007). The majority of defective proteins implicated in CNMs are involved in various aspects of membrane trafficking and remodeling and are relevant to essential cellular processes including endocytosis, intracellular vesicle trafficking and autophagy (Romero and Laporte, 2013). To date, the main proteins implicated in CNMs are phosphatidylinositol phosphatase Myotubularin coded by *MTM1* gene (Laporte et al., 1996); GTPase dynamin-2 involved in endocytosis and cell motility, and coded by *DNM2* gene (Bitoun et al., 2005); amphiphysin-2 nucleocytoplasmic adaptor protein, coded by *BIN1* gene (Nicot et al., 2007) and the principal sarcoplasmic reticulum calcium release channel, ryanodine receptor 1, coded by *RYR1* gene (Wilmshurst et al., 2010; Bevilacqua et al., 2011).

Myonuclei spatial organization can contribute to muscle fibers functionality as growing evidences support a direct connection between myonuclear positioning and normal function of muscles (Metzger et al., 2012; Falcone et al., 2014; Janin and Gache, 2018; Robson et al., 2016). Additionally, T-tubule organization and efficiency are highly impacted in CNM (Chin et al., 2015; Al-Qusairi et al., 2009). Finally, besides abnormal nuclear positioning and T-tubules abnormalities, altered autophagy is frequently described in CNM (Jungbluth and Gautel, 2014).

SH3KBP1, also known as Ruk/CIN85 (Cbl-interacting protein of 85 kDa) is a ubiquitously expressed adaptor protein, involved in multiple cellular processes including signal transduction, vesicle-mediated transport and cytoskeleton remodeling (Havrylov et al., 2010; Buchman et al., 2002). SH3KBP1 protein is composed of three SH3 domains at the N-terminus followed by a proline-rich (PR) domain, a serine-rich (SR) domain, and a C-terminus coiled-coil (CC) domain. Functions of SH3KBP1 as an adaptor protein are mainly linked to endocytosis trafficking and degradative pathway through the recruitment of Cbl (E3 ubiquitin ligase), endophilin and dynamin (Schroeder et al., 2010; Sun et al., 2015; Zhang et al., 2009). SH3KBP1 protein is also associated with several compartments involved in membrane trafficking such as the Golgi complex and is mainly concentrated in COPI-positive subdomains (Havrylov et al., 2008). The role of SH3KBP1 during the formation of muscle fibers has never been investigated.

In the present study, we show that the adaptor protein SH3KBP1, through its N-terminus part, is able to scaffold endoplasmic reticulum (ER) probably *via* an interaction with Calnexin. SH3KBP1 also governs myonuclei motion and spatial organization as well as myoblast fusion. Additionally, we observed that SH3KBP1 interacts with Dynamin 2 (DNM2) and organizes T-tubule formation in skeletal muscle. Moreover, its down-regulation contributes to an increase of CNM-like phenotypes in a mouse model expressing the most frequent mutation causing autosomal dominant centronuclear myopathy (AD-CNM).

Results

SH3KBP1 is required for precocious myonuclear positioning steps and controls fusion parameters during muscle fiber formation.

To identify new factors that contribute to myonuclear spreading and alignment in muscle fibers, we performed a large siRNA screen on candidates expected to affect myonuclei repartition in nascent myotubes. Briefly, primary myoblasts were isolated from young pups and induced to differentiate *in vitro* for 3 days before analysis (Falcone et al., 2014) (Fig.1A). This cell culture technique leads to an accumulation of heterogeneous myotubes regarding

myonuclei number and myotubes length (Blondelle et al., 2015). To precisely characterize the early steps of myonuclei positioning in myotubes, we developed an image-J® plugin that automatically extracts different myotubes parameters (such as myotubes lengths/areas and myonucleus localization). Data were then classified and analyzed according to myonuclei content using a homemade program in R-Studio® (Fig.1D-F). This analysis allowed us to track myonuclei accretion during elongation of myotubes in a window from 3 to 11 myonuclei per myotubes. Isolated murine myoblasts were then treated with short interfering RNA (siRNA) targeting either a scrambled sequence or candidate genes. Among candidates from the siRNA screen, efficient *sh3kbp1* depletion appears to strongly modify myonuclear positioning (Fig1. B-C, Fig.S1A). In control condition, we observed a nearly linear relation between addition of myonuclei into myotubes and expansion of myotubes length, with an average of nearly 10 % increase of length after each myonucleus accretion (Fig. 1D). In *sh3kbp1* depleted myotubes, length repartition is homogenously extended to an increase of 46.8% ±3.3 in myotubes containing up to 11 myonuclei (Fig. 1D). Quantification of the mean distance between all myonuclei inside myotubes indicate a burst of spacing (+103.5% ±11.6, data not shown) concomitantly with an escape from the center of myotubes reflected by (i) the mean distance between myotube centroid and each myonuclei (DMcM) (+111.5% ±12.5) (Fig. 1E) and (ii) the Myonuclei Spreading Graphic (MSG) representation (Fig. 1F). MSG shows statistical probability to find one myonucleus along the all length of myotubes and allow the extraction of "statistical clustering zones" (colors code in Fig. 1F) that we estimate as four zones in the case of scramble myotubes *versus* eight zones in *sh3kbp1* depleted myotubes (Fig. 1F). Thus, *sh3kbp1* depleted myotubes failed to homogeneously spread myonuclei along myotubes length that tends to accumulate at myotubes tips (Fig. 1C, arrows). Overall, these data suggest that for a defined myonuclei content in myotubes, SH3KBP1 acts as "anti-elongation" factor and contributes to myonuclei spreading in myotubes.

Myoblasts/myotubes elongation and alignment is a key process that controls myoblast/myotubes fusion (Louis et al., 2008). As *sh3kbp1* depletion led to myotubes length increase, we wondered if fusion aspects were modified during differentiation. Indeed, myotubes elongation can contribute to increase myotubes/myoblast contacts that thus will modulate membrane fusion and ultimately modify myonuclei accretion speed (Kim et al., 2015). We evaluated fusion capacity of primary myoblasts isolated from young pups after *in vitro* differentiation induction (Fig.S1B-G). After 3 days of differentiation, isolated myoblasts treated with siRNA targeting *sh3kbp1* mRNA are similarly stained for myosin heavy chain antibodies compare to control cells treated with siRNA scramble sequences, indicating normal myoblast commitment into muscle differentiation process (Fig. S1B-D). Fusion index was increased in *Sh3kbp1* depleted myotubes, assessed by the total number of myonuclei in myotubes (Fig. S2E) and the average number of myonuclei per myotube (Fig. S2F). Accordingly, in *sh3kbp1* depleted conditions, distribution of myotubes with respect to myonuclei content revealed much more myotubes with ≥10 nuclei when compared to controls (Fig. S2G). Altogether, this data suggests that *sh3kbp1* acts also as an "anti-fusion" factor as expected for an anti-elongation factor.

SH3KBP1 governs myonuclei velocity that contributes to myonuclei positioning in mature myofibers.

To investigate the role of *sh3kbp1* in late steps of differentiation, primary mouse myotubes were maintained in differentiation media for 5 to 10 days as previously described (Pimentel et al., 2017; Falcone et al., 2014) Fig. 2A.

In 5-day differentiated myofibers, myonuclei clustering and velocity was addressed (Fig. 2B-F). First, we observed twice more myonuclei clustered in myotubes treated with shRNA targeting *sh3kbp1* gene compared to control, confirming a role of *sh3kbp1* on myonuclei spreading (Fig. 2B & E, white asterisk). As myonuclei within myofibers have different behaviors (Gache et al., 2017), we next investigated the impact of *sh3kbp1* depletion on myonuclei movements in 5-day differentiated myofibers. Myoblasts were transfected with RFP-lamin-chromobody® to visualize myonuclei concomitantly with shRNA targeting scramble or *Sh3kbp1*, both GFP-tagged. Myotubes containing both constructions (GFP and RFP-lamin-chromobody®) were selected for fewer analyses (Fig.2C-F). After 5 days of differentiation, myonuclei were tracked every 20 minutes for a time period of 14 hours (Fig. 2E). Myonuclei displacements parameters were analyzed using SkyPad method (Cadot et al., 2014). We found that in control condition, myonuclei are in motion during nearly 35 % of the time (a movement is defined as a displacement more than 30 µm) at a median speed of 0.232 ±0,014 µm/min. Depletion of *sh3kbp1* increased from more than 20% the percentage of time myonuclei are in motion of and by more than 30% median speed that reach 0.313 ±0,014 µm/min outside myonuclei clusters (Fig.2C-D). Indeed, because of high myonuclei concentration inside myonuclei clusters, we could not technically access to myonuclei motion and speed. To further investigate the implication of *sh3kbp1* in late steps of differentiation, primary mouse myotubes were maintained in differentiation media for 10 days as previously described (Pimentel et al., 2017) (Fig. 2G). In these maturation conditions, myonuclei are compressed between myofiber plasma membrane and contractile apparatus and adopt a flatten architecture all along myofibers length (Roman et al., 2017). This long-term differentiation approach allow to confirm that *sh3kbp1* controls myonuclear positioning during maturation of myofibers as *sh3kbp1* depletion using either siRNA or shRNA caused a significant reduction in the mean distance between adjacent myonuclei (Fig. 2G-H). Additionally, *Sh3kbp1* depletion significantly reduce by more than 30 % myofibers width (Fig. 2I). These results suggest that SH3KBP1 contributes to nuclear spreading and to the reduction of myonuclei movements and motion during muscle fibers maturation.

Next, we focused on the expression of both SH3KBP1 protein and *Sh3kbp1* mRNA in the time course of *in vitro* myotubes formation using C2C12 cells. These analyses showed a slight enhancement of SH3KBP1 production during early stages of myotubes formation (Fig. 3A). These results were confirmed using RT-qPCR techniques where a two-fold increase was observed in mRNA expression at the onset of differentiation step (Fig3B-C). To confirm *Sh3kbp1* functions during muscle cell differentiation, we stably knocked-down *Sh3kbp1* mRNA expression in C2C12 cells using a small hairpin interfering RNA (shRNA) (Fig. 3D). As observed in primary cells, after 3 days of differentiation, myoblasts entered the "muscle differentiation program", illustrated by the detection of myosin heavy chain-positive (MHC+) cells (Fig. 3E, day3). Although intensity of staining is reduced, we do not observe any alteration of myotubes size repartition in *Sh3kbp1* knocked-down compared to control conditions (Fig. S2A). After 6 days of differentiation, we clearly see a breaking event in fusion capacity correlated with *Sh3kbp1* knockdown (Fig. 3E). In control conditions, myonuclei spread along thin myotubes length while *Sh3kbp1* knockdown gives rise to huge myotubes with clustered myonuclei areas (Fig. 3E, day6). Distribution of myotubes with respect to their myonuclei content reveals also a significant increase in the number of myotubes with high myonuclei content compared to controls (Fig. S2B). In control condition, we observed a limited accumulation of clustered myonuclei along myotubes length, with a majority of clusters containing 4 to 6 myonuclei (Fig. 3F). On the opposite, in *Sh3kbp1* knockdown, we observe a clear increase in the proportion of

clusters containing more than 15 myonuclei (Fig. 3F). To address the specificity of myonuclei clustering phenotype in *Sh3kbp1* depleted conditions, we re-expressed full-length SH3KBP1 proteins in *Sh3kbp1* depleted murine myotubes and show that we rescue even better than in control the number of clustered myonuclei by myotubes (Fig. S2C-D). Together, these results show that *Sh3kbp1* is essential during myotube formation, both in primary myoblasts and in C2C12 cell cultures, to control myoblasts fusion and myonuclear positioning during skeletal muscle formation.

SH3KBP1 is an endoplasmic reticulum scaffolding protein that interacts with ER72 and Calnexin.

Several studies show that SH3KBP1 is distributed between different membrane trafficking compartments such as the Golgi Complex (Havrylov et al., 2008). The three SH3 domains localized in the N-terminal part of SH3KBP1 are responsible for its high capacity to interact with diverse regulatory partners (Havrylov et al., 2009) while the C-terminus part, containing a coiled-coil domain allows its targeting to endosomal membranes (Zhang et al., 2009). As no role of SH3KBP1 was previously described in skeletal muscle, we analyzed its localization during the time course of muscle formation using both C2C12 myoblast cell line and murine primary myoblasts (Fig. 4 A-B). In growing conditions, SH3KBP1 is localized in the cytoplasm with an apparent higher concentration at the vicinity of nuclei both in primary and in C2C12 myoblasts and some dots inside nucleus are also visible (Fig. 4A-B). During early myotubes formation, SH3KBP1 seems to spread along myotubes length, exhibit a weak perinuclear accumulation and myonuclei still exhibits dots inside myonuclei (Fig. 4A-B, Day3 and Day2). In 5 days differentiation C2C12 myotubes, perinuclear accumulation of SH3KBP1 is stronger and we still observe some accumulation inside some myonucleus as dots or line (Fig. 4A, Day5). In primary myoblasts induced to differentiate into “mature-like” fibers organized with myonuclei at periphery, SH3KBP1 was still detected at myonuclei vicinity but more accumulated at the interface between myonuclei “bottom” and muscle fiber interior and it also exhibited longitudinal/transversal staining (Fig. 4B, Day10). We thus wondered what kind of compartments could be controlled by SH3KBP1. To answer this question, we used stable C2C12 cell-line depleted for *Sh3kbp1* to investigate altered compartment phenotypes (Fig. 4C-D). We observed that, even if myonuclei are clustered in myotubes depleted for *Sh3kbp1*, Golgi marker RCAS1 was still mainly localized around myonuclei, as previously described for Golgi elements (Fig. 4C)(Ralston et al., 1999). On the contrary, the ER marker ERP72 that showed perinuclear localization in control myotubes was completely dispersed in *Sh3kbp1-depleted* myotubes (Fig. 4D). This result indicates a role for *Sh3kbp1* in the upkeep of ERP72-containing ER specifically at the vicinity of myonuclei, independently of Golgi complex architecture.

ERP72 (also called PDIA4) is a disulfide isomerase that acts as a folding chaperone for newly synthesized secretory proteins in the ER compartment (Satoh et al., 2005). Endogenous ERP72 co-immunoprecipitated with exogenous full-length GFP-tagged SH3KBP1 (Fig. 4E-G). Using a panel of SH3KBP1 deletion mutants, we determined that ERP72 interacts with the C-terminal part of SH3KBP1, independently of its C-terminus coiled-coil domain (Fig. 4E-G). ERP72 is described as an intraluminal ER protein that interacts with calnexin ER-chaperone (Penga et al., 2014). Interestingly, the C-terminus part of Calnexin is cytosolic and thus could be the cytoplasmic linker between SH3KBP1 and ERP72-containing Endoplasmic Reticulum (Wada et al., 1991). We next tested if SH3KBP1 physically interacts with Calnexin (Fig. 4E-G) and observed that endogenous Calnexin, as ERP72, co-immunoprecipitated with exogenous full-length GFP-tagged SH3KBP1 constructs. In addition, we also

identified the C-terminal part of SH3KBP1, independently of the C-terminus coiled-coil domain as the Calnexin-interacting domain (Fig. 4E-G). Therefore, Proline-and Serine-Rich domains of SH3KBP1 mediate the interaction with ERP72-positive ER through Calnexin binding.

SH3KBP1 progressively accumulates at the Z-line and interacts with DNM2.

We next investigated SH3KBP1 localization *in vivo*, in mature myofibers from adult skeletal muscle. SH3KBP1 accumulated specifically at the vicinity of myonuclei, forming a "cage" around myonuclei in *Tibialis Anterior* (TA) muscle (Fig. 5A-B, asterisks). This staining was confirmed in human muscle biopsies where we observed that myonuclei are positive for SH3KBP1 (Fig. S3G). In TA longitudinal section, SH3KBP1 exhibited a striated pattern at the I-band/Z-line zone, in between the staining of the voltage-dependent calcium channel, DHPRα, which labels T-tubules and forms a doublet band indicating that SH3KBP1 does not colocalize with DHPRα but follow, in a close proximity, T-tubules structures (Fig. 5C-E). To determine domains of SH3KBP1 responsible for this particular localization, we next tested *in vitro* expression of full-length SH3KBP1 or associated fragments into primary myoblasts induced to differentiate into "mature-like" fibers with peripheral myonuclei and proper sarcomere organization, reflected by striated actin staining (Fig. 5F-G). In this myofibers, full-length SH3KBP1 was present as small aggregation patches close to myonuclei, combined with striated pattern and accumulated at the Z-line with no overlap with actin staining (Fig. 5F-G, SH3KBP1-FL). N-terminus fragment of SH3KBP1 containing SH3 domains was only present as striated patterns with no particular accumulation at myonuclei vicinity, while the C-terminus SH3KBP1 fragments strongly accumulated at the periphery of muscle fibers, at the vicinity of myonuclei and at the Z-line with striated patterns (Fig. 5.F). Numerous proteins accumulate at the I-band/Z-line zone and participate in myofibers structuration (Burgoyne et al., 2015). Among them, Dynamin 2 (DNM2), a large GTPase implicated in cytoskeleton regulation and endocytosis, was previously described in HeLa cells as a SH3KBP1 interacting protein, through its proline-rich domain (Schroeder et al., 2010). To this end, we expressed, in C2C12 cells, full-length GFP-tagged-DNM2 with fragments of FLAG-tagged SH3KBP1 and immunoprecipitated SH3KBP1 constructs. This experiment confirmed that DNM2 interacts with SH3KBP1 through its N-terminal part (Fig. 5H-I). Therefore, in mature myotubes, SH3KBP1 accumulate at the Z-line where it forms a protein complex with DNM2.

SH3KBP1 is required in mature fibers for the maintenance of T-tubules.

We next assessed the impact of *Sh3kbp1* depletion on internal cell architecture. To this end, we used our *in vitro* model assay on mature fibers using primary myoblasts (Fig. 6A). Myofibrillogenesis in *Sh3kbp1* depletion condition was normal after 10 days of differentiation, reflected by F-actin staining (Fig. 6B). In control condition, we also observed that DHPRα staining which labels T-tubule, forms transversal doublet bands alternatively with actin staining (Fig. 6A). Quantification of the staining indicated that in control conditions, using either siRNA or shRNA scramble, nearly 30% of formed myofibers exhibit a transversal DHPRα staining, reflecting formation of mature T-tubules (Fig. 6A & C). On the contrary, in *Sh3kbp1*-depleted myofibers, DHPRα staining is much more punctuated, indicating the absence of mature T-tubules aligned with sarcomere structures (Fig. 6B) and suggesting a role of SH3KBP1 in T-tubule formation. Indeed, in *Sh3kbp1*-myofibers, we observed a drop of myofibers with transversal staining of DHPRα to nearly 5% of myofibers, correlating with an increase in random

DHPRα staining as dots along myofibers (Fig. 6C, Fig. S2E). To confirm these results we depleted *Sh3kbp1* from mature myofibers using shRNA electroporation technique directly in TA skeletal muscle of two-month-old mice (Fig. 6D). First, after 15 days of *Sh3kbp1* inhibition, an atrophic muscle fiber effect was observed in electroporated TA muscles fibers, reflected by a 35% decrease of the mean muscle fibers cross section area in *Sh3kbp1* fibers compared to controls (Fig. 6F), an effect that we previously observed *in vitro* (Fig. 2I). Moreover, T-tubule architecture appears perturbed in *Sh3kbp1* fibers, illustrated by an unequal DHPRα staining along fibers (Fig. 6D). Together, these results show that Sh3kbp1 contribute to T-tubule formation and maintenance in skeletal muscle fibers.

Sh3kbp1 is up regulated in a murine model of AD-CNM and inhibits CNM phenotypes.

Our data show that *Sh3kbp1* controls myonuclei dynamics and reticulum spatial organization and interacts with DNM2 which is mutated in dominant centronuclear myopathy characterized by myonuclear centralization (Romero and Bitoun, 2011). Heterozygous AD-CNM-Knock-In-*Dnm2*^{R465W} mouse model (KI-*Dnm2*$^{R465W/+}$) progressively develop muscle atrophy, impairment of contractile properties, histopathological abnormalities including slight disorganization of T-tubules and reticulum, and elevated cytosolic calcium concentration (Durieux et al., 2010). We first analyzed *Sh3kbp1* mRNA expression in TA skeletal muscle during mice development and aging (Fig. 7A). To our surprise, *Sh3kbp1* mRNA was progressively reduced from more than 30 % in 8 months old mice compare to 2 months old mice (Fig. 7A), suggesting a progressive loss of SH3KBP1 pool during aging. More interestingly, we also showed that in this KI-*Dnm2*$^{R465W/+}$ model, *Sh3kbp1* mRNA is significantly up-regulated during the first 4 months of mice development (Fig. 7A), suggesting a compensation mechanism, that can explain the limited ratio of atrophic fibers and absence of centralized myonuclei in this CNM model (Durieux et al., 2010). To address the role of SH3KBP1 in long-term muscle homeostasis in both wild type and KI-*Dnm2*^{R465W} mice, we investigated *in vivo* depletion of Sh3kbp1 protein. Down-regulation of *Sh3kbp1* was achieved using intramuscular TA muscle injections of an AAV cognate vector expressing shRNA targeting *Sh3kbp1* mRNA (AAV-shSh3kbp1) either in wild type or KI-*Dnm2*^{R465W} mice at 5 weeks of age, an age where muscle mass is nearly fully developed. This allowed addressing the role of *Sh3kbp1* specifically in adult skeletal muscle during the first three months of mice development and specifically in a period where we observed *Sh3kbp1* mRNA up-regulation in KI-*Dnm2*^{R465W} model (Fig. 7A). In wild type mice, *Sh3kbp1* mRNA level was decreased by 2.7 fold compared to PBS-injected muscles (Fig. S3A, WT). In KI-*Dnm2*^{R465W} mice, *Sh3kbp1* mRNA levels showed a 5.4 fold decrease compared to PBS-injected TA-muscles (Fig. S3A, WT, KI-*Dnm2*^{R465W}). No significant change of body weight was observed between AAV-shSh3kbp1-injected and PBS-injected conditions in both genotypes (Fig. S3B). However, a significant decrease in absolute force (g) developed by TA muscles specifically in KI-*Dnm2*^{R465W} mice depleted for *Sh3kbp1* was observed (Fig. 7D) suggesting a specific impact of *Sh3kbp1* down-regulation in the KI-*Dnm2*^{R465W} mice model. Interestingly, we observed a significant decrease of TA muscle mass of about 20%, when *Sh3kbp1* is depleted in both WT and KI-*Dnm2*^{R465W} mice (Fig. 7E). Cross-sectional areas of TA-muscle fibers were determined using transverse sections stained with laminin antibodies to define muscle fibers border (Fig. 7B-C). Global decrease in median myofibers area was observed in AAV-shSh3kbp1 injected TA-muscles compared to control muscles in WT (-30%) and KI-*Dnm2*^{R465W} (-20%) mice (Fig. 7F). Analysis of muscle fibers area repartition showed a significant increase in atrophic fibers in AAV-shSh3kbp1

injected muscles (Fig. S3C). Additionally, we observed a significant reduction of about 25% in the total number of fibers specifically in KI-*Dnm2*^{R465W} model depleted for *Sh3kbp1* (Fig. S3D). DNM2-CNM patients exhibit a predominance of type 1 muscle fibers (Romero and Bitoun, 2011). Thus, we investigated the ratio of slow fiber types in AAV-shSh3kbp1 injected TA-muscles, reflected by the expression of myosin heavy chain type 1 (Fig. 7C-D & G). In wild type conditions, slow fiber type accounted for 5 % of total muscle fibers. We observed that in AAV-shSh3kbp1 injected muscles, this ratio was slightly increased to reach 6.4 % of total muscle fibers, which is the same as what was observed in KI-*Dnm2*^{R465W} mice (Fig. 7G). However, when *Sh3kbp1* is depleted in KI-*Dnm2*^{R465W} muscle, this ratio increases drastically to reach 12% of total fibers (Fig. 7G). In the Knock-in mouse model, DNM2 mutation leads to autophagy impairment (Rabai et al., 2019; Durieux et al., 2010). During autophagosome formation, LC3-I (Microtubule-associated protein 1A/1B-light chain 3) is converted to LC3-II by conjugation to phosphatidylethanolamine lipid. To assess the impact of *Sh3kbp1* depletion on autophagy, LC3-II positive fibers was determined in Sh3kbp1 depleted fibers in both WT and KI-Dnm2^{R465W} mice. We observed an increase in number of LC3-II positive fibers in both genotypes but more pronounced in KI-*Dnm2*^{R465W} mice (Fig. 7H). Our *in vitro* data show that *Sh3kbp1* depletion increase fusion and alter myonuclei spreading (Fig. 1-3). We thus investigate the impact on the number of myonuclei and the ratio of internalized myonuclei by fibers in *Sh3kbp1* depleted myofibers but did not find any evidence for alteration compare to control conditions (Fig. S3E-F). Altogether, our data suggest that *Sh3kbp1* mRNA increase observed in AD-CNM model could be an attempt of compensatory mechanism as normalization of *Sh3kbp1* expression intensified muscle phenotype.

Discussion

Myonuclei movement's during muscle cell formation have been related to the activity of numerous microtubule binding proteins such as Motors and Maps (Gache et al., 2017). In immature myotubes, microtubules are organized into antiparallel arrays between adjacent myonuclei and contribute to the polarization/elongation of myotubes, alignment of myonuclei and ultimately organization of myosin filaments during sarcomere formation (Pizon et al., 2005; Metzger et al., 2012; Wang et al., 2013). This new orientation/architecture of the microtubule network directly influences myoblasts/myotubes fusiform shape, as microtubule network forces are applied at the extremity of polarized myotubes and also in-between myonuclei (Metzger et al., 2012); it also contributes to myonuclei spreading along myotubes length (Tassin et al., 1985). This precise myonuclei organization in muscle fibers gives rise to the formation of so-called "MyoNuclear Domains" (MNDs) wherein each myonucleus is responsible for gene expression in its surrounding cytoplasm and guaranties functional integrity of muscles (Qaisar, 2012; Liu et al., 2009). However, regulation of processes involved in myonuclei positioning in developing muscle fibers, not directly linked to the microtubule network, are still unknown.

The present study demonstrates that a protein related to the endoplasmic reticulum (ER) network controls both myotubes elongation and myonuclei localization/spreading in developing myofibers, two processes that are closely linked as they both depends on microtubule network organization. Early steps of myonuclei positioning in myotubes depend on an interplay between microtubules, microtubules-associated-proteins such as MAP4, MAP7 and motors proteins such as Dynein and Kif5B (Gimpel et al., 2017; Mogessie et al., 2015; Metzger et al., 2012; Cadot et al., 2012; Wang et al., 2013; Wilson and Holzbaur, 2014a). This process also depends on

myonuclei membrane associated components such as Nesprin-1 or AKAP9 (Gimpel et al., 2017; Wilson and Holzbaur, 2014b; Doñate Puertas et al., 2018). Here, we show that SH3KBP1 depletion leads to longer and thinner myotubes without significant alteration of the microtubules network compared to control (Fig. 1-3 & data not shown). We find that the C-terminus part of SH3KBP1 is associated with ERP72-positive ER probably through its binding to Calnexin (Fig. 4E-G). This association scaffolds ERP72-associated ER specifically at myonuclei vicinity, without affecting Golgi apparatus integrity (Fig. 4A-D). Recently, ER has been implicated in governing both microtubule alignment and cytoplasmic streaming (Kimura et al., 2017). Kimura *et al* propose that local cytoplasmic flow generated along microtubules is transmitted to neighboring regions through the ER and in turn, aligns microtubules and self-organizes the collective cytoplasmic flow. SH3KBP1, by shaping and maintaining ER clustering during myofibers development could contribute to prevent microtubules network anchoring at the nucleus membrane and thus local microtubule network organization. In this view, SH3KBP1, during myoblasts fusion process could disorganize parallel microtubules organization and thus decrease forces applied on myotubes tips extremity. This phenomenon could lead to the control of myotubes length, but also of both myonuclei motility and velocity (Fig. 2).

SH3KBP1 staining is diffuse in dividing cells, while it progressively accumulates at the vicinity of myonuclei during differentiation process (Fig. 4). A few proteins have been shown to form a flexible perinuclear shield that can protect myonuclei from extrinsic forces (Wang et al., 2015; Ghasemizadeh et al., 2019). To note, recent data show that disruption of one component of this perinuclear shield, MACF1 protein, increases myonuclei velocity (Ghasemizadeh et al., 2019). Consequently, SH3KBP1 probably belongs to the group of proteins that contribute to the stability of this perinuclear shield through the maintenance of ER at the vicinity of myonuclei. In accordance with this preferential localization at the proximity of myonuclei, SH3KBP1 staining in transversal *Tibialis Anterior* muscle section is very intense at myonucleus site whereas nuclei outside the fiber remains negative (Fig. 5A-B). In human muscle biopsies, this localization around myonuclei is maintained even in centralized nuclei from CNM patient (Fig. S3G). The three SH3 domains of SH3KBP1 have been shown to cluster multiple proteins and protein complexes that can also contributes to the stability of those interactions. Havrylov *et al* identified using mass spectrometry, few microtubule-binding-proteins such as MAP7 and MAP4 that can potentially interact with SH3 domains of SH3KBP1 and have already been shown to control myonuclei positioning in myotubes (Metzger et al., 2012; Mogessie et al., 2015; Havrylov et al., 2009). However, we failed to confirm the interaction of SH3KBP1 with either MAP7 or MAP4 in muscle cells (data not shown). Alternatively, SH3KBP1 also interacts with dynamin-2 (DNM2) and has been shown to participate in dynamics instability of microtubules (Tanabe and Takei, 2009) and microtubule nucleation (Thompson et al., 2004). The failure of recruiting DNM2 at the right place during myotubes formation after SH3KBP1 depletion could also contribute to the aberrant myonuclei spreading (Fig. 1). Interestingly, in CNM-KI-*Dnm2*^{R465W} mouse model, Fongy *et al* show that myonuclei move and spread properly in heterozygous myotubes but hypothesize a defect in nuclear anchoring at the periphery (Fongy et al., 2019). Several studies pointed the importance of cytoskeleton, including MAPs, microtubules and intermediate filaments, in the nuclear anchorage in mature muscle (Ghasemizadeh et al., 2019; Roman et al., 2017). SH3KBP1 dependent ER-scaffolding could participate in myonuclei anchoring at the periphery of myofibers and thus in the recruitment and stabilization of a network of proteins at the vicinity of myonuclei. This hypothesis is supported by our data showing an increase in the percentage of the time in motion

of myonuclei, in the absence of SH3KBP1 (Fig. 2D), correlated with the strong staining of myonuclei in mouse and human models (Fig. 5A & S3G).

In mature myofibers, SH3KBP1 depletion leads to more aggregated myonuclei phenotype, suggesting that a failure in the early phases of myonuclear positioning is difficult to compensate (Fig.2G). Interestingly, *sh3kbp1* depletion in long-term primary myofibers culture induces a reduction in myofibers width (Fig. 2I). These results are confirmed *in vivo* as *sh3kbp1* down regulation in *Tibialis Anterior* muscle reduce from more than 30% the average cross section areas of myofibers (Fig. 6E-F & 7F). Moreover, SH3KBP1-depleted mature myofibers show disorganized perinuclear endoplasmic reticulum (ER) (Fig 4). Of interest, ER is one initiation site for autophagic process and ER selective autophagy (called ER-phagy or reticulophagy) has been described to control ER shape and dynamics through ER-phagy receptors that address ER portions to the autophagosomes (Grumati et al., 2018). SH3KBP1 depletion increases the number of LC3II positives myofibers in *Tibialis Anterior* muscle (Fig. 7H), suggesting a possible increase of autophagosomes number. Additionally, SH3KBP1 interacts with dynamin-2 (Fig. 5-G), which is also involved in the autophagic lysosome reformation (Schulze et al., 2013). This autophagy-dependent modulation of muscle homeostasis could first explain the decrease of Cross Section Area and myofibers width that we observed and ultimately the reduction of muscle myofibers (Fig. 2I, 7E-F & S3C). Interestingly, autophagy genes have been involved in muscle myonuclei positioning during Drosophila metamorphosis (Fujita et al., 2017). Whether this process is involved in SH3KBP1-dependent myonuclei positioning will be the subject of further investigations.

SH3KBP1 depletion shows that T-tubule formation is dramatically impaired both *in vitro* and *in vivo* (Fig. 6). Myofibrils provide the contractile force under the control of the 'excitation-contraction coupling' system that includes two membranous organelles: the sarcoplasmic reticulum (SR) and Transverse (T)-tubules (Al-Qusairi and Laporte, 2011). These two-membrane systems are structurally associated to form the triads of skeletal muscle cells. SR is a complex network of specialized smooth endoplasmic reticulum, essential to transmit the electrical impulse as well as in the storage of calcium ions. SR is built from the formation and maturation of two distinct and functionally related domains: the longitudinal SR and the junctional SR that together wrap the contractile apparatus. T-tubule network is continuous with the muscle cell plasma membrane (PM) and begins from the invagination of PM in a repeated pattern at each sarcomere (Barone et al., 2015). These two-membrane systems are structurally associated to maintain their typical organization in muscle cells. SH3KBP1 depletion seems to alter more specifically junctional SR rather than longitudinal SR as it specifically alters transversal organization of T-tubules (Fig. 6A-C). One hypothesis, recently suggested by Quon *et al*, is that non-vesicular lipid transport and lipid biosynthesis could intersect at ER-PM membrane contact sites and would serve as a nexus, coordinating requirements in the PM for lipids with their production in the ER (Quon et al., 2018).

Autosomal dominant CNM is caused by heterozygous mutations in the *DNM2* gene, which encodes the Dynamin 2 (DNM2) GTPase enzyme (Romero, 2010). *DNM2*-related autosomal dominant (AD)-CNM was initially characterized as a slowly progressing muscle weakness affecting distal muscles with onset in early adulthood. DNM2-R465W missense mutation represents the most frequent mutation in humans and a knock-in (KI) mouse

model expressing this mutation has been generated that develops a progressive muscle weakness (Durieux et al., 2010). Expressing DNM2-R465W mutation in mice leads to contractile impairment that precedes muscle atrophy and structural disorganization that mainly affects both mitochondria and endo/sarcoplasmic reticulum. Interestingly, CNM- KI-*Dnm2*^{R465W} mouse model exhibits twice more Sh3kbp1 mRNA amount in the first 4 months than control mice before normalization after 8 months (Fig. 7A). Of note, this increase is concomitant with transient transcriptional activation of both ubiquitin–proteasome and autophagy pathways at 2 months of age in the TA muscle of the KI-Dnm2 mice (Durieux et al., 2010). One can hypothesize that this elevated amount of *sh3kbp1* is one of the factors that limits activation of autophagy pathway activation and thus slows-down CNM associated phenotype. In accordance with this hypothesis, we find that *sh3kbp1* depletion increase CNM phenotype (Fig. 7D-H). In conclusion, increased amount of SH3KBP1 could delay the CNM phenotype development by stabilizing Triads and the braking of the autophagy response.

Finally, our data show that *Sh3kbp1* depletion increases fusion events in transfected primary myoblasts and stable cell line. *In vivo,* when *Sh3kbp1* is depleted from mature myofibers in a period of time characterized by minimal myonuclei accretion in muscle fibers, we observe a tendency to slightly increase the percentage of myonuclei per myofibers in both WT and KI-*Dnm2*^{R465W} conditions (Fig. S3E). These data suggest that SH3KBP1 could contribute to fusion efficiency by a still unknown mechanism. The role of ER on myoblast fusion is poorly documented and its effect seems to be more indirectly linked to pathways related to physiologic ER stress signaling and SARC (stress-activated response to Ca^{2+}) body formation more than a direct impact on myoblast fusion (Bohnert et al., 2017; Nakanishi et al., 2007; 2015). Alternatively, our *in vitro* data suggest that the global microtubule network organization is not changed but that dynamics of organelles related to microtubules pathways are improved, reflected by the increase of myonuclei dynamics in the absence of SH3KBP1 (Fig. 2A-F). There is also no evidence of a clear specific role of microtubules network on the fusion potential, however, the modification of microtubule dynamics/orientation by different MAPs are known to alter fusion potential (Mogessie et al., 2015; Straube and Merdes, 2007; Cadot et al., 2012). Fusion processes require remodeling of both membranes and actin cytoskeleton polymerization at the site where two membrane will fuse (Sampath et al., 2018). One can hypothesize that SH3KBP1 could contribute to the fusion process through the control of membrane remodeling on specifics PM-ER sites. Incidentally, we noticed that in absence of SH3KBP1, myotubes are longer, increasing consequently the fusiform shape of cells (Fig. 1D). As fusion mainly occurs at the tips of myotubes (Cadot et al., 2015; 2012), this increase of myotubes polarization could contribute to accumulate proteins involved in fusion specifically at the tips of myotubes and consequently favor fusion capacity.

Altogether these data are in agreement with an involvement of *Sh3kbp1* in muscle fibers formation and maintenance. In the present study, we show that the adaptor protein SH3KBP1, through its N-terminus part, is able to scaffold ER *via* an interaction with Calnexin. SH3KBP1 also governs myonuclei motion and spatial organization as well as myoblast fusion. Additionally, we observed that SH3KBP1 interacts with DNM2 and organizes T-tubule formation in skeletal muscle; moreover, its down-regulation contributes to an increase of the CNM-like phenotype in the most frequent mutation model (KI-*Dnm2*^{R465W}) of autosomal dominant centronuclear myopathy. Altogether, our data suggest that SH3KBP1 increase observed in AD-CNM model could be an attempt

of compensatory mechanism in CNM- KI-*Dnm2*^{R465W} model and could be used as a preventing factor in the development of CNM phenotype.

Figures

Figure 1: Myonuclear positioning during primary myotubes formation is controlled by *sh3kbp1.* (A) Scheme of sequential steps in order to obtain immature myotubes from primary myoblasts. siRNAs were transfected 24 hours before myoblasts fusion. (B-C) Representative immunofluorescence staining of myosin heavy chain (green) and myonuclei (red) in primary myotubes treated for scramble (B) or a pool of 2 individual siRNAs targeting *Sh3kbp1* mRNA (C) after 3 days of differentiation, white arrows indicate "tips-aggregated myonuclei". Scale Bar: 150µm. (D-E) Myotubes lengths and Mean distances between each myonuclei and myotube's centroid (DMcM) ranked by myonuclei content per myotubes were quantified after 3 days of differentiation in cells treated with a scramble or *Sh3kbp1* siRNAs. Data from three independent experiments were combined. Scramble siRNA cells (n=1010) and *Sh3kbp*1 siRNA cells (n=1093), Unpaired t-test, ***$p < 0.001$. Center lines show the medians; box limits indicate the 25th and 75th percentiles as determined by R software; whiskers extend 1.5 times the interquartile range from the 25th and 75th percentiles, outliers are represented by dots. (F) Myonuclei Spreading Graph (MSG) represents statistical spatial distribution of myonuclei along myotubes in scramble and in *Sh3kbp1* siRNA-treated myotubes; white-line represents the mean value of the statistical frequency.

Figure 2: Myonuclei localization and motion are affected in *sh3kbp1* depleted primaries myofibers and lead to myonuclei aggregation. (A) Scheme of sequential steps in order to obtain mature myofibers from primary mice myoblasts. siRNAs or shRNA were transfected during precocious steps of myoblasts fusion. (B-F) Primary myoblasts were treated with scramble or *Sh3kbp1* shRNA tagged with GFP (Green) and co-transfected with RFP-lamin-chromobody® (red) and were induced to differentiate for 5 days into myofibers. (B-D) Quantification of myonuclei clustering by myotubes (B), myonuclei time in motion (C) and myonuclei speed (D) were quantified using SkyPad analysis (Cadot et al., 2014). Data from three independent experiments were combined. Unpaired t-test, ***$p < 0.001$, **$p < 0.01$. (E) Representative immunofluorescence staining of RFP-lamin-chromobody® (red) and shRNA tagged with GFP (Green) in primary myotubes treated with scramble or *Sh3kbp1* shRNA after 5 days of differentiation into myofibers. Scale Bar: 150µm. (Asterisks represents myonuclei clustering) (F) Frames from a 16h time-lapse movie in two channels (shRNA in green and lamin-chromobody® in red) of primary myotubes. In the first frame (on the left), myofibers are selected in white, which corresponds to the region used to create the adjacent kymograph. Scale Bar: 30µm. (Asterisks 1-5 are examples of individual myonuclei tracking). (G) Four representative images of 10 days differentiated myofibers transfected with either scramble or *Sh3kbp1* shRNA tagged with GFP, shRNA (Green) myonuclei (red). Scale Bar: 10µm. (Asterisks are individual myonuclei) (H-I) Quantification of the mean distance between pairwise myonuclei (H) and mean myofibers width (I) in 10 days differentiated myofibers treated with scramble siRNA or shRNA, a pool of 2 individual siRNAs or an individual shRNAs targeting *Sh3kbp1*. Data from three independent experiments were combined. Center lines show the medians; box limits indicate the 25th and 75th percentiles as determined by R

493 software; whiskers extend 1.5 times the interquartile range from the 25th and 75th percentiles, outliers are
494 represented by dots. Unpaired t-test, ***p < 0.001, **p < 0.01, *p < 0.05.
495
496 **Figure 3: SH3KBP1 is induced during myotubes differentiation and controls myonuclei aggregation in**
497 **C2C12 cells.** (A) Western blot analysis of SH3KBP1 protein expression in total protein extracts from
498 proliferating (P) or differentiating C2C12 cells for up to 5 days. C2C12 differentiation is assessed by Myogenin
499 expression and Tubulin is used as loading control. (B-C) qRT-PCR analysis of *Sh3kbp1* (B) and *Myogenin* (C) gene
500 expression level relative to *CycloB, Gapdh, GusB, Rpl41* and *Tbp* gene in proliferating C2C12 cells (P) or
501 differentiating C2C12 cells for up to 5 days. (D) Representative western blots analysis of SH3KBP1 protein down-
502 regulation in stable cell line constitutively expressing shRNA construct targeting *Sh3kbp1.* Tubulin is used as
503 loading control. (E) Representative immunofluorescence staining of myosin heavy chain (green) and myonuclei
504 (red) in 3 or 6 days cultured C2C12 stable cell lines expressing scramble shRNA or shRNA targeting *Sh3kbp1.*
505 Zooms 1 & 2 are magnifications of images in white dots rectangle in 6 days old myotubes. Scale bars, 150 µm and
506 15 µm in zoom. (F) Quantification of the number of myonuclei by clusters in C2C12 cells stable cell line
507 expressing scramble shRNA or shRNA targeting *Sh3kbp1* after 5 days of differentiation. Data from three
508 independent experiments were combined. Unpaired t-test, ***p < 0.001, *p < 0.05. Center lines show the
509 medians; box limits indicate the 25th and 75th percentiles as determined by R software; whiskers extend 1.5
510 times the interquartile range from the 25th and 75th percentiles, outliers are represented by dots.
511 **Figure 4: SH3KBP1 is localized near and inside myonuclei and controls ERP72 positives Endoplasmic**
512 **reticulum through Calnexin interaction during *in vitro* muscle fibers differentiation.** (A-B) Representative
513 immunofluorescent staining of SH3KBP1 (green), Actin (Red) and myonuclei (blue) in the course of myotube
514 formation in C2C12 cells line in proliferation (P) or after 2 and 5 days of differentiation (A) or in the course of
515 myofibers formation in primary myoblast cultures in proliferation (P) or after 3 and 10 days of differentiation
516 (B). Scale bars, 10 µm. (C-D) Representative Immunofluorescent staining of Golgi Marker (RCAS1, for receptor
517 binding cancer antigen expressed on SiSo cells, red) (C) and Endoplasmic Reticulum (ERP72, for Endoplasmic
518 reticulum resident protein 72, red) (D) and myonuclei (blue) in 6 days cultured C2C12 stable cell line expressing
519 either scramble shRNA or shRNA targeting *Sh3kbp1* gene (GFP-shRNA). Scale bars, 100 µm. (E) Scheme of
520 SH3KBP1 constructs, labeled with GFP in the N-terminus part, used for immunoprecipitation assay in (F-G). FL:
521 full length. (F) Representative western blot with indicated antibodies (right) in C2C12s expressing GFP-
522 SH3KBP1 constructs (top). (G) Representative western blot with indicated antibodies (right) of GFP-SH3KBP1
523 constructs immunoprecipitation using C2C12 expressing indicated constructs (top). Blots were repeated more
524 than 3 times.
525
526 **Figure 5: SH3KBP1 is localized near myonuclei and at I-band/Z-line zone in muscle fibers *in vivo* and**
527 **interact with DNM2.** (A-B) Representative images of *Tibialis Anterior* muscle transversals cross-section stained
528 for SH3KBP1 (green) and myonuclei (red). Asterisks show myonuclei inside myofibers. Scale bars, 150 µm. (C-E)
529 Representative images of *Tibialis Anterior* muscle longitudinal cross-section stained for SH3KBP1 (red) and
530 DHPR1α, for DyHydroPyridine Receptor alpha (green). Scale bars, 150 µm. (F) Representative
531 immunofluorescent staining of long term expression of SH3KBP1 constructs (listed in Fig. 4E) in green (GFP-
532 constructs), Actin (red) and myonuclei (blue) in 10 days differentiated primary myofibers. Scale bars, 10 µm. (G)

Line scan of the yellow boxes to visualize transversal organization of SH3KBP1 (green) and actin (red) staining. (H) Western blot with indicated antibodies (right) in C2C12 cells expressing Flag-SH3KBP1 constructs (top) and GFP-DNM2. (I) Representative western blot with indicated antibodies (right) of DNM2-GFP constructs immunoprecipitation using C2C12 expressing indicated constructs (top).

Figure 6: SH3KBP1 controls T-tubule organization during muscle fibers formation and in mature myofibers. (A-B) Representative immunofluorescent image of DHPR1-α (green), Actin (red) and myonuclei (blue) staining in 10 days cultured primary myotubes after scramble siRNA (A) or *Sh3kbp1* siRNA (B) transfection. Scale bars, 20 μm. (C) Quantification of DHPR-α staining aspects in mature myofibers treated with either scramble siRNA, a pool of 2 individual siRNAs targeting *Sh3kbp1* mRNA, scramble shRNA or an individual shRNA targeting *Sh3kbp1* mRNA. Data from three independent experiments were combined. Unpaired t-test, ***p < 0.001, **p < 0.01. Details for different categories are available in Fig. S2E. (D-E) Representative images of transversals (left) cross-section of *Tibialis Anterior* muscle electroporated with scramble or an individual shRNAs targeting *Sh3kbp1 and* stained for GFP (green) and myonuclei (blue). Scale bars, 50 μm (F) Quantification of muscle fibers electroporated with scramble or an individual shRNAs targeting *Sh3kbp1*. Center lines show the medians; box limits indicate the 25th and 75th percentiles as determined by R software; whiskers extend 1.5 times the interquartile range from the 25th and 75th percentiles, outliers are represented by dots. Unpaired t-test, ***p < 0.001. (G-H) Representative images of longitudinal cross-section of *Tibialis Anterior* muscle electroporated with scramble or an individual shRNAs targeting *Sh3kbp1 and* stained for GFP and DHPR-α. Scale bars, 20 μm.

Figure 7: *sh3kbp1* silencing worsened CNM phenotype in KI-DNM2^{R465W} mice model. (A) qRT-PCR analysis of *Sh3kbp1* gene expression relative to *Nat10* gene *Tibialis Anterior* muscles from WT or KI-*Dnm2*^{R465W} mice at 1, 2, 4 and 8 months of age. Non-parametric one-way Anova used for statistical significance ***p < 0.001, **p < 0.01, *p < 0.05. (B-C) Representative images of *Tibialis Anterior* muscle cross-section from WT or KI- *Dnm2*^{R465W} mice at the age of 4 months, injected with either PBS or AAV cognate vector expressing shRNA targeting *SH3KBP1* mRNA (Sh3kbp1-shRNA) for 3 months and stained for Dapi (Blue), Laminin (green) and MyHC (red). Scale Bars = 150 μm. (D-H) Quantification of Absolute force (P0) (D), *Tibialis Anterior* muscle mass (E), mean cross-sectioned myofibers areas (F), percentage of slow fibers (MHC1 positives) (G) and percentage of LC3II-positive fibers (H) of *Tibialis Anterior* muscles from WT or KI- *Dnm2*^{R465W} mice at the age of 4 months, injected with either PBS or AAV cognate vector expressing shRNA targeting *SH3KBP1* mRNA (Sh3kbp1-shRNA) for 3 months. Data from at least 4 mice in each condition were combined. Unpaired t-test, ***p < 0.001, **p < 0.01, *p < 0.05. Center lines show the medians; box limits indicate the 25th and 75th percentiles as determined by R software; whiskers extend 1.5 times the interquartile range from the 25th and 75th percentiles, outliers are represented by dots.

Supplementary figure 1: SH3KBP1 affects myoblast fusion. (A) Representative western blot analysis of SH3KBP1 protein expression in total protein extracts from differentiating primary myotubes treated with scramble or siRNA (#1 & #2) or a pool of siRNA targeting *SH3KBP1* mRNA. Loading control is tubulin. (B-C) Representative immunofluorescent images of 3 days of primary differentiated myotubes stained for myosin heavy chain (green) and myonuclei (red) and treated with scramble (B) or with a pool of 2 individual *Sh3kbp1*

siRNAs. Scale Bar: 50µm. (D-G) Quantification of differentiation index (percentage of nuclei in Myosin Heavy Chain positives cells) (D), Fusion index (percentage of nuclei inside myotubes) (E), Average number of nuclei by myotubes (F) and distribution of myotubes classified depending on the number of nuclei in myotubes (G). Data from three independent experiments were combined. Unpaired t-test, **p < 0.01, *p < 0.05. Center lines show the medians; box limits indicate the 25th and 75th percentiles as determined by R software; whiskers extend 1.5 times the interquartile range from the 25th and 75th percentiles, outliers are represented by dots.

Supplementary figure 2: SH3KBP1 affects myoblast fusion and localization of myonuclei in C2C12 cells. (A-B) Distribution of 3 days differentiated C2C12 myotubes formed from stable cell line expressing either scramble or *Sh3kbp1* shRNAs and classified depending on nuclei content inside myotubes after (A) 3 days or (B) 5 days of differentiation. (C) Representatives immunofluorescent staining of myosin heavy chain (green) and myonuclei (red) in stable cell line expressing *Sh3kbp1* shRNA (top) or co-transfected with full-length SH3KBP1 (bottom) after 5 days of differentiation. Scale Bar: 50µm. (D) Quantification of the percentage of nuclei by clusters in stable cell line expressing *Sh3kbp1* shRNA and co-transfected with mCherry or full-length SH3KBP1 plasmid. Data from three independent experiments were combined. Unpaired t-test, ***p < 0.001, **p < 0.01, *p < 0.05. Center lines show the medians; box limits indicate the 25th and 75th percentiles as determined by R software; whiskers extend 1.5 times the interquartile range from the 25th and 75th percentiles, outliers are represented by dots. (E) Representatives immunofluorescent categories of staining for DHPR-alpha in 10 days differentiated myofibers. Scale Bar: 2µm.

Supplementary figure 3: *sh3kbp1* silencing worsened CNM phenotype in KI-DNM2^{R465W} mice model. (A) qRT-PCR analysis of *Sh3kbp1* gene expression relative to Nat10 gene in 4 months *Tibialis Anterior* muscles from WT or KI- *Dnm2*^{R465W} mice injected with either PBS or AAV cognate vector expressing shRNA targeting *SH3KBP1* mRNA (Sh3kbp1-shRNA). ***p < 0.001. (B-F) Quantification of total body mass (B), distribution of cross-sectioned myofibers areas (C), number of fibers by muscles (D), number of myonuclei by fiber (E) and number of internalized myonuclei (F) in *Tibialis Anterior* muscles from WT or KI-*Dnm2*^{R465W} mice at the age of 4 months, injected with either PBS or AAV cognate vector expressing shRNA targeting *SH3KBP1* mRNA (AAV-SH3KBP1) for 3 months. Data from at least 4 mice in each condition were combined. Unpaired t-test, ***p < 0.001, **p < 0.01, *p < 0.05. Center lines show the medians; box limits indicate the 25th and 75th percentiles as determined by R software; whiskers extend 1.5 times the interquartile range from the 25th and 75th percentiles, outliers are represented by dots. (G) Immunofluorescent staining of SH3KBP1, Actin and nuclei in two control human patient and in two patients expressing DNM2-R465W point mutation.

Materials and methods

Cell culture

Primary myoblasts were collected from wild type C57BL6 mice as described before (Falcone et al., 2014; Pimentel et al., 2017). Briefly, Hindlimb muscles from 6 days pups were extracted and digested with collagenase (Sigma, C9263-1G) and dispase (Roche, 04942078001). After a pre-plating step to discard contaminant cells such as fibroblasts,

myoblasts were cultured on matrigel coated-dish (Corning, 356231) and induced to differentiate in myotubes for 2-3 days in differentiation media (DM: IMDM (Gibco, 21980-032) + 2% of horse serum (Gibco, 16050-122) + 1% penicillin-streptomycin (Gibco, 15140-122)). Myotubes were then covered by a concentrated layer of matrigel and maintained for up to 10 days in long differentiation culture medium (LDM: IMDM (Gibco, 21980-032) + 2% of horse serum (Gibco, 16050-122) + 0.1% Agrin + 1% penicillin-streptomycin (Gibco, 15140-122)) until the formation of mature and contracting myofibers. LDM was changed every two days.

Mouse myoblast C2C12 cells were cultured in Dulbecco's modified Eagle's medium (DMEM (Gibco, 41966029) + 15% fetal bovine serum (FBS) (Gibco, 10270-106) + 1% penicillin-streptomycin (Gibco, 15140-122))) and were plated on 0.1% matrigel-coated dishes for 1-2 days before differentiation. Differentiation was induced by switching to differentiation media (DMEM + 1% horse serum).

Cell transfection

For C2C12 cells, 3 different siRNAs Silencer per gene were transfected using Lipofectamine 2000 (ThermoFisher Scientifics, 11668-019) at the final concentration of 10 nM, following manufacturer instructions, 2 days before differentiation. For shRNA cDNA (Geneocopia) transfection, Lipofectamine 2000 (ThermoFisher Scientifics, 11668-019) was used following manufacturer instructions.
For primary cells, siRNA were transfected using Lipofectamine 2000 (ThermoFisher Scientifics, 11668-019) at the final concentration of 2 nM. shRNA (Geneocopia), Eb1 or RFP-Lamin-chromobody (Chromotek) cDNA were transfected using Lipofectamine 3000 (ThermoFisher Scientifics, L3000-008). For the list of siRNA, shRNA and DNA constructs, refer to supplementary table 1.

Protein sample preparation

For primary cultured cells or C2C12 cell lines, cells were harvested, using Trypsin for 5min at 37°C and centrifuged at 1500RPM for 5min at 4°C. Cell pellets were diluted and incubated in the optimal volume of RIPA lysis buffer containing phosphatases inhibitors (Sigma, P5726-5mL) and proteases inhibitors (Sigma, P8340) for 10min at 4°C. Following a sonication and a centrifugation at 12000RPM for 10min at 4°C, protein samples were collected for further uses. The concentration of proteins was determined using BCA protein assay kit (Thermo Fisher Scientifics, 23225) as described by the manufacturer.

Western blot

To carry out western blots, the same amount of sample were loaded in 6% acrylamide gels and were migrated at 130V for 10min followed by 160V for 90min. iBlot 2 mini slacks (Thermo Fisher Scientifics, IB23002) semi-dry system was used to transfer the proteins to nitrocellulose membranes. Membranes were then saturated in 5% milk in TBS for 1h at room temperature (RT) and were incubated in primary antibodies in 5% milk in TBS over night at 4°C. Following washes by 0.1% Tween-20-1X TBS, the membranes were incubated in HRP conjugated secondary antibodies in 5% milk in TBST for 1h at room temperature (RT). Following washes by 0.1% Tween-20-1X TBS the detection of the target proteins was carried out using Super Signal West Femto (Thermo Fisher Scientifics, 34095) and ChemiDoc imaging system (BioRad).

Antibodies

Cells were fixed in 4%PFA in PBS for 20min at 37°C followed by washes with PBS and permeabilization with 0.5% Triton-X100 in PBS for 5min at RT. Following washes with PBS, cells were saturated with 1% BSA in PBS for 30min at 37°C and incubated in primary antibodies over night at 4°C. Following washes with 0.05% Triton-X100 in PBS, cells were incubated in secondary antibodies or dyes for 2hrs at RT followed by washes with 0.05% Triton-X100 in PBS and a last wash in PBS. Cultured myofibers were imaged using either Z1-AxioObserver (Zeiss) or confocal SP5 microscope (Leica). For the list of antibodies and dilution, refer to supplementary table 2.

Video-Microscopy

Time-lapse images were acquired using Z1-AxioObserver (Zeiss) with intervals of 20 minutes. Final videos were analyzed using Metamorph (Zeiss) and SkyPad plugin as described before (Cadot et al., 2014).

Adeno-Associated Virus production and *in vivo* transduction

A cassette containing the small hairpin (sh) RNA under the control of H1 RNA polymerase III promoter was inserted in a pSMD2 expression plasmid. AAV vectors (serotype 1) were produced in HEK293 cells after transfection of the pSMD2-shRNA plasmid, the pXX6 plasmid coding for viral helper genes essential for AAV production and the pRepCap plasmid (p0001) coding for AAV1 capsid as described previously (Riviere et al, 2006). Viral particles were purified on iodixanol gradients and concentrated on Amicon Ultra-15 100K columns (Merck-Millipore). The concentration of viral genomes (vg/ml) was determined by quantitative real-time PCR on a LightCycler480 (Roche diagnostic, France) by using TaqMan probe. A control pSMD2 plasmid was tenfold serially diluted (from 10^7 to 10^1 copies) and used as a control to establish the standard curve for absolute quantification. Male wild type and heterozygous KI-*Dnm2*^{R465W} mice were injected under isoflurane anesthesia. Two intramuscular injections of 30 µl within 24h interval were performed using 29G needle in TA muscles corresponding to 10^{11} viral genomes per muscle. All of the experiments and procedures were conducted in accordance with the guidelines of the local animal ethics committee of the University Claude Bernard – Lyon 1 and in accordance with French and European legislation on animal experimentation and approved by the ethics committee CECCAPP and the French ministry of research.

Muscle contractile properties

The isometric contractile properties of TA muscles were studied *in situ* on mice anesthetized with 60 mg/kg pentobarbital. The distal tendon of the TA muscle was attached to a lever arm of a servomotor system (305B Dual-Mode Lever, Aurora Scientific). The sciatic nerve was stimulated by a bipolar silver electrode using a supramaximal (10 V) square wave pulse of 0.1 ms duration. Absolute maximal isometric tetanic force was measured during isometric contractions in response to electrical stimulation (frequency of 25–150 Hz; train of stimulation of 500 ms). All isometric contraction measurements were made at optimal muscle length. Force are expressed in grams (1 gram = 9.8

mNewton). Mice were sacrificed by cervical dislocation and TA muscles were weighted. Specific maximal force was calculated by dividing absolute force by muscle weight.

RNA extraction

After the addition of Trizol (Sigma, T9424-200mL) on each sample, lysing matrix D and fast prep system (MPbio, 6913-100) were used for sample digestion and pre-RNA extraction. In order to extract RNA, samples were incubated in chloroform for 5min at RT, centrifuged for 15min at 12000 rcf at 4°C and incubated in the tubes containing isopropanol (precipitatation of RNA) for 10min at RT. following a centrifuge of samples for 15min at 12000rcf at 4°C, samples were washed 2 times with 70% ethanol and the final RNA pellets were diluted in ultra-pure RNase free water (Invitrogen, 10977-035). RNA concentration was calculated using Nanodrop (ThermoFisher Scientifics).

RT-q-PCR on cells

Goscript Reverse Transcriptase System (Promega, A5001) was used, as described by the manufacturer to produce the cDNA. Fast Start Universal SYBR Green Master (Rox)(Roche, 04913914001) and CFX Connect™ Real-Time PCR Detection System (BioRad) were used to carry out the quantitative PCR using the following primer sets. The CT of target genes were normalized on 3 control genes. For the list of primers used, refer to supplementary table 1.

RT-q-PCR on muscle samples

50 longitudinal sections (12 µm) of TA muscles were cut and used for RNA isolation and RT-qPCR. Total RNA was extracted from muscle by using NucleoSpin (Macherey-Nagel). RNA (200 ng) was reverse transcribed using Reverse Transcription Core Kit (Eurogentec). Real-time PCR was performed in a 20 µL final volume using the Takyon No Rox SYBR kit (Eurogentec). Fluorescence intensity was recorded using a CFX96 Real-Time PCR Detection System (Bio-Rad) and the data analyzed using the ΔΔCt method of analysis. Reference gene 18s was used to normalize the expression level of the gene of interest as previously described (Pfaffl et al., 2001). The selected forward and reverse primer sequences are listed in Table 1. Statistical analyses were performed using GraphPad PRISM 5.0 (La Jolla). Data were analyzed for normal distribution using Shapiro-Wilk test. Non-parametric one-way Anova (n = 4-6) was used to determine transcripts expression level. Primers were designed using Primer 3 software from gene sequences obtained from Genebank. Primer specificity was determined using a BLAST search. For the list of primers used, refer to supplementary table 1.

Histological staining and analysis

Tibialis anterior muscles were collected, embedded in tragacanth gum, and quickly frozen in isopentane cooled in liquid nitrogen. Cross-sections (10µm thick) were obtained from the middle portion of frozen muscles and processed for histological, immunohistochemical, enzymohistochemical analyses according to standard protocols. The fibre cross-sectional area and the number of centrally nucleated fibers were determined using Laminin and Dapi-stained sections. Fluorescence microscopy and transmission microscopy were performed using Axioimager Z1 microscope with CP Achromat 5x/0.12, 10x/0.3 Ph1, or 20x/0.5 Plan NeoFluar objectives (Zeiss). Images were captured using a charge-

coupled device monochrome camera (Coolsnap HQ, Photometrics) or color camera (Coolsnap colour) and MetaMorph software. For all imaging, exposure settings were identical between compared samples. Fiber number and size, central nuclei and peripheral myonuclei were calculated using ImageJ software.

Quantification methods for myonuclei spreading in myotubes

Quantifications in immature myotubes were assessed using an homemade analysis tool. An image analysis performed in ImageJ® software is combined with a statistical analysis in RStudio® software. This provides quantifications of parameters, ranked by myonuclei content per myotubes, regarding phenotype of myotubes (area, length) and their respective myonuclei positioning compare to centroid of myotubes (DMcM).

MSG diagrams were obtained through the normalization of lengths of all analyzed myotubes (independently to their myonuclei content) to 100%. White lines represent myonuclei density curves assessing the statistical frequency for myonuclei positioning along myotubes. Each color group reflects statistical estimation of myonuclei clustering along myotubes.

Additional information

Competing interests

The authors declare no competing interests.

Funding

This work was funded by grants from ATIP-AVENIR Program and Association Française contre les Myopathies (MyoNeurAlp Alliance).

Acknowledgements

We thank the Penn Vector Core, Gene Therapy Program (University of Pennsylvania, Philadelphia, US) for providing pAAV1 plasmid (p0001), and Sofia Benkhelifa-Ziyyat for AAV production, the Imaging facilities of Lyon, PLATIM and CICLE, the animal facility of Lyon, PBES, and particularly, Christophe Chamot and Claire Burny for building the macros in ImageJ and R-Studio.

Author contributions

Conceptualization, A.G., M.B. and V.G. ; Methodology, A.G., N.C., M.B., A.G., A-C.D.and V.G. Formal Analysis, A.G., M.B., A.G., A-C.D., D.A., E.C. and V.G. Investigation, G., E.C., M.B., N.C., C.K-R, A.J., A.G., A-C.D, D.A., N-B. R., M-T. B., L.J., M.B. and V.G. Writing – Original Draft, V.G., V.B., and M.B. Funding Acquisition V.G.

References

Al-Qusairi, L., and J. Laporte. 2011. T-tubule biogenesis and triad formation in skeletal muscle and implication in human diseases. *Skelet Muscle*. 1:26. doi:10.1186/2044-5040-1-26.

Al-Qusairi, L., N. Weiss, A. Toussaint, C. Berbey, N. Messaddeq, C. Kretz, D. Sanoudou, A.H. Beggs, B. Allard, J.-L. Mandel, J. Laporte, V. Jacquemond, and A. Buj-Bello. 2009. T-tubule

755 disorganization and defective excitation-contraction coupling in muscle fibers lacking
756 myotubularin lipid phosphatase. *Proc. Natl. Acad. Sci. U.S.A.* 106:18763–18768.
757 doi:10.1073/pnas.0900705106.

758 Barone, V., D. Randazzo, V. Re, V. Sorrentino, and D. Rossi. 2015. Organization of junctional
759 sarcoplasmic reticulum proteins in skeletal muscle fibers. *Journal of muscle research and*
760 *cell motility*. 36:501–515. doi:10.1007/s10974-015-9421-5.

761 Bevilacqua, J.A., N. Monnier, M. Bitoun, B. Eymard, A. Ferreiro, S. Monges, F. Lubieniecki, A.L.
762 Taratuto, A. Laquerrière, K.G. Claeys, I. Marty, M. Fardeau, P. Guicheney, J. Lunardi, and
763 N.B. Romero. 2011. Recessive RYR1 mutations cause unusual congenital myopathy with
764 prominent nuclear internalization and large areas of myofibrillar disorganization.
765 *Neuropathol. Appl. Neurobiol.* 37:271–284. doi:10.1111/j.1365-2990.2010.01149.x.

766 Bitoun, M., S. Maugenre, P.-Y. Jeannet, E. Lacène, X. Ferrer, P. Laforêt, J.-J. Martin, J. Laporte, H.
767 Lochmüller, A.H. Beggs, M. Fardeau, B. Eymard, N.B. Romero, and P. Guicheney. 2005.
768 Mutations in dynamin 2 cause dominant centronuclear myopathy. *Nature genetics*.
769 37:1207–1209. doi:10.1038/ng1657.

770 Blondelle, J., Y. Ohno, V. Gache, S. Guyot, S. Storck, N. Blanchard-Gutton, I. Barthélémy, G.
771 Walmsley, A. Rahier, S. Gadin, M. Maurer, L. Guillaud, A. Prola, A. Ferry, G. Aubin-
772 Houzelstein, J. Demarquoy, F. Relaix, R.J. Piercy, S. Blot, A. Kihara, L. Tiret, and F. Pilot-
773 Storck. 2015. HACD1, a regulator of membrane composition and fluidity, promotes
774 myoblast fusion and skeletal muscle growth. *J Mol Cell Biol*. 7:429–440.
775 doi:10.1093/jmcb/mjv049.

776 Bohnert, K.R., J.D. McMillan, and A. Kumar. 2017. Emerging roles of ER stress and unfolded
777 protein response pathways in skeletal muscle health and disease. *J. Cell. Physiol*. 233:67–
778 78. doi:10.1002/jcp.25852.

779 Bruusgaard, J.C., K. Liestøl, and K. Gundersen. 2006. Distribution of myonuclei and
780 microtubules in live muscle fibers of young, middle-aged, and old mice. *Journal of Applied*
781 *Physiology*. 100:2024–2030. doi:10.1152/japplphysiol.00913.2005.

782 Bruusgaard, J.C., K. Liestøl, M. Ekmark, K. Kollstad, and K. Gundersen. 2003. Number and
783 spatial distribution of nuclei in the muscle fibres of normal mice studied in vivo. *The*
784 *Journal of Physiology*. 551:467–478. doi:10.1113/jphysiol.2003.045328.

785 Buchman, V.L., C. Luke, E.B. Borthwick, I. Gout, and N. Ninkina. 2002. Organization of the
786 mouse Ruk locus and expression of isoforms in mouse tissues. *Gene*. 295:13–17.
787 doi:10.1016/S0378-1119(02)00821-1.

788 Burgoyne, T., E.P. Morris, and P.K. Luther. 2015. Three-Dimensional Structure of Vertebrate
789 Muscle Z-Band: The Small-Square Lattice Z-Band in Rat Cardiac Muscle. *Journal of*
790 *molecular biology*. 427:3527–3537. doi:10.1016/j.jmb.2015.08.018.

791 Cadot, B., V. Gache, and E.R. Gomes. 2014. Fast, multi-dimensional and simultaneous
792 kymograph-like particle dynamics (SkyPad) analysis. *PLoS ONE*. 9:e89073.
793 doi:10.1371/journal.pone.0089073.

794 Cadot, B., V. Gache, and E.R. Gomes. 2015. Moving and positioning the nucleus in skeletal

muscle - one step at a time. *Nucleus*. 6:373–381. doi:10.1080/19491034.2015.1090073.

Cadot, B., V. Gache, E. Vasyutina, S. Falcone, C. Birchmeier, and E.R. Gomes. 2012. Nuclear movement during myotube formation is microtubule and dynein dependent and is regulated by Cdc42, Par6 and Par3. *EMBO Rep.* 13:741–749. doi:10.1038/embor.2012.89.

Chin, Y.-H., A. Lee, H.-W. Kan, J. Laiman, M.-C. Chuang, S.-T. Hsieh, and Y.-W. Liu. 2015. Dynamin-2 mutations associated with centronuclear myopathy are hypermorphic and lead to T-tubule fragmentation. *Hum. Mol. Genet.* 24:5542–5554. doi:10.1093/hmg/ddv285.

Doñate Puertas, R., G. Millat, I. Ernens, V. Gache, S. Chauveau, E. Morel, E. Christin, N. Couturier, Y. Devaux, and P. Chevalier. 2018. Atrial Structural Remodeling Gene Variants in Patients with Atrial Fibrillation. *Biomed Res Int*. 2018:4862480–12. doi:10.1155/2018/4862480.

Durieux, A.-C., A. Vignaud, B. Prudhon, M.T. Viou, M. Beuvin, S. Vassilopoulos, B. Fraysse, A. Ferry, J. Lainé, N.B. Romero, P. Guicheney, and M. Bitoun. 2010. A centronuclear myopathy-dynamin 2 mutation impairs skeletal muscle structure and function in mice. *Hum. Mol. Genet.* 19:4820–4836. doi:10.1093/hmg/ddq413.

Falcone, S., W. Roman, K. Hnia, V. Gache, N. Didier, J. Laine, F. Aurade, I. Marty, I. Nishino, N. Charlet-Berguerand, N.B. Romero, G. Marazzi, D. Sassoon, J. Laporte, and E.R. Gomes. 2014. N-WASP is required for Amphiphysin-2/BIN1-dependent nuclear positioning and triad organization in skeletal muscle and is involved in the pathophysiology of centronuclear myopathy. *EMBO Mol Med*. 6:1455–1475. doi:10.15252/emmm.201404436.

Fongy, A., S. Falcone, J. Lainé, B. Prudhon, A. Martins-Bach, and M. Bitoun. 2019. Nuclear defects in skeletal muscle from a Dynamin 2-linked centronuclear myopathy mouse model. *Scientific Reports*. 9:1580. doi:10.1038/s41598-018-38184-0.

Fujita, N., W. Huang, T.-H. Lin, J.-F. Groulx, S. Jean, J. Nguyen, Y. Kuchitsu, I. Koyama-Honda, N. Mizushima, M. Fukuda, and A.A. Kiger. 2017. Genetic screen in Drosophila muscle identifies autophagy-mediated T-tubule remodeling and a Rab2 role in autophagy. *Elife*. 6:e23367. doi:10.7554/eLife.23367.

Gache, V., E.R. Gomes, and B. Cadot. 2017. Microtubule motors involved in nuclear movement during skeletal muscle differentiation. *Mol. Biol. Cell*. mbc.E16–06–0405. doi:10.1091/mbc.E16-06-0405.

Ghasemizadeh, A., E. Christin, A. Guiraud, N. Couturier, V. Risson, E. Girard, C. Jagla, C. Soler, L. Laddada, C. Sanchez, F. Jaque, A. Garcia, M. Lanfranchi, V. Jacquemond, J. Gondin, J. Courchet, L. Schaeffer, and V. Gache. 2019. Skeletal muscle MACF1 maintains myonuclei and mitochondria localization through microtubules to control muscle functionalities. *bioRxiv*. 12:636464. doi:10.1101/636464.

Gimpel, P., Y.L. Lee, R.M. Sobota, A. Calvi, V. Koullourou, R. Patel, K. Mamchaoui, F. Nedelec, S. Shackleton, J. Schmoranzer, B. Burke, B. Cadot, and E.R. Gomes. 2017. Nesprin-1α-Dependent Microtubule Nucleation from the Nuclear Envelope via Akap450 Is Necessary for Nuclear Positioning in Muscle Cells. *Current biology: CB*. doi:10.1016/j.cub.2017.08.031.

835 Grumati, P., I. Dikic, and A. Stolz. 2018. ER-phagy at a glance. *J. Cell. Sci.* 131:jcs217364.
836 doi:10.1242/jcs.217364.

837 Gundersen, K. 2016. Muscle memory and a new cellular model for muscle atrophy and
838 hypertrophy. *Journal of Experimental Biology*. 219:235–242. doi:10.1242/jeb.124495.

839 Havrylov, S., F. Ichioka, K. Powell, E.B. Borthwick, J. Baranska, M. Maki, and V.L. Buchman.
840 2008. Adaptor protein Ruk/CIN85 is associated with a subset of COPI-coated membranes
841 of the Golgi complex. *Traffic*. 9:798–812. doi:10.1111/j.1600-0854.2008.00724.x.

842 Havrylov, S., M. Jolanta Redowicz, and V.L. Buchman. 2010. Emerging Roles of Ruk/CIN85 in
843 Vesicle-Mediated Transport, Adhesion, Migration and Malignancy. *Traffic*. 11:721–731.
844 doi:10.1111/j.1600-0854.2010.01061.x.

845 Havrylov, S., Y. Rzhepetskyy, A. Malinowska, L. Drobot, and M.J. Redowicz. 2009. Proteins
846 recruited by SH3 domains of Ruk/CIN85 adaptor identified by LC-MS/MS. *Proteome Sci*.
847 7:21. doi:10.1186/1477-5956-7-21.

848 Janin, A., and V. Gache. 2018. Nesprins and Lamins in Health and Diseases of Cardiac and
849 Skeletal Muscles. *Front Physiol*. 9:97. doi:10.3389/fphys.2018.01277.

850 Jungbluth, H., and M. Gautel. 2014. Pathogenic mechanisms in centronuclear myopathies.
851 *Front Aging Neurosci*. 6:339. doi:10.3389/fnagi.2014.00339.

852 Jungbluth, H., H. Zhou, C.A. Sewry, S. Robb, S. Treves, M. Bitoun, P. Guicheney, A. Buj-Bello, C.
853 Bönnemann, and F. Muntoni. 2007. Centronuclear myopathy due to a de novo dominant
854 mutation in the skeletal muscle ryanodine receptor (RYR1) gene. *Neuromuscular*
855 *Disorders*. 17:338–345. doi:10.1016/j.nmd.2007.01.016.

856 Kim, J.H., P. Jin, R. Duan, and E.H. Chen. 2015. Mechanisms of myoblast fusion during muscle
857 development. *Curr. Opin. Genet. Dev.* 32:162–170. doi:10.1016/j.gde.2015.03.006.

858 Kimura, K., A. Mamane, T. Sasaki, K. Sato, J. Takagi, R. Niwayama, L. Hufnagel, Y. Shimamoto, J.-
859 F. Joanny, S. Uchida, and A. Kimura. 2017. Endoplasmic-reticulum-mediated microtubule
860 alignment governs cytoplasmic streaming. *Nat. Cell Biol.* 19:399–406.
861 doi:10.1038/ncb3490.

862 Laporte, J., L.J. Hu, C. Kretz, J.L. Mandel, P. Kioschis, J.F. Coy, S.M. Klauck, A. Poustka, and N.
863 Dahl. 1996. A gene mutated in X-linked myotubular myopathy defines a new putative
864 tyrosine phosphatase family conserved in yeast. *Nature genetics*. 13:175–182.
865 doi:10.1038/ng0696-175.

866 Liu, J.-X., A.-S. Höglund, P. Karlsson, J. Lindblad, R. Qaisar, S. Aare, E. Bengtsson, and L. Larsson.
867 2009. Myonuclear domain size and myosin isoform expression in muscle fibres from
868 mammals representing a 100,000-fold difference in body size. *Experimental physiology*.
869 94:117–129. doi:10.1113/expphysiol.2008.043877.

870 Louis, M., N. Zanou, M. Van Schoor, and P. Gailly. 2008. TRPC1 regulates skeletal myoblast
871 migration and differentiation. *J. Cell. Sci.* 121:3951–3959. doi:10.1242/jcs.037218.

872 Metzger, T., V. Gache, M. Xu, B. Cadot, E.S. Folker, B.E. Richardson, E.R. Gomes, and M.K.

873 Baylies. 2012. MAP and kinesin-dependent nuclear positioning is required for skeletal
874 muscle function. *Nature*. 484:120–124. doi:10.1038/nature10914.

875 Mogessie, B., D. Roth, Z. Rahil, and A. Straube. 2015. A novel isoform of MAP4 organises the
876 paraxial microtubule array required for muscle cell differentiation. *Elife*. 4:e05697.
877 doi:10.7554/eLife.05697.

878 Nakanishi, K., K. Kakiguchi, S. Yonemura, A. Nakano, and N. Morishima. 2015. Transient Ca
879 2+depletion from the endoplasmic reticulum is critical for skeletal myoblast
880 differentiation. *The FASEB Journal*. 29:2137–2149. doi:10.1096/fj.14-261529.

881 Nakanishi, K., N. Dohmae, and N. Morishima. 2007. Endoplasmic reticulum stress increases
882 myofiber formation in vitro. *The FASEB Journal*. 21:2994–3003. doi:10.1096/fj.06-
883 6408com.

884 Nicot, A.-S., A. Toussaint, V. Tosch, C. Kretz, C. Wallgren-Pettersson, E. Iwarsson, H. Kingston,
885 J.-M. Garnier, V. Biancalana, A. Oldfors, J.-L. Mandel, and J. Laporte. 2007. Mutations in
886 amphiphysin 2 (BIN1) disrupt interaction with dynamin 2 and cause autosomal recessive
887 centronuclear myopathy. *Nature genetics*. 39:1134–1139. doi:10.1038/ng2086.

888 Penga, L., M.I. Rasmussena, A. Chailyana, G. Houenb, and P. Højrupa. 2014. Probing the
889 structure of human protein disulfide isomerase by chemical cross-linking combined with
890 mass spectrometry. *J Proteomics*. 108:1–16. doi:10.1016/j.jprot.2014.04.037.

891 Pimentel, M.R., S. Falcone, B. Cadot, and E.R. Gomes. 2017. In Vitro Differentiation of Mature
892 Myofibers for Live Imaging. *Journal of visualized experiments: JoVE*. e55141–e55141.
893 doi:10.3791/55141.

894 Pizon, V., F. Gerbal, C.C. Diaz, and E. Karsenti. 2005. Microtubule-dependent transport and
895 organization of sarcomeric myosin during skeletal muscle differentiation. *EMBO J.*
896 24:3781–3792. doi:10.1038/sj.emboj.7600842.

897 Qaisar, R. 2012. Myonuclear Organization and Regulation of Muscle Contraction in Single
898 Muscle Fibres: Effects of Ageing, Gender, Species, Endocrine Factors and Muscle Size. 1–
899 64.

900 Qaisar, R., and L. Larsson. 2014. What determines myonuclear domain size? *Indian J. Physiol.*
901 *Pharmacol.* 58:1–12.

902 Quon, E., Y.Y. Sere, N. Chauhan, J. Johansen, D.P. Sullivan, J.S. Dittman, W.J. Rice, R.B. Chan, G. Di
903 Paolo, C.T. Beh, and A.K. Menon. 2018. Endoplasmic reticulum-plasma membrane contact
904 sites integrate sterol and phospholipid regulation. *PLoS Biol.* 16:e2003864–41.
905 doi:10.1371/journal.pbio.2003864.

906 Rabai, A., L. Reisser, B. Reina-San-Martin, K. Mamchaoui, B.S. Cowling, A.-S. Nicot, and J.
907 Laporte. 2019. Allele-Specific CRISPR/Cas9 Correction of a Heterozygous DNM2 Mutation
908 Rescues Centronuclear Myopathy Cell Phenotypes. *Mol Ther Nucleic Acids*. 16:246–256.
909 doi:10.1016/j.omtn.2019.02.019.

910 Ralston, E., Z. Lu, and T. Ploug. 1999. The organization of the Golgi complex and microtubules
911 in skeletal muscle is fiber type-dependent. *J. Neurosci.* 19:10694–10705.

912 Robson, M.I., J.I. de Las Heras, R. Czapiewski, P. Lê Thành, D.G. Booth, D.A. Kelly, S. Webb,
913 A.R.W. Kerr, and E.C. Schirmer. 2016. Tissue-Specific Gene Repositioning by Muscle
914 Nuclear Membrane Proteins Enhances Repression of Critical Developmental Genes during
915 Myogenesis. *Mol. Cell*. 62:834–847. doi:10.1016/j.molcel.2016.04.035.

916 Roman, W., J.P. Martins, F.A. Carvalho, R. Voituriez, J.V.G. Abella, N.C. Santos, B. Cadot, M. Way,
917 and E.R. Gomes. 2017. Myofibril contraction and crosslinking drive nuclear movement to
918 the periphery of skeletal muscle. *Nat. Cell Biol.* 152:1376–33. doi:10.1038/ncb3605.

919 Romero, N.B. 2010. Centronuclear myopathies: a widening concept. *Neuromuscular disorders:*
920 *NMD*. 20:223–228. doi:10.1016/j.nmd.2010.01.014.

921 Romero, N.B., and J. Laporte. 2013. Centronuclear Myopathies. 14. Wiley-Blackwell, Oxford,
922 UK. 11 pp.

923 Romero, N.B., and M. Bitoun. 2011. Centronuclear myopathies. *Semin Pediatr Neurol*. 18:250–
924 256. doi:10.1016/j.spen.2011.10.006.

925 Sampath, S.C., S.C. Sampath, and D.P. Millay. 2018. Myoblast fusion confusion: the resolution
926 begins. 1–10. doi:10.1186/s13395-017-0149-3.

927 Satoh, M., A. Shimada, H. Keino, A. Kashiwai, N. Nagai, S. Saga, and M. Hosokawa. 2005.
928 Functional characterization of 3 thioredoxin homology domains of ERp72. *Cell Stress*
929 *Chaperones*. 10:278–284. doi:10.1379/CSC-116R.1.

930 Schroeder, B., S.G. Weller, J. Chen, D. Billadeau, and M.A. McNiven. 2010. A Dyn2-CIN85
931 complex mediates degradative traffic of the EGFR by regulation of late endosomal
932 budding. *EMBO J.* 29:3039–3053. doi:10.1038/emboj.2010.190.

933 Schulze, R.J., S.G. Weller, B. Schroeder, E.W. Krueger, S. Chi, C.A. Casey, and M.A. McNiven.
934 2013. Lipid droplet breakdown requires dynamin 2 for vesiculation of autolysosomal
935 tubules in hepatocytes. *J. Cell Biol.* 203:315–326. doi:10.1083/jcb.201306140.

936 Straube, A., and A. Merdes. 2007. EB3 regulates microtubule dynamics at the cell cortex and is
937 required for myoblast elongation and fusion. *Current biology: CB*. 17:1318–1325.
938 doi:10.1016/j.cub.2007.06.058.

939 Sun, Y., N.T. Leong, T. Wong, and D.G. Drubin. 2015. A Pan1/End3/Sla1 complex links Arp2/3-
940 mediated actin assembly to sites of clathrin-mediated endocytosis. *Mol. Biol. Cell*.
941 26:3841–3856. doi:10.1091/mbc.E15-04-0252.

942 Tanabe, K., and K. Takei. 2009. Dynamic instability of microtubules requires dynamin 2 and is
943 impaired in a Charcot-Marie-Tooth mutant. *J. Cell Biol.* 185:939–948.
944 doi:10.1083/jcb.200803153.

945 Tassin, A.M., M. Paintrand, E.G. Berger, and M. Bornens. 1985. The Golgi apparatus remains
946 associated with microtubule organizing centers during myogenesis. *J. Cell Biol.* 101:630–
947 638.

948 Thompson, H.M., H. Cao, J. Chen, U. Euteneuer, and M.A. McNiven. 2004. Dynamin 2 binds
949 gamma-tubulin and participates in centrosome cohesion. *Nat. Cell Biol.* 6:335–342.

950 doi:10.1038/ncb1112.

951 Wada, I., D. Rindress, P.H. Cameron, W.J. Ou, J.J. Doherty, D. Louvard, A.W. Bell, D. Dignard, D.Y.
952 Thomas, and J.J. Bergeron. 1991. SSR alpha and associated calnexin are major calcium
953 binding proteins of the endoplasmic reticulum membrane. *J. Biol. Chem.* 266:19599–
954 19610.

955 Wang, S., A. Reuveny, and T. Volk. 2015. Nesprin provides elastic properties to muscle nuclei
956 by cooperating with spectraplakin and EB1. *J. Cell Biol.* 209:529–538.
957 doi:10.1083/jcb.201408098.

958 Wang, Z., J. Cui, W.M. Wong, X. Li, W. Xue, R. Lin, J. Wang, P. Wang, J.A. Tanner, K.S.E. Cheah, W.
959 Wu, and J.-D. Huang. 2013. Kif5b controls the localization of myofibril components for
960 their assembly and linkage to the myotendinous junctions. *Development*. 140:617–626.
961 doi:10.1242/dev.085969.

962 Wilmshurst, J.M., S. Lillis, H. Zhou, K. Pillay, H. Henderson, W. Kress, C.R. Müller, A. Ndondo, V.
963 Cloke, T. Cullup, E. Bertini, C. Boennemann, V. Straub, R. Quinlivan, J.J. Dowling, S. Al-
964 Sarraj, S. Treves, S. Abbs, A.Y. Manzur, C.A. Sewry, F. Muntoni, and H. Jungbluth. 2010.
965 RYR1 mutations are a common cause of congenital myopathies with central nuclei. *Annals*
966 *of neurology*. 68:717–726. doi:10.1002/ana.22119.

967 Wilson, M.H., and E.L.F. Holzbaur. 2014a. Nesprins anchor kinesin-1 motors to the nucleus to
968 drive nuclear distribution in muscle cells. *Development*. 142:218–228.
969 doi:10.1242/dev.114769.

970 Wilson, M.H., and E.L.F. Holzbaur. 2014b. Nesprins anchor kinesin-1 motors to the nucleus to
971 drive nuclear distribution in muscle cells. *Development*. 142:218–228.
972 doi:10.1242/dev.114769.

973 Zhang, J., X. Zheng, X. Yang, and K. Liao. 2009. CIN85 associates with endosomal membrane
974 and binds phosphatidic acid. *Cell Research*. 19:733–746. doi:10.1038/cr.2009.51.

975

Figure 1

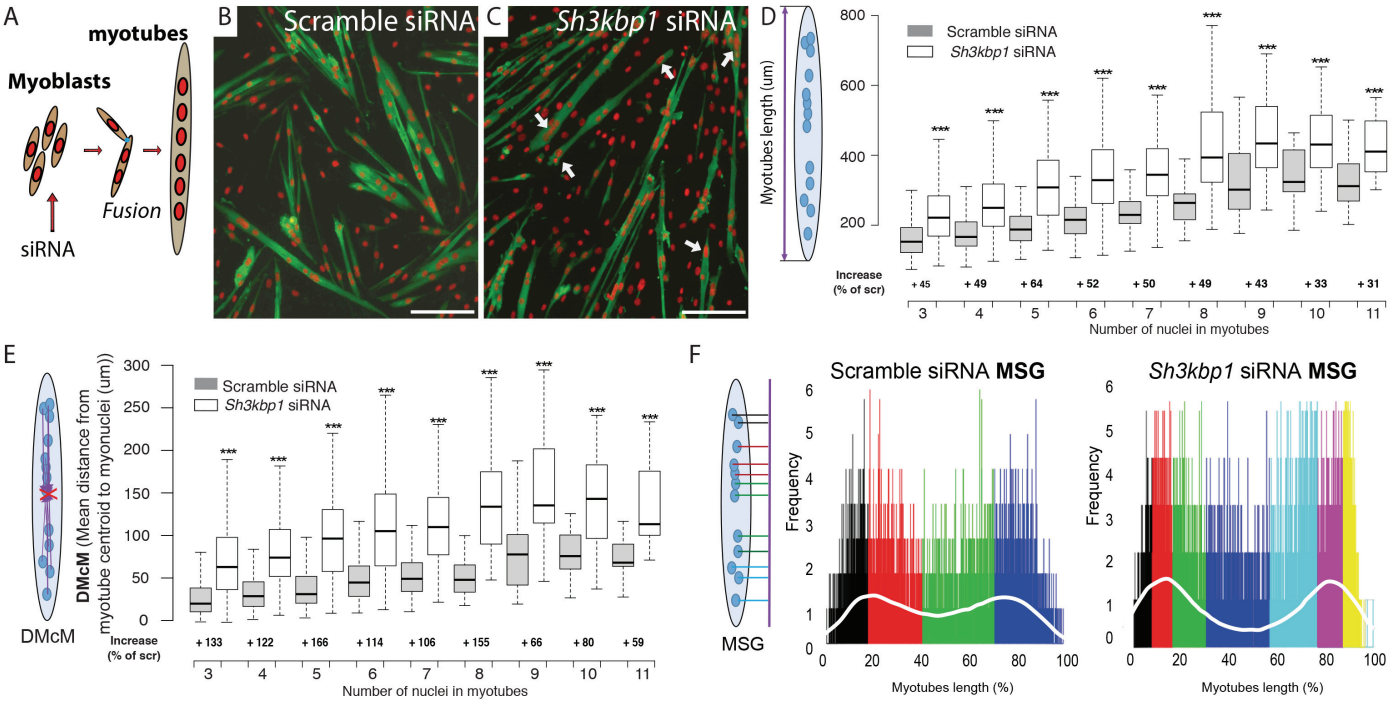
A
myotubes
Myoblasts
Fusion
siRNA
B
Scramble siRNA
C
Sh3kbp1 siRNA
D
Myotubes length (um)
Scramble siRNA
Sh3kbp1 siRNA
Increase (% of scr)
+ 45
+ 49
+ 64
+ 52
+ 50
+ 49
+ 43
+ 33
+ 31
Number of nuclei in myotubes
E
DMcM
DMcM (Mean distance from myotube centroid to myonuclei (um))
Scramble siRNA
Sh3kbp1 siRNA
Increase (% of scr)
+ 133
+ 122
+ 166
+ 114
+ 106
+ 155
+ 66
+ 80
+ 59
Number of nuclei in myotubes
F
MSG
Scramble siRNA MSG
Sh3kbp1 siRNA MSG
Frequency
Myotubes length (%)

Figure 2

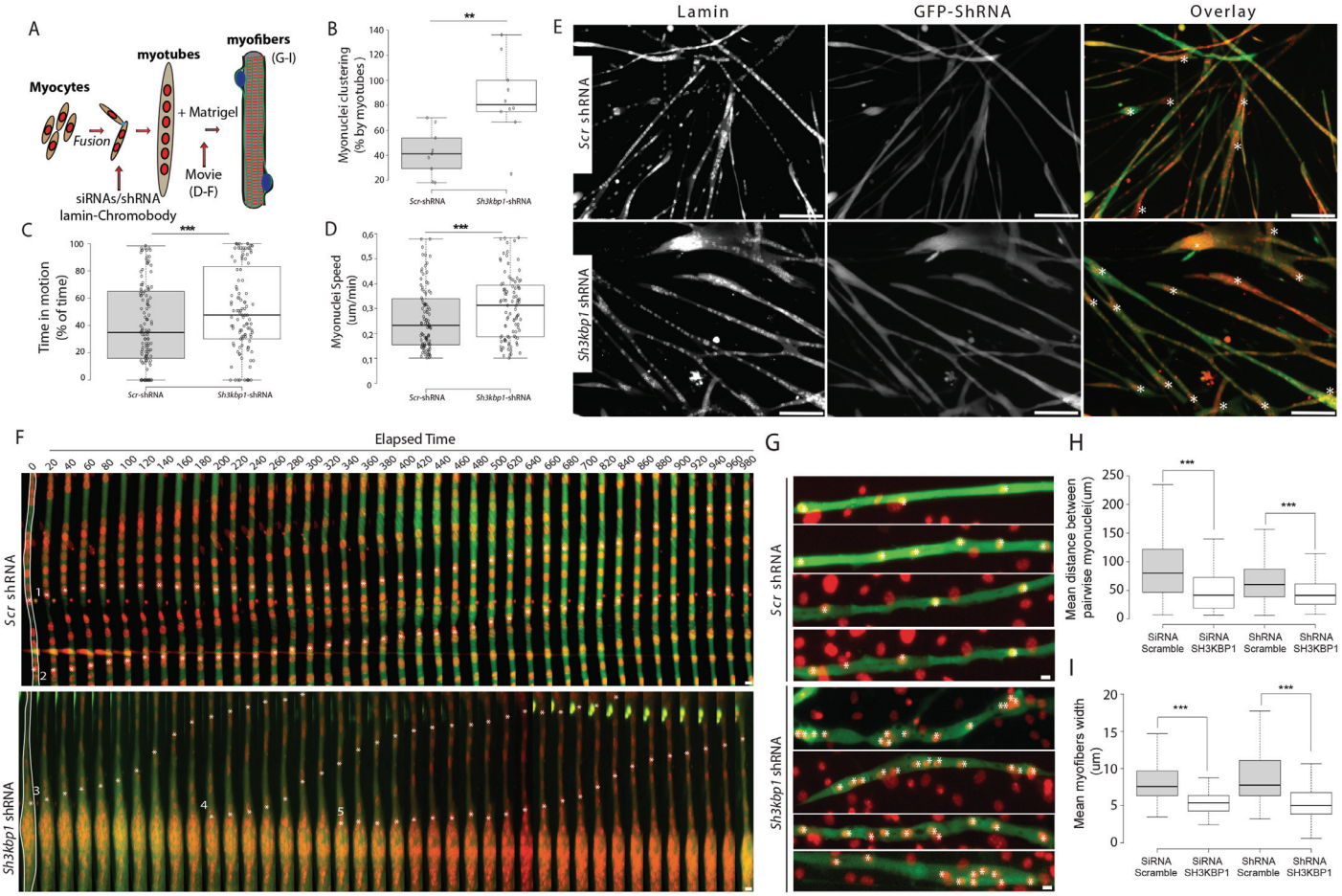
A
myotubes
myofibers
(G-I)
Myocytes
Fusion
+ Matrigel
Movie
(D-F)
siRNAs/shRNA
lamin-Chromobody
B
Myonuclei clustering
(% by myotubes)
Scr-shRNA
Sh3kbp1-shRNA
C
Time in motion
(% of time)
D
Myonuclei Speed
(um/min)
E
Lamin
GFP-ShRNA
Overlay
Scr shRNA
Sh3kbp1 shRNA
F
Elapsed Time
G
H
Mean distance between
pairwise myonuclei(um)
SiRNA
Scramble
SiRNA
SH3KBP1
ShRNA
Scramble
ShRNA
SH3KBP1
I
Mean myofibers width
(um)

Figure 3

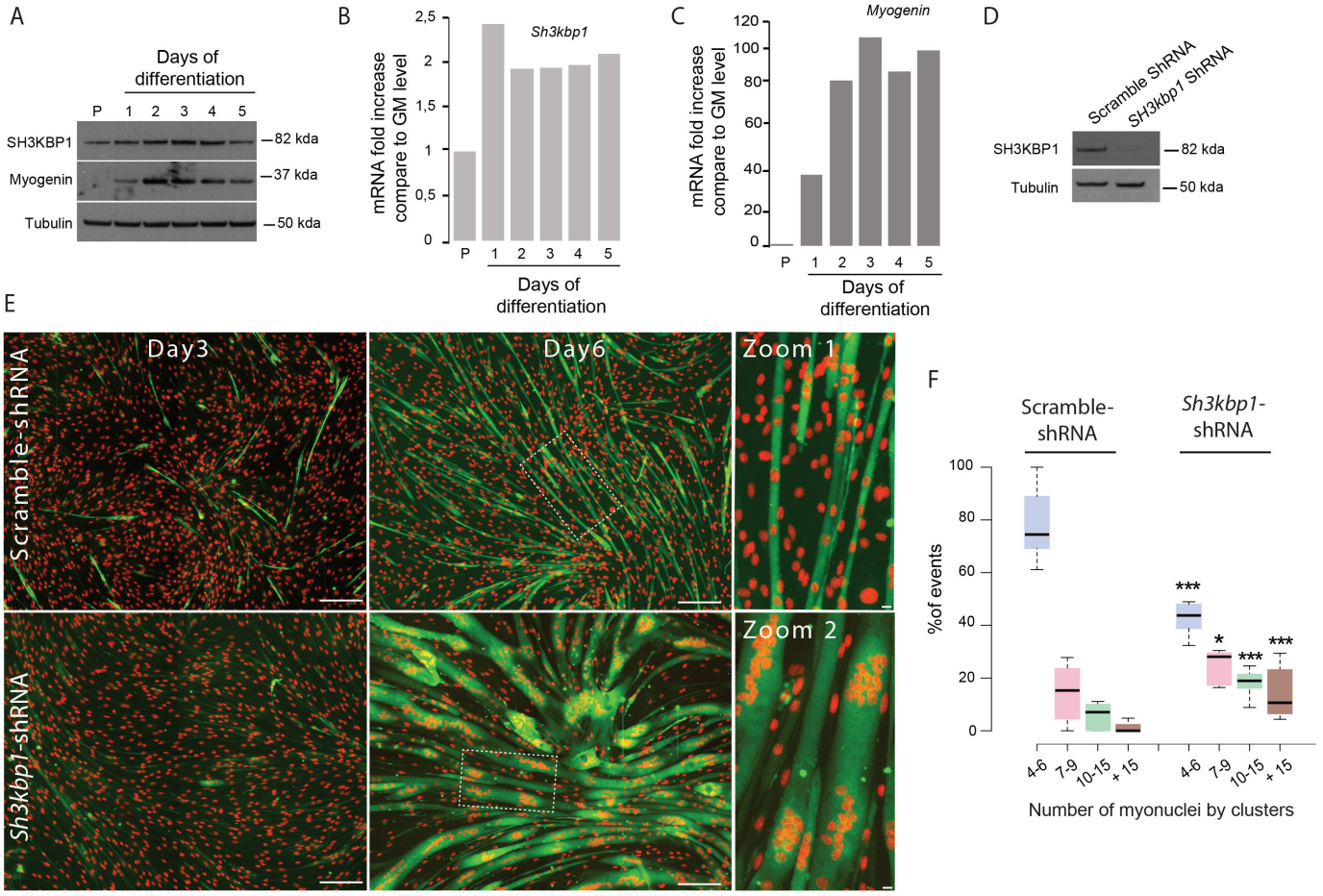
A
Days of differentiation
P 1 2 3 4 5
SH3KBP1
Myogenin
Tubulin
82 kda
37 kda
50 kda
B
Sh3kbp1
mRNA fold increase compare to GM level
2,5
2
1,5
1
0,5
0
P 1 2 3 4 5
Days of differentiation
C
Myogenin
mRNA fold increase compare to GM level
120
100
80
60
40
20
0
P 1 2 3 4 5
Days of differentiation
D
Scramble ShRNA
Sh3kbp1 ShRNA
SH3KBP1
Tubulin
82 kda
50 kda
E
Day3
Day6
Zoom 1
Zoom 2
Scramble-shRNA
Sh3kbp1-shRNA
F
Scramble-shRNA
Sh3kbp1-shRNA
%of events
100
80
60
40
20
0
***
*
***
***
4-6 7-9 10-15 + 15
4-6 7-9 10-15 + 15
Number of myonuclei by clusters

Figure 4

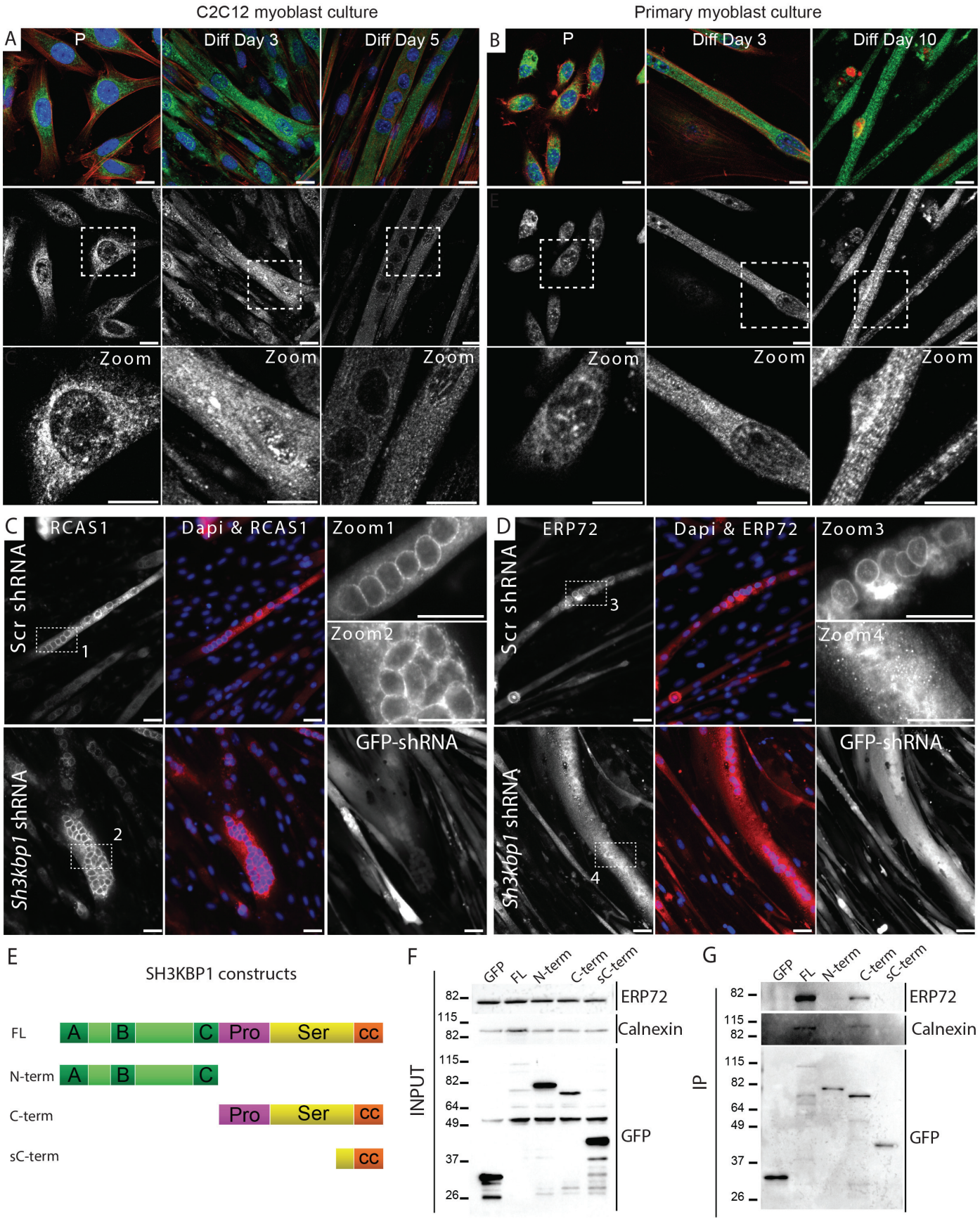
C2C12 myoblast culture
Primary myoblast culture
A
P
Diff Day 3
Diff Day 5
B
P
Diff Day 3
Diff Day 10
Zoom
Zoom
Zoom
Zoom
Zoom
Zoom
C
RCAS1
Dapi & RCAS1
Zoom1
Zoom2
Scr shRNA
1
Sh3kbp1 shRNA
2
GFP-shRNA
D
ERP72
Dapi & ERP72
Zoom3
Zoom4
Scr shRNA
3
Sh3kbp1 shRNA
4
GFP-shRNA
E
SH3KBP1 constructs
FL
N-term
C-term
sC-term
A
B
C
Pro
Ser
cc
F
GFP
FL
N-term
C-term
sC-term
INPUT
82
115
82
115
82
64
49
37
26
ERP72
Calnexin
GFP
G
GFP
FL
N-term
C-term
sC-term
IP
82
115
82
115
82
64
49
37
26
ERP72
Calnexin
GFP

Figure 5

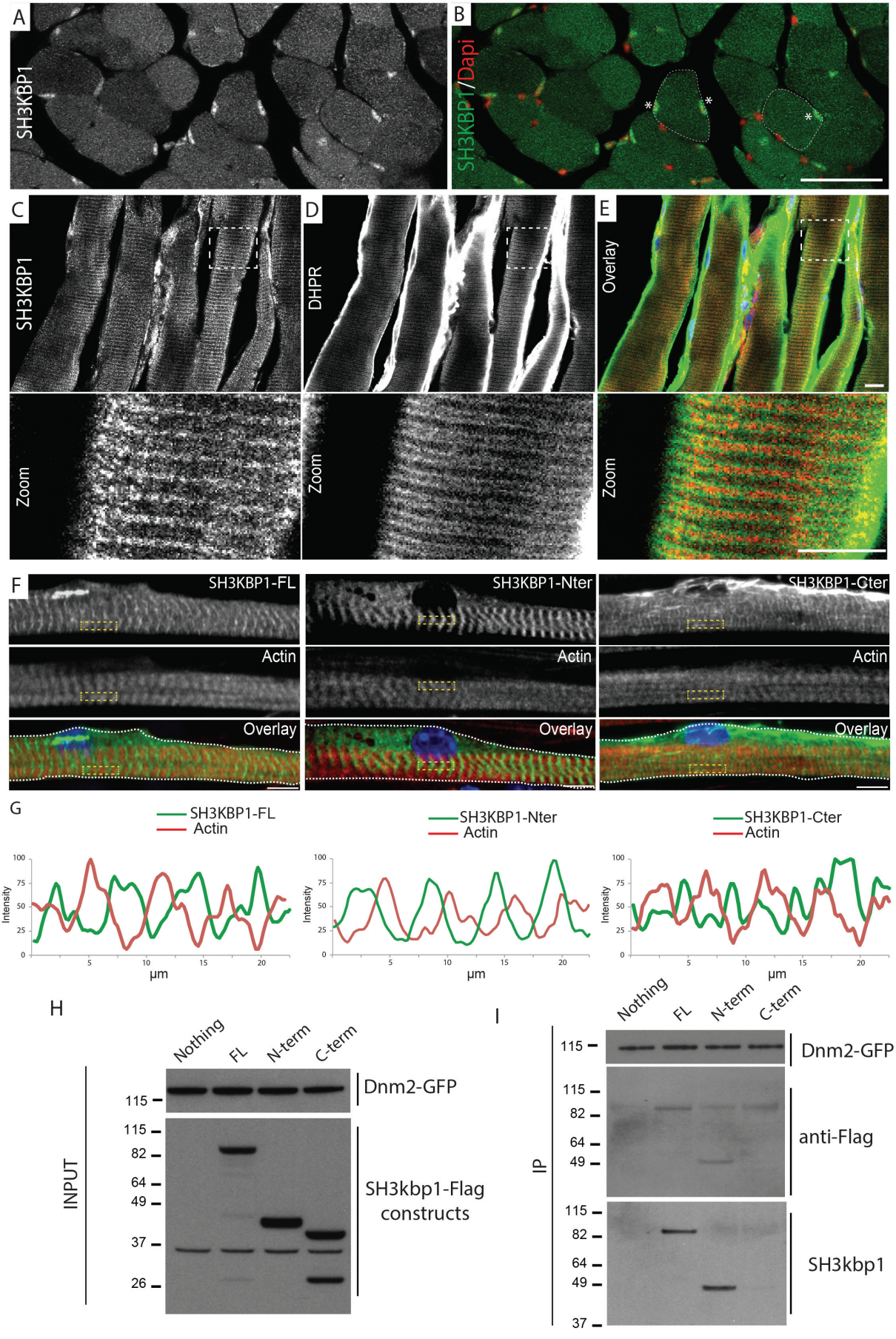
A
SH3KBP1
B
SH3KBP1/Dapi
C
SH3KBP1
D
DHPR
E
Overlay
Zoom
Zoom
Zoom
F
SH3KBP1-FL
SH3KBP1-Nter
SH3KBP1-Cter
Actin
Actin
Actin
Overlay
Overlay
Overlay
G
SH3KBP1-FL
Actin
SH3KBP1-Nter
Actin
SH3KBP1-Cter
Actin
Intensity
µm
H
Nothing
FL
N-term
C-term
INPUT
Dnm2-GFP
SH3kbp1-Flag
constructs
115
82
64
49
37
26
I
Nothing
FL
N-term
C-term
IP
Dnm2-GFP
anti-Flag
SH3kbp1
115
82
64
49
37

Figure 6

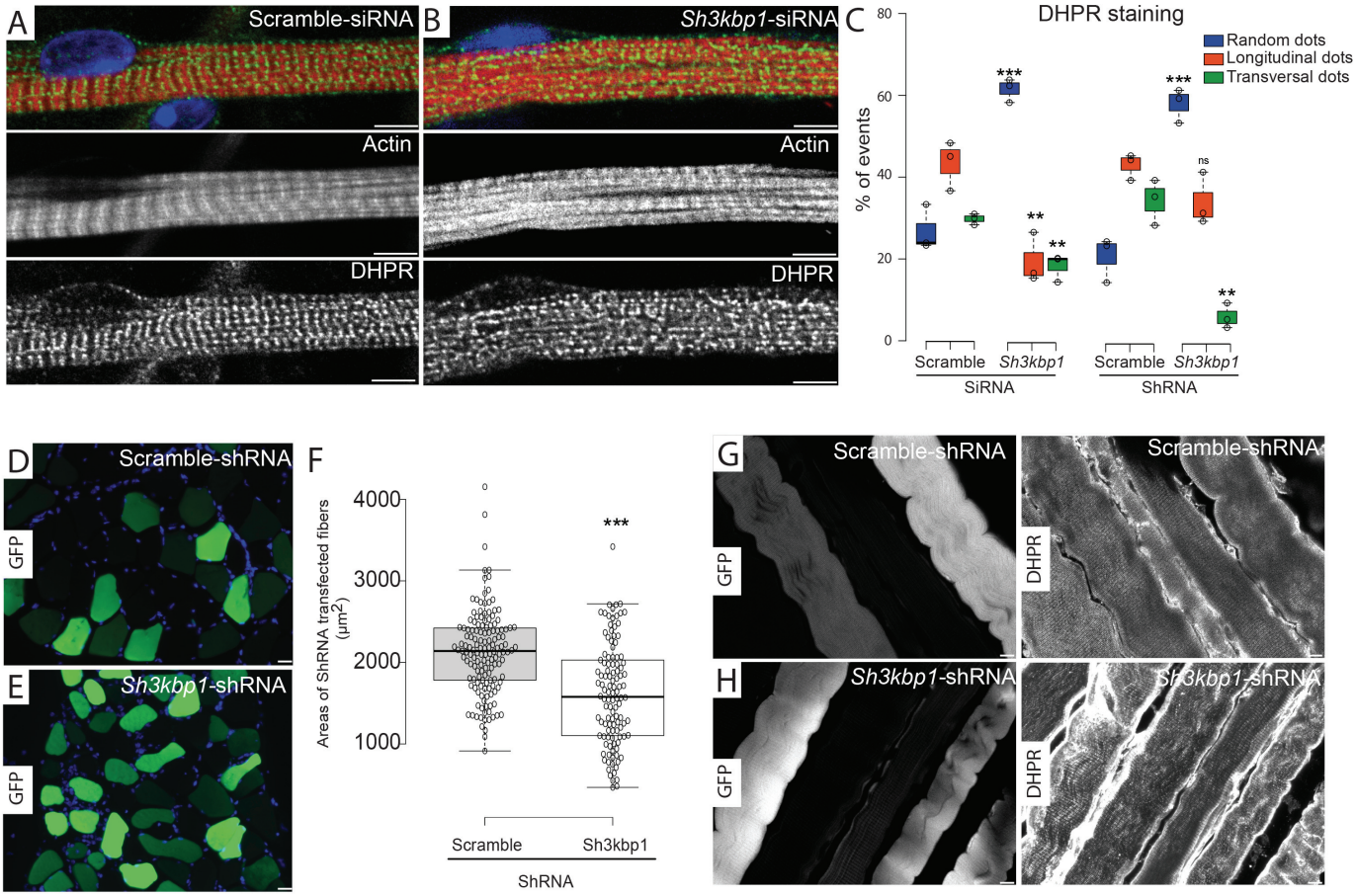
A
Scramble-siRNA
Actin
DHPR
B
Sh3kbp1-siRNA
Actin
DHPR
C
DHPR staining
Random dots
Longitudinal dots
Transversal dots
% of events
80
60
40
20
0
***
**
**
***
ns
**
Scramble
Sh3kbp1
Scramble
Sh3kbp1
SiRNA
ShRNA
D
Scramble-shRNA
GFP
E
Sh3kbp1-shRNA
GFP
F
Areas of ShRNA transfected fibers (µm2)
4000
3000
2000
1000
***
Scramble
Sh3kbp1
ShRNA
G
Scramble-shRNA
GFP
Scramble-shRNA
DHPR
H
Sh3kbp1-shRNA
GFP
Sh3kbp1-shRNA
DHPR

Figure 7

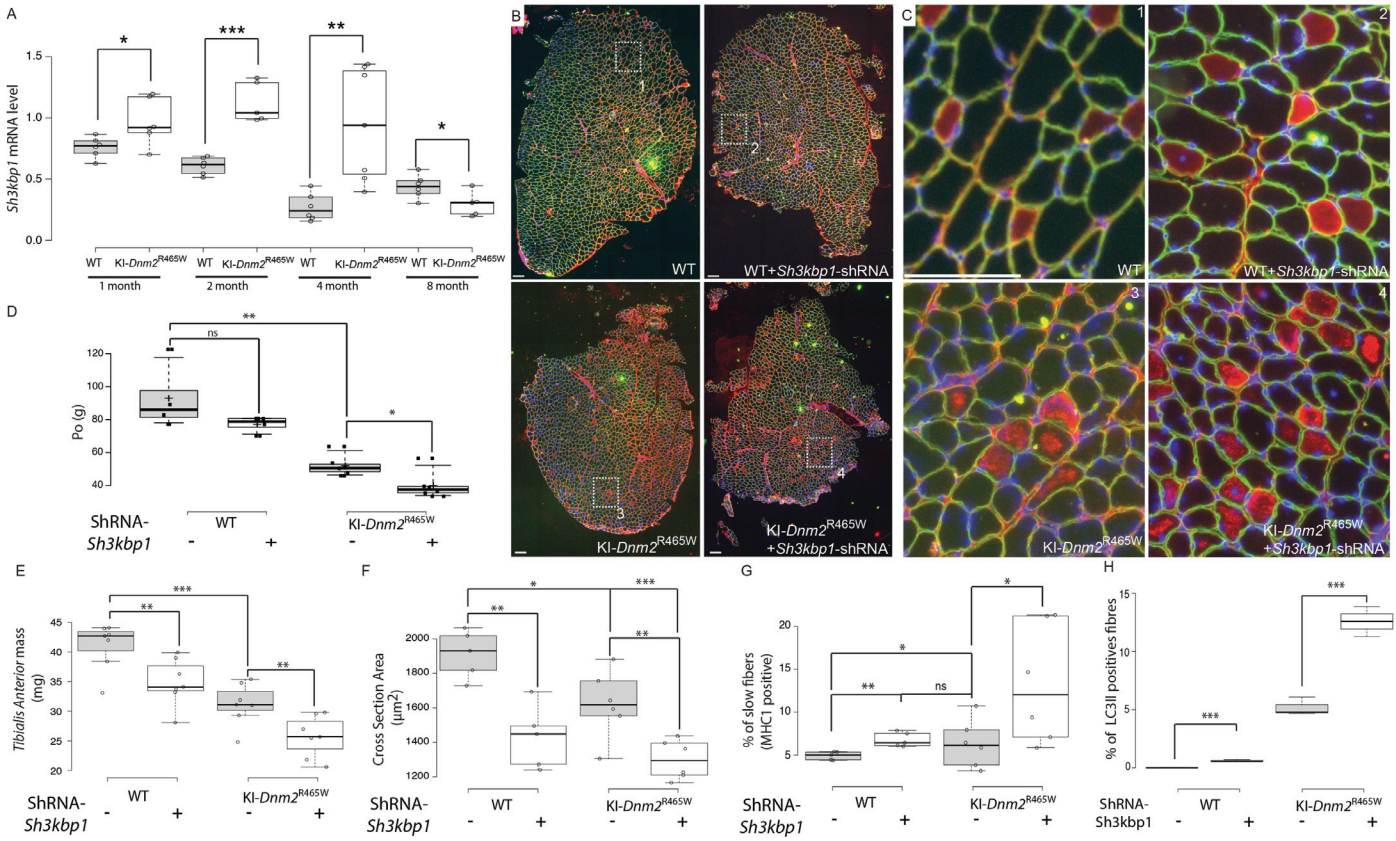
A
Sh3kbp1 mRNA level
WT
KI-Dnm2R465W
1 month
2 month
4 month
8 month
B
WT
WT+Sh3kbp1-shRNA
KI-Dnm2R465W
KI-Dnm2R465W +Sh3kbp1-shRNA
C
D
Po (g)
ShRNA-Sh3kbp1
E
Tibialis Anterior mass (mg)
F
Cross Section Area (µm2)
G
% of slow fibers (MHC1 positive)
H
% of LC3II positives fibres
ShRNA-Sh3kbp1

Supplementary Figure 1

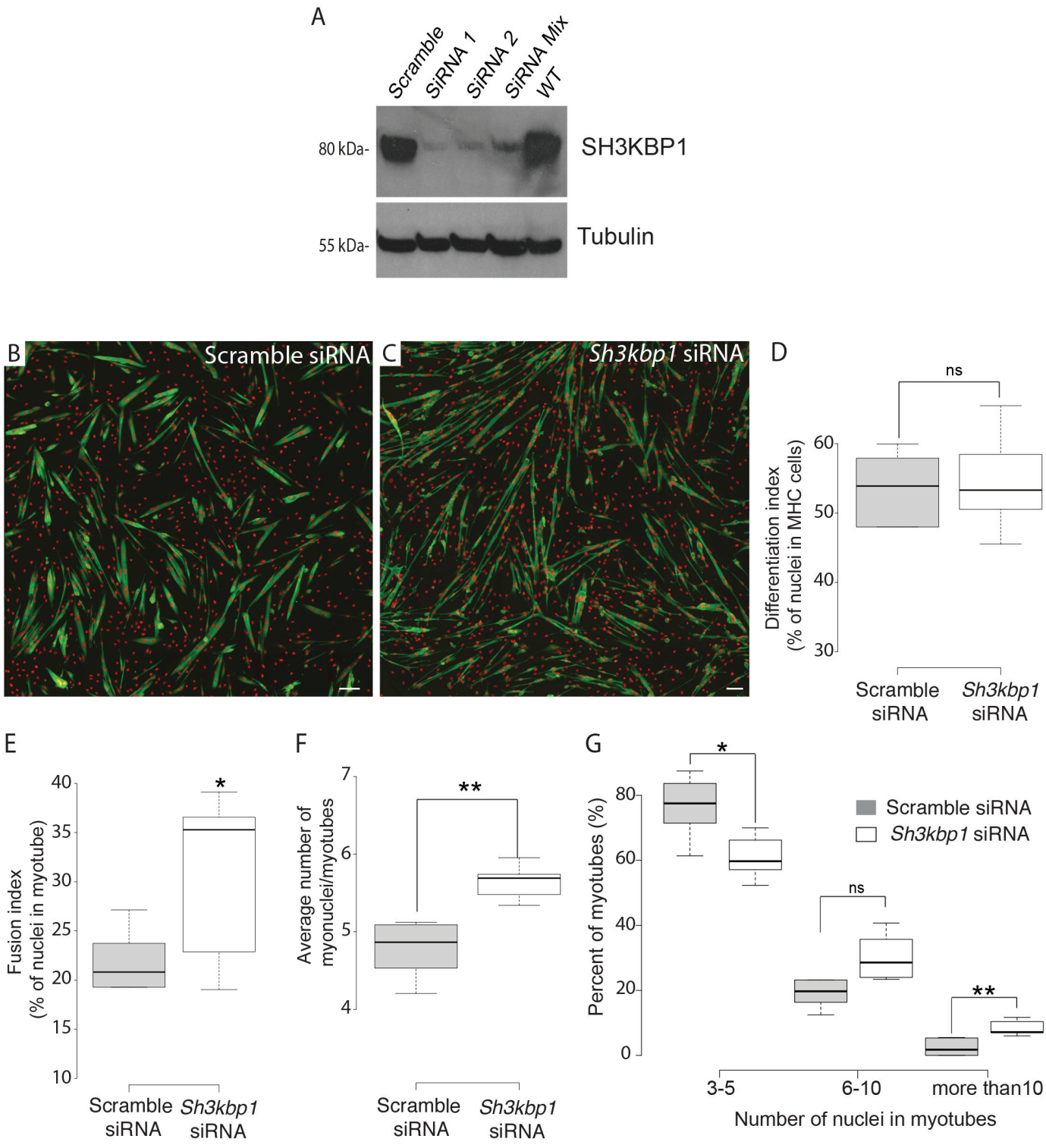

Supplementary Figure 2

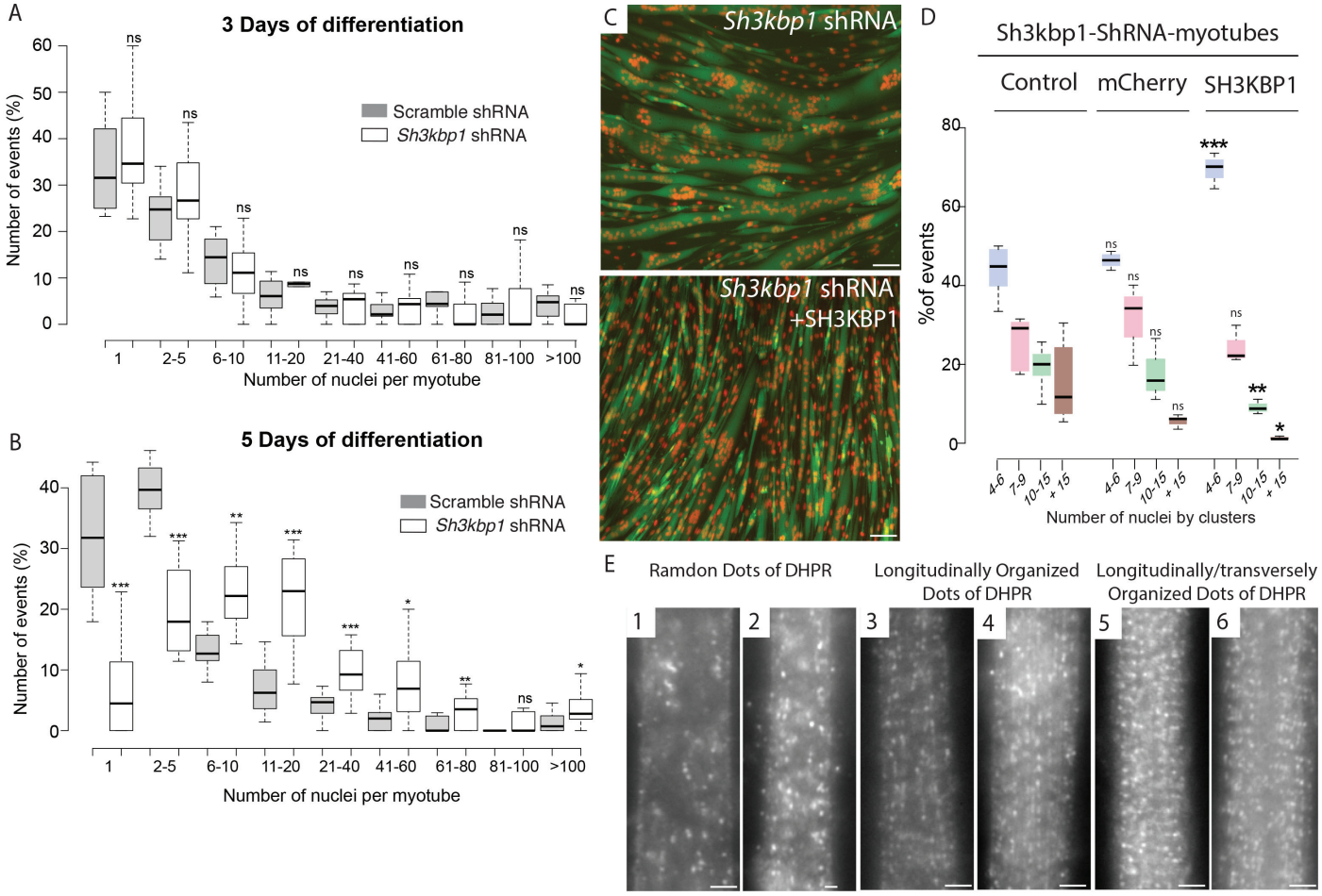

Supplementary Figure 3

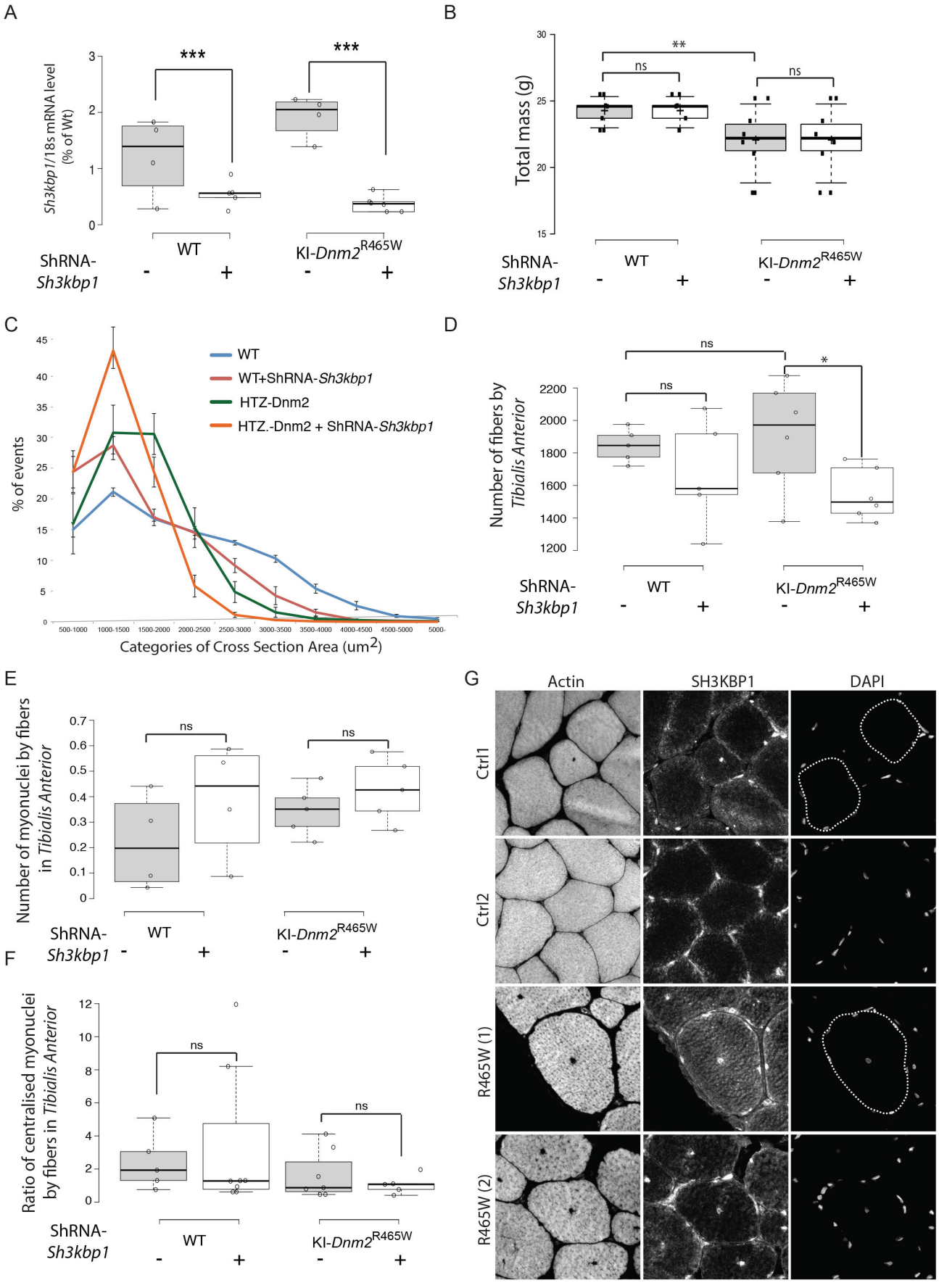

Supplementary Table 1

siRNA/shRNA sequence

siRNA	Sense oligonucleotide sequence	Anti-Sense oligonucleotide sequence
SH3KBP1 #1	GGUUGUAGGAGAGGUAGAGtt	CUCUACCUCUCCUACAACCtc
SH3KBP1 #2	GGUUUUGACUCUGUGAUAUtt	AUAUCACAGAGUCAAAACCtt
SH3KBP1 #3	GGUCGAUUGAAGUGGAAAAtt	UUUUCCACUUCAAUCGACCtt
shRNA	**Clone Name**	**Target Sequence**
SH3KBP1	MSH032547-2-CU6(OS308398)	ttacctccagctacatcaa

DNA constructs

Name	Company/collaborators
SH3KBP1-Full length-GFP	Buchman VL Lab Gift
SH3KBP1-Full length-M2	Buchman VL Lab Gift
SH3KBP1-C-terminal-GFP	Buchman VL Lab Gift
SH3KBP1- C-terminal -M2	Buchman VL Lab Gift
SH3KBP1- N-terminal -GFP	Buchman VL Lab Gift
SH3KBP1-N-terminal -M2	Buchman VL Lab Gift
SH3KBP1- CC -GFP	Buchman VL Lab Gift
SH3KBP1-CC -M2	Buchman VL Lab Gift
DNM2-GFP	Laporte J Lab Gift

Primers sequences

Primers	Sequence
SH3KBP1 F	AATACCGGTTCTTCCTCGGC
SH3KBP1 R	CATCCTCCACCAACTCGGAC
Gusb F	GAGGATTGCCAACGAAACCG
Gusb R	GTGTCTGGGGACCACCTTTGA
GAPDH F	AACTTTGGCATTGTGGAAGG
GAPDH R	ACACATTGGGGGTAGGAACA
RpL4 F	GCCATGAGAGCGAAGTGG
RpL4 R	CTCCTGCAGGCGTCGTAG

18 s	Forward	CGC CGC TAG AGG TGA AAT C
	Reverse	CCA GTC GGC ATC GTT TAT GG
Sh3Kbp1	Forward	CCA TGC ACG ATG TAT CCA GTG
	Reverse	GTC GTT CTC CTC GTT TAT TGG TT

Supplementary Table 2

Antibody or Dye	Species and Utility	Dilution Factor	Manufacturer and Reference
Anti-SH3KBP1	Rabbit	1:100	Sigma- HPA003355
Anti-SH3KBP1 (Cin85 H-300)	Rabbit	1:1000	Santa Cruz, sc-48746
Anti-SH3KBP1 (SETA/Cin85/Ruk/SH3KBP1 Antibody clone 179.1.E1) 05-731	Mouse	1:1000	Merck 05-731
Anti-α-Tubulin	Mouse - primary	1:1000	Sigma T6074-200uL
Anti-myogenin (F5D)	Mouse	1:100	Santa Cruz sc-12732
Anti-RCAS1 (D2B6N)	Rabbit	1:200	Cell Signaling #12290
Anti-ERP72 (D70D12)	Rabbit	1:100	Cell Signaling #5033
Anti-laminin	Rat	1:200	Sigma
Anti-GFP (3H9)	Rat	1:1000	Chromotek
Anti-Flag M2	Mouse	1:1000	Sigma F1804
Anti-Calnexin (C5C9)	Rabbit	1:100	Cell Signaling #2679
Anti-LC3II/LC3I	Rabbit - primary	1:250	Sigma L7543
Anti-Myosin skeletal slow	Mouse	1:100	Sigma M8421
MF20	Mouse-primary	1:10	DSHB
Anti-DHPR	Rabbit	1:10	DSHB (IIID5E1)
Dapi-brilliant blue	Dye	1:50000	Thermo Fisher Scientifics D1306
Phalloidin-Alexa Fluorr 647	Dye	1:100	Thermo Fisher Scientifics A22287
Anti-mouse-HRP	Goat - secondary	1:3000	Invitrogen 62-6520
Anti-rabbit-HRP	Goat - secondary	1:3000	Invitrogen 65-6120
Anti-rat-Alexa Fluor 488	Donkey - secondary	1:500	Thermo Fisher Scientifics A-21208
Anti-rabbit-Alexa Fluor 647	Goat - secondary	1:500	Thermo Fisher Scientifics A-21245
Anti-mouse-Alexa Fluor 647	Goat - secondary	1:500	Thermo Fisher Scientifics A-21240